

Volume 19 Supplement Number 1 1997

International Journal of Fatigue

Materials • Structures • Components

Fatigue

DISTRIBUTION STATEMENT A

Approved for public release;
Distribution Unlimited

PROFESSIONAL QUALITY INSPECTION

ELSEVIER

International Journal of
Fatigue

Materials Structures Components

Editor

Dr Les P. Pook

Department of Mechanical
Engineering
University College London
Torriington Place
London WC1E 7JE, UK
Telephone: 0171 380 7184
Telefax: 0171 383 0831

North American Editor

Professor K. L. Reifsnider

Department of Engineering Science
and Mechanics
Virginia Polytechnic Institute
and State University
Blacksburg
Virginia 24061-0219, USA
Telephone: 540 231 9187
Telefax: 540 231 5316

Japanese Editor

Professor Y. Murakami

Department of Mechanical Science
and Engineering
Kyushu University
6-10-1 Hakozaki, Higashi-ku,
Fukuoka, 812 Japan
Telephone: 092 641 1101
Telefax: 092 641 9744

Editorial Advisory Board

Dr M. H. Aliabadi
University of London, UK

Professor J. T. Barnby
Astbury, Bridgnorth, UK

Professor D. J. Burns
University of Waterloo, Canada

Professor O. Buxbaum
Fraunhofer Institut für
Betriebsfestigkeit, Germany

Professor A. Carpinteri
Università Degli Studi di Parma, Italy

Dr H.D. Chandler
University of the Witwatersrand, South Africa

Professor N. E. Dowling
Virginia Tech, USA

Professor P. J. Haagensen
University of Trondheim, Norway

Dr M. A. Hicks
Rolls Royce plc, UK

Professor D. W. Hoepner
University of Utah, USA

Professor M. N. James
University of Plymouth, UK

Mr R. Jeal
Technology Management Pty Ltd, Australia

Professor M. Jono
Osaka University, Japan

Professor K. Koibuchi
University of Tokyo, Japan

Professor K. Komai
Kyoto University, Japan

Professor J. Lankford
Southwest Research Institute, San Antonio, USA

Professor A. McEvily
University of Connecticut, USA

Dr T. Nicholas
Wright-Patterson AFB
OH 45433-7817, USA

Dr H. L. J. Pang
Nanyang Technological University, Singapore
2263

Professor A. Plumtree
University of Waterloo, Canada

Dr J. Polák
Academy of Sciences of the Czech
Republic, Czech Republic

Professor R. A. Smith
University of Sheffield, UK

Professor R. Stickler
Universität Wien, Austria

Professor T. Tanaka
Ritsumeikan University, Japan

Professor D. Taylor
Trinity College, Dublin, Ireland

Professor V. T. Troshchenko
National Academy of Sciences of Ukraine,
Ukraine

Professor A. K. Vasudevan
Office of Naval Research, VA 22217-5660,
USA

Dr R. J. H. Wanhill
National Aerospace Laboratory NLR,
The Netherlands

Aims and Scope

International Journal of Fatigue publishes refereed papers dealing both with the fundamental aspects of the fatigue of materials and, more importantly, with the relevance of fatigue to engineering and design. Papers on fatigue-related topics such as fracture mechanics, stress analysis and compliance are also welcomed, especially if they discuss potential or actual applications. The approach is therefore interdisciplinary, and all classes of materials are included.

Submissions

Authors wishing to submit a paper for publication should send 3 copies of their manuscript to Dr L. P. Pook, Professor K. L. Reifsnider, or Professor Y. Murakami. Detailed Notes for Authors appear on the inside back cover of the journal.

International Journal of Fatigue is abstracted and indexed in: Science Citation Index, SciSearch, Current Contents (Engineering, Computing and Technology), Research Alert, Materials Science Citation Index, Cambridge Scientific Abstracts, Chemical Abstracts, AS, Engineering Index, FIZ, INSPEC, Materials Information/Metals Abstracts

UNITED ENGINEERING TRUSTEES, INC.

ENGINEERING SOCIETIES LIBRARY

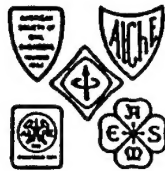
ENGINEERING FOUNDATION

UNITED ENGINEERING CENTER

345 EAST 47TH STREET, NEW YORK, N.Y. 10017

212-705-7828

FAX 212-705-7441



April 23, 1998

Defense Technical Information Center
8725 John J. Kingman Road
STE 0944
Ft. Belvoir, VA 22060-6218

Re: N00014-96-1-0811

Dear Sir/Madam:

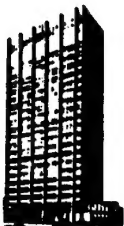
Enclosed please find a copy of the proceedings for the conference **International Conference on Fatigue Damage in Structural Materials** which satisfies the requirements to close out this grant.

Thank you in advance for your attention to this request.

Sincerely,


Jerome Fishel
Secretary & General Manager

c: C.V.Freiman
E. Rosenberg
A.K. Vasudevan



United Engineering Center
"for the advancement of America's engineering leadership"
at United Nations Plaza and 47th Street, New York City

Fatigue is an international journal published 10 times a year, in January, February, March, April, May, July, August, September, October and November, by Elsevier Science Ltd.

Publishing and Subscriptions offices: Elsevier Science Ltd., The Boulevard, Langford Lane, Kidlington, Oxford OX5 1GB, UK. Tel. (+1865) 843000, Fax: (+1865) 843010.

Publishing Editor (Elsevier Science Ltd): Dean Eastbury

Address for submissions: See Notes for Authors.

Subscription Information: Annual Institutional Subscription Rates 1998: Europe; The CIS and Japan 1548 Dutch Guilders. All other countries US\$890. Associated Personal Subscription rates are available on request for those whose institutions are library subscribers. Dutch Guilder prices exclude VAT. Non-VAT registered customers in the European Community will be charged the appropriate VAT in addition to the price listed. Prices include postage and insurance and are subject to change without notice.

For orders, claims, product enquiries (no manuscript enquiries) please contact the Customer Support Department at the Regional Sales Office nearest to you:

The Americas: Elsevier Science Customer Support Department, 655 Avenue of the Americas, New York, NY 10010, USA [Tel: (+1) 212-633-3730/1-888 4ES-INFO. Fax: (+1) 212-633-3680. E-mail: usinfo-f@elsevier.com].

Japan: Elsevier Science Customer Support Department, 9-15 Higashi-Azabu 1-chome, Minato-ku, Tokyo 106, Japan [Tel: (+3) 5561-5033. Fax: (+3) 5561-5047. E-mail: info@elsevier.co.jp].

Asia Pacific (excluding Japan): Elsevier Science (Singapore) Pte Ltd, No. 1 Temasek Avenue, 17-01 Millenia Tower, Singapore 039192. [Tel: (+65) 434-3727. Fax: (+65) 337-2230. E-mail: asiainfo@elsevier.com.sg].

Rest of the World: Elsevier Science Customer Service Department, PO Box 211, 1001 AE Amsterdam, The Netherlands. [Tel: (+31) 20-485-3757. Fax: (+31) 20-485-3432. E-mail: nlinfo@elsevier.nl].

Back issues: Back issues of all previously published volumes are available direct from Elsevier Science Offices (Oxford and New York). Complete volumes and single issues can be purchased for 1992-1996. Earlier issues are available in high quality photo-duplicated copies as complete volumes only. Back volumes on microfilm are available from UMI, 300 North Zeeb Road, Ann Arbor, MI 48106, USA.

Periodicals postage paid at Newark, New Jersey. International Journal of Fatigue (ISSN 0142-1123) is published 10 issues per year in January, February, March, April, May, July, August, September, October and November, by Elsevier Science Ltd., The Boulevard, Langford Lane, Kidlington, Oxford OX5 1GB, UK. The annual subscription in the USA is \$890. International Journal of Fatigue is distributed by Mercury Airfreight International Ltd., 10 Campion Road, Irvington, New Jersey 07111-1105. POSTMASTER: please send address corrections to International Journal of Fatigue, c/o Elsevier Science Inc., RSO, Customer Support Department, 655 Avenue of the Americas, New York, NY 10010, USA [Tel: (+1) 212-633-3730/1-888 4ES-INFO. Fax: (+1) 212-633-3680. E-mail: usinfo-f@elsevier.com].

Copyright © 1998 Elsevier Science Ltd. All rights reserved.

This journal and the individual contributions contained in it are protected by the copyright of Elsevier Science Ltd, and the following terms and conditions apply to their use:

Photocopying

Single photocopies of single articles may be made for personal use as allowed by national copyright laws. Permission of the publisher and payment of a fee is required for all other photocopying, including multiple or systematic copying, copying for advertising or promotional purposes, resale, and all forms of document delivery. Special rates are available for educational institutions that wish to make photocopies for non-profit educational classroom use.

222 Rosewood Drive, Danvers, MA 01923, U.S.A. In the U.K., users may clear permissions and make payment through the Copyright Licensing Agency Rapid Clearance Service (CLARCS), 90 Tottenham Court Road, London W1P 9HE. In other countries where a local copyright clearance exists, please contact it for information on required permissions and payments.

Derivative works

Subscribers may reproduce tables of contents or prepare lists of articles including abstracts for internal circulation within their institutions. Permission of the publisher is required for resale or distribution outside the institution. Permission of the publisher is required for all other derivative works, including compilations and translation.

Electronic storage

Permission of the publisher is required to store electronically any material contained in this journal, including any article or part of an article. Contact the publisher at the address indicated.

Except as outlined above, no part of this publication may be reproduced, stored in a retrieval system or transmitted in any form or by any means, electronic, mechanical, photocopying, recording or otherwise, without prior written permission of the publisher.

Notice

No responsibility is assumed by the Publisher for any injury and/or damage to persons or property as a matter of products liability, negligence or otherwise, or from any use or operation of any methods, products, instructions or ideas contained in the material herein.

Although all advertising material is expected to conform to ethical (medical) standards, inclusion in this publication does not constitute a guarantee or endorsement of the quality or value of such product or of the claims made of it by its manufacturer.

© The text paper used in this publication meets the minimum requirements of American National Standard for Information Sciences—Permanence of Paper for Printed Library Materials, ANSI Z39.48-1984.

The Item-fee Code for this publication is: 0142-1123/97 \$17.00+ 0.00

ISSN 0142-1123

This journal is printed on acid free, low chlorine bleach, wood free paper. Typeset by Photo-graphics, Honiton, Devon, UK.

Printed by Page Brothers, Norwich, Norfolk, UK.

International Journal of Fatigue

Materials Structures Components

Contents

Volume 19

Supplement Number 1

1997

S1 Foreword

General Topics

- S3** Fatigue issues in aircraft maintenance and repairs
U.G. Goranson

- S23** Fatigue crack initiation in alpha-beta titanium alloys
J.A. Hall

- S39** Fretting fatigue in engineering alloys
T.C. Lindley

Fatigue Crack Initiation

- S51** Effects of grain size on cyclic plasticity and fatigue crack initiation in nickel
D.J. Morrison and J.C. Moosbrugger

- S61** Microstructural fracture in metal fatigue
L. Lawson, E.Y. Chen and M. Meshii

- S69** A new life extension method for high cycle fatigue using micro-martensitic transformation in an austenitic stainless steel
T.H. Myeong, Y. Yamabayashi, M. Shimojo and Y. Higo

- S75** Fatigue microcrack distributions and the reliability of a nickel base superalloy
E.Y. Chen, S. Sauer, M. Meshii and W.T. Tucker

- S83** Dwell sensitive fatigue in a near alpha titanium alloy at ambient temperature
M.R. Bache, M. Cope, H.M. Davies, W.J. Evans and G. Harrison

- S89** Damage mechanisms of single and polycrystalline nickel base superalloys SC16 and IN738LC under high temperature LCF loading
R.P. Wahi, J. Auerswald, D. Mukherji, A. Dudka, H.-J. Fecht and W. Chen

- S95** Fatigue crack initiation in Ti-5Al-4Sn-2Zr-1Mo-0.7Nd-0.25Si high temperature titanium alloy
J.F. Lei, Z.G. Wang, D. Li and Z.Q. Hu

Short Fatigue Cracks

- S99** Short crack growth and internal stresses
K. Sadananda and A.K. Vasudevan

- S109** Fatigue performance of 6261-T6 aluminium alloy - constant and variable amplitude loading of parent plate and welded specimens
M.N. James and A.E. Paterson

- S119** Fatigue growth of small corner cracks in aluminium 6061-T651
R.L. Carlson, D.L. Steadman, D.S. Dancila, G.A. Kardomateas

- S127** Multiaxial small fatigue crack growth in metals
D.L. McDowell

- S137** Effective strain-fatigue life data for variable amplitude fatigue
T.H. Topper and T.S. Lam

Long Fatigue Cracks

- S145** Fatigue crack growth threshold: implications, determination and data evaluation
H. Döker

- S151** Role of microstructures on the growth of long fatigue cracks
A.K. Vasudevan, K. Sadananda and K. Rajan

- S161** Physical meaning of ΔK_{RP} and fatigue crack propagation in the residual stress distribution field
M. Toyosada, T. Niwa and J. Sakai
- S167** The growth of cracks in Ti-6Al-4V plate under combined high and low cycle fatigue
B.E. Powell, M. Hawkyard and L. Grabowski
- Environmental Effects on Fatigue**
- S177** Environmental interactions with fatigue crack growth in alpha/beta titanium alloys
W.J. Evans, M.R. Bache, M. McElhone and L. Grabowski
- S183** Analysis of high temperature fatigue crack growth behavior
K. Sadananda and A.K. Vasudevan
- Fatigue Crack Closure**
- S191** Introducing the compliance ratio concept for determining effective stress intensity
J.K. Donald
- S197** Fatigue crack growth from stage I to stage II in a corrosive environment
R. Hamano
- S205** Characterization of crack tip and geometry induced closure
W.J. Evans and S.H. Spence
- S211** The effect of stress ratio on fatigue crack growth rate in the absence of closure
R. Sunder, J. Porter and N.E. Ashbaugh
- Microscopy in Fatigue**
- S223** Observation of fatigue damage in structural steel by scanning atomic force microscopy
Y. Nakai, S. Fukuhara, K. Ohnishi
- S237** Assessment of fatigue load spectrum from fracture surface topography
T. Kobayashi, D.A. Shockley, C.G. Schmidt and R.W. Klopp
- Fatigue Damage Modeling**
- S245** Cyclic relaxation in compression-dominated structures
E.J. Tuegel and C.L. Brooks
- S253** Cumulative fatigue damage modeling — crack nucleation and early growth
G.R. Halford
- S261** Analytical modeling for life extension of aging equipment
R.A. Sire and S.W. Hopkins
- S267** Modeling of cyclic stress-strain behavior and damage mechanisms under thermomechanical fatigue conditions
H.J. Maier and H.-J. Christ
- S275** Analysis and prediction of microstructural effects on long-term fatigue performance of an aluminium aerospace alloy
P.E. Magnusen, R.J. Bucci, A.J. Hinkle, J.R. Brockenbrough and H.J. Konish
- S285** Microstructure based fatigue life predictions for thick plate 7050-T7451 airframe alloys
M.A. Prystupa, R.J. Bucci, P.E. Magnusen and A.J. Hinkle
- S289** The effects of load sequencing of the fatigue life of 2024-T3 aluminium alloy
R.A. Everett Jr
- Applications**
- S295** Prediction uncertainties at variable amplitude fatigue
T. Svensson
- S303** Unique fatigue threshold and growth properties of welded joints in a tensile residual stress field
A. Ohta, N. Suzuki and Y. Maeda
- S311** Thickness effects on the fatigue strength of welded steel cruciforms
D.P. Kihl and S. Sarkani
- S317** Fatigue analysis and the local stress-strain approach in complex vehicular structures
F.A. Conle and C.-C. Chu
- S325** Multiaxial fatigue life prediction method in the ground vehicle industry
C.-C. Chu
- S331** Fatigue crack initiation and growth in riveted specimens: an optical and acoustic microscopic study
Z.M. Connor, W. Li, M.E. Fine and J.D. Achenbach
- S339** Epilogue

The *International Journal of Fatigue* homepage can be found at <http://www.elsevier.com/locate/ijfatigue/>
The Structural Integrity Network website can be found at <http://www.elsevier.com/locate/sinet/>
The Elsevier Science catalogue can be found at <http://www.elsevier.nl/gopher.elsevier.com>



ContentsDirect, the free e-mail alerting service, delivers the table of contents of this journal directly to your PC, prior to publication. The quickest way to register for ContentsDirect is via the Internet at: <http://elsevier.nl/locate/ContentsDirect>. If you don't have access to the Internet you can register for this service by sending an e-mail message to csubs@elsevier.co.uk - specifying the title of the publication you wish to register for

**First International Conference on
Fatigue Damage in Structural Materials**

**22-27 September 1996
Hyannis, Massachusetts**

Guest Editors

**AK Vasudevan
JT Cammett
CA Bigelow
T Nicholas**

DTIC QUALITY INSPECTED

19980428 120



Foreword

The Engineering Foundation First International Conference on Fatigue Damage in Structural Materials was held at the Tara Hotel, Hyannis, MA, USA on September 22–27, 1996. The conference was organized in order to bring together experts from around the world in academia, government, and industry to address current issues in fatigue of structural materials with particular emphasis on in-service fatigue failures in both military and civilian applications including air, sea, and land vehicles. The failures which have occurred have resulted in substantial unscheduled maintenance costs as well as requiring redesigns and newer hardware in some cases. In a few cases, operational safety and readiness have been raised as concerns. With this as background, the conference organizers felt that it was an opportune time to explore all matters pertinent to the analysis and the prediction of fatigue damage of critical components under service environments, including some review of current analytical methods, development of new methods, and identification of technical gaps in areas of fatigue crack nucleation and growth. The papers which were presented at the conference are presented in this volume.

The general purposes of the conference were to provide a forum for current research in fatigue and to explore fatigue issues relevant to existing and new structural materials. The conference was truly international in participation. Seventy-four delegates attended from

eight countries: Australia, Canada, Great Britain, France, Germany, Japan, Sweden and the United States. Forty-two papers were presented in eight sessions: Overviews, Fatigue Initiation, Short Crack Growth, Long Crack Growth (two sessions), Microscopy, Modeling and Probability and Statistics. Sessions were organized to provide ample opportunity for discussion and there was much of that stimulated by presentations. Subsequent to the conference all papers were reviewed and revised as appropriate prior to this publication. The conference organizers have appreciated the assistance provided by the Engineering Foundation. We are especially appreciative of the participation of the delegates and the contributions from authors and reviewers to the success of this conference.

The conference was jointly organized and sponsored by the United States Air Force, the United States Navy and the Federal Aviation Agency. Conference arrangements were made by Ms. Barbara Hickernell, Engineering Foundation, New York. The organizers thank Mr Dean Eastbury and Prof. K. Riebsnider of the *International Journal of Fatigue* for publishing the articles.

Conference Editors

AK Vasudevan, Office of Naval Research
JT Cammett, Naval Aviation Depot
CA Bigelow, Federal Aviation Agency
T Nicholas, Air Force Wright Laboratory

PII: S0142-1123(97)00029-7

Fatigue issues in aircraft maintenance and repairs

Ulf G. Goranson

Boeing Commercial Airplane Group, Seattle, WA, USA
(Received 10 February 1997)

Many design considerations are involved in ensuring structural integrity of Boeing jet transports, which have common design features validated by extensive analyses, tests, and service performance. Designing for continued structural integrity in the presence of damage such as fatigue or corrosion is an evolutionary process. Performance demands, increasing structural complexity, and aging fleet reassessments have required development of standards suitable for application by large teams of engineers. This presentation is focused on such methods with special emphasis on practical fatigue reliability considerations. Durability evaluations are based on quantitative structural fatigue ratings which incorporate reliability considerations for test data reduction and fleet performance predictions. Fatigue damage detection assessments are based on detection reliability estimates coupled to damage growth and residual strength evaluations. Data are presented to airline operators on detection check forms which permit efficient maintenance planning to achieve required fatigue damage detection reliability levels. © 1998 The Boeing Company. Published by Elsevier Science Ltd.

(Keywords: fatigue and damage tolerance; damage detection reliability; airline maintenance planning)

OVERVIEW

Criteria and procedures used in commercial jet transport design and manufacture over the last four decades have resulted in fail-safe/damage-tolerant structures with a credible safety record, *Figure 1*. Advancements in the capability to characterize structural performance by analysis have spurred adaptation of traditional fatigue and fracture mechanics technologies with large test and service databases to achieve development of technology standards over the last two decades. Major Boeing efforts have been focused on capturing lessons learned for future continuous design improvements with standardized durability and damage tolerance checking procedures similar to traditional strength checking procedures. The challenge of successfully implementing technology standards hinges on a practical balance

between simplicity and technical credibility aimed at providing structural engineers with useful and service/test validated analysis tools. This paper provides fundamental principles behind durability and damage tolerance technology standards, as well as examples of test and service validation.

DESIGN CONSIDERATIONS

Structural integrity

Two basic structural integrity issues must be addressed. The first is to design and verify the ultimate strength of the undamaged structure for specified design maneuvers, gusts, flutter, ground loads, and pressurization. The second is to design the structure to sustain fail-safe loads with limited damage for a period of service prior to detection and repair. All Boeing jet transports are designed to this fail-safe principle, which requires fail-safe load capability at all times and restoration of the structure to ultimate load capability after damage detection. The fail-safe load factor is 2.5 g for maneuver design conditions, and an additional safety factor of 1.5 is applied to obtain the ultimate load requirement. The fail-safe (limit) load levels are selected to represent conditions that may occur once in a lifetime for a fleet of airplanes. Design gust levels are based on a similar remote probability of occurrence criterion. Static strength design criteria existing today, including the factor of safety, have worked well, and concerns about static overload failures have essentially been eliminated in present-day commercial airplanes.

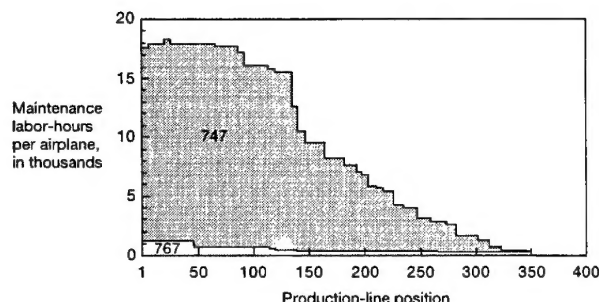


Figure 1 Safety record – worldwide commercial jet fleet

Several sources of damage must be evaluated to ensure structural safety during service. Both accidental damage and environmental deterioration are random events during the operational life of the airplane, and maintenance requirements must reflect inspectability for these types of damage. Fatigue damage is a cumulative process, and some cracking is expected in large fleets designed to reach an economic life goal with high reliability. Consequently, supplemental fatigue damage inspections may be required for older airplanes. The inspectability and accessibility characteristics of the structure must be such that general visual methods of damage detection can be confidently employed for most of the structure. Directed inspections involving sophisticated damage detection equipment may be acceptable in areas where inaccessibility dictates infrequent inspection.

Structural durability

Interaction between structural damage tolerance and durability characteristics must be recognized in the design, manufacturing, and operation of modern jet transports. Design evolution and maintenance requirements are motivated by both safety and economic concerns. Damage tolerance is primarily governed by certification requirements, while durability characteristics mainly influence the airplane cost of ownership and are dictated by the requirements of a competitive international market. There is no limit to the service life of damage-tolerant (fail-safe) airplane structures, provided the necessary inspections are carried out along with timely repairs and comprehensive corrosion prevention programs. Since operational efficiency is impacted by the cost and frequency of repair, durability may limit the productive life of the structure.

Fatigue tests of components or the entire airframe are extremely valuable in the early life of a given model, but proof of quality stems from the accumulated experience of maturing fleets, *Figure 2*. The Boeing Commercial Airplanes durability system was developed in the early 1970s to serve as a corporate memory of past design, *Figure 3*. Highlighted key parameters provide the means of timely extension and transfer of experience to new design and/or operating usage. The Boeing fleet is surveyed continuously and the information is summarized in terms of service-demonstrated fatigue lives of various components.

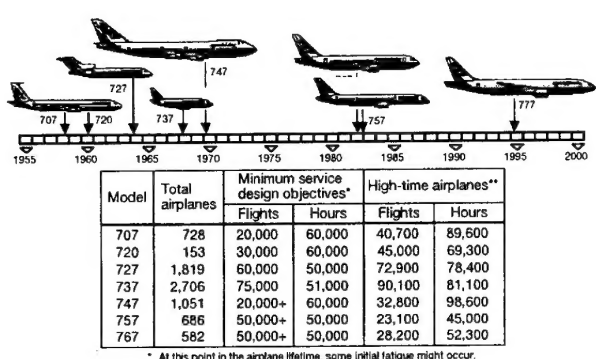


Figure 2 Boeing commercial jet fleet summary

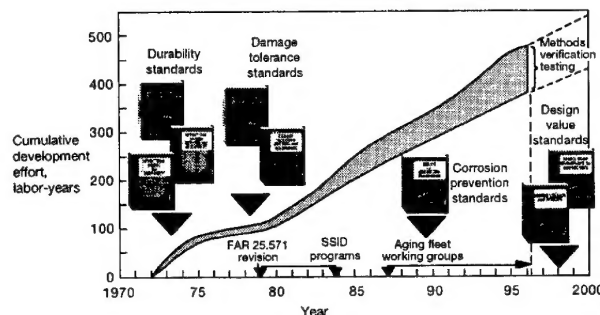


Figure 3 Boeing technology standards development

Damage tolerance

Certification of commercial jet transports requires damage-tolerant designs in all instances where they can be used without unreasonable penalty. The technical capability has now evolved to use damage growth to determine inspection requirements, which in the past were based on service experience. Appropriate multiple site damage must be considered in both new design and structural reassessments of older models.

Damage tolerance comprises three distinct elements of equal importance for achieving the desired level of safety:

- Damage limit – the maximum damage, including multiple secondary cracks, that the structure can sustain under limit load conditions;
- Damage growth – the interval of damage progression, from the detection threshold to damage limit; it varies with the magnitude of operating loads, sequence of loads, and environmental influences;
- Inspection program – a sequence of inspections of a fleet of airplanes with methods and intervals selected to achieve timely detection of damage.

These elements of damage tolerance are merged at Boeing Commercial Airplanes by a Damage Tolerance Rating (DTR) system to provide a quantitative measure of fatigue damage detection reliability, *Figure 4*.

STRUCTURAL DURABILITY ASSESSMENTS

Fatigue ratings and allowables

Long-life structures are achieved by balancing detail design practices with the operating stress environment,

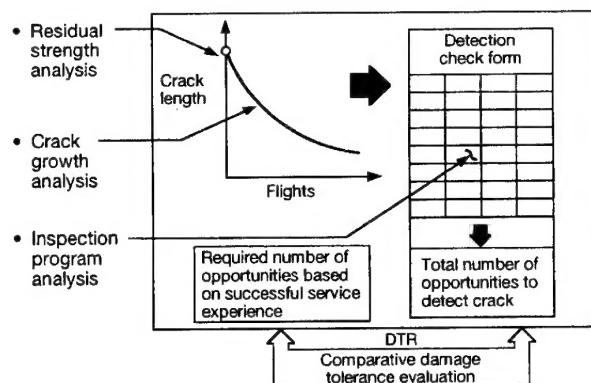


Figure 4 Damage detection evaluation

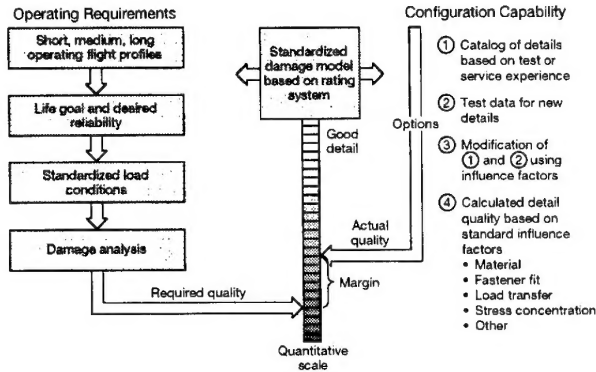


Figure 5 Durability design evaluation

Figure 5. Experience has shown that incompatibility between operating stresses and fatigue allowables causes 85% of the service problems. Standardizing the fatigue analysis process allows the service requirement analysis to be conducted independently of and prior to structural capability analysis. This design process provides the following benefits.

- Early attention directed toward fatigue prevention.
- Fatigue methods and allowables available to all structural engineers.
- Common quantifiable base for decision making.
- Emphasis on detail design to achieve minimum design service objectives.
- Trade studies leading to efficient weight/cost designs.

Structural configurations are selected to meet minimum design service objectives. This implies that some specific level of structural fatigue quality must be achieved, with the desired level of confidence and reliability, to provide competitive economic structures with very limited cracking during the anticipated service life. Service life calculations are based on fatigue damage models representing known test and service experience. The focal point in the damage model is defined by a Detail Fatigue Rating (DFR). A comprehensive inventory of service and test-proven design allowables is based on a family of damage curves for various mean and alternating stress combinations uniquely defined by given DFR values. Such DFRs permit quantitative compilation of the cumulative fatigue and design experience as shown in *Figure 6*.

Analytical fatigue allowables are also available to

structural engineers to modify existing configurations proven by test and fleet experience, or to derive fatigue ratings for a completely new design. Base ratings are established for notches and mechanically fastened structures, and comprehensive libraries of modification factors accounting for different design parameters such as the type of detail, amount of load transfer, fastening system, surface finish, and material alloy type are provided.

Fatigue reliability considerations

The structural design service objective is a minimum of 20 years of airline operation with only a small percentile of the population subject to repair because of the initiation of detectable fatigue cracks. This percentile varies from less than 5% for those structures that are easy to inspect and repair to extremely low percentiles for structures with difficult access. To obtain these levels of reliability, every structural engineer is required to design for fatigue prevention. This requirement has necessitated the use of straightforward procedures that are easily applied at the design stage.

The ‘scatter factor’ approach to structural fatigue reliability has been used in the airplane industry for decades, and scatter factors such as 2 and 4 are well established. Therefore, in deference to structural engineer familiarity, this approach of using statistically and physically meaningful scatter factors has been retained.

The two-parameter Weibull distribution is used for the structural life distribution mode. In this application structural life is defined as the operational life to initiation of a fatigue crack of detectable size. The Weibull distribution was selected after considerable USAF-sponsored research in the late 1960s and early 1970s. Furthermore, the two-parameter model was chosen to recognize the conservative possibility of a detectable fatigue crack being present at zero life.

Predefined shape parameters are used for the design process. These parameter values were established after reviewing literally thousands of fatigue test results and determining that the parameter was material dependent, and in the case of high strength steel was also stress concentration dependent. Design scatter factors are based on shape parameters that range from 2.2 for high strength steels to 4 for aluminum.

The scale parameter β defines the central tendency (characteristic) fatigue life of a structure and depends upon the quality of the structure and the stresses to which the structure is subjected during its operation. The characteristic fatigue life is either calculated by the designer or determined by testing. For design purposes, characteristic life is related to fatigue lives at higher levels of structural reliability via appropriate scatter factors.

The fatigue design procedure is divided into two major steps. The first step establishes a structure’s minimum design service objective in terms of operational flights with high structural reliability. The second step determines the structural fatigue quality required to attain this design objective. Scatter factors are used in both steps.

The first step uses a factor known as the Fatigue Reliability Factor (FRF). This factor has been normalized so that a value of unity translates to a minimum level of reliability of 95% over the structure’s

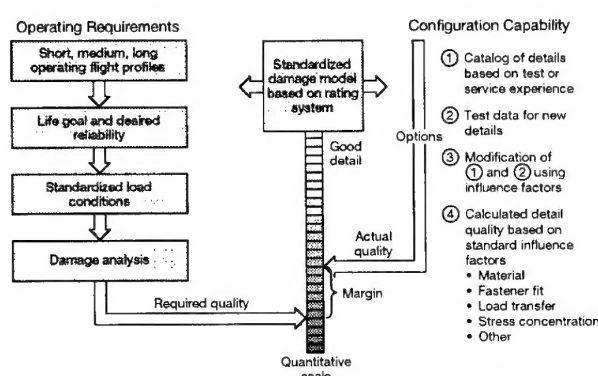


Figure 6 Normalized fatigue ratings

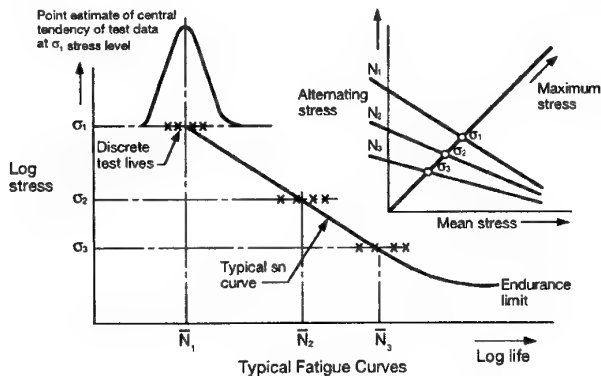


Figure 7 Fatigue damage model

operational lifetime. FRF = 1 is limited to structures in which fatigue cracks are easily detected and repaired. Structural engineers are required to use FRFs that are increasingly greater than unity when establishing life goals for structures that are increasingly difficult to inspect and repair. This simple approach results in the more difficult structures being designed for longer lives. Therefore, at any time during an airplane's operational lifetime, a difficult-to-inspect/repair structural part would have less expectation of fatigue cracking, i.e. higher reliability, than an easy-to-inspect/repair part.

The second step of the fatigue design process requires fatigue allowables in order to determine the structural quality needed to achieve the economic design service objective. These allowables are usually referred to as SN curves, and they define the life of a structure at any given level of stress, *Figure 7*.

Fatigue design allowables (DFR curves) identify for any level of operational stress a minimum fatigue life that can be comfortably exceeded by all but the weakest extreme members of the structural population. These allowables are developed empirically from fatigue test results of structurally representative specimens subject to realistic operational loads. The fabrication and testing of specimens are carefully monitored and documented and the test results verified before acceptance as valid data. Four separate 'scatter factors' are used to reduce valid fatigue life data to reliable design allowables. As shown in *Figure 8*, these factors are as follows.

- Establish a lower bound interval estimate of central tendency fatigue life from the results of a limited

number of test specimens. In keeping with long-established static strength allowables practice, the confidence bound is set at the 95% level.

- Account for the degree of simplification used in the fatigue test representation of the actual structural part and the real operational load conditions.
- Account for the influence of population size on fatigue life. This factor distinguishes between the fatigue performances of typically small test specimens, which contain few potential crack initiation locations, and large full-scale structures with their multitude of potential sizes for initiation of the earliest fatigue cracks.
- Establish the structure's design allowable fatigue life at the 95% reliability level; that is, the life at which 95% of the population of structures will be free of fatigue cracks of detectable size. The 95% reliability level was adopted for fatigue allowables as a simplification of the A and B basis static strength allowables, which have been set for decades at reliability levels of 99% and 90% respectively.

The fatigue design procedure can be simply summarized as follows. The structural engineer first establishes a minimum design service objective for the structure per appropriate Design Requirements and Objectives document for each model. This design objective is then entered in an appropriate DFR curve and the design allowable stress determined. This stress is then compared to the actual stress that will be imposed on the structure during its operation, and a resultant fatigue margin is calculated by dividing the allowable stress by the operational stress. Clearly this margin must equal or exceed unity to attain the structure's reliability and life goal requirements.

Fatigue performance validation

Technology standards. Since the early 1970s, Boeing has devoted extensive efforts to developing methods and allowables that enhance analysis capability for new and aging airplane structures, see *Figure 3*. ('Allowables' are material properties and specific strength data used for design and analysis of airplane structures.)

Significant amounts of testing served as verification and validation of technology standards development. This testing included coupon, component, and full-scale fatigue testing and teardown inspections. ('Coupons' are small material test specimens used to determine allowables.)

Durability standards were developed first, followed by damage tolerance standards. These two standards were incorporated into the designs of the second generation of Boeing jet transports, the 757 and 767. The damage tolerance standards were utilized in the certification of the 757 and 767 as damage tolerant. This damage tolerance was certified per the US Federal Aviation Administration (FAA) Federal Airworthiness Regulation 25.571, Amendment 25-45. The Boeing damage tolerance standards were also utilized in the Supplemental Inspection Documents of aging airplane programs for the Boeing 707, 727, 737, and 747.

Since the early 1970s, corrosion has been recognized as one of the dominant factors in the inspection and maintenance activities of airline operations. Boeing has devoted extensive resources to the technology standards development in the areas of corrosion prevention and

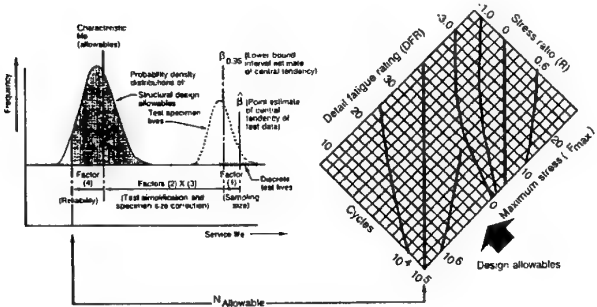


Figure 8 Fatigue design allowables considerations

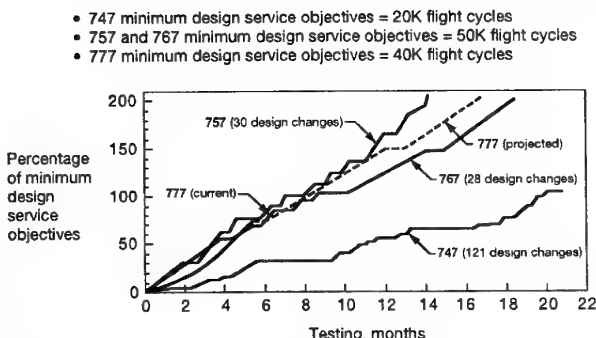


Figure 9 Major airframe fatigue tests

corrosion control. Expanded corrosion coverage, as a result of the corrosion standards development, has been incorporated into the production lines of all current production airplanes as well as the Aging Fleet Structures Working Groups. These groups include representatives from airframe manufacturers, airline operators, and regulatory agencies.

Figure 9 illustrates the significance of durability standards development to the structural improvement process. For example, the second generation 757 and 767 were tested to *twice* their respective Design Service Objectives (DSOs) in flight cycles; improved testing technology allowed this testing to be completed in less time than it took to test the first generation 747 to its *one* DSO in flight cycles. More significantly, the design changes identified in the 757 and the 767 fatigue testing in two DSO flight cycles are far fewer than the design changes identified for the 747 during fatigue testing for its one DSO in flight cycles. This improvement was possible because durability technology standards were incorporated into the original designs of both the 757 and 767.

Another measurement for the effectiveness of the design improvements is 'maintenance labor hours per airplane' compared for the initial 10 years of operation for each model, *Figures 10* and *11* show significant order of magnitude improvements between first and second generation wide and standard body airplanes. These improvements are a result of implementation of lessons learned from past design practices for new airplanes.

Full-scale fatigue testing. Full-scale fatigue testing of airplanes is a major part of structural performance data development. In addition to providing the vali-

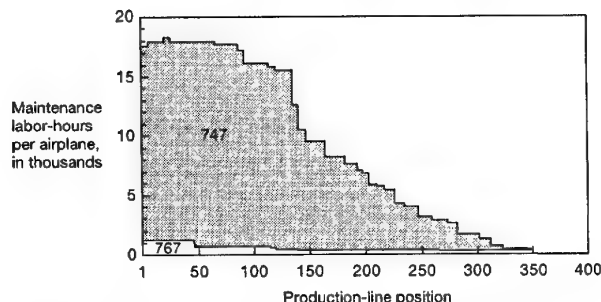


Figure 10 747/767 service bulletin: labor hours after 10 years of service to address corrosion and fatigue

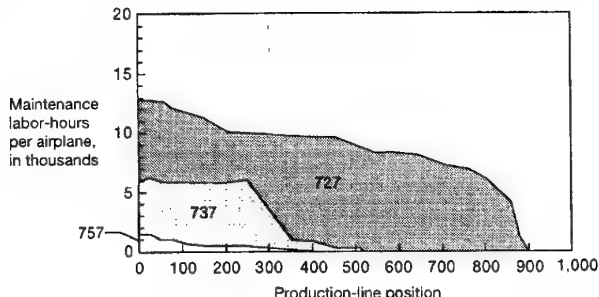


Figure 11 727/737/757 service bulletin: labor hours after 10 years of service to address corrosion and fatigue

dation of aircraft design concepts, full-scale fatigue testing is often used to identify any preventative maintenance actions for the fleet, if the fatigue testing is done at the time of certification of a new model of jet transport (which is often the case at Boeing).

Figure 12 shows the minimum DSO in flight cycles and the full-scale fatigue testing in flight cycles. It may be seen from *Figure 12* that full-scale fatigue testing is generally accomplished to twice the minimum DSO, with two exceptions. The first exception is the model 727, which was originally fatigue tested to its DSO of 60,000 flight cycles. However, approximately two years ago, a 727 airplane with 47,000 accumulated flight cycles was acquired and the fuselage cyclic pressure tested to an additional 76,000 cycles. The second exception is the model 747, which was also originally fatigue tested to the DSO of 20,000 flight cycles. As in the case of the 727, a 747 airplane with 20,000 accumulated flight cycles was acquired and the fuselage cyclic pressure tested to an additional 20,000 cycles. In addition, the fuselage sections 41 and 42 of the derivative model 747-400 were cyclic pressure tested to 60,000 cycles, representing three DSOs.

Teardown inspections. Since the introduction of the 707, several teardown inspections and evaluations of high-time airplanes have been conducted as part of a continuing assessment of airplane structure. These inspections permit a detailed examination of structural performance, and provide much useful information for forecasting future structural maintenance requirements. Sophisticated inspection techniques, capable of finding

Airplane	Minimum design service objective	Fatigue test cycles	Remarks
707	20,000	50,000	Fuselage Hydro-fatigue test
727	60,000	(a) 60,000 (b) 170,000	Complete airframe Complete fuselage 47,000 cycles in service, plus 123,000 pressure test cycles
737	75,000	(a) 150,000 (b) 129,000	Fuselage section/pressure and shear Complete aft fuselage 59,000 cycles in service, plus 70,000 pressure test cycles
747	20,000	(a) 20,000 (b) 40,000 (c) 60,000	Complete airframe Complete fuselage 20,000 cycles in service, plus 20,000 pressure test cycles 747-400 sections 41 and 42 pressure test cycles
757	50,000	100,000	Complete airframe
767	50,000	100,000	Complete airframe
777	44,000	60,000 (ongoing)	Complete airframe (test in progress for early 1997 completion)

Figure 12 Full-scale fatigue test programs

smaller cracks than typically found during routine airline inspections, are used on the disassembled structure. Teardowns also provide an excellent database for calibrating analysis tools, and developing structural modifications on future production airplanes, if required. Major teardown inspections supplementing normal fleet surveillance activities have been conducted on several models:

● 707 wing plus center section	1965
● 707 wing	1968
● 707 wing plus center section and fuselage	1973
● 707 empennage	1978
● 727 forward fuselage	1978
● 737 wing plus center section, forward fuselage, and empennage	1987
● 737 aft fuselage	1988
● 747 wing and empennage	1989
● 747 fuselage	1991
● 727 wing and empennage	1994
● 727 fuselage	1995

Concerns related to an increased number of airplanes being used beyond their original design life objectives have spurred further activities to obtain airframes retired from service for teardown inspections. Boeing will continue to monitor the aging fleet to verify the effectiveness of preventative modifications incorporated as retrofit on older models and/or new model production improvements. Findings will be disseminated to operators by service bulletins as required and incorporated in maintenance recommendations.

Fleet surveys. The aging fleet surveys by engineering teams were initiated in 1986 to gain a better understanding of the condition of structures and systems and to observe the effectiveness of corrosion prevention features and other corrosion control actions taken by the operators, *Figure 13*. All manufacturers continually review reported service data and other first-hand information from customer airlines in order to promote safe and economic operation of the worldwide fleet. These surveys were primarily prompted by the projected upward trend in airplane age towards and beyond original design service objectives.

The initial fleet surveys showed that the majority of the airplanes were well maintained and in relatively good condition. However, there were a number of airplanes whose condition showed that finding corrosion discrepancies and repairing them was accepted

practice and little or no attempt was made to apply any preventative measures. From the surveys and some similar incidents it became apparent that some airplanes were continually operating with significant structural corrosion and that this was on the increase as airplanes age. This in turn could significantly influence the fatigue cracking and damage tolerance capability of principal structural elements. Boeing formed a special Corrosion Task Force in 1988 and held meetings with airline maintenance executives as a result of these surveys.

Service-demonstrated fatigue lives. The commercial jet fleet is used as a large group of specimens loaded in real-life environments to demonstrate service-demonstrated fatigue life and to predict future fatigue performance. This fleet represents a database of over 8000 delivered airplanes, with a total fleet experience exceeding 150 million flight cycles, and daily utilization exceeding 23,000 flights, see *Figure 2*.

Where a statistically significant number of fatigue cracks have been reported in a fleet, maximum likelihood estimates of the Weibull shape and scale parameters are used to determine fleet-demonstrated DFR values. This provides a means of relating service experience for one model to other models with different utilization characteristics. Significant fleet findings, often augmented by extensive teardown inspections, are used to modify fatigue methods and allowables described previously. When no fatigue cracks have been observed, a simpler approach based on the design shape parameter is used to estimate service-demonstrated lives. Such information provides a fundamental check and balance for the fatigue analysis system, and new design and/or redesign evaluations can be related to accumulated fleet performance, *Figure 14*.

DAMAGE TOLERANCE ASSESSMENTS

Jet transports are designed to be damage tolerant, a concept that evolved from the fail-safe design principle introduced in the 1950s. The ability to analyze damaged structure has improved steadily through more sophisticated application of fracture mechanics. Timely detection of damage is the ultimate control in ensuring structural safety. However, traditional damage growth and residual strength evaluations have failed to incorporate damage detection parameters that influence maintenance planning.

The effects of accidental, environmental, and fatigue

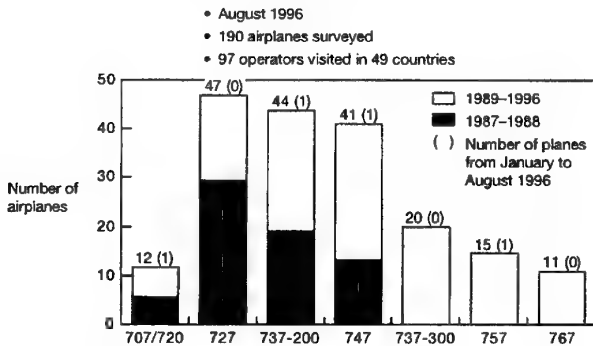


Figure 13 Boeing fleet surveys

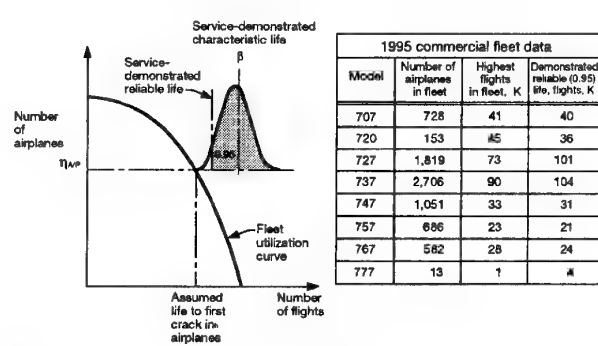


Figure 14 Service-demonstrated fatigue lives

damage must be assessed to achieve a balanced inspection program. Of these, fatigue damage, characterized by the initiation and subsequent growth of a crack, is the most amenable to rigorous analytical treatment. Major efforts during the last 15 years have focused on establishing quantitative damage detection rating systems that measure the efficiency of inspection programs. Extensive statistical evaluations of reported service data have resulted in estimates of damage detection reliability for different inspection methods.

Fatigue damage detection is normally considered in terms of a single event involving inspection for a given size of crack with a specified method. However, airline maintenance practices consist of multiple inspection levels, varying inspection intervals, and different methods of inspection. In addition, fatigue cracking is generally found on more than one airplane in the fleet within a relatively short period of time. This multiplicity of events significantly influences the timely detection of fatigue damage and needs to be reflected in damage detection assessments. It must be shown that there is a high probability of detecting fatigue damage in the fleet before such damage reduces airplane residual strength below specified levels. A DTR system suitable for ensuring timely detection of fatigue damage in the fleet was developed to accommodate these concepts, see *Figures 3 and 4*.

Elements of damage tolerance

The key objective for airplane structures designed to the damage tolerance concept has always been to carry regulatory fail-safe loads until detection and repair of any fatigue cracks, corrosion, or accidental damage occurring in service. The ability to analyze damaged structures has progressed significantly during the last 20 years through the evolution of fracture mechanics. Assessments now consider residual strength, damage growth, interactive multiple damage sites and quantitative structural maintenance evaluations. Structural maintenance is the cornerstone for ensuring continued airworthiness of damage-tolerant structures.

Residual strength. The maximum allowable damage that a structure can sustain at a critical fail-safe level is the key to the level of damage growth and inspection needed to ensure damage detection. Built-up airplane structures consist of multiple sheet, stiffener, and fastener elements. Interaction between these cracked and uncracked elements causes significant redistribution of stresses. Failures are often precipitated by local exhaustion of plastic strain capability of the most critical elements, and/or net section failures involving a mixture of fracture mechanics and transitional behavior in some elements, *Figure 15*.

Crack growth. The rate of damage propagation is a function of material properties, structural configuration, environment, crack length of primary and secondary cracks, and operating stress exposure. Damage detection assessments require crack growth data from detection threshold lengths to the allowable damage determined by residual strength analyses. Use of normalized damage models for calculating relative growth per flight, including load sequence effects, permits separation of the material, geometry, and stress parameters, *Figure 16*.

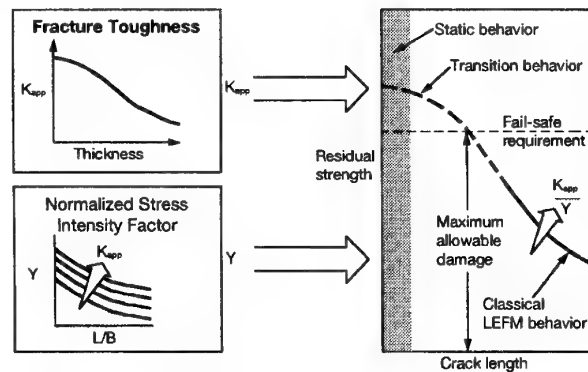


Figure 15 Residual strength evaluation

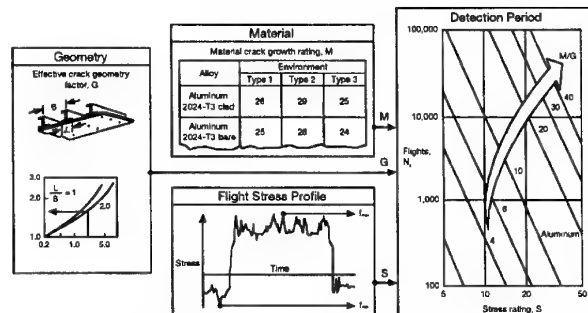


Figure 16 Crack growth evaluation

Damage detection. Both accidental damage and most forms of environmental damage can be considered as random events that can occur at any time during the operational life of an airplane. Fatigue damage is characterized by cumulative progression relating to airplane usage measured in flights. Detection ratings have been developed for accidental and environmental damage. A quantitative fatigue damage detection rating system is known as the DTR system. Damage detection is a function of fleet size, number of cracks, and number and type of inspections, *Figure 17*.

Structural maintenance considerations

Structural maintenance and inspections are the cornerstones of continuing airworthiness of jet transport structures. The advent of fracture mechanics technology

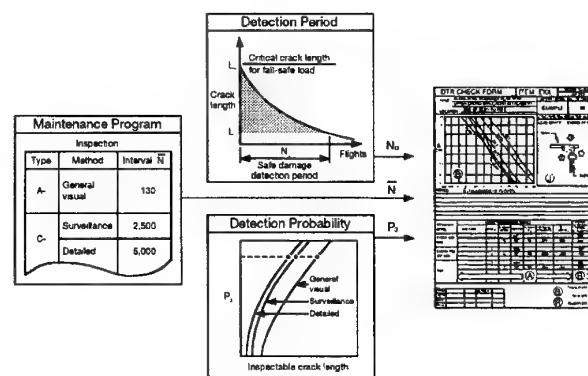


Figure 17 Damage detection

has accelerated the knowledge for determination of crack growth rates and maximum allowable damage at limit load conditions. The research community has expanded the understanding and modeling of these structural characteristics. Although elastic-plastic analyses have their place, the added accuracy is often not consistent with the accuracy of other significant parameters governing residual strength. Significant understanding exists today to properly plan fatigue and crack growth tests in order to recognize sequence effects caused by spectrum loads. While analysis models can yield reasonable correlation with laboratory loading environments and simplified structural configurations, it is easy to have large uncertainties due to local load redistributions in cracked structures, flaw shapes, cracking patterns and a host of external and environmental characterization problems. While progress must be encouraged, it is truly necessary to pay attention to the overall sensitivity of stress histories and analysis assumptions in the final answer. In summary, prediction of fatigue crack growth for a host of complex structural details within a factor of 2 is not always as easy as advertised by complex models.

The practising structural maintenance engineer is charged with development of inspection programs from the time of airplane introduction into service. Three principal forms of structural damage must be evaluated to achieve a balanced structural inspection program for timely detection of environmental deterioration, accidental damage, and fatigue damage.

Environmental deterioration actually involves two forms of damage, corrosion and stress corrosion. Corrosion may or may not be time- and/or usage-dependent. For example, deterioration resulting from a breakdown in a surface protection system is more probable as calendar age increases; conversely, corrosion due to spillage or a leaking seal is treated as a random discrete event.

Accidental damage can also be considered in two categories. First, discrete source or large-scale damage, such as that caused by a large bird strike or uncontaminated engine disintegration, involves special regulations. Such damage detection is considered obvious, but it must be shown that a flight can be safely completed after it has occurred. Second, more general forms of accidental damage, such as dents and scratches, occurring during routine operation of the airplane must be considered in the inspection program.

Both accidental and most forms of environmental damage are random events that can occur at any time during the operation life of an airplane. However, experience has shown that some structural areas are more susceptible than others to these types of damage. This information is used to develop suitable inspection tasks.

Fatigue damage is characterized as the initiation of a crack, with subsequent propagation. This is a result of a continuous process whose effect is cumulative with respect to airplane usage (measured in flights or flight-hours). Comprehensive fatigue life, crack growth and residual strength evaluations are required. Using previous service experience to improve detail design results in a high level of structural durability. Large-scale panels and full-scale airplane fatigue tests are used to identify areas in which this durability is significantly lower than predicted. Changes to the pro-

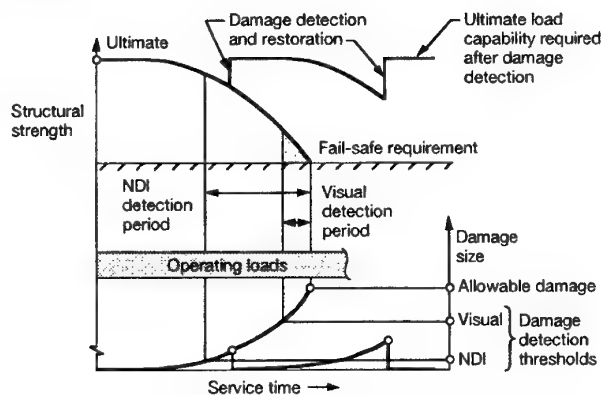


Figure 18 Strength requirements for damage-tolerant structure

duction airplanes to rectify problems usually result. Most airplanes in the fleet are then expected to exceed the fatigue service objective without significant cracking. This does not preclude anticipated cracking before all airplanes reach the design life objective.

For safety critical structures, it must be demonstrated that there is a high probability of timely detection of any cracking throughout the operational life of the fleet, *Figure 18*. This means that the inspection program must be capable of timely detection of initial damage in the fleet. Subsequent action is necessary to detect or prevent any damage in the fleet.

The conflicts in structural maintenance planning often occur because of the focus on fracture mechanics-based damage tolerance evaluations. Inspection programs in place to provide timely detection of corrosive or accidental damage are often not addressed by the scientifically oriented structural engineer, who may be satisfied with inspection thresholds based on universally applied initial flaws and inspection intervals based on simple factoring of the damage detection period from an assumed detectable/inspectable damage size to the damage allowed at limit load conditions.

This section addresses some key issues related to inspection thresholds and intervals with emphasis on quantifying detection reliability aspects and sensitivity to key parameters and variables.

Structural characteristics

Airplane structures can be categorized for the purpose of determining safety analysis requirements, *Figure 19*. Any structural detail, element or assembly is

Structural category		Technique of ensuring safety	Safety analysis requirements	Structural classification examples
Structurally significant items or principal structural elements (primary structure)	① Secondary structure	Design for loss of component or safe separation	• Continued safe flight	Wing spoiler segment (safe separation or safe loss of function)
		Adequate residual strength with extensive damage obvious during walkaround or indicated by malfunction	• Residual strength	Wing fuel leaks
		Inspection program matched to structural characteristics	• Residual strength • Crack growth • Inspection program	All primary structure not included in categories ② or ④
	④ Safe-life design	Conservative fatigue life	• Fatigue	Landing gear structure (conservative fatigue life)

Figure 19 Structural classification examples

classified as a Structurally Significant Item (SSI) if its failure reduces airplane residual strength below regulatory levels or results in an unacceptable loss of function. Most SSIs require damage tolerance evaluations comprising residual strength for Category 2 structures and all three elements of damage tolerance for Category 3 structures.

The structure of each airplane model undergoes a thorough examination to ascertain the functions of its components and, as necessary, to classify those components. For the new models, this evaluation is performed using the FAA approved guidelines of MSG3. These evaluations are conducted, in support of a Structures Working Group established jointly by Boeing and its operators, to develop the structural maintenance program. As a consequence of examinations, some 80 to 100 SSIs can typically be identified on each airplane model. As an example, 33 SSIs for a typical outer wingbox are shown in *Figure 20*. Each SSI may cover a broad expanse of structure. For example, the entire wing rear spar lower chord and skin may represent a single SSI. In consequence, the SSI may be divided into a number of details based on access, inspectability, stress level, material, and detail design differences. This example in *Figure 20* shows three details in a single rib bay. Detail A shows a typical rear spar structure; detail B shows the rear spar at a rib where internal inspection is restricted; detail C shows the rear spar at a rib where a main landing gear trunnion support fitting additionally restricts external inspection. Within each detail, the inspectable initial damage is assumed to occur in the most difficult location from the viewpoint of inspectability, regardless of the relative fatigue life of the component. In the selected lower chord example, crack growth calculations are performed for cracks in the chord itself, in the skin, and as appropriate in the web. These cracks grow interactively, with each influencing to some degree the behavior of the others. Separate analyses may occasionally be required to accommodate crack growth data necessary to evaluate the effectiveness of selected nondestructive testing techniques. Thus, in summary, a formal damage tolerance evaluation of an airplane structure may involve crack growth and probability of detection determination at several hundred details with two to three times as many crack growth curves to represent adjacent structural elements. Some 150 to 250 of these, representing the most critical, are published in formal certification docu-

mentation. Each crack growth analysis must take into account the unique aspects of load spectrum, stress level, material, geometry and interaction between adjacent structural elements.

Fatigue inspection threshold

The design service objectives are established for high utilization operators in terms of flight cycles for short, medium and long flights. Design service objectives are established with a minimum of 95% reliability. For typical aluminum alloys this implies a characteristic life of at least twice the design service objective excluding additional factors applied to achieve 99% reliability for most principal structural elements. Supplemental structural fatigue inspections based on fatigue principles are often initiated when the fleet leaders reach 75% of the design service objective. At this time the fleet exceeding 50% of the design objectives is included in a so-called candidate fleet. These principles were initially developed more than 10 years ago for the first generation of supplemental inspection programs. The rate of findings of previously unknown cracking does not support an often-advocated abandoning of this approach in favor of initial flaw growth periods critically factored by 2. While some provisions exist to adjust the initial flaw for inherent manufacturing quality and life enhancements, the end product of such assessments offers little advantage over service/test-demonstrated fatigue initiation data.

Increasing concerns for widespread fatigue damage have promulgated more pressure to establish thresholds for such structural damage which can significantly reduce the residual strength and accelerate damage progression link-up of adjacent cracks.

Widespread fatigue damage in a structure is characterized by the presence of multiple structural details with cracks that are of sufficient size and diversity whereby the structure will no longer meet its damage tolerance requirement (e.g. maintaining the required residual strength after partial failure), *Figure 21*. There are two distinct types of WFD:

- Multiple Site Damage (MSD) – simultaneous presence of fatigue cracks in the same structural elements;
- Multiple Element Damage (MED) – simultaneous presence of fatigue cracks in adjacent structural elements.

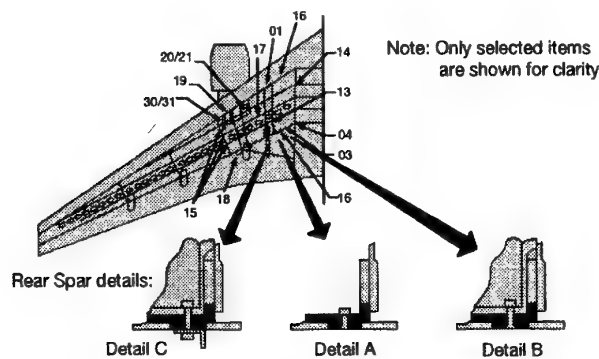


Figure 20 Structurally significant item examples for wingbox

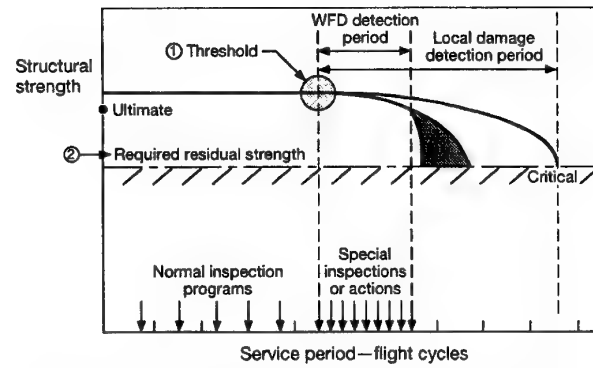


Figure 21 Damage detection comparisons for local and widespread fatigue damage

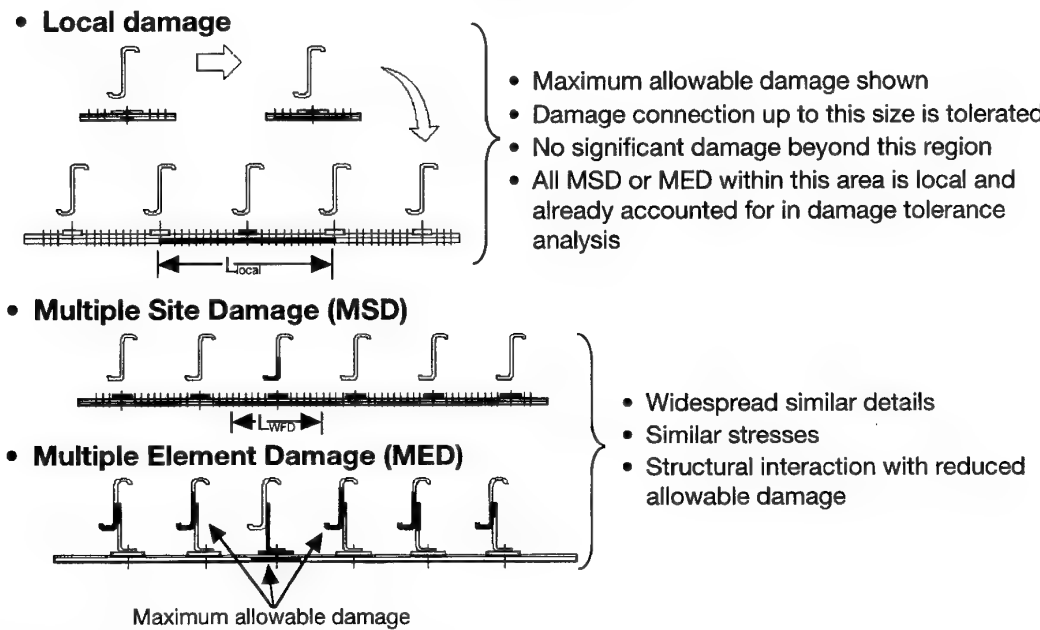


Figure 22 Example of local versus widespread MSD or MED

Dependent types of MSD and MED that are within the extent of existing damage tolerance regulation compliance assumptions are labeled 'local'. Such dependent damage is characterized by retention of residual strength capability after link-up of adjacent finite cracks. Independent types of WFD may reduce the residual strength and corresponding critical crack length substantially, *Figure 22*.

The concern for WFD thus exists when regions with similar structural details have the same high stress levels. Coalescence of multiple damage origins may potentially be catastrophic, and there is a lack of confidence in damage detection before such unsafe conditions may develop. *Figure 23* shows a typical trend for allowable local versus widespread damage which is discussed in more detail later.

Structural design philosophy is focused on the early, i.e. extreme, event, and consequently fatigue design criteria are in place which reflect this philosophy. For example, the statistical model used is Weibull, one of the family of extreme value distributions, instead of the log-normal distribution which is in more common use in the aviation industry. It should be noted that

fleet data are monitored for lessons learned, to analyze early fatigue incidents when necessary, and develop and document the demonstrated fatigue ratings of the structures. This activity has been ongoing for very many years, resulting in design standards reflecting lessons learned from a large maintained database, and high confidence in the correlation between fatigue analysis prediction and service demonstrated performance.

Given this background, it is believed that a similar designer/analyst-oriented procedure could be used for predicting thresholds for WFD. Structural design criteria specify that any structural component must equal or exceed a specific level of reliability for the duration defined by the minimum DSO. These levels of reliability range from high to very high depending upon the criticality of the component. The concept of widespread fatigue damage may add another dimension, namely a consideration of order statistics. When designing for reliability today designers/analysts must select from a menu of fatigue reliability factors that are appropriate for their structural applications. These factors are Weibull based in order to provide sufficiently high levels of reliability in the fleet without the need to address fleet size, i.e. reliability in terms of percentage, e.g. 99%. However, in the case of WFD consideration may have to be given to the first, second, or *i*th event in a fleet of *n* structures. This would force unfamiliar scenarios on designers/analysts, such as the number of fatigue events within any single component, or within *n* components per airplane, or *m* airplanes in the fleet.

The Weibull parameters characterizing structural fatigue have already been known, verified and used over the past 30 years. It was therefore logical to expand on existing fatigue reliability factor design procedures to include a WFD threshold factor which considers *i* events in samples of size *n*. A nomograph was selected as the medium to present the WFD

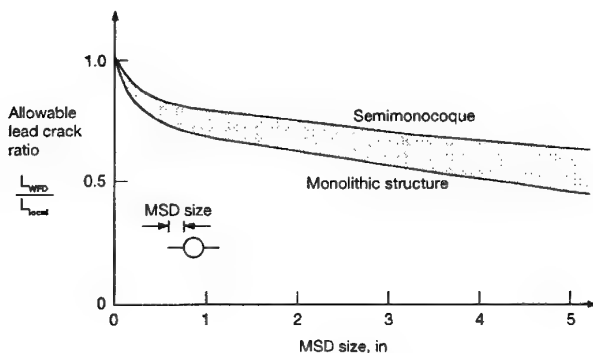


Figure 23 MSD influence on allowable lead crack size

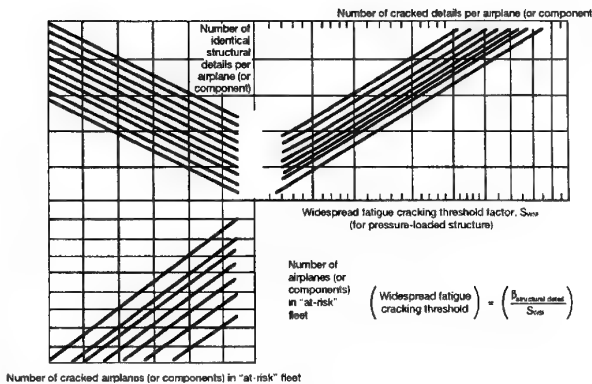


Figure 24 Nomograph for estimating WFD threshold factor for pressurized structures

threshold factor. This was done to provide the designer/analyst with a visual aid (*Figure 24*) to the interactive relationships between i fatigue events and n sample size, whether it be details per component, or components per airplane, or airplanes per fleet. The initial nomograph was developed for application to fuselage structures, i.e. predominantly pressure-loaded structural details such as fuselage lap joints, circumferential splices, and frames (*Figure 25*). The underlying assumption for the nomograph is based on the observation that airplane-to-airplane variation in fatigue is greater than component-to-component variation within the same airplane. Therefore, the graph was developed using the inverse Weibull function and a series of Weibull shaped parameters:

$$\text{Reduction factor: } \left(\frac{\beta_{\text{pop}}}{\beta_i} \right)_{\text{STR}} = [\ln(1 - F_{\text{STR}}(x_i))]^{-1} \alpha_{\text{STR}}$$

in which the subscript STR represents structural detail, structural component, or airplane. For each structural category, β_{pop} = population characteristic life to specified damage for STR, β_i = characteristic life to i th occurrence of damaged STR in a sample of n STRs, x_i = expected life to i th occurrence of damaged STR in a sample of n STRs, $F_{\text{STR}}(x_i)$ = probability of damage for an STR at x_i flights = $i/(n + 0.5)$, α_{STR} = shape parameter for STR = 8.0 for rivet holes in a

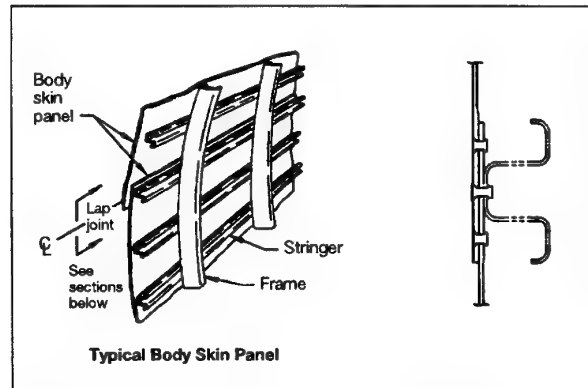


Figure 25 Typical body-skin panel – longitudinal

lap joint, 6.0 for lap joints in an airplane, 5.0 for airplanes in a fleet.

Analysts supporting the standard body and wide body airplane programs have been evaluating this procedure to ascertain the level of correlation between predictions based on the nomograph and observed fleet history. Some difficulties were encountered due to a lack of consensus on what damage extent constituted WFD. As is seen from *Figure 24*, the analyst must make certain decisions regarding sample size at risk of fatigue cracking and the WFD limit in terms of number of cracks. Nevertheless, predictions were found to be encouraging although somewhat more conservative than intended.

The example is based on a fleet of 323 airplanes with six identical lap joints per airplane and 380 equally critical rivet connections per lap joint. It was assumed that the WFD threshold was consistent with small cracks initiated at 10%, i.e. 38, of the rivet holes in a lap. *Figure 26* is a plot comparing the cracking history predicted via the factors from the nomograph against the service history as reported by the airplane operators. It is noted that the correlation at the first event is very close, but from there on the prediction becomes increasingly conservative.

Several other examples have been undertaken by program personnel and are at different stages of completion. To date all feedback indicates that the proposed S_{WSF} factor provides conservative estimates relative to service history; however, data are insufficient to proceed with refinement of the procedure. A nomograph for gust critical structures, e.g. wings, has also been developed and provided to airplane program personnel for evaluation, but there has been no feedback at this time.

Damage detection

Three principal sources of damage to airplane structures must be considered independently, *Figure 27*. Both accidental damage and most forms of environmental damage can be considered as random events that can occur at any time during the operational life of an airplane. Fatigue damage is characterized by a cumulative progression relating to airplane usage measure in flights. Detection ratings have been developed for accidental and environmental damage. A quantitative fatigue damage detection rating system is known as the DTR system. The concepts of this system have been described in earlier publications and this review

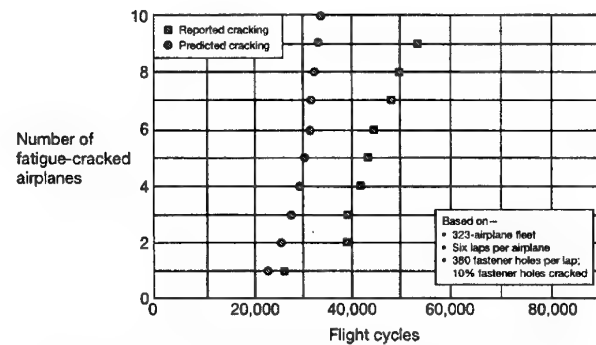


Figure 26 Comparison of predicted and actual cracking histories for example problem

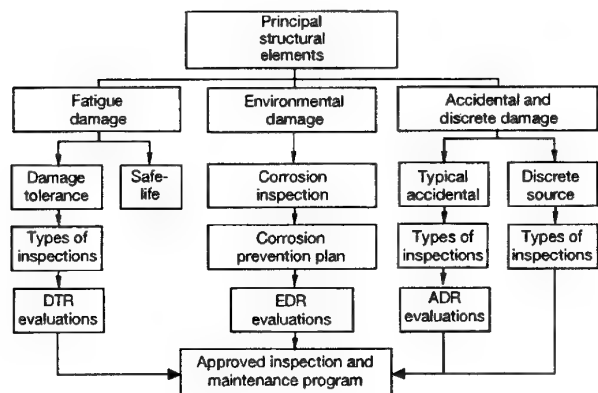


Figure 27 Principal damage sources for maintenance planning considerations

focuses on application examples that demonstrate major features.

Damage detection is a function of fleet size, number of cracks, and number and type of inspections. Three independent probabilities determine the certainty of damage detection:

- P_1 : probability of inspecting an airplane with damage;
- P_2 : probability of inspecting a detail containing a crack;
- P_3 : probability of detecting a crack in the detail.

For a single inspection of the detail considered on an airplane with damage, the probability of detection P_3 is a function of crack length, inspection check level, and detection method.

P_3 for visual inspections is based on an extensive review and analysis of fatigue cracks detected in service. Account has been taken of cracks remaining undetected during inspections prior to detection, including those assumed to have occurred but not yet detected, *Figure 28*. Detection thresholds and characteristic crack lengths are defined by a three-parameter Weibull distribution.

Detection standards used for fleet safety evaluations must recognize that many service inspections fail to detect damage beyond the detection threshold. A mean crack growth curve shape was used to describe the crack growth history prior to detection. Crack length,

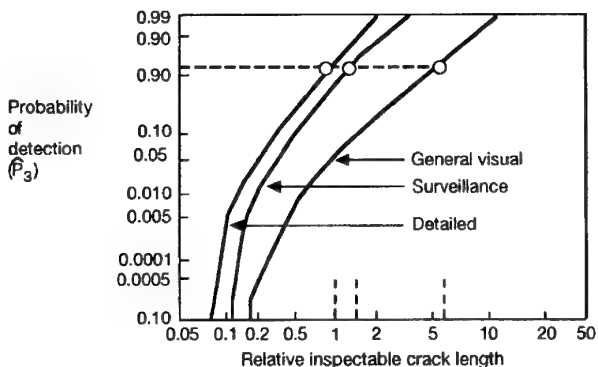


Figure 28 Relative probability of detection for visual inspection methods

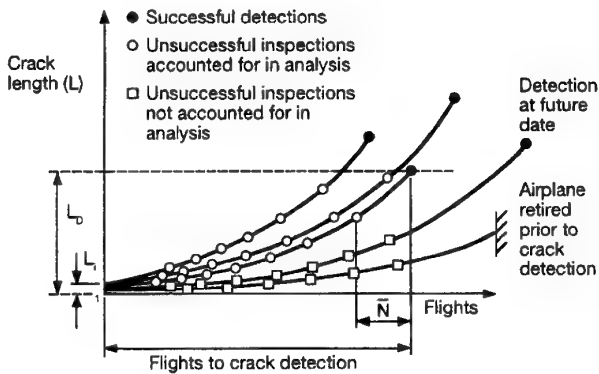


Figure 29 Detection and nondetection events

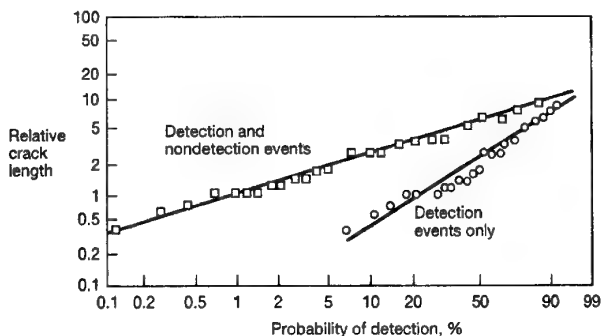


Figure 30 Effect of nondetection events on probability of detection

total flights at detection, and an assumed detection threshold after an appropriate period of service provided the necessary crack growth curve constants, *Figure 29*. Previous unsuccessful inspections correspond to nondetections that are usually 20 to 50 times more numerous than the detection events. Allowance was made for escalation in inspection intervals for the relevant period of collected service data and for cracks currently being missed that will be detected in the future. This latter point was demonstrated by successive elimination of detection events and analysis of the reduced sample. The total influence of the nondetection events is substantial, as illustrated in *Figure 30*.

Use of Nondestructive Inspection (NDI) procedures such as ultrasonic or low frequency eddy current may significantly increase the damage detection period, *Figure 31*. NDI procedures allow detection of smaller

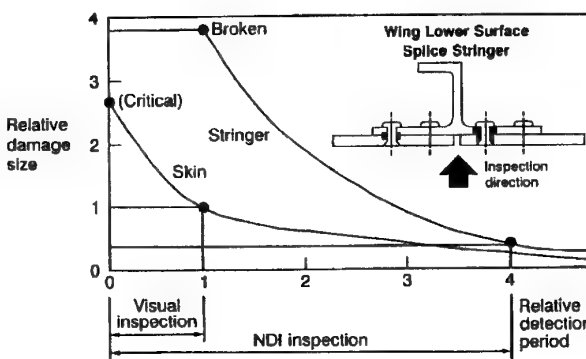


Figure 31 Visual versus NDI damage detection periods

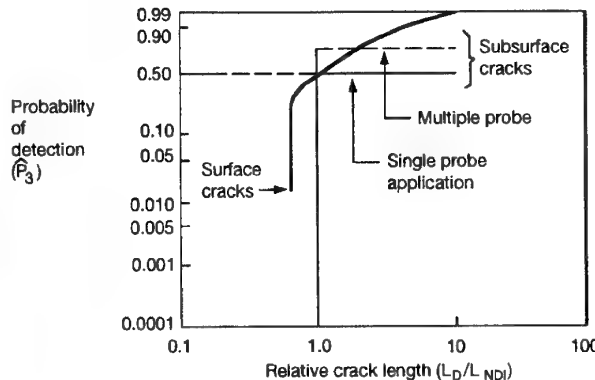


Figure 32 Probability of detection for NDI inspections

surface cracks than with visual inspection, and also allow subsurface crack detection. Therefore, an equal probability of detecting damage can be achieved with a reduced inspection frequency. Damage detection reliabilities have been established for different crack lengths in relation to the minimum detectable for typical inspection techniques and structural configurations, *Figure 32*. These P_3 curves are appropriately modified to account for visual detection of surface cracks and multiple probe applications at different locations along the same crack during the same inspection of subsurface cracks.

The crack length at the time of inspection is random. The last inspection occurs at some point during the final inspection interval, \bar{N} , *Figure 33*. Since P_3 varies significantly, the average value is determined by integrating individual P_3 s over the interval. Previous inspection detection contributions can be approximated by the P_3 values for the midpoints of each inspection interval. The cumulative probability of crack detection in at least one of several inspections is $P_3 = 1 - \prod(1 - \hat{P}_{3i})$. In some cases the inspection interval \bar{N} is greater than the damage detection period N_0 , and the probability that the inspection will occur is accounted for by calculating the average \hat{P}_3 for the inspection interval assumed equal to N_0 and using $P_3 = \hat{P}_3 N_0 / \bar{N}$ for damage detection assessments.

The calculated probability of detection does not provide a convenient measure of maintenance actions and requires products of nondetection probabilities to combine effects of types and/or levels of inspection. The

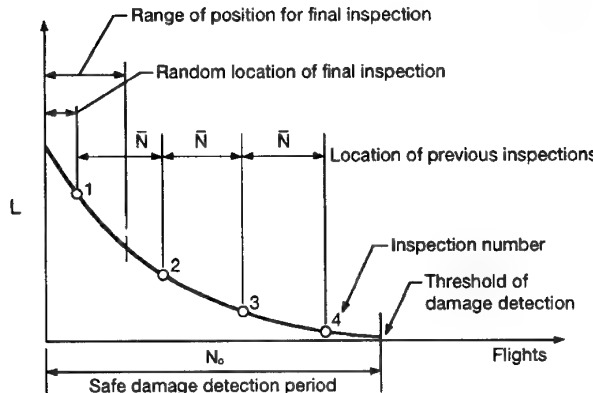


Figure 33 Multiple inspection detection consideration

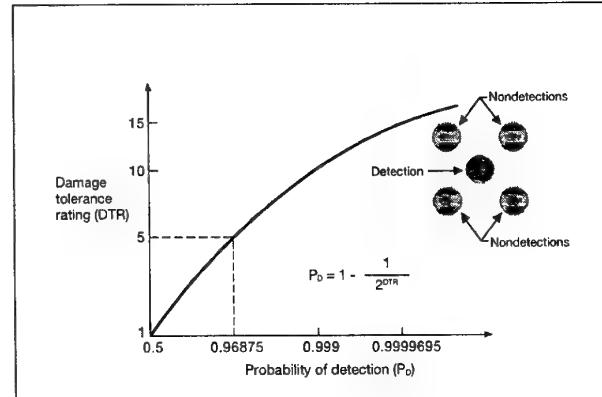


Figure 34 Probability of detection measurements

DTR is a measure of detecting at least one fatigue crack. The measuring units are the equivalent number of opportunities for detection, each with an equal chance of detection or nondetection:

$$P_D = 1 - \frac{1}{2^{DTR}}$$

where $P_D = 1 - \prod(1 - P_{di})$, $P_{di} = P_1 \cdot P_2 \cdot P_3$ for all applicable inspections.

The measurement of detectability by DTR values provides a better comparison between P_D levels on a suitable engineering scale, *Figure 34*. The detection evaluation can be performed for varying inspection intervals and methods which are summarized in a form suitable for individual operator use, *Figure 35*.

Inspection intervals

Structural inspection program planning involves fracture mechanics evaluations of crack growth and residual strength characteristics coupled to a damage

DTR CHECK FORM		ITEM W-XX	MODEL/SERIES 727-XXX																																	
TITLE WING LOWER SURFACE REAR SPAN CHORD AND SKIN		OPERATOR/DRY NO. OF CAND. AIR.	EXAMPLE XX																																	
LOCATION _____		STRUCTURE AND INSPECTION DETAILS LEAD CRACK SKIN FLANGE OF CHORD																																		
NOTES: _____																																				
INSPECTION PROGRAM DETAILS <table border="1"> <thead> <tr> <th>STRUCTURE DETAIL</th> <th>JOB CARD</th> <th>DRBC</th> <th>CHORD LEVEL</th> <th>INSPECTION METHOD</th> <th>N-1</th> <th>FREQUENCY</th> <th>N - 1</th> <th>DAMAGEMODELLING PERIOD</th> <th>N-1</th> <th>DRR</th> </tr> </thead> <tbody> <tr> <td>SPIN</td> <td>1</td> <td>C</td> <td>DIET</td> <td>100</td> <td>3000</td> <td>3000</td> <td>8000</td> <td>3.3</td> <td></td> <td></td> </tr> <tr> <td>SPAR CHORD</td> <td>3</td> <td>C</td> <td>IFEC</td> <td></td> <td></td> <td></td> <td></td> <td></td> <td></td> <td></td> </tr> </tbody> </table>				STRUCTURE DETAIL	JOB CARD	DRBC	CHORD LEVEL	INSPECTION METHOD	N-1	FREQUENCY	N - 1	DAMAGEMODELLING PERIOD	N-1	DRR	SPIN	1	C	DIET	100	3000	3000	8000	3.3			SPAR CHORD	3	C	IFEC							
STRUCTURE DETAIL	JOB CARD	DRBC	CHORD LEVEL	INSPECTION METHOD	N-1	FREQUENCY	N - 1	DAMAGEMODELLING PERIOD	N-1	DRR																										
SPIN	1	C	DIET	100	3000	3000	8000	3.3																												
SPAR CHORD	3	C	IFEC																																	
DATA CONTROL: <ul style="list-style-type: none"> (A) INDIVIDUAL OPERATOR (B) BOEING (J) JOINT BOEING/ALL OPERATORS (R) JOINT BOEING/REGULATORY AGENCY 																																				
B FUEL LEAK DTR 2 TOTAL DTR 5.3 R REQUIRED DTR 4																																				

Figure 35 Damage-tolerance rating check form for detection assessments

detection assessment. Residual strength and fatigue crack growth evaluations are combined with service-based crack detection data to produce detection reliability representing multiple type and intervals of inspections in a fleet of airplanes subjected to exploratory inspections. Such data give operators freedom to adjust quantitatively their maintenance program in any manner that is desired as long as the required reliability of damage detection is preserved.

Traditional damage tolerance evaluations often concentrate predominantly on the fracture mechanics aspects and the inspection intervals are often simply chosen to reflect half of the damage growth period from detectable to critical damage sizes. Such evaluations often fail to reflect the combined benefits of visual inspections performed during normal maintenance programs focused primarily on corrosion and accidental damage sources. The value of cumulative contributions of multiple inspections in a fleet of airplanes must also be recognized by accounting for such additional detection opportunities before the most critical change in one airplane reaches limit load damage containment capability. Several of these damage detection considerations are discussed in the following sections.

Damage detection considerations

The inspectable crack length at the time of inspection may be significantly different from the total crack length obtained by fracture mechanics calculations, depending on several factors such as location of the cracks and direction and method of inspection. For example, consider the inspectable crack length for the detail shown in *Figure 36*. If inspected visually, the crack would be detectable past A or B, depending on the side of the detail inspected. The crack must grow far enough that the tip is beyond any obstruction, in this case the sheet and sealant on the top and the sealant over the fastener on the bottom. The inspectable crack length is zero when the tip clears the obstruction edge (locations A and B), even though the actual length is significantly greater. For inspections from the bottom of the detail after the crack tip reaches C, the inspectable length will not increase, because the crack past that point will not be visible.

Design objectives for damage tolerant structures include emphasis on accessibility and inspectability. The operator desires flexible maintenance programs which allow inspection intervals for fatigue damage

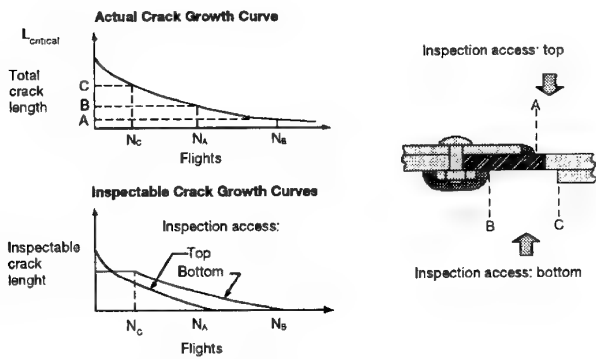


Figure 36 Inspectable crack length considerations

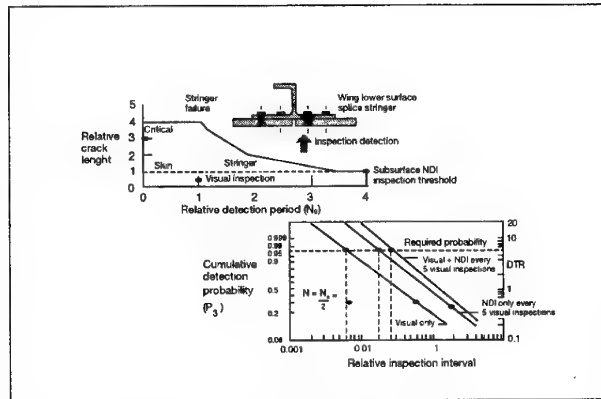


Figure 37 Cumulative detection probability – inspection method variation

inspections which are compatible with typical intervals used for corrosion and accidental damage inspections.

Changes in stress levels of about 15% can easily change the damage detection period by a factor of 2. Improved material properties can also influence the damage detection period by similar factors. Lack of accessibility for visual inspection can be alleviated by deploying nondestructive inspection techniques. Multiple site damage scenarios often lead to rapid linking of cracks in combination with reduced residual strength capability, i.e. smaller critical crack lengths.

The commonly used practice of setting inspection intervals to half the damage detection period fails to provide a quantitative damage detection reliability. Required detection probabilities result in quite different inspection intervals compared with simple factoring of the detection period by 2.

Damage detection requirements can often be met by a combination of visual and nondestructive inspections. See *Figure 31* for a simple example of visual external inspections and/or external NDI inspections. *Figure 37* shows the cumulative probabilities of detection for different combinations of inspections. It should again be noted that simple factoring of the visual or NDI detection periods by 2 gives quite different detection reliabilities.

Visual inspections can often be performed from different directions and the cumulative detection reliability must be derived accordingly. *Figure 38* shows a wing center section rear spar example for different cracking patterns (lead crack assumptions). Actual and

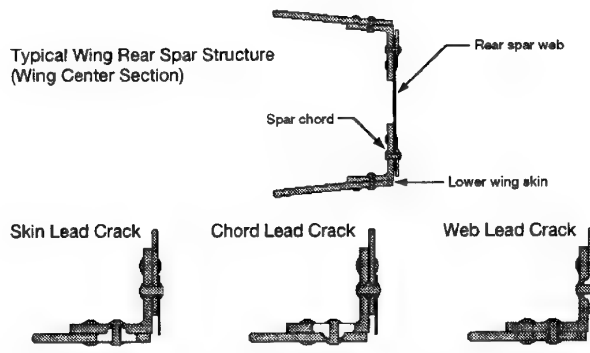


Figure 38 Wing spar chord cracking pattern examples

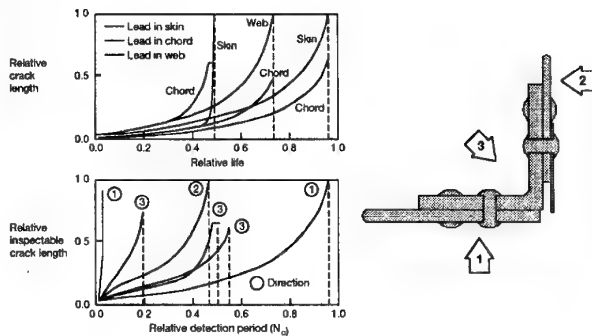


Figure 39 Spar chord crack growth curve examples – wing center section

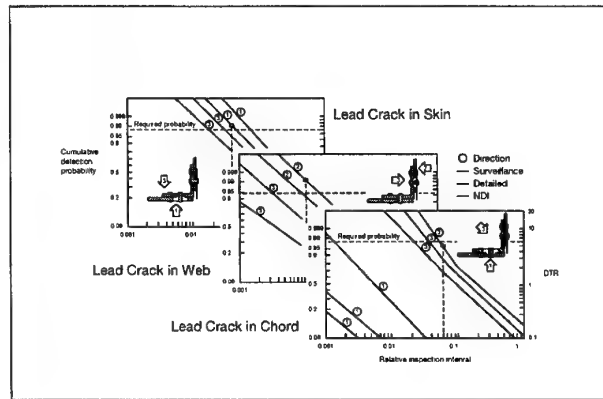


Figure 40 Cumulative detection probability – cracking pattern

inspectable crack growth curves for directions 1, 2 and 3 are shown in *Figure 39* for these three cracking patterns. Corresponding cumulative detection probabilities for different inspection options are shown in *Figure 40*. An example maintenance program providing sufficient detection probabilities is shown in *Figure 41*.

Fleet cracking detection contributions

Experience has shown that when damage is detected in the fleet, further inspections generally reveal additional damage in the same detail on other airplanes and/or in similar detail at another location. Additional damage in the fleet increases the probability of detecting at least one crack. The number of flights between occurrences in the fleet of fatigue damage to the same detail, ΔN , can be derived from actual fleet

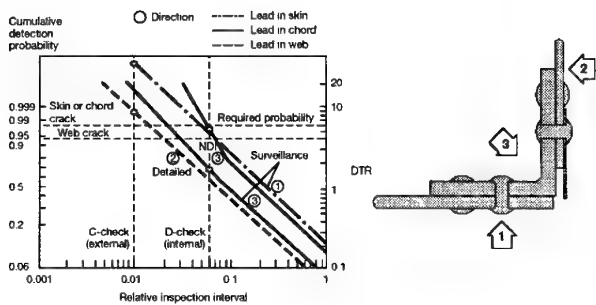


Figure 41 Cumulative detection probability pattern/variation inspection direction combinations – cracking

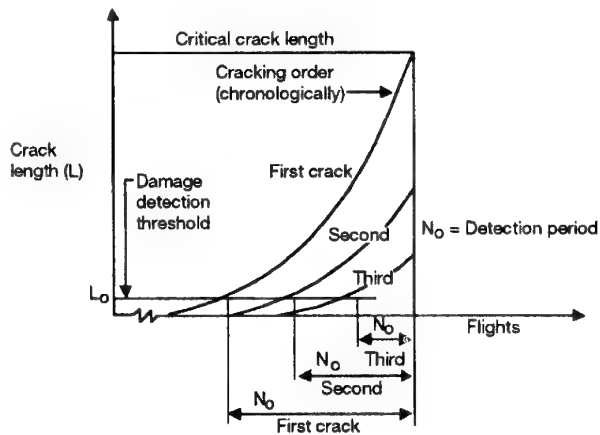


Figure 42 Multiple cracking in the fleet

cracking statistics or from fleet usage and fatigue-life distribution. If the first damage is detectable at N_1 flights, the second damage will reach the same level of detectability at $N_1 + \Delta N$, and the third at $N_1 + 2\Delta N$, *Figure 42*.

Each successive crack occurring during the damage detection period, N_0 for the first crack, has a reduced interval for detection and a shorter crack length, *Figure 43*. Taking this into consideration, the cumulative probability of detection can be determined for each crack using the same procedure. From this the probability of crack detection in the fleet is calculated, using a given inspection method and frequency, as shown below:

$$P_3 = 1 - \prod_{i=1}^m \prod_{j=1}^n (1 - \hat{P}_{3ij})$$

where \hat{P}_{3ij} is the probability of detection during the i th inspection of the j th cracked airplane during the damage detection period N_0 ; m is the number of cracked airplanes; and n is the number of inspections performed on the j th cracked airplane.

For convenience an equivalent constant probability of detection for each inspection can be defined by

$$\bar{P}_3 = 1 - (1 - \hat{P}_3)\bar{N}/N_0$$

Considering all levels of inspection in the fleet (A, B, C and D), the cumulative probability of damage detection is given by

- Number of flights available for detection of:
 - First crack in the fleet = N_0
 - Second crack in the fleet = $N_0 - \Delta N$
 - Third crack in the fleet = $N_0 - (2 \Delta N)$

Figure 43 Multiple fleet cracking contributions to damage detection

$$P_D = 1 - \prod(1 - P_{di})$$

where $P_D = P_1 \cdot P_2 \cdot P_3$, $i =$ applicable inspections.

CONTINUING AIRWORTHINESS INITIATIVES

Continuing airworthiness concerns for aging jet transports has received attention over the last 15 years. Supplemental structural inspection programs were developed in the late 1970s to address fatigue cracking detection in airplanes designed to the fail-safe principles. These evaluations were performed in accordance with updated damage tolerance regulations to reflect the state-of-the-art in residual strength and crack growth analyses based on fracture mechanics principles. Damage at multiple sites was also addressed in terms of dependent damage size distributions in relation to assumed lead cracks in different structural members. Structural audits were performed in the mid 1980s to ascertain whether these supplemental inspection programs addressed independent multiple site damage in similar structural details subjected to similar stresses.

Boeing initiated aging fleet surveys by engineering teams in 1986 to gain a better understanding of the condition of structures and systems and to observe the effectiveness of corrosion prevention features and other corrosion control actions taken by the operators. Boeing, like other manufacturers, continually reviews reported service data and other first-hand information from customer airlines in order to promote safe and economic operation of the worldwide fleet. These surveys were primarily prompted by the projected upward trend in airplane age toward and beyond original design service objectives.

Extensive industry actions were initiated in 1988 to address aging fleet airworthiness concerns prompted by the explosive decompression of a 737 over Hawaii. Model-specific Structures Working Groups have demonstrated a cooperative determination over the last five year period to make the right things happen within and across models and throughout the industry. The achievements have been impressive in the accomplishing of results in five original tasks chartered by the Airworthiness Assurance Task Force, now known as the Airworthiness Assurance Working Group, Figure 44.

Service bulletin reviews and mandatory inspections

Continuing airworthiness of jet transport structures designed to the fail-safe principles has traditionally

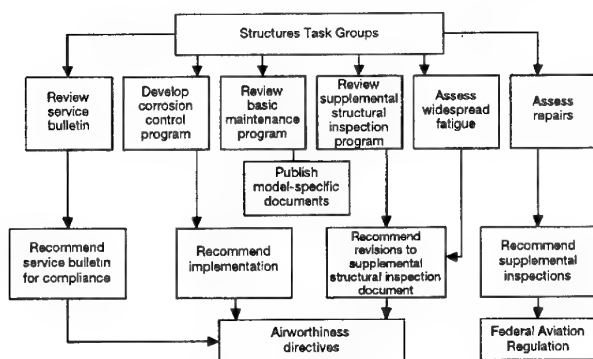


Figure 44 Continued airworthiness industry initiatives

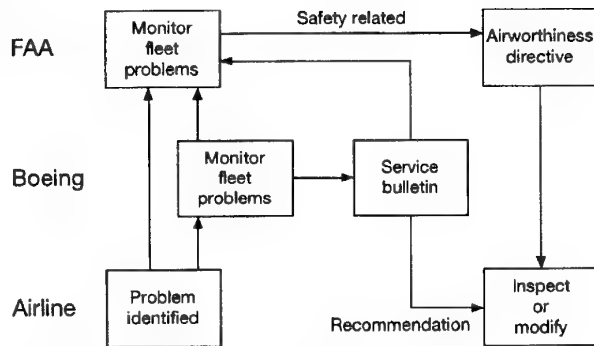


Figure 45 In-service problem actions

been ensured by inspection programs. In the event of known, specific fatigue cracking and/or corrosion problems, that if not detected and repaired had the potential to cause a significant degradation in airworthiness, the normal practice in the past was to introduce a service bulletin, Figure 45.

The net result of this process was to carry out inspections of all affected airplanes until damage was detected and then to perform the repair. Thus, continuing structural airworthiness was totally dependent on repetitive inspections. Aging airplane concerns prompted reassessment of the viability of indefinite repetitive inspections.

Aging fleet service bulletin summary documents were released in 1989 for each model formalizing Structures Working Group (SWG) recommendations for mandatory modifications or inspections, Figure 46.

It is important to note that cumulative service experience is incorporated in the design and reflected by less inspection/modification for later production units. In turn, these service experiences are incorporated in new models, often with orders of magnitude reduction in later modification efforts.

Corrosion prevention and control programs

While corrosion has always been recognized as a major factor in airplane maintenance, each airline has addressed it differently according to its operating environment and perceived needs. Manufacturers have published corrosion prevention manuals and guidelines to assist the operators, but until now there have never been mandatory corrosion control programs.

It became apparent that without effective corrosion

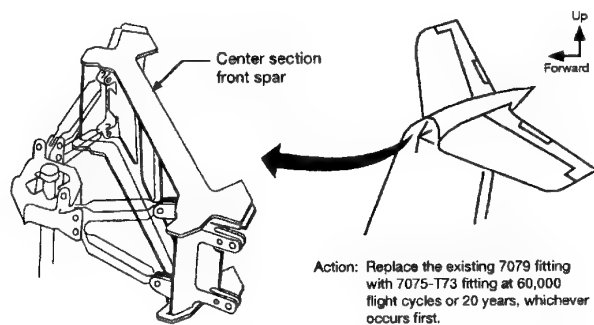


Figure 46 Mandatory service bulletin modification example for 727 horizontal stabilizer front spar center section with stress corrosion problems

control programs, the frequency and severity of corrosion were increasing with airplane age and, as such, corrosion was more likely to be associated with other forms of damage such as fatigue cracking. This, if allowed to continue, could lead to an unacceptable degradation of structural integrity, and in an extreme instance, the loss of an airplane.

The working groups have recognized the need for a universal baseline minimum corrosion control program for all airplanes to prevent corrosion from affecting airworthiness. Maximum commonality of approach within and between each manufacturer to ensure consistent and effective procedures throughout the world has been a key objective for the working groups. The program requirements apply to all airplanes that have reached or exceeded the specified implementation age threshold for each airplane area. The specific intervals and thresholds vary between models, but all programs follow the same basic philosophy.

The corrosion control and prevention program provides structural access and inspections of internal structure and structure hidden by fairings in a disciplined and consistent manner. While many operators may already have covered these areas in existing maintenance programs, the net effect has been an increased awareness for the value of Corrosion Prevention and Control Programs (CPCPs), Figure 47.

There is general agreement in the airplane industry that corrosion prevention and control procedures are needed on all current in-production airplanes and for future generations of airplanes.

Supplemental fatigue inspection programs

Supplemental structural inspection documents were released between 1979 and 1983 for all aging Boeing jet transport models. Their purpose was to ensure continued operation of the aging fleet by timely detection of new fatigue damage locations. These documents have been updated on a regular basis to reflect service experience and operator inputs. In the light of current aging fleet concerns, these inspection programs were to ensure adequate protection of the aging fleet. The major focus of these reviews was:

- adequacy of the present fleet leader sampling;
- inclusion/deletion of principal structural elements.

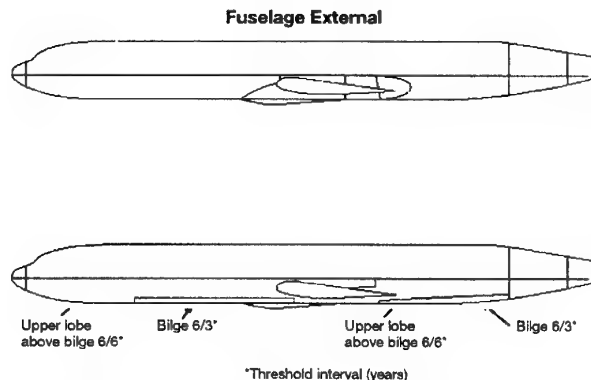


Figure 47 727 corrosion control program – example

Revisions to 707, 727, 737 and 747 SSIDs included changes to approximately 10 significant structural items for each model. Some PSEs were not included in the original SSID on the basis that damage would be obvious before safety was affected. A review of those items resulted in adding several items to the SSID, primarily some hidden wing structures previously deleted on the basis of fuel leaks to signify fatigue damage.

Thin gauge fuselage structure was not included in the initial SSIDs on the basis of test and service evidence that skin cracks would turn at frame locations and result in a safe decompression. Consideration of aging fleet damage in adjacent bays prompted coverage of thin gauge fuselage structure, 1.4 mm thick or less for models 727 and 737. The 747 fuselage skins were already included in the initial SSID because of thicker gauges.

Widespread fatigue damage

The present rules for airplane structural design have evolved from successful experience and lessons learned in service. As opposed to earlier commercial airplanes, the first generation of jet transports have not become technically obsolete before portions of the worldwide fleet have reached and exceeded original design service objectives. Dependent damage at multiple sites was recognized in revised damage tolerance regulations in the late 1970s. Independent damage in similar details subjected to similar stresses has long been recognized as a potential continuing airworthiness problem. Fuselage structure is typically more susceptible to WFD because of numerous similar details subjected to pressure cycle loads with moderate flight-by-flight variations.

An international task group was chartered in 1990 composed of manufacturers and operators to investigate and propose appropriate actions to address WFD concerns by timely discovery of any aging fleet problems. The Structural Audit and Evaluation Task Group (SAETG) performed an extensive data collection and analysis activity to determine candidate options that have applicability to the identified concerns. While all the adopted SAETG options are valid to some extent in predicting the onset and location of multiple site damage and multiple element damage, none of the options provides foolproof safeguards. Ultimately conscientious and reliable inspections of the airplane structure are the key to confidence in ensuring continuing airworthiness.

Structural repair assessments

Inevitably airplanes accumulate repairs. For each model, Structural Repair Manuals (SRMs) assist the operator in ensuring that typical repair action maintains the airframe structural integrity. Other larger repairs are handled by individually prepared and approved engineering drawings. Traditionally, these repairs have primarily focused on static strength and fail-safe aspects of the structure after repair, with commonsense attention to durability considerations. For several years, however, there has been an additional emphasis on the need for structures to be damage tolerant. Achieving damage tolerance demands knowledge of potentially critical structural elements, an understanding of damage

growth and critical size, and an inspection program to ensure timely detection.

Repairs may affect damage tolerance in different ways. An external patch on the fuselage can hide the primary structure to an extent that supplemental inspections may be required, *Figure 48*. Other repairs may interfere with obvious means of detecting damage such as skin repairs on the lower wing with sealant that prevents fuel leakage. Repairs located in low stress areas with slow crack growth rate can have damage tolerance provided by existing maintenance. Several Structures Task Groups (STGs), manufacturer and AAWG subcommittee meetings were held during 1990 and 1991. Industry concern for the direction of these activities resulted in formation of the Repair Assessment Task Group (RATG). The thrust of these activities has been focused on updates of the SRMs and model-specific repair assessment documents approved by the FAA.

Model-specific SRMs are being updated by the manufacturers to reflect damage tolerance repair considerations. The goal is to complete these with initial emphasis on fuselage pressure boundary structures. Separate model-specific documents outside the SRMs have been prepared by Boeing for four aging airplane models. The uniformity/similarity of these repair assessment procedures are important to simplify operator workload. The manufacturers have spent considerable time over the last three years to achieve commonality of the repair assessment process.

Thresholds for assessments of existing repairs are based on fatigue damage considerations and specified for each model in flight cycles. While threshold recommendations vary between manufacturers, they are typically 75% of design service objectives and range from 15,000 to 60,000 flight cycles for long and short haul airplanes respectively. Guidance material documents for each model provide a list of structures for which repair assessments are required. *Figure 49* shows one example of model-specific Boeing repair assessment guidelines for inspection interval selections.

CONCLUSIONS

Timely damage detection is the key element in ensuring structural damage tolerance. Extensive testing, analysis and service records have been employed to provide new technology and procedures that meet damage tolerance regulations for new and aging jet transports.

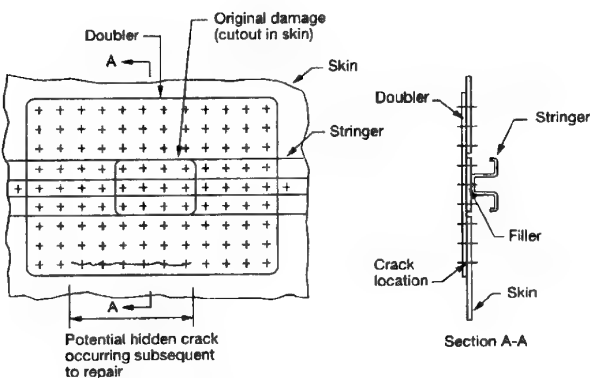


Figure 48 Typical fuselage external skin repair

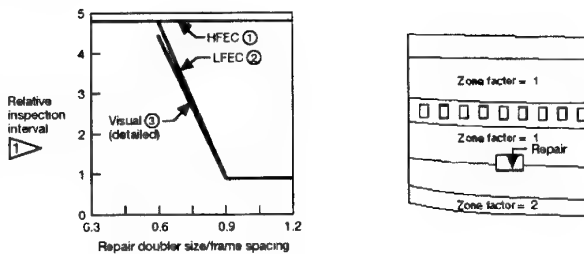


Figure 49 Inspection options for fuselage skin repairs requiring supplemental inspections

Damage detection assessments for environmental, accidental and fatigue damage sources should reflect a rational coupling between structural characteristics and maintenance program parameters.

Damage tolerance verification includes assessments of allowable damage, damage detection periods for different cracking patterns, and inspection program efficiency. Traditional fracture mechanics research and applications tend to focus on structural characteristics, and the practising engineer is often encouraged to recommend inspections based on simple factoring of damage detection periods. This practice tends to result in variable and unknown fatigue damage detection reliability levels. This review has provided some examples of a more rational approach to development of flexible maintenance programs without compromising safety.

Continuing airworthiness challenges for aging airplanes have been addressed over the last 15 years. Aging fleet concerns have resulted in joint industry, operator and airworthiness authority actions. Mandatory modifications in lieu of continued inspections as well as mandated corrosion prevention programs are examples of prudent actions to permit continued safe operation of jet transports until their retirement from service for economic reasons. Structural repair assessment guidelines have also been established to ensure damage detection by supplemental inspections for some categories of repair.

Additional challenges of local damage tolerance capabilities have been addressed in recent years to establish positive initiatives to control widespread fatigue damage effects on continuing airworthiness.

The design, construction, operation and maintenance of airplanes take place in a changing and dynamic arena, with new technology needs and new players. The structural safety system may never be perfect, but it has produced an enviable record. Damage detection is a key element of damage tolerance assurance. Vigilance must be exercised to maintain focus on prudent inspections and preventative actions for environmental, accidental and fatigue damage.

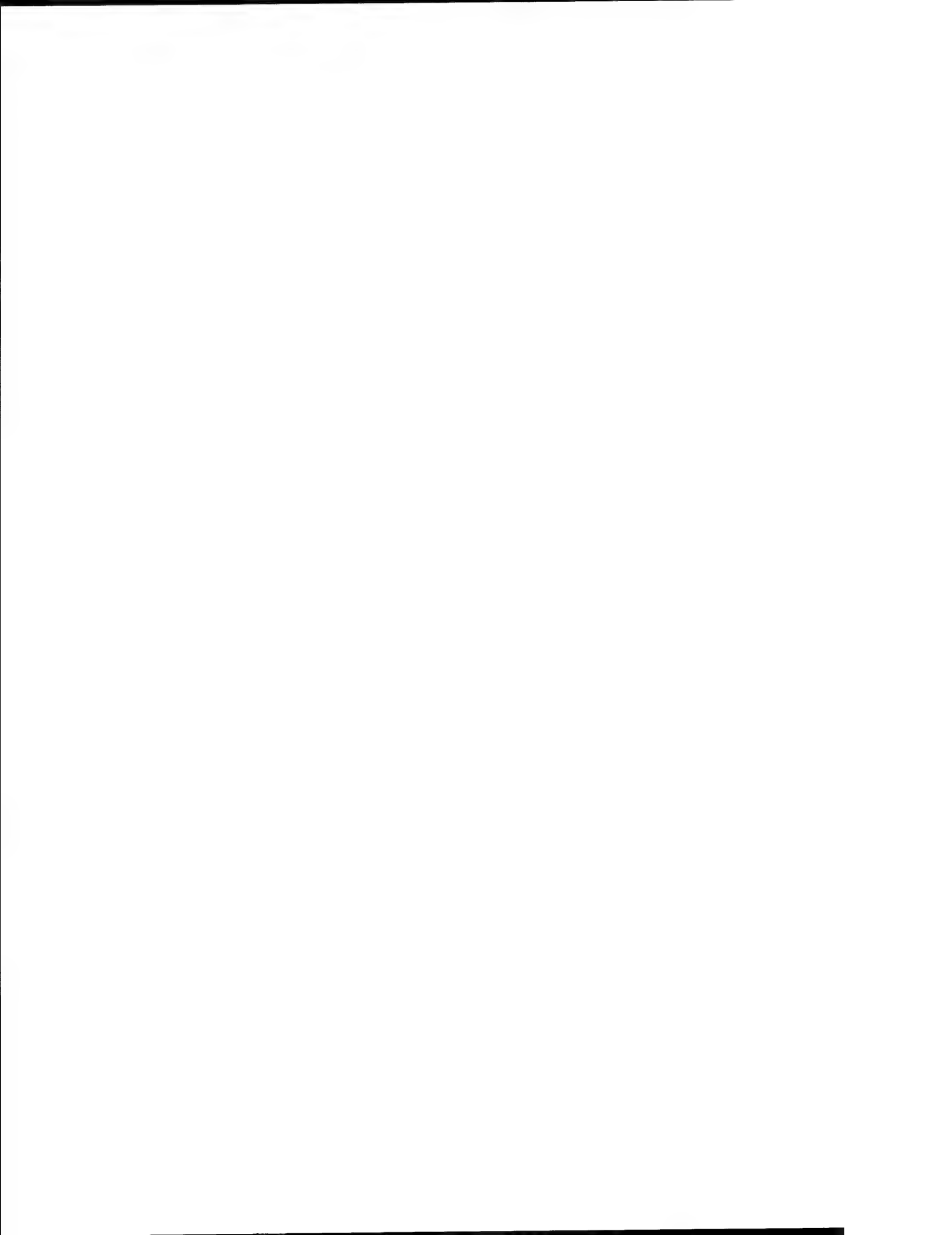
ACKNOWLEDGEMENTS

The author would like to acknowledge the graphics and publications support from Mr W.J. Brewer from the Structures Engineering organization of Boeing Commercial Airplane Group, and Mr Floyd Stewart

and staff from Boeing Information and Support Services, Graphic and Media Design Resources.

REFERENCES

- 1 Whittaker, I. C. and Besuner, P. M., A reliability analysis approach to fatigue life variability of aircraft structures. Air Force Materials Laboratory Technical Report AFML-TR-69-65, April 1969.
- 2 Whittaker, I. C., Development of titanium and steel fatigue variability model for application of reliability analysis approach to aircraft structures. Air Force Materials Laboratory Technical Report AFML-TR-72-236, October 1972.
- 3 Broek, D., Damage tolerance in practice, AGARD Lecture Series No. 97 on Fatigue Mechanics in Practice. Delft, The Netherlands, October 1978.
- 4 Craig, L. E. and Goranson, U. G., Airworthiness assessment of Boeing jet transport structures. 10th Symposium of the International Committee on Aeronautical Fatigue (ICAF), Brussels, Belgium, May 1979.
- 5 Goranson, U. G., Hall, J., Maclin, J. R. and Watanabe, R. T., Long life damage tolerant jet transport structures. ASTM Symposium on Design of Fatigue and Fracture Resistant Structures, November 10–11, 1980.
- 6 Galda, K. H., Maintenance system by means of damage tolerance principle. 13th Symposium of the International Committee on Fatigue (ICAF), Pisa, Italy, May 22–24, 1985.
- 7 Broek, D. *Elementary Engineering Fracture Mechanics*, 4th edn. Martinus Nijhoff, 1987.
- 8 Miller, M., Luthra, V. K. and Goranson, U. G., Fatigue crack growth characterization of jet transport structures. 14th Symposium of the International Committee on Aeronautical Fatigue (ICAF), Ottawa, Canada, June 8–12, 1987.
- 9 Swift, T., Damage tolerance in pressurized fuselages. 11th Planetea Memorial Lecture, 14th Symposium of the International Committee on Aeronautical Fatigue (ICAF), Ottawa, Canada, June 8–12, 1987.
- 10 Goranson, U. G. and Miller, M., Aging jet transport structural evaluation programs. 15th Symposium of the International Committee on Aeronautical Fatigue (ICAF), Jerusalem, Israel, June 21–23, 1989.
- 11 Whittaker, I. C., Miller, M. and Goranson, U. G., Durability and damage tolerance evaluations of jet transport structures. 5th International Conference on Structural Safety and Reliability (ICOSSAR), San Francisco, CA, August 1989.
- 12 Sampath, S. G. and Broek, D., The prospect of detecting and dealing with widespread fatigue damage: threshold for inspecting MSD susceptible lap splices. International Conference on Aircraft Damage Assessment and Repair, Melbourne, Australia, August 26–28, 1991.
- 13 Whittaker, I. C., Stilwell, P. B. and Sizemore, D. R., Fleet fatigue cracking threshold prediction. 16th Symposium of the International Committee on Aeronautical Fatigue (ICAF), Tokyo, Japan, May 20–24, 1991.
- 14 Schijve, J., Multiple site fatigue damage of riveted joints. Proceedings of the International Workshop on Structural Integrity of Aging Airplanes, Atlanta, GA, March 31–April 2, 1992.
- 15 Schmidt, H. J. and Brandecker, B., Results of the AAWG industry committee on widespread fatigue damage. Proceedings of the International Workshop on Structural Integrity of Aging Airplanes, Atlanta, GA, March 31–April 2, 1992.
- 16 Swift, T., Unarrested fast fracture. Proceedings of the International Workshop on Structural Integrity of Aging Airplanes, Atlanta, GA, March 31–April 2, 1992.
- 17 Broek, D., The effects of multi-site-damage on the arrest capability of aircraft fuselage structures. Fracture Research TR9302, June 1993.
- 18 Goranson, U. G., Damage tolerance facts and fiction. 17th Symposium of the International Committee on Aeronautical Fatigue, Engineering Material Advisory Service Ltd., 17-1 (1993–1996).
- 19 Thomson, D., Hoadley, D. and McHatton, J., Load tests of flat and curved panels with multiple cracks. Foster-Miller Draft Final Report to the FAA Center, September 1993.
- 20 Bigelow, C. A. and Tan, P. W., An integrated methodology for assessing widespread fatigue damage in aircraft structures. Proceedings of the FAA-NASA 6th International Conference on the Continued Airworthiness of Aircraft Structures, Atlantic City, NJ, June 27–28, 1995, pp. 121–138.
- 21 deWit, R., Fields, R. J., Low III, S. R., Harne, D. E. and Foecke, T., Fracture testing of large-scale thin-sheet aluminum alloy. NIST Report 5661, Prepared for FAA, May 1995.
- 22 Goranson, U. G., Aging aircraft airworthiness initiatives. *The Japan Society of Mechanical Engineering Journal*, 1995, **98-915**, 101.
- 23 Gruber, M. L., Mazur, C. J., Wilkins, K. E. and Worden, R. E., Investigation of fuselage structure subject to widespread fatigue damage. Final Report to the FAA, DOT/FAA/AR-95/47, October 1995.
- 24 Harris, C. E., Starnes Jr., J. H. and Newman Jr., J. C., Development of advanced structural analysis methodologies for predicting widespread fatigue damage in aircraft structures. Proceedings of the FAA-NASA 6th International Conference on the Continued Airworthiness of Aircraft Structures, Atlantic City, NJ, June 27–28, 1995, pp. 139–164.
- 25 Newman Jr., J. C. and Dawicke, D. S., Fracture analysis of stiffened panels under biaxial loading with widespread cracking. NASA Report TM 110197, November 1995.
- 26 Wang, L., Brust, F. W. and Atluri, S. N., Computational predictions of the NIST multiple site damage experimental results. FAA Center of Excellence Report, Georgia Institute of Technology, August 1995.
- 27 McGuire, J. F. and Varanasi, S. R., Boeing structural design and technology improvements. *The Boeing Airliner*, April–June 1996.
- 28 Gruber, M. L., Wilkins, K. E. and Worden, R. E., Investigation of fuselage structure subject to widespread fatigue damage. Proceedings of the FAA-NASA Symposium on Continued Airworthiness of Aircraft Structures, Atlanta, GA, August 1996.
- 29 Whittaker, I. C. and Chen, H. C., Widespread fatigue damage threshold estimates. Proceedings of the FAA-NASA Symposium on Continued Airworthiness of Aircraft Structures, Atlanta, GA, August 1996.



PII: S0142-1123(97)00047-9

Fatigue crack initiation in alpha-beta titanium alloys

J.A. Hall

OREMET Titanium, 530 34th Avenue SW, Albany, OR 97321 USA (formerly
AlliedSignal Engines, Phoenix, AZ, USA)

Fatigue crack initiation constitutes that part of total life, which includes the nucleation life, N_n , of an initial crack-like-discontinuity (CLD) and the growth life, N_s , of the CLD to an observable size called an initiated crack. This sequence dominates the total fatigue life of defect-free alpha-beta titanium alloys. The mechanisms of CLD formation and its growth to the initiated crack at room temperature are reviewed in light of controlling microstructure and other metallurgical features. Recommendations are made for improving fatigue crack initiation resistance with consideration to practical limitations. © 1998 Elsevier Science Ltd.

(Keywords: titanium; fatigue; microstructure)

INTRODUCTION

When considering those factors which influence total fatigue history of a metallic component, the total life, N_t , can be partitioned into at least four components as outlined in *Table 1* and illustrated in *Figure 1*.

Table 1 outlines the concept of total fatigue life that involves an understanding a material's intrinsic defects, as well as those influenced by manufacturing, maintenance and service. This extends to understanding the growth of these defects to a size detectable by applicable inspection procedures. This point is often defined as the initiation life in fatigue, N_i . From this point on, cracks are often described using linear elastic fracture mechanics (LEFM). Exercise caution when in the region where small crack behavior is evident¹⁻⁴.

This paper discusses the early components of fatigue life (N_n and N_s) in titanium alloys leading up to the detectable fatigue crack, a_i . This important phase of fatigue life will be addressed in light of reported

mechanisms and potential metallurgical influences on them. Examples of behavior, with discussions on how the alloy's characteristics, including structure and its manufacturing methods, are presented in this paper. The final discussions will focus on practical issues associated with applying the best, or ideal, microstructure for fatigue crack initiation resistance.

FATIGUE CRACK NUCLEATION, N_n , THE GENERATION OF CRACK-LIKE-DISCONTINUITY (CLD) OF SIZE, A_n

Some time in a fatigue-loaded component's service life there becomes a physically present, although perhaps not detectable, CLD. This is the nucleus of a crack. These nuclei may pre-exist any service exposure. In fact, the nuclei may be a remnant of the material's manufacturing history.

The incidence of melting and processing induced

Table 1 Components of total fatigue life

$$N_t = N_n + N_s + N_\sigma + N_\delta, \text{ where:}$$

N_t = Total number of cycles of fatigue life which must be defined relative to some criteria

N_n = Number of cycles to nucleate a CLD of dimension a_n . An understanding of how the CLDs relate to imposed fields of cyclic and static stress, intrinsic and extrinsic environments. It is an important area of study and is seldom quantitatively integrated into structural integrity philosophies.

N_s = Number of cycles of small crack growth, where growth is very dependent upon structure of the material and where the behavior of such cracks (commonly described as small crack behavior) deviates from extrapolations of conditions described by LEFM. These deviations are usually non-conservative^{3,4}.

N_σ = Number of cycles of crack growth characterized by LEFM. In general, the material can be considered as a continuum; the cracks are large by the definition of Ref. 4.

N_δ = Number of cycles of growth characterized by plasticity, wherein the crack size is too large to be well described by LEFM analysis. Here, elastic-plastic crack mechanics (EPCM) or fully plastic crack mechanics (FPCM) is applied.

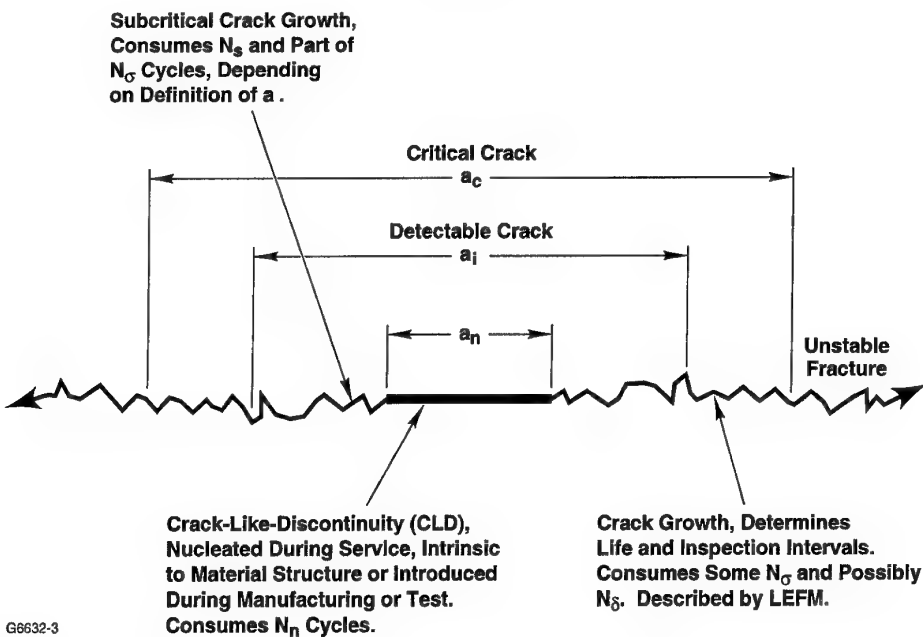


Figure 1 Schematic concept of a CLD and its extension to critical size, characterized by unstable crack growth

defects is small. The titanium and forging industries are rapidly moving toward their elimination through improved ingot manufacturing methods and improved forging practices, inspection and process control. It is appropriate to consider, in the design life calculations, the generation of a CLD of size a_n , in defect-free material to take maximum advantage of the intrinsically available N_n .

In the remaining paragraphs, normally occurring microstructures in titanium alloys will be discussed, in anticipation of the arrival of defect-free forgings. Reference will be made to the controlling microstructural elements in the processes associated with crack nucleation.

Among these, in alpha or alpha-beta alloys, are:

- D_α , [or D_a in Figure 2(a)] the primary alpha grain size;
- D_c , in Figure 2(b), the packet or colony size of alpha platelets or needles;
- D_β , [or D_b in Figure 2(c)] the prior beta grain size.

When the microstructure contains large domains in which the bulk of the alpha phase is crystallographically aligned or nearly aligned, the controlling element is likely to be that domain, D_t in Figure 2(d). D_t and D_c may be identical in some cases, or at least closely related.

LOW CYCLE FATIGUE (LCF) CRACK NUCLEATION IN LEAN ALPHA-BETA ALLOYS

Eylon and Pierce, in Ti-6Al-4V, demonstrated that the portion of life attributed to crack nucleation and growth to a detectable flaw size is $> 85\%$ ⁵; Figure 3 illustrates this point and gives emphasis to the importance of crack nucleation⁵. Note that the a_i in Figure 3 is ca 67% of the widely published detection limits of conventional non-destructive evaluation (NDE), (0.75 mm). Yet $> 85\%$ of the specimen's total life is

expended getting there. A close analysis of the information reveals less scatter and slightly higher N_i/N_f ratio with finer, equiaxed structures⁵.

Many studies of fatigue crack nucleation in alpha and alpha-beta titanium alloys attribute the process, in part, to the occurrence of heterogeneous deformation in the form of intense slip bands. The slip bands interact with phase boundaries, accumulated deformation debris, and tensile stress components in the generation of CLDs⁵⁻²⁵.

Crack nucleation sites

For notched ($K_t = 2$, $R = -1$) fatigue tests on mill annealed Ti-6Al-4V, Benson *et al.*, demonstrated that for all but the lowest stresses, the nucleation sites at room temperature and at 315°C were slip bands in the alpha phase⁶. Surface replicas from electropolished surfaces, examined with optical microscopy techniques, revealed small cracks on the slip bands as early as 3% of the total life. It was further revealed that these cracks were seldom deeper than one grain diameter before propagating across the notch width⁶. Alpha-beta interfaces served as initiation sites only at very low stress, in room temperature tests, with no detectable slip bands⁶.

Early work by Wells and Sullivan on Ti-6Al-4V, with LCF tests at a variety of temperatures to 315°C and at room temperature in salt water, revealed some fundamental information on crack nucleation²². In all cases, the dominant crack nucleation mechanism includes the working of persistent slip bands, as revealed by transmission electron microscopy on surface replicas. When an occasional alpha particle boundary separation was the nucleation event, the separation was preceded by slip in the alpha phase. Figure 4 shows transmission electron microscopy (TEM) replica micrographs of specimens with low and high strain range LCF on smooth specimens. Slip bands are evident in both cases. In Figure 4(b), slip traces appear

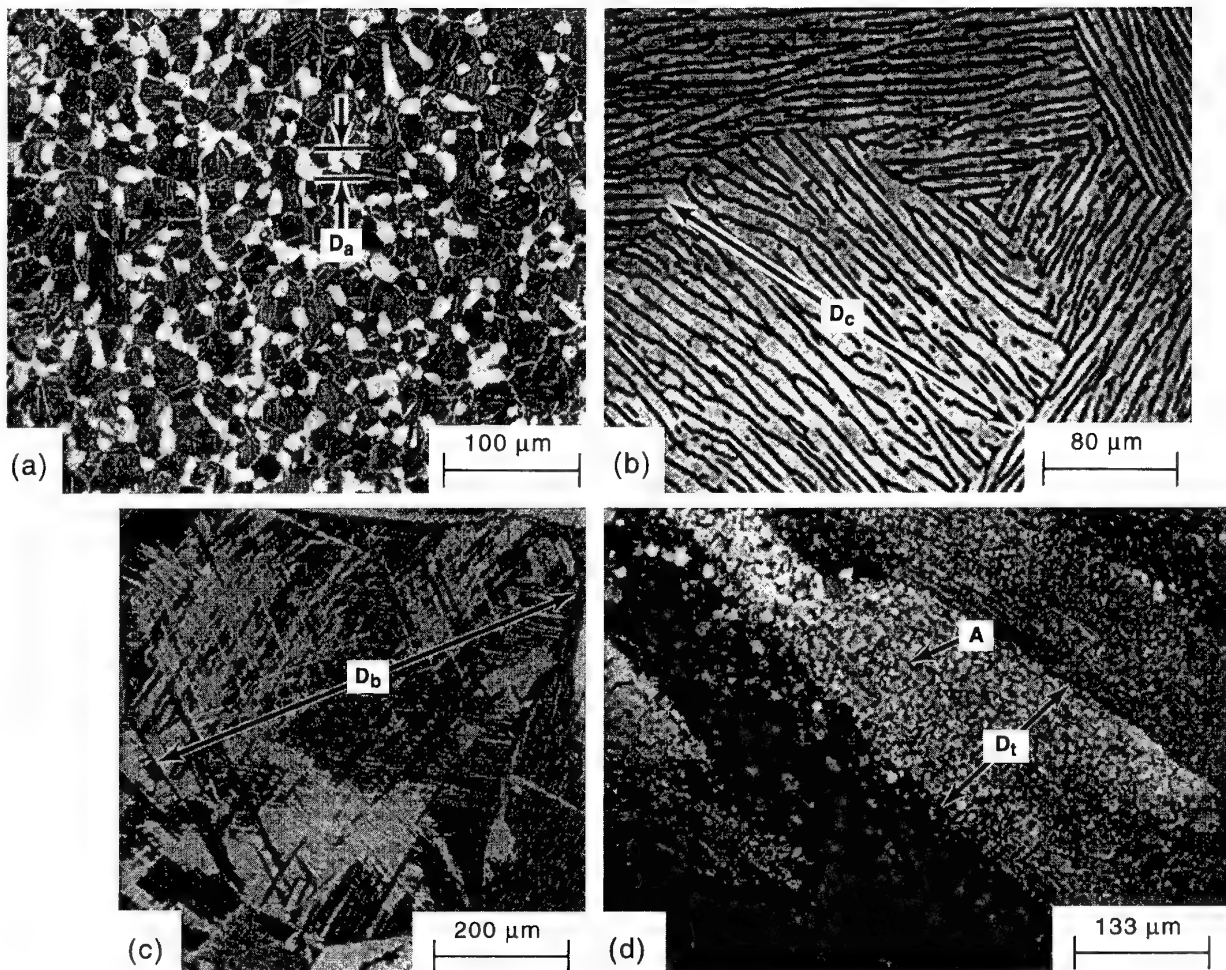


Figure 2 (a) Near-alpha alloy, processed high in the alpha-beta phase field. D_a defines the primary alpha grain size. (b) Near-alpha alloy, beta processed with obvious colony microstructure. D_c defines colony size. (c) Beta heat treated Ti-6Al-4V. Prior beta grain is outlined with grain boundary alpha. D_b defines the beta grain size. (d) Fine alpha grain Ti-6Al-4V, viewed using polarized light, showing large texture domain. Small alpha grain D_a , at A. D_t defines the texture domain size which may be effectively larger than D_b

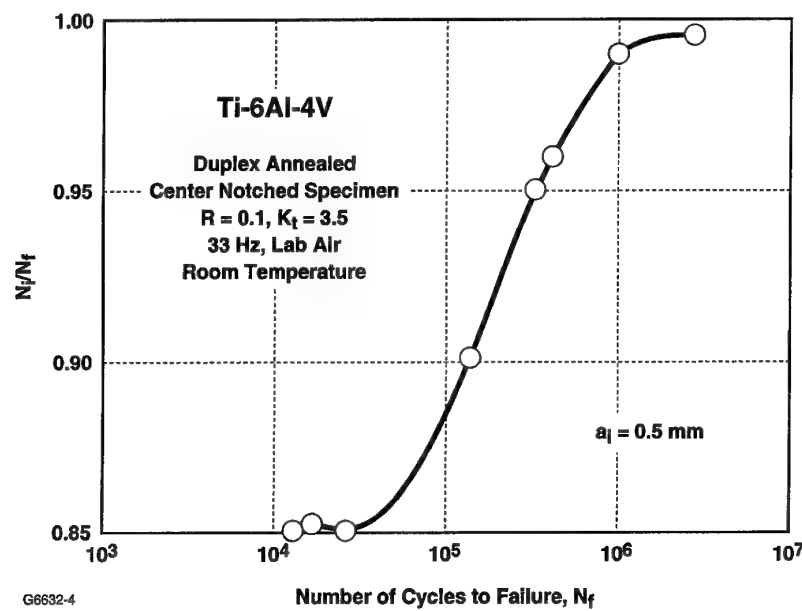


Figure 3 Fraction of total life consumed initiating a 0.5 mm crack, a_i , in flat, center notched, $K_t = 3.5$ LCF, tested at room temperature⁵

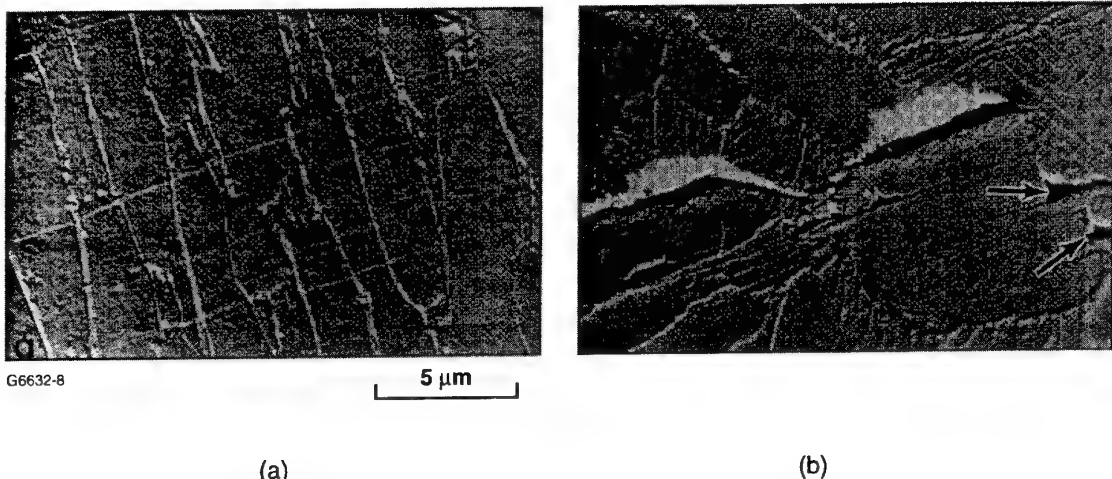


Figure 4 Ti-6Al-4V, room temperature LCF, $R = -1.0$, TEM replica micrograph from polished gage section. (a) $\Delta\epsilon_i = 0.009$, $N = 10\,419$. Note the persistent intra-alpha particle slip bands. (b) $\Delta\epsilon_i = 0.016$, $N = 1204$. Note the persistent slip bands associated with both boundary and intra-alpha particle crack nucleation²²

to have been associated with even the interface separation²². *Figure 5* illustrates the relationship of intense slip with the nucleation of a_n in a beta annealed + aged, near alpha, alloy tested in smooth, LCF⁸.

In these cases, intense slip plays an important role in creating the CLD of dimension a_n , associated with fatigue crack nucleation. Even the case of alpha boundary nucleation is not clearly separable from this mechanism. In the work by Benson *et al.*, it was reported that at low cyclic strains, interface nucleation was observed in the absence of detectable slip lines⁶. In the report, local strain levels were such that the inelastic strain portion of the total strain was small, leaving slip traces of a small dimension that escapes observation by the optical replica techniques used.

Hydrogen effects

In addition, internal and external hydrogen may play a role in creating CLD. For example, where there is a hydrostatic tension component of a local stress,

hydrogen will tend to migrate to these regions. Due to the interaction of this interstitial atom with dislocations, cross slip becomes energetically unfavorable, further intensifying the slip bands²⁶.

Hydrogen effects on CLD becomes important during application of dwell at maximum load, with low frequency LCF and an effectively high local mean stress (high R). In theory, where D is large and the resultant slip path is long, basal slip intensification would occur with possible enhanced hydrogen transport through a continuous beta phase. Therefore, refined structure (small D_α , D_c , D_β and D_t) would be beneficial.

Substructure effects

To clarify LCF crack nucleation, examine the work of Chu *et al.* on Ti-6Al-2Nb-1Ta-0.8Mo⁷. Room temperature creep strain was applied to various levels up to 2.7%, prior to LCF testing. A definite increase in life was found if the prior creep strain had exceeded 0.2%. The results are reproduced in *Figure 6*. The authors attribute the increased life to the generation of a reasonably stable homogeneous dislocation network. The network delayed the generation of planar slip bands under fatigue cycling, postponing the onset of the CLD nucleation events. TEM observations proved the dislocation substructures of specimens subjected to both creep + LCF and LCF alone. Dislocation substructure observations gives evidence that preconditioning and/or periodic reconditioning of titanium alloy components establishes controlled dislocation arrays may offer some component LCF life advantages.

HIGH CYCLE FATIGUE (HCF) CRACK NUCLEATION IN LEAN ALPHA-BETA ALLOYS

Peters *et al.* studied HCF in highly textured Ti-6Al-4V, with $R = -1$, in vacuum, laboratory air and in salt water environments¹⁵. They found that moist air is an aggressive environment, especially where the stress and crystallographic orientations favor basal plane fracture. In both air and salt water tests, basal plane cracks were the observed CLDs. However, little basal plane cracking was observed in vacuum tests.

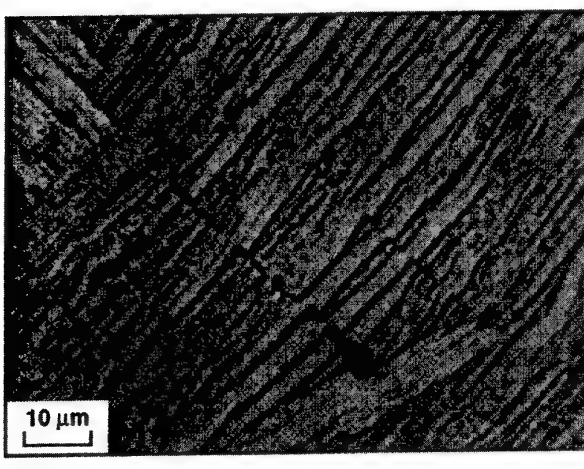


Figure 5 Beta annealed, near alpha, alloy. Slip bands in alpha colony and crack nucleation at colony boundary. LCF, $K_t = 1.0$, $R = 0.3$, room temperature⁸

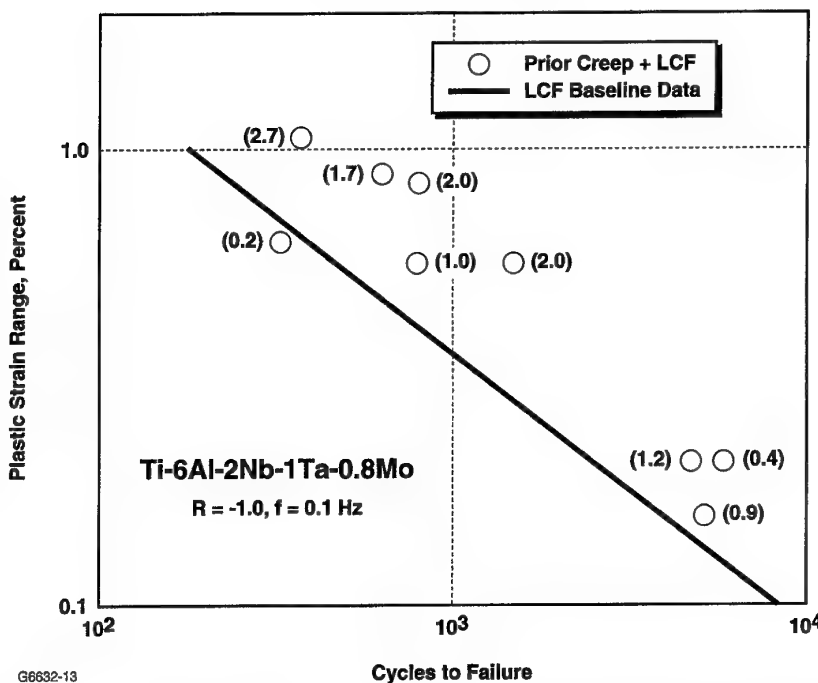


Figure 6 Low cycle fatigue data on a near-alpha alloy, Ti-6Al-2Nb-1Ta-0.8Mo. Prior creep is beneficial to fatigue life. Numbers indicate prior room temperature creep strain, in percent⁷

This difference was more obvious with higher fatigue stresses, *Figure 7*. In all cases, nucleation was reported as due to reversible slip over whatever slip distances the microstructure/textures allowed. If texture or coarseness of the structure was favorably arranged for high tensile stress across the basal plane, strong environmental influences were noted. Otherwise, slip on other planes performed the nucleation job, although at a higher N_n . Hydrogen is considered to play a role by promoting slip heterogeneity as postulated by Postans and Jeal²⁶. The primary alpha size in the alloy of this study was very fine ($D_\alpha = 2 \mu\text{m}$). However, due to a strong texture, D_t was evidently large, diminishing the advantage of the fine alpha.

Wagner *et al.*, when studying the influence of surface treatments on HCF of Ti-6Al-4V in rotating beam fatigue tests, found a positive effect of pre-inducing high, but homogeneous, dislocation densities in inhibiting crack nucleation²⁷. This added to the positive influence of compressive residual stresses and served to counter the negative effects of surface roughness introduced during the deformation where the dislocations were introduced (e.g. shot peening).

HIGH STRENGTH ALPHA-BETA ALLOYS

When considering fatigue behavior of higher strength alpha-beta alloys, such as Ti-17 and Ti-6Al-2Sn-4Zr-6Mo (Ti6246), used in highly stressed rotating components of gas turbine engines where LCF is a definite design factor, there are a number of microstructural features which separate these alloys from their leaner relatives. There is a greater volume fraction of the beta or aged beta phase which has considerably higher strength than the alpha. The spatial separation of primary alpha particles is greater, permitting less interac-

tion among them. Therefore, we shall consider the high strength alpha-beta alloys separately.

While studying LCF behavior of age hardened Ti-17, Funkenbush and Coffin examined the nucleation of CLDs as it is influenced by microstructure²³. They tested the three basic structures shown in *Figure 8*, using metallographically prepared specimen gage sections strained in bending.

Figure 9 contains examples of each of the nucleation sites reported for Ti-17²³. In this figure, there is evidence that slip band crack nucleation has occurred. This indicates that slip band separation due to accumulated fatigue damage may be the operating mechanism. This is seen only with fine equiaxed alpha particles and in the absence of large planar alpha-aged beta interfaces. When the microstructure contains large planar interfaces, or alpha plates, unlike the near alpha alloys, the dominant CLD is an extrusion along such interfaces, as seen in *Figure 9(c)*. The interface separation in *Figure 9(b)* appears without extrusions, indicating some sort of de-cohesion mechanism, perhaps associated with the build up of strain at alpha slip band intersections with the aged beta matrix. Mahajan and Margolin observed, in low strain range LCF on equiaxed Ti6246 with equiaxed primary alpha, intense slip bands within the alpha particles with little penetration into the aged beta matrix¹³. In these cases, alpha-beta interfaces were dominant nucleation sites. These latter investigators reported qualitatively similar results in Ti6246 as reported for Ti-17^{13,14,23}. They did, however, report that with larger plastic strains there appeared to be significant slip band nucleation. The slip band nucleation increased with larger alpha particles and with grain boundary alpha. The qualitative agreement in operative nucleation mechanisms between Ti-17 and Ti6246 is joined by observations on a series of Ti-Mn binary alloys¹⁷.

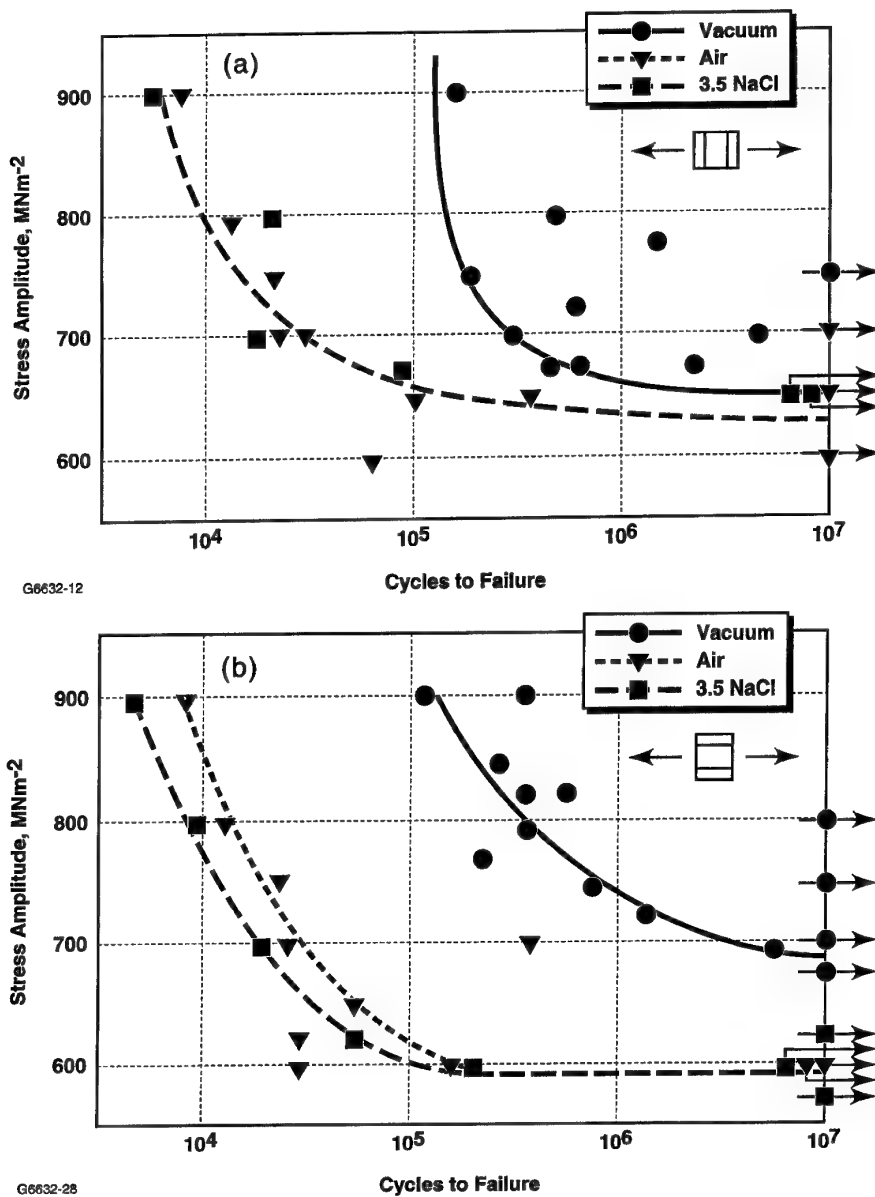


Figure 7 (a) HCF tests on smooth, polished, rotating beam, specimens from highly textured Ti-6Al-4V forgings. The microstructure is fine ($D_a = 2 \mu\text{m}$) and the loading is parallel to the basal plane. The environment influence is most evident at the higher stresses and the laboratory air and salt water environments have nearly identical effects¹⁵. (b) HCF tests on smooth, polished, rotating beam, specimens from highly textured Ti-6Al-4V forgings. The microstructure is fine ($D_a = 2 \mu\text{m}$) and the loading is normal to the basal plane. The environment influence is most evident at the stresses and the laboratory air and salt water environments have nearly identical effects¹⁵

From these observations on high-strength alpha-beta alloys, alpha-beta interface strength can influence N_f . Hall showed that the energy necessary to fracture such an interface depends on the composition profile of nominal alloy ingredients in the vicinity of the interface²⁸. The profile is seldom at an equilibrium state in conventionally processed alloys. Therefore, added to the microstructural dimensions which affect slip associated behavior, are considerations of interface strength, which may not be evident from microstructural examination. The strength is a product of the material's thermal history and phase chemistry.

In addition to the cited observations on surface nucleation sites, Saleh and Margolin, in Ti-Mn alloys,

reported that subsurface nucleation was similar to the surface mechanisms only when examining equiaxed microstructures¹⁷. However, microstructures which contained Widmanstatten alpha exhibited considerable cross-colony nucleation on slip bands in subsurface sites. The surface sites appeared to be of the interface kind associated with extrusions described in Ref. ²³. They attribute this to the relaxed elastic constraints at the specimen surface¹⁷.

SUMMARY OF CLD FORMATION IN FATIGUE

Fatigue crack nucleation is inhibited, in all cases of HCF and LCF, by fine structures (D_α , D_β , D_c and D_i)

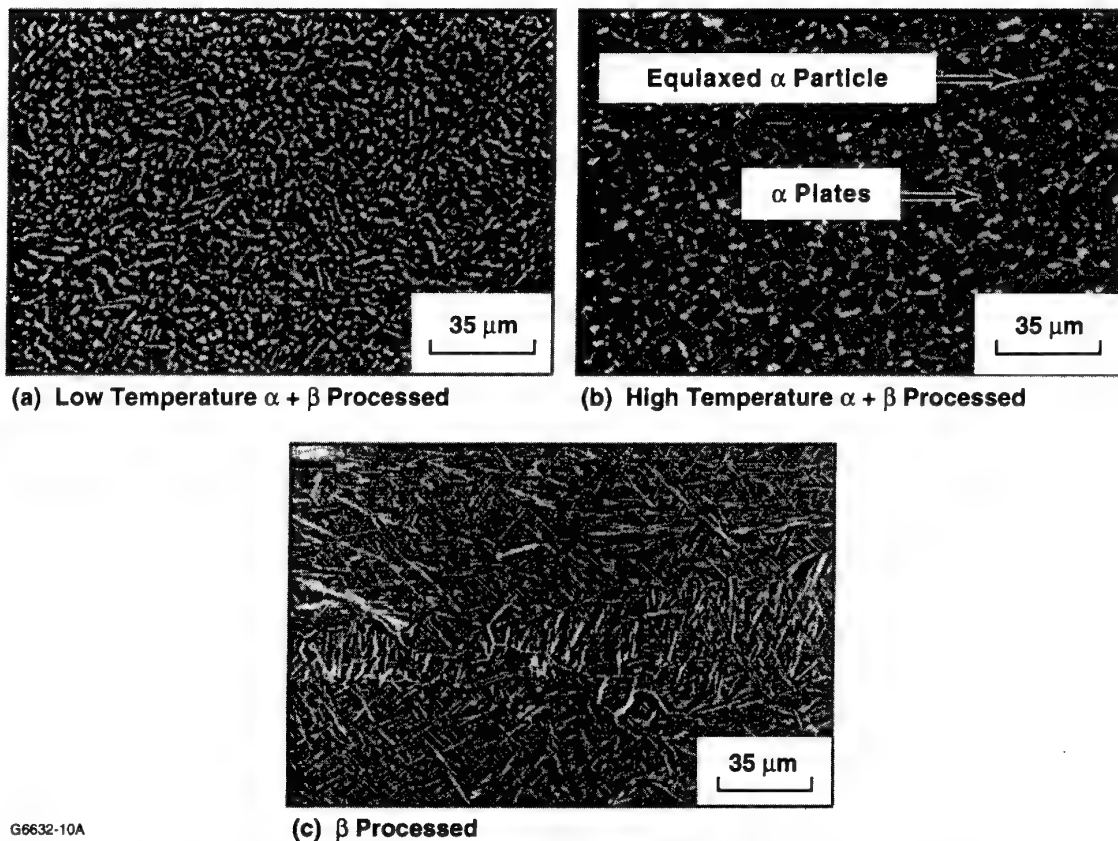


Figure 8 Microstructures of high strength alloy, Ti17 (Ti-5Al-2Sn-2Zr-4Mo-4Cr). LCF tested at room temperature²³

reducing slip distances and eliminating large planar interfaces. Secondary effects (i.e. intrinsic boundary strength and resistance to planar slip which are alloy and process dependent) are superimposed on the microstructural effects. This leaves the qualitative mechanism of fatigue crack nucleation common to all alpha-beta titanium alloys. Optimizing any alloy for maximum N_n will involve microstructure refinement at all structure levels.

INITIAL SHORT CRACK GROWTH, N_s , THE PROPAGATION OF A CRACK UNTIL ITS BEHAVIOR IS DESCRIBED BY LEFM

Growth of small CLDs into recognizable cracks with behavior described by LEFM, N_s , is now receiving attention from the metallurgical and design communities³.

Total fatigue life is dominated by the time or number of cycles when incipient cracks are small, *Figure 3*. This includes propagation of a small fatigue generated CLD of size, a_n , nucleated under conditions described in the previous section, to one characterized by LEFM.

A definition of small cracks is suggested by Suresh and Ritchie²⁹. Cracks are short when:

1. length is small compared to relevant microstructure dimensions (a continuum mechanics limitation);
2. length is small compared to the scale of local plasticity (a linear elastic fracture mechanics limitation);
3. length is small (0.5–1.0 mm or smaller).

All three describe cracks that propagate faster than, or at least at the same rate as, corresponding long fatigue cracks subjected to the same nominal driving force²⁹. Suresh and Ritchie propose that part of the reason for this behavior is a result of the absence of roughness-induced crack closure effects observed in low R , large crack behavior³⁰.

Tokaji *et al.*, found that in high strength, low alloy, steels with fine and coarse austenite grain sizes, the surface crack was less than three grain diameters in length³¹. The grain boundaries provided crack arrest or deceleration points. Slightly longer cracks were not strongly influenced by the microstructure. The longer cracks grew faster than projected from LEFM extrapolations of long crack data until surface lengths exceeded several grain diameters, D . They concluded that after the surface crack reached *ca* $3D$, some crack closure began to be effective and that this effect saturated after another 150 μm of growth. Then LEFM adequately described crack growth. From this point, grain boundaries become less important as crack growth inhibitors. Wagner *et al.* investigated equiaxed Ti-8.6Al in a similar manner and found grain boundaries to provide substantial resistance to growth of very short cracks²⁰. They also examined the total shape of surface cracks, finding them not to conform to an expected uniform a/c ratio²⁰. *Figure 10* shows the way surface cracks are periodically arrested by grain boundaries until the grain is cracked to its fullest depth. This illustration shows how the surface cracks grow in a discontinuous manner and how the initial crack shape can deviate

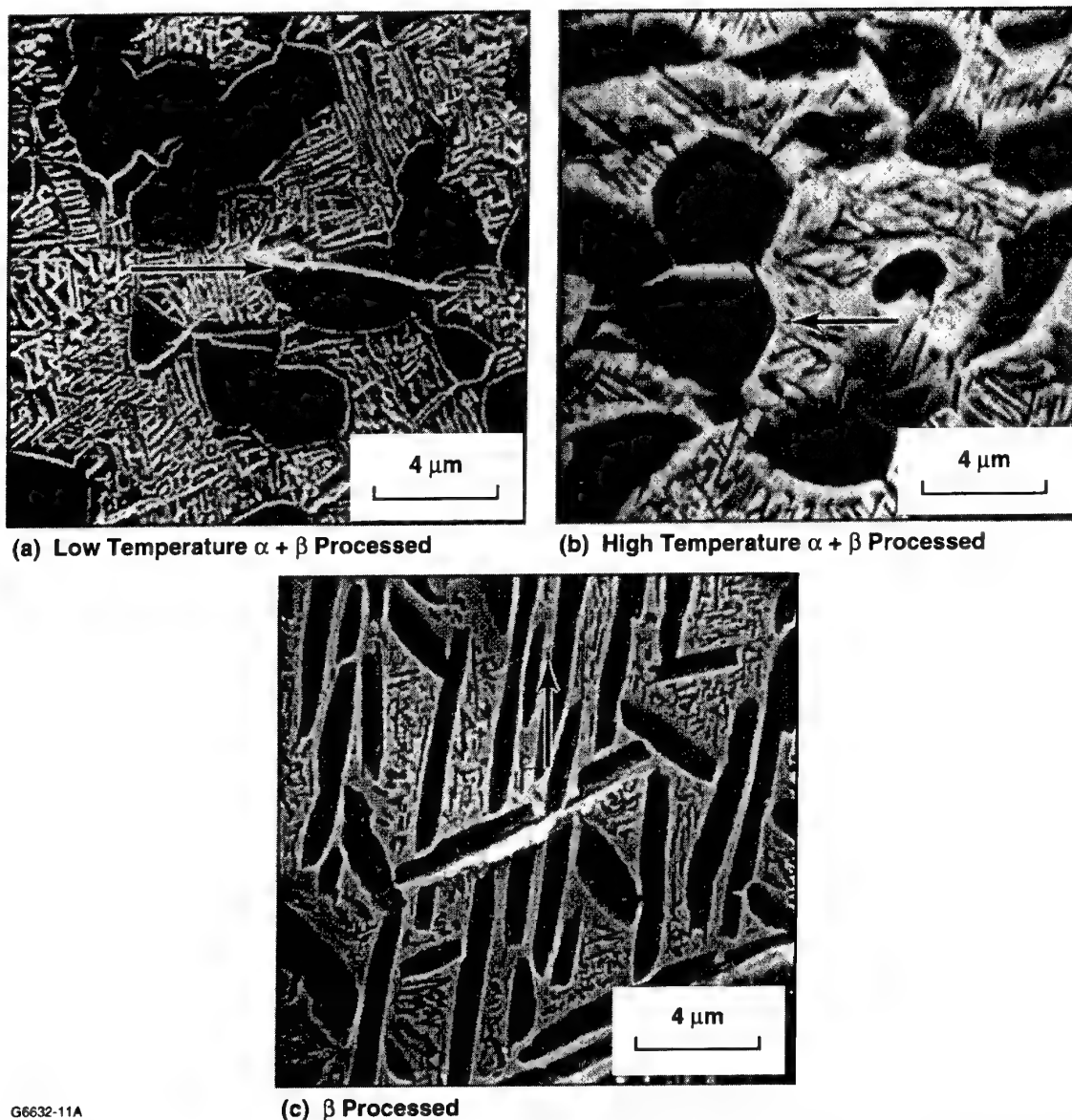


Figure 9 Nucleation sites in Ti17 LCF specimens. Note that the interface site in equiaxed structure (b) does not exhibit extrusions like those seen in platelet alpha containing structures²³

from that expected from LEFM. Not only in the equiaxed structures of Wagner's alloys, but in other alloys with colony microstructures, there is reported evidence of such discontinuous small crack growth, with arrest at grain or colony boundaries^{34,35}. In each case, arrest is followed by severe acceleration of the surface crack, to the next boundary where the crack is again arrested. This is a common observation for short cracks in titanium alloys which exhibit extended planar slip^{8,9,20,33,34}. Slower short crack growth in the finer grain material was reported, consistent with having more grain boundary arrest points^{20,31}. This is counter to the accepted experience with long fatigue cracks where coarse microstructures result in a roughness-induced closure and lower crack growth rates^{12,32}.

Larsen *et al.*, after accounting for crack closure with large and small cracks in equiaxed alpha alloys, Ti-4Al and Ti-8Al, still found that small cracks, with the

surface crack length, $2C$, less than *ca* $3D_\alpha$, grew faster than their long counterparts³³. They attribute this to a continuum mechanics limitations of the stress intensity factor, K . They point to no abrupt change in material behavior, only to the manner in which it is described.

Short crack growth can be placed into perspective by a schematic illustration of the life of a fatigue-loaded component^{1,2,32}. Figure 11 summarizes the phases of fatigue and, when examined along with Figure 1, provides a total description of crack size and fatigue life. Note that the structure dominated part of surface crack growth, N_s , is discontinuous, consistent with the observations of several workers^{20,31,33-36}.

The work of Hicks and Brown, on IMI685 in a colony microstructure, is summarized in Figure 12³⁵. The faster growing short cracks tend to follow slip bands across alpha colonies. Alpha has limited availability of slip systems and this necessitates re-initiating

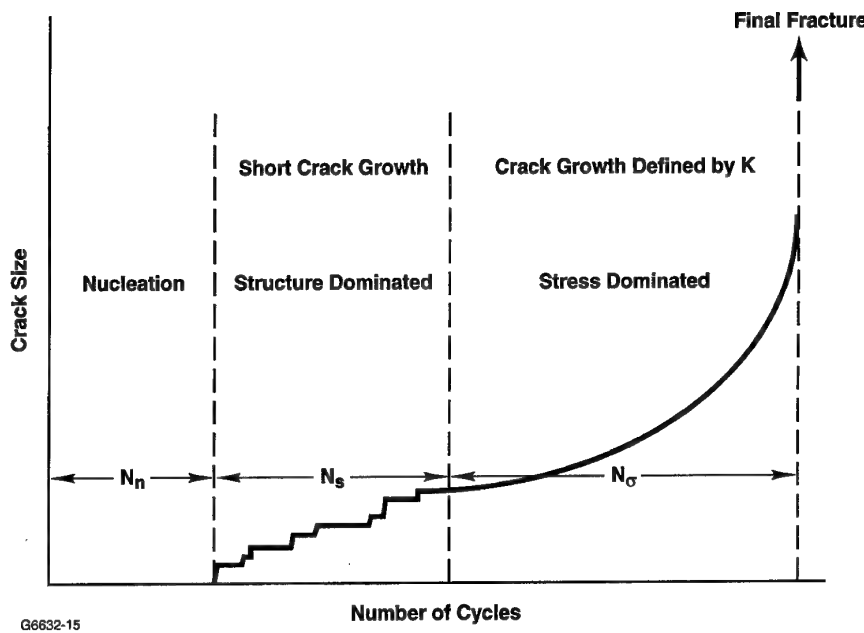


Figure 10 Schematic diagram of observed fatigue crack growth behavior in Ti-8.6Al with an equiaxed microstructure. Note crack arrest at boundaries²⁰

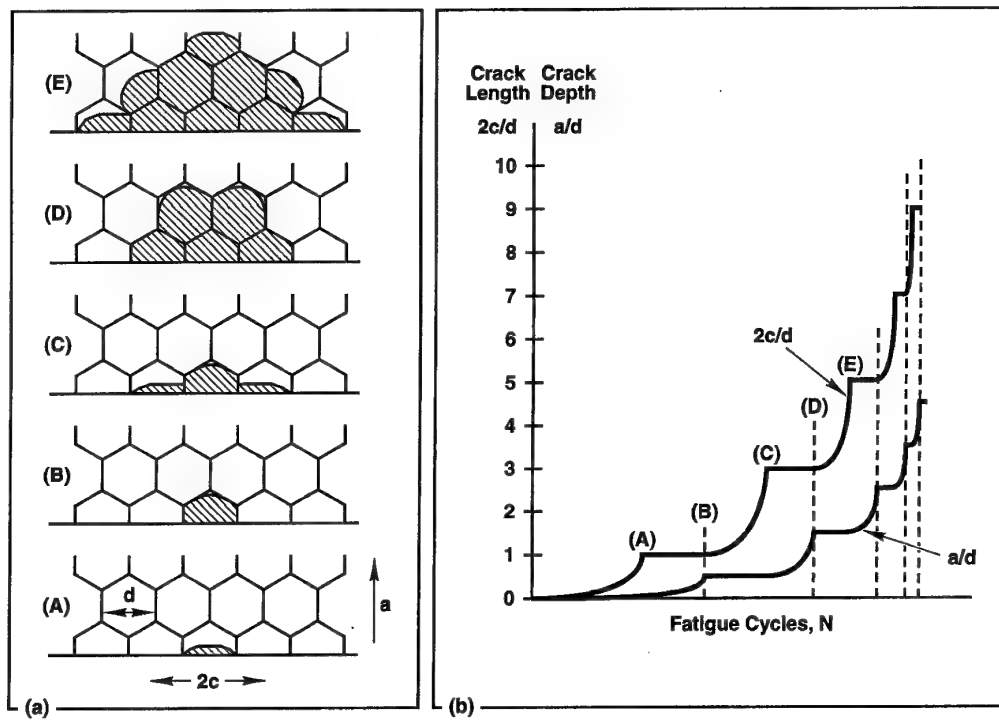


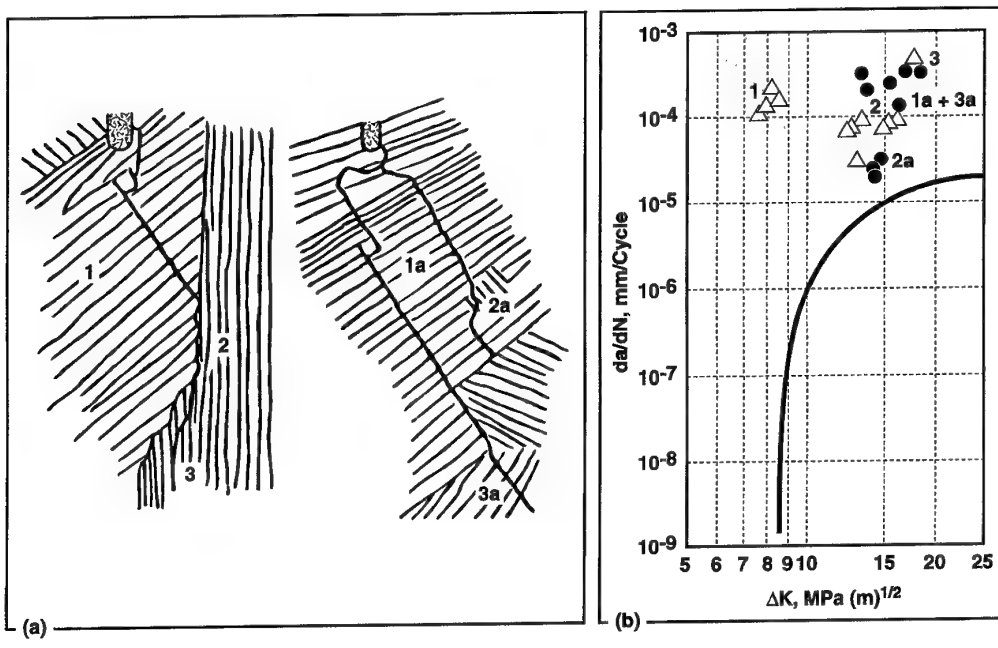
Figure 11 Schematic portrayal of the phases of crack nucleation and growth²

the slip at colony boundaries. There are a number of fatigue cycles required for this re-initiation and sustaining of slip bands in the adjacent, differently-oriented, colony. The result is a tortuous crack path with an erratic growth rate.

Fine grain titanium alloys, where extended slip paths are not evident, also exhibit short crack behavior.

Howland *et al.* shows long and short crack growth curves for fine grain, equiaxed, Ti-6Al-4V and colony microstructures of IMI685³². Both materials exhibit the short crack behavior with higher growth rates, but the effect magnitude is less with the finer grain material. Their data is combined and replicated in *Figure 13*.

Plumbridge in IMI829 with basketweave structure



G6632-16

Figure 12 Alloy IMI685. (a) Sketch of actual crack paths showing crack path through an alpha colony microstructure. (b) Plot of the local growth rate of the small cracks in (a) on same scale as long crack growth for the same material. Note the rapid growth rate for the short cracks³⁵

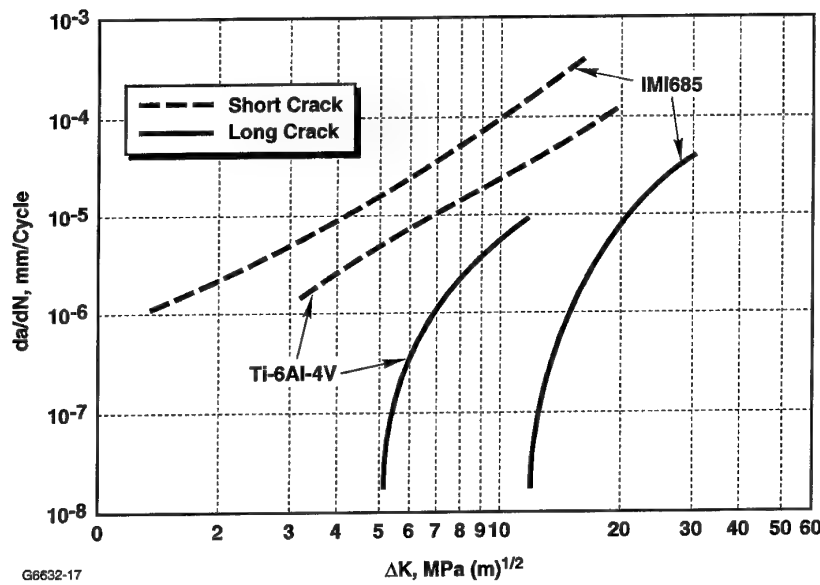


Figure 13 Short and long crack growth in equiaxed Ti-6Al-4V and colony microstructure IMI685, respectively³²

of limited continuous alpha slip distances, reported early crack growth to follow slip bands within the alpha particles¹⁶. These factors did not create large deviations in crack path because the particles were small. Similarly, Mahajan and Margolin in Ti6246, when the LCF strain range was high, reported that early crack paths tended to follow slip bands within the primary alpha¹³. Similar behavior was reported in Ti-Mn alloys, where surface and interior cracking was reported along slip bands in the equiaxed alpha phase with some interface cracking¹⁷. On the other hand, Widmanstatten microstructures seemed to exhibit initial

surface crack paths along the length of alpha plates where, in the interior of the specimen, cracking occurred on slip bands across alpha colonies¹⁷.

Except for mechanisms associated with roughness induced crack closure, the reasons for the additional short crack effect are not clear³. Both short and long cracks in materials were observed with strong planar slip characteristics, like titanium, tend to follow persistent slip bands^{34,35}. These slip bands are generated during fatigue and the accumulation of damage within the bands, and eventually reduces the transverse strength of the materials in these bands; therefore,

cracks easily propagate along the bands. This fracture proceeds rapidly until the slip-induced damage is insufficient to reduce the local toughness below the locally applied, stress intensity. For small cracks, this occurs at one of the boundaries, where the crack is arrested. The crack must then await slip-imposed damage to occur in an adjacent microstructural element for the process to repeat itself. The effectiveness of the barrier at the boundary is dependent upon the relative crystallographic orientations of the adjacent colonies and the colony size.

In the case of large cracks, there are many points on the crack front where boundaries are continuously encountered and local arrest is attempted. The result is an overall retardation. When added to the roughness induced closure, which has been shown to account for only part of the entire reduced growth rate of long cracks compared to short crack, the differences may be qualitatively accounted³⁰.

Both short and long crack behavior will be modified by geometric factors such as grain or colony boundaries and roughness-induced crack closure. These latter two factors can oppose each other under circumstances where grain size or of the controlling microstructural feature is very small and fracture surface roughness is insufficient to induce closure effects.

Once the crack reaches a size larger than the relevant microstructure, its fracture behavior is described by LEFM tools and the subject is studied. In this well-known regime of behavior that most current materials behavior and life prediction practices and their associated damage tolerance or safelife design practices operate. They do not consider, in a quantitative way, the major portions of fatigue life associated with N_n and N_s . Older and still popular concepts of designing for fatigue initiation do incorporate, in a non-quantitative way, elements of N_n and N_s in their life prediction by including them in the 'scatter' associated with fatigue design data. These utilize fatigue design without fracture mechanics and assume nothing about initial flaws or crack growth rates. The uncontrolled nature of the causes for the scatter in fatigue crack initiation, which may not be identically incorporated in both the material from which the design data is gathered, and in the component as it enters service, reduces the quality of fatigue life prediction.

PRACTICAL IMPLICATIONS IN THE APPLICATION OF MICROSTRUCTURE CONTROL TO IMPROVE FATIGUE PROPERTIES

The material's fatigue properties include:

1. Most of the total life is consumed creating the first CLD so $S-N$ curves reflect the useful fatigue life of a material. The remainder of life associated with crack growth is useful in establishing inspection intervals but not in predicting the total fatigue life.
2. There is a great deal of scatter in the data used for design as depicted, schematically, in *Figure 14(a)* and (b).

Figure 14(a) illustrates the scatter in life for given test conditions and clearly illustrates the greater scatter at the longer life conditions. Modeling of the data with scatter is often made easier by describing the scatter band as seen in *Figure 14(b)*. Contributing to the

scatter are extrinsic factors associated with specimen preparation methods, test equipment variables and the details of the test methods used.

There is also a family of intrinsic variables such as microstructure, macrostructure, texture and other metallurgical factors. An approach to reducing scatter is through close control of these intrinsic metallurgical factors. In the following paragraphs are descriptions of a few of the challenges associated with these controls.

Microstructure and HCF

HCF in Ti-6Al-4V is influenced by the volume fraction of primary alpha and the cooling rate from the solution temperature. Rudinger and Fischer experimented with various solution temperatures and cooling rates from the solution treatment³⁷. They created several distinct microstructures characterized by their percent of primary alpha and the morphology of the secondary alpha. *Figure 15* is an extraction and replot of their data comparing 10^7 runout stress and volume fraction of primary alpha. Both air cooled and water quenched 100 mm bars were examined. For primary alpha contents < 85%, a water quenched condition is superior but with a decreasing advantage as the volume fraction of primary alpha increases. However, an opposite trend is noted for the air cooled microstructures. Convergence occurs at ca 85% primary alpha. From this observation, in order to seek the best HCF strength, one rapidly cooling from a temperature as close to the beta transus as is practical with the available controls, would be most desirable. However, if consistency is more important, a lower solution temperature will produce a microstructure with less variability in HCF strength and less sensitivity to cooling rate or section size. Other properties must be considered as many are also influenced strongly by microstructure.

Chemistry and transus

There have been a number of attempts to relate the beta transus temperature to alloy chemistry. One approximation is seen in *Table 2*. The approximation resulted from a linear regression analysis of a number of heats of Ti-6Al-4V and reflects the major alloying elements and impurities commonly encountered. While it is only approximate, the relative values of the coefficients are indicative of the effect each element has on the beta transus of this alloy.

As seen in the equation of *Table 2*, the alloy chemistry can have a large effect on the actual beta transus. At the extremes of alloy chemistry permitted by specification, it is possible to have a variation in beta transus as high as 60°C. These extremes are seldom encountered in practice.

Chemical segregation of the alloying elements during solidification, or changes in bulk or local interstitial content during processing, can have profound effects on local transformation temperatures. The degree that titanium alloy products can be made with uniform chemistry is limited by practical considerations of formulation, solidification and environments encountered during processing at elevated temperatures. It is prudent, then, to determine the overall effect on the beta transus by dealing directly with the alloy's transus uniformity. *Table 3* shows the results of a study on eight Ti-6Al-4V ingots where the beta transus was

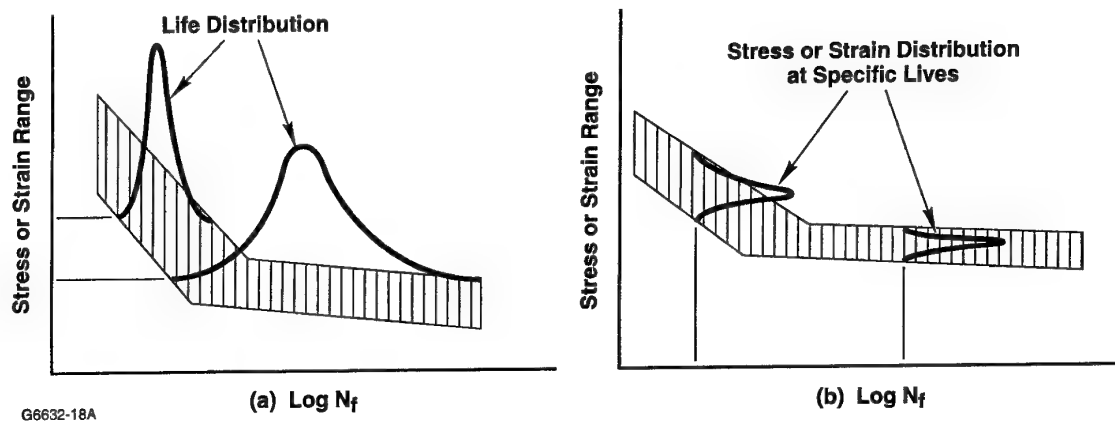


Figure 14 Typical means of expressing scatter in fatigue data. The scatter on the independent test variable is often used for convenience in modeling the data scatter and developing design allowables

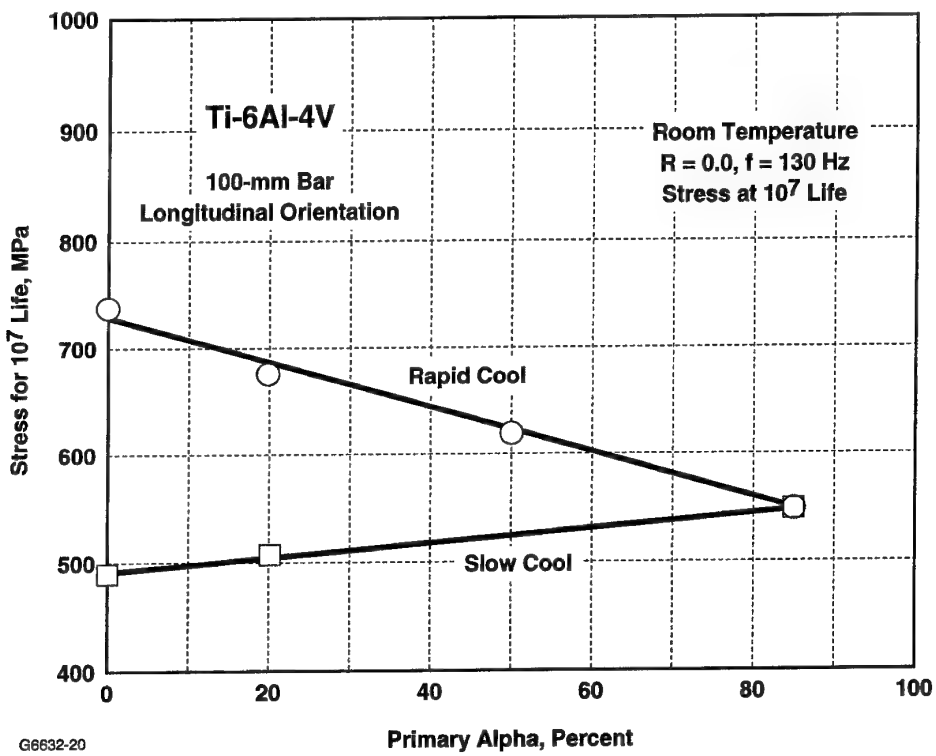


Figure 15 High cycle fatigue life is affected by the microstructure and the cooling rate from solution treatment. All were aged at 700°C for 2 h and air cooled prior to testing³⁷

Table 2 Approximate beta transus for Ti-6Al-4V, based on chemistry

$$T_b(\text{°C}) = 882.2 - 13.9(\%V) + 22.2(\%Al) - 13.9(\%Fe) + 183.3(\%O) + 500(\%N) + 255.5(\%C) - 1250(\%H)$$

$$T_b(\text{°F}) = 1620 - 25(\%V) + 40(\%Al) - 25(\%Fe) + 330(\%O) + 900(\%N) + 460(\%C) - 2250(\%H)$$

Note: all compositions are in weight percent

measured at four locations, top to bottom and at three radial locations, at each ingot length position. Although not as large as possible, the results indicate a wide variation not only from heat to heat but within a heat. This variation makes tight control of the microstructure

difficult with fixed forging and/or heat treatment temperatures. The problem is exaggerated as the requirement for a low level of primary alpha emerges in an attempt to maximize fatigue or creep properties.

To specify a heat treatment by a particular tempera-

Table 3 Typical beta transus variations

Ti-6Al-4V Eight production heats	
Transus range within a heat (maximum–minimum)	
High	27.8°C (50°F)
Low	16.7°C (30°F)
Average	21.8°C (39°F)
Transus variation from heat to heat (at the middle of the ingot, mid radius position)	
High transus	999°C (1830°F)
Low transus	986°C (1806°F)
Overall range of beta transus	
High transus reading, all heats	1014°C (1857°F)
Low transus reading, all heats	973°C (1783°F)
Overall range	41°C (74°F)

Transus measured at the top, 25% from top, middle, 75% from top and bottom ingot positions, each at the center, mid-radius and outside radial

Same ‘fixed’ practice for formulation and melting of all heats

ture alone may result in a wide variation in microstructure, as depicted by vol% primary alpha, when a logical range of beta transus from heat to heat can be as high as 41°C if a uniform microstructure is needed. It is important to characterize the beta transus of each ingot by location within the ingot and then adjust the heat treatment to give the desired microstructure.

Transus approach curve

A useful characterization of an alloy is the beta transus approach curve as seen in *Figure 16*³⁸. This plot illustrates a typical beta transus approach curve for a common near-alpha titanium alloy. The plot shows how the amount of primary alpha changes as the exposure temperature departs from the beta transus temperature. A steep slope implies that small variations in temperature will yield large differences in primary

alpha content. Conversely, a less steep curve will have less sensitivity as to the amount of primary alpha with variations in processing temperature. The latter, all else equal, is the desirable situation for microstructure control. Some of the new, high-performance, near-alpha alloys currently do require tight microstructure controls. Melting and mill practices were adjusted to accommodate these needs. In some cases, alloy compositions were adjusted to create a beta transus approach curve with temperature sensitivity to the amount of primary alpha phase present at working or heat treatment temperatures³⁹.

The problem associated with controlling the microstructure is intensified further by difficulties in maintaining, in production furnaces, tight temperature uniformity requirements. A typical specification range of temperature permitted in a production heat treatment furnace is $\pm 14^\circ\text{C}$. Using *Figure 16*, this range of 28°C could result in primary alpha content varying as much as 35% within a single heat treatment lot, even if the alloy’s chemistry would be without variation.

For many alloys, it is common to have a far from ideal distribution of microstructure. *Figure 17(a)* is a cross section of a typical forging of Ti-6Al-2Sn-4Zr-2Mo showing the flow lines which are a result of distorting the original macrostructure of the billet as the forging is made. There are three specific areas marked where detailed micrographs were taken. *Figure 17(b)* is a photomicrograph of the Area 2, showing a primary alpha content of over 50%. *Figure 17(c)* from Area 6 exhibits ca 27% primary alpha. Area 4 is not shown, but its primary alpha content was close to 40%. From early work on this alloy, the range of primary alpha content will result in a minimum creep rate change of a factor of at least two³⁸.

A logical extension of the HCF-microstructure

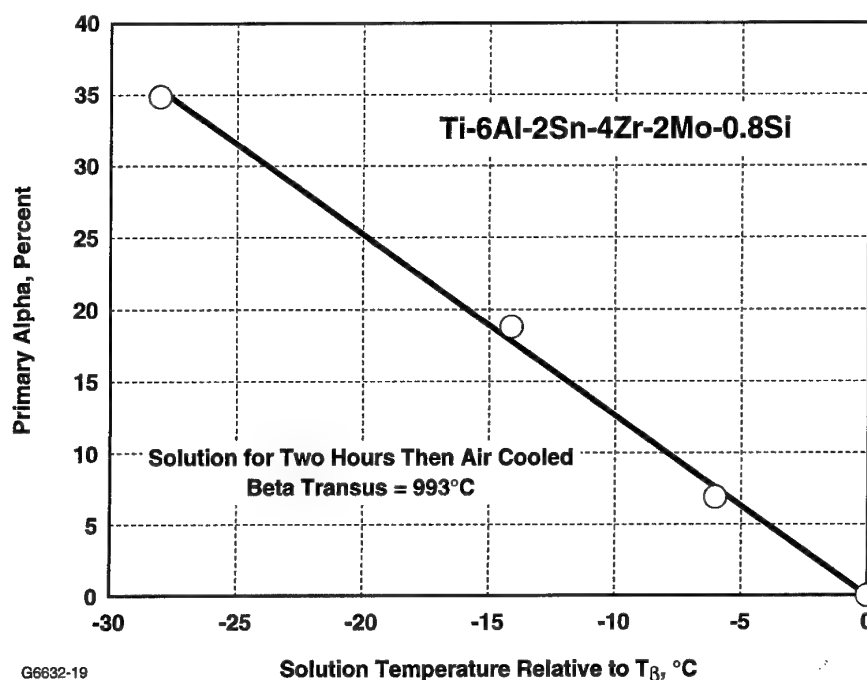


Figure 16 Beta transus approach curve for Ti-6Al-2Sn-4Zr-2Mo-0.08Si, relative to a beta transus of 993°C³⁸

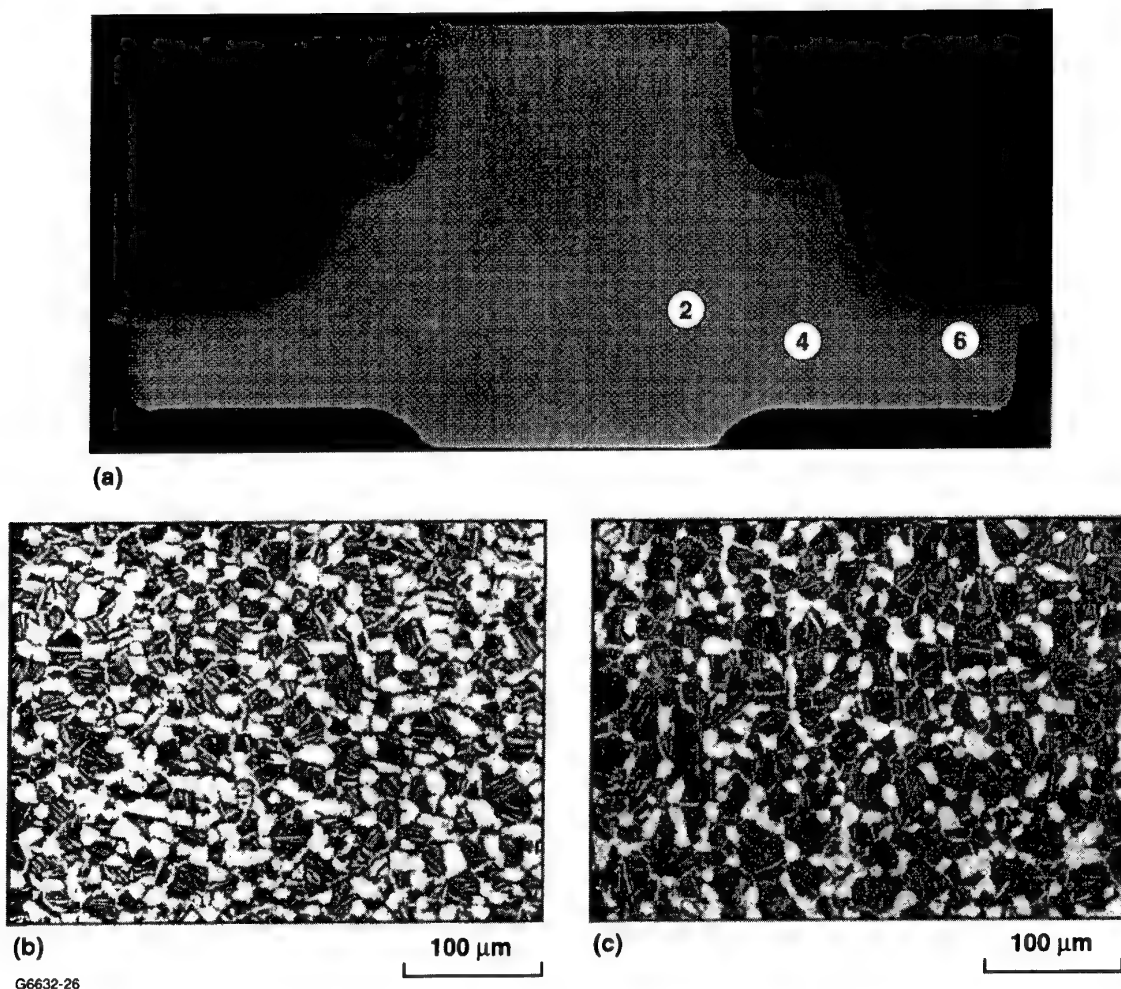


Figure 17 (a) Cross-section of a rotor forging of Ti-6Al-2Sn-4Zr-2Mo-0.08Si. The marked locations, 2, 4 and 6 are where the microstructure was examined in detail. (b) and (c) are photomicrographs at locations 2 and 6, respectively. The primary alpha content for locations 2, 4 and 6 is 52, 40 and 27%

relationships of *Figure 15* is that a similar relationship exists for both Ti-6Al-4V and Ti-6Al-2Sn-4Zr-2Mo-0.08Si. The microstructure variations in this forging will result in an 80 MPa (11.5 KSI) difference in stress for 10^7 cycle HCF life.

CONCLUSIONS AND RECOMMENDATIONS

The events in a component's total fatigue life leading up to the presence of an observable crack, a_i , are loosely identified as fatigue crack initiation life. Fatigue life prediction practices based on fracture mechanics and limits of NDE begin with a_i . Prediction ignores a major portion of the intrinsic fatigue life available to a defect-free component. a_i is often defined as being quite large, on the order of 0.5 mm, depending on the method of observation and the configuration of the part at inspection.

The dominant portion of total fatigue life, the events of crack nucleation, and short crack growth must be considered in order to predict the whole fatigue life. For titanium alloys, microstructure and associated crystallographic texture dominate the fatigue behavior in its early stages; nucleation of early CLD and their growth to large cracks.

It is also important for the metallurgist to know and use the understanding of these behaviors. Then the metallurgist can devise manufacturing processes to optimize the material's intrinsic fatigue strength. Among these requirements is the need to be consistent. The structure, at all scales of observation, must be reproduced in all manufactured parts. This structure must reliably represent that from which the behavior models were derived.

The desired microstructure for fatigue crack nucleation and early growth resistance in alpha-beta titanium alloys is fine, with short interfaces, small grains, and without texture on a micro- or a macroscale. Alloy chemistry, microstructures and substructures which discourage planar slip or development of intense slip bands, are beneficial.

From practical considerations, there are necessary compromises that occur due to economic reasons. There are reasons for robust processes that are less sensitive to variables but give repeatable results despite use of an extended range of process variables. There is no doubt that as process controls and understanding of the structure-property relationships improve, titanium alloy parts and confidently can be designed with an increasing and more predictable fatigue lives.

REFERENCES

- 1 Hoepner, D.W., Parameters that input to application of damage tolerance concepts to critical engine components, in *Tolerance Concepts for Critical Engine Components*. AGARD Conference Proceedings No. 393, Damage, San Antonio, TX, USA, 22-26 April, 1985.
- 2 Jeal, R.H., The specification of gas turbine forgings. *Metals and Materials*, 1985, September, 528.
- 3 Ritchie, R.O. and Yu, W., Short cracks in fatigue: a consequence of crack tip shielding, in *Small Fatigue Cracks* (Eds Ritchie, R.O. and Lankford, J.), *Proceedings, 2nd Engineering Foundation International Fatigue Conference/Workshop*, Santa Barbara, CA, January 1986, TMS-AIME, Warrendale, PA, 1986.
- 4 Suresh, S. and Ritchie, R. O., *International Metals Reviews*, 1984, **29**, 445.
- 5 Eylon, D. and Pierce, C. M., *Metal Transactions*, 1976, **7A**, 111.
- 6 Benson, D. K., Grosskreutz, J. C. and Shaw, G. G., *Metal Transactions*, 1962, **3A**, 1239.
- 7 Chu, H.P., MacDonald, B.A. and Arora, O.P., Titanium Science and Technology, Vol. 4 (Eds Lutjering, G., Zwicker, U. and Bunk, W.), Deutsche Gesellschaft Fur Metallkunde E.V., 1985, *Proceedings of the 5th International Conference on Titanium*, Munich, September 1984, p. 2395.
- 8 Eylon, D. and Hall, J. A., *Metal Transactions*, 1977, **8A**, 981.
- 9 Eylon, D., Hall, J. A., Pierce, C. M. and Ruckle, D. L., *Metal Transactions*, 1976, **7A**, 1817.
- 10 Eylon, D., Rosenblum, M.E. and Fujishiro, S., *Titanium '80, Science and Technology*, Vol. 3 (Eds Kimura, H. and Izumi, O.), TMS-AIME 1980, *Proceedings of the 4th International Conference on Titanium*, Kyoto, Japan, May 1980, p. 1845.
- 11 Grosskreutz, J. C., *Metal Trans.*, 1972, **3A**, 1255.
- 12 Lutjering, G. and Gysler, A. *Titanium Science and Technology*, Vol. 4, *Proceedings of the 5th International Conference on Titanium*, Munich, September 1984, p. 2065.
- 13 Mahajan, Y. and Margolin, H., *Metal Transactions*, 1982, **13A**, 257.
- 14 Mahajan, Y. and Margolin, H., *Metal Transactions*, 1982, **13A**, 269.
- 15 Peters, M., Gysler, A. and Lutjering, G., *Metal Transactions*, 1984, **15A**, 1597.
- 16 Plumbridge, W. J. and Stanley, M., *International Journal of Fatigue*, 1966, **8**, 209.
- 17 Saleh, Y. and Margolin, H., *Metal Transactions*, 1983, **14A**, 1481.
- 18 Shih, D.S., Lin, F.S. and Starke, E.A., *Titanium Science and Technology*, Vol. 4, *Proceedings of the 5th International Conference on Titanium*, Munich, September 1984, p. 2099.
- 19 Takemoto, T., Jing, K. L., Tsakalacos, T., Weissman, S. and Kramer, I. R., *Metal Transactions*, 1983, **14A**, 127.
- 20 Wagner, L., Gregory, J.K., Gysler, A. and Lutjering, G., in *Small Fatigue Cracks* (Eds Ritchie, R.O. and Lankford, J.), *Proceedings, 2nd Engineering Foundation International Fatigue Conference/Workshop*, Santa Barbara, CA, January 1986, TMS-AIME, Warrendale, PA, 1986, p. 117.
- 21 Walcher, J.C. and Finnerty, D.L., SAE Paper 821437, *Proceedings Aerospace Congress and Exposition*, Anaheim, CA, October, 1982.
- 22 Wells, C. H. and Sullivan, C. P., *Transactions of ASM*, 1969, **62**, 263.
- 23 Funkenbush, A. W. and Coffin, L. E., *Metal Transactions*, 1978, **9A**, 1159.
- 24 Bania, P.J., Bidwell, L.R., Hall, J.A., Eylon, D. and Chakrabarti, A.K., in *Titanium and Titanium Alloys: Scientific and Technical Aspects*, Vol. 1 (Eds Williams, J.C. and Belov, A.F.), Plenum, 1982, *Proceedings 3rd International Conference on Titanium*, Moscow, May 1976, p. 663.
- 25 Bania, P.J. and Antolovich, S.D., in *Titanium Science and Technology*, Vol. 4, *Proceedings of the 5th International Conference on Titanium*, Munich, September 1984, p. 2305.
- 26 Postans, P.J. and Jeal, R.H., in *Titanium Science and Technology '72*, Vol. 1 (Eds Jaffee, R.I. and Burte, H.M.), *Proceedings of the 2nd International Conference on Titanium*, Boston, May 1972, Plenum Press, New York, 1973, p. 192.
- 27 Wagner, L., Gerdes, C. and Lutjering, G., in *Titanium Science and Technology, Proceedings, 5th International Conference on Titanium*, Vol. 4, p. 2147.
- 28 Hall, J.A., Influence of alpha-beta interface composition profile on specific interface fracture energy in the Ti-Mo alloy system, Ph.D. Dissertation, Ohio State University, August, 1979.
- 29 Suresh, B. and Ritchie, R. O., *International Reviews*, 1984, **29**, 445.
- 30 Suresh, B. and Ritchie, R. O., *Metal Transactions*, 1982, **13A**, 1627.
- 31 Tokaji, K., Ogawa, T., Harda, Y. and Anso, Z., *Fatigue and Fracture of Engineering Materials and Structures*, 1986, **9**, 1.
- 32 Howland, C., Hicks, M.A. and Jeal, R.H., in *Small Fatigue Cracks* (Eds Ritchie, R.O. and Lankford, J.), *Proceedings, 2nd Engineering Foundation International Fatigue Conference/Workshop*, Santa Barbara, CA, January 1986, TMS-AIME, Warrendale, PA, 1986, p. 607.
- 33 Larsen, J.M., Nicholas, T., Thompson, A.W. and Williams, J.C., in *Small Fatigue Cracks* (Eds Ritchie, R.O. and Lankford, J.), *Proceedings, 2nd Engineering Foundation International Fatigue Conference/Workshop*, Santa Barbara, CA, January 1986, TMS-AIME, Warrendale, PA, 1986, p. 499.
- 34 Eylon, D. and Bania, P. J., *Metal Transactions*, 1978, **9A**, 1273.
- 35 Hicks, M.A. and Brown, C.W., *International Journal of Fatigue* 1982, July, 167.
- 36 Chesnutt, J.C., in *Titanium Science and Technology*, Vol. 4, *Proceedings of the 5th International Conference on Titanium*, Munich, September, 1984, p. 2227.
- 37 Rudinger, K. and Fischer, D., in *Titanium Science and Technology*, Vol. 4, *Proceedings of the 5th International Conference on Titanium*, Munich, September 1984, p. 2123.
- 38 Bania, P.J. and Hall, J.A., in *Titanium Science and Technology*, Vol. 4, *Proceedings of the 5th International Conference on Titanium*, Munich, September 1984, p. 2371.
- 39 Neal, D.F., *6th World Conference on Titanium*, Vol. 1, *Proceedings of the 6th World Conference on Titanium*, Cannes, June 1988, p. 253.

PII: S0142-1123(97)00039-X

Fretting fatigue in engineering alloys

T.C. Lindley

Imperial College of Science and Technology, Department of Materials, Prince Consort Road, London SW7 2BP, UK

The experimental procedures which have been used to carry out fretting fatigue tests are reviewed and the preferred specimen and contact pad geometries and method of testing are identified. The $S-N$ curves generated with and without fretting and subsequent analysis have been used to satisfy a number of objectives: (1) to establish the important variables which can significantly affect fretting fatigue behaviour; (2) to increase our fundamental understanding of the fretting fatigue process; and (3) to give a ranking of a diverse range of materials in terms of their resistance to fretting fatigue. The analytical methods which have been used to predict fretting fatigue crack initiation are briefly discussed. With some specimen/fretting pad material combinations, small fretting fatigue cracks are introduced at a very early stage in life and fracture mechanics methods are developed in order to model their growth. Analytical procedures for fretting fatigue based on either $S-N$ endurance or fracture mechanics methodologies are discussed. © 1998 Published by Elsevier Science Ltd.

(Keywords: fretting fatigue; engineering alloys; fatigue strength reduction; fracture mechanics; growth of short cracks)

INTRODUCTION

Fretting is the oscillatory sliding motion of small 'slip' amplitude between two contacting surfaces¹. It is promoted by high frequency, low amplitude vibratory motion and commonly occurs in clamped joints and 'shrunk-on' components found, for example, in keyways, splines and dovetail joints². The surface damage produced by fretting can take the form of fretting wear (with or without environmental assistance) or fretting fatigue where the material fatigue properties can be seriously degraded. Early research on fretting employed a contact pad clamped to a fatigue specimen in order to measure $S-N$ curves, with and without fretting, and thereby establish the fatigue strength reduction factor for a particular material combination of interest³⁻⁵. The extent of this reduction⁶ was found to be particularly affected by the following variables: (a) slip amplitude; (b) magnitude and distribution of contact pressure; (c) the particular material combination and condition of the mating surfaces; (d) frictional forces and near surface stresses; (e) cyclic frequency; (f) temperature; and (g) environment.

Several investigators have attempted to quantify fretting fatigue in terms of these parameters, particularly the slip amplitude, but they have achieved limited success⁷. A number of models based on $S-N$ data and the relative slip amplitude will be reviewed in order to highlight the strengths and weaknesses of such approaches.

EXPERIMENTAL METHODS

Fatigue specimen

Specimens have often been prepared with the gauge length having machined parallel 'flats' which are then polished on silicon carbide papers, typically down to a 600 grade finish, and finally degreased so as to provide a 'standard' surface. The stress concentration associated with the specimen corners is small compared with that due to the fretting contact.

Fretting contact pads

Since several investigators (see data compilation in Ref. 8) have concluded that the range of slip is an important parameter influencing fretting fatigue behaviour, fretting contact has often been achieved using a bridge type pad which is particularly convenient for studying the effect of slip amplitude. The pad feet are often ground to a 600 SiC grit finish and then degreased to obtain a 'standard' finish. The bridge is usually 'anchored' in some way, possibly with a stiff spring, but 'floating' bridges have also been employed. The bridge feet may be flat and of restricted height so as to minimise elastic deflection. Cylindrical or chamfered feet have also been used. A wide variation in slip amplitude value can be readily achieved by changing the length dimension of the bridge. The bridge type contact is also useful in that the wide range in values of achievable slip amplitude allows control of the relative contributions to damage from fretting fatigue and fretting wear. Spink⁹ found that the wear damage increased progressively with increasing slip amplitude,

but that fretting fatigue cracks always initiated away from areas of maximum wear. Major disadvantages with bridge pads having flat contact surface include: (a) good alignment between pad and specimen with loading direction is difficult to achieve; (b) the stress singularities associated with the pad corners; and (c) the difficulty of defining stick-slip zones in the fretting contact. It has been argued¹⁰ that in fundamental studies of fretting fatigue, the specimen/contact pad geometries should provide a well-defined stress field, and in this respect 'ball on flat' or 'cylinder on flat' are recommended.

Method of testing

In order to achieve controlled fretting between the specimen/pad contacting surfaces, two distinct methods have traditionally been used. Many of the earlier studies² involved clamping pads against a fatigue specimen using a previously calibrated steel proving ring, the resulting assembly then being mounted in a standard uniaxial fatigue machine. Loads are usually applied under either load, or very occasionally displacement control in push-pull (direct stress) or rotating bend. A more sophisticated option² is to use a biaxial test machine with two pairs of independently controlled actuators on the horizontal and vertical axes which will have a number of advantages, i.e. (a) more precise control and measurement of relative slip between pad and specimen, (b) the ability to apply large contact loads (up to 250 kN) which sometimes occur under service conditions, (c) constant contact loads can be achieved even in the presence of substantial fretting wear which would otherwise result in load relaxation, (d) tests can be temporarily interrupted to enable inspection of surface damage, (e) variable amplitude loadings can be applied to pad and specimen, (f) both in-phase and out-of-phase loading can be achieved.

Fretting wear debris

The amount of wear debris will depend upon the particular materials in contact, range of slip, contact pressure and other factors. In some cases, the debris can escape from the contact and clamping pressure will reduce. If, however, debris is retained then it will often occupy a greater volume than the material it replaces and contact pressure will increase. The role of the debris will be discussed further in the modelling section.

Frictional force measurement

Strain gauges are bonded to the underside of a bridge type contact pad in order to measure pad deflection and hence frictional forces between pad and specimen¹¹. The change in frictional force during a fretting fatigue test can be used to detect crack initiation and also to monitor subsequent crack development². Additionally, measured frictional forces are used in modelling of crack growth under fretting conditions using fracture mechanics concepts^{2,11}. For constant amplitude loading, the approximately sinusoidal output from the pad strain gauge is fed to an x-time recorder/plotter via a transient recorder. This allows the range of surface strain ($\Delta\epsilon_B$) from the bottom surface of the pad to be determined continuously for each pad throughout the fretting fatigue test. At each fretting pad foot, the frictional force results in both uniaxial extension and

bending of the pad. The pad strain ($\Delta\epsilon_B$) is then given by

$$E_{PAD}\Delta\epsilon_B = C_B \frac{\Delta F_t}{BD} \quad (1)$$

where E_{PAD} is the Young's modulus of the pad material and B and D are the pad thickness and height respectively. The term C_B is a correction factor which accounts for the bending contribution pad deformation, and is related to the pad span such that as $S \rightarrow \infty$, $C_B \rightarrow 1$. The factor C_B was measured experimentally using a split fretting fatigue specimen in which the static load applied to the specimen is diverted entirely through the pads. During a fretting fatigue test, the change in frictional force is measured as a fretting scar develops¹¹. Frictional forces increase during the initial 'bedding in' period followed by a 'plateau' region where they are approximately constant (Figure 1). This plateau value will be maintained throughout the test unless crack initiation occurs. In this case, fretting pad strain and frictional force will decrease rapidly at the pad where initiation occurs².

The plateau value of frictional force for the contacting materials of interest can be determined as a function of alternating fatigue stress, contact pressure and pad span. The resulting measurements indicate that at low contact pressure the peak frictional force $\Delta F_t/2$ increases with applied stress and achieves a limiting value approximately equal to the applied contact load on each foot². This implies that a maximum coefficient of friction equal to unity is achieved under fretting conditions at an applied stress amplitude greater than some critical value. This critical value is itself dependent on pad span and pad material. By varying pad material and geometry and contact pressure, it is poss-

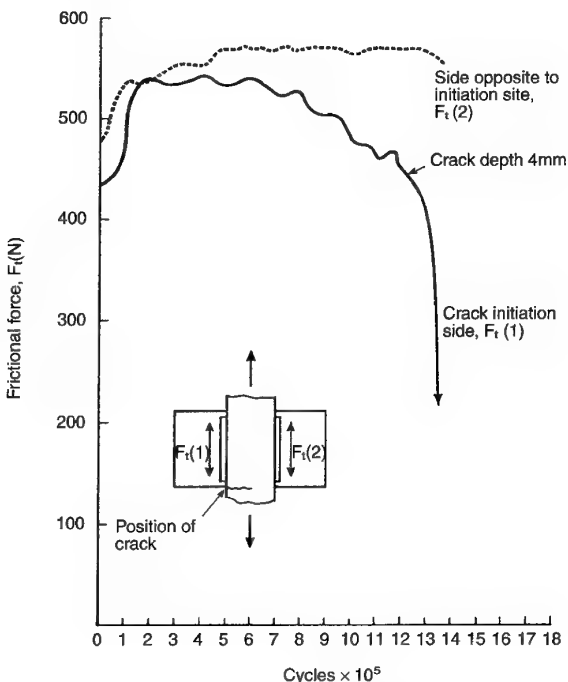


Figure 1 Frictional force variation in a fretting fatigue test with 2014A aluminium specimen and 3.5%NiCrMoV bridge pads (after Ref.²)

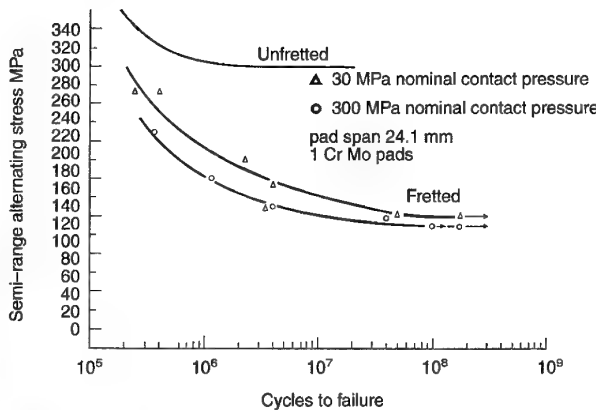


Figure 2 Fatigue *S-N* curves with and without fretting for 3.5%NiCrMoV steel specimen and 1%CrMo steel bridge pads at zero mean stress (after Ref. ¹⁴)

ible to generate a range of values for frictional force and relative slip amplitude. This method of controlling frictional force and slip amplitude can be used to study their influence on the initiation of fretting cracks ^{7,9}.

Fatigue *S-N* data with and without fretting

The materials of interest are tested with their contacting surfaces in the 'standard' condition. The particular fatigue (body) mean stress and the contact stresses are often dictated by the service conditions being simulated. Several series of specimens are tested in order to establish the fatigue *S-N* curves with and without fretting and a range of contact pressures and contact pad spans (if bridge type pads are used) are often investigated. The vast majority of data in the literature relates to air environment. The reduction in fatigue strength for a 3.5%NiCrMoV steam turbine rotor steel in contact with a 1%CrMo steel ² is shown in *Figure 2*, and details including fretting fatigue strength reduction factors are given in *Table 1*. The

substantial effect of pad span on fatigue behaviour is given in *Figure 3* for 2014A (BS L65) specimens fretted against BS S98 steel ¹². Data is also given for Ti6Al4V fretted against itself ¹³.

The nominal range of slip δ at each end of a bridge pad is given as $\delta = \sigma x/E$ where σ is the applied stress amplitude, x the mean pad span and E is Young's modulus. True slip ranges can be found by correcting for pad deflection. Early fretting researchers suggested that slip of the order of 9 to 15 μm commonly gives the maximum reduction in fatigue strength (see Ref. 8).

Metallography and fractography

Fretting between each contact pad foot and the fatigue specimen results in a fretting scar in the surface. In general, slip only occurs over part of the fretting interface and a boundary will develop between the slip and nonslip (stick) regions. In practice, the position of

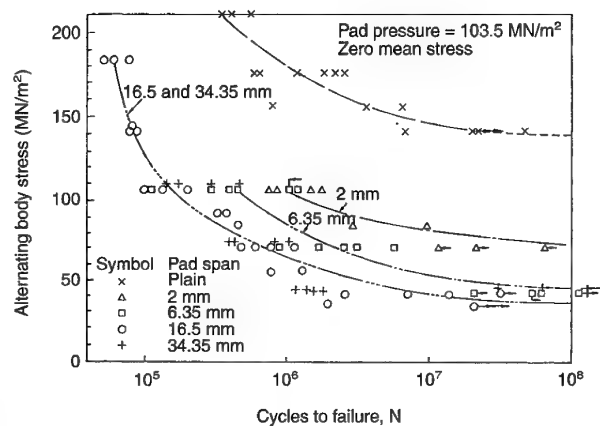


Figure 3 Effect of bridge pad span on fretting fatigue life during constant amplitude loading for a 2014A aluminium specimen and BS S98 steel bridge pads (after Ref. ¹²)

Table 1 Fatigue strength reduction factors due to fretting in various engineering alloys

Fatigue specimen	Contact pad	Contact pressure (MPa)	Fatigue mean stress (MPa)	Fatigue strength unfretted (MPa)	Fatigue strength fretted (MPa)	Strength reduction factor	Relative slip range (μm)
Steels ²							
3.5NiCrMoV	1CrMo	30	0	± 300	± 140	2.1	15
3.5NiCrMoV	1CrMo	30	300	± 215	± 60	3.6	6.2
3.5NiCrMoV	1CrMo	300	0	± 300	± 130	2.3	12
3.5NiCrMoV	1CrMo	300	300	± 215	± 60	3.6	4
3.5NiCrMoV	2014A	30	0	± 300	± 140	2.1	13.5
3.5NiCrMoV	2014A	30	300	± 215	± 75	2.9	6.8
18Mn4Cr	3.5NiCrMoV	20.7	0	± 250	± 100	2.5	10
18Mn4Cr	3.5NiCrMoV	20.7	300	± 125	± 50	2.5	4.5
18Mn18Cr	3.5NiCrMoV	20.7	0	± 250	± 165	1.5	17.4
18Mn18Cr	3.5NiCrMoV	20.7	300	± 185	± 70	2.6	6.7
Aluminium ³¹							
2014A Al	3.5NiCrMoV	30.8	75	± 140	± 15	9.3	2
2014A Al	3.5NiCrMoV	30.8	125	± 135	± 12.5	10.8	1.5
2014A Al peened	3.5NiCrMoV	30.8	125	± 135	± 50	2.7	9.6
Aluminium ¹²							
2014A	BS S98	103.5	0	± 148	± 72	2.05	2
2014A	BS S98	103.5	0	± 148	± 47	3.14	4.2
2014A	BS S98	103.5	0	± 148	± 36	4.11	8.35
2014A	BS S98	103.5	0	± 148	± 36	4.11	17.4
Titanium ¹³							
Ti6Al4V	Ti6Al4V	20	61.25	± 260	± 125	2.1	30

this boundary can move, possibly as a result of change in coefficient of friction or because of changes in local stresses accompanying crack initiation.

With small slip range ($\delta \leq 10 \mu\text{m}$), fretting scars tend to be patchy with little fretting wear. At higher values of slip range ($\delta \geq 20 \mu\text{m}$), considerable wear is encountered over the whole contact area. For any specimen/pad combination examined, surface damage from wear is greater in the softer material. If metal transfer occurs from one component in a fretting assembly to the other, then it is invariably from the softer to the harder material. The surface damaged regions in steel specimens had an overlay of brown debris which was identified by X-ray analysis as α - and γ - Fe_2O_3 and particulate iron.¹⁴ The fine iron particles can rapidly oxidise and provide an oxide abrasive which promotes the fretting wear process. Large slip displacements will tend to encourage the disruption of existing oxide films, thereby allowing metal to metal contact, possibly local welding and metal transfer. The role of the oxide debris can be highly specific to the material combination in contact and also to the state of stress. In some alloy systems, the 'glaze' oxides produced during fretting can substantially lower the coefficient of friction.⁶ Cellulose acetate replicas can be taken from the fretted scar areas and it has been demonstrated¹⁴ that microcracks often initiate at the slip/no slip boundary (see Figure 4). Some tests can be periodically interrupted in order to take acetate replicas of the fretted region which can then be examined in the scanning electron microscope (SEM), demonstrating that in several materials small cracks are present at an early stage in fretting fatigue life ($< 20\%$). Small, nonpropagating cracks have also been found in fretted specimens 'running out' at 10^8 cycles, when tested below the fretting fatigue limit.^{7,15}

Metallographic sections taken through a fretting scar show that the small crack initially grows at a shallow angle to the specimen surface whilst it is under the influence of the shear stresses resulting from the contact pad. As the crack develops and the shear mode diminishes, it assumes an orientation perpendicular to the applied (body) fatigue stress.

Fractographic observations were made using scanning electron microscopy of 'broken-open' fretting defects produced during interrupted fatigue tests carried out at stresses below the fretting fatigue limit (Figure 5). The defect containing specimen can be broken open after cooling in liquid nitrogen and the tip of the defect is thereby 'marked' in steels by the change in fracture

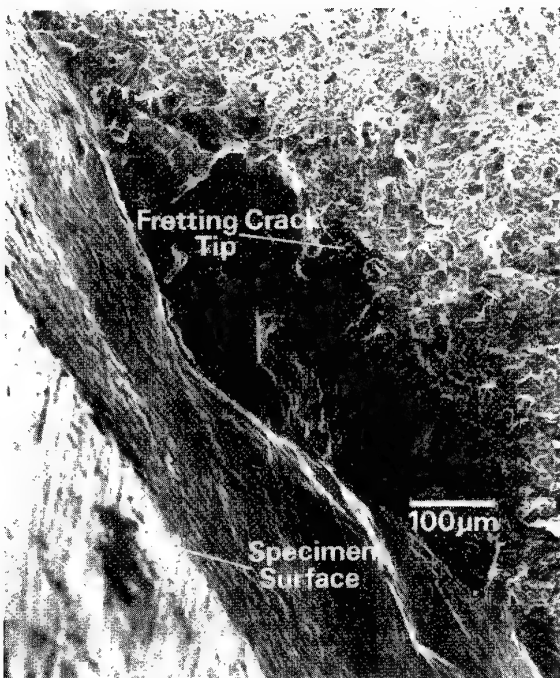


Figure 5 Small fretting fatigue defect (about 0.25 mm deep) in 3.5%NiCrMoV steel specimen with 1%CrMo steel bridge pad, tested below the fretting fatigue limit (stress $0 \pm 130 \text{ MPa}$ and contact pressure 300 MPa) and subsequently broken open in liquid nitrogen (after Ref. 7)

mode. Alternatively, fretting defects can be broken open by removing the fretting pads and continuing the fatigue test at a much higher stress. The tip of the fretting defect which makes a shallow angle with the specimen surface is then marked by an abrupt change in angle, the 'break open' fracture being perpendicular to the specimen surface.

The depths (measured perpendicular to the specimen surface) and the aspect ratio (depth divided by semi-surface length) of defects revealed by breaking open in the interrupted tests were measured on the fracture surface. The observations indicate that a number of defects will be created in each specimen, and it will be the largest defect which is likely to promote 'break open'. The defect size results are given in Table 2 for a steel and an aluminium alloy as a function of the fretting conditions.

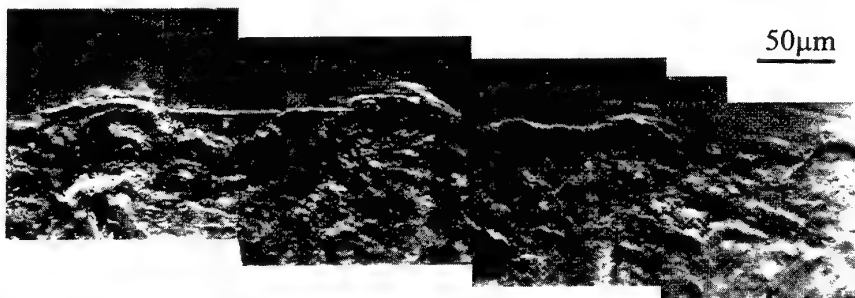


Figure 4 Cellulose acetate replica showing crack of approximately 0.4 mm surface length at front foot of bridge pad and near slip/no slip boundary. Specimen 3.5%NiCrMoV steel and 1%CrMo steel pad with fatigue stress $308 \pm 65 \text{ MPa}$ and 300 MPa contact pressure (after Ref. 14)

Table 2 Defect sizes measured in interrupted fretting fatigue tests

Maximum defect depth (mm)	Defect aspect ratio	Applied stress (MPa)	Applied contact pressure (MPa)	Pad span (mm)	Plateau ΔF_i (N)	Slip range δ (μm)
Specimen: 3.5NiCrMoV steel; Pad: 1CrMo Steel ²						
0.08	0.14	150 ± 90	30	25.4	621	9.5
0.10	0.70	0 ± 90	30	25.4	617	9.5
0.11	0.28	0 ± 90	300	25.4	2110	6.11
0.13	0.40	0 ± 110	30	25.4	714	11.7
0.16	0.18	0 ± 80	30	50.8	892	16.4
0.16	0.4	0 ± 90	30	50.8	893	18.8
0.18	0.25	0 ± 140	30	25.4	827	15.0
0.20	0.06	0 ± 110	300	25.4	2050	8.7
0.22	0.30	0 ± 130	300	25.4	2319	10.5
Specimen: 2014A Al; Pad: 3NiCrMoV steel ³¹						
0.12	0.96	75 ± 10	30.8	25.4	246	2.44
0.15	0.57	75 ± 12.5	30.8	25.4	380	2.75
0.15	0.46	75 ± 20	30.8	12.7	338	2.32
0.19	0.74	75 ± 14	30.8	25.4	401	3.19
0.25	0.39	75 ± 12.5	30.8	25.4	371	2.79

Fretting fatigue analysis: the S-N approach

The conventional method of establishing the important variables which can affect fretting fatigue has been to generate *S-N* curves, with and without fretting, thereby allowing fretting fatigue strength reduction factors to be established. Such information is given in *Table 1* for important practical assemblies found in large electrical turbogenerators and jet engines. This method is particularly important for ranking the various combinations in terms of fretting fatigue performance. An indication is given of material combinations where significant fretting problems will arise or which should be avoided altogether. Since they have been perceived to be the parameters of great importance, the roles of frictional force, contact pressure and range of slip have received much attention ^{1-9,14,15}.

It is widely recognised that the initiation of fretting fatigue cracks is strongly influenced by the alternating shear stresses in the surface which arise from the frictional forces promoted by the oscillatory movement. Nishioka and Hirakawa ^{15,16} measured the alternating stress σ_{fw1} required to initiate a fretting fatigue crack for the case of a cylindrical pad in contact with the plane surface of a fatigue specimen. They derived the expression

$$\sigma_{fw1} = \sigma_{w1} - 2\mu p_0 [1 - \exp(-S/k)] \quad (2)$$

where σ_{w1} is the fatigue strength in the absence of fretting, μ is the coefficient of friction, p_0 the contact pressure, S the amplitude of slip and k is a constant, determined experimentally. The additional stress introduced into the surface by the fretting contact is given by the term $2\mu p_0 [1 - \exp(-S/k)]$ and is greater the higher the values of contact pressure and coefficient of friction. For large values of slip amplitude, S , the exponential term becomes insignificant. When slip amplitude, S , is greater than 20 μm , the fretting fatigue strength σ_{fw1} reaches a constant value of 90 MPa with $\sigma_{w1} = 736$ MPa, $\mu = 0.67$, $p_0 = 500$ MPa and $k = 3.38 \times 10^{-3}$. This result is consistent with the experimental findings of Field and Waters ¹⁸, who found that the minimum fretting fatigue strength for steels occurred for a slip amplitude between 8 and 14 μm . Support for the idea that a minimum value in fretting fatigue strength occurs at a particular value of slip amplitude

is given by the work of Duquette and coworker ^{19,20}. For contact pressures between 20 and 41 MPa, he found a minimum fretting fatigue strength at a slip amplitude of 20 μm . He further suggested that the fatigue strength increases at higher values of slip amplitude due to the excessive wear which can abrade away previously initiated fretting fatigue cracks. A simple schematic ²¹ indicating the interrelation between wear and fretting fatigue life as a function of slip amplitude is given in *Figure 6*. The various regimes of stick, mixed stick and slip, gross slip, reciprocating sliding are found from the Mindlin analysis ²².

It should be noted that the analysis of Nishioka and Hirakawa ^{15,16,17} predicts that if the fatigue strength increases then there will be a corresponding increase in fretting fatigue strength which is contrary to experimental observations reported in the literature ⁶.

Wharton *et al.* ²³ presented an approach which is based on the fatigue strength without fretting, σ_{wo} , being reduced by the added tangential stress determined by the contact load L , the breadth b of the contact region for a cylindrical pad, the coefficient of friction

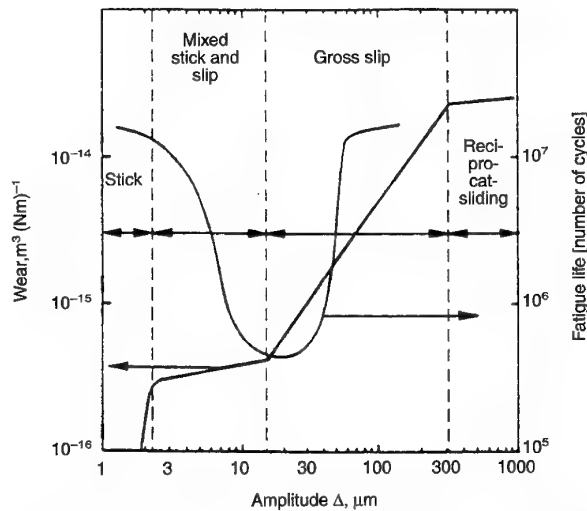


Figure 6 Relation between fretting fatigue and wear as a function of slip amplitude (after Ref. ²¹)

μ and a notch sensitivity factor q to give the following relation for fretting fatigue strength σ_{wf} :

$$\sigma_{wf} = \sigma_{wo} - q \left(\frac{8\mu L}{\pi b} \right) \quad (3)$$

This relation is consistent with the experimental observation that a material with a high plain fatigue strength does not necessarily have a high fretting fatigue strength, the notch sensitivity q accounting for this feature.

Nowell and Hills²⁴ have emphasised that fretting fatigue crack initiation will only occur when a critical contact width is exceeded and that the amplitude of slip between the two surfaces has a significant influence on the initiation process. However, crack initiation is a microscopic process taking place at asperity level (in terms of surface roughness) whereas elastic stress analysis predicts 'bulk' properties for a smooth contact. As a consequence, quantifying crack initiation using bulk properties will inevitably result in empirical relationships.

In the UK, the Engineering Sciences Data Unit (ESDU) have used the experimental data of the researchers at the National Engineering Laboratory^{3,18} to forward a predictive methodology which relates the fatigue strength reduction factor K_{ff} , due to fretting, to the slip amplitude δ . Based on experimental results on a low carbon steel, $K_{ff} = 2$ at low fatigue mean stress and 4 at high mean stress when $\delta \leq 5 \times 10^{-3}$. When $\delta \geq 5 \times 10^{-3}$ then $K_{ff} = 2$ at low mean stress and 10 at high mean stress. A major problem arises in that the fretting fatigue reduction factor found for a simple specimen geometry is expected to be quite different from the much more complex geometries found in real components. In brief, Lindley and Nix⁸ have concluded that K_{ff} factors are only meaningful for ranking the susceptibility to fretting of various contacting material combinations. Difficulties stemming from both geometry and 'volume of material sampled' found in plain fatigue are also found in fretting fatigue.

In carrying out extensive research into the fretting behaviour at the dovetail fixing of a turbine blade and a disk, Ruiz and coworkers²⁵⁻²⁷ have developed the concept of a fretting fatigue damage parameter (FFDP). Here, it was argued that it is not the slip δ nor the interface shear stress τ alone that causes the damage, but a combination of the two. It has been shown that the severity of surface damage as characterised by the surface roughness depends entirely on the product $\delta\tau$. The amount of work done in overcoming friction per unit surface area in the slip zone varies with position and can be characterised by the product of τ , the maximum traction attained during one cycle at that point, and δ , the relative slip amplitude between the surfaces at the same position. The parameter $\tau\delta$ then gives a measure of the amount of fretting damage per cycle at any point on the surface. It will be seen that no fretting will occur when $\tau\delta$ is zero, that is in the stick zone ($\delta = 0$) and outside the contact (where $\tau = 0$). Ruiz and coworkers²⁵⁻²⁷ also argued that a crack is more likely to initiate in a region of bulk tensile stress compared to one where the stress parallel to the surface is compressive. Furthermore, the growth of cracks developing from the surface damage is also controlled by the tangential stress σ_t along the line of

contact, leading to the combined (initiation and growth) damage parameter (FFDP):

$$\text{FFDP} = \sigma_t \tau \delta \quad (4)$$

A crack is predicted to initiate at the point where the maximum value of $\sigma_t \tau \delta$ reaches a critical value. Ruiz and coworkers²⁵⁻²⁷ and Kuno *et al.*²⁸ have found good agreement between the locations of maxima of $\sigma_t \tau \delta$ and the sites of crack initiation. This is demonstrated by the results of Ruiz and coworkers²⁵⁻²⁷, Figure 7 giving values of σ_t and $(\tau\delta)$ and $(\sigma_t \tau \delta)$ along the interface in the blade/disk contact of a dovetail joint. It can be seen that there is good agreement between the cracking position and the maximum value of $\sigma_t \tau \delta$.

In order to simulate the fretting conditions in a real component, it is necessary to reproduce each of the three parameters in a laboratory test.

Ruiz and coworkers²⁵⁻²⁷ have suggested that their FFDP, $\sigma_t \tau \delta$, can be used as a basis for design against fretting fatigue and the likelihood of fretting fatigue can be reduced in two ways: (1) reducing the slip amplitude and/or the shear stress will thereby reduce the severity of fretting $\tau\delta$; (2) the stress in the surface σ_t should be minimised by placing contacting surfaces in low tensile regions or in compressive fields. Until methods based on micromechanics are developed, the FFDP $\sigma_t \tau \delta$ can provide a useful guide to design engineers.

For the blade/disk dovetail joint, Ruiz and coworkers²⁵⁻²⁷ carried out analyses of tests at both room temperature and 600°C. They concluded that the fretting fatigue parameter $\sigma_t \tau \delta$ controlled behaviour at room temperature whereas the peak stress (fatigue only) becomes the overriding parameter at 600°C. However, the changing stress/temperature/contact profile during the various stages of operation of a jet engine means that both parameters (fretting fatigue or fatigue only) must be considered.

Fretting fatigue analysis: the fracture mechanics approach

Several studies^{29,30} have demonstrated that fretting fatigue cracks can be initiated at a very early stage (< 5%) of fretting fatigue life. The cracks propagate obliquely to the specimen surface under the combined action of tangential fretting forces and the cyclic body stresses. When the crack reaches a certain depth, which depends upon the applied and mean body stresses as well as the prevailing contact conditions (contact pressure, value of friction, slip amplitude), further crack propagation occurs perpendicular to the applied stress since the friction forces will then be insignificant. As well as accelerating crack initiation, fretting can also increase the rate of crack propagation. Additionally, a crack which might be dormant under simple fatigue loading might resume propagation under fretting fatigue conditions⁶. The S-N tests previously described and the associated metallography have demonstrated that small fretting cracks, typically up to 0.5 mm deep, initiate rapidly at a small fraction (5–10%) of fretting fatigue life. Nix and Lindley^{7,31} used interrupted testing and metallographic examination of sections through fretting damage to demonstrate that fretting cracks could form at stresses considerably below the fatigue limit. As well as measuring crack size, angle to the

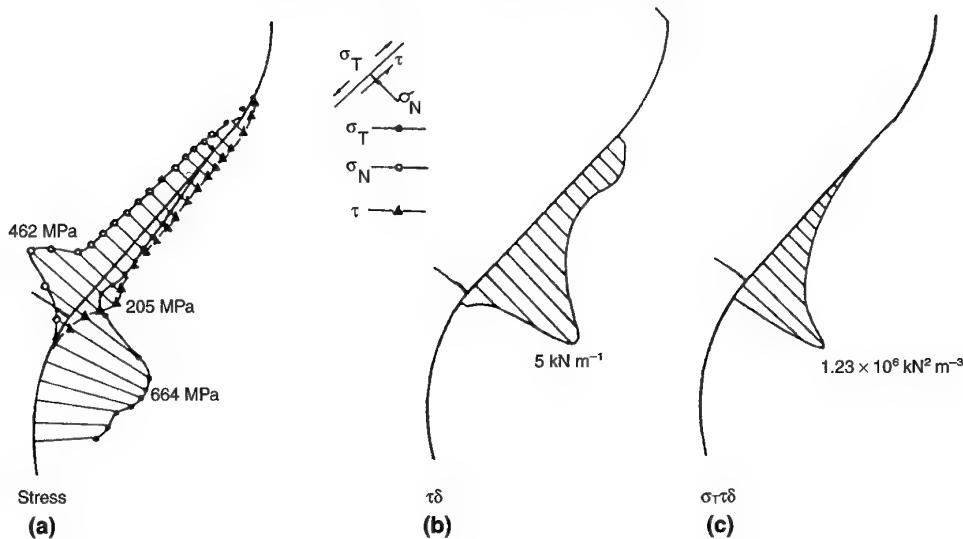


Figure 7 Turbine blade/disk dovetail joint under 40 kN biaxial load showing (a) distribution of stresses, (b) fretting damage parameter $\tau\delta$, (c) combined fatigue and fretting damage parameter $\sigma_T\delta$ (after Refs^{25–27})

specimen surface and crack aspect ratio, the frictional forces required to introduce such cracks were also found (see *Table 2*). Other workers have independently shown that cracks could initiate very early in fretting fatigue life ($< 5\text{--}10\%$) and at stresses well below the fretting fatigue limit (to give rise to nonpropagating cracks) and attention was then focussed on the apparently easier task of modelling fretting fatigue crack growth using fracture mechanics. In a fracture mechanics model^{11,31}, the stress intensity factor at the tip of a crack growing beneath a fretting contact will arise not only from the body stresses but also from contributions arising from the tangential and vertical forces due to the fretting contact. This composite stress intensity factor can be evaluated^{33–36} by several distinct methods: (1) finite element stress analysis which might be necessary for the highly complex assemblies found in practice; (2) by using stress intensity factors arising from the tangential and normal forces at the fretting position using Green's functions; (3) the use of distributed dislocation methods. In a fracture mechanics model of fretting fatigue, it is necessary to have a knowledge of frictional forces at the contact in either specimens or component. The cyclic stress intensity factor ΔK_{app} is then given by contributions from the alternating body stresses σ_a and frictional forces F_t , and if A is the specimen cross-sectional area:

$$\Delta K_{app} = Y\sigma_a\sqrt{\pi a} + F_t K_{tp} - Y\frac{F_t}{A}\sqrt{\pi a} \quad (5)$$

The mean stress intensity factor K_m due to the mean body stress σ_m and normal contact force F_n is given by

$$K_m = Y\sigma_m\sqrt{\pi a} + F_n K_{np} \quad (6)$$

where a is the crack length and Y is a surface and crack shape correction factor.

The stress intensity factor components due to frictional (F_t) and normal (F_n) loads (per unit load) are K_{tp} and K_{np} respectively. The terms K_{tp} and K_{np} depend on the distribution of stresses beneath the contact and the measured frictional forces are required to scale K_{tp}

and K_{np} as indicated in Equations (5) and (6) above, a detailed explanation being given in Ref.³². Crack propagation lives can then be found in principle by integrating a fretting fatigue crack growth law, and Edwards¹¹ was able to successfully predict experimentally derived *S-N* curves, thereby providing validation of the fracture mechanics methodology. Alternatively, the composite ΔK_{app} can be compared with the experimentally determined fatigue crack growth threshold ΔK_{th} in order to predict the balance between crack growth or arrest^{2,32}. If $\Delta K_{app} > \Delta K_{th}$, then sustained growth of a fretting fatigue crack will occur (see *Figure 8*). The fracture mechanics model demonstrates that the applied stress intensity factor for a small crack, ΔK_{app} , will be increased under fretting conditions, possibly promoting growth, whereas the crack would remain dormant in a nonfretting situation. Such analyses will require a knowledge of both short and long crack behaviour and the valid application of linear elastic fracture mechanics will need to be demonstrated.

A major factor impeding progress toward a better understanding of fretting fatigue is the limited direct

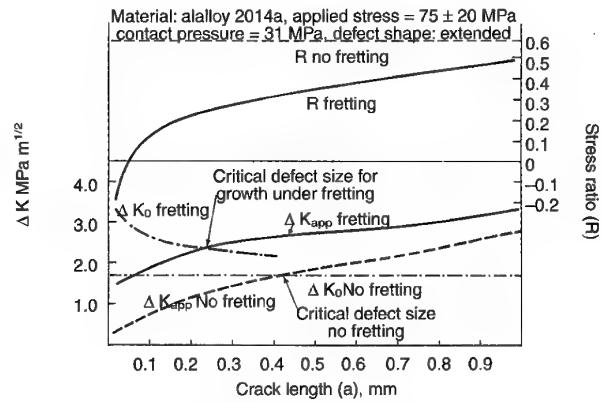


Figure 8 Applied stress intensity factor ΔK_{app} and threshold parameter for fatigue crack growth ΔK_{th} as a function of crack depth for conditions with and without fretting (after Ref.³²)

observation information, even at room temperature and in air environment. Small crack growth is initially controlled by a combination of shear and tensile forces. Eventually the crack changes direction under the contact, at which point the tensile forces predominate. Although it would constitute a vital step toward understanding fretting fatigue, only limited progress has been made in evaluating the growth of small cracks under mixed mode loading without fretting.

In general terms, fretting fatigue strength reduction factors are generally limited to ranking, in a qualitative manner, the susceptibility of different contacting combinations to fretting fatigue. Despite these various complications, Lindley and Nix^{2,32} have met with some success in modelling fretting fatigue damage in turbogenerators. However, the following simplifications were made in their analysis, each item requiring substantial further research.

- (a) Cracks were assumed to propagate at right angles to the surface rather than the 10–45° found in practice.
- (b) Only mode I stress intensity factors were used in the analysis, a consequence of the lack of experimental data for mixed mode I/II loading under fretting fatigue conditions.
- (c) Multiple cracking commonly occurs under fretting conditions which would introduce crack tip shielding.^{37,38}
- (d) Fretting involves multiaxial fatigue³⁹ whereas uniaxial models only are generally used in analysis.

As a small fretting crack grows in the region of contact, the crack tip will experience mode II as well as mode I stress intensity factors. Nowell and coworkers⁴⁰ have used the experimental data of Bramhall⁴¹ to calculate K_I and K_{II} factors for a crack at cylinder/flat contact and then to present the information in terms of contour maps. Figure 9 is a polar map giving values of K_I and K_{II} as a function of the ratio b/a where b is the crack length and a is the half-contact width. The maximum value of K_{II} occurs when the crack is inclined at an angle of about 45° to the

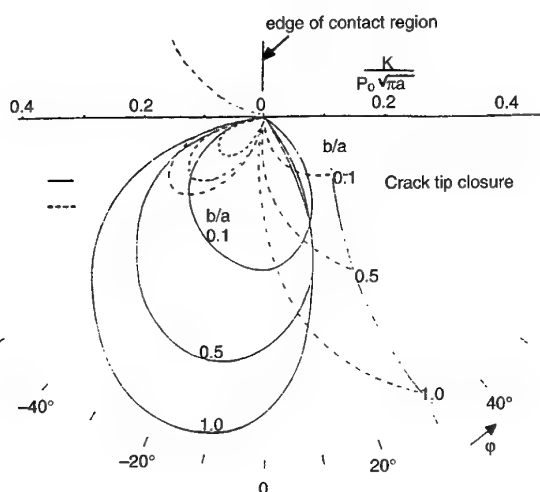


Figure 9 Polar plots of K_I and K_{II} stress intensity factors (normalised with respect to contact half-width a) for a crack of length b propagating from the trailing edge of a contact (cylindrical pad against a flat specimen, after Ref. 40)

free surface, and from this aspect growth under the contact is clearly favoured. The calculated K_I reaches a maximum for a crack approximately at right angles to the free surface, and K_I becomes negative for a crack inclined beneath the contact. Even in the very early stages of crack growth, a small K_I component is needed in order to 'unlock' the crack faces. For an inclined crack growing under the contact under mixed mode I/II loading, the predicted crack closure condition is always in proximity. If the transition from mode II to mode I growth does not occur at an early stage in crack propagation life, then closure and a nonpropagating crack are likely to result. The diagram can correctly predict the observed direction of crack propagation in several experiments.

Therefore fracture mechanics potentially provides an attractive assessment route to model the growth of fretting cracks, but there are substantial qualifications.

Microstructural fracture mechanics

Plain fatigue. In a polycrystalline material, plastic deformation is triggered in certain favourably oriented surface grains to form so-called 'persistent slip bands'. Intrusions and extrusions (1–10 μm in size) are created where the persistent slip bands (PSBs) intersect the free surface. Since the intrusions are stress raisers on a microscopic scale, they will develop by promoting more plastic deformation. The initiation and early growth of such defects will depend upon the material's plastic deformation characteristics, i.e. whether slip is planar or wavy, the cyclic hardening or softening response and in some cases the ability to strain age. Although 'natural' defects can develop at PSBs in pure metals, crack initiation can occur more readily at inclusions in commercial materials, plastic deformation processes again being operative.

Forsyth⁴² showed that in high purity AlZnMg alloys, the initiation and early growth of microcracks could occur by the activation of a single slip system (stage 1 crack growth), the controlling shear stresses thereby creating PSBs in a favourably oriented surface grain with microcracks angled to the specimen surface. As the stage 1 crack approached the first grain boundary, multiple slip systems were activated at the crack tip causing a transition to stage 2 growth normal to the specimen surface and controlled by the tensile stress.

In many commercial alloys, microcracks initiate at inclusions and the stage 1 period of growth can be eliminated. The tendency toward inclusion cracking rather than slip band (stage 1) cracking was found to depend on stress level and inclusion content, slip band cracking being promoted by high stresses and higher purity content.⁴³ Stress concentrations such as notches can also eliminate the stage 1 phase of growth.

As a microcrack develops, it will encounter microstructural barriers such as grain and colony boundaries and possibly twins, which it may or may not overcome. Countering these microstructural effects will be mechanical factors such as crack closure. The reduced constraint associated with a surface microcrack will result in less crack closure, a major factor contributing to the faster growth rates found for small cracks.

A starting point in attempts to model the growth of small cracks has been the application of linear elastic fracture mechanics (LEFM), and in particular the cyclic stress intensity factor ΔK . However, it must be remem-

bered that the crack size should be larger than the microstructural unit (often the grain size). LEFM is applicable to cracks which have already propagated through several grains. Breakdown of LEFM can occur at crack sizes of $100 \mu\text{m}$ in medium strength steels and as low as $10 \mu\text{m}$ in high strength engineering alloys under conditions of constant small amplitude stresses in high cycle fatigue.

Fretting fatigue. Fretting fatigue involves a highly complex interplay between mechanical, metallurgical and environmental factors and their individual contributions can be quite different from those operative in plain fatigue. The initial angled crack followed by eventual cracking normal to the specimen surface are again encountered and designated stage 1 (shear stresses predominant) and stage 2 (tensile stresses predominant) respectively.

A feature of fretting is that existing oxide films can be disrupted allowing metal to metal contact, possibly local welding and metal transfer across the interface between the contacting bodies. Shearing of the welds will give particle detachment and surface roughness including pitting. Pits are known to be highly detrimental in the case of plain fatigue. Very high dislocation densities will be introduced due to extensive plasticity at asperity contacts, and in steel/steel assemblies white etching layers have been seen⁶, indicating very high hardness.

Since cracks tend to develop beneath the fretting contact, the level of crack closure will be a major factor determining continued growth or arrest as already indicated⁴⁰. The observation that frictional forces and therefore surface stresses change with accumulating fatigue cycles is a further complication. It is probable that the barriers which impede the development of a fretting fatigue crack are likely to be mechanical in origin rather than microstructural. The author believes that in some practical fretting problems the long crack threshold for fatigue crack growth with fretting ΔK_{th} can be compared with the applied ΔK_{app} in order to predict crack arrest or continued growth of a stage 2 crack. However, in other cases fretting crack initiation and stage 1 growth will be the critical events leading to failure. Care should be exercised in integrating a fretting fatigue crack growth law in order to predict an $S-N$ curve, since it is likely that the K_I and K_{II} factors will not be valid over all the (short) crack sizes involved.

Palliatives to combat fretting fatigue. Fretting fatigue problems should be eliminated or minimised by good design involving reduction of local stresses and avoidance wherever possible of contacting interfaces. In situations where fretting fatigue remains a threat, then palliatives can be considered.

The $S-N$ methodology already developed can be used to assess the performance of various palliative treatments which may be used to reduce or eliminate fretting degradation of fatigue properties. The benefits from palliative action fall into two categories. (a) Those which reduce friction at the fretting interface (Figure 10) and therefore the stresses available to promote fatigue crack initiation and early crack growth. In the presence of surface lubricants such as molybdenum disulphide or PTFE, the relative slip amplitude

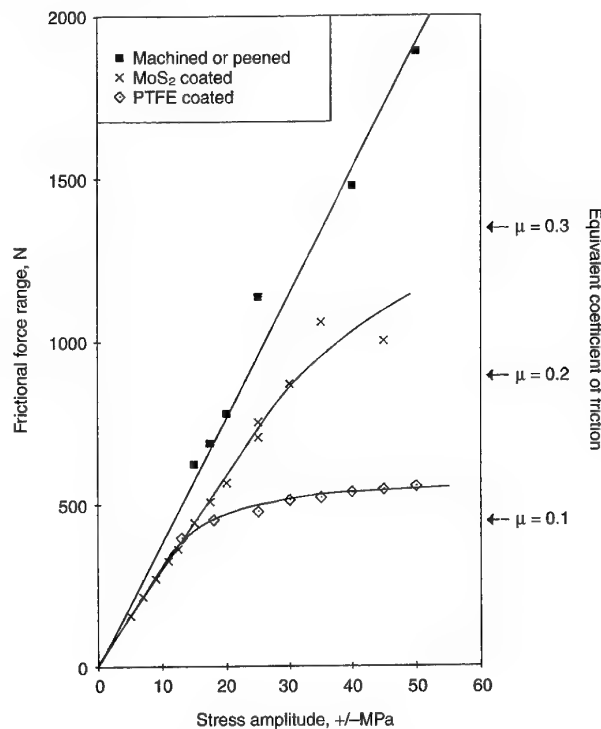


Figure 10 The effect of various palliative treatments on the plateau value of frictional force as a function of applied stress for a 2014A aluminium specimen and 3.5%NiCrMoV bridge contact pad (after Ref. ²)

increases under conditions of low friction (Figure 11). (b) Those which improve the near surface fatigue properties by introducing compressive residual stresses. For the case of 2014A³¹ aluminium alloy in contact with 3.5NiCrMoV pads, small fretting cracks can still initiate after glass bead peening but they are unable to grow in the presence of the compressive residual stresses. For 2014A alloy, the most effective single palliative treatment to combat fretting fatigue was found to be glass bead peening (Figure 12). It should be noted that the high rates of wear associated with large slip amplitudes can negate the benefits of peening by removing the near surface layer.

The fretting fatigue damage parameter of Ruiz and coworkers²⁵⁻²⁷ can be used to rationalise palliative action in combatting fretting where it should be noted that a lubricant which lowers the coefficient of friction will have opposite effects on τ and δ , and hence the combined effect must be carefully considered.

CONCLUSIONS

- Preferred experimental procedures including specimen and contact pad geometry requirements have been identified with the objective of generating $S-N$ curves with and without fretting.
- The important variables which significantly affect fretting fatigue behaviour, including contact pressure, slip amplitude and frictional forces in the contact interface, are identified.
- Analytical procedures for fretting fatigue based on either crack initiation or crack growth are critically examined.

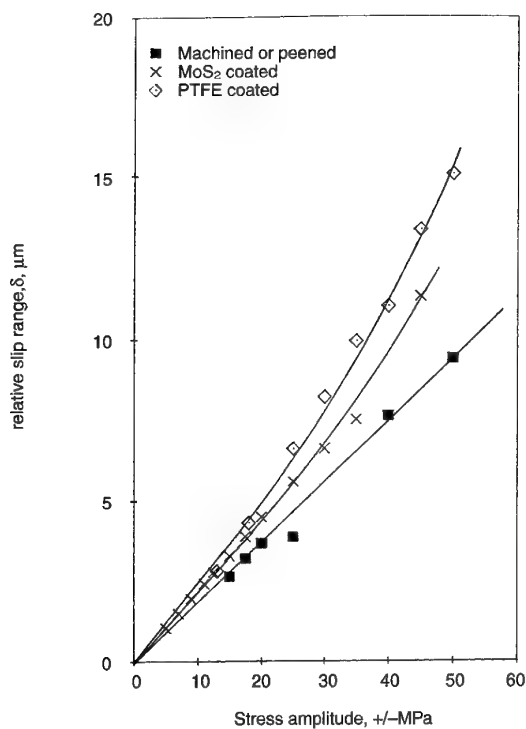


Figure 11 The relationship between relative slip and applied stress for a 2014A aluminium specimen and 3.5%NiCrMoV bridge pad after palliative treatment (after Ref. ²)

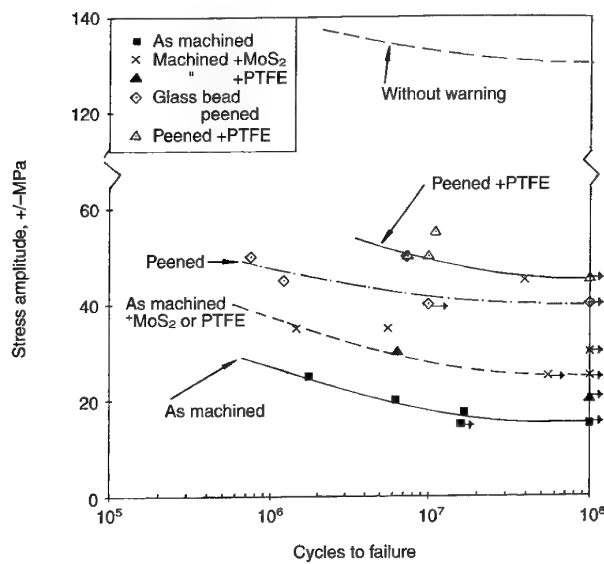


Figure 12 The effect of various palliative treatments on fretting fatigue $S-N$ curves for a 2014A aluminium specimen and 3.5%NiCrMoV bridge pad (after Ref. ²)

REFERENCES

- 1 Waterhouse, R. B. *Fretting Corrosion*. Pergamon Press, Oxford, 1972.
- 2 Lindley, T. C. and Nix, K. J., Fretting fatigue in the power generation industry. In *Standardisation of Fretting Fatigue Test Methods and Equipment*, eds H. A. Attia and R. B. Waterhouse. ASTM STP 1159, 1992, pp. 153–169.
- 3 Fenner, A. J. and Field, J. E., Fatigue under fretting conditions. *Revue Metallurgique*, 1958, **55**, 475–478.
- 4 Nishioka, K. and Hirakawa, K., Fundamental investigation of fretting fatigue: Part 2, Fretting fatigue test machines and some results. *Bulletin of Japan Society of Mechanical Engineers*, 1969, **12**(50), 180–187.
- 5 Endo, K., Goto, H. and Nakamura, T., Fretting fatigue strength of several material combinations. *Bulletin of Japan Society of Mechanical Engineers*, 1973, **16**(92), 143–150.
- 6 Waterhouse, R. B., Fretting fatigue. *International Metallurgical Reviews*, 1992, **37**(2), 77–97.
- 7 Nix, K. J. and Lindley, T. C., The influence of relative slip and contact materials on the fretting fatigue of a 3.5%NiCrMoV rotor steel. *Wear*, 1988, **125**, 147–162.
- 8 Lindley, T. C. and Nix, K. J., An appraisal of the factors which influence the initiation of cracking by fretting fatigue in power plant. In *Fretting Fatigue*. MEP Publications, London, 1992, pp. 239–256.
- 9 Spink, G. M., Fretting fatigue of a 2.5%NiCrMoV low pressure turbine shaft steel: The effect of different contact pad materials and of variable slip amplitude. *Wear*, 1990, **136**, 281–297.
- 10 Hills, D. A. and Nowell, D., A critical analysis of fretting fatigue experiments. In *Fretting Fatigue*. MEP Publications, London, 1992, pp. 171–182.
- 11 Edwards, P. R., The application of fracture mechanics to predicting fretting fatigue. In *Fretting Fatigue*. Applied Science Publishers, London, 1981, pp. 67–97.
- 12 Rayaprolu, D. B. and Cook, R., A critical review of fretting fatigue investigations at the Royal Aerospace Establishment. In *Standardisation of Fretting Fatigue Test Methods and Equipment*. ASTM STP 1159, Philadelphia, PA, 1992, pp. 129–152.
- 13 Nakazawa, K., Sumita, M. and Maruyama, N., Effect of contact pressure on fretting fatigue of high strength steel and titanium alloy. In *Standardisation of Fretting Fatigue Test Methods and Equipment*. ASTM STP 1159, Philadelphia, PA, 1992, pp. 115–125.
- 14 King, R. N. and Lindley, T. C., Fretting fatigue in a 3.5%NiCrMoV rotor steel. *Advances in Research*, ICF 5. Pergamon Press, Oxford, 1980, pp. 631–640.
- 15 Nishioka, K. and Hirakawa, K., Proceedings of International Conference on Mechanical Behaviour of Materials, Kyoto, Japan, 1972, pp. 308–318.
- 16 Nishioka, K. and Hirakawa, K., Fundamental investigation of fretting fatigue: Part 5, The effect of relative slip. *Bulletin of Japan Society of Mechanical Engineers*, 1969, **12**(52), 692–697.
- 17 Nishioka, K. and Hirakawa, K., Fundamental investigation of fretting fatigue: Part 6, Effect of contact pressure and hardness of materials. *Bulletin of Japan Society of Mechanical Engineers*, 1972, **15**(80), 135–144.
- 18 Field, J. E. and Waters, D. M., Fretting fatigue strength of En26 steel: Effect of mean stress, slip amplitude and clamping conditions. National Engineering Laboratory Report No. 275, UK, 1967.
- 19 Duquette, D. J. *Strength of Materials and Alloys*. Pergamon Press, 1980, p. 214.
- 20 Sproles, F. S. and Duquette, D. J., The mechanism of material removal in fretting. *Wear*, 1978, **49**, 339–352.
- 21 Vingsbo, O. and Soderberg, D., On fretting maps. *Wear*, 1988, **126**, 131–147.
- 22 Mindlin, R. D., Compliance of elastic bodies in contact. *Journal of Applied Mechanics*, 1949, **16**, 259–268.
- 23 Wharton, M. H., Waterhouse, R. B., Hirakawa, K. and Nishioka, K., The effect of different contact materials on the fretting fatigue strength of an aluminium alloy. *Wear*, 1973, **26**, 253–260.
- 24 Nowell, D. and Hills, D. A., Crack initiation criteria in fretting fatigue. *Wear*, 1990, **136**, 329–343.
- 25 Ruiz, C., Boddington, P. H. B. and Chen, K. C., An investigation of fatigue and fretting in a dovetail joint. *Experimental Mechanics*, 1984, **24**, 208–217.
- 26 Ruiz, C. and Chen, K. C., Life assessment of dovetail joints between blades and disks in aero-engines. Proceedings of International Conference on Fatigue and Structures, I. Mechanical Engineering, London, 1986.
- 27 Ruiz, C., Wang, Z. P. and Webb, P. H., Techniques for the characterisation of fretting fatigue damage. In *Standardisation of Fretting Fatigue Test Methods and Equipment*, eds H. A. Attia and R. B. Waterhouse. ASTM STP 1159, 1992, pp. 170–177.
- 28 Kuno, M., Waterhouse, R. B., Nowell, D. and Hills, D. A., Initiation and growth of fretting fatigue cracks in the partial slip regime. *Fatigue and Fracture of Engineering Materials and Structures*, 1989, **12**(5), 387–398.

- 29 Endo, K. and Goto, H., Initiation and propagation of fretting fatigue cracks. *Wear*, 1976, **38**, 311–320.
- 30 Endo, K., Practical observations of initiation and propagation of fretting fatigue cracks. In *Fretting Fatigue*. Applied Science Publishers, London, 1981, pp. 127–141.
- 31 Nix, K. J. and Lindley, T. C., The role of fretting in the initiation and growth of defects in an aluminium alloy. *Proceedings of Conference on Crack Initiation under Complex Loading, Paris, 1984*. Société Française de Métaux et Matériaux, pp. 233–246.
- 32 Nix, K. J. and Lindley, T. C., The application of fracture mechanics to fretting fatigue. *Fatigue and Fracture of Engineering Materials and Structures*, 1985, **8**(2), 143–160.
- 33 Rooke, D. P., The development of stress intensity factors. In *Fretting Fatigue*. MEP Publications, London, 1992, pp. 23–58.
- 34 Dai, D. N., Hills, D. A. and Nowell, D., Stress intensity factors for three dimensional fretting fatigue cracks. In *Fretting Fatigue*. MEP Publications, London, 1992, pp. 59–72.
- 35 Faanes, S. and Harkegard, G., Simplified stress intensity factors in fretting fatigue. In *Fretting Fatigue*. MEP Publications, London, 1992, pp. 73–82.
- 36 Sheikh, M. A., Fernando, U. S., Brown, M. W. and Miller, K. J., Elastic stress intensity factors for fretting fatigue using the finite element method. In *Fretting Fatigue*. MEP Publications, London, 1992, pp. 83–102.
- 37 Dubourg, M. -C. and Villechaise, B., Analysis of multiple fatigue cracks: Part 1, Theory. *Journal of Tribology*, 1992, **114**, 455–461.
- 38 Dubourg, M. -C., Godet, M. and Villechaise, B., Analysis of multiple fatigue cracks: Part 2, Results. *Journal of Tribology*, 1992, **114**, 462–468.
- 39 Fourny, S., Kapsa, Ph., Vincent, L. and Dang Van, K., Theoretical analysis of fatigue under dry friction for fretting loading conditions. *Wear*, 1996, **195**, 21–34.
- 40 Hills, D. A., Nowell, D. and O'Connor, J. J., On the mechanics of fretting fatigue. *Wear*, 1988, **125**, 129–146.
- 41 Bramhall, R., Studies in fretting fatigue. Ph.D. Thesis, Department of Engineering Science, Oxford University, 1973.
- 42 Forsyth, P. J. E., A two stage process of fatigue crack growth. *Acta Metallurgica*, 1963, **11**, 703–707.
- 43 Kung, C. Y. and Fine, M. E., Fatigue crack initiation and microcrack growth in 2024-T4 and 2124-T4 alloys. *Metallurgical Transactions A*, 1979, **10**, 603–610.

PII: S0142-1123(97)00034-0

Effects of grain size on cyclic plasticity and fatigue crack initiation in nickel

D.J. Morrison and J.C. Moosbrugger

Department of Mechanical and Aeronautical Engineering, Clarkson University,
Potsdam, NY 13699-5725, USA

Fatigue experiments were conducted on polycrystalline nickel of two grain sizes, 24 and 290 μm , to evaluate the effects of grain size on cyclic plasticity and fatigue crack initiation. Specimens were cycled at room temperature at plastic strain amplitudes ranging from 2.5×10^{-5} to 2.5×10^{-3} . Analyses of the cyclic stress-strain response and evolution of hysteresis loop shape indicate that the back stress component of the cyclic stress is significantly affected by grain size and plastic strain amplitude, whereas these parameters have little effect on friction stress. A nonlinear kinematic hardening framework was used to study the evolution of back stress parameters with cumulative plastic strain. These are related to substructural evolution features. In particular, long range back stress components are related to persistent slip bands. The difference in cyclic plasticity behavior between the two grain sizes is related to the effect of grain size on persistent slip band (PSB) morphology, and the effect this has on long range back stress. Fine grain specimens had a much longer fatigue life, especially at low plastic strain amplitude, as a result of the influence of grain size on fatigue crack initiation characteristics. At low plastic strain amplitude (2.5×10^{-4}), coarse grain specimens initiated cracks where PSBs impinged on grain boundaries. Fine grain specimens formed cracks along PSBs. At high plastic strain amplitude (2.5×10^{-3}), both grain sizes initiated cracks at grain boundaries. © 1998. Published by Elsevier Science Ltd.

(Keywords: fatigue; cyclic plasticity; crack initiation)

INTRODUCTION

Numerous studies on cyclic plasticity and fatigue crack initiation of monocrystalline metals, especially copper, have produced a general understanding of the fundamental response of these materials to cyclic loading¹⁻⁷. More recently, attention has been directed toward developing a fundamental understanding of polycrystal cyclic plasticity and fatigue crack initiation phenomena⁸⁻²⁷. Basic mechanisms derived from monocrystal studies provide the foundation for understanding the considerably more complex polycrystal behavior. The objective of the present research was to determine the influence of a fundamental microstructural variable, grain size, on fundamental cyclic plasticity and crack initiation mechanisms. The results of this study, as well as other previous work, clearly indicate that grain size influences cyclic plasticity and fatigue crack initiation mechanisms^{11-14,18-22}.

EXPERIMENTAL PROCEDURES

The experimental details used for this study have been fully described elsewhere^{21,22}. Briefly, fatigue tests were accomplished at room temperature on fine grain (24 μm) and coarse grain (290 μm) nickel-270 (99.98% Ni). Grain size measurements represent the average

linear intercept and include twin boundaries. The coarse grain material was texture-free, but the fine grain material had a $\langle 111 \rangle - \langle 100 \rangle$ fiber texture with both components approximately three times random density. Fatigue specimens with cylindrical gage sections were cycled under fully-reversed tension-compression at constant plastic strain amplitudes, $\epsilon_{pa} = (\epsilon_{p,max} - \epsilon_{p,min})/2$, ranging from 2.5×10^{-5} to 2.5×10^{-3} . Periodically during the fatigue experiments, hysteresis loops were digitally recorded. Several parameters defining the shape of the hysteresis loops were calculated, including the loop shape parameter, V_H , which is defined as the ratio of the area enclosed by the loop to the area of the parallelogram that circumscribes the loop⁵. Acetate replicas were obtained from the surface of the gage section at periodic intervals. The replicas were vacuum evaporation coated with Au-30% Pd at a 30° shadow angle along the direction of the tensile axis.

CYCLIC PLASTICITY BEHAVIOR

The cyclic stress-strain responses of the specimens at cyclic saturation (stabilization of stress amplitude, σ_a , with continued cycling) are shown in the cyclic stress-strain (CSS) curves in Figure 1, where saturation stress amplitude, $\sigma_{a,sat}$, is plotted vs. the plastic strain ampli-

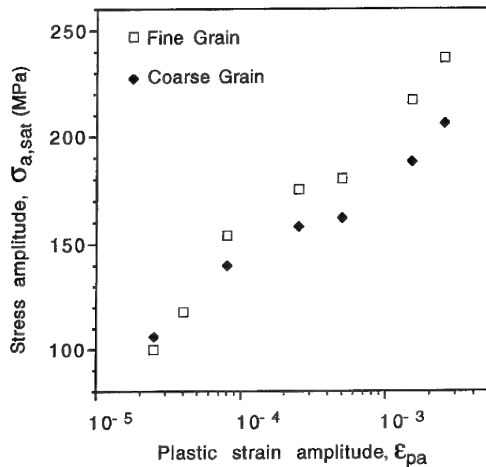


Figure 1 Cyclic stress-strain (CSS) curves of fine and coarse grain nickel

tude at which the test was accomplished. Details concerning the cyclic hardening characteristics (i.e. change in σ_a with continued cycling) of the individual specimens have been reported previously.^{21,22} Figure 1 indicates that $\sigma_{a,sat}$ increases with increasing ϵ_{pa} , and that a short plateau is evident between ϵ_{pa} of approximately 2×10^{-4} and 8×10^{-4} . It has been well established in monocrystal studies that the plateau is caused by the localization of plastic strain in persistent slip bands (PSBs).^{3,28} Figure 1 also indicates that $\sigma_{a,sat}$ was higher in the fine grain nickel, except at very low ϵ_{pa} . The $\langle 111 \rangle\langle 100 \rangle$ texture of the fine grain material would be expected to account for some of the higher $\sigma_{a,sat}$. Juul Jensen *et al.*²⁹ calculated Taylor factors for textures similar to those of the specimens of this study. Based on those Taylor factors, the fine grain texture would be expected to increase the strength by about 3%.

In order to gain insight into the fundamental mechanisms responsible for the differences in the CSS curves, hysteresis loops were analyzed to determine the contributions of friction stress and back stress to the CSS response. Friction and back stresses were calculated using the Cottrell method.³⁰ This method relies on an accurate measurement of the stress at which reverse plastic deformation occurs upon load reversal. In the present work, this stress was defined as the point where the unloading-reloading stress-strain path deviated from the extended linear elastic modulus line by a strain offset of 5×10^{-6} . The friction and back stress components of the CSS curve are presented in Figure 2, which shows that the saturation friction stress is quite insensitive to grain size and ϵ_{pa} , whereas the back stress component is primarily responsible for the differences in CSS behavior.

The evolution of the back stress component within a hysteresis loop was analyzed using a nonlinear back stress evolution equation framework. In the modeling of cyclic plasticity, one of the most popular approaches for modeling back stress evolution is the use of uncoupled nonlinear kinematic hardening rules of the Armstrong-Frederick³¹ type, with the superposition suggested by Chaboche and Rousselier.³² In this

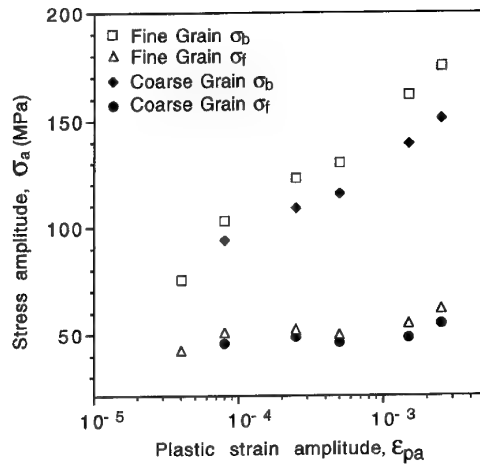


Figure 2 Friction stress (σ_f) and back stress (σ_b) components of the CSS curves

approach, the uniaxial back stress, α , evolves according to

$$\dot{\alpha}_i = C_i [b_i \operatorname{sgn}(\dot{\epsilon}_p) - \alpha_i] \dot{p}, \quad \alpha = \sum_{i=1}^N \alpha_i \quad (1)$$

where $\dot{p} = |\dot{\epsilon}_p|$, $\operatorname{sgn}(\dot{\epsilon}_p) = \dot{\epsilon}_p / |\dot{\epsilon}_p|$, and $\dot{\epsilon}_p$ is the uniaxial plastic strain rate $\dot{\epsilon}_p = \dot{\epsilon} - \dot{\sigma}/E$ where $\dot{\epsilon}$ is the total strain rate, $\dot{\sigma}$ is the stress rate, and E is Young's modulus. The uniaxial stress is then

$$\sigma = \sigma_f \operatorname{sgn}(\dot{\epsilon}_p) + \alpha \quad (2)$$

where σ_f is the friction stress. The selection of parameters C_i and b_i , $i = 1, 2, \dots, N$, provides for nonlinear back stress evolution which matches experiments, and the memory feature of Equation (1) provides for a Bauschinger effect. Furthermore, multiple nonlinear kinematic hardening rules are appealing for their connection to microphenomenological approaches.³³⁻³⁵ Accordingly, Equation (1) has various back stress components evolving with a hardening-dynamic recovery format.

A recent approach for determining the parameters in Equation (1) from experiments allows for a direct experimental extraction of these parameters from a hysteresis loop. They can then be studied with respect to their variation with cumulative plastic strain ($\epsilon_{p,cum} = 4n\epsilon_{pa}$, where n is the cycle number), hence providing a connection to an evolving dislocation substructure. The basis for this approach and details are given elsewhere³⁶, but a brief summary is appropriate. Define the saturation distance for the i th back stress as

$$d_i = |b_i \operatorname{sgn}(\dot{\epsilon}_p) - \alpha_i| \quad (3)$$

thus the evolution of the i th back stress is given by

$$\dot{\alpha}_i = C_i d_i \dot{\epsilon}_p$$

The friction stress σ_f changes little as a function of ϵ_p within a given cycle, so from Equation (2)

$$\frac{d\sigma}{d\epsilon_p} = \frac{d\alpha}{d\epsilon_p} = \sum_{i=1}^N C_i d_i \quad (4)$$

The C_i are ordered so that $C_{i+1} < C_i$. Thus, in a half-cycle loading segment from $-\epsilon_{pa}$ to ϵ_{pa} , all but one

of the back stress components α_j , $j < N$, saturate and cycle between $-b_j$ and b_j . The most slowly evolving back stress cycles between $-\alpha_{Na}$ and $\alpha_{Na} < b_N$. This leads to a predicted hardening modulus variation at low $d\sigma/d\epsilon_p$ which is linear in d_N since $d_j = 0$, $j < N$, and then $d\sigma/d\epsilon_p = C_N d_N$ by Equation (4). We further define a saturation level for stress if the plastic straining were to continue past ϵ_{pa} as

$$\sigma_{sat} = \sigma_f + \sum_{i=1}^N b_i \quad (5)$$

(Note: do not confuse this σ_{sat} with $\sigma_{a,sat}$ used previously with the CSS curve) and define the total saturation distance

$$d = \sum_{i=1}^N d_i = |\sigma_{sat} \operatorname{sgn}(\dot{\epsilon}_p) - \sigma| = |\sigma_a \operatorname{sgn}(\dot{\epsilon}_p) - \sigma + \Delta\alpha_N| \quad (6)$$

where $\Delta\alpha_N = (b_N - \alpha_{Na}) \operatorname{sgn}(\dot{\epsilon}_p) = (\sigma_{sat} - \sigma_a) \operatorname{sgn}(\dot{\epsilon}_p)$. Equation (6) also holds for a segment between $+\epsilon_{pa}$ and $-\epsilon_{pa}$ (i.e. a compression-going branch). With these definitions, the predicted hardening modulus variation at low $d\sigma/d\epsilon_p$ is

$$\left(\frac{d\sigma}{d\epsilon_p} \right)_{low} = C_N d_N = C_N d = C_N |\sigma_a \operatorname{sgn}(\dot{\epsilon}_p) - \sigma + \Delta\alpha_N| \quad (7)$$

From Equation (7), a plot of $d\sigma/d\epsilon_p$ vs. $|\sigma_a \operatorname{sgn}(\dot{\epsilon}_p) - \sigma|$ will yield C_N and $|\Delta\alpha_N|$ as slope and $|\sigma_a \operatorname{sgn}(\dot{\epsilon}_p) - \sigma|$ intercept, respectively, of the curve at low $d\sigma/d\epsilon_p$ as illustrated schematically in Figure 3.

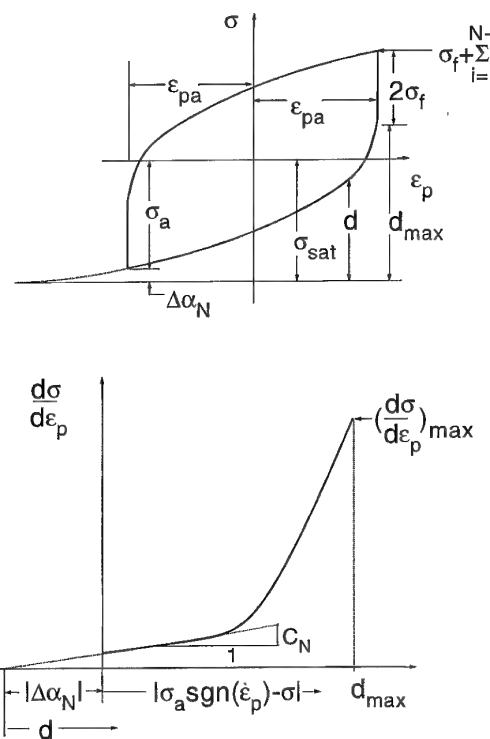


Figure 3 Schematic representation of parameters used to model the evolution of back stress in a hysteresis loop

After determining C_N and $|\Delta\alpha_N|$ we can determine b_N and α_{Na} from

$$b_N - \alpha_{Na} = |\Delta\alpha_N| \quad (8)$$

and

$$2\alpha_{Na} = (b_N + \alpha_{Na})(1 - e^{-C_N 2\epsilon_{pa}}) \quad (9)$$

Equation (9) is the solution to Equation (1) for $i = N$ and a path from $p = 0$ at $-\epsilon_{pa}$ to $p = 2\epsilon_{pa}$ at $+\epsilon_{pa}$ assuming $\alpha_N = -\alpha_{Na}$ at $p = 0$ and $\alpha_N = \alpha_{Na}$ at $p = 2\epsilon_{pa}$. That is, assuming a symmetric response which is consistent with small cyclic hardening *within* a cycle.

For $N \geq 2$ we can employ the following additional equations:

$$\sum_{i=1}^{N-1} b_i = \sigma_{sat} - (\sigma_f + b_N) \quad (10)$$

and

$$\left(\frac{d\sigma}{d\epsilon_p} \right)_{max} = \sum_{i=1}^{N-1} C_i 2b_i + C_N d_{N,max} \quad (11)$$

where $d_{N,max} = \alpha_{Na} + b_N$ and $(d\sigma/d\epsilon_p)_{max}$ is an experimental result as illustrated in Figure 3. For $N = 2$, Equations (8)–(11) constitute a linear system sufficient to determine b_1 , b_2 , C_1 , and α_{2a} with C_2 determined as in Figure 3. For $N > 2$ additional conditions are required.³⁶ In this manner, we can determine the amplitudes of the long range and short range back stress components, the long range being the more slowly evolving with reversed plastic strain.

The back stress evolution parameters were determined in this way as a function of $\epsilon_{p,cum}$ for $\epsilon_{pa} = 2.5 \times 10^{-4}$ where $N = 2$ was found to be the required number of back stresses. Figure 4 shows the variation of b_1 and b_2 , and Figure 5 shows the variation of C_1 and C_2 . Figures 6a and b compare the model (Equations (1) and (2)) and experimental hysteresis loops for the coarse and fine grain specimens at representative cycles. Figure 6c and d show similar comparisons for $d\sigma/d\epsilon_p$ vs. d . As can be seen in Figure 4b, the variation of b_2 mimics the cyclic hardening behavior of the two grain sizes at this plastic strain amplitude, indicating the connection of the more slowly evolving or ‘long range’^{35,37,38} back stress component to cyclic hardening. Plots of loop shape parameters, V_H , vs. $\epsilon_{p,cum}$ based on model and experimental loops are shown in Figure 7a and 7b for the coarse and fine grain specimens, respectively. Clearly, the model reflects the evolution of V_H . It has been shown previously in single crystals^{5,28} and in the polycrystalline nickel used in this study³⁹ that the increase in V_H between $\epsilon_{p,cum} = 1$ and $\epsilon_{p,cum} = 10$ is caused by the localization of plastic strain in PSBs. The V_H increase is especially pronounced in the coarse grain response of Figure 7a. Furthermore, Figure 5b shows that the variation of C_2 closely mimics that of V_H , indicating the connection of the long range back stress to the nucleation and evolution of PSBs.

FATIGUE CRACK INITIATION BEHAVIOR

Fatigue crack initiation characteristics were analyzed for specimens cycled at $\epsilon_{pa} = 2.5 \times 10^{-4}$ (hereafter referred to as low strain) and $\epsilon_{pa} = 2.5 \times 10^{-3}$ (high

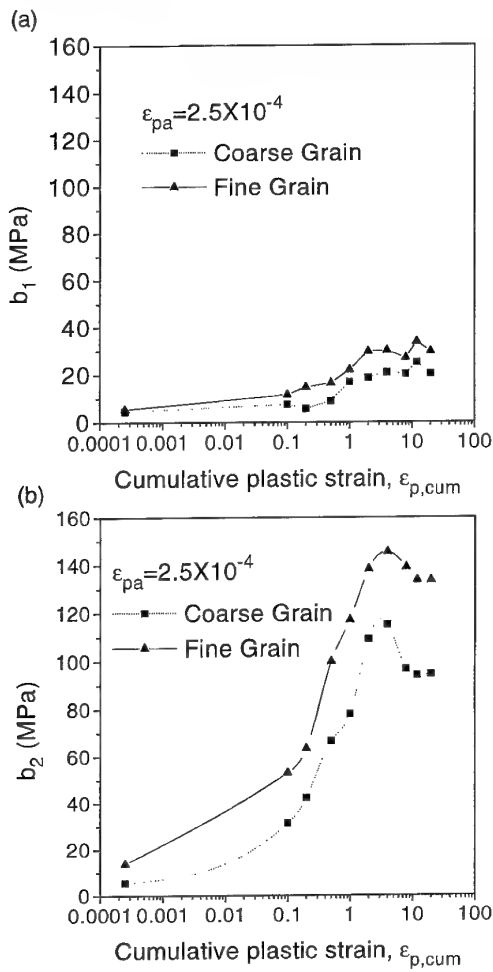


Figure 4 Variation of model parameters b_1 (a) and b_2 (b) with $\epsilon_{p,cum}$ for coarse and fine grain nickel cycled at $\epsilon_{pa} = 2.5 \times 10^{-4}$

strain). Figure 8 shows the length of the longest crack (measured circumferentially) vs. the number of cycles. The Coffin–Manson plots in Figure 9 show cycles to failure, n_f , which was defined as the cycle at which the peak tensile stress decreased to 90% of the peak compressive stress. Table 1 summarizes the information in Figures 8 and 9. The fatigue crack initiation life, n_i , listed in Table 1, is defined as the number of cycles to grow a 200 μm crack. This value was selected because it was observed that cracks 200 μm long usually continued to grow while the growth of shorter cracks was frequently arrested.

Figure 9 and Table 1 indicate that grain refinement significantly increased fatigue life, especially at low strain amplitude, primarily as a result of the large n_i in the fine grain specimen cycled at low strain. At high strain amplitude, the influence of grain size was minor. However, even at the high strain amplitude, grain refinement significantly increased n_i . The results also show that at low strain amplitude, a large fraction of the fatigue life is spent in initiating the crack.

Typical fatigue crack initiation and growth characteristics of the fine and coarse grain specimens cycled at the low plastic strain amplitude ($\epsilon_{pa} = 2.5 \times 10^{-4}$) are shown in the replica micrographs of Figures 10 and 11. The vertical dimension of each micrograph in this

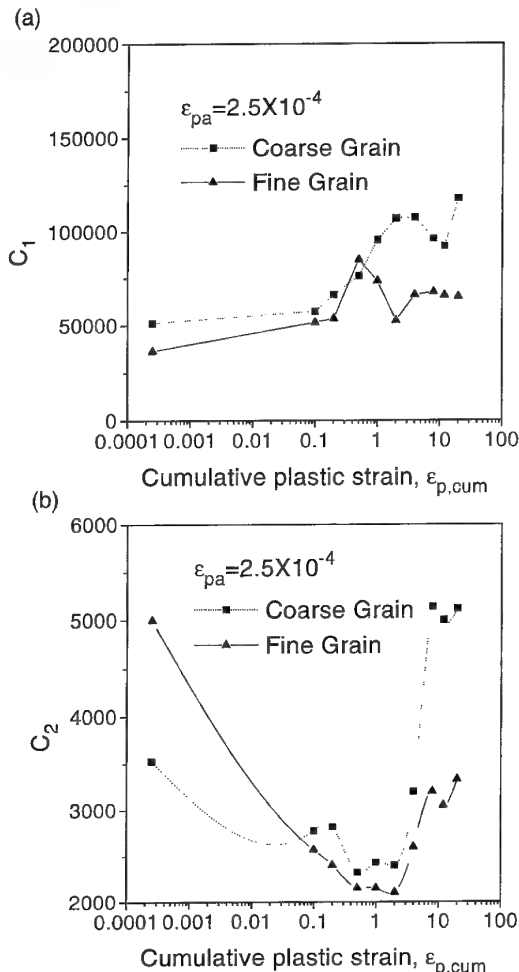


Figure 5 Variation of model parameters C_1 (a) and C_2 (b) with $\epsilon_{p,cum}$ for coarse and fine grain nickel cycled at $\epsilon_{pa} = 2.5 \times 10^{-4}$

report is aligned with the applied stress direction. For the coarse grain/low strain specimen, crack initiation occurred almost exclusively at grain boundaries where PSBs impinged. An example is shown in the replica micrograph of Figure 10a, which was obtained after 12,000 cycles. The gray ‘shadow’ identified by the arrows unambiguously identifies the region of the grain boundary crack. Figure 10b shows another typical crack in the same specimen after 50,000 cycles. The crack propagated along grain boundaries with occasional linking of cracks along slip bands. The preferred mode of crack initiation and growth in the fine grain/low strain specimen was along PSBs. Figure 11a shows cracks that formed along PSBs after 140,000 cycles. As shown in Figure 11b, the crack also propagated along PSBs. Occasionally, PSB cracks would be linked along grain boundaries as shown by the ‘gb’ arrow in Figure 11b.

Crack initiation and growth phenomena for the specimens cycled at the high strain amplitude (2.5×10^{-3}) are shown in Figures 12 and 13. Cracks initiated along grain boundaries in the coarse grain/high strain specimen. A typical example of this behavior is shown in Figure 12a, where the initiation site is identified with an arrow. This replica micrograph was obtained

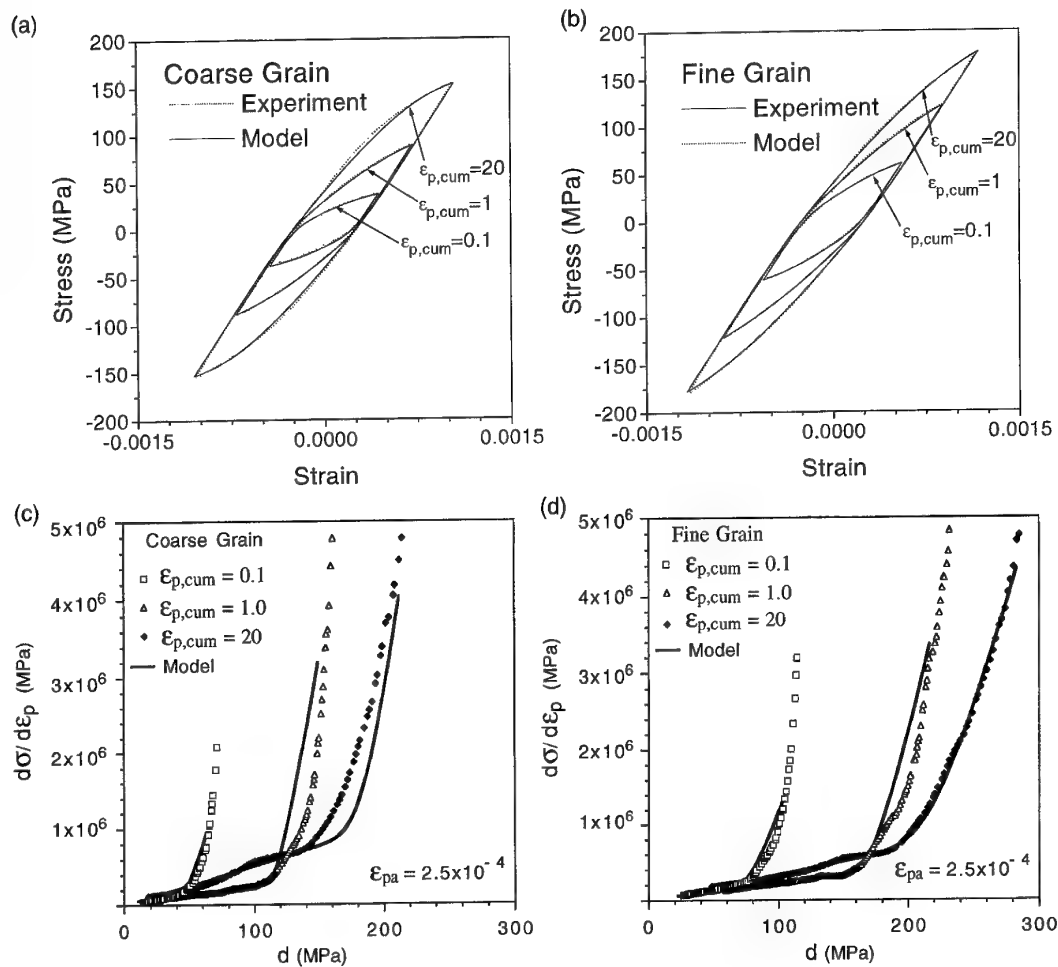


Figure 6 Comparison of model and experimental hysteresis loops for coarse grain (a) and fine grain (b) nickel and comparison of model and experimental plots of $d\sigma/d\epsilon_p$ vs. d for coarse grain (c) and fine grain (d) nickel cycled at $\epsilon_{pa} = 2.5 \times 10^{-4}$

after 200 cycles. *Figure 12b* shows the same crack after 4000 cycles. The crack propagated exclusively along grain boundaries. For the fine grain/high strain specimen, cracks also tended to initiate at grain boundaries. *Figure 13a* shows the formation of a grain boundary crack after 1200 cycles. Crack propagation in the fine grain/high strain specimen occurred along grain boundaries as shown in *Figure 13b*, which was obtained after 4000 cycles.

DISCUSSION OF RESULTS

When discussing the results of this study, it is important to recall that the fine grain nickel had a modest $\langle 111 \rangle$ - $\langle 100 \rangle$ fiber texture. Based on Taylor factor differences discussed earlier, the texture would be expected to have a minor influence. Nonetheless, recent studies have addressed the effects of texture on cyclic hardening and only present a qualitative description.^{19,20,22} At present, it is not possible to quantitatively separate the effects of texture and grain size on cyclic plasticity. Therefore, reference to the fine grain nickel implicitly includes the effects of the $\langle 111 \rangle$ - $\langle 100 \rangle$ texture.

Low strain amplitude

At low plastic strain amplitude, the crack initiation behavior is clearly dominated by the localization of plastic strain in PSBs. Numerous studies have demonstrated that PSBs are favored sites for fatigue crack initiation in monocrystals.⁴⁰⁻⁴⁴ In addition, it has been shown that cracks initiate along PSBs in polycrystalline materials.^{12,42,45-48} A fatigue crack initiation model proposed by Tanaka and Mura⁴⁹ and later refined by Lin *et al.*⁵⁰ and Mura and Nakasone⁵¹ essentially models the PSB as a plate-like distribution of dislocation dipoles of vacancy type. As cycling continues, the accumulation of dislocation dipoles increases the internal tensile stress. Eventually, a fracture criterion is satisfied that causes crack initiation. The Tanaka and Mura model predicts that at constant shear stress amplitude, n_i is proportional to $(1/D)$ where D is the grain size. Therefore, grain refinement leads to a longer crack initiation life. It has also been proposed that PSBs can initiate grain boundary cracks as a result of large stresses that develop in the region where PSBs impinge on grain boundaries (PSB/grain boundary crack). Mughrabi⁵² presented a PSB/grain boundary crack initiation model based on a dislocation model of

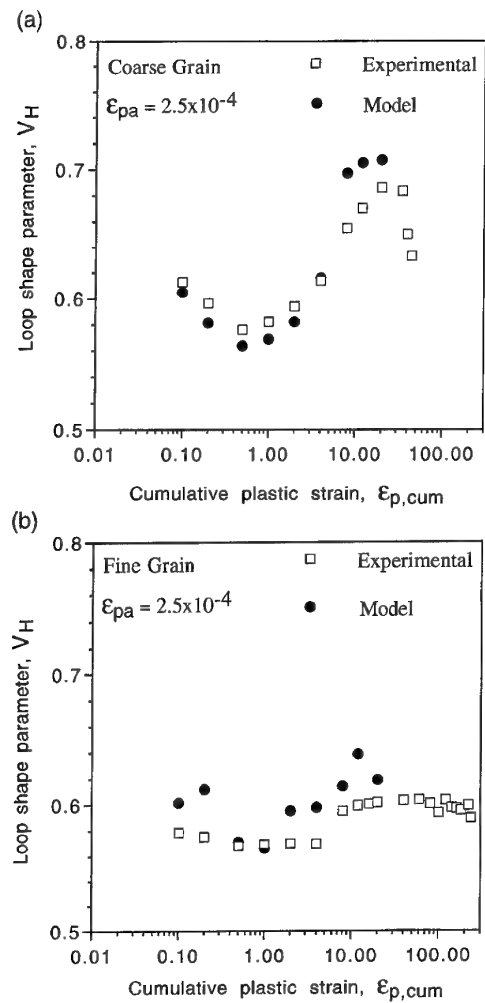


Figure 7 Comparison of model and experimental values of V_H for coarse grain (a) and fine grain (b) nickel cycled at $\epsilon_{pa} = 2.5 \times 10^{-4}$

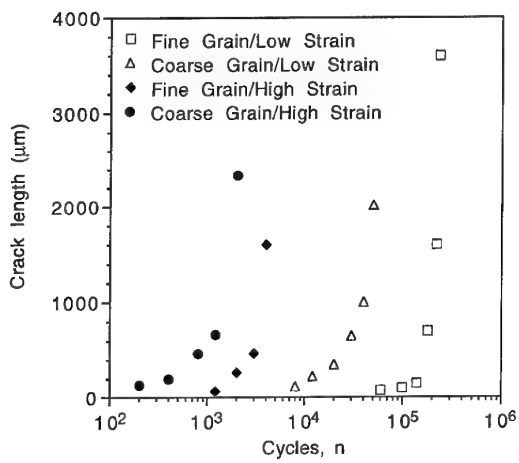


Figure 8 Length of longest crack vs. number of cycles for fine and coarse grain nickel cycled at $\epsilon_{pa} = 2.5 \times 10^{-4}$ (low strain) and $\epsilon_{pa} = 2.5 \times 10^{-3}$ (high strain)

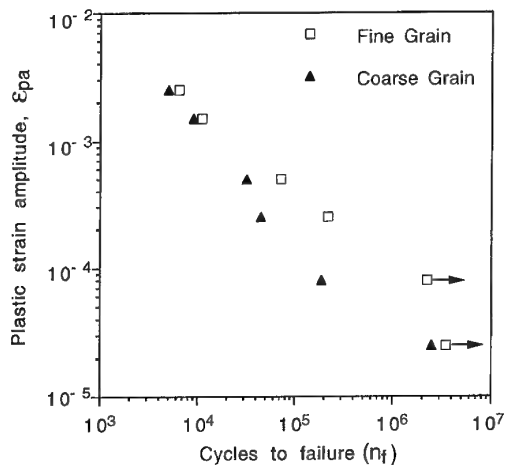


Figure 9 Coffin–Manson plots of ϵ_{pa} vs. number of cycles to failure (n_f)

PSB extrusion morphology by Essmann *et al.*⁵³ and Stroh's theory of grain boundary fracture caused by dislocation pile-ups⁵⁴. Based on studies of polycrystalline copper, Mughabgi's model predicts that n_i is proportional to $(1/D)^3$. Once again, grain size has a significant effect on n_i . Based on the $(1/D)$ and $(1/D)^3$ relationships for PSB and PSB/grain boundary crack initiation, it can be hypothesized that there is a critical grain size above which PSB/grain boundary cracks form and below which the preferred mode of fatigue crack initiation is on PSBs. The results presented in Figures 10 and 11 are consistent with this hypothesis.

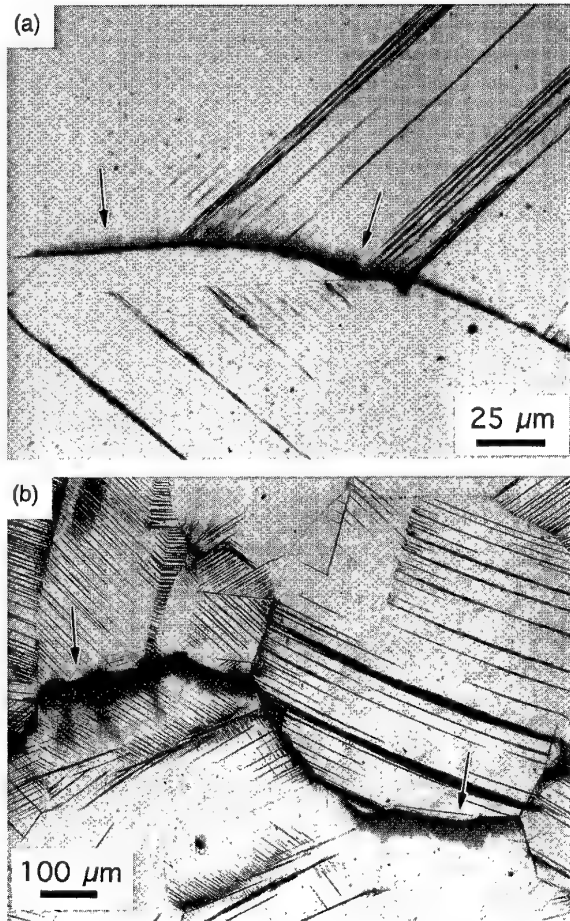
The effect of grain size in determining cyclic plasticity behavior at small strain amplitude is also apparently the result of the dependence of PSB morphology on grain size. The long range back stress amplitude (reflected by b_2) accounts for the cyclic hardening and the difference in cyclic hardening between fine and coarse grain microstructures. Likewise, evolution of C_2 , which largely reflects the behavior of $d\sigma/d\epsilon_p$ for the bulk of reversed plastic strain at a given $\epsilon_{p,cum}$, closely mimics the evolution of the loop shape parameter V_H . Furthermore, the difference in evolution of C_2 between the two grain sizes closely resembles the difference in evolution of V_H between the two grain sizes. This implies that the long range back stress α_2 is related to compatibility stresses resulting from the localization of plastic strain in PSBs. The difference in PSB morphology in the two grain sizes results in different compatibility stresses. This is consistent with Mughabgi's³⁸ models for long range back stress and Pedersen and coworkers'^{6,55} models of the CSS curve.

High strain amplitude

The high strain fatigue crack initiation behavior of the nickel in this study closely parallels that reported by Kim and Laird⁸ for high strain fatigue of polycrystalline copper. In that study, it was shown that cracks form at high angle grain boundaries where the dominant slip system of one or both of the grains is directed at the intersection of the grain boundary and the specimen surface. These conditions lead to the formation of a grain boundary step with a sharp root radius. Compatibility-induced multiple slip in the grain bound-

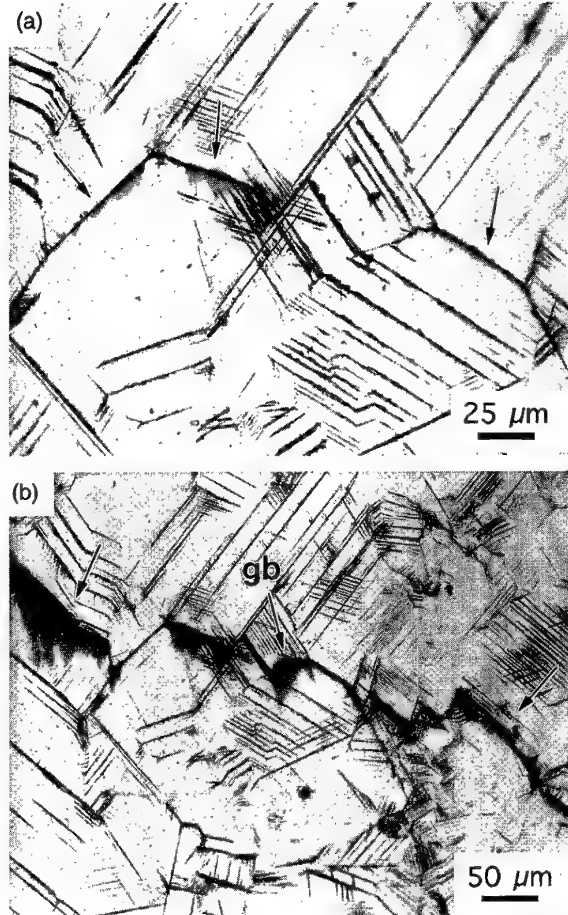
Table 1 Summary of fatigue cycles for crack initiation (n_i), growth (n_g), and failure (n_f) for fine and coarse grain nickel

Specimen	n_i	n_g	n_f	n_i/n_f
Fine grain/high strain	1700	4700	6400	0.27
Coarse grain/high strain	400	4600	5000	0.08
Fine grain/low strain	145000	75000	220000	0.66
Coarse grain/low strain	12000	33000	45000	0.27

**Figure 10** Fatigue cracks in the coarse grain/low strain specimen after 12,000 cycles (a) and 50,000 cycles (b). Arrows identify the locations of cracks

ary region promotes strain irreversibility that enhances the growth of the step and leads to the nucleation of a crack⁸. The larger grain boundary compatibility strain in a coarse grain material caused by the larger ‘effective gage length’ of large grains¹⁴, coupled with the longer slip length in a coarse grain material, accelerates the crack initiation process in a coarse grain material⁵⁶.

Preliminary efforts to model the cyclic plasticity behavior at high strain amplitude indicate that the differences in the two grain sizes are not nearly as pronounced or as easily interpreted as the low strain case, even though the fine grain specimen exhibited a significantly higher $\sigma_{a,sat}$. Analyses similar to those reported here for the low strain amplitude case reveal subtle differences in cyclic hardening between the two grain sizes which appear in the most slowly evolving

**Figure 11** Fatigue cracks in the fine grain/low strain specimen after 140,000 cycles (a) and 235,000 cycles (b). The arrow marked ‘gb’ identifies a grain boundary crack

back stress amplitude. The loop shape parameter decreases continuously with $\epsilon_{p,cum}$ and the difference in V_H between grain sizes seems to be reflected in an intermediate range back stress. This is consistent with more homogeneous deformation and hardening and less discernible differences between dislocation substructures in the two grain sizes in the high strain case^{22,57}. These issues are currently being investigated and more details will be given in a subsequent report.

CONCLUSIONS

From the results of this study the following conclusions are made.

1. Except at very low ϵ_{pa} , fine grain nickel has a higher $\sigma_{a,sat}$ than coarse grain nickel. The back stress component of $\sigma_{a,sat}$ is primarily responsible

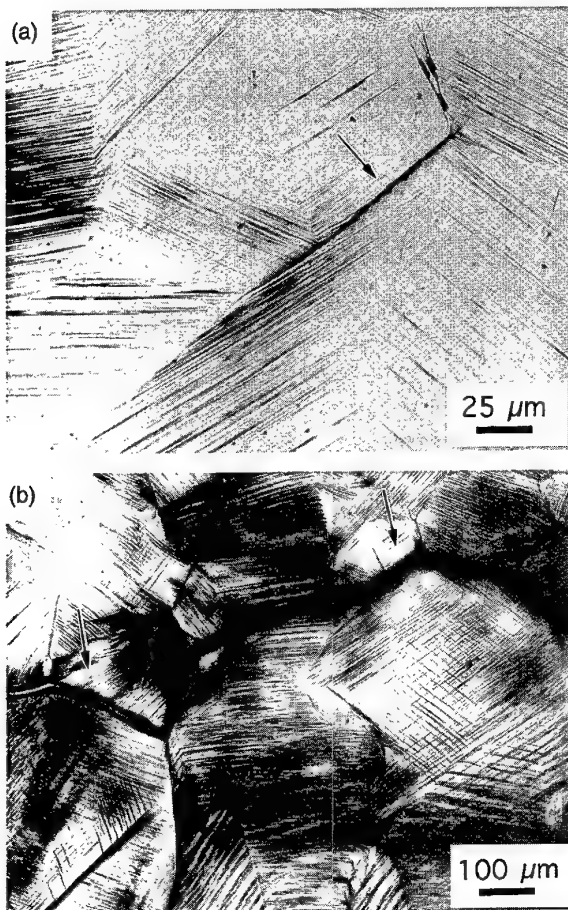


Figure 12 Fatigue cracks in the coarse grain/high strain specimen after 200 cycles (a) and 4000 cycles (b)

for the influences of ϵ_{pa} and grain size on $\sigma_{a,sat}$. The friction stress component is not appreciably affected by ϵ_{pa} or grain size.

2. The evolution of the back stress component within a cycle can be modeled using superposition of Armstrong–Frederick type kinematic hardening rules. Evolution of parameters affecting the long-range component of back stress with cumulative plastic strain is related to the evolution of PSBs. Differences in long range back stress behavior due to grain size are caused by the influence that grain size has on PSB morphology.
3. At low plastic strain amplitude ($\epsilon_{pa} = 2.5 \times 10^{-4}$), fatigue crack initiation is influenced by strain localization in PSBs. In coarse grain nickel, cracks initiated at grain boundaries where PSBs impinged. In the fine grain nickel, cracks initiated transgranularly along PSBs. At high plastic strain amplitude ($\epsilon_{pa} = 2.5 \times 10^{-3}$), cracks initiated along grain boundaries in fine and coarse grain nickel.

ACKNOWLEDGEMENTS

This work was supported by the US Air Force Office of Scientific Research through Air Force Engineering Research Initiation Grants RI-B-90-15 (J.M.) and RI-B-90-2 (D.M.) administered by the Engineering Foundation. Additional support was provided by the

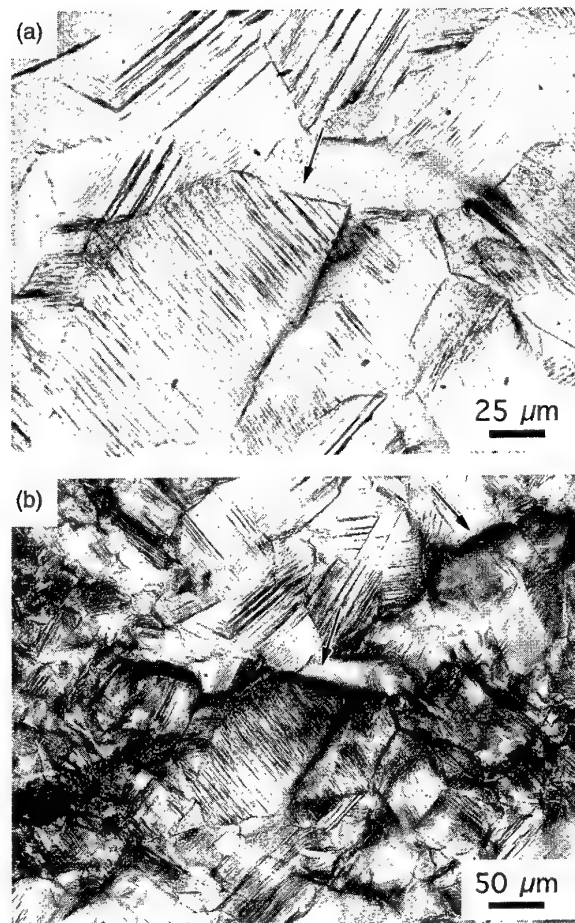


Figure 13 Fatigue cracks in the fine grain/high strain specimen after 1200 cycles (a) and 4000 cycles (b)

National Science Foundation through Grants MSS 9108695 and CMS 9634707. The assistance of S. Mascaro in obtaining replica micrographs is gratefully acknowledged.

REFERENCES

- 1 Lukas, P., Klesnil, M. and Krejci, J., Dislocations and persistent slip bands in copper single crystals fatigued at low stress amplitude. *Physica Status Solidi*, 1968, **27**, 545–558.
- 2 Basinski, S. J., Basinski, Z. S. and Howie, A., Early stages of fatigue in copper single crystals. *The Philosophical Magazine*, 1969, **19**, 889–924.
- 3 Winter, A. T., A model for the fatigue of copper at low plastic strain amplitudes. *The Philosophical Magazine*, 1974, **30**, 719–738.
- 4 Laird, C., Charsley, P. and Mughrabi, H., Low energy dislocation structures produced by cyclic deformation. *Materials Science and Engineering*, 1986, **81**, 433–450.
- 5 Mughrabi, H., The cyclic hardening and saturation behaviour of copper single crystals. *Materials Science and Engineering*, 1978, **33**, 207–223.
- 6 Pedersen, O. B., Mechanism maps for cyclic plasticity and fatigue of single phase materials. *Acta Metallurgica et Materialia*, 1990, **38**, 1221–1239.
- 7 Basinski, Z. S. and Basinski, S. J., Fundamental aspects of low amplitude cyclic deformation in face-centered cubic crystals. In *Progress in Materials Science*, Vol. 36. Pergamon Press, 1992, pp. 89–148.
- 8 Kim, W. H. and Laird, C., Crack nucleation and stage I propagation in high strain fatigue II. Mechanism. *Acta Metallurgica*, 1978, **26**, 789–799.
- 9 Winter, A. T., Pedersen, O. B. and Rasmussen, K. V., Dislo-

- cation microstructures in fatigued copper polycrystals. *Acta Metallurgica*, 1981, **29**, 735–748.
- 10 Figueroa, J. C. and Laird, C., Crack initiation mechanisms in copper polycrystals cycled under constant strain amplitudes and in step tests. *Materials Science and Engineering*, 1983, **60**, 45–58.
- 11 Lukas, P. and Kunz, L., Effect of grain size on the high cycle fatigue behaviour of polycrystalline copper. *Materials Science and Engineering*, 1987, **85**, 67–75.
- 12 Mughrabi, H. and Wang, R., Cyclic stress-strain response and high-cycle fatigue behaviour of copper polycrystals. In *Basic Mechanisms in Fatigue of Metals*, Materials Science Monographs, Vol. 46. Elsevier, 1988, pp. 1–14.
- 13 Christ, H. J., Mughrabi, H. and Witig-Link, C., Cyclic deformation behavior, microstructure and fatigue crack initiation of copper polycrystals fatigued in air and vacuum. In *Basic Mechanisms in Fatigue of Metals*, Materials Science Monographs, Vol. 46. Elsevier, 1988, pp. 83–92.
- 14 Liang, F. L. and Laird, C., Control of intergranular fatigue cracking by slip homogeneity in copper. I: Effect of grain size. *Materials Science and Engineering A*, 1989, **117**, 95–102.
- 15 Ma, B. T., Laird, C. and Radin, A. L., Dependence of fatigue failure mechanism on the cyclic history of polycrystalline copper. *Materials Science and Engineering A*, 1990, **123**, 159–167.
- 16 Liu, W., Bayerlein, M., Mughrabi, H., Day, A. and Quested, P. N., Crystallographic features of intergranular crack initiation in fatigued copper polycrystals. *Acta Metallurgica et Materialia*, 1992, **40**, 1763–1771.
- 17 Polak, J., Obertlik, K., Hajek, M. and Vasek, A., Cyclic stress-strain response of polycrystalline copper in a wide range of plastic strain amplitudes. *Materials Science and Engineering A*, 1992, **151**, 19–27.
- 18 Rolim Lopes, L. C. and Charlier, J., Effect of grain size and intergranular stresses on the cyclic behavior of a ferritic steel. *Materials Science and Engineering A*, 1993, **169**, 67–77.
- 19 Llanes, L., Rollett, A. D., Laird, C. and Bassani, J. L., Effect of grain size and annealing texture on the cyclic response and the substructure evolution of polycrystalline copper. *Acta Metallurgica et Materialia*, 1993, **41**, 2667–2679.
- 20 Llanes, L., Bassani, J. L. and Laird, C., Cyclic response of polycrystalline copper – composite-grain model. *Acta Metallurgica et Materialia*, 1994, **42**, 1279–1288.
- 21 Morrison, D. J. and Chopra, V., Cyclic stress-strain response of polycrystalline nickel. *Materials Science and Engineering A*, 1994, **177**, 29–42.
- 22 Morrison, D. J., Influence of grain size and texture on the cyclic stress-strain response of nickel. *Materials Science and Engineering A*, 1994, **187**, 11–21.
- 23 Lukas, P. and Kunz, L., Comparison of fatigue behavior of single crystals and polycrystals. *Materials Science and Engineering A*, 1994, **189**, 1–7.
- 24 Liu, C. D., You, D. X. and Bassim, M. N., Cyclic strain hardening in polycrystalline copper. *Acta Metallurgica et Materialia*, 1994, **42**, 1631–1638.
- 25 Polak, J. and Vasek, A., Fatigue damage in polycrystalline copper below the fatigue limit. *International Journal of Fatigue*, 1994, **16**, 403–408.
- 26 Kage, M., Miller, K. J. and Smith, R. A., Fatigue crack initiation and propagation in a low carbon steel of two different grain sizes. *Fatigue and Fracture of Engineering Materials and Structures*, 1992, **15**, 763–774.
- 27 Turnbull, A. and De Los Rios, E. R., The effect of grain size on the fatigue of commercially pure aluminum. *Fatigue and Fracture of Engineering Materials and Structures*, 1995, **18**, 1455–1467.
- 28 Blochwitz, C. and Veit, U., Plateau behaviour of fatigued FCC single crystals. *Crystal Research and Technology*, 1982, **17**, 529–551.
- 29 Juul Jensen, D., Thompson, A. W. and Hansen, N., The role of grain size and strain in work hardening and texture development. *Metallurgical Transactions A*, 1989, **20**, 2803–2810.
- 30 Cottrell, A. H. In *Dislocations and Plastic Flow in Crystals*. Clarendon Press, 1953, pp. 111–125.
- 31 Armstrong, P. J. and Frederick, C. O., A mathematical representation of the multiaxial Bauschinger effect. Central Electricity Generating Board Report CEBR RD/B/N 731, UK, 1966.
- 32 Chaboche, J. -L. and Rousselier, G., On the plastic and viscoplastic constitutive equations – Part I. Rules developed with internal variable concept. *ASME Journal of Pressure Vessel Technology*, 1983, **105**, 153–158.
- 33 Aifantis, E., The physics of inelastic deformation. *International Journal of Plasticity*, 1987, **3**, 211–247.
- 34 Moosbrugger, J. C. and McDowell, D. L., On a class of kinematic hardening rules for nonproportional cyclic viscoplasticity. *ASME Journal of Engineering Materials Technology*, 1989, **111**, 87–98.
- 35 McDowell, D. L. and Moosbrugger, J. C., Continuum slip foundations of elasto-viscoplasticity. *Acta Mechanica*, 1992, **93**, 73–87.
- 36 Moosbrugger, J. C. and Morrison, D. J., Nonlinear kinematic hardening rule parameters – direct determination from completely reversed proportional cycling. *International Journal of Plasticity*, in press, 1997.
- 37 Mughrabi, H., Ackermann, F. and Herz, K., Persistent slip bands in fatigued face-centered and body-centered cubic metals. In *Fatigue Mechanisms*, ed. J. T. Fong. ASTM-STP 675, American Society for Testing and Materials, 1979, pp. 69–105.
- 38 Mughrabi, H., Dislocation clustering and long range internal stresses in monotonically and cyclically deformed metal crystals. *Review of Physical Applications*, 1988, **23**, 367–379.
- 39 Morrison, D. J., Jones, J. W. and Was, G. S., Cyclic strain localization in ion beam microalloyed nickel. *Scripta Metallurgica*, 1990, **24**, 2309–2314.
- 40 Cheng, A. S. and Laird, C., Fatigue life behavior of copper single crystals Part II. Model for crack nucleation in persistent slip bands. *Fatigue of Engineering Materials and Structures*, 1981, **4**, 343–353.
- 41 Ma, B. T. and Laird, C., Overview of fatigue behavior in copper single crystals – I. Surface morphology and stage I crack initiation sites for tests at constant strain amplitude. *Acta Metallurgica*, 1989, **37**, 325–336.
- 42 Laird, C. and Duquette, D. J., Mechanisms of fatigue crack nucleation. In *Corrosion Fatigue*. National Association of Corrosion Engineers, 1972, pp. 88–117.
- 43 Polak, J., Lepisto, T. K. and Kettunen, P., Surface topography and crack initiation in emerging persistent slip bands in copper single crystals. *Materials Science and Engineering*, 1985, **74**, 85–91.
- 44 Thompson, N., Wadsworth, N. and Louat, N., The origin of fatigue fracture in copper. *Philosophical Magazine Series 8*, 1956, **1**, 113–126.
- 45 Stubbington, C. A. and Forsyth, P. J. E., Some metallographic observations on the fatigue behavior of copper and nickel and certain of their alloys. *Journal of the Institute of Metals*, 1957/58, **86**, 90–94.
- 46 Mughrabi, H. and Wang, R., Cyclic strain localization and fatigue crack initiation in persistent slip bands in face-centered-cubic metals and single phase alloys. In *Defects and Fracture*. Martinus Nijhoff, 1982, pp. 15–22.
- 47 Fine, M. E. and Kwon, I. B., Fatigue crack initiation along slip bands. In *Small Fatigue Cracks*. The Metallurgical Society, 1986, pp. 29–40.
- 48 Bayerlein, M. and Mughrabi, H., Fatigue crack initiation and early crack growth in copper polycrystals – effects of temperature and environment. In *Short Fatigue Cracks*. ESIS 13, Mechanical Engineering Publications, 1992, pp. 55–82.
- 49 Tanaka, K. and Mura, T., A dislocation model for fatigue crack initiation. *Journal of Applied Mechanics*, 1981, **48**, 97–103.
- 50 Lin, M. R., Fine, M. E. and Mura, T., Fatigue crack initiation on slip bands, theory and experiment. *Acta Metallurgica*, 1986, **34**, 619–628.
- 51 Mura, T. and Nakasone, Y., A theory of fatigue crack initiation in solids. *Journal of Applied Mechanics*, 1990, **57**, 1–6.
- 52 Mughrabi, H., A model of high cycle fatigue-crack initiation at grain boundaries by persistent slip bands. In *Defects, Fracture, and Fatigue*. Martinus Nijhoff, 1983, pp. 139–146.
- 53 Essmann, U., Goesele, U. and Mughrabi, H., A model of extrusions and intrusions in fatigued metals – I. Point-defect production and the growth of extrusions. *The Philosophical Magazine A*, 1981, **44**, 405–426.
- 54 Stroh, A. N., *Advances in Physics*, 1957, **6**, 418–465.
- 55 Pedersen, O. B., Rasmussen, K. V. and Winter, A. T., The cyclic stress strain curve of polycrystals. *Acta Metallurgica*, 1982, **30**, 57–62.
- 56 Kim, W. H. and Laird, C., The role of cyclic hardening in crack nucleation at high strain amplitude. *Materials Science and Engineering*, 1978, **33**, 225–231.
- 57 Feltner, C. E. and Laird, C., Cyclic stress-strain response of FCC metals and alloys – II. Dislocation structures and mechanisms. *Acta Metallurgica*, 1967, **15**, 1633–1653.

PII: S0142-1123(97)00037-6

Microstructural fracture in metal fatigue

L. Lawson*, E.Y. Chen† and M. Meshii‡

*226 Interstate Parkway, Bradford, PA 16701, USA

†General Electric Corporate Research & Development, P.O. Box 8, Schenectady, NY 12301, USA

‡Department of Materials Science and Engineering, Northwestern University, Evanston, IL 60208, USA

The growth rates of microstructurally short fatigue cracks often appear to show less sensitivity to length than would be expected on the basis of a relaxed microstructure. In addition to stress enhancements provided by dislocation theory, recently purely elastic mechanisms have been shown to generate stress singularities as well. Incorporation of such singularities into a Monte Carlo simulation of an evolving microcrack distribution improves the ability of the model to replicate actual distributions obtained experimentally for 304 stainless steel. Furthermore, it allows the use of a single set of Paris constants for both long and short cracks. © 1998 Elsevier Science Ltd.

(Keywords: metal fatigue; Monte Carlo method; stress singularities; 304 stainless steel)

INTRODUCTION

Attempts to explain the anomalous behavior of microstructurally small cracks literally fills volumes. This work reports that it is apparently possible to use a single Paris equation for both large and small fatigue cracks and to successfully describe the evolution of fatigue crack distributions in 304 stainless steel. Using a Monte Carlo model previously developed for predicting microcrack length distributions in 304 SS and advanced materials, it was found that inclusion of the stress intensities characteristic of singularities, either known or predicted to exist, resulted in realistic length distributions using only the long crack Paris equation constants where previously special experimentally derived microcrack constants had been required. Furthermore, this new approach allowed replication of known behavior previously not easily replicable.

The motivation for this work comes in part from the recent publication of a number of articles by Picu and Gupta¹⁻⁵ examining elastic stress singularities which may occur in materials at points of special symmetry. These add to an already established list of singularities related to plasticity. The predicted existence of 'supersingularities' having absolute exponents greater than 1/2 provides a ready means for crack nucleation following that of the classical Zener-Stroh crack⁶. These may also be relevant to questions about length scales. Recently, Sadananda and Vasudevan⁷ have advanced the cause of the proposed unification of the long and short crack regimes around a single pair of Paris parameters and the presence of stress singularities within the microstructure of the material.

BACKGROUND AND NUMERICAL METHOD

The empirical Paris relationship continues to be the best known descriptor of fatigue crack growth despite its use of an elastic quantity, the stress intensity factor K , to describe a plastic process, and concerns over the fractional and ill-defined dimensionality of its coefficient^{8,9}. The constants in this relation have sometimes been taken as dependent on the length scale of the crack being described. This however lacks justification and is physically displeasing⁷. Long cracks average the microstructure over the length of the active faces at their tips, allowing faster growing segments to drag those which would otherwise grow slowly if at all¹⁰. Small cracks lack this averaging and hence might be expected to show greater dispersion due to the effects of local stresses and microstructural variation. Because large cracks can drag otherwise nongrowing face segments, their average growth rate at a given ΔK should be somewhat less than that of growing small cracks. Given this inconsistency, *ceteris paribus*, the growth rates of small and large cracks ought to be similar for the same ΔK . Provided, of course, that ΔK , a continuum elastic measure of Linear Elastic Fracture Mechanics (LEFM), is applicable on a microstructural length scale? This question is more easily viewed in hindsight, and will be discussed in the conclusion of this paper.

In order to analyze the effects of local variations of stress and microstructure on the crack growth rate, these may be separated from the Paris relation using a stochastic model. While the model is intended to apply to cracks the size of microcracks, it reduces to

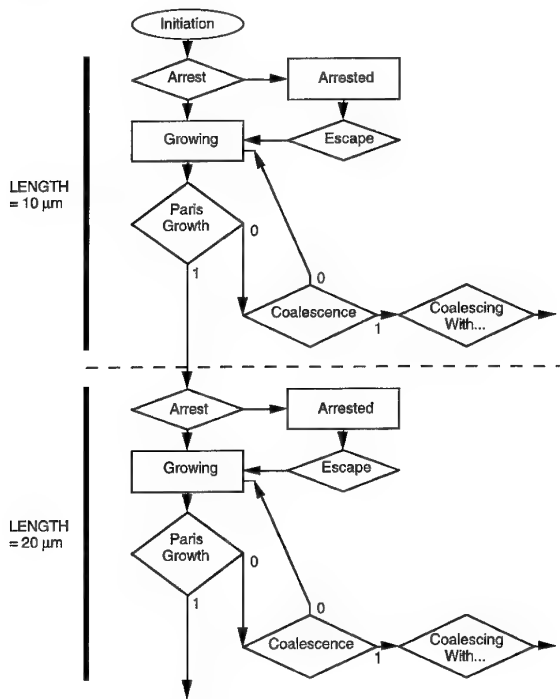


Figure 1 Abbreviated flow chart for crack growth starting at initiation and progressing through two steps in length. The actual program repeats the process for 200 length steps. Coalescence is based a stereological model and dimensional analysis¹³. Once it is determined that a crack will coalesce in a given step, the mating crack is chosen at random subject to distributional constraints on its length

the long crack Paris relation when applied to long cracks. The simplest such model is a direct Monte Carlo simulation. In this model, previously reported¹¹, the elements of the problem have been taken as initiation, Paris relation growth, arrest/escape and coalescence; these events have been assigned probabilities. *Figure 1* illustrates part of the program flow

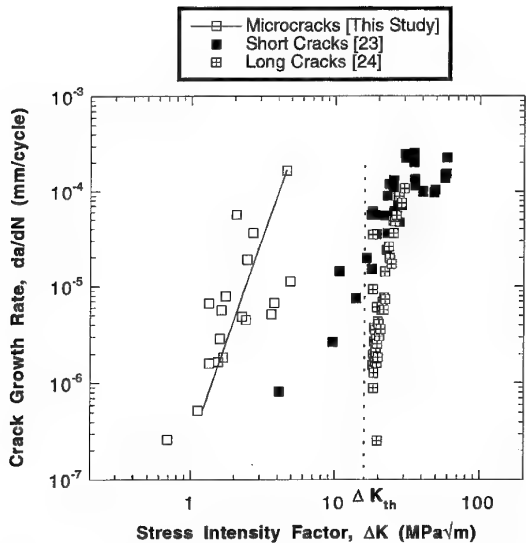


Figure 2 Growth rates of cracks of three different length categories in 304 stainless steel

chart for the Monte Carlo simulation used in this work. Paris relation growth is reduced to a probability of growing a single length increment per cycle. The constants used originally¹² were based on direct measurement of the growth rates of *growing* small cracks. A difficulty with the Paris constants for these small cracks was their reflection of the apparent insensitivity of the growth rate of the very small cracks to their length. This insensitivity gave lower Paris exponents for short cracks than for long cracks and often quizzical results such as negative exponents for individual microcracks. Using average values of these Paris parameters for small cracks did give an acceptable prediction of microcrack length distributions in a previous version of the model. But, on close inspection, that version showed a dependence of growth rate on length which was much stronger than reality. The introduction into the model of stress singularities of the type described by Picu – and assuming these to be at the origin of the crack – eliminated this dependence and allowed long crack Paris parameters to predict short crack behavior.

The singularities described by Picu have the property of being able to change sign with the applied remote stress with or without a time lag. In contrast, the Zener–Stroh coalescence of dislocations applies typically a fixed stress intensity which sums with that of the changing remote stress. Pile-ups of mobile dislocations can amplify either the positive or negative half of an applied stress cycle, and Picu-type singularities can amplify both halves. Their inclusion in the crack distribution model to some extent represents the combined effects of these other singularities as well. Apart from the tip stress intensity, microcrack growth is strongly affected by local variations in a material's resistance to crack growth. Local variations in crack plane due to crystallographic orientation is but one example. These variations appear experimentally through partial arrest which may be real or apparent. The probabilities of arrest and escape from the arrested state were estimated experimentally by tracking the growth of individual cracks using acetate replicas. These estimates were refined through correlation with distribution data. The probability of arrest was made a function of length. Obstacles were of three different 'heights' (corresponding to three different maximum lengths) in terms of cyclic K_{\max} with decreasing probability of encounter with increasing height. The escape probability was made a constant since the raw data could not support a picture more detailed than that of an average residence time at each obstacle. This approach subsumes the contribution, if any, of crack closure. Also important, coalescence was less critical to the model in the early stages of fatigue than the probabilities of growth and arrest. Also, it seems to be better understood. It is discussed in detail in Ref.¹³. The appearance of innate singularities is not new. One type has been analyzed by Tvergaard and Hutchinson¹⁴. Other types have been calculated to exist in slip bands¹⁵ and can be found latent in the well-known Fourier treatment of grain boundary sliding by Raj and Ashby¹⁶.

Numerical models of microcrack distributions have been developed by researchers to deal with the random diversity of microstructure, and stochastic simulation has become the major tool to work with it. The model

of Cox and Morris^{10,17} provides an excellent example of how factors such as roughness induced crack closure can be subsumed into a probability of growth concept. These authors tracked the evolution of a control variable related to crack length as a semi-Markovian process. Monte Carlo simulations, because they utilize decision trees, tend to be Markovian. Bataille and Magnin¹⁸, for example, used a model of grid elements to track the growth of individual cracks over a 2-D surface and model their interactions – particularly coalescence. An approach allowing for a greater number of effects to be considered was introduced by Chen *et al.*¹¹, which gains its economy through treating cracks as indistinguishable except for their surface length. This model is the one used here.

STRESS INTENSITY INDUCED BY SINGULARITIES

Perhaps the best known examples of self-initiating cracks associated with stress singularities are Zener–Stroh cracks. For this reason they are a good first example. Defining the negative of the singularity exponent as its ‘strength’, we see that the Zener–Stroh crack applies a crack tip singularity of 0.5 strength but originates from an innate singularity of unity strength, a superdislocation. Weertman⁶ calculated the value of K associated with the externally loaded Zener–Stroh crack to be the sum of that for the corresponding Griffith-type crack and that of the Zener–Stroh crack itself. Unloaded, the stress intensity of the Zener–Stroh crack is itself singular

$$K_{zs} = \frac{b_T G}{2(1-\nu)(\pi a)^{0.5}} \quad (1)$$

where b_T is the total Burgers vector equivalent of the singularity being modeled, G is the shear modulus, ν is Poisson’s ratio, and a is the crack length. Notice that K diminishes with crack length. The driving force for crack growth goes to infinity as the crack length approaches zero. There is thus always a crack.

In order, for the sake of the model, to generalize to singularities of other strengths, we may use a Westergaard stress function^{19,20} as a local mean field approximation based on an averaged modulus. This is theoretically justifiable in several common individual cases and is done whenever materials are treated as isotropic. The Westergaard stress function is a complex stress function which automatically satisfies the stress equilibrium and strain compatibility requirements. In addition, the Westergaard stress function takes a form particularly suited to crack problems where the traction forces must be zero along portions of the x -axis where the crack is located. The proposed function is

$$Z(z) = Hz^{1-p}(z^2 - a^2)^{-0.5} \quad (2)$$

where z is a point on the complex plane, a is the half-length of the crack, p is the strength of the source singularity, and H is a constant. The mode I stress at the crack plane is found as

$$\sigma_{yy,y=0} = \operatorname{Re}\{Z(z)\} - \operatorname{Re}\{Z(x^*)\} \quad (3)$$

where x^* is any value x such that $a \geq |x|$. Evidently, the second term on the right must be a constant over that interval in order for the stress function to be valid. The stress intensity of the crack is given by

$$K_I = (2\pi)^{0.5} \lim_{z \rightarrow a} (z-a)^{0.5} Z(z) \quad (4)$$

The two important limiting cases are those where $p \rightarrow 0$ and $p \rightarrow 1$. In the first case, the mode I stress $\sigma_{yy,y=0} = H_G \frac{x}{(x^2 - a^2)^{0.5}}$ is that for a Griffith center crack, where no applied singularity exists. The Westergaard stress function provides the unique elastic solution in which there is no singularity other than that at the crack tip. For the case where $p = 1$, the mode I stress is

$$\sigma_{yy,y=0} = H_{zs}(x^2 - a^2)^{-0.5} \quad (5)$$

This stress distribution is that of the Zener–Stroh crack. There is evidently a singularity of unity strength at $x = 0$, $y = 0$ when the crack has zero length. As $a \rightarrow 0$, the stress distribution (5) becomes that of an edge superdislocation as expected. Substituting Equation (2) into Equation (4) gives Equation (1) for a Zener–Stroh crack. The stress intensity for the general case of a singularity of power p at the origin is found similarly from Equation (2)

$$K_I = \pi^{0.5} Ha^{0.5-p} \quad (6)$$

For $p > 0.5$ there is a pole at zero and a crack (or a BCS/Dugdale zone²¹ if the equilibrium length is of atomic dimensions) must form spontaneously. For $p = 0.5$, the stress intensity is constant. For $p < 0.5$ the crack behavior is little different from that of a remote-loaded crack, except that the stress is local and decays at a rate which slows the growth of stress intensity with length.

The form of expression used in the model to calculate the applied stress intensity is

$$K_I = H_G a^{0.5} + H_p a^{0.5-p} \quad (7)$$

Because of the possibility of stress relaxation or modification at grain boundaries, the stress intensity given by Equation (7) is not likely to persist in the same form across them or similar features. This is one likely cause of the dip frequently seen in da/dN vs. a near the transition from the ‘short’ to the ‘long’ crack regimes. A second cause is related to the form of Equation (7), which has a minimum with respect to a for any value of $p > 0.5$, suggesting that the crack growth rate for a cyclic load also has a minimum. Setting this minimum to correspond to the experimentally observed minimum at $a = 200 \mu\text{m}$ (see for example figures 9.1 and 9.3 in Suresh²²) allowed H_p to be estimated from the known H_G . The simulation results reported here are based on $p = 1$ where H_G is the same as that for large cracks. Setting p to other values between 0.5 and 1 had little effect other than making the minimum less pronounced.

EXPERIMENTAL

Figure 2 illustrates growth data for cracks of different size ranges in ingot 304 stainless steel. In spite of the high relative mean stress for the long cracks, the threshold evident for the long cracks is not apparent for microcracks. Two causal factors can be identified. For the same stress intensity, the applied stress level must go up as the length of the cracks becomes shorter.

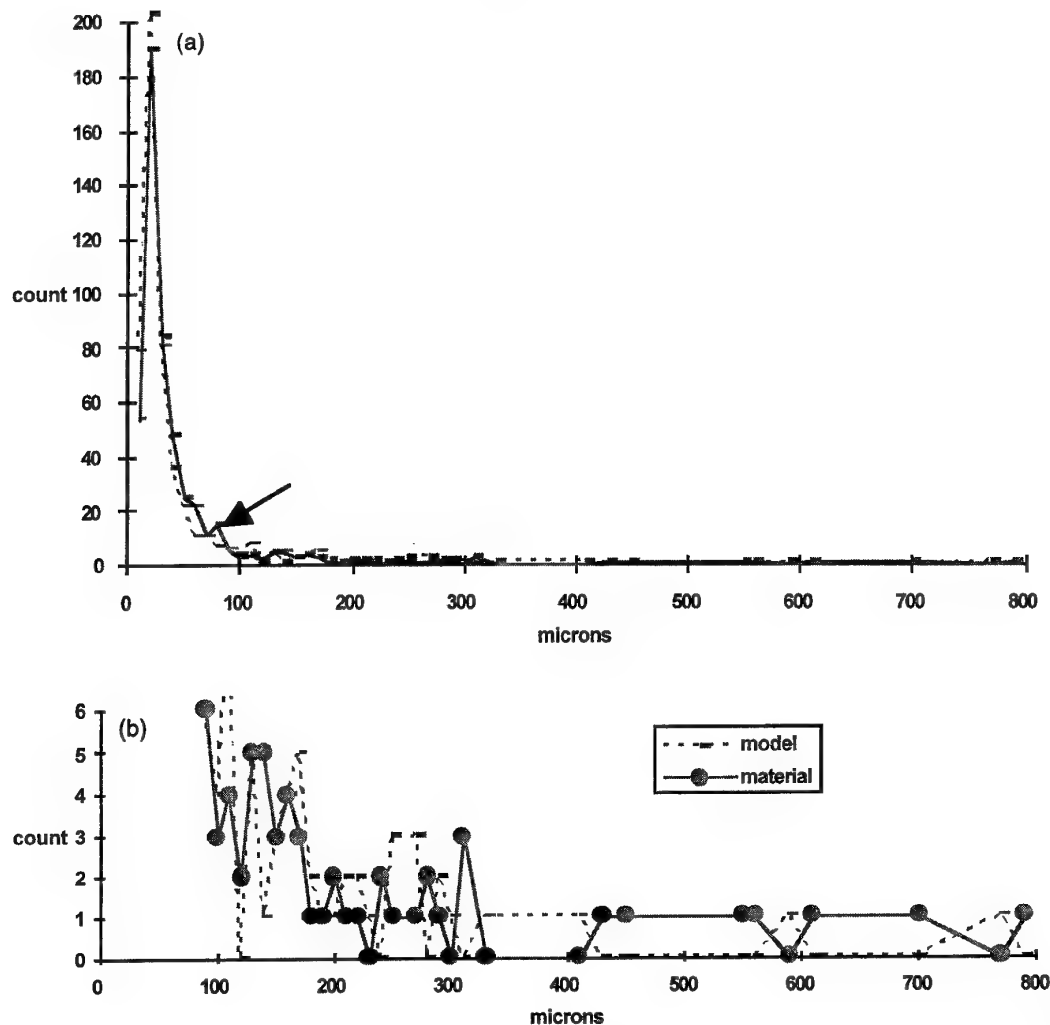


Figure 3 (a) Histogram of microcrack lengths (μm) for 304 stainless steel cycled for 4260 cycles at a stress amplitude of 346 MPa, $R = -1$. The arrow indicates a line of experimental data. The dotted line indicates the Monte Carlo simulation. Cracks of lengths 1.52 and 4.71 mm appeared in the sample, but cracks of that length were beyond the bounds of the array used in the simulation. (b) Close up of the same histogram showing the region above 90 μm

Also, the relative size of the microstructure length scale increases as the length of the crack decreases. As mentioned before, the apparent Paris exponent is smaller for the microcracks. It should be noted that the measured growth rates and Paris constants for microcracks are those for microstructurally favored microcracks; those which are not so favored are not measurable because they do not grow.

The crack growth data used in this study was obtained from an ingot stainless steel provided by Carpenter Technology Corporation having a rated yield strength of 259 MPa and a mixed grain size of 90 and 180 μm . These values and the mean distance to an inclusion or similar obstacle, 20 μm , were used in the calculation of the probability of microstructural crack arrest. Smooth electropolished specimens of the material were fatigued at a stress amplitude of 346 MPa ($R = -1$, $\Delta\sigma = 692$ MPa). During continued cycling, acetate replicas were taken of the surface. These replicas were plated, shadowed and examined in the electron microscope. Tables of microcrack lengths and their

growth rates were prepared. The number of cycles to failure was above 4000 in these tests.

RESULTS AND DISCUSSION

Figures 3–5 compare the crack length histograms obtained by actual counting with those generated by the simulation. These results of the typical simulation run are consistent with the actual counts within the run-to-run variations of each. We may gain inference about the physics of the growth of microcracks from the behavior of the simulation. For example, in the simulation, the increase in the number of cracks with increasing length up to a peak near 20 μm is the result of the innate singularity which tends to allow the newly generated crack to overcome all obstacles. This peak is a feature of the experimental data which previous versions of the simulation could not reproduce.

Another such feature is the weakness of the effect of length on growth rate in the length range below 200 μm . The program used Paris equation constants

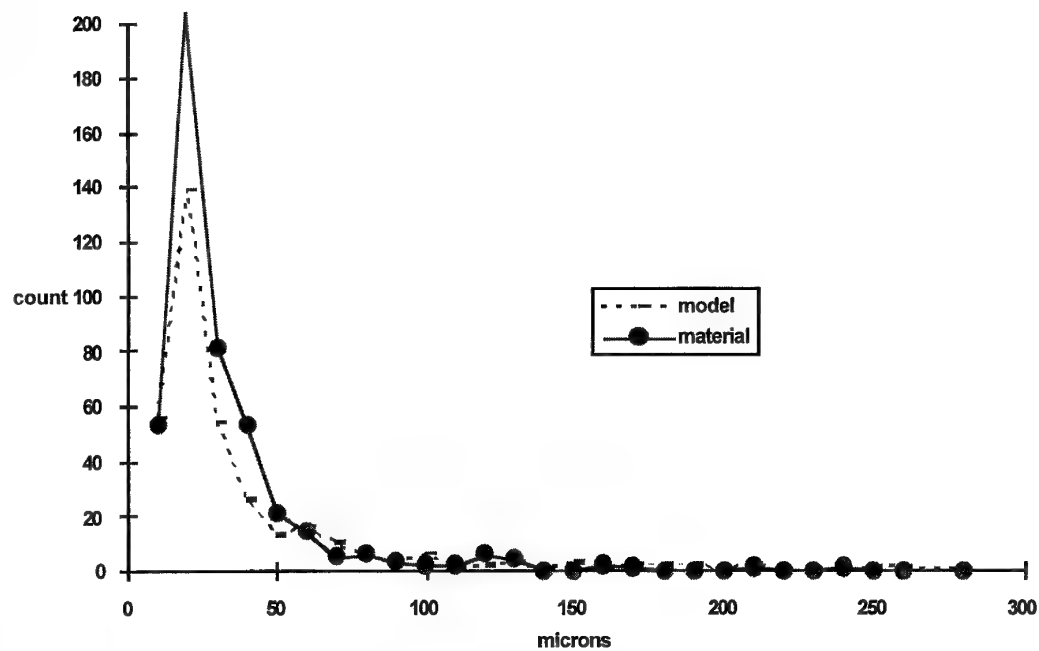


Figure 4 Histogram of microcrack lengths (μm) for 304 stainless steel cycled for 3100 cycles at a stress amplitude of 346 MPa, $R = -1$. The dotted line indicates the Monte Carlo simulation

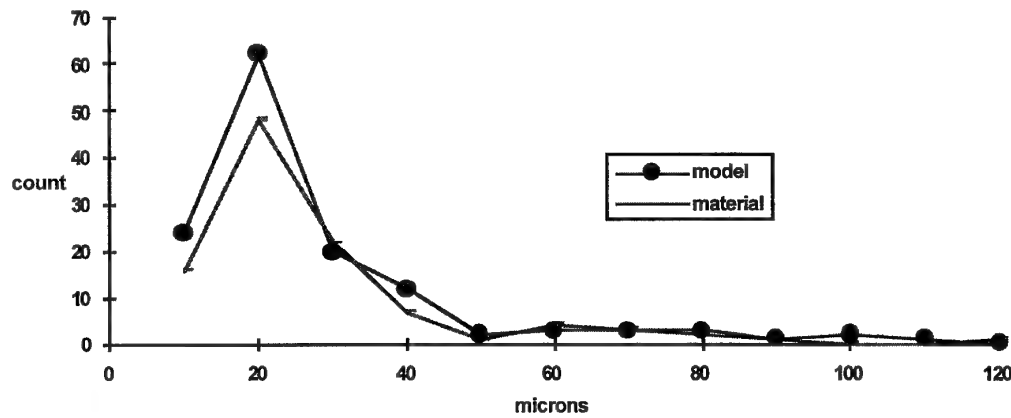


Figure 5 Histogram of microcrack lengths (μm) for 304 stainless steel cycled for 1250 cycles at a stress amplitude of 346 MPa, $R = -1$. The dotted line indicates the Monte Carlo simulation

Table 1 Probabilities per fatigue cycle (per crack)

Crack length range (μm)	Arrest	Escape from arrested state
10–20	0.035	0.00045
30–90	0.0001	0.00045
90–170	0.00001	0.00045
170 and above	0	0.00045

from long crack data, $C = 1.2 \times 10^{-9} \text{ mm cycle}^{-1}$, $m = 3.34$, the Paris exponent. Using these in combination with the observed crack growth rate minimum near 200 μm in length resulted in a range of lengths in the simulation between 70 and 500 μm in which the variation in growth rate would be small in the

absence of microstructural obstacles. Reducing the strength of the singularity increases the flatness of ΔK vs. crack length under the assumptions used here.

From the standpoint of the simulation, trapping dominates growth in the length range 20 to 100 μm . This creates an apparent growth law with what would appear to be a smaller Paris exponent than that of long cracks. Because of their larger ΔK (and larger K_{\max}) the larger cracks have a lesser probability of being trapped. The experimentally estimated trapping probabilities are given in Table 1.

CONCLUSION

Comparison of microcrack growth data for ingot 304 SS (cycled above the nominal yield stress at 346 MPa = $0.5\Delta\sigma = \sigma_{\max}$) with a stochastic model incorporating

stress singularities known to exist in polycrystalline materials resulted in a self-consistent prediction of small crack growth using Paris relation constants derived from large crack behavior. In the model, cracks are considered to originate at singularities having a strength greater than 0.5. Such singularities overcome the nucleation barrier experienced by Griffith cracks. Once the crack is nucleated, it experiences an induced stress intensity which diminishes with length by an inverse power smaller than that of the originating singularity. This induced stress intensity sums with that from the applied remote stress, resulting in a minimum at a length near 200 μm for these tests in this material. As this length is exceeded, the decaying stress intensity of the source singularity is lost beneath the effects of grain boundaries and similar features. In this approach self-consistency of the Paris relation was achieved by offsetting the accelerating effect of the source singularities with the observed interruptions due to microstructural arrest.

A considerable obstacle in understanding microstructurally small crack behavior comes from the approach of the length scale to atomic dimensions. In part, this was obviated here by treating cracks as indistinguishable, allowing a mean field treatment. At the length scale of atomic dimensions, molecular dynamics studies of fracture have supported the notion that continuum elasticity is a good approximation of the mean field^{25,26}. But the question remains of why the LEFM measures, K and ΔK , appear to work for small cracks where plasticity is presumed significant? This question may be related to that of why the J -integral can be applied to fatigue – where it is undefined? A complete answer is not available – at least here. Remember that continuum plasticity is an artifice and, at dimensions even somewhat larger than the atomic scale, plasticity vanishes, being replaced by discrete displacement discontinuities, i.e. dislocations. The spacing between the physical tip of the crack and the nearest functioning slip plane is likely to be significantly large; the crack tip is immediately surrounded by an elastic enclave²⁷. Plasticity appears as a convenience on a somewhat large scale, as a limiter of the applied stress and a provider of defects which feed fatigue crack growth.

On this scale we may examine K which is a measure of the (square root of the) free energy available for crack growth. It is also a prefactor in the equations describing the LEFM elastic stress field. Although the LEFM stress field would not be that of the sample in plasticity, how much work of unloading is required to convert the sample from a plastic to an elastic state? The upper bound on recoverable energy would be that in the elastic state plus any lost in the unloading. But actual hysteresis curves for fatigue do not indicate any transition from plasticity to elasticity in unloading. Hence, while the energy may be internally redistributed somewhat, the total available elastic energy for crack growth must be nearly the same in the two states. ΔK is a more abstruse matter. It is used as a measure of a generalized force for fatigue damage. Since fatigue damage requires plasticity, it becomes, in effect, an LEFM measure of plasticity and is therefore a mixed entity. The experimental evidence this work has provided has shown that the ΔK - da/dN relationship, called the Paris relation, can persist on very small length scales. Furthermore, it was the elastic energy definition

of ΔK rather than its customary form containing the square root of a length which was operative on the smaller scale. But, the direct role of elastic energy may be overstated in the theory of fatigue based on ΔK . K is also a number, a weighted measure, which labels the portion of a stress state related to a crack. ΔK is a measure of the difference between two such stress states. ΔJ is another weighted measure of stress. Frequently, especially in numerical problems, two similar weighted measures of a potential yield similar predictions for a system's evolution and can be chosen for mathematical convenience. For this reason alone it should not be surprising that both measures, K and J , are useful outside the province of their definitions. For instance, fracture mechanicians often assume Weibull distributed variates. But the Weibull distribution is wholly fictitious! (except as an asymptote).

ACKNOWLEDGEMENTS

This work was supported in part by the National Institute for Standards and Technology under Contract Number 70NNNANB9H0916. The authors thank Catalin Picu of Brown University and S. Leigh Phoenix of The Department of Theoretical and Applied Mechanics, Cornell University for their assistance.

REFERENCES

- 1 Picu, C., Interface crack impinging on a triple junction. *International Journal of Solids Structures*, 1996, **33**, 1563.
- 2 Picu, C. and Gupta, V., Stress singularities at triple junctions with freely sliding grains. *International Journal of Solids Structures*, 1996, **33**, 1535.
- 3 Picu, C. and Gupta, V., Crack nucleation on columnar ice due to elastic anisotropy and grain boundary sliding. *Acta Metallurgica et Materialia*, in press.
- 4 Picu, C., Stress singularities at vertices of conical inclusions with freely sliding interfaces. *International Journal of Solids Structures*, 1996, **33**, 2453.
- 5 Picu, C., Singularities at grain triple junctions in two-dimensional polycrystals with cubic and orthotropic grains. *Journal of Applied Mechanics*, 1996, **63**, 295.
- 6 Weertman, J., Zener-Stroh crack, Zener-Holomon parameter, and other topics. *Journal of Applied Physics*, 1986, **60**, 1877.
- 7 Sadananda, K. and Vasudevan, A. K., A unified framework for fatigue crack growth. Proceedings of Fatigue '96, Sixth International Fatigue Congress, Berlin, Germany, May 6–10, 1996, p. 375.
- 8 Rocha, M. M. and Schüller, G. I., A probabilistic criterion for evaluating the goodness of fatigue crack growth models. *Engineering Fracture Mechanics*, 1966, **53**, 707.
- 9 Paris, P., Fracture mechanics and fatigue: A historical perspective. Unpublished research, Washington University, St. Louis, MO, 1995.
- 10 Cox, B. N. and Morris, W., Model-based statistical analysis of short fatigue crack growth in Ti6Al-2Sn-4Zr-6Mo. *Fatigue and Fracture of Engineering Materials and Structures*, 1987, **10**, 429.
- 11 Chen, E. Y., Lawson, L. and Meshii, M., Comparison of the growth of an individual and average microcracks in the fatigue of Al-SiC composites. *Metallurgical and Materials Transactions A*, 1995, **26**, 3163.
- 12 Chen, E. Y., Impact of fatigue microcracks on the application of Al-SiC composites in unified life cycle engineering. Ph.D. Dissertation, Northwestern University, Evanston, IL, 1995.
- 13 Chen, E. Y., Lawson, L. and Meshii, M., The effect of fatigue microcracks on rapid catastrophic failure in Al-SiC composites. *Materials Science and Engineering A*, 1995, **200**, 192.
- 14 Tvergaard, V. and Hutchinson, J., Microcracking in ceramics induced by thermal expansion or elastic anisotropy. *Journal of the American Ceramic Society*, 1988, **71**, 157.
- 15 Brown, L. M. and Ogin, S., Role of internal stresses in the nucleation of fatigue cracks. In *Fundamentals of Deformation and Fracture*, eds B. Bilby, H. Miller and J. Willis. Cambridge University Press, Cambridge, UK, 1985, p. 501.

- 16 Raj, R. and Ashby, M., On grain boundary sliding and diffusional creep. *Metallurgical Transactions*, 1971, **2**, 1113.
- 17 Cox, B. N. and Morris, W., A probabilistic model of short fatigue crack growth. *Fatigue and Fracture of Engineering Materials and Structures*, 1987, **10**, 419.
- 18 Bataille, A. and Magnin, T., Surface damage accumulation in low-cycle fatigue: physical analysis and numerical modeling. *Acta Metallurgica et Materialia*, 1994, **42**, 3817.
- 19 Parker, A. P. *The Mechanics of Fracture and Fatigue*. E.&F.N. Spon Ltd., London, 1981.
- 20 Westergaard, H., Bearing pressures and cracks. *Journal of Applied Mechanics*, 1939, **6**, 49.
- 21 Weertman, J. and Weertman, J. R. *Dislocation Based Fracture Mechanics*. World Scientific Publishing, River Edge, 1996.
- 22 Suresh, S. *Fatigue of Materials*. Cambridge University Press, NY, 1991.
- 23 McGuire, S., Ph.D. Dissertation. Northwestern University, Evanston, IL, 1993.
- 24 Buck, O., Personal communications, 1992.
- 25 Ashurst, A. and Hoover, W., *Physics Review B*, 1976, **14**, 1465.
- 26 Paskin, A., Massoumzadeh, B., Shukla, K., Sieradzki, K. and Dienes, G. J., *Acta Metallurgica*, 1987, **1985**, 33.
- 27 Weertman, J., Personal communication (course lecture), 1988.

PII: S0142-1123(97)00060-1

A new life extension method for high cycle fatigue using micro-martensitic transformation in an austenitic stainless steel[‡]

T. H. Myeong*, Y. Yamabayashi*, M. Shimojot and Y. Higot

*Tokyo Institute of Technology, 4259 Nagatsuta-cho, Midori-ku, Yokohama, 226, Japan

^tPrecision and Intelligence Laboratory, Tokyo Institute of Technology, 4259 Nagatsuta-cho, Midori-ku, Yokohama, 226, Japan

Most of the conventional strengthening methods for metals and alloys such as work hardening, precipitation hardening, cause a decrease in ductility and are not very effective for cyclic loading. In this study, a new strengthening method, which is effective for high cycle fatigue, has been developed. The intersections of dislocations in a stainless steel are freezed by very fine martensite particles, which are supposed to suppress dislocation motion at low stress amplitudes. Fatigue life in a high cycle regime increased > 60 times, and no decrease in ductility was observed in tensile tests, as compared to a work-hardened stainless steel. © 1998 Elsevier Science Ltd.

(Keywords: fatigue life extension; martensitic transformation; austenitic stainless steel; cyclic plastic deformation)

INTRODUCTION

A number of the conventional structural materials against fatigue have been designed on the basis of the strengthening methods for monotonic loading such as work hardening, precipitation or dispersion strengthening or solid solution strengthening, etc. The basis for these methods is to increase the monotonic strength to build up a microstructure that contains effective obstacles for dislocation motion¹. These methods improve tensile properties by suppressing dislocation motion with an attendant decrease in ductility. However, under cyclic loading these methods are not so effective as under monotonic loading.

Prior to the onset of precipitation strengthening, some amount of dislocation motion is required, or the dislocations will move until they encounter obstacles. Though they are stopped by any obstacles, they could move in a reverse direction under the reversed stress of cyclic loading. Such a small amount of cyclic dislocation motion may be enough to cause fatigue crack initiation. Once a crack has initiated, a reduction in ductility which generally occurs with strengthening degrades the fatigue crack growth resistance of the material. It is also known that cyclic softening gener-

ally occurs in work-hardened materials due to a continual change in the dislocation structure until a saturated state is reached¹. This means that dislocations get to move easily inside the dislocation sub-structures. To summarize the discussion so far:

1. one of the differences of cyclic loading to monotonic loading is the to-and-fro motion of dislocations (although the motion may be small);
2. the conventional strengthening methods do not stop this small dislocation motion under cyclic loading; and
3. a small amount of cyclic dislocation motion may cause fatigue crack initiation.

It is well known that an austenitic stainless steel is quasi-stable at room temperature. When it is quenched below the M_s temperature or worked between the M_s and M_d temperatures, a Martensitic transformation occurs. M_s is the temperature for spontaneous transformation and M_d is the maximum temperature at which the transformation can be induced by plastic deformation. Also when an austenitic stainless steel is cooled down and kept around the M_s temperature without any load, α martensitic transformation occurs, which is called isothermal martensite transformation². According to Olson and Cohen³, in stainless steel with low stacking fault energy, the nucleation sites of a embryos were placed at two intersecting shear systems

[‡]This work was carried out as a part of the Ph.D. thesis of one of the authors (T.H.M.).

Table 1 Chemical composition of the austenitic stainless steel employed (wt%)

C	Si	Mn	P	S	Ni	Cr	Fe
0.06	0.31	1.31	0.034	0.028	8.11	18.41	Bal.

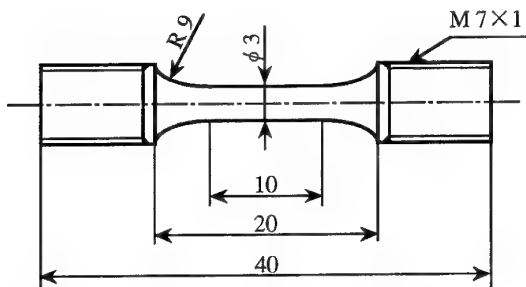


Figure 1 The dimension of the tensile specimen (mm)

in austenite. That is, on the basis of the double shear mechanism proposed by Bogers and Burgers⁴, in which b.c.c.-like stacking is formed at the intersection of two shear bands (1/18a[112]shear and 1/12a[112]shear). This has been confirmed on single crystals of a stainless steel (Fe-17.7Cr-13.6Ni) by Higo *et al.*⁵. Because the intersection of two partial dislocations has a b.c.c.-like stacking, which is similar to the structure of α martensite, it is thought that the intersection of two partial dislocations can also be a nucleation site of α martensite. α martensite, which has a b.c.c. or b.c.t. structure, is incoherent to the matrix of the f.c.c. structure, so that high energy or stress is needed the emission of dislocations from the α martensite. It is thought that α martensite particles pin the intersections of dislocations and suppress cyclic dislocation motion if α martensite particles are formed at the intersections of dislocations.

The objective of this study is to develop a new strengthening method which is effective in cyclic loading by pinning the intersections of dislocations.

EXPERIMENTAL

The material used was an austenitic stainless steel (Fe-18Cr-8Ni) rod, which was drawn in order to increase dislocation density. The applied plastic strain was *ca* 2%. [If the pre-strain is increased, the fatigue life may increase, however, transmission electron microscope (TEM) observation, which is described below, will be difficult.] The chemical composition of this material is shown in *Table 1*. Specimens for tensile tests and fatigue tests were removed from the material. The dimensions of the tensile specimen and the fatigue specimen are shown in *Figures 1* and *2*, respectively.

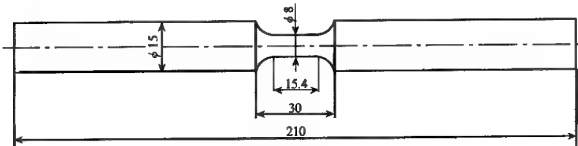


Figure 2 The dimension of the specimen for the fatigue life tests (mm)

A subzero heat treatment was carried out on the specimens to produce martensite particles at the intersections of the dislocations. In order to make the martensite particles as small as possible, the specimens were cooled down to -76°C for a period of 3 h. In the material used in our research, the temperature at which martensite nucleation starts was $>-76^{\circ}\text{C}$, however, the M_s temperature, which is normally defined as the temperature at which martensite is observed on surfaces of specimen using an optical microscope, was between -76 and -196°C (liquid nitrogen). The M_d temperature of this material was between room temperature and 120°C .

Metallographic observation was carried out to examine the microstructure and to measure the average grain size of the material using a laser microscope. Specimens for the observation were sectioned parallel and perpendicular to the drawing direction, polished by $1\ \mu\text{m}$ diamond paste and etched using a hydrochloric acid + methanol + picric acid solution. The average grain sizes were *ca* $54\ \mu\text{m}$ on the section parallel to the drawing direction and *ca* $51\ \mu\text{m}$ on the section perpendicular to it.

Transmission electron microscope observation was also carried out. The specimens (with diameter 3 mm) for the TEM observation were ground using emery papers until the thickness became *ca* $0.2\ \text{mm}$ and then electro-polished by a twin jet electro-polisher in a glacial acetic acid + perchloric acid electrolytic solution.

Tensile tests were performed on both non-subzero treated and subzero treated specimens using an Instron type tensile testing machine in laboratory air (temperature = 11 – 15°C and relative humidity = 55 – 65%) at a cross head speed of $0.5\ \text{mm min}^{-1}$ (strain rate = $8 \times 10^{-4}\ \text{s}^{-1}$).

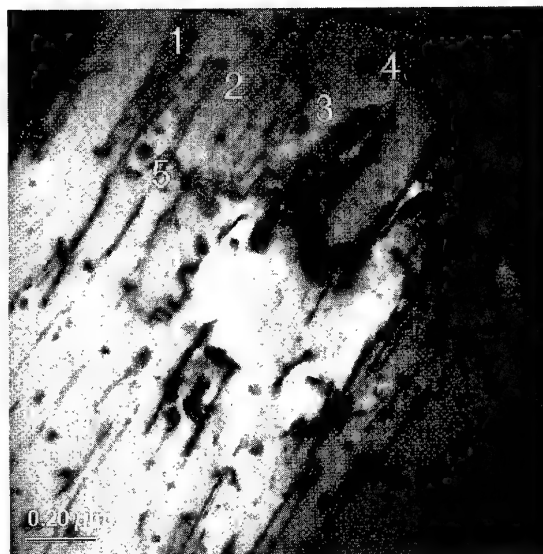
Fatigue life tests were performed on both non-subzero treated and subzero treated specimens using a rotary four point bend fatigue testing machine at an *R*-ratio of -1 . The temperature of the specimen surface was measured using an infrared temperature sensor. The test frequency, that is, the revolution speed of the fatigue life tests was determined so that the temperature of the specimen surface did not exceed 35°C , and thus the frequency was in a range of 2 – $10\ \text{Hz}$.

RESULTS

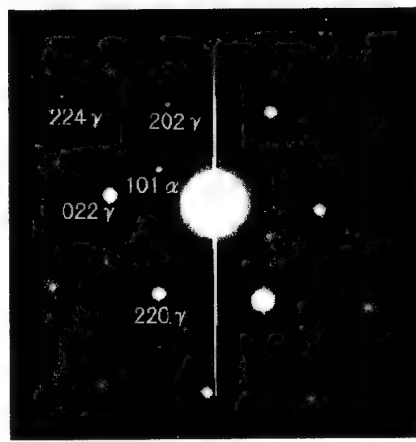
Polished surfaces of both subzero and non-subzero treated specimens were observed using a laser microscope, however, no difference was observed. Thus, no large martensite was formed by the subzero treatment.

A bright field TEM image of a subzero treated specimen is shown in *Figure 3(a)*. Dislocations and small dots are observed. The size of these dots was *ca* 0.02 – $0.1\ \mu\text{m}$ in diameter. In order to identify the small dots, the diffraction pattern of this image is analysed. The result is shown in *Figure 3(b)* in which two sets of diffraction patterns exist. One is a diffraction pattern of austenite and the other is of a martensite. The orientation relationship between the austenite matrix and the martensite observed in the figure is close to the Nishiyama relationship⁶, which is $(111)\gamma//(110)\alpha$, $[112]\gamma//[110]\alpha$.

A dark field image generated by a spot in the diffraction pattern of martensite is shown in *Figure 4*.



(a)



(b)

Figure 3 (a) A bright field TEM image and (b) the diffraction pattern of the image of a subzero treated specimen

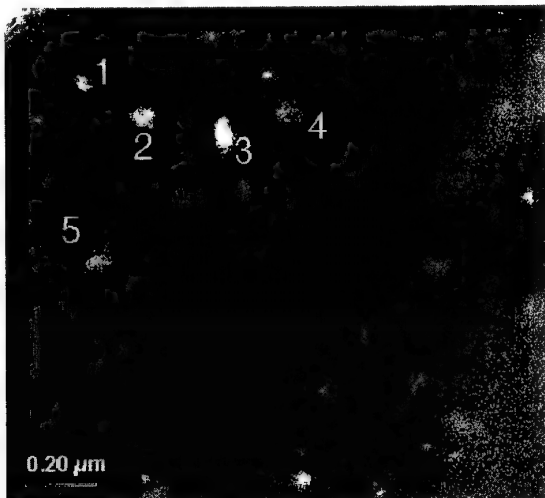


Figure 4 A dark field image using a spot in the diffraction pattern of martensite

Some bright and small dots were observed. Comparing the positions of the bright and small dots in *Figure 4* with those of the dark and small dots in *Figure 3(a)*, it was confirmed that the positions of the dots in *Figure 4* coincide with some of the dots in *Figure 3(a)*. However, all of the dots in *Figure 4* do not correspond to the dots in *Figure 3(a)*. This may be because of the existence of martensite of another variant which was not related to the analysed orientation. According to Higo *et al.*⁵, the martensite variants formed by plastic deformation strongly depend on the direction of the stress applied. In the present study, since the martensite transformation is induced by the subzero treatment and not by plastic deformation there is a possibility of the appearance of all martensite variants for minimizing the transformation strain.

The results of the tensile tests performed on both

the non-subzero treated and subzero treated specimens at room temperature are shown in *Figure 5*. The tensile properties of the subzero treated specimen were almost the same as those of the non-subzero treated specimen in all respects such as yield stress, tensile strength and elongation.

An *S-N* curve (fatigue lives vs maximum stress) is shown in *Figure 6*. The fatigue lives of subzero treated specimens did not increase in a low cycle regime ($< 10^4$ cycles) as compared to those of the non-subzero treated specimens. However, in a high cycle regime ($> 10^4$ cycles), the fatigue lives of subzero treated specimens are much longer than those of non-treated specimens. At a maximum stress of 350 MPa, the number of cycles to the failure of subzero treated specimens are about four and five times larger than that of the non-subzero treated specimens. At a maximum stress of 310 MPa, which is just above the

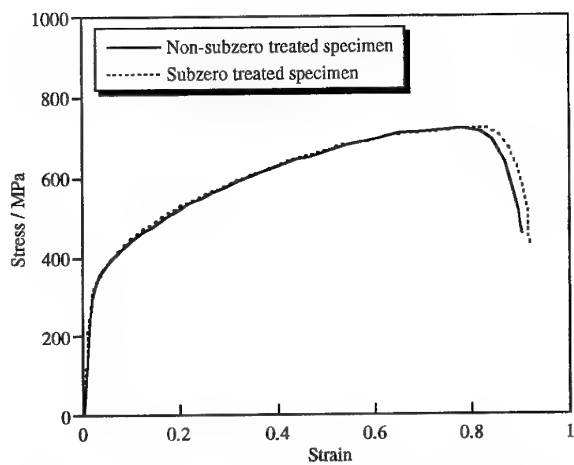


Figure 5 Stress-strain curves of a non-subzero treated specimen and a subzero treated specimen

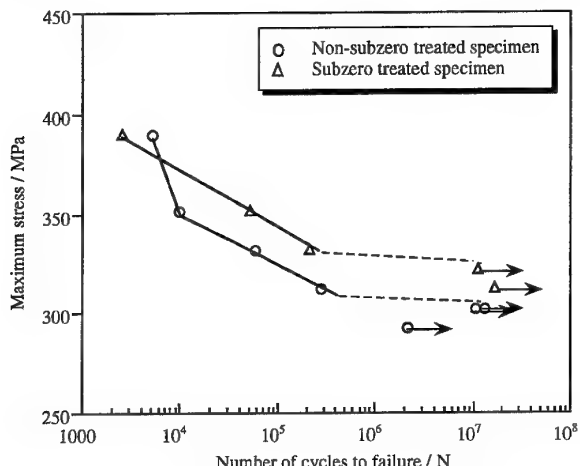


Figure 6 Fatigue life of non-subzero and subzero treated specimens

fatigue limit, the number of cycles to the failure of the non-subzero treated specimen was 2.8×10^5 cycles, and the subzero treated specimen did not fail at 1.7×10^7 cycles, which is > 60 times longer.

DISCUSSION

The TEM observation revealed that very fine martensite particles existed in subzero treated specimens. According to the mechanism proposed by Bogers and Burgers⁴, these fine martensite particles are thought to be nucleated at intersections of dislocations. Due to the fact that the fatigue lives of subzero treated specimens increase at lower stress amplitudes as compared to the non-treated specimens, it is suggested that these martensite particles suppress dislocation motion.

At higher stress amplitudes, however, the fatigue lives of subzero treated specimens are almost the same as those of non-treated specimens. It is thought that dislocations come off the martensite particles at higher stresses because the particles are so small that the pinning force is small. This agrees with the fact that the tensile properties of subzero treated specimens are

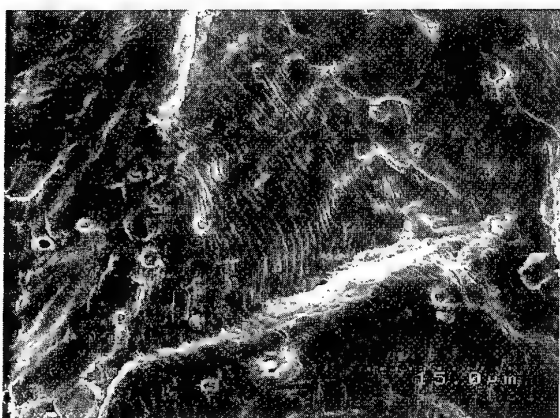
the same as those of non-treated specimens. During the tensile test, because the stress exceeded the pinning force, dislocations are thought to come off the martensite particles and to move easily. Thus, the pinning effects diminished and the tensile properties became the same. This does not necessarily mean that this method has a deficiency. Because there is no decrease in elongation or fracture strain, this implies that there is little decrease in fracture toughness after the subzero treatment, though the conventional strengthening methods, in general, decrease the fracture strain.

Fracture surfaces of specimens tested at a stress of 330 MPa for both subzero and non-subzero treatments observed using a SEM are shown in Figure 7. No difference was observed on the fracture surfaces of subzero and non-subzero treated specimens. This is also because once cracks were initiated, the plastic strain at the crack tips were so large due to the stress concentrations that the dislocation locking mechanism proposed in this study no longer operates at the crack tips.

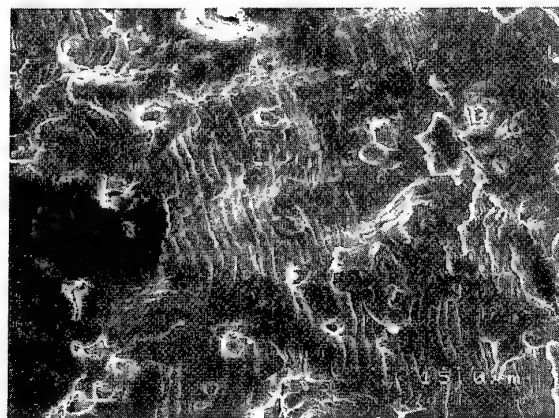
It has been reported that plastically induced ϵ martensitic transformation makes elongation much larger in tensile tests⁷. According to the large elongation in the tensile tests in this study, ϵ martensitic transformation which is induced by plastic deformation may have occurred in both subzero treated and non-treated specimens. Thus, ϵ martensitic transformation might occur during fatigue tests. This is not, however, the reason for the fatigue life extension at lower stress amplitudes, because this transformation could occur in both the specimens and this transformation could occur more in high stress amplitudes.

The pinning force generated by the martensite particles depends on the distance between two pinning points which is often explained as the Orowan mechanism⁸ in precipitate strengthened materials. In the method used in this study, the average pinning distance can be controlled by changing the initial dislocation density. For future work, it may be possible to increase the fatigue strength more by optimizing or by increasing the initial dislocation density, which can be controlled by cold working.

In a conventional strengthening method such as pre-



(a)



(b)

Figure 7 Fractographs of (a) a non-subzero treated specimen and (b) a subzero treated specimen

cipitation hardening, dislocations must move until the dislocations encounter precipitates. Such a hardening method is not very effective for suppressing cyclic dislocation motion, which occurs under cyclic loading. In conventional martensite hardened material, martensite particles are relatively large and brittle so that the particles may act as crack initiation sites. However, with this new strengthening method developed in this study, martensite particles are very small and are supposed to be located at the intersections of dislocations. Thus, this does not cause any brittleness, although cyclic dislocation motion is suppressed under high cycle fatigue loading.

CONCLUSIONS

A new strengthening method, which is effective for high cycle fatigue ($> 10^4$ cycles), has been developed. In this method, a subzero treatment is performed and the intersections of dislocations are locked by very fine martensite particles, which suppress dislocation motion at low stress amplitudes. The fatigue life at a low stress amplitude was increased > 60 times as compared to non-treated specimens. Furthermore, no decrease in ductility was observed in the tensile tests.

ACKNOWLEDGEMENTS

This study was partly supported by a Grant-in-Aid for COE Research from the Ministry of Education, Science, Sports and Culture, Japan (No. 07CE2003, 'Ultra-parallel Optoelectronics').

REFERENCES

- 1 Klesnil, M. and Lukas, P., Materials science monographs, 7. *Fatigue of Metallic Materials*, 1992, 88–101.
- 2 Imai, Y. and Izumiya, M., *Journal of the Japan Institute of Metal*, 1963, **27**, 170–176.
- 3 Olson, G. B. and Cohen, M., *Journal of the Less-Common Metals*, 1972, **28**, 107–118.
- 4 Bogers, A. J. and Burgers, W. G., *Acta Metallurgica*, 1964, **12**, 255–261.
- 5 Higo, Y., Lecroisey, F. and Mori, T., *Acta Metallurgica*, 1974, **22**, 313–323.
- 6 Nishiyama, Z., *Martensite Transformation* (in Japanese). Marzen, Tokyo, 1971, p. 5.
- 7 Higo, Y., Mori, T. and Nakamura, T., *Journal of the Iron and Steel Institute of Japan*, 1975, **11**, 37–54.
- 8 Orowan, E., Causes and effects of internal stresses. In *Internal Stresses and Fatigue in Metals*, ed. G. M. Rasswelier and W. L. Grube. Elsevier, New York, pp. 59–80.

PII: S0142-1123(97)00015-7

Fatigue microcrack distributions and the reliability of a nickel base superalloy

E.Y. Chen*†, S. Sauer*‡, M. Meshii* and W.T. Tucker§

*Department of Materials Science and Engineering, Northwestern University,
Evanston, IL 60208, USA

§Management Science and Statistics, GE Corporate Research & Development,
Schenectady, NY 12301, USA

Low cycle fatigue failure in nickel base superalloys is strongly influenced by the initiation, growth and interaction of a high density of distributed microcracks. The latter is of immense significance late in the fatigue life as several microcracks can link together to form a rapidly growing critical crack. This study details the room temperature growth behavior of microcracks in populations on the surface of a Ni base superalloy selected for use in advanced turbine engines. Gathered with the needs of the reliability engineer in mind, it is shown that the growth patterns of these microcracks needs to be considered in order to avoid making nonconservative fatigue lifetime predictions. © 1998 Elsevier Science Ltd.

(Keywords: microcracks; Ni superalloy; reliability)

INTRODUCTION

Nickel base superalloys have been used extensively in the aerospace industry because of their outstanding properties in high temperature and harsh operating conditions. These materials have been specifically employed for critical applications such as turbine disks of advanced military aircraft engines due to their high temperature strength (deformation behavior), creep rupture strength, and fatigue resistance¹. In fatigue restricted situations, the ability to predict the growth rates of cracks from the microcrack[¶] initiation stage through to final failure is a necessity². To achieve this, an understanding of the growth behavior of microcracks in Ni superalloys is required.

The microcrack growth regime is often the longest

stage of the fatigue life in metals. In Ni base superalloys, particularly during the period just after crack initiation, it is still not well understood. Microcracks growing from defects have been found to propagate at different rates to those from slip bands in the same material³. While the growth behavior of long cracks can be approximately described by the Paris-Erdogan equation³, microcracks have growth behaviors not well characterized when linear elastic fracture mechanics (LEFM) is directly applied, because factors such as crack coalescence cannot be taken into account in the framework of the so-called ‘small crack problem’. Coalescence can play a significant role because crack growth often consists of several microcracks linking together to create a larger crack. This leads to ‘jumps’ in the crack growth rate not accounted for when using empirical expressions such as the Paris equation, which tends to ‘smooth’ out the data^{4–8}. As a result of coalescence, crack propagation lives are shorter than would be expected for a single, isolated growing long crack⁹. This can lead to overestimates on the expected fatigue lifetimes of components.

Several works on small crack growth in Ni base superalloys have been found in the literature^{9–16}. Most of these studies examined short crack growth using bending or notched fatigue specimens. Smooth specimens, however, are preferred over bending specimens to investigate microcrack growth because the volume of material which experiences the maximum stress is higher¹⁰. Their use is also favored over that of notched specimens since the introduction of a localized region

†Present address: Physical Metallurgy Laboratory, GE Corporate Research and Development, Schenectady, NY 12301, USA. Phone: + (518) 387-4121; Fax: + (518) 387-6232; E-mail: eychen@crd.ge.com.

‡Present address: Universität Stuttgart, Eschenauer Strasse 15, 70437 Stuttgart, Germany. Phone: + (49) 711-872666.

¶Crack sizes will be distinguished by a terminology similar to that set in Ref.². Microcracks refer to mechanically and microstructurally small cracks which are less than 100 µm in length and depth, on the order of the grain size, and of sizes comparable to their own crack tip plastic zones. Short cracks are physically small cracks which are 100 to 500 µm in either length or depth directions. Long cracks have lengths and depths which are greater than 500 µm, satisfy the requirements of linear elastic fracture mechanics, and have growth rates which can be described by the Paris-Erdogan equation³. The term ‘small cracks’ refers to both short cracks and microcracks.

of very high stress concentration into the latter means that the critical crack will always initiate at the notch, thus eliminating subsurface defects and other factors as important crack initiation sites. On predicting the growth rates of microcracks in Ni superalloys, there is a dearth of information available. Most studies uncovered in the literature emphasized the correlation (or lack of correlation) between small and long crack growth rates through the use of the stress intensity factor (ΔK) or modified versions of ΔK to account for factors such as crack closure (e.g. ΔK_{eff}). One study¹¹ indicated that for Ni superalloys there is little evidence of crack closure for microcracks of up to 250 μm .

To assist in improving our understanding of the mechanics of microcrack growth in Ni base superalloys, this paper examines how they initiate, grow, and interact in distributions on the surfaces of smooth fatigue specimens. By characterizing the growth of microcracks both individually and as a part of the evolving crack population, the process by which the critical cracks (i.e. those that lead to failure) emerge and the rate at which they grow can be established. Such detailed microcrack growth studies can provide valuable insights into improving fatigue lifetime predictions as well as help to achieve a better control over fatigue failure than researches based primarily on macrocracks are capable of to date. This is because all macrocracks are inherently the net products of the distribution of microcracks. The information gathered here will eventually be applied to a computational methodology (not discussed here) devised to assist the reliability engineer in scheduling safety inspections more effectively^{7,17}. The strategy is to closely reproduce the experimentally obtained microcrack distributions so that the number of cracks of a particular length, especially those which may go critical, can be estimated at any given point in the fatigue life. One other important contribution of this type of research lies in the design of state-of-the-art alloys. Materials with microstructures in which microcracks can only nucleate and grow with great difficulty would undoubtedly possess superior fatigue properties, particularly in low cycle fatigue where the contribution of microcracks to failure is often much higher.

EXPERIMENTAL DETAILS

The material studied here is the Ni base superalloy designated René 88†, which was obtained from General Electric Aircraft Engines (Evendale, OH) in 1995. René 88, or R'88DT, is processed by powder metallurgy, and is extruded and isoforged (see Ref. 18 for a detailed description of the processing technique for this material). This particular stock is γ' (Ni-Al-Ti) and solid solution (Mo, W) strengthened. Table 1 shows the mechanical properties at various temperatures¹⁹. The grain size is ASTM 6-9 with a line intercept average of 21 μm . Figure 1 is a micrograph of the R'88DT microstructure after etching with waterless Kalling's reagent.

Fatigue testing was performed using sheet specimens based on the ASTM Standards E606 design²⁰ (Figure

2). These specimens were machined from the as-received stock material by electro-discharge machining. For preparation, the specimens were polished from 240 grit down to 600 grit using SiC paper. Fine polishing was then performed with diamond slurries of 6 and 1 μm on TEXTMET 1000‡ polishing cloth. The fatigue tests were conducted in room temperature air under fully-reversed loading ($R = -1$) at a maximum stress of 960 MPa (approximately $0.9\sigma_y$) using a computer-controlled MTS§ Axial-Torsion Materials Test System, a servo-hydraulic mechanical testing machine. The testing frequency was chosen as 1 Hz since this provided sufficient time to examine the growth of the microcracks optically, allowed for environmental effects at room temperature air, and even made it easier to hold the specimen in the fixture. Although MTS 647 hydraulic wedge grips were used, the hardness of the material made it necessary to increase the friction at grip/specimen interface to prevent the specimen from sliding out during loading. This was done by gluing (with superglue) Al_2O_3 powder (particle size $\approx 0.5 \mu\text{m}$) onto the grip sections of each specimen.

To obtain microcrack growth and distribution data, cellulose acetate replicas were employed. Replicas were typically made at every 1000 cycles in fatigue testing. To do this, the fatigue tests were interrupted and the specimens were loaded to the maximum applied stress. This allowed the replicas, when softened with acetone, to penetrate as deep as possible into the opened microcracks on the specimen surface. After the replicas were made for the four sides of each specimen, they were vacuum coated and shadowed, respectively, with Al and Au so that they could be examined in a Hitachi S-570 scanning electron microscope (SEM). The coordinate controls on the specimen stage of the SEM allowed the same microcracks to be tracked on each set of replicas with respect to a reference point. The scale of resolution for pinpointing microcracks depends on the SEM magnification employed. For example, at a magnification of 150 times, microcracks of at least 50 μm could be positively identified as such in the SEM. Higher magnifications could be used for greater resolution, however, this limited the number of microcracks in the surface population which could be sampled. For this particular work, microcracks of 20 μm and larger (up to several millimeters) were counted. Data obtained from the replicas by this analysis method include information on microcrack initiation, growth, and distributions on the specimen surfaces.

EXPERIMENTAL RESULTS AND DISCUSSION

Evolution and characterization of microcrack distributions

Figure 3 shows an example of a replica sequence of microcrack growth as obtained during fatigue testing. From these micrographs the initiation and growth of the same slip band microcrack on the surface of the R'88DT can be followed until it becomes the critical crack which leads to failure. These micrographs

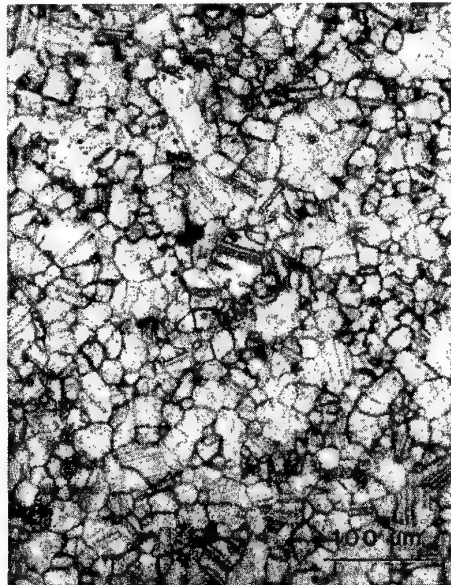
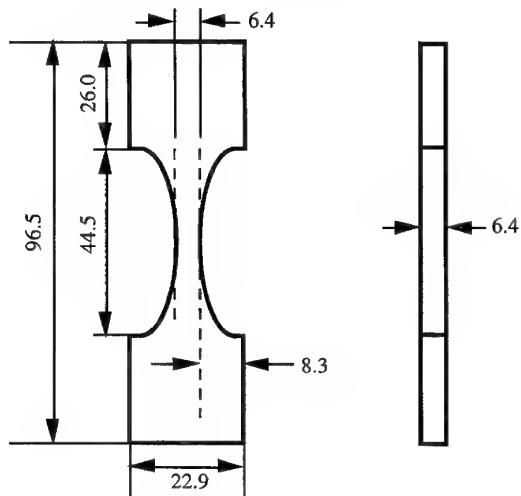
†TEXTMET 1000 is a trademark of Buchler Ltd. (Lake Bluff, IL).

‡MTS is a trademark of MTS Systems Corporation (Minneapolis, MN).

§René 88 is a trademark of General Electric Company.

Table 1 Mechanical properties of R'88DT Ni superalloy¹⁹

Property	Temperature (K)		
	477	672	925
0.2% yield strength, σ_y (MPa)	1110	1103	1027
Ultimate tensile strength, σ_u (MPa)	1476	1482	1462

**Figure 1** Microstructure of R'88DT after etching with waterless Kalling's reagent**Figure 2** Fatigue specimen design for microcrack studies in the R'88DT (unit = millimeters)

also indicate that there is a continuously changing density of surface microcracks which becomes very large late in the fatigue life (over 200 microcracks mm^{-2} at $N/N_f = 0.98$ when viewed at a magnification of 150 times). Many of these cracks were greater than 100 μm near the end of the fatigue life. As for the microcrack shown in Figure 3a, the majority of the microcracks

appear to have initiated at slip bands. Others emerged at grain and twin boundaries. Microcracks which initiated from inclusions at the surface were seen, but were few in number compared to the former. Initiation at subsurface defects was not immediately seen from the replicas.

Crack coalescence was a significant factor in the growth of microcracks, particularly late in the fatigue life when the total length density of microcracks present is high.[†] In the example of Figure 3, the critical crack was the result of over 10 sets of linkages between microcracks of various lengths at different stages in its growth. Microcracks from the slip bands and grain/twin boundaries appear to grow in a zig-zag manner, as commonly seen by other researchers studying Ni superalloys^{13,14}. This is partly due to the coalescence of microcracks along different planes. Fracture surface analyses (not given here) also confirmed the importance of coalescence during the fatigue damage process. In most of the specimens studied, the critical crack was a product of the coalescence between several large cracks (as distinguished on the fracture surface by the overlapping of cracks on different planes). Another feature of interest is that there were usually several other long cracks present, in addition to the one which became critical. These other long cracks could be on the same or a different side of the specimen with the critical crack. It was not immediately clear as to why one long crack instead of another became the critical crack. Coalescence with another long crack, however, could be one explanation.

To analyze the evolving distributions of microcracks, the length of each microcrack present in a given area was measured. Figure 4 shows an example of how the distribution changes over time. Following a sharp initial rise in the number of microcracks (Figure 4a), the crack density remains relatively unchanged (Figure 4b). Near the end of the fatigue life (Figure 4c), the crack density actually decreases. An explanation for this can be related to the contributions of initiation and coalescence to the fatigue damage process. Initiation introduces new cracks of the smallest sizes into the system, leading to the large peak seen in the distribution. Coalescence, on the other hand, reduces the number of cracks as two or more cracks are 'absorbed' into one. Along with individual microcrack growth, this process broadens the distribution. With continued fatigue cycling, the number of favorable sites for crack initiation is expected to decline and the number of new cracks entering the system decreases. While the rate of change in crack density is positive for most of the life, the probability of crack coalescence rises

[†]Ref. 8 examines similar crack coalescence mechanisms in an advanced composite material.

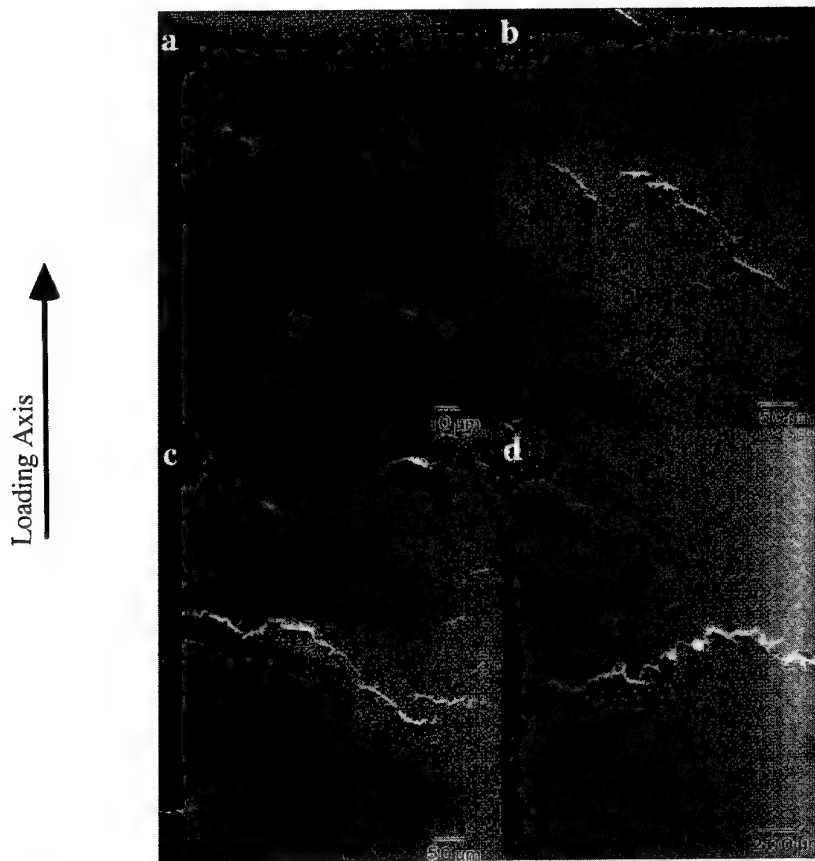


Figure 3 Evolution of a fatigue microcrack population on the surface of the R'88DT as seen from micrographs of replicas at (a) $N/N_f = 0.20$, (b) $N/N_f = 0.49$, (c) $N/N_f = 0.69$, and (d) $N/N_f = 0.98$. In this case, a single slip band microcrack initiates, grows on its own, interacts and coalesces with other microcracks to become the critical crack which led to failure. $R = -1$, $\sigma_{max} = 960$ MPa, $N_f = 10,168$ cycles

proportionally. Eventually, the rate of coalescence exceeds that of initiation and the density of cracks shrinks. Another factor which must be considered for the observed decrease in crack density late in the life is crack tip shielding. In many cases, small microcracks became shielded ahead of the tips of larger microcracks and macrocracks. Although these microcracks were still present when the maximum stress was applied, they were at least partially closed and not easily revealed by the replicas when examined in the SEM.

Figure 5 shows the evolving crack population over time as divided into microcrack, short crack, and long crack categories to highlight the importance of the microcracks. From this figure, microcracks are seen to dominate the total crack population for up to 60% of the life. Most cracks remained small (i.e. less than 500 μm) for the entire fatigue life. The fraction of long cracks in the total population is always less than 10%. Long cracks also do not begin to emerge from the small cracks until about $N/N_f = 0.70$. This suggests that long crack growth behavior (e.g. Paris-type crack growth) may not be seen in the R'88DT until over 70% of the fatigue life has expired.

One way to characterize microcrack distributions to allow their use in the previously mentioned methodology for reliability inspection scheduling is to evaluate them statistically²¹. The statistical investigation included here consists of studying the use of probability distributions to describe the microcrack growth behavior in the microcrack distributions of Figure 4.

At this point only two distributions have been considered for the R'88DT: Weibull and log-normal. The various probability plots (not shown here) indicate that the log-normal distribution fits over the complete range of growth much better than the Weibull (at 95% confidence level). Other distributions, however, still need to be considered. It would also be very useful to have a physical basis for any distribution employed. Even at this stage of analysis the results for the log-normal distribution are very interesting. This is seen by considering the summary plot showing the estimated location and scale parameters for two different specimens N2 and N3 tested under the same conditions (Figure 6). After a reasonable percentage of life has been accrued (20 to 30%) the scale parameter (representing scatter in the data) stabilizes. The location parameter, however, increases to a plateau just before specimen failure. The location parameter represents the 'average' size or length of the microcracks at a given percentage of life. Its increase over time is consistent with the individual growth and coalescence of the microcracks. The observed plateau could suggest that at this point in the life a dominant critical crack has emerged. The presence of a dominant critical crack leads to a significantly decreased rate at which new cracks (if any) are initiated into the specimen (shielding effects). As a result, the distribution peak decreases in height and broadens as cracks grow from it into the lower tail of the distribution, while little or no new cracks are initiated. The consistency of these prelimi-

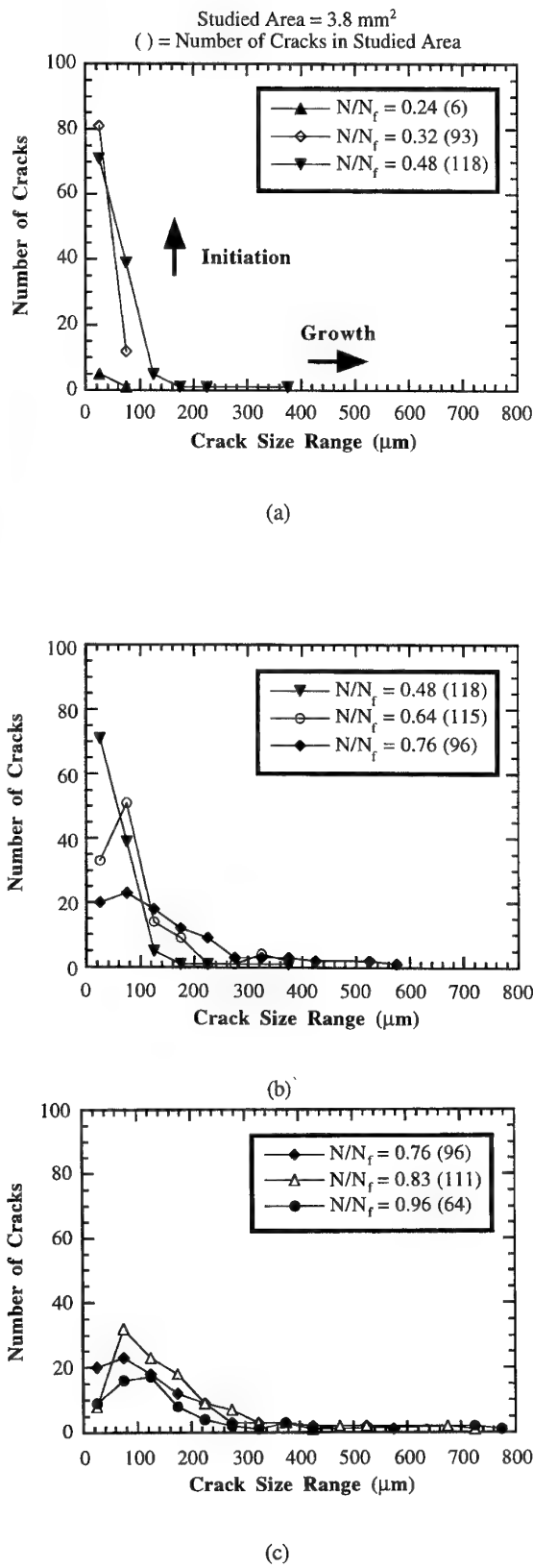


Figure 4 Change in microcrack length distributions in the R'88DT. Data taken from replicas. $R = -1$, $\sigma_{\max} = 960 \text{ MPa}$, $N_f = 12,506$ cycles

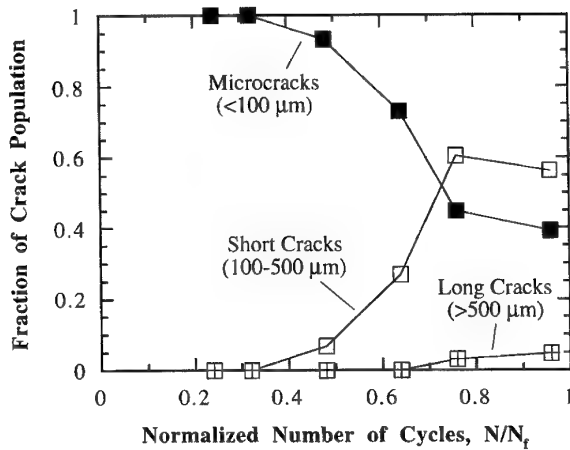


Figure 5 Fraction of cracks of different sizes at various stages in the fatigue life of a Ni base superalloy. Data taken from replicas. $R = -1$, $\sigma_{\max} = 960 \text{ MPa}$, $N_f = 12,506$ cycles

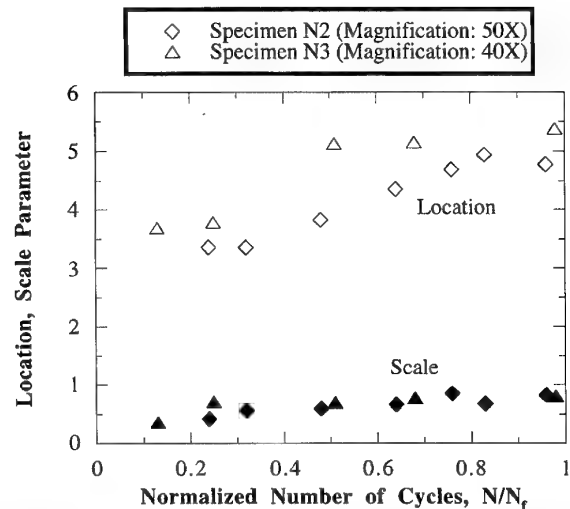


Figure 6 Change in location and scale parameters of the log-normal distribution function used to fit the observed microcrack distributions in two different specimens (N2 and N3) of the R'88DT. $R = -1$, $\sigma_{\max} = 960 \text{ MPa}$

nary results is very pleasing, and they give a good probabilistic description of microcrack growth in the distributions. As a result, it may be possible to apply the log-normal distribution to represent actual microcrack distributions in the R'88DT.

Growth of individual microcracks in the distributions

The growth behavior of individual microcracks can be followed on the replicas from initiation to failure. Figure 7 shows the change in surface crack length (b) versus the number of fatigue cycles (N) for the critical cracks in three different specimens. A total of 49 cracks, both small and long, was followed. Figure 7 shows that even the critical cracks remained less than 200 μm in length for over 50% of the fatigue life. Since 200 μm is the threshold value for many NDE techniques, this suggests it may not be cost effective to schedule reliability inspections prior to this stage in the fatigue life. Another common characteristic of the microcracks was that they all exhibited some instances

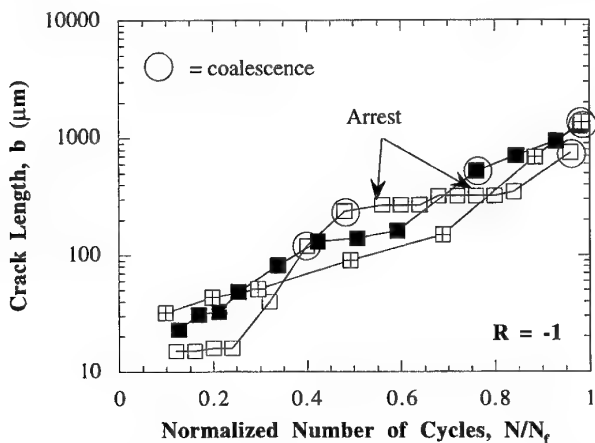


Figure 7 Growth behavior of critical cracks in the fatigue of the R'88DT. The circles indicate that coalescence with another crack took place in the interval prior to which the replica was made. Data taken from replicas. $R = -1$, $\sigma_{\max} = 960$ MPa

of arrest or coalescence. Even the critical cracks in *Figure 7* showed periods of little or no growth on the surface up to 20% of the life. After crack linkages, a jump in the crack length can be seen.

To examine whether or not the growth rates of microcracks can be predicted by the use of an empirical power law, the crack growth rate for all the studied microcracks (49 total microcracks) was determined by differentiating the b vs N plots. *Figure 8* shows the log-log scale plot of the crack growth rate along the surface length (db/dN) vs ΔK as compared with long crack data obtained from single edge-notched (SEN) specimens at elevated temperatures between 420 and

1000 K.^{19,*} The calculations of ΔK for the microcracks were taken for semi-elliptical cracks²² based on the shape of the critical crack as seen from the fracture surface.[‡] Since only the surface crack length can be accurately measured from the replicas, it was assumed that the crack depth was 1/4 the size of the crack length since most microcracks in this material were longer than they were deep. The shape of the scatter for the individual microcrack data points in *Figure 8* is roughly triangular (i.e. for large values of ΔK the band is narrow whereas for small values a very broad range of scatter is seen). The slope of the scatter at large ΔK values seems to correlate well with the long crack data. If extrapolation from the upper bound of the long crack data into the long crack threshold (i.e. microcrack) regime is made using a power law expression, it is seen that such prediction would be nonconservative compared to the upper bound of possible microcrack growth rates. This means that predictions of microcrack growth based on such extrapolations may result in overly optimistic fatigue lifetime predictions.

To address the question of at what point in fatigue life or at what length microcracks begin to exhibit Paris-type crack growth (i.e. when the crack growth rates of microcracks can be fitted by a power law on a log da/dN vs log ΔK plot as in *Figure 8*), the growths of microcracks that became long cracks were examined more closely. Of the 49 total microcracks studied, 14 of these cracks became long. To assess these cracks, the term ‘incubation’ is introduced and will be defined as the interval prior to which microcracks begin to demonstrate Paris-type growth (this could also represent the transition from small to long crack growth). For example, incubation period refers to the time prior to which the growth rate of a microcrack could be described with a Paris equation. *Figure 9* shows the resulting incubation properties of microcracks which eventually displayed Paris-type growth in the R'88DT. From *Figure 9a*, the incubation period is usually over 60% of the fatigue life. This means that most of the microcracks which became long did not do so until almost 2/3 of the lifetime had expired. This is consist-

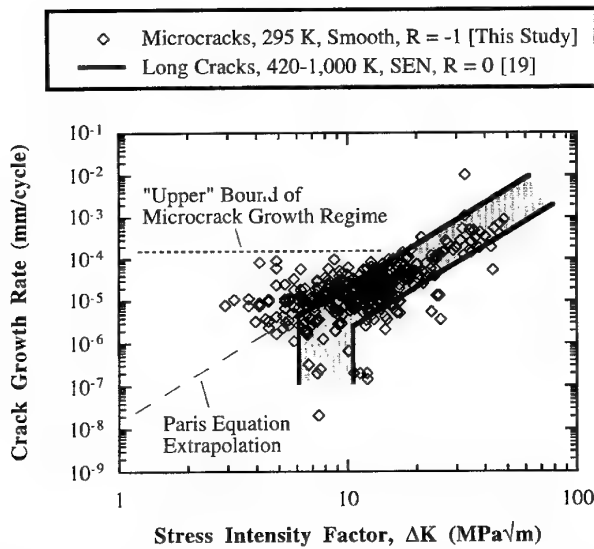


Figure 8 Comparison of microcrack and long crack growth rates in the R'88DT. Long crack data were obtained from SEN specimens at temperatures between 420 and 1000 K.

*Long crack growth rate data at room temperature is not immediately available. However, the Paris exponent for the slope of the long crack growth rate (da/dN) vs ΔK curve at room temperature would be expected to be similar to those obtained at higher temperatures and fast frequencies. The threshold value, however, may be smaller. The crack propagation mechanisms are expected to be similar as well. Therefore, the elevated temperature results can be expected to be close to that at room temperature.

†The choice of ΔK as the crack driving force parameter here is somewhat arbitrary. While it seems to ignore plasticity, it is an accessible parameter and one that it is well-defined for the asymptotic case of long cracks in an elastic matrix. It is accessible because it can be calculated, at least nominally, from physical measurements of the remote load and the size and shape of the crack. The parameter ΔJ accommodates plasticity better but is less easily measured and would be expected to be proportional to ΔK^2 as the asymptotic case is approached. Plasticity is a macroscopic phenomenon which may not really be suited to modeling the tips of very small cracks, because it must be replaced by dislocation elasticity on an atomic level. Furthermore, the J -integral is based on the Hencky deformation theory of plasticity and is not theoretically sound for cases where unloading occurs such as fatigue. Experimentally, it does work as a tool to model fatigue when it can be evaluated. But ΔK also works much of the time and is easier to evaluate for small cracks. One virtue of the J -integral for describing the growth of small cracks would be that it need not be inherently length dependent.

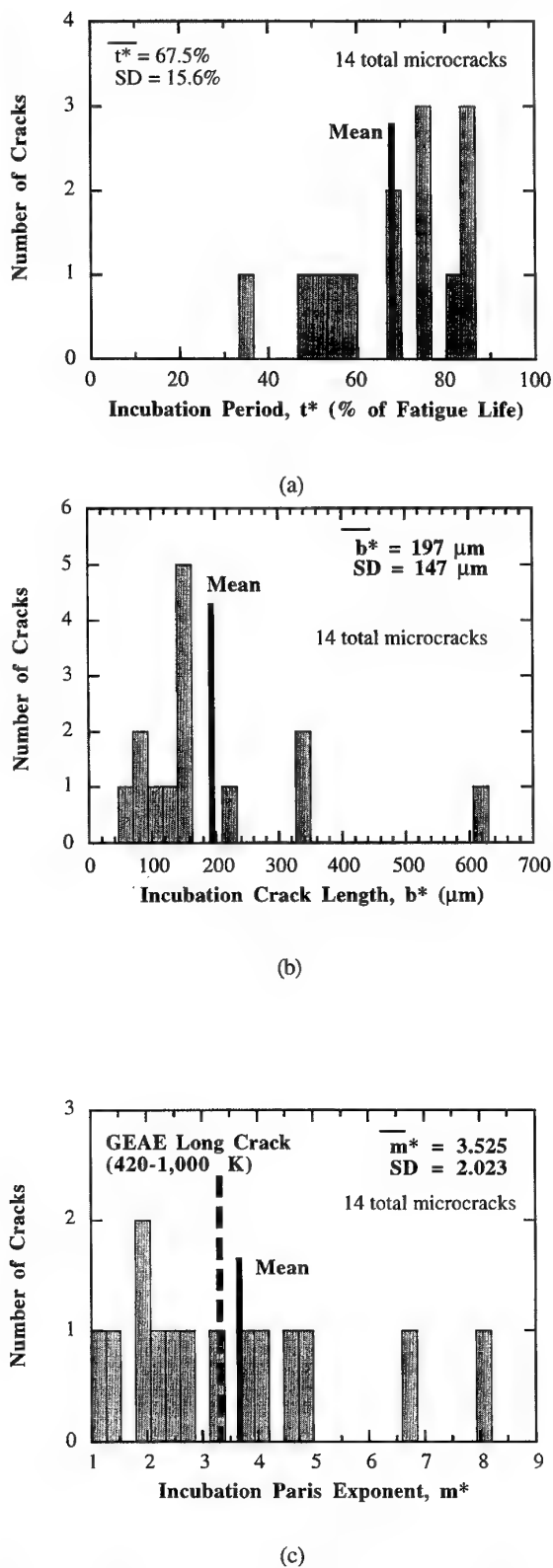


Figure 9 Incubation properties of fatigue cracks in the R'88DT. $R = -1$

ent with the results of *Figure 5*. In terms of crack growth rate predictions, this indicates that the use of the Paris equation to directly predict the growth rate of microcracks may not be reliable for over half of

the lifetime. In *Figure 9b*, it is seen that microcracks as small as $50 \mu\text{m}$ can exhibit Paris-type growth behaviors. The mean crack length of the examined microcracks was $197 \mu\text{m}$, or approximately the threshold size of NDE detection methods. Finally, *Figure 9c* shows the Paris exponents (m) of those microcracks which eventually exhibited Paris-type growth. Although the average m of 3.5 was similar to that of the long crack, $m = 3.3$, for long cracks between 420 and 1000 K, the scatter in m could range from 1.1 to 8.0 in value. Thus, the similar values of the average m and the long crack m was most likely just a coincidence.

CONCLUDING REMARKS

This work demonstrated that fatigue failure in room temperature air of the Ni base superalloy R'88DT is strongly influenced by the initiation, growth, and interaction of a high density of distributed microcracks. The latter was of immense significance late in the fatigue life when several microcracks would link together to form a rapidly growing critical crack. As shown in this study, microcrack initiation and growth regime can dominate the fatigue damage process for a majority of the life (60% in some cases) in the R'88DT. This is of consequence to the reliability engineer as the fraction of macrocracks present which are potentially detectable by NDE during inspections is always less than 10% of the total crack population. Furthermore, arrest and coalescence play important roles in the growth of all cracks, even those which eventually became critical. This can have a substantial impact since long crack growth rate data obtained from notched fatigue specimens are often extrapolated to microcracks using a Paris-type LEFM expression. It was shown in this study that the resulting crack growth rate predictions for microcrack growth rates by this approach could be nonconservative. A term ‘incubation’ was also introduced here to describe the length and time prior to which microcracks began to exhibit Paris-type growth. The results indicate that microcracks as small as $50 \mu\text{m}$ could exhibit Paris growth, and almost two thirds of the fatigue life typically expired before this occurred. Finally, statistical analyses of microcrack distributions for application to a microcrack-based reliability inspection scheduling strategy were discussed. The consistency of these preliminary results may provide a good probabilistic description of microcrack growth in the distributions. Future studies will implement the data discussed here to a Monte Carlo simulation developed for reproducing the microcrack distributions¹⁷ to obtain further insights into microcrack growth in the R'88DT, particularly on the arrest and coalescence mechanisms.

ACKNOWLEDGEMENTS

This work was supported by the National Institute of Standards and Technology under Contract No. 70NNANB9H0916. Thanks are due to Dr P.A. Domas (GEAE), Dr M.F. Henry (GCRD), Professor M.E. Fine (NU), and Dr L. Lawson (NU) for many useful discussions. Appreciation is also due to Dr D.K. Hsu and Mr B. Larsen at the Center of NDE (Iowa State University) and Mr M. Seniw and Mr R. Kraemer (NU) for technical assistance. This work made use of

MRL Central Facilities supported by the National Science Foundation, at the Materials Research Center of Northwestern University, under Award No. DMR-9120521.

REFERENCES

- 1 Tien, J. K. and Caulfield, T. *Superalloys, Supercomposites and Superceramics*. Academic Press, San Diego, 1989.
- 2 Ritchie, R. O. and Lankford, J. *Small Fatigue Cracks*, eds R. O. Ritchie and J. Lankford. The Metallurgical Society of AIME, Warrendale, PA, 1986, p. 1.
- 3 Paris, P. C. and Erdogan, F., *Journal of Basic Engineering*, 1963, **85D**, 528.
- 4 Miner, R. V. *Superalloys II*, eds C. T. Sims, N. S. Stoloff and W. C. Hagel. John Wiley, New York, 1987, p. 263.
- 5 Woolin, P. and Knott, J. F. *Proceedings of Fatigue '87*, Charlottesville, VA, eds R. O. Ritchie and E. A. Starke Jr. Engineering Materials Advisory Services Ltd., West Midlands, UK, 1987, p. 1087.
- 6 Fine, M. E., Kung, C. Y., Padragas, M. I. and Achenbach, J. D. *Durability of Metal Aircraft Structures*, eds S. N. Althuri, C. E. Harris, A. Hoggard, N. Miller and S. G. Sampath. Atlanta Technology Publications, Atlanta, GA, 1992, p. 297.
- 7 Chen, E. Y., Lawson, L. and Meshii, M., *Metallurgical and Materials Transactions*, 1995, **26A**(12), 3163.
- 8 Chen, E. Y., Lawson, L. and Meshii, M., *Materials Science and Engineering A*, 1995, **200**, 192.
- 9 Konig, G. W. and Bergmann, J., Impact of materials defects on engine structures integrity. Paper presented at 74th SMP Meeting, Patras, Greece, 27–28 May, AGARD-R-790, 1993.
- 10 Kendall, J. M. and King, J. E., *International Journal of Fatigue*, 1988, **7**, 163.
- 11 Newman, P. and Beevers, J. C. *Small Fatigue Cracks*, eds R. O. Ritchie and J. Lankford. The Metallurgical Society of AIME, Warrendale, PA, 1986, p. 97.
- 12 McCarver, J. F. and Ritchie, R. O., *Materials Science and Engineering*, 1982, **55**, 63.
- 13 Brown, C. W., King, J. E. and Hicks, M. A., *Metallurgical Science*, 1984, **18**(7), 374.
- 14 Boyd-Lee, A. D. and King, J. E. *Proceedings of Fatigue '90*, eds H. Kitagawa and T. Tanaka. Materials and Component Engineering Publications Ltd., Birmingham, UK, 1990, p. 1205.
- 15 Mei, Z., Krenn, C. and Morris Jr., J. W. *Advances in Cryogenic Engineering*, Vol. 40, eds R. P. Reed et al. Plenum Press, New York, 1994, p. 1299.
- 16 Healy, J. C., Grabowski, L. and Beevers, C. J., *International Journal of Fatigue*, 1991, **13**(2), 133.
- 17 Chen, E. Y. Ph.D. Thesis, Northwestern University, Evanston, IL, 1996.
- 18 Krueger, D. D., Kissinger, R. D. and Menzies, R. G. *Superalloys 1992*, eds S. D. Antolovich, R. W. Sturud, R. A. MacKay, D. L. Anton, T. Khan, R. D. Kissinger and D. L. Klarstrom. The Mineral, Metals and Materials Society, Warrendale, PA, 1992, p. 277.
- 19 Domas, P. A., Personal communications, 1995.
- 20 ASTM Designation E606-80. In *Annual Book of ASTM Standards*, Vol. 03.01. American Society for Testing and Materials, Philadelphia, 1990, p. 603.
- 21 Chen, E. Y., Lawson, L. and Meshii, M., *Scripta Metallurgica Materialia*, 1994, **30**(6), 737.
- 22 Nisitani, H. and Isida, M. *Proceedings of Joint JSME-SESA Conference on Experimental Mechanics*, Part I, 1982, p. 150.



PII: S0142-1123(97)00020-0

Dwell sensitive fatigue in a near alpha titanium alloy at ambient temperature

M.R. Bache*, M. Copet, H.M. Davies*, W.J. Evans* and G. Harrison†

*IRC in Materials for High Performance Applications, University of Wales,
Swansea SA2 8PP, UK

†Rolls Royce plc, P.O. Box 31, Derby DE2 8EJ, UK

‡Structural Materials Centre, Defence Research Agency, Farnborough, Hampshire
GU14 0LS, UK

The ambient temperature fatigue performance of the near alpha titanium alloy IMI834 was evaluated using laboratory specimens manufactured from two material sources: rolled bar stock and an isothermally forged compressor disc. The effect of dwell periods imposed at peak stress and R value were assessed. Significant differences were defined between the two variants with respect to their sensitivity to dwell loading. Variations in microstructural form together with a localised texture within the disc material are considered responsible for controlling the dwell performance in each case. The findings are consistent with a previously proposed model for facet development in this class of material. © 1998 Elsevier Science Ltd.

(Keywords: dwell; facets; micro-texture; basal slip)

INTRODUCTION

The near alpha titanium alloy IMI834 was developed specifically for service in high pressure (HP) compressors of aero gas turbine engines to address the need for enhanced operating temperatures approaching 650°C. It was recognised, however, that such improvements in temperature capability almost inevitably require a trade-off in low temperature fatigue performance. To offset this limitation the alloy was given a fine bimodal microstructure consisting of equiaxed primary alpha grains in a fully transformed beta matrix. It was anticipated that such a microstructure would also reduce the susceptibility to low temperature dwell sensitive fatigue, a phenomenon observed in previous coarser grained near alpha variants.

The objectives of the current programme of research were to explore the ambient temperature low cycle fatigue performance of the alloy, to characterise cyclic deformation and crack development mechanisms and to investigate how these processes are affected by load ratio (R) and the imposition of dwell loading. To this end a comprehensive database was developed using specimens manufactured from two sources of IMI834. These were rolled bar stock and an isothermally forged compressor disc supplied by Rolls Royce plc.

Tests were performed under load control and the accumulation of strain monitored throughout the lifetime of the individual tests. The development of sub-surface quasi-cleavage facets was fully characterised in

both variants of the material. Evidence to support the implicit role of strain accumulation and basal plane slip in their formation will be presented in the form of $S-N$ data, strain-cycle records and fractographic observations. Measurements of the crystallographic orientations of facets and neighbouring features, as determined through electron backscattered diffraction (EBSD), reinforce the model previously proposed by Evans and Bache for facet formation based upon the pile-up of dislocations at grain boundaries¹. The role of localised microstructural texture is also considered for the disc material.

It is argued that the current interest in combining initiation based lifting methods with damage tolerance failure criteria requires a better understanding of the faceting process and of the local conditions that control the crack growth kinetics. On this basis, the present findings have clear implications not only with respect to understanding crack development in titanium alloys but also with respect to the construction of appropriate numerical models.

EXPERIMENTAL METHODS

Plain cylindrical low cycle fatigue specimens, *Figure 1*, were manufactured from IMI834 supplied in the form of 30 mm round bar stock. Pre-machined specimen blanks were solution heat treated in air at 1025°C for 2 h, oil quenched, aged at 700°C for 2 h and air cooled to laboratory temperature. This produced a fine,

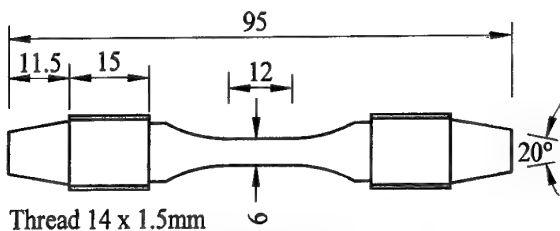


Figure 1 Plain LCF specimen design

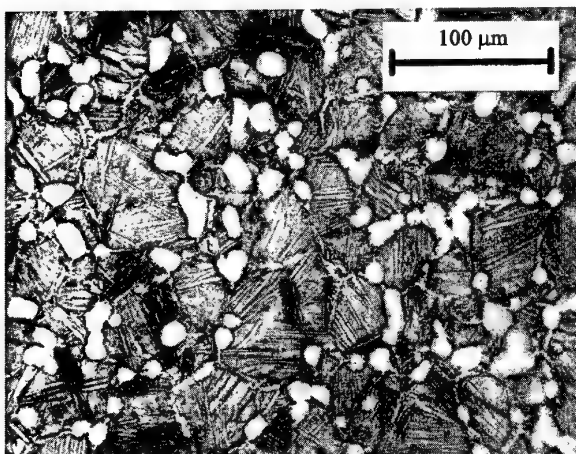


Figure 2 Bimodal microstructure of IMI834 bar stock material

bimodal microstructure of 15% equiaxed primary alpha within a fine transformed beta matrix, *Figure 2*. The prior β grain size was approximately $60 \mu\text{m}$.

Identical specimens were also machined from the isothermally forged compressor disc. In this case, specimen blanks were cut in a 'radial normal' orientation, i.e. their longitudinal axis was tangential to both the bore and rim of the disc. The forged disc, which had received an additional post-weld heat treatment of 640°C for 2 h, also possessed a fine grained bimodal microstructure. An important difference in this material was a localised microstructural texture highlighted by the aggregation of elongated primary alpha grains, *Figure 3*.

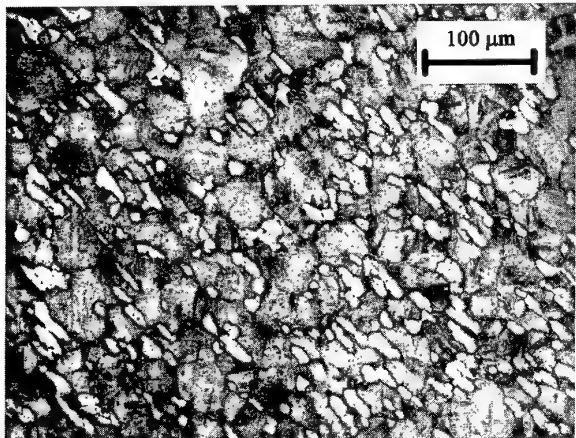


Figure 3 Aggregation of elongated alpha grains in IMI834 bar stock material

All the low cycle fatigue tests were conducted at laboratory temperature under load control on a closed-loop servohydraulic machine with a maximum load capacity of 100 kN. The majority of tests employed standard 'cyclic' or '2 min dwell' fatigue waveforms with a load ratio $R = 0.1$, as shown in *Figure 4*. Each incorporated a 2 s rise and fall between peak and minimum stress. The 1 s hold at peak load for cyclic loading was to facilitate data acquisition. Data from the dwell tests were taken shortly before the end of the dwell period. A small number of tests were performed with dwell times of 15 s and 5 min at peak stress, but always with identical rise and fall ramps. A limited number of specimens were tested with load ratios of $R = 0.5$ and $R = -0.5$. Axial strain accumulation was monitored by means of a commercial strain gauge bridge extensometer. Through the application of in-house software, cyclic fatigue lives and strain-time records were obtained.

Optical and scanning electron microscopy were used to examine the fracture surfaces of all failed specimens. In addition, selected test pieces were analysed to obtain crystallographic orientation measurements of planar faceted features and neighbouring grains. The microtexture technique, based upon electron backscattered diffraction (EBSD), is documented elsewhere and specific details of its application to titanium alloys are also available².

RESULTS

The LCF response of IMI834 bar stock to 'cyclic' and '2 min dwell' loading is illustrated in *Figure 5*. A fatigue limit is apparent for the cyclic data ($N_f > 10^6$ cycles) at an approximate peak applied stress of 700 MPa. This compares favourably with previously published data for the cyclic yield stress³. For applied

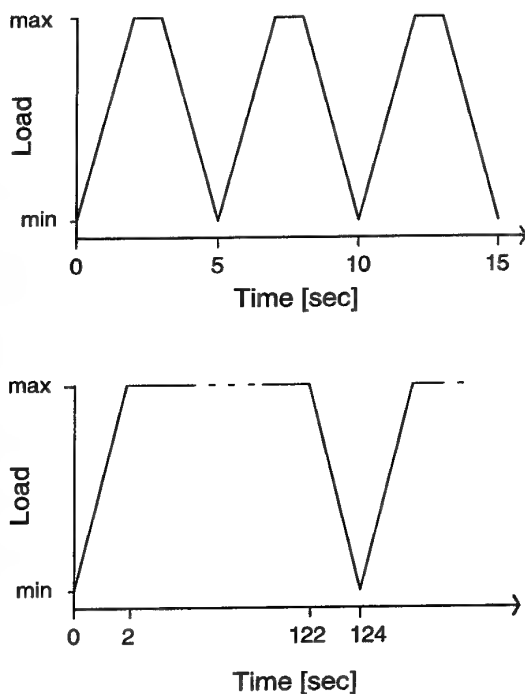


Figure 4 Cyclic and 2 min dwell loading waveforms

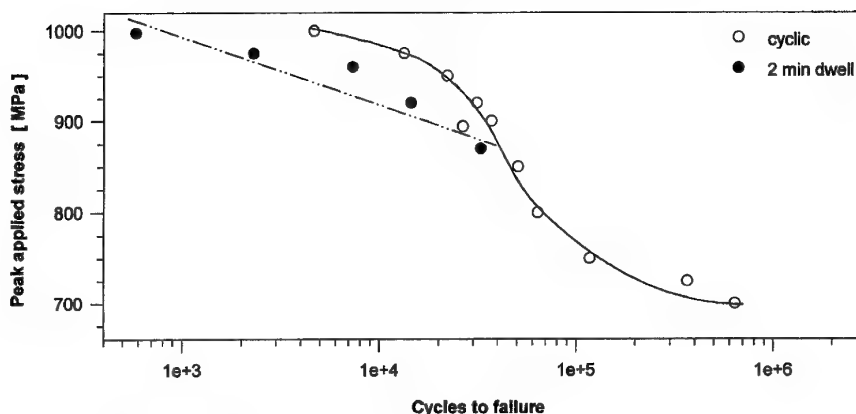


Figure 5 Cyclic and 2 min dwell fatigue data for bar stock material

stresses greater than 900 MPa a knee in the graph is evident as the tensile strength is approached. A best fit curve has been drawn through the cyclic points by eye. A best fit line has also been drawn through the 2 min dwell data such that it extrapolates to the measured monotonic ultimate tensile strength (1180 MPa) at one half cycle. The dwell line merges with the cyclic curve at approximately 850 MPa.

A similar comparison between cyclic and 2 min dwell data is made for the disc material in *Figure 6*. In this case, significantly reduced lives are evident under dwell loading at all applied stress levels above 700 MPa. Best fit lines have again been drawn through the cyclic and dwell data points. The UTS in this case was 1046 MPa. If the bar and disc data are plotted on a normalised stress basis (the peak applied stress divided by the appropriate tensile UTS) it is found that the bar and disc cyclic data superimpose, *Figure 7*. However, for the dwell data the enhanced sensitivity of the disc material is reinforced for the relatively low applied stresses. The effect of variations in the length of dwell periods is explored for the disc material in *Figure 8*. The inverse trend between dwell time and fatigue life is evident. An additional factor was that for these tests, performed at 880 MPa and $R = 0.1$, the rate of tensile strain accumulation is significantly greater for the longer dwell times.

The effect of load ratio on fatigue response under 2 min dwell tests is illustrated in *Figure 9*. The

regression line drawn through the $R = 0.1$ data in *Figure 6* is included for comparison. Tests were performed at peak stress levels of 800 and 880 MPa. In contrast to the generally accepted view on fatigue, the positive R ratio is more damaging even though the cyclic stress range is reduced, whereas the negative R ratio and large stress range extends the life to failure, particularly at the lower stress.

The fracture surface studies revealed that a dominant characteristic of all bar and disc failures was the formation of quasi-cleavage facets. In bar stock failures the facets were comparable in size to primary alpha grains (approximately 30 μm across), *Figure 10*. They were predominantly orientated perpendicular to the principle tensile axis at the lower applied stresses, but at the higher stresses inclined facets were also in evidence. EBSD confirmed that the plane was [0001]². In the disc material the elongated primary alpha grains influenced the shape of facets, *Figure 11*. EBSD measurements were taken at random from 60 such facets within this particular band. The resultant pole diagram, *Figure 12*, illustrates a strong near-basal orientation for the facets. After light etching, the exposed subsurface microstructure demonstrated that these facets extended beyond the primary alpha grains into the neighbouring regions of transformed α/β laths, *Figure 13*.

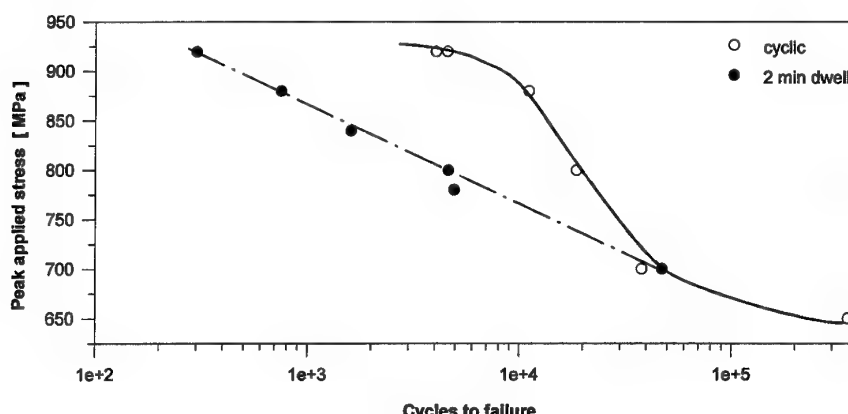


Figure 6 Cyclic and 2 min dwell fatigue for disc material

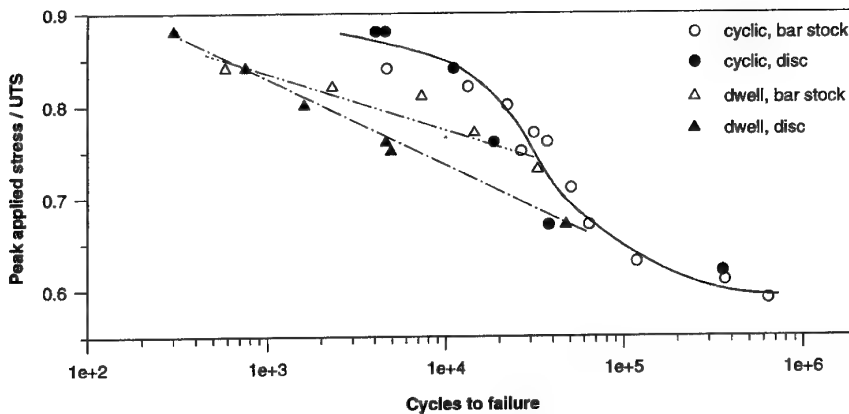


Figure 7 Normalised bar stock and disc data, plotted as a function of peak applied stress/UTS

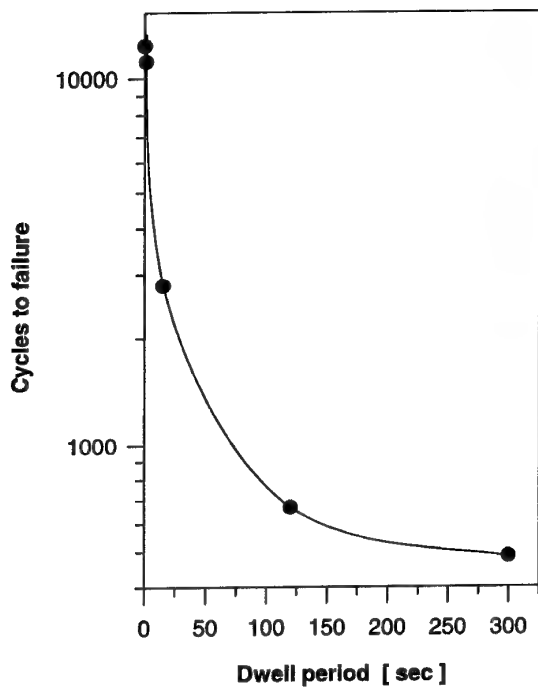


Figure 8 The effect of dwell period on fatigue life in disc material

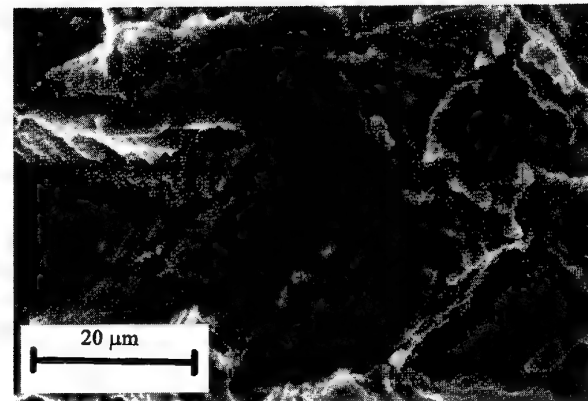


Figure 10 Quasi-cleavage facet in IMI834 bar stock

DISCUSSION

Important differences have been demonstrated between the low cycle fatigue behaviour of IMI834 material in bar stock and forged disc conditions, both with respect to their sensitivity to dwell loading and the microstructural influence on facet formation. In the case of bar stock, dwell periods only marginally reduce the lives compared to the baseline cyclic data. Furthermore, the reduction is only evident at relatively high stresses above the monotonic yield (850 MPa). The disc

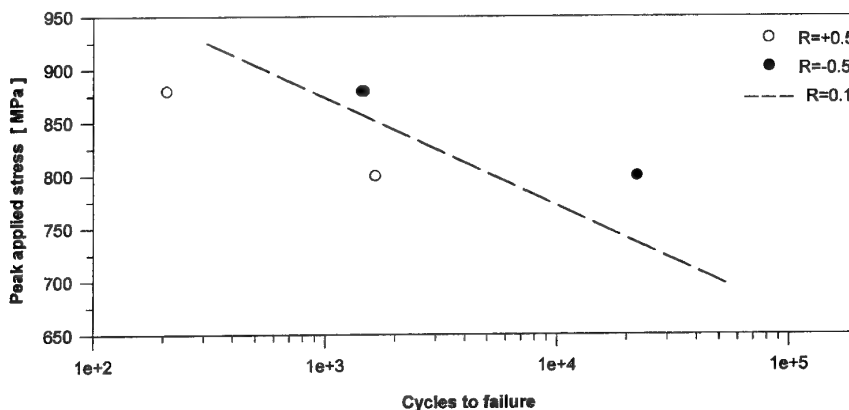


Figure 9 The effects of R value for dwell loading of disc specimens

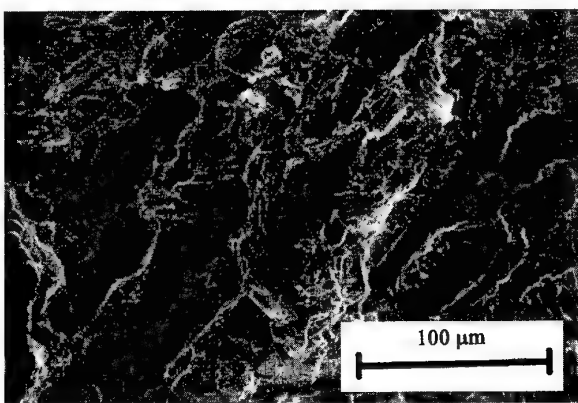


Figure 11 Elongated facets in disc material

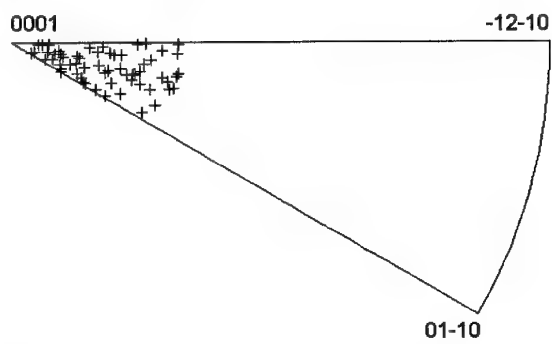


Figure 12 EBSD measurements from a banded region on a disc specimen fracture surface

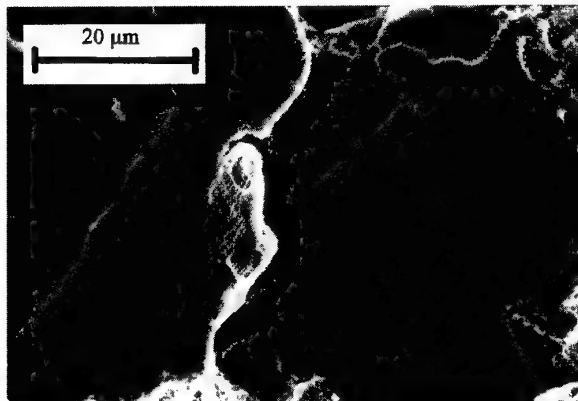


Figure 13 Etched facet in disc material illustrating underlying alpha (right-hand side) and transformed beta microstructure

material, on the other hand, displays a significant dwell effect at stresses as low as the cyclic yield stress (700 MPa). This sensitivity is confirmed by expressing the data in a normalised stress format in order to allow for the relative differences between the tensile strengths of the two forms of material.

The implicit role of facet formation in the dwell sensitivity of near alpha titanium alloys has received much attention in previous publications by the authors^{1,2,5}. The present results are consistent with our earlier work, in that for the two variants of IMI834 numerous small scale quasi-cleavage facets were evident on all

the fracture surfaces and at applied stresses less than the monotonic yield these facets were essentially perpendicular to the principle tensile stress. The preferred plane for facet development has again been demonstrated to be [0001]. It has been argued that their formation requires slip to occur on the basal plane even though it may not be favourably orientated with respect to planes of maximum shear as in the present case. The Stroh pile-up model⁴, as modified by Evans and Bache¹, accounts for the transfer of a shear stress onto unfavourably orientated planes. Furthermore, it introduces a tensile stress component which in conjunction with the applied stress causes a crack to develop within the resultant slip band. In essence, stress is redistributed from favourably orientated or 'weak' grains onto 'hard' grains with their basal planes perpendicular to the applied stress. Dwell loading assists this process by encouraging bulk strain accumulation.

One prediction of the model is that the shear and tensile stresses induced in the hard grain where the facets develop are directly proportional to the pile-up size in the source or weak grain. This is effectively the grain diameter, so faceting should be comparatively easier in coarse grained alloys. In addition, facets formed in these coarse alloys will be physically larger and, for a given testpiece or component section size, would have a bigger impact in terms of damage tolerance and residual propagation life. Experimental evidence supports these arguments. Near alpha alloys most susceptible to dwell notably include the coarse grained varieties, i.e. IMI685 and IMI829¹. Large scale facets develop in these alloys which rapidly promote complete failure in laboratory specimens. In the present study, the IMI834 bar stock evaluated has a small grain size and is relatively dwell insensitive. Previous work on facet initiated failures in this material has demonstrated that Stage II fatigue crack growth makes a more dominant contribution to the total life⁵. The intriguing observation, however, is that the IMI834 disc material has a comparable microstructural size and yet suffers from an increased dwell sensitivity. It is suggested that this difference may be due to the subtle differences in microstructure as a result of the isothermal forging operation. Firstly, the elongated alpha grains observed in this material are approximately twice the size of the equiaxed examples in bar stock. Secondly, even though global X-ray texture measurements for the disc indicate no significant forging texture, the metallographic studies demonstrate significant local banding of the elongated primary alpha grains on a local scale. The EBSD measurements show that the bands have a preferred orientation that facilitates the formation of basal plane facets. These elongated facets then extend beyond the alpha phase boundaries into the surrounding transformed matrix material. This would suggest that the primary alpha and transformed region have a common basal plane. In essence, the forging operation has failed to break up the original prior beta grains and so the disc alloy behaves more like the coarser IMI685 and IMI829 near alpha variants.

Finally, the results from the tests under different R ratios are also consistent with the facet formation model. Thus the untypical result that fatigue life is reduced by a high R ratio ($R = 0.5$) can be attributed to the fact that a high mean stress encourages strain accumulation and associated dislocation movement in

the source grain, thereby facilitating stress redistribution. In contrast, a negative ratio ($R = -0.5$) promotes slip reversal in the source grain so that pile-up stress fields relax and the tendency for facet formation is reduced.

CONCLUSIONS

1. IMI834 bar stock, heat treated to produce a bimodal microstructure of 15% primary alpha within a transformed alpha/beta matrix, has been shown to be relatively insensitive to dwell loading. Reduced lives were only noted at high stress levels above monotonic yield.
2. In contrast, fatigue lives measured under dwell conditions in the disc material were significantly reduced. Best fit curves drawn through cyclic and dwell data appear to coincide at the approximate cyclic yield stress for the alloy.
3. In disc material, the extent of the dwell period at peak stress clearly affects the fatigue performance with increasing periods inducing shorter lives. Dwell sensitivity is also dependent on R ratio. On a peak tensile stress basis, a high positive ratio ($R = 0.5$) produced a decrease in life while the negative equivalent ($R = -0.5$) slightly improved the performance.
4. Important differences were noted in the microstructural form of the disc material. Individual alpha

grains were elongated to almost double the size of the equiaxed bar stock. EBSD analysis demonstrates that aggregates of such alpha grains can be highly textured on a localised scale. These differences have important implications concerning facet formation. A model based upon dislocation pile-ups predicts that facet development should be enhanced due to these microstructural variations.

5. Crack initiation in titanium alloys is dominated by the development of facets. The relatively early formation of larger facets in the disc variant and their subsequent influence on Stage II crack propagation life may explain the differences between the dwell sensitive behaviour of the bar stock and disc materials.

REFERENCES

- 1 Evans, W. J. and Bache, M. R., *International Journal of Fatigue*, 1994, **16**, 443.
- 2 Bache, M. R., Evans, W. J. and Davies, H. D. *Journal of Materials Science*, 1997, **32**, 3435.
- 3 Bache, M. R., Evans, W. J. and Rees, G. S. In *Proceedings of International Symposium on Air Breathing Engines*, Melbourne, Australia, ed. F. S. Billig. American Institute of Aeronautics and Astronautics, Washington, DC, 1995, p. 195.
- 4 Stroh, A. N., *Proceedings of the Royal Society, London*, 1954, **223**, 404.
- 5 Bache, M. R., Davies, H. D. and Evans, W. J. In *Titanium '95, Proceedings of 8th World Conference on Titanium*, Birmingham, UK, eds P. A. Blenkinsop, W. J. Evans and H. M. Flower. Institute of Materials, London, 1995, p. 1347.

PII: S0142-1123(97)00038-8

Damage mechanisms of single and polycrystalline nickel base superalloys SC16 and IN738LC under high temperature LCF loading

R.P. Wahi*, J. Auerswald*, D. Mukherji*, A. Dudka†, H.-J. Fecht† and W. Chent

*Hahn-Meitner Institute Berlin GmbH, Glienicker Straße 100, D-14109 Berlin, Germany

†Institute of Metal Research, Technical University Berlin, PN 2-3, Hardenbergstraße 36, D-10623 Berlin, Germany

The mechanical behaviour of polycrystalline and single crystal nickel base superalloys, IN738LC and SC16, respectively, has been investigated under strain controlled LCF loading at 1223 K. The alloys showed a very similar stress response: a long stable stress amplitude period preceded by either cyclic hardening at higher strain amplitudes or by cyclic softening at lower strain amplitudes. The fatigue life of the single crystal alloy was, however, measured to be about 10 times higher than that of the polycrystalline variant. This can be attributed to the differences in deformation and damage processes observed in the two alloys. © 1998 Elsevier Science Ltd.

(Keywords: superalloys; high temperature LCF; damage)

INTRODUCTION

The application of single crystal blades in gas turbines for aerospace engines is nowadays well established due to their excellent high temperature properties and lower life-cycle costs. To transfer the benefits of single crystal technology to land based gas turbines, a single crystal nickel base superalloy SC16¹ has recently been developed in Europe with the aim of replacing polycrystalline superalloys such as IN738LC. Initial tests on the single crystal superalloy SC16 revealed that under tensile and creep loading the alloy provided improved high temperature mechanical properties^{1,2}, as compared to IN738LC. In the present study the mechanical behaviour of both the alloys was investigated under LCF loading at various temperatures from ambient temperature to 1223 K. In this paper the fatigue life and the damage behaviour of both the alloys at 1223 K are reported, compared and discussed in the light of characteristic deformation mechanisms observed.

EXPERIMENTAL

The chemical compositions of IN738LC and SC16 are given in *Table 1*. Both the alloys were supplied by Thyssen Guss AG at Bochum and the specimens were machined by Motoren und Turbinen Union at Munich. The alloys were subjected to specific heat treatments in order to produce similar initial γ/γ' microstructures:

unimodally distributed, cuboidal γ' precipitates with an average edge length of 450 nm and a volume fraction of about 40% embedded in a γ matrix^{3,4}. The axis of the single crystal specimens tested in the present study had a crystallographic orientation of $\langle 001 \rangle$ with a maximum deviation of about 6° with respect to the tensile loading axis. The mechanical tests were conducted on a servohydraulic MTS testing system under total axial strain controlled symmetric loading ($R_s = -1$) using a constant strain rate of 10^{-3} s^{-1} . The total strain amplitudes used in this study were varied between 0.4 and 1.0%. All the tests presented in this paper were carried out at 1223 K in air.

The microstructures of the deformed specimens were examined using transmission and scanning electron microscopy techniques reported elsewhere^{2,3}.

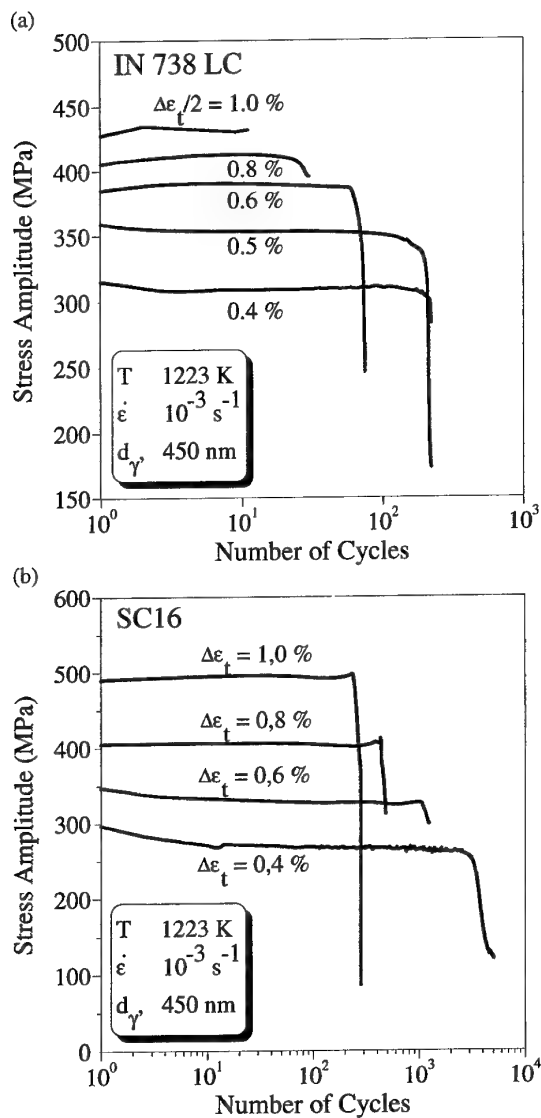
RESULTS AND DISCUSSION

Mechanical behaviour

The cyclic stress response of both the alloys under high temperature LCF loading is plotted in *Figure 1a* (IN738LC) and *Figure 1b* (SC16). No significant difference in cyclic deformation behaviour can be detected. Both the alloys reached similar stress levels at the same total strain amplitudes. They show a stable stress response over a large number of cycles preceded by a region of small cyclic hardening at the higher

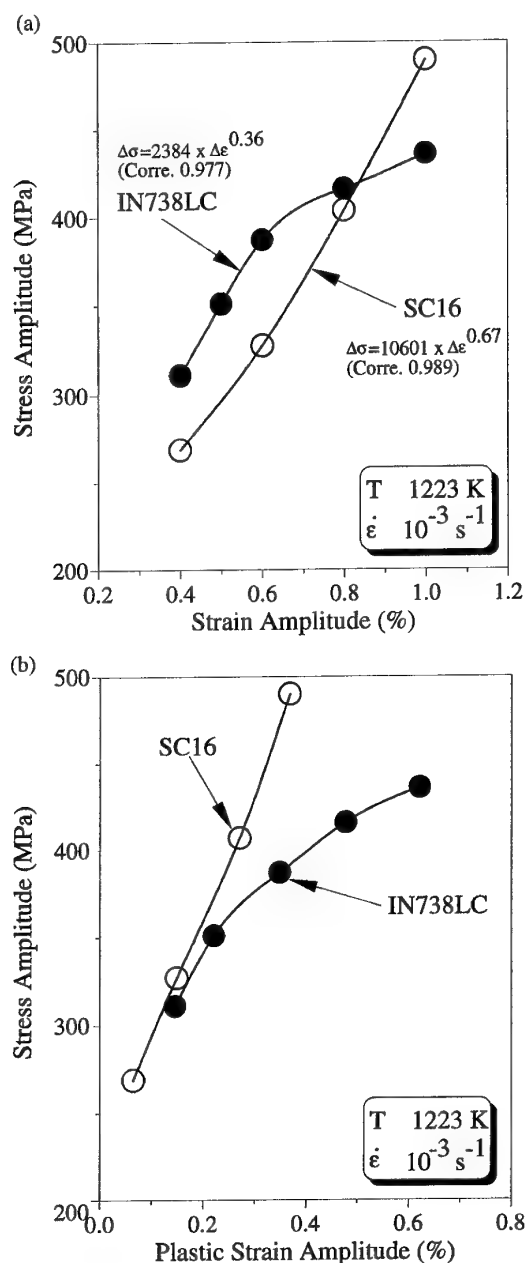
Table 1 Chemical composition of superalloys IN738LC and SC16 (wt.%)

	Al	B	C	Co	Cr	Mo
IN738LC	3.50	0.01	0.11	8.60	16.0	1.80
SC16	3.50	—	—	—	16.0	3.00
	Nb	Ta	Ti	W	Zr	Ni
IN738LC	0.80	1.80	3.50	2.60	0.04	bal.
SC16	—	3.50	3.50	—	—	bal.

**Figure 1** Cyclic stress response of superalloys IN738LC (a) and SC16 (b)

strain amplitudes or softening at the lower strain amplitudes.

Figure 2a shows the cyclic stress-strain curves of both the alloys. In the lower strain amplitude region

**Figure 2** Cyclic stress-strain curves of superalloys IN738LC and SC16. (a) Stress amplitude vs. total strain amplitude; (b) stress amplitude vs. plastic strain amplitude

the stress amplitude of SC16 is lower than that of IN738LC under comparable strain amplitudes. At these strain levels, plastic deformation in the alloys is very small. Therefore, the stress amplitudes under cyclic loading are mainly determined by elastic properties of the alloys. Since the single crystal SC16 with an orientation of $\langle 001 \rangle$ exhibits a relatively lower Young's modulus ($E \approx 90$ GPa at 1223 K) than that of IN738LC ($E \approx 115$ GPa at 1223 K), it is expected that in the present case the single crystal specimens have a lower stress amplitude. The major difference in the cyclic stress-strain behaviour has been found in cyclic work hardening. The single crystal SC16 showed higher work hardening in the larger strain amplitude region. This is clearly seen in Figure 2b. A similar effect was also observed in the work hardening behaviour of both the alloys under monotonic loading. The higher work hardening rate of the $\langle 001 \rangle$ oriented single crystal alloy is obviously related to the larger number of slip systems activated in this alloy. It is to be expected that the recovery behaviour of the two alloys, which contributes to the net work hardening, is also influenced by the difference in number of active slip systems. Further experiments are in progress to clarify the difference in work hardening behaviour of the two alloys.

The dependence of fatigue life (number of cycles to fracture) on plastic strain amplitude is represented by a Coffin-Manson plot for two alloys in Figure 3. The number of cycles to fracture for the alloy SC16 has been measured to be about 10 times higher than that for IN738LC. The Coffin-Manson exponents for both the alloys were around -0.61. Values of -0.5 to -0.6 have been reported previously for nickel base superalloys in the literature⁵.

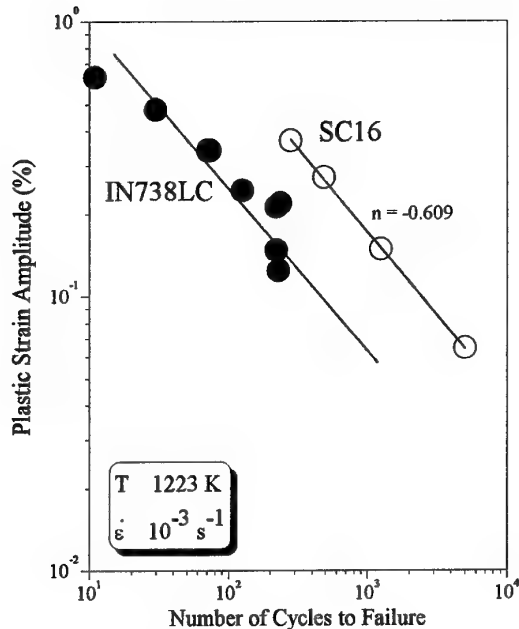


Figure 3 Fatigue response of IN738LC and SC16

Deformation and damage mechanisms

The plastic deformation in both the alloys under all experimental conditions used in this study was found to occur on the $\{111\}\langle 110 \rangle$ slip systems⁶⁻⁸.

In the alloy IN738LC the deformation under all the strain amplitudes employed was found to be concentrated in discrete slip bands running across γ and γ' phases, Figure 4a⁶. A detailed examination of the dislocation substructure in these slip bands revealed that shear of the γ' phase was associated with the formation of stacking faults, Figure 4b⁶.

The optical and scanning electron microscopic examinations revealed that in polycrystalline alloy IN738LC crack initiation took place essentially at the intersections of grain boundaries with the specimen surface due to preferential oxidation, Figure 5a. The crack propagation path was found to be governed by either grain or dendrite boundaries irrespective of the test conditions. Figure 5b shows a typical fracture surface with features characteristic of a dendrite boundary failure morphology. Macroscopically, fracture surfaces under all test conditions were found to be very rough with the plane of fracture generally perpendicular to the load axis, Figure 5c.

The deformation mechanism in the single crystal alloy SC16 was found to be strongly dependent on the strain amplitude. At the smaller strain amplitudes up to 0.6%, the deformation was essentially concentrated in the γ channels perpendicular to the load axis $\langle 001 \rangle$, Figure 6a. The γ' phase remains undeformed during the test. At higher strain amplitudes

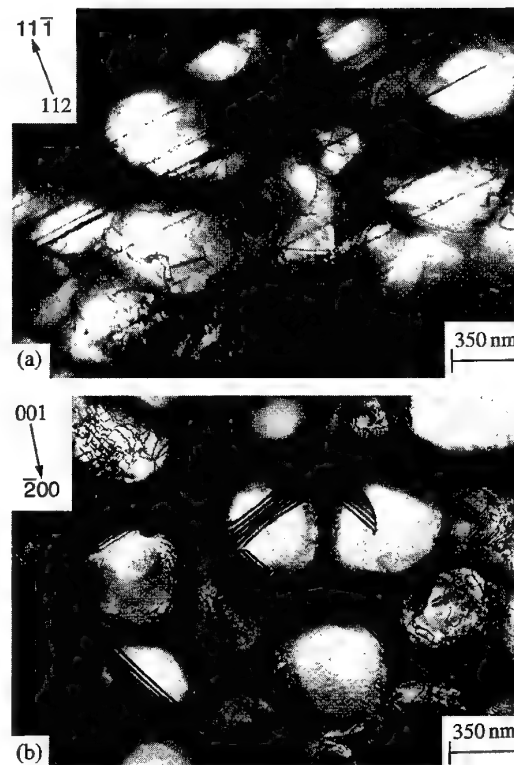


Figure 4 Deformation substructure in fatigued IN738LC specimens. (a) Slip bands ($T = 1223$ K, $\dot{\epsilon} = 10^{-3}$ s $^{-1}$, $\Delta\epsilon_t = 1.0\%$); (b) stacking faults ($T = 1223$ K, $\dot{\epsilon} = 10^{-3}$ s $^{-1}$, $\Delta\epsilon_t = 1.0\%$)

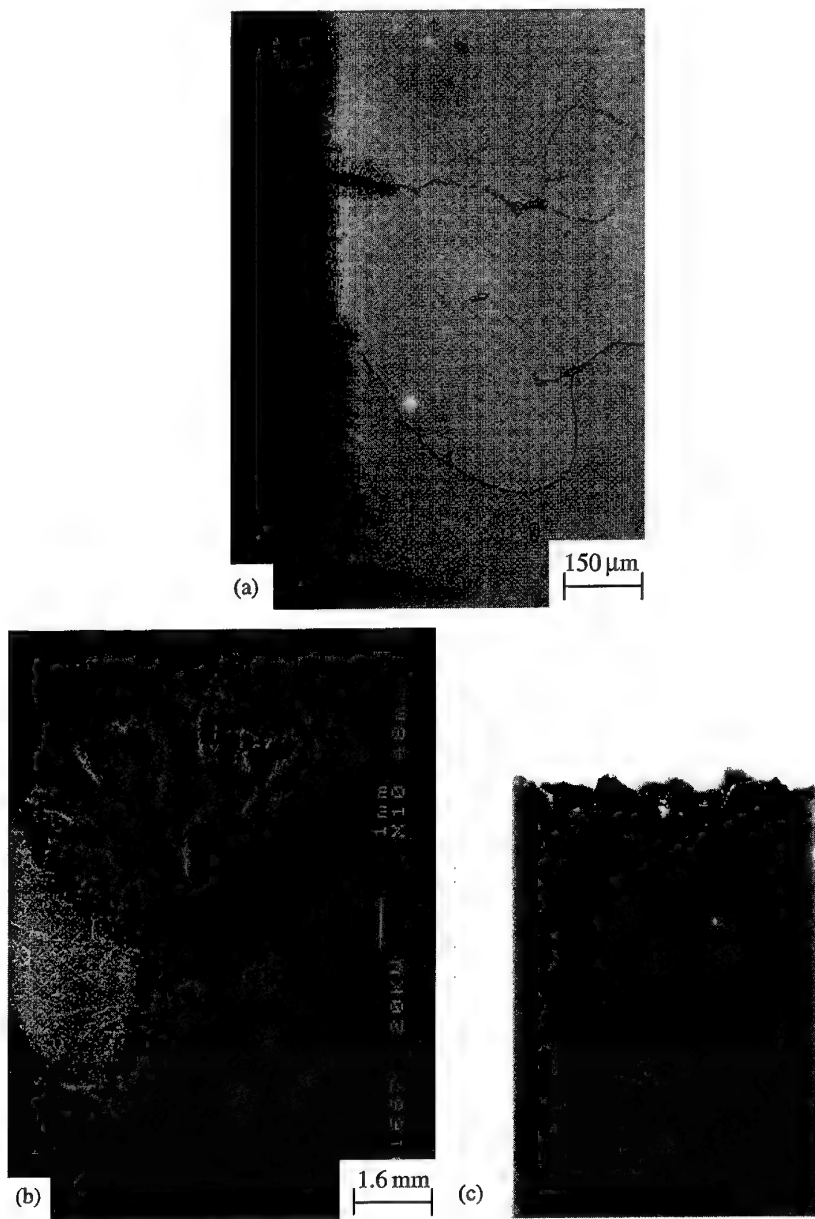


Figure 5 Micrographs showing (a) crack initiation site, (b) propagation path in IN738LC and (c) macrograph showing the fatigued specimen

is concentrated in slip bands extending across both the γ and γ' phases, *Figure 6b*. The shear of the γ' phase is associated with the formation of stacking faults, *Figure 6c*.

In the single crystal SC16 grain boundaries do not exist. Both casting pores (*Figure 7a*) and microcracks in oxide layers on the specimen surface (*Figure 7b*) become potential crack initiation sites. The latter were observed predominantly in the specimens tested at the higher strain amplitudes. It is obvious that a definite high strain level is required in order to cause cracking of the oxide layer. The cracks grew initially more or less perpendicular to the load axis at all the strain amplitudes. This trend remained until fracture in the tests with lower strain amplitudes (*Figure 8a*), whereas at higher strain amplitudes the further growth of cracks occurred at an angle of about 54° to the load axis $\langle 001 \rangle$ (*Figure 8b*). It is to be noted that the angle

between (001) and (111) planes is 54.7° . Evidently the crack propagation, in this case, occurs along (111) slip planes running through γ and γ' phases.

The above observations very clearly show the interdependence of the crack growth path and microscopic deformation mechanisms in the single crystal alloy SC16. At lower strain amplitudes deformation and damage is concentrated in (001) γ channels perpendicular to the load axis, therefore the crack propagates along these channels. At higher strain amplitudes the cracks grow along the (111) slip bands due to the concentration of deformation and damage there. In the polycrystalline alloy IN738LC the fracture is more or less independent of the deformation mechanisms observed. The presence of grain/dendrite boundaries, which are generally considered to be weak regions at high temperatures, obviously determines the crack propagation path.

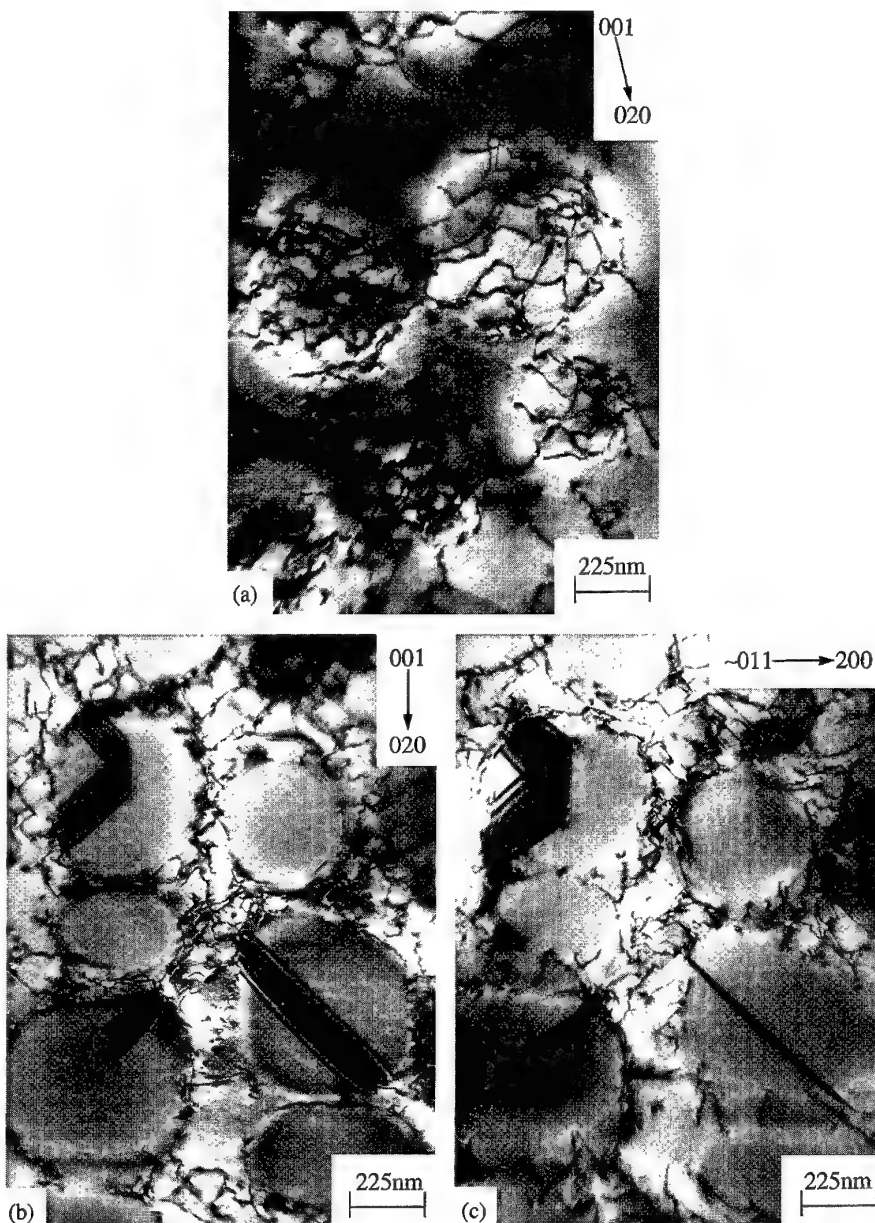


Figure 6 Deformation substructure in fatigued SC16 specimens. (a) Dislocation networks at γ/γ' interfaces ($T = 1223\text{ K}$, $\dot{\epsilon} = 10^{-3}\text{ s}^{-1}$, $\Delta\epsilon_r = 0.6\%$), (b) and (c) stacking faults in γ' ($T = 1223\text{ K}$, $\dot{\epsilon} = 10^{-3}\text{ s}^{-1}$, $\Delta\epsilon_r = 0.8\%$)

CONCLUDING REMARKS

The fatigue behaviour of two superalloys, the polycrystalline alloy IN738LC and the single crystal alloy SC16, with similar chemical compositions has been investigated under high temperature LCF loading. The following main results were obtained.

- Both the alloys showed a stable cyclic stress response.
- SC16 exhibited a higher cyclic work hardening rate.
- The fatigue life of SC16 was measured to be about 10 times higher than that of IN738LC.
- In IN738LC crack initiation and propagation occurred at grain/dendrite boundaries.

- Crack initiation sites in SC16 were casting pores and microcracks in the surface oxide layer. Crack propagation was controlled by deformation mechanisms.

ACKNOWLEDGEMENTS

The authors would like to express their thanks to Ms Maaß, Weimann and Mr Seiler for their technical assistance and to the Deutsche Forschungsgemeinschaft for their financial support of the project. One of the authors, A.D., is thankful to the Deutsche Akademische Austauschdienst (DAAD) for financial help.

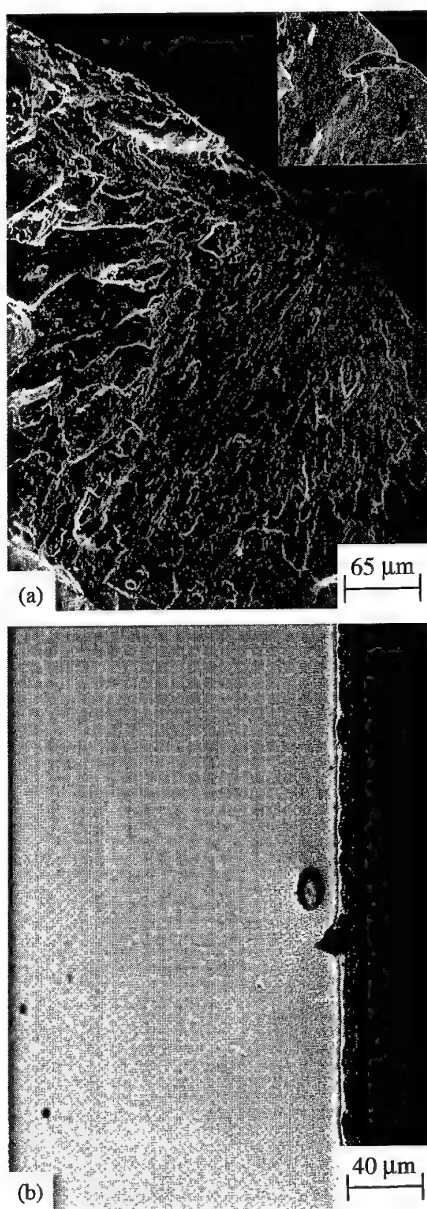


Figure 7 Micrographs showing (a) casting pores as crack initiation sites and (b) microcracks in the oxide layer on the specimen surface

REFERENCES

- 1 Khan, T. and Caron, P., Development of a new single crystal superalloy for industrial gas turbines. In *High Temperature Materials for Power Engineering 1990*, Vol. 2, eds E. Bachelet et al. Kluwer Academic, Dordrecht, 1990, pp. 1261–1270.
- 2 Rumi, M., Chen, W., Mukherji, D., Kuttner, T., Wahi, R. P. and Wever, H., Influence of strain rate on the fracture behaviour of the single crystal superalloy SC16 under tensile loading. In *Materials for Advanced Power Engineering 1994*, Vol. 2, eds D. Coutouradis et al. Kluwer Academic, Dordrecht, 1994, pp. 1165–1174.
- 3 Mukherji, D., Jiao, F., Chen, W. and Wahi, R. P., Stacking fault formation in γ' phase during monotonic deformation of IN738LC at elevated temperatures. *Acta Metallurgica et Materialia*, 1991, **39**, 1515–1524.
- 4 Malow, T., Zhu, J. and Wahi, R. P., Influence of heat treatment on the microstructure of the single crystal nickel base superalloy SC16. *Z. Metallkd.*, 1994, **85**, 9–19.
- 5 Singh, V., Sundararaman, M., Chen, W. and Wahi, R. P., Low-cycle fatigue behavior of nimonic PE16 at room temperature. *Metallurgical Transactions*, 1991, **22A**, 499–506.
- 6 Jiao, F., Elektronenmikroskopische Untersuchung der Hochtemperatur-Verformungsmechanismen an der Nickelbasislegierung IN738LC. Doctor Thesis, Technical University Berlin, 1992.
- 7 Jiao, F., Zhu, J., Wahi, R. P., Chen, H., Chen, W. and Wever, H., Low cycle fatigue behaviour of IN738LC at 1223 K. In *Low Cycle Fatigue and Elasto-Plastic Behaviour of Materials*, ed. K.-T. Rie. Elsevier Applied Science, London, 1992, pp. 298–330.
- 8 Auerswald, J., Mikrostrukturuntersuchungen an der einkristallinen Nickelbasislegierung SC16 nach Kurzzeitermüdung (LCF). Diploma Thesis, Technical University Berlin, 1996.

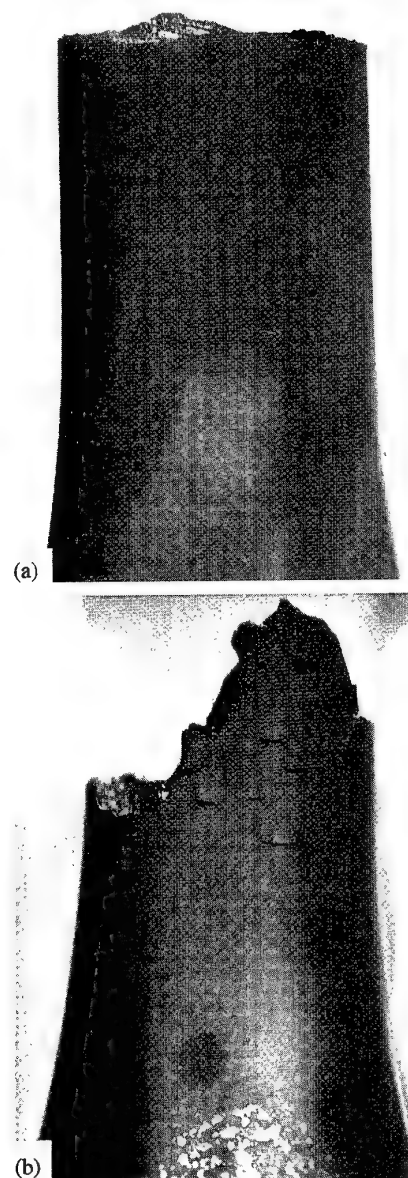


Figure 8 Macrographs showing the failed specimens of SC16 tested (a) at $\Delta\epsilon_i = 0.4\%$ and (b) at $\Delta\epsilon_i = 1.0\%$

PII: S0142-1123(97)00036-4

Fatigue crack initiation in Ti-5Al-4Sn-2Zr-1Mo-0.7Nd-0.25Si high temperature titanium alloy

J.F. Lei, Z.G. Wang, D. Li and Z.Q. Hu

State Key Laboratory for Fatigue and Fracture of Materials, Institute of Metal Research, Academia Sinica, Shenyang 110015, P.R. China

Ti-5Al-4Sn-2Zr-1Mo-0.7Nd-0.25Si alloy is a new high temperature titanium alloy for aeroengine use. In this paper, the fatigue crack initiation in this alloy was investigated. At applied maximum nominal stresses less than 500 MPa, most cracks initiate in the matrix away from the Nd-rich particles. Initiation of these cracks is related to the cracking of equiaxed α phase on the prior β grain boundaries. At high applied stresses, almost half of the cracks initiate in the matrix away from the Nd-rich particles and the other half initiate near Nd-rich particles. The probability that an Nd-rich particle initiates a fatigue crack decreases very rapidly as the particle size falls below 12 μm . © 1998 Elsevier Science Ltd.

(Keywords: Ti-5Al-4Sn-2Zr-1Mo-0.7Nd-0.25Si high temperature titanium alloy; fatigue crack initiation; Nd-rich particles)

INTRODUCTION

With the increasing demand of the aeronautical industry, high temperature titanium alloys are widely used for their excellent properties such as low density and high oxidation resistance. Ti-5Al-4Sn-2Zr-1Mo-0.7Nd-0.25Si alloy (hereafter called Ti-55 alloy) is a newly developed near alpha high temperature titanium alloy for use at 550°C. It is mainly used for making aeroengine blades. As is well known, fatigue failures continue to plague many aeroengine materials. Since fatigue crack initiation is the crux of fatigue failure, it is very important to study the fatigue crack initiation in Ti-55 alloy. Generally, constituent particles are often preferential sites for fatigue crack initiation. The main purpose of this paper is to report some observations on the fatigue crack initiation under different stresses in Ti-55 alloy, in particular the fatigue crack initiation related to Nd-rich particles, and to present a preliminary interpretation. It is very interesting to find that the Nd-rich particles in the Ti-55 alloy have better resistance to fatigue crack initiation than the matrix at low stresses (less than 500 MPa of maximum nominal stress). This result has been analyzed by using a current theory of stress distribution around a particle in the matrix.

MATERIAL AND EXPERIMENTAL PROCEDURE

Ti-55 alloy shows excellent tensile strength and creep resistance up to 823 K as well as good fatigue strength. Typical mechanical properties of Ti-55 alloy are shown

in Table 1. A feature of Ti-55 alloy is that it contains the rare earth element Nd which forms Nd-rich particles and strengthens the alloy by refining the grains. The Nd-rich particles strongly collect O and Sn, improving the thermal stability of the alloy. Therefore, the Nd-rich particles play a key role in assuring the excellent properties of Ti-55 alloy.

The material used for the present experiments was in the form of rods 23 mm in diameter rolled from a 2 ton ingot of Ti-55 alloy. Fatigue specimens were machined and smoothly ground from short bars which had been solution treated at 1266 K for 1 h and air cooled, and then aged at 873 K for 2 h and air cooled. The microstructure of the Ti-55 alloy under the optical microscope is shown in Figure 1. The matrix consists of equiaxed α phase (white) and acicular transformed β . The black particles in Figure 1 were identified as Nd-rich particles. These ellipsoidal particles are uniformly distributed in the matrix. Image analysis indicated that the equivalent circular diameters of the Nd-rich particles range from about 3 to 25 μm with an average value of about 9 μm . The microhardness of the Nd-rich particle is about one third that of the matrix. The equivalent circular diameter distribution of the Nd-rich particles is shown in Figure 2.

The plate specimen with a hollow was employed (see Figure 3). The Neuber stress concentration factor of the hollow is about 1.05. The hollow surface was polished metallographically by hand before tests.

Acetate replicas and a scanning electron microscope (SEM) were employed to monitor the fatigue crack initiation. The tests were periodically interrupted in

Table 1 The mechanical properties of Ti-55 alloy

Tensile	Temperature (K)	room temperature	823
	YS $\sigma_{0.2}$ (MPa)	950	547
	UTS σ_u (MPa)	1013	658
	Elongation (%)	16	21
	Area reduction (%)	35	48
Creep	Temperature (K)	813	823
	Time (h)	100	100
	Stress (MPa)	343	294
Fatigue	Total plastic strain (%)	0.190	0.163
	Temperature (K)	room temperature	823
	Fatigue strength (MPa)	456	420

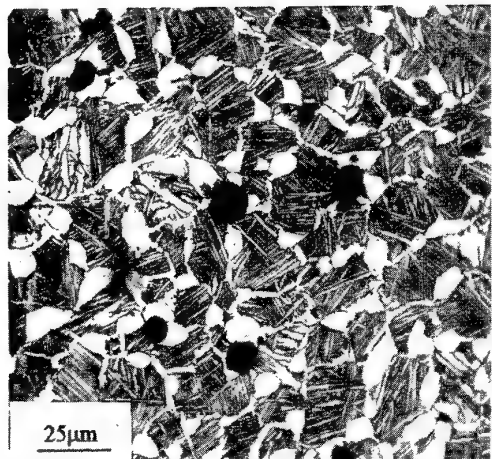


Figure 1 Typical microstructure of Ti-55 alloy, showing equiaxed α (white), acicular transformed β (laminated) and Nd-rich particles (black)

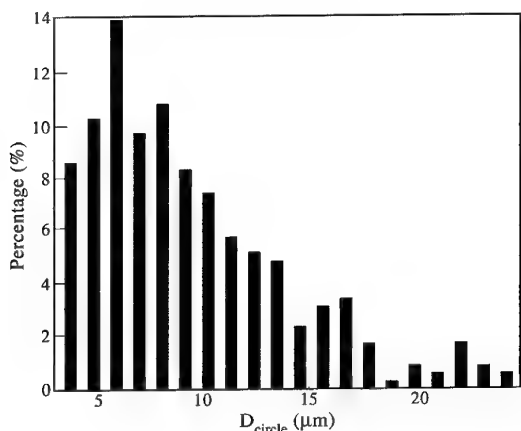


Figure 2 The Nd-rich particle size distribution in Ti-55 alloy, with the percentage plotted against the equivalent circular diameter

order to replicate the specimen's hollow with AC paper (acetate film), and then the replica was observed under an optical microscope, or the specimen was removed from the testing machine and directly observed in the SEM. All fatigue tests were conducted on a Schenck closed loop electrohydraulic system of 40 kN capacity in laboratory air at room temperature. The frequency of the tension-tension loading was 20 Hz and an R ratio of 0.1 was employed. The maximum nominal stress in the experiment ranged from 450 to 650 MPa.

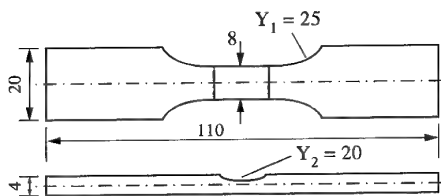


Figure 3 Specimen dimension (mm)

RESULTS AND DISCUSSION

Fatigue crack initiation mode

Examination of replicas under the optical microscope revealed that there are two modes of fatigue crack initiation in Ti-55 alloy. One mode is not associated with the Nd-rich particles, since the cracks initiated in the matrix, as shown in *Figure 4*. The crack illustrated is more than 200 μm in length. Around the crack there are some Nd-rich particles (some particles were clearly removed to produce pits). Detailed investigation showed that this mode of crack initiation is related to the cracking of equiaxed α particles on the prior β grain boundaries. The second mode is associated with the Nd-rich particles, since the crack nucleated near the Nd-rich particles, as shown in *Figure 5*. The crack in *Figure 5* occurred on both sides of the cracked Nd-rich particle and propagated.

It was found that the mode of the fatigue crack initiation depends on the stress level. At low stresses, it was observed that a dominant crack is usually not associated with Nd-rich particles and most of the cracks initiated in the matrix. At high stresses, almost half of

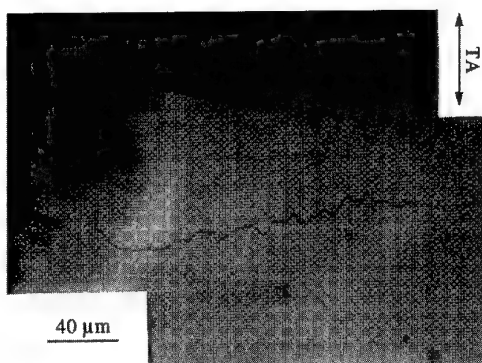


Figure 4 Crack initiation in the matrix away from the Nd-rich particles. The fatigued specimen was not etched. TA represents the tensile axis

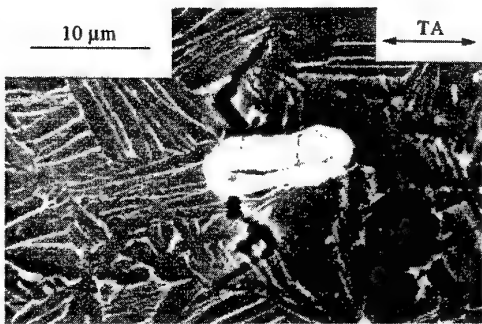


Figure 5 SEM image showing crack initiation near an Nd-rich particle. The fatigued specimen was etched to reveal the microstructure of Ti-55 alloy. TA represents the tensile axis

the cracks were found to initiate at or near the Nd-rich particles. The probability that an Nd-rich particle initiates a fatigue crack increases with stress, as shown in *Figure 6*. The probability of particle induced initiation was obtained by dividing the number of cracks related to the Nd-rich particles by the total crack number. When the maximum nominal stress is less than 500 MPa, the Nd-rich particles display an improved resistance to the fatigue crack initiation compared with the matrix.

The stress distribution around an Nd-rich particle has been calculated by using a current mechanics theory^{2,3}. Because the Nd-rich particle is much softer than the matrix, the stress on the Nd-rich particle is about 60% of the applied stress. When the applied stress is lower, the Nd-rich particle does not crack or debond from the matrix, thus the Nd-rich particle does not cause the fatigue crack. However, in this case a region of equiaxed α phase on the prior β grain boundaries may crack due to the stress concentration and result in a first mode crack. As the applied stress is increased, the stress on the Nd-rich particle increases too. Hence, the probability of fatigue crack initiation related to the Nd-rich particles increases.

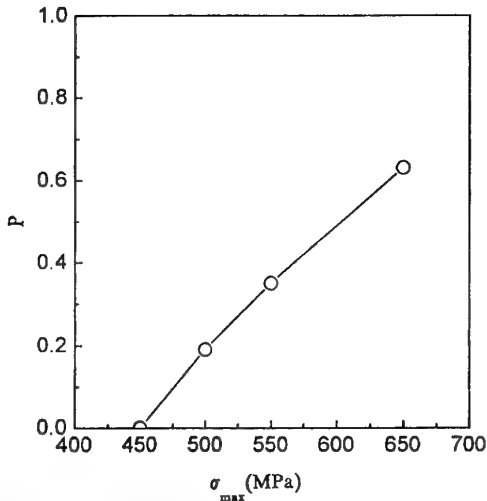


Figure 6 The relationship between the probability of fatigue crack initiation at Nd-rich particles (P) and the maximum nominal stress (σ_{\max})

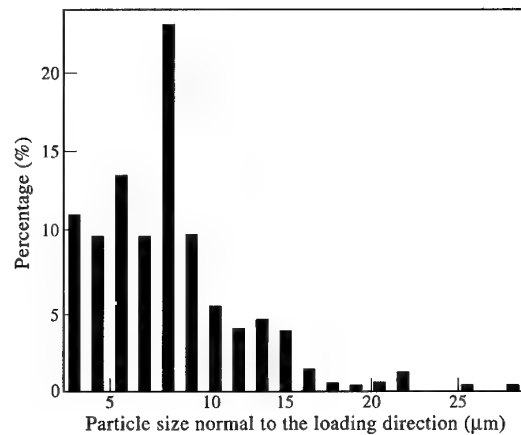


Figure 7 The Nd-rich particle size distribution normal to the loading direction

The effect of the Nd-rich particle size on the second mode crack initiation

The specific influence of the Nd-rich particles on fatigue crack initiation has been investigated further. Initially, the Nd-rich particle size distribution normal to the loading direction was determined. The results are shown in *Figure 7*. The relative fatigue crack initiation probability vs. the Nd-rich particle dimension normal to the loading direction is plotted in *Figure 8*. The relative fatigue crack initiation probability was obtained by dividing the number of cracked particles having induced cracks in the matrix by the total number of particles for a given particle size range (the particle size range in *Figures 7* and *8* is taken as 1.3 μm). The data in *Figure 8* are scattered, but the trend is obvious. The relative fatigue crack initiation probability increases with the particle size. According to the Weibull model of particle cracking^{4,5}, we have

$$p = 1 - \exp \left\{ - \left(\frac{d}{d_0} \right)^3 \left(\frac{\sigma}{\sigma_0} \right)^m \right\} \quad (1)$$

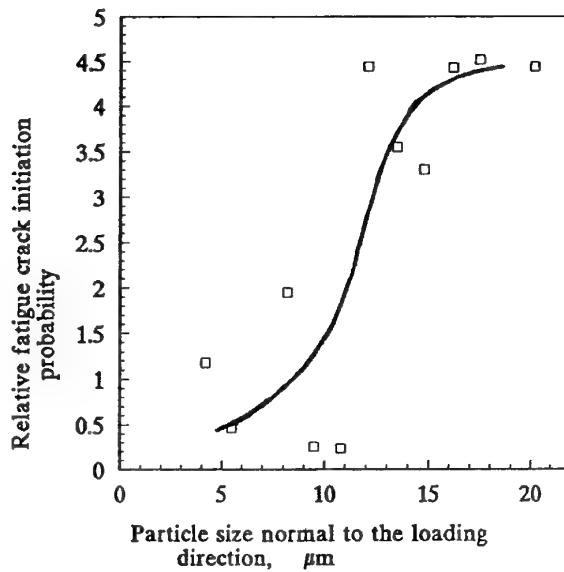


Figure 8 The relationship between Nd-rich particle size and fatigue crack initiation

Here, p is the particle cracking probability, d is the particle diameter, σ is the applied stress, d_0 and σ_0 are the normalizing parameters and m is the Weibull modulus. It can be seen from Equation (1) that the larger the particle, the higher the particle cracking probability. We know that particle cracking is often an important reason for fatigue crack initiation related to particles. So the larger the particle size, the higher the probability that the particle initiated a fatigue crack, as depicted in *Figure 8*. According to the probability distribution in *Figure 8*, the second mode crack initiation probability rapidly decreases as the particle size falls below 12 μm .

CONCLUSIONS

The Nd-rich particles in the Ti-55 alloy are uniformly distributed in the matrix and their sizes are from 3 to 25 μm with an average value of about 9 μm in diameter for a 2 ton ingot. The fatigue crack initiation mode depends on the stress level. At the applied maximum nominal stresses less than 500 MPa, most of the cracks initiate in the matrix away from the Nd-rich particles. The Nd-rich particles display better resistance to fatigue

crack initiation than the matrix. At high applied stresses, approximately half of the cracks initiate near the Nd-rich particles. The probability that an Nd-rich particle initiates a fatigue crack decreases rapidly as the particle size falls below 12 μm .

ACKNOWLEDGEMENTS

This paper was submitted following an invitation from Dr A.K. Vasudevan, chair of the "Fatigue Damage in Structural Materials" Conference. Mr Lei would like to express his gratitude to Dr A.K. Vasudevan for this invitation and also thanks Dr R. Yang and two reviewers for their patient grammatical corrections.

REFERENCES

- 1 Lei, J. F., Liu, Y. Y., Guan, S. X., Wang, Q. J., Wang, Z. G., Li, D. and Hu, Z. Q. *Journal of Materials Science and Technology*, 1996, **13**, 238.
- 2 Goodier, J. N., *Journal of Applied Mechanics*, 1993, **1**, 39.
- 3 Melander, A., *International Journal of Fatigue*, 1990, **12**, 154.
- 4 Lewis, C. A. and Withers, P. J., *Acta Metallurgica et Materialia*, 1995, **43**, 3685.
- 5 Wallin, K., Saario, T. and Torronen, K., *International Journal of Fracture*, 1987, **32**, 201.



PII: S0142-1123(97)00057-1

Short crack growth and internal stresses

K. Sadananda* and A.K. Vasudevant

*Material Science and Technology Division, Code-6323, Naval Research Laboratory, Washington, DC 20375, USA

†Materials Division, Code-332, Office of Naval Research, Arlington, VA 22217, USA

Short crack growth behavior has been examined using the two parametric approach developed earlier by the authors. It is commonly accepted that there is a lack of similitude in the description of the short crack growth behavior. Contrary to this understanding, it is shown that there is no anomaly in the short crack growth behavior. The apparent anomaly arises because of ignoring: (1) the second parameter associated with the threshold K_{\max}^* ; and (2) the existence of internal stresses in the crack tip field where the short cracks nucleate and grow. In the case of short cracks nucleating from notches the internal stresses can be pre-existing or can be generated *in situ* if they form at a free surface. In the latter case, formation of intrusions and extrusions at the persistent slip bands are the precursors for the crack nucleation providing the necessary internal stresses. Thus short cracks grow under a total force, consisting of both internal and applied stresses, satisfying the same two thresholds for long cracks. Examples are provided from the literature to illustrate the concepts. It is shown that the internal stresses decrease as a short crack grows out of the existing stress field. These internal stresses can be predicted using elastic or elastic-plastic continuum approximations. Application of this concept is extended to understand the role of: (1) residual stresses; and (2) the transformation induced internal stresses on the crack growth. Based on the analysis, we restate the similitude concept as: *equal crack tip forces result in equal crack growth rates for the same crack growth mechanism, provided all the contributing forces are taken into consideration.* © 1998 Published by Elsevier Science Ltd.

(Keywords: two threshold ΔK and K_{\max} parameters; short and long cracks; elastic and elastic-plastic analysis; internal stresses; autofrattage; phase transformation; steels; titanium and aluminum alloys)

Fatigue damage normally involves stages pertaining to crack nucleation, short crack growth and long crack growth finally leading to the failure. In service, the crack nucleation stage is either circumvented or cut short by the presence of sharp stress concentrations, such as scratches, dents, holes etc., which act as nucleation sites. In the absence of such stress concentrations, microstructural inhomogeneities, such as inclusions or cast porosities, could provide these stress raisers. For example, in a recent Delta airline crash, retained β phase in a Ti-disk alloy lead to the gas turbine disk failure¹.

In an ideally smooth specimen, it is well known² that intrusions and extrusions form at the persistent slip bands giving rise to stress concentrations. In essence, a crack, being a high energy defect, requires concentrated energy in the form of stress concentrations to initiate and sustain that crack. During cyclic loading, irreversible plastic flow in each cycle helps to accumulate these internal stresses in the form of dislocation pile-ups and dipole bundles. The observed phenomenological relation between the plastic strain range per cycle and the number of cycles to failure (Coffin-Manson relation³) exemplifies an interrelation between the cumulative plastic flow and the fatigue damage process.

Traditionally, the design of load-bearing structures has been based on 'stress versus number of cycles' to failure⁴, which, for the most part, involves crack nucleation life. Any safe life design approach normally involves the judicious use of optimum safety factors without significantly increasing the structural weight and the associated operational costs. These safety factors are intended to cover the unknown or unquantifiable internal stresses arising from the variations in alloy chemistry, processing and/or fabrication, during part assembly and maintenance. It is interesting to note that in the history of civilian aircraft many fatigue failures have been attributed⁵ to the inadvertent introduction of stress concentrations during maintenance operations. Common use of the $S-N$ curves may be adequate at the design level, but is inadequate to predict the remaining life of a component in service, since the load-history is generally unknown. The use of fracture mechanics then provides a better methodology, wherein the existence of a crack of a detectable size can be assumed, and the number of remnant cycles needed for its growth can be computed. For such computation, knowledge of crack growth kinetics is a prerequisite.

Short crack growth refers to the growth of a crack

nucleated in some stress concentration area of a component. Traditionally, the short crack growth has been considered separate from the long crack growth, since its behavior on the ΔK basis was found to be different⁶. Such differences manifest in several ways as in:

1. an excessive scatter in the short crack growth data⁷⁻⁹;
2. the growth occurring at stress intensity ranges below that of a long crack growth threshold;
3. high growth rates occurring even at these low ΔK levels;
4. high growth rates decreasing with an increase in the applied driving force, violating mechanics principles;
5. plastic zone sizes comparable to the crack lengths invalidating the small scale yielding approximations; and
6. pronounced interaction with microstructures (such as grain boundaries etc.) when the crack length is of the order of the microstructural scale.

Next to crack nucleation, short crack growth is of technological importance, since a major part of fatigue life is spent in this regime. Orders of magnitude of scatter in the short crack growth data makes it impossible to predict accurately the life of a component. Furthermore, the demarcation between crack nucleation and the short crack growth stage is ambiguous, and is intimately tied to the sensitivity of the crack detection technology. Even after the crack has been detected, an analytical methodology is still required to predict the growth kinetics of this short crack to estimate the remnant life of a component. Hence, a clear understanding of the short crack growth kinetics become important for life prediction and design.

Linear fracture mechanics has provided a powerful tool for predicting crack growth rates in a structure. To a large extent, the approach is successful because the crack growth rate can be represented in terms of specimen geometry independent stress intensity parameters. Hence the crack growth rates observed in a laboratory coupon can be directly related to that in a complicated structural component, if the driving forces expressed in terms of ΔK are same. Life prediction of a component then becomes easier. Unfortunately, these advantages were lost when the crack closure corrections were introduced in the early 1970s to account for the load ratio dependence on ΔK ¹⁰. Here the closure stresses were used to correct the applied ΔK to arrive at the true crack tip driving forces. Experimentally, for a given material, crack closure values were observed to vary with specimen geometry, crack length, load and environment¹¹. In spite of such variance, crack closure has been assumed to be responsible for several fatigue phenomena such as:

1. load-ratio dependence on ΔK ;
2. environmental effect;
3. temperature effect;
4. overload and under-load effects;
5. short crack growth behavior, etc.

Even though it has been attributed to a wide range of applications, closure is one of the least understood concepts. Interestingly, there has been one analytical paper in support of the concept¹². Experimental difficulties in measuring crack closure accurately has led

ASTM to form a round robin on crack closure measurements involving 10 laboratories using three different methods on a single alloy of 2024-T351 with the same loading history. Unfortunately, the 10 different labs provided 30 different crack closure values¹³. This may possibly be due to the magnitude of the closure being small leading to a high degree of scatter.

Contrary to current models, we have recently shown that plasticity originating from a crack-tip cannot contribute to its closure^{14,15}. Asperities due to surface roughness cause premature contact of the mating surfaces, but their effects on stress fields at the crack tip are significantly small. Hence, it was concluded that closure is either non-existent as in plasticity-induced closure or insignificant as in asperity-induced closure. To account for such discrepancies, a new concept was proposed that required two driving forces for an advancing fatigue crack¹⁶. This involves an amplitude term ΔK , and a peak load term K_{\max} . Both being LEFM parameters, the specimen and load geometry independence is preserved, and the need for crack closure measurements is eliminated. This analysis has been extended to the growth of short cracks¹⁷ as well as crack nucleation¹⁸. Additional data is presented to support the analysis of short crack growth behavior and the nature of internal stresses. The concept of internal stresses provides a powerful tool to understand not only the growth behavior of short cracks, but also many other crack growth variations resulting from overloads, under-loads, effect of cold-work or stress induced transformations, etc.

SHORT CRACK GROWTH

The anomaly in the short crack growth behavior is attributed predominantly to the absence of plasticity induced closure, because of the lack of plasticity in the wake of the crack. By this explanation, the short crack growth is represented as an intrinsic material behavior. In contrast, the long crack growth is considered to be extrinsic because the behavior is modified by the significant contribution from closure. In order to make the long cracks behave in an intrinsic manner, similar to the short cracks, closure corrections are to be made to the applied ΔK .

Large experimental scatter is generally observed in the short crack growth behavior. This is explained in terms of a short crack encountering microstructural obstacles such as grain boundaries. Arrest of short cracks is also believed to occur when the cracks encounter grain boundaries during their growth. Finally, the overall behavior is related to the plasticity induced crack closure which is a major source for the violation of the similitude concept¹⁹. The similitude concept states that *equal crack tip forces should result in equal crack growth rates*. After careful analysis, one can consider the short crack problem with a different view point. First, let us define that long crack growth represents the fundamental material behavior, instead of the short cracks. This assumption can be reasonably justified in the following manner:

1. From dislocation theory, plasticity originating from a crack tip cannot cause closure;
2. There is no unique closure value that one can associate with long cracks; as an example from the ASTM round robin¹³ closure measurements;

3. There is less experimental scatter in the long crack growth data from specimen to specimen or from laboratory to laboratory for a given material;
4. Long cracks have unique thresholds for a given R ratio (and grow without retardation or arrest) while short cracks have none;
5. On the other hand, scatter is significant in the short crack growth data taken with the same specimen;
6. Crack growth rates can decrease with increasing driving force for short cracks;
7. Short crack growth data from tests of various alloys fall within the same scatter band, or for the same alloy with different microstructures showing no unique behavior.

Thus, long crack growth behavior is more consistent and predictable, justifying the view that it represents a fundamental behavior of a material under fatigue conditions.

The decrease in short crack growth rates with increase in ΔK leading to their arrest have been attributed to microstructural obstacles. These obstacles are grain boundaries whose grain orientation changes²⁰ where a short crack can get arrested. The microstructure can play a significant role in the growth of short cracks, when the length of short cracks are less than the grain size. But this decrease and arrest was also found for a small through thickness crack, where the specimen thickness is larger than several grains. In this case, the reason for deceleration and the arrest of a growing small crack should be related to the causes other than the microstructure. Here, we bring to the reference a classic work by Pippin *et al.*²¹ on Armco iron. They considered a small through thickness crack, otherwise known as a mechanically short crack, with a specimen thickness much larger than the grain size. Figure 1 shows a typical crack growth behavior for Armco iron, for various constant ΔK tests at $R = -1$. The results indicate that for a given constant $\Delta K = 4 \text{ MPa}\sqrt{\text{m}}$, the crack starts growing at a higher growth rate of $ca 2 \times 10^{-6} \text{ mm cycle}^{-1}$. The crack quickly decelerates with an increase in crack length until complete crack arrest occurs at $ca 5 \times 10^{-10} \text{ mm cycle}^{-1}$. From their paper, we observe that the authors have discarded all the data that did not represent the through thickness cracks. Since crack length along the thickness direction spans over several grain sizes the crack arrest cannot necessarily be related to the grain boundary or other sub-microstructural obstacles. Figure 1 indicates

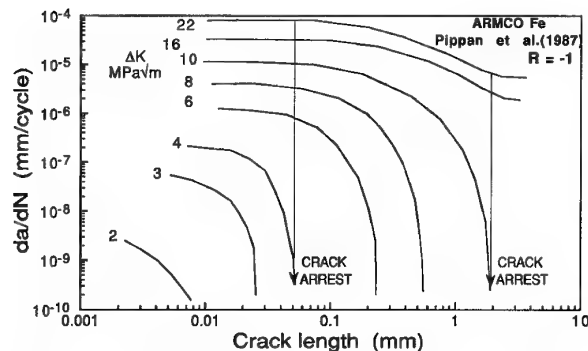


Figure 1 Short crack growth data on Armco Fe at various constant ΔK

that the crack arrest occurs for $\Delta K \leq 10 \text{ MPa}\sqrt{\text{m}}$. At $\Delta K \geq 16 \text{ MPa}\sqrt{\text{m}}$, there is a small decrease in crack growth rate leveling off to a constant value. The trend in the results are similar at other R ratios.

The reason for the crack arrest becomes evident from Figure 2, extracted from Pippin's data²¹. For $R = -1$, the figure shows that the long crack threshold is *ca* $12 \text{ MPa}\sqrt{\text{m}}$, slightly above $10 \text{ MPa}\sqrt{\text{m}}$. Note that the upper bound for short crack growth data follow closely the high R-ratio data, even though the background is $R = -1$. This upper bound observation is taken from the highest crack growth rates at each ΔK in Figure 1 when the crack lengths are small, *ca* 0.005 mm . This similarity in growth rates for short cracks at low R and that of long cracks at high R is used to strengthen the argument that in both cases closure is absent. But, according to closure proponents closure exists only for long cracks at low R-ratios. We can attribute this similarity neither to closure nor lack of it, but to the presence of high local R-ratio. When cracks are small, the local R differs from the remote R-ratio, which is $R = -1$ in this case. As the crack length increases, the local R-ratio decreases approaching the remote R-ratio.

In terms of a crack arrest phenomenon, Figure 2 also shows that for $\Delta K \leq 10 \text{ MPa}\sqrt{\text{m}}$, crack arrest occurs as indicated by the downward arrow. These ΔK values are less than the long crack threshold ($\sim 12 \text{ MPa}\sqrt{\text{m}}$) at $R = -1$ for causing arrest. On the other hand, at $\Delta K = 16$ or $22 \text{ MPa}\sqrt{\text{m}}$, the growth decreases from the upper bound limiting value approaching the long crack growth rates at which point they remain constant, since ΔK is constant, Figure 1. Hence Pippin's data establishes an important fact that it is not necessarily the microstructural obstacles that cause short crack arrest, but the fact that the driving forces are less than the long crack thresholds. The reason for this experimental observation is given below.

SHORT CRACKS WITHIN INTERNAL STRESS FIELDS

Considering that long crack growth behavior is fundamental and that plasticity does not contribute to crack closure, we postulate that crack growth occurs in all cases only when the two critical thresholds are met simultaneously. One can show that short cracks are no exception to this rule. Most of the anomaly is a result of ignoring the second threshold, K_{\max}^* , in addition to

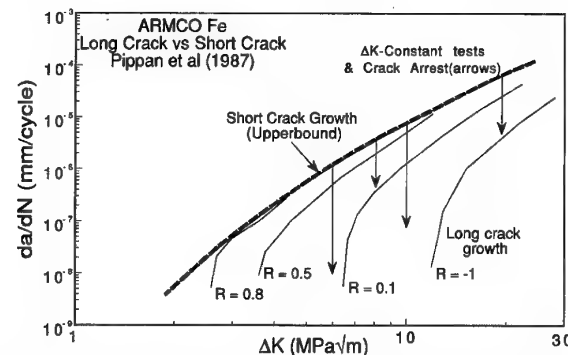


Figure 2 Comparison of long and short crack growth rates on Armco Fe

ΔK . Short crack growth behavior with its associated arrest phenomenon, results from the consideration of the second threshold requirement for K_{\max}^* . Figure 3 shows the general behavior of short cracks irrespective of their source or classification. Based on their size and origin, short cracks have been classified as small cracks, physically short, mechanically short, microstructurally short and short-short cracks¹⁹. Similar trends in the behavior is also observed from small cracks starting at notches²². Generality of the behavior is such that from the data, it is difficult to distinguish the nature of the short crack for which the data has been obtained. The generic features common to all short cracks are:

1. they have a high initial crack growth rate;
2. growth rates decrease with increase in ΔK , sometimes reaching a minimum;
3. crack arrest occurs in some cases; and
4. growth rates increase after reaching a minimum converging to the long crack growth rates.

Since the behavior is the same irrespective of their source or classification, we seek a generic explanation applicable to all short cracks, whether they are initiated from free surfaces, corners or notches; whether they are mechanically short, microstructurally short, physically short or short-short cracks. It is known that (1) small cracks initiating from notches behave similar to short cracks and (2) these cracks are growing in the internal stress field gradients of the notches super imposed on the applied stresses. From (1) and (2) we can postulate that all short cracks are growing in some kind of internal stress fields giving rise to a behavior similar to the cracks starting from notches.

Figure 3(a) schematically shows a few examples of

short crack growth behavior that differs from the long crack growth. Growth rates decelerate to a minimum and then accelerates. In some cases the crack deceleration can lead to an arrest without exhibiting a minimum. From the above postulate, the driving force for a short crack involves an applied ΔK identified along the X-axis in Figure 3(a), plus an internal stress. Normally the source of internal stresses are stress concentrations from notches or holes or inclusions etc. The internal stress fields decrease with distance away from their source. From the crack growth data, one can estimate the magnitude of the internal stress acting at the crack tip, as a difference in ΔK values between the long crack growth and short crack growth data, at the same crack growth rate. This implies that for the same crack growth rate, the driving forces are the same, for both short and long cracks. As the short crack growth data merges with the long crack growth data, the internal stress computed as a difference between them approaches zero.

The schematic in Figure 3(b) shows the crack tip stress as a function of distance, where the internal stress decreases to zero with distance from the source. As the crack length increases, the driving force from the applied stress, ΔK_{app} increases, while the internal stress decreases; and the resulting total stress passes through a minimum. Hence, the initial decrease in growth rate comes from the rapid decrease in the internal stress as the crack tip moves away from the source; and the subsequent acceleration then comes from the increase in the applied stress contribution. For a short fatigue crack to grow the driving forces must exceed the long crack thresholds, ΔK_{th}^* and K_{\max}^* . Due to high internal stresses at small crack lengths, K_{\max}^* can also exceed to provoke the condition

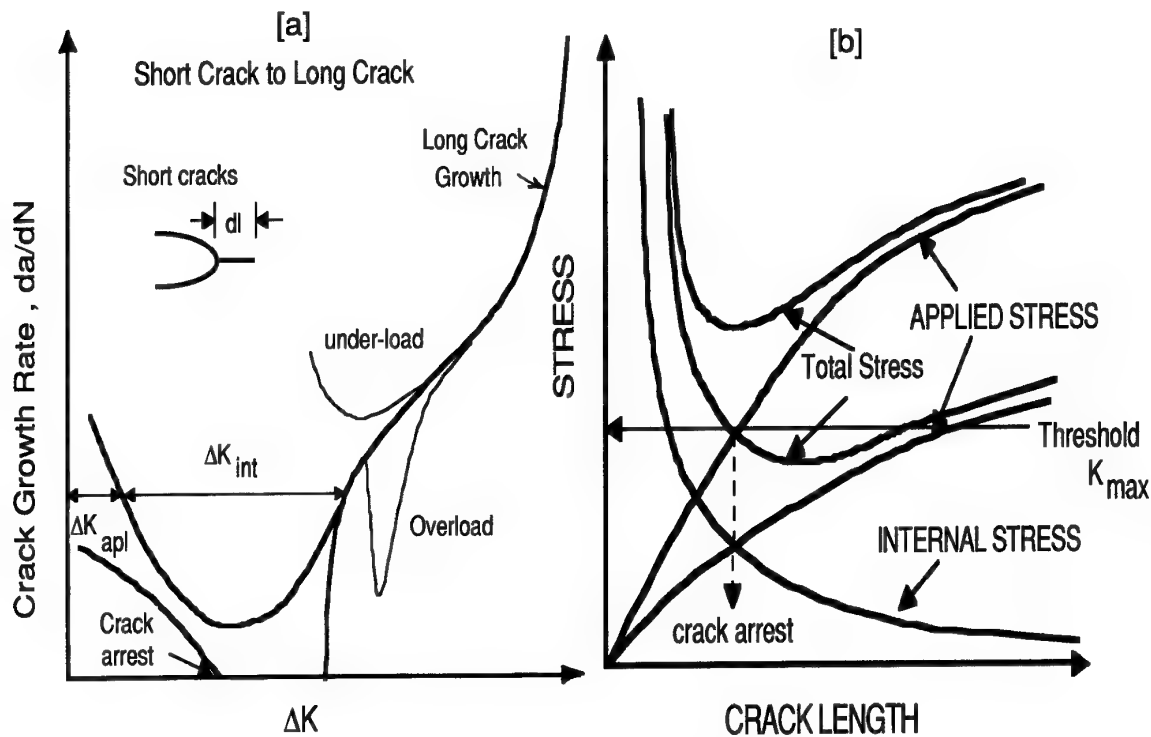


Figure 3 Schematic illustration of (a) long and short crack growth rates and (b) the role of internal stress in short crack behavior

for the crack growth to occur. As the crack length increases, a small crack moves away from the source of the internal stress. The contribution from the internal stress decrease allowing for the effect from the remote stress to dominate. If the total stress intensity is below the K_{\max}^* , as may be the case at low applied stresses, the cracks stop growing resulting in non-propagating short cracks. If the stress intensity minimum is above the threshold, then cracks will continue to grow and accelerate as the applied stress contribution increases. When the internal stress goes to zero, the total stress now consisting of only the applied stress approaches that for a long-crack. Of the two thresholds ΔK_{th}^* is very small and consequently K_{\max}^* plays a major role. For example, in Al-base alloys, ΔK_{th}^* is *ca* 1 MPa \sqrt{m} , very small compared to $K_{\max}^* > 3\text{--}4 \text{ MPa}\sqrt{m}$; hence ΔK_{th}^* is easily met by the applied stress. It is the K_{\max}^* that becomes responsible for the observed non-propagating cracks.

Internal stresses that can be related to dislocation density gradients, normally enhance K_{\max} and K_{\min} , thereby affecting mostly the local R -ratio, but not ΔK . Hence, due to the presence of internal stress, the local R -ratio will be higher than the remote R ratio. Convergence of short crack growth rate data (upper bound in *Figure 2*) to the long crack growth rate data at high R -ratio, is therefore a natural phenomenon. In some cases ΔK can also be affected by the internal stresses, if the dislocation density or distribution is markedly affected by the loading and unloading.

We therefore conclude that:

1. the same two thresholds apply for both long and short cracks;
2. the short cracks are growing in the presence of an internal stress gradient and therefore;
3. there is nothing anomalous about the short crack behavior if one considers the total forces acting on the crack in terms of the applied and internal forces.

We reinforce the similitude concept by restating that:

Equal crack tip forces lead to equal crack growth rates for the same crack growth mechanism if all the forces are included.

This statement has a more general bearing if one can also include the chemical forces on the crack growth. To add a chemical force term to the applied ΔK requires a consideration from the time-dependent aspect of damage, the scope of which is beyond the current discussion.

EXPERIMENTAL EVIDENCE

In support of the discussed analysis, we now present some examples taken from the literature. *Figure 4* shows the experimental data from McClung and Sehitoglu²³, where tests were done using a notched specimen. As in *Figure 3(a)*, the internal stress value at each crack growth rate is arrived at by subtracting ΔK value of short cracks from the value from the long crack data, taken at the same growth rates for a notch factor of $K_t = 3.0$. In *Figure 4*, the internal stress is plotted in the normalized coordinates; the length scale being normalized with the size of the notch. There is a sharp increase and gradual decrease in the internal stress

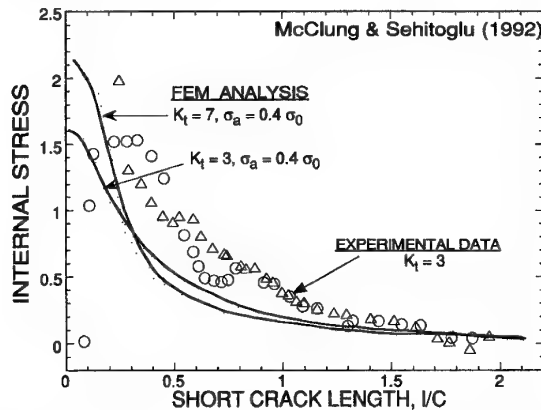


Figure 4 Comparison of internal stress computed from data to FEM analysis with the experiment

with increase in crack length due to decrease in the notch tip stress field. For lengths greater than twice the radius of the notch, the internal stresses become negligible, as expected. McClung and Sehitoglu²³ have independently calculated the stress field of the notch using finite element analysis with elastic-plastic approximation. The solid curves show the results of calculations on the same scale. Other than the use of their raw experimental data to compute the internal stresses and their independent FEM analysis data, the data has not been manipulated to arrive at the figure. *Figure 4* indicates that: (a) internal stresses do decrease rapidly with increase in crack length; (b) the stresses computed independently using elastic-plastic approximation match reasonably with the experimental data confirming that the internal stress hypothesis is correct. Notwithstanding the inherent limitations of the FEM in the computation of the stresses, the *Figure 4* supports the use of internal stress concept in the analysis of short cracks.

We show a second example in *Figure 5* with the data taken from Larson's work²⁴. The purpose here is to show that in some cases internal stresses could be of a simpler form with \sqrt{r} singularity, similar to the crack tip stress field. *Figure 5(a)* shows the Ti-8Al alloy data²⁴ at two different R -ratios for both short and long cracks. The internal stress for each short crack is deduced by taking its corresponding long crack data as a reference. In *Figure 5(b)*, these internal stresses are plotted as a square root of the crack length. Note that the internal stresses decrease linearly with the square root of crack length with both R -ratio data falling on the same line. Thus the nature of the internal stress is the same in these two tests. The linear relationship implies that the internal stress in this case is of the same form as the crack tip stress fields. The applied stress increases linearly with square root of crack length. The sum of the internal and applied stresses is equal to that required for a long crack. The combined results in *Figures 4* and *5(b)* indicate that the use of linear elastic or elastic-plastic approximations can predict, to a degree of accuracy, the internal stresses aiding the growth of short cracks.

Recalling the Armco Fe data from Pippan *et al.*²¹ in *Figures 1* and *2*, the internal stress from their short crack growth data is determined as a function of crack length and the result is shown in *Figure 6*. All the

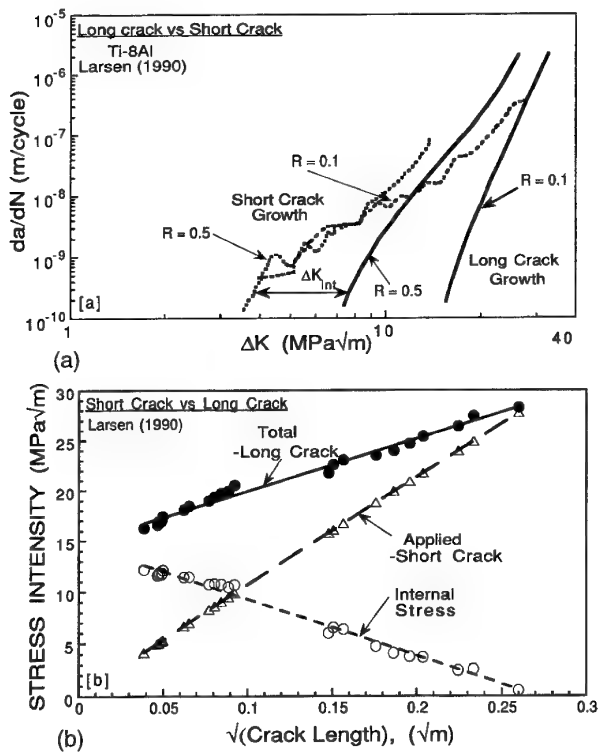


Figure 5 (a) Long and short crack growth data on Ti-8Al alloy, and (b) the computed internal stress variation with crack length

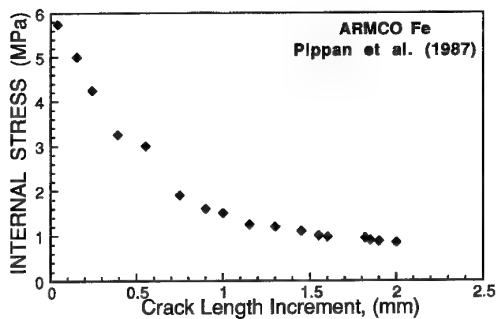


Figure 6 Computed internal stress for Armco Fe, from Figures 1 and 2

calculated internal stress data fall on a single curve suggesting that the source of the internal stress is same. Although the authors claim that they have annealed the sample to relieve all the residual stresses, that the stresses are fully relieved is only an assumption. Their short crack growth data shows that either the stress relief experiment is either incomplete or additional internal stresses were introduced, probably *in situ* via cyclic plasticity.

Figure 7 shows the classic data on low carbon steel from Tanaka and Nakai²⁵ where the short cracks are growing from different sources using different specimens. They have systematically studied a crack growing from a notch, from a free surface and from the corner of a notch. For each of these cases Figure 7(a) shows the summary of all the short crack growth data with the observed experimental scatter, along with the long crack growth data. The internal stress computed

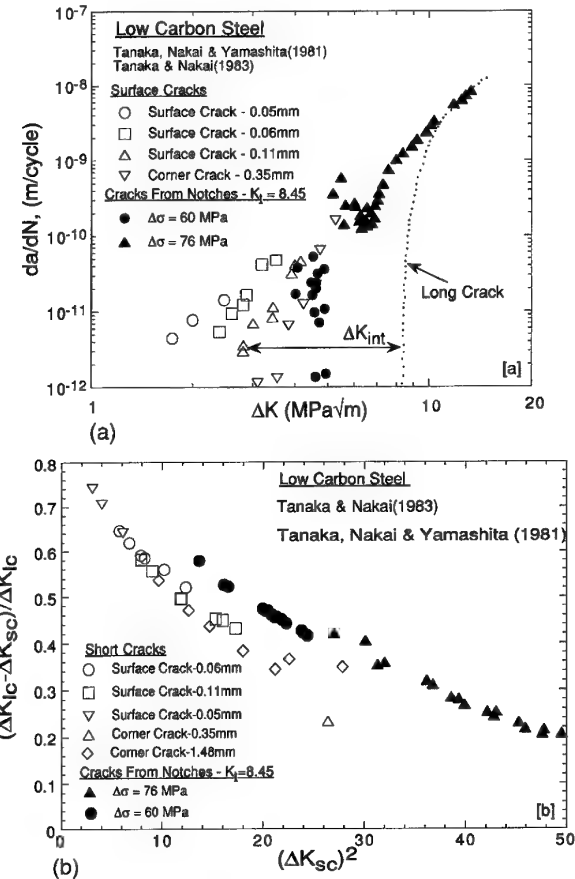


Figure 7 (a) Comparison of long and short crack growth rates for a low carbon steel and (b) the related internal stresses

for each of the cases is plotted in Figure 7(b) as a function of a parameter that is proportional to the crack length. Surprisingly, inspite of the diverse nature of stress concentrations that produced these short cracks, Figure 7(b) shows that all the internal stresses fall on a unique curve. This behavior is a pleasant surprise and indicates that the gradient of internal stresses are essentially similar in all the cases, and may follow a similar relation.

Short crack growth behavior has been studied extensively since 1975. Using the published data one can determine the internal stresses using the raw crack growth data and show that in each one of the cases the internal stresses show similar behavior. For brevity, we have provided only selective examples that illustrate the basic concepts. Although we have not independently determined the internal stresses, FEM analysis and the examples shown here indicate that internal stresses are deterministic and are of a simpler form, which can be computed to a degree of approximation for engineering analysis. Unfortunately, there are no direct experimental methods that can be used to measure the internal stress gradients. This is because the gradients extend only a millimeter or so, and this limited length scale offers difficulty to the measurements. We next illustrate this internal stress concept with two other examples: (1) autofrettage in a thick walled tube; and (2) stress induced phase transformation. These two examples show how one can utilize

this approach to arrive at the nature and mechanism of the origin of the internal stresses.

CRACK GROWTH UNDER RESIDUAL STRESSES

Stacey and Webster²⁶ have studied the effect of residual stresses on crack growth in a low alloy steel. Significant compressive residual stresses were generated during autofrettage in a thick wall tube and the specimens were sectioned from the tube with cracks starting from the inner wall. The long crack growth rates were studied with identical specimens before and after the introduction of the residual stresses. Figure 8 shows the crack growth rate data with and without the compressive stresses. Both plots correspond to the long crack growth data. There is no crack closure involved in these tests other than the pre-existing internal stresses in the material with its own characteristic gradient. One can consider that these compressive internal stresses have made the material extra stiff, requiring higher driving forces for crack growth. As before, the difference in ΔK value between the two curves at the same crack growth rates estimates the magnitude of internal stress as a function of crack length, and the result is plotted in Figure 8(b). Comparison with Figure 4 shows that the nature of the internal stresses is qualitatively similar to that in Figure 8(b).

Interestingly, Stacey and Webster have determined

the change in the stiffness of the material due to autofrettage using compliance type of measurements. The internal stress curve in Figure 8(b) follows closely the change in the measured specimen compliance due to autofrettage. This confirms that the crack growth rate curves in Figure 8(a) reflect accurately the internal stress gradient introduced by the autofrettage process. One can extend the application of these concepts to quantify the effects of overloads and under-loads which introduce internal stresses of different magnitudes and signs that can affect the crack growth rates.

INTERNAL STRESSES FROM STRESS INDUCED TRANSFORMATION

The internal stress concept can be extended to understand the effect of stress induced transformation on fatigue crack growth. Stress or strain induced phase transformation can occur in the stress field of a crack. The resulting transformation subsequently induces stresses that are proportional to the volume of the material transformed, which is related to the stress field or strain field of the original crack. It is believed that transformation can affect fatigue crack growth by three different processes:

1. inducing compressive stresses that can enhance crack closure;
2. increasing resistance to crack growth due to superimposed compressive stresses ahead of the crack tip; and
3. introducing a new material different from the matrix which has different fracture properties.

Mei and Morris²⁷ have analyzed this problem using a 304L type stainless steel that has been annealed, quenched and strained to undergo martensitic transformation at liquid nitrogen temperature. The data was compared with the untransformed material tested at room temperature. Figure 9(a) shows the effect of transformation on the resulting crack growth rate. As before, Figure 9(a) was used to calculate the transformation stresses that are affecting the crack growth in a similar way to the short cracks.

In Figure 9(b) shows the R -ratio effect of this material at 77°C. The solid points are based on the author's data which are limited to the three R -ratios tests, while the rest of the data points are fitted by linear extrapolation. Interestingly, at low crack growth rates near threshold ($da/dN = 5 \times 10^{-8} \text{ mm cycle}^{-1}$), all the data fall on a single line. At intermediate crack growth rates ($1 \times 10^{-5} \text{ mm cycle}^{-1}$), there appears to be a bilinear behavior indicative of some change in the crack growth mechanism. In this bi-linear curve, the slope at low R -ratio (low K_{\max}) is similar than at threshold. However, the slope at high R -ratio is steeper with ΔK decreasing more rapidly. We observed that in a similar plot (not shown) at a still higher crack growth rates ($da/dN = 1 \times 10^{-3} \text{ mm cycle}^{-1}$), all the data again fell on a single line, with a steeper slope. Thus, even though the data is very limited, there appears to be two distinct mechanisms operating with a gradual change occurring from the lower growth rates to higher growth rates. This change seems to occur with an increase in K_{\max} reflected in the R -ratio effect, evidenced by the bi-linear curve in Figure 9(b).

Figure 9(c) gives an additional support for this

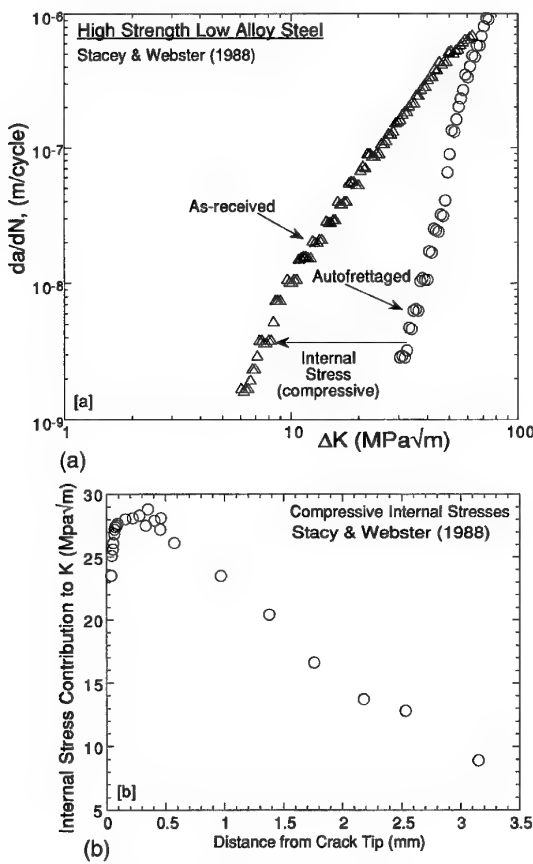


Figure 8 (a) Long crack growth rates for high strength low alloy steel under autofrettaged condition and (b) the resulting internal stress variation with distance from the crack tip

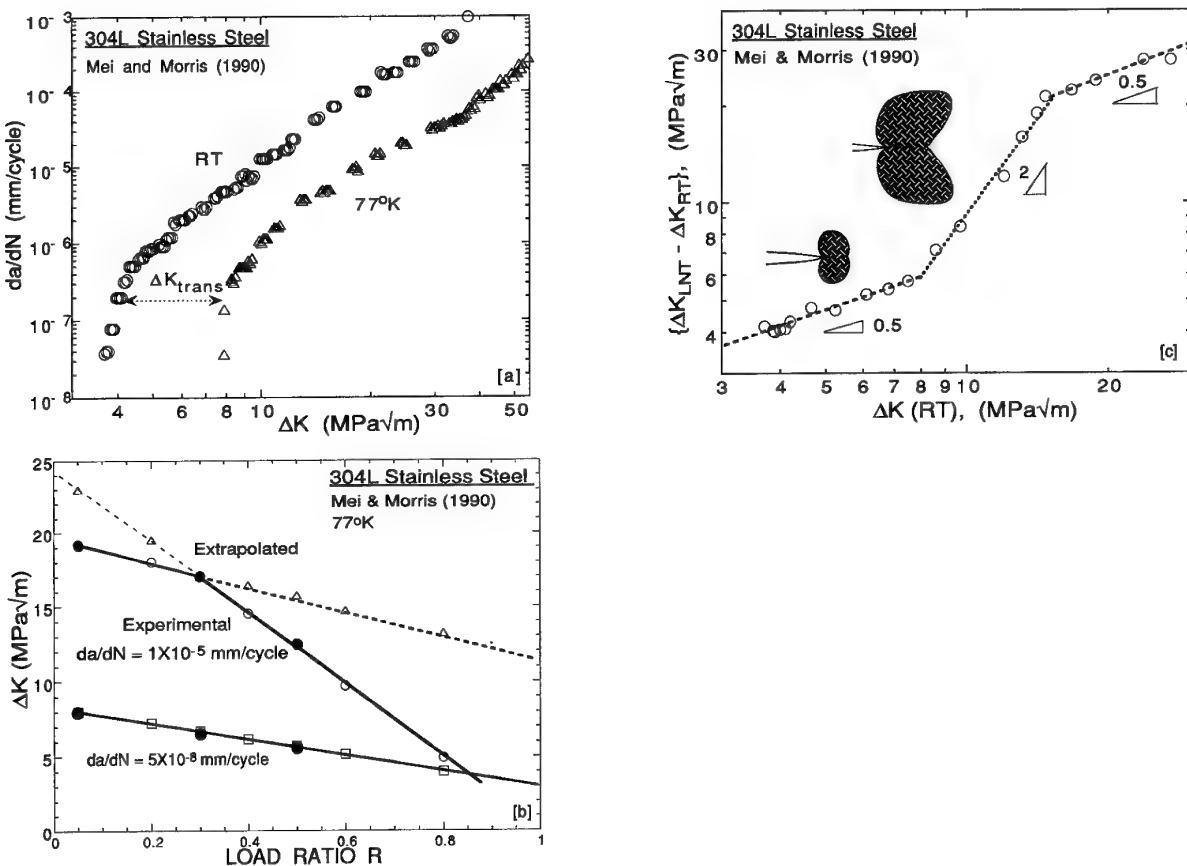


Figure 9 (a) Long crack growth results from a stress induced phase transformed 304L stainless steel, (b) representation of ΔK with load ratio R and (c) the variation of the internal stresses suggesting three distinct regions of behavior

hypothesis. The transformation internal stresses, measured as the difference between ΔK at liquid nitrogen temperature and room temperature, are plotted as a function of ΔK at room temperature. We have selected $\Delta K(RT)$ along the X-axis, since the extent of transformation is a function of the stress. Interestingly, the data falls on three linear segments. At ΔK close to the threshold, the slope is *ca* 0.5, changing to 2 in the intermediate range, and then falling back to 0.5 at a still higher ΔK . The magnitude of the slopes appear to be a reflection of some changes in the physics of the damage process rather than due to any artifacts or crack closure. All the data in *Figure 9(a)* and hence *Figure 9(c)* correspond to one R -ratio. Unfortunately the authors did not perform tests at other R -ratios to compute the transformation stresses as a function of R .

Based on *Figure 9(b)* and *(c)*, it is clear that not one mechanism, but at least two mechanisms are operating. One mechanism operating at low $\Delta K < 8$ MPa \sqrt{m} and the other at intermediate $\Delta K \sim 8-15$ MPa \sqrt{m} . Because of the lack of further information like microstructural analysis, one can only speculate on the mechanisms involved. Close to the threshold at $\Delta K < 8$ MPa \sqrt{m} , crack growth rates are influenced by the transformation stresses that are proportional to the background crack tip stresses which varies with square root of crack length. At intermediate stresses ($\Delta K \sim 8-15$ MPa \sqrt{m}) the transformation volume itself is proportional to the strains which are parabolically related to the background stress. Thus the transformed

material behavior may be entering into crack growth kinetics. At very high $\Delta K > 15$ MPa \sqrt{m} , other fracture process may be controlling to cause a slope of 0.5. Thus the analysis points to a methodology that can provide a powerful tool to evaluate the mechanisms governing the deviations in crack growth behavior.

APPLICATION TO LIFE PREDICTION

Recognizing that the long crack growth behavior is fundamental to the damage of a material, we find that any deviations from this is a result of superimposed stresses, either *in situ* generated or pre-existing. This gives a basis for developing a life prediction methodology based on the two parametric approach. This is illustrated schematically taking a Class-III type of an alloy²⁸ that gives a perfect L-shape curve on a $\Delta K - K_{max}$ plot. *Figure 10* shows a constant crack growth rate plot in terms of ΔK^{total} and K_{max}^{total} , where the superscript 'total' includes contributions from both applied and internal stresses. With an increase in da/dN , the curve moves to higher ΔK and K_{max} . Thus, one can draw at each crack growth rate, a similar $\Delta K - K_{max}$ plot. The L-shaped curve at the threshold growth rate represents a lower bound below which no crack growth occurs. One can determine the L-shaped curve either by doing a constant ΔK test, or a constant K_{max} test, or a constant R -ratio test or any combination of the these; since the final $\Delta K - K_{max}$ curve is independent of these tests. In all these tests, one moves

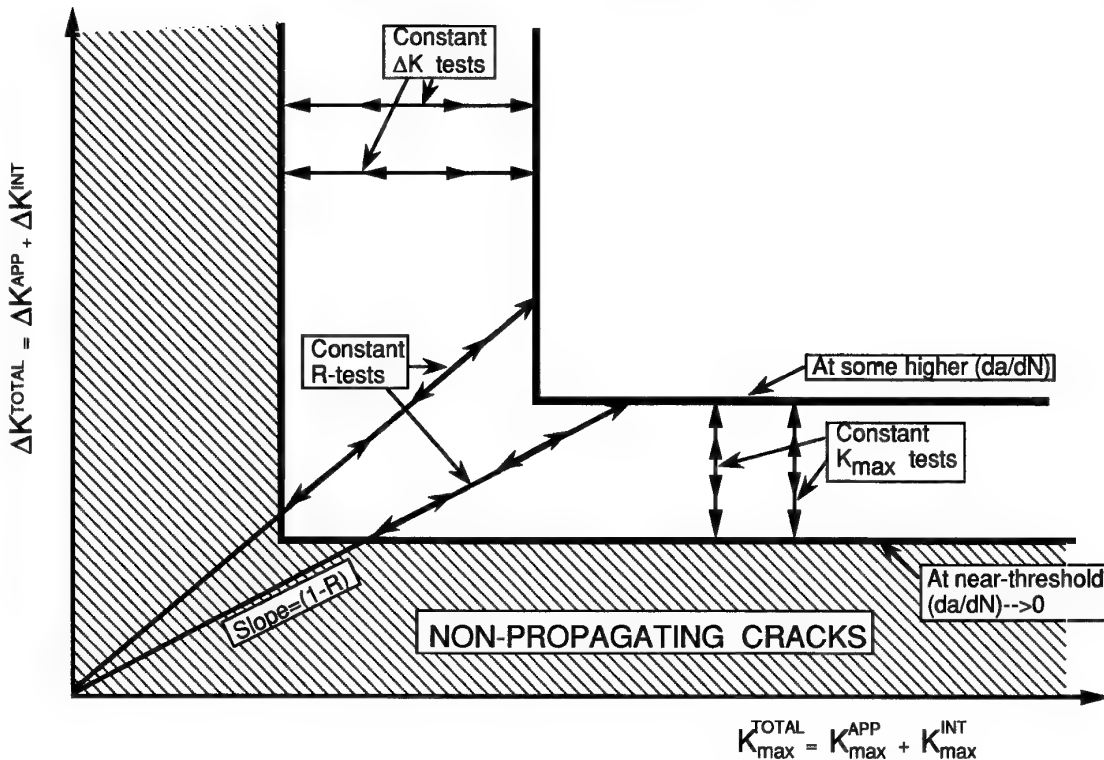


Figure 10 Schematic representation of constant crack growth rate plots in terms of the total $\Delta K - K_{\text{max}}$ that includes the internal stress contribution, for a Class-III type of material behavior

continuously from one (da/dN) curve to the next along a particular $\Delta K - K_{\text{max}}$ trajectory, as illustrated in Figure 10.

Crack growth rates can be predicted by developing a (da/dN) relation with ΔK and K_{max} using laboratory data. In order to develop such relations a complete range of data for all R -ratios is needed. To illustrate this point, we can represent the (da/dN) relation in terms of ΔK and K_{max} in terms of a power law of the form:

$$(da/dN) = A(\Delta K - \Delta K_{\text{th}}^*)^n(K_{\text{max}} - K_{\text{max}}^*)^m \quad (1)$$

Where ΔK_{th}^* and K_{max}^* are the two critical thresholds, A , n and m are material dependent constants. Using the above relation, one can arrive at $\Delta K - K_{\text{max}}$ plots representative of a material behavior. At the threshold, $(da/dN) \Rightarrow 0$ and the relation (1) reduces to:

$$\Delta K = \Delta K_{\text{th}}^* + B/(K_{\text{max}} - K_{\text{max}}^*)^m \quad (2)$$

where for simplicity we have assumed $n = 1$. Figure 11 shows a typical plot generated using the above equation for an Al-9.5Si alloy data taken from Usami²⁹. For a general case, actual material data from several R -ratio tests can be used to arrive at the values for the material constants. Integration of Equation (1) from the initial crack length to final, gives the number of cycles for crack growth. Thus, the current life prediction methodologies can be applied to predict the life by substituting Equation (1) for representing the crack growth rate. For short cracks, overloads etc. the description of ΔK and K_{max} should include the total stresses rather than the applied stress alone, while the same long crack thresholds are valid for all cracks.

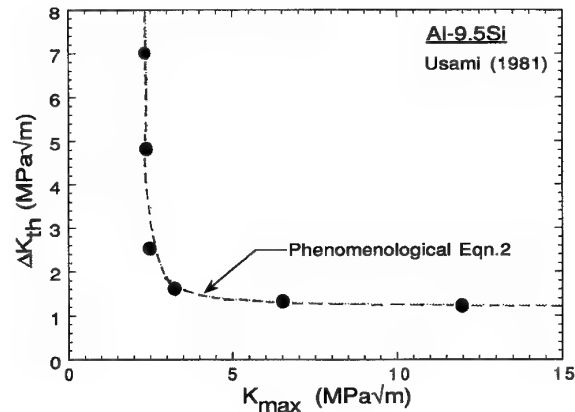


Figure 11 Representation of the experimental Al-9.5Si data in agreement with Equation (2) on a $\Delta K - K_{\text{max}}$ plot

SUMMARY

A unified frame work of analysis for short and long cracks is provided using the two parameter approach. Long crack growth behavior is assumed to represent the fundamental material behavior with the same two thresholds valid for all cracks, short or long. Deviation from the long crack behavior, as in the case of short cracks, arises due to the presence of additional internal stresses. These internal stresses are relatable to notch tip stresses as in the case of short cracks originating from notches, or to other stress concentrations. Without these internal stresses, high energy defects such as cracks cannot be initiated. For example, in the case of

smooth specimens, intrusions and extrusions along the persistent slip bands provide the necessary stress concentrations for the nucleation of cracks. Deceleration of short cracks is related to rapid decrease in the internal stresses. Their arrest can occur when the total force due to internal and applied stresses falls below the K_{\max}^* . Even for short cracks of the order of microstructural scale (grain size), where the crack growth is crystallographic, changes in the grain boundary orientation may provide the necessary physical obstacle. But arrest should occur only when the total crack tip force is less than the threshold for that new grain orientation. Hence the anomaly observed with short cracks is not real and is a result of: (a) not including the simultaneous requirement for the two critical thresholds for fatigue crack growth; and (b) ignoring the relevant internal stresses that cause a higher crack tip driving force and a higher local R -ratio. The concept of internal stresses is significantly important and can explain the effects of residual stresses introduced under various circumstances such as cold-working or overloads or underloads. Likewise, the effects of superimposed transformation induced stresses could also be analyzed. Based on our analysis we reaffirm the similitude concept in the following form:

Equal crack tip forces result in equal crack growth rates, provided the mechanism of growth remains the same.

REFERENCES

- 1 Hall, J., Titanium alloy microstructures in design. International Journal of Fatigue, in press.
- 2 Wood, W. A., *Bulletin of the Institute of Metals*, 1955, **3**, 5.
- 3 Coffin, L.F., *Transactions of the American Society of Mechanical Engineering*, 1954, **76**, 931-950; Manson, S.S., *National Advisory Commission on Aeronautics*, Report 1170, Cleveland, 1954.
- 4 Goranson, U., Issues in aircraft maintenance and repairs, International Journal of Fatigue, in press.
- 5 Pelloux, R.M., In *Fatigue '93*, Vol. III (Eds J.P. Bailon and J.I. Dickson). Engineering Materials Advisory Services Ltd, West Midlands, UK, 1993, pp. 1727-1739.
- 6 Ritchie, R.O. and Lankford, J. (Eds), *Small Fatigue Cracks*, AIME-Metallurgical Society, Warrendale, PA, 1986.
- 7 Morris, W. L., Buck, O. and Marcus, H. L., *Metallurgical Transactions*, 1976, **7a**, 1161.
- 8 Lankford, J., *Fatigue Engineering Materials Structure*, 1982, **5**, 233.
- 9 Brown, C. W. and Hicks, M. A., *Fatigue Engineering Materials Structure*, 1983, **6**, 67.
- 10 Elber, W., *Engineering Fracture Mechanics*, 1970, **2**, 37.
- 11 Banerjee, S., *A Review of Crack Closure*. AFWAL-TR-84-4031. Air Force Materials Laboratory, Dayton, OH, 1984
- 12 Budiansky, B. and Hutchinson, J. W., *Journal of Applied Mechanics*, 1978, **45**, 267.
- 13 *Mechanics of Fatigue Crack Closure*. ASTM STP-982, American Society of Testing Materials, Philadelphia, 1988; and Phillips, E.P., Results of the Round Robin on Opening-load Measurement Conducted by ASTM Task Group E24.04.04 on Crack Closure Measurements and Analysis. Report NASA TM-101601, May 1989.
- 14 Louat, N., Sadananda, K., Vasudevan, A. K. and Duesbery, M., *Metallurgical Transactions*, 1993, **24A**, 2225.
- 15 Weertman, J., *Physics Status Solidi B*, 1992, **172**, 27-40.
- 16 Vasudevan, A. K., Sadananda, K. and Louat, N., *Material Science Engineering*, 1994, **A188**, 1.
- 17 Sadananda, K. and Vasudevan, A.K., ASTM STP-1296. American Society of Testing Materials, Philadelphia, 1997, pp. 301-316.
- 18 Sadananda, K. and Vasudevan, A.K., *Fatigue 96* (Eds Lutjering, G. and Nowack, H.), Vol.1. Pergamon, Berlin, 1996, pp. 375-380.
- 19 Suresh, S. and Ritchie, R. O., *International Metal Review*, 1984, **29**, 445-476.
- 20 Lankford, J. and Davidson, D.L. In *Small Fatigue Cracks* (Eds Ritchie, R.O. and Lankford, J.), AIME-Metallurgical Society, Warrendale, PA, 1986, pp. 51-73.
- 21 Pippin, R., Berger, M. and Stuwe, H. P., *Metallurgical Transactions*, 1987, **18A**, 429.
- 22 El-Haddad, M. H., Topper, T. H. and Smith, K. N., *Engineering Fractures*, 1979, **11**, 573.
- 23 McClung, R. C. and Schitoglu, H., *Journal of Engineering Materials Technology*, 1992, **114**, 1-7.
- 24 Larson, J.M., Ph.D. Thesis, Carnegie Mellon University, Pittsburgh, PA, 1987.
- 25 Tanaka, K. and Nakai, Y., *Fatigue Engineering Materials Structure*, 1983, **6**, 315.
- 26 Stacey, A. and Webster, G., ASTM STP 1004. American Society of Testing Materials, Philadelphia, 1988, pp. 107-121.
- 27 Mei, Z. and Morris, J. W., *Metallurgical Transactions*, 1990, **21A**, 337.
- 28 Vasudevan, A. K. and Sadananda, K., *Metals and Materials Transactions*, 1995, **26A**, 1221.
- 29 Usami, S., In *Fatigue Thresholds* (Eds Backlund, J., Blom, A. and Beevers, C.J.), Vol. 1, EMAS Ltd, UK, 1982, p. 205.



PII: S0142-1123(97)00042-X

Fatigue performance of 6261-T6 aluminium alloy – constant and variable amplitude loading of parent plate and welded specimenst

M.N. James* and A.E. Paterson†

*School of Manufacturing, Materials and Mechanical Engineering, University of Plymouth, Drake Circus, Plymouth, Devon PL4 8AA, UK

†Aluminium Federation of South Africa, Box 423, Isando 1600, South Africa

The work reported in this paper is a summary of the results obtained from several projects run over a five year period. A number of thrusts were encompassed in the project scope, which was to examine the fatigue strength of extruded 6261-T6 I-beams with centrally located, welded cover plates under constant amplitude (CA) and variable (two-level repeated block) amplitude (VA) loading. The CA part of the work examined the effect of cover plate geometry, specimen size, thermal and vibratory stress relief, and differences in fabrication quality on fatigue performance. A number of cases were identified which gave rise to cross-overs in performance in moving from shorter to longer fatigue lives. The aim of the VA part of the work was to identify situations which might give rise to fatigue lives shorter than predicted by linear damage summation models, such as Miner's rule. Two such cases were identified: specimens which had been subjected to vibratory stress relief; and specimens in which weld 'quality' (as assessed by profile, heat affected zone hardness, extent and microstructure) varied. Explanations for these observations are proposed and supported by interpretation of a two-level block of small fatigue crack growth. © 1998 Elsevier Science Ltd.

(Keywords: variable amplitude loading; welded cover plates; vibratory stress relief; crack initiation; nonconservative linear damage summation)

INTRODUCTION

The 6 × 61 series of aluminium alloys are widely used and readily weldable structural Al-Mg-Si alloys. 6261 is a variant in this series which, in the specimens used in the work described in this paper, contained typically 0.74–0.82 Mg, 0.63–0.67 Si, 0.19–0.29 Fe, 0.26–0.34 Cu, 0.25–0.30 Mn, 0.025–0.120 Zn and 0.016–0.040 Ti. It is usually used in the peak aged T6 condition and mechanical properties of the specimens used were typically a 0.2% proof stress between 282 and 320 MPa, tensile strength between 301 and 367 MPa, and elongation of 10–15% over a 20 mm gauge length. These variations in properties and composition arose because the specimens were obtained from several heats of the alloy, in a number of different product forms (three sizes of I-beam and four plate sizes).

The work reported in this paper is a summary of the results obtained from several projects run over a

period of five years. The purpose is to provide an overview of the programme and to link short fatigue crack effects with observed variations in fatigue performance of the welded joints. This linkage is accomplished through an explanation for the observed stress-life ($S-N$) cross-overs, in terms of fatigue crack initiation and small crack growth phenomena. Whilst this linkage is not conclusively proven, it is clear that significant benefits in weld optimisation procedures could arise from further work in the area of crack initiation at aluminium weldments, particularly studies of the effects of changes in local geometry, size and softening in the heat affected zone (HAZ), and crack initiation and small crack growth under variable amplitude (VA) loading.

A number of thrusts were encompassed in the project scope, which was to examine the fatigue strength of extruded 6261-T6 I-beams with centrally located, welded cover plates under constant amplitude (CA) and variable (two-level repeated block) amplitude (VA) loading. The CA part of the work highlighted a number of factors which can cause a cross-over in fatigue performance in going from shorter to longer fatigue

^tThis work was performed while M.N.J. was with the School of Process and Materials Engineering, University of the Witwatersrand, WITS 2050, South Africa.

lives. The aim of the VA part of the work was to identify situations which might exacerbate such effects by giving rise to fatigue lives shorter than predicted by linear damage summation (LDS) models, such as Miner's rule.

Such models are important because design codes like BS CP 118 and BS 8118^{1,2} use Miner's rule to make life predictions for welded details subject to VA loading. This is generally reasonable where fatigue life is dominated by crack growth, as growth rate retardations are usually dominant in such cases, leading to conservative linear damage calculations. This would tend to be true, for example, for steel weldments where crack initiation is often bypassed by weld toe intrusions³. It is, however, recognised that under certain specific conditions linear damage calculations may be nonconservative. One such case occurs in two-level block loading of unwelded specimens where the higher amplitude stress is applied first for some proportion of the expected life and the lower amplitude stress is then applied until failure⁴. This appears to be related to the effect of higher amplitude cycles during the crack initiation and early growth phase of life (defined here as the development of a crack perhaps 0.5 mm in surface length).

In this regard, detailed experimental and analytical work was carried out by Grimshaw et al.⁵ on the effect of a single spike overload or a single block of high amplitude loads on the growth of small fatigue cracks approaching the first few microstructural barriers in a steel. This indicated clearly that acceleration in growth rate following a higher amplitude load was dependent on the position of the crack tip relative to microstructural barriers and the ratio of high-to-low load amplitude. The maximum effect often occurred just as the crack tip was approaching the first barrier. Such accelerations in growth rate can be several orders of magnitude, depending on the ratio of high-to-low load amplitudes⁶. Accelerated growth rate in this critical region could lead to a significant shortening of overall life, when quantified on the basis of linear damage summation.

Presumably, therefore, VA loading could give non-conservative Miner's rule predictions in situations where crack initiation and small crack growth are important factors in overall fatigue life. This should occur, under certain conditions, in aluminium weldments where weld toe intrusions are often absent and crack initiation occupies a substantial part of the lifetime⁷. Important life factors would then include local weld geometry, weld 'quality' and residual stress level, as these influence cross-over behaviour under CA loading, and hence should have an effect on the correlation between observed fatigue lives and those predicted by LDS.

The S-N test programme was structured to provide insight into the effects of some of these factors, while the potential importance of the crack initiation/small crack growth phase of life was examined separately, due to the difficulty of following the growth of small fatigue cracks at weld toes. Hence unwelded specimens of the parent alloy were used in a study of the behaviour of small fatigue cracks under CA and VA (two-level repeated block) loading. This part of the work revealed some interesting behaviour and will be extended in the future.

Crack closure effects are recognised as generally important influences on the crack growth transients which occur in VA loading, and limited information regarding crack closure and growth rate behaviour subsequent to single and repeated high amplitude loads was obtained from single-edge-notch bend (SENB) specimens of 6261-T6 in both the welded and unwelded condition.

While sections of this work have already been published^{6,8,9}, this paper provides an overview of the results of the complete programme to date and links crack initiation and small crack growth rate phenomena with observed behaviour of welded joints. It also presents new data on the influence of size on the fatigue strength of I-beams containing a centrally located welded cover plate, growth rate data for the parent plate and HAZ, and limited information on the closure and growth rate response subsequent to the application of single spike and 10 cycle block overloads of various amplitudes. The information obtained in the various parts of the programme is reviewed and summarised in the following sections.

OVERVIEW OF WELDED I-BEAM PROGRAMME

Constant amplitude loading of I-beam specimens (S-N testing)

Full experimental details are available in Refs^{8,9}. Around 80 specimens were used in this section of the work, which encompassed the following thrusts.

*The effect on CA fatigue strength of different cover plate geometries*⁸. S-N curves were developed at $R = 0.1$ for one size of I-beam specimen with centrally located welded cover plates of five different shapes (Figure 1). The I-beam was 100 mm deep, 75 mm wide with flange/web thicknesses of 4.2 mm. Cover plates had a maximum width of 40 mm and were 3 mm thick. S-N data were compared with the design curves from BS CP 118 and BS 8118 for welded details of the appropriate class⁸. BS 8118 is a limit-state code, i.e. its purpose is to define a condition beyond which the structure is unfit for its intended purpose, while CP 118 is predicated on the basis of permissible stresses. As both codes are extant, it is of some interest to determine what differences in life prediction may arise from the two codes when they are applied to widely used welded joints.

This can be determined from Figure 2, which shows a comparison between the results of the I-beam test programme and applicable design curves from CP 118 and BS 8118. Note that in all figures, to enable comparison with the relevant codes, nominal stresses are shown. It is interesting to note that for both as-extruded and welded I-beams, the CP 118 design curves corresponding to $R = 0.1$ are conservative only up to lives of around 2×10^6 cycles, and become unsafe at longer lives. It is generally accepted that the presence of residual stresses at the weld results in a high local stress ratio, irrespective of that in the applied stress cycle. Hence, following the suggestion of Armstrong¹⁰, a more appropriate design curve should be that for $R = 0.5$ in CP 118. This line is also shown in the figure, and certainly provides a better fit to the experimental data. The safety margin in strength prediction is, however, still negligible at lives $> 2 \times 10^6$ cycles.

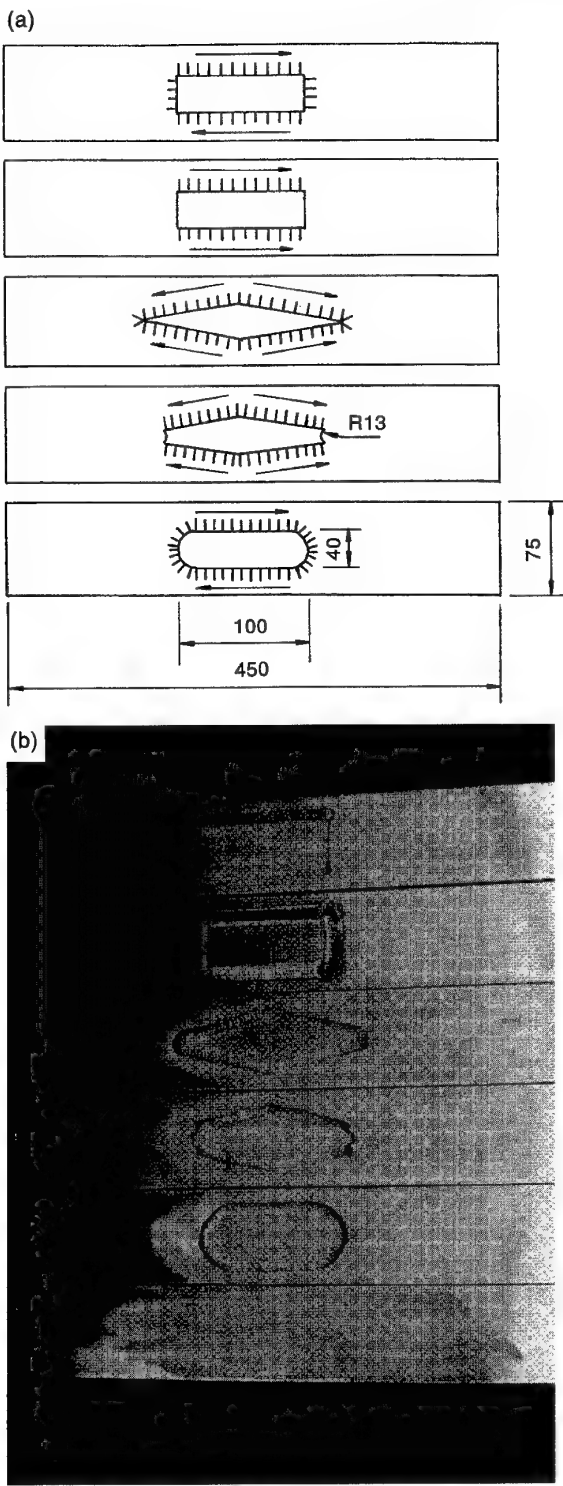


Figure 1 (a) Schematic drawing showing the five cover plate geometries used in this work on the $100 \times 75 \text{ mm}^2$ I-beam specimens. The arrows show the welding directions. (b) Actual cover plate specimens, showing the general quality of welds from Fabricator 2

In contrast, the design curves from BS 8118 (mean minus two standard deviations) are conservative at all lives and have slopes more compatible with those of the experimental data.

Table 1 gives the fatigue strength of the various cover plate geometries at lives of 10^5 cycles and 2×10^6

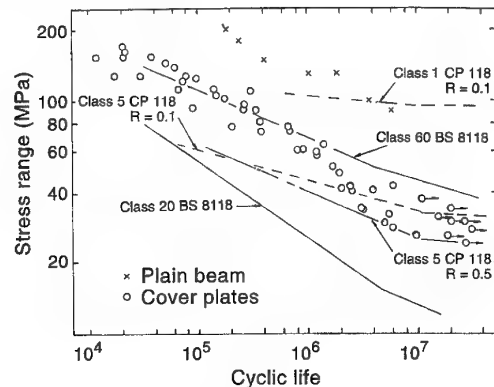


Figure 2 Comparison between the results of the CA S-N testing and the design curves from CP 118 and BS 8118

Table 1 Fatigue strengths of the various cover plate geometries⁷

Cover plate	End weld	Fatigue strength (MPa)	
		10^5 cycles	2×10^6 cycles
None		220	110
Rectangular	Yes	95	50
	No	120	43
Rhomboid	Yes	112	53
	No	114	48
Oval	Yes	100	50

10^6 cycles. Clearly, there are significant gains in fatigue strength that could derive from careful choice of cover plate geometry (some 26% at a life of 10^5 cycles and 23% at 2×10^6 cycles). A cautionary note must be added, however, in so far as a larger data set would be required to provide statistically reliable design curves. Equally, the ranking of the details changes in going from shorter to longer lives, i.e. there are cross-overs in fatigue performance in going from the shorter to the longer lives.

Data reported by Gurney³ for steel cover plates show very similar trends to those shown by the aluminium details. However, steel cover plates with unwelded ends showed higher fatigue strengths at both lives, whereas the aluminium data show that unwelded ends have a higher fatigue strength at 10^5 cycles, but not at 2×10^6 cycles. The difference in fatigue strength between welded and unwelded ends also depends strongly on the shape of cover plate termination; the difference is much more marked at 10^5 cycles for the gradual transition of the rhomboid cover plate. It can be surmised that such behaviour reflects the combined influence of overall stress flow, local stress concentration and weld 'quality' on crack initiation and small crack growth in the aluminium alloy (which is obviated in steel welds by toe intrusions³). This stage of crack growth is more extensive at longer lives, and hence long life data will show the effect of crack initiation influences more strongly than shorter life data.

The size effect on fatigue life. This was examined by the use of three different sized I-beams with a common cover plate and end detail geometry (rectangular with end weld). I-beam dimensions ranged

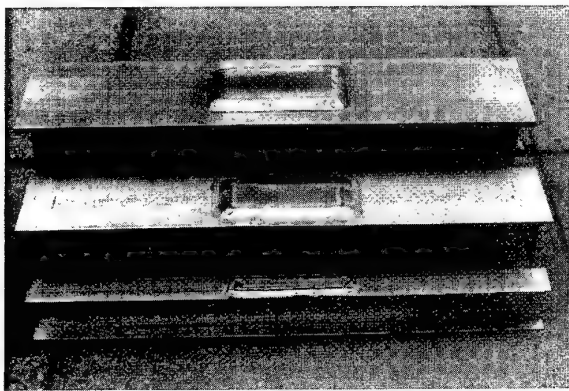


Figure 3 Illustration of the three different sized I-beams, with rectangular fully welded cover plates, used in the CA test programme

from $48 \times 27 \times 1.5 \text{ mm}^3$, through $100 \times 75 \times 4.2 \text{ mm}^3$ to $150 \times 101 \times 6.5 \text{ mm}^3$. Cover plates were consistently 100 mm long, but the width and thickness varied from $13 \times 1.5 \text{ mm}$, through $40 \times 3 \text{ mm}$ to $53 \times 5 \text{ mm}$. These dimensions were chosen because they corresponded to standard extrusion products, and were therefore more likely to represent commercial practice than if standardised ratios of cover plate to I-beam dimensions had been used.

Figure 3 shows samples of the three different sized I-beams used in this programme, all of which had rectangular cover plates with end welds, while Figure 4 shows relevant $S-N$ data with mean lines fitted by regression analysis. It is clear that a significant size effect exists, and that fatigue strength does not scale with size. It is also interesting that while the data for the $150 \times 101 \text{ mm}^2$ and $100 \times 75 \text{ mm}^2$ I-beams have approximately the same slope of mean line, that for the $48 \times 27 \text{ mm}^2$ I-beam does not. Indeed, from the limited data available, it appears that the smaller I-beam may show higher fatigue strengths than the $100 \times 75 \text{ mm}^2$ I-beam at lives $> 10^7$ cycles.

A simple finite element analysis was performed to model the cover plate and top flange of the three sizes of I-beam. Reasonable assumptions were made regarding the weld profile (based on sectioning of specimens) and values of the stress concentration factor

(k_t) at the weld toe were obtained. This indicated that typical stress concentration factors were $k_t = 3.5$ for the $48 \times 27 \text{ mm}^2$ specimens, $k_t = 2.7$ for the $150 \times 101 \text{ mm}^2$ specimens and $k_t = 2.3$ for the $100 \times 75 \text{ mm}^2$ specimens. Although this may explain why the data for the larger specimens falls below that for the $100 \times 75 \text{ mm}^2$ specimens, it does not clarify the situation regarding the smaller specimens. As discussed below, it is believed that an interaction between size and hardness of the HAZ, and local stress concentration (toe geometry), is leading to differences in initiation behaviour and early crack growth. More sophisticated modelling which includes microstructural parameters would be required to predict the fatigue life variations observed in this test programme.

The effect on fatigue strength of weld 'quality'. The effect on fatigue strength of the interaction between microstructural parameters and local stress concentration factors was examined in more detail through the concept of weld 'quality'. This was done for one cover plate geometry (rectangular with end weld), by using I-beam specimens from two different fabricators. 'Quality' was assessed in terms of weld toe angle and leg length (i.e. local stress concentration at the weld toe) and HAZ hardness and grain size (preheat and heat input effects). These differences were used to explain variations in observed fatigue life between specimens from the two fabricators, designated Fabricator 1 and Fabricator 2⁹. Fabricator 1 welds were made without preheat in a single pass around the periphery of the cover plate. They had a more variable profile than welds made by Fabricator 2, which used 40°C of preheat and made the weld in two passes (stop/start positions at opposite corners of the cover plates).

This profile difference was quantified in terms of the angle that the weld made with the I-beam flange at the toe, and the leg length on the flange. This was done destructively after testing, by sectioning the weld end region. Whereas the angle found with Fabricator 2 welds was fairly consistently around 30°, the angle at Fabricator 1 welds generally varied between about 24 and 48°, although isolated regions of undercut were observed. Similar observations applied to the leg length, which was consistently close to 7.5 mm for Fabricator 2 welds, but varied between 7 and 10 mm on Fabricator 1 welds. The inference of these observations is that local weld toe stress concentrations would be more variable, and higher in places, for Fabricator 1 welds than for those made by Fabricator 2.

However, fatigue performance in terms of crack initiation is also dependent on the hardness of the alloy and grain size, which are governed by heat input and preheat. Measurements of grain size in the HAZ, hardness values and extent of softened region⁹ indicated that Fabricator 2 welds had a more extensive, and softer, HAZ than did Fabricator 1 welds. The interaction between weld geometry (local k_t) and heat input/preheat led to a cross-over occurring in the CA $S-N$ data for I-beams welded by the two different fabricators.

This effect can be seen in Figure 5, where it appears that Fabricator 1 specimens have superior fatigue strengths at lives $> 10^5$ cycles, while Fabricator 2 specimens perform better at lives $< 10^4$ cycles. An

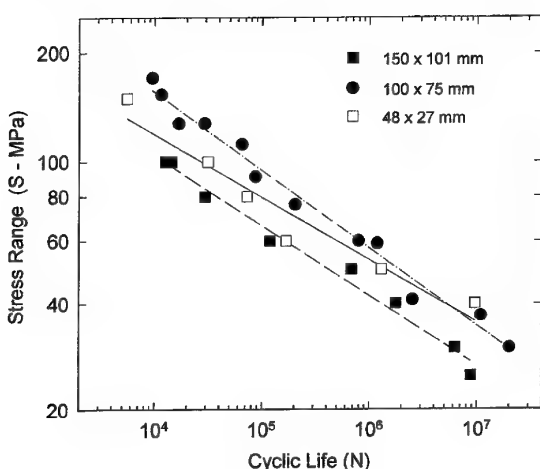


Figure 4 CA $S-N$ data for the three sizes of I-beam specimen

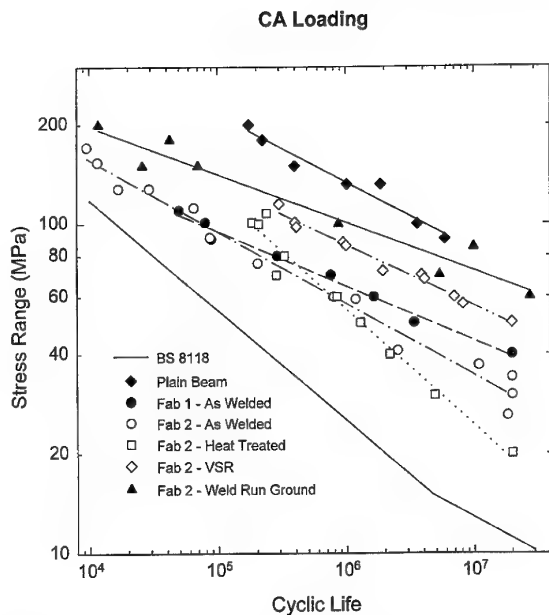


Figure 5 CA S-N results showing the effect on fatigue strength of different fabricators, vibratory and thermal stress relief

explanation can be proposed based on the softer, larger grained and more extensive HAZ in Fabricator 2 welds, which allows easier crack initiation than is the case for Fabricator 1 welds. At long lives, where crack initiation dominates life, the fatigue performance of Fabricator 1 welds is then better despite the slightly higher stress concentration associated with a larger weld toe angle. Conversely, at short lives, where crack initiation accounts for a smaller life percentage, the higher stress concentration of Fabricator 1 welds exerts an influence during the short crack growth regime and leads to poorer fatigue performance than for welds made by Fabricator 2. In real terms the difference in fatigue strength at 2×10^7 cycles is around 25%, with welds made by Fabricator 1 showing a fatigue strength of perhaps 40 MPa while those of Fabricator 2 average around 30 MPa.

The effect on fatigue strength of subresonant vibratory stress relief (VSR) and heat treatment (a full T6 thermal cycle). This work used I-beam specimens with a rectangular end weld cover plate geometry⁹. VSR appears to confer a significant increase in fatigue strength over the range of lives examined (2×10^5 – 2×10^7 cycles). The gain in fatigue strength at 2×10^7 cycles is around 15 MPa – an increase of approximately 50% over the strength of the untreated weld. The slope of the line is very similar to that of the as-welded I-beams, indicating that VSR would give an advantage at all lives. Thus in this case, at least, it is clear that VSR has not ‘consumed’ any of the fatigue life but has beneficially increased fatigue performance by reducing tensile residual stresses, even though the applied stress ratio has a positive value of 0.1.

In contrast, restoring the hardness of the HAZ through a second T6 heat treatment (although with lower tensile properties) has led to quite a severe reduction in fatigue performance at lives $> 8 \times 10^5$ cycles. At 2×10^7 cycles the fatigue strength is down

to 20 MPa, a reduction in strength of some 33% over the as-welded I-beams. Interestingly, the slope of the curve is very different to that found for the other cases examined, and at lives shorter than 8×10^5 cycles the heat treated I-beams appear to perform better than those in the as-welded condition. Indeed, assuming that the trend continues along the linear regression line shown, the performance of VSR and heat treated specimens would become the same at lives of around 10^5 cycles.

The conclusion from this observation of similar fatigue strengths at shorter lives is that the reduction in residual stresses is more influential in this region than a decrease in tensile and yield strengths, i.e. that the main effect of the reduction in residual stresses is on crack growth. Equally, lower tensile properties would encourage earlier crack initiation and lead to a marked decrease in fatigue performance of the heat treated specimens at longer lives, where the initiation phase is a major part of the overall life.

Two-Level repeated block loading of I-beam specimens (S-N testing)

In the VA part of the testing programme, two-level repeated block loading was applied until failure to as-welded specimens from both fabricators, and to VSR and heat treated specimens from one of the fabricators⁹. The number of high-to-low amplitude cycles in a single two-level block ranged from 1/20, through 10/20 to 1/1000 and 1/50,000. Load amplitude increases of 25%, 75% and 150% were considered. Test parameters were similar to those above, in particular R was maintained at 0.1 for both high and low amplitudes. However, testing was performed at 20–40 Hz using a computer controlled servohydraulic testing machine. The higher frequency was used for longer life tests (high-to-low amplitude load ratios of 1/1000 and 1/50,000). Some 90 specimens were manufactured for this part of the test programme.

This work is reported in detail in Ref.⁹, and the important results can be summarised as follows. Miner’s rule life predictions, based on the CA data, are conservative with the exception of I-beams welded by Fabricator 1 and I-beams which were given VSR. For the VSR specimens it should be noted, however, that although linear damage summation gave values < 1 , the observed lives were still generally better than those found with the as-welded I-beams under similar VA test conditions. Thus its use in increasing fatigue life is not in doubt in these particular tests. Nonetheless, the issue of why LDS is nonconservative in these two cases remains an interesting, and unanswered, question. It is not clear also whether the nonconservatism arises in the crack initiation or crack growth stages of life, or both. There is a clear need for further experimental work in this area, preferably coupled with finite element modelling.

In general, the Miner’s life prediction became more conservative as the number of low amplitude cycles increased in a VA block (from 1/20, through 10/20 to 1/1000 and 1/50,000). This is in accord with the normal observation that growth rate retardation in VA loading increases with increase in number of low amplitude cycles.

CRACK GROWTH RATE TESTING OF SENB SPECIMENS

Fatigue cracks in the welded I-beam specimens invariably initiated in the HAZ at the weld toe. Crack growth rate tests were therefore performed on SENB specimens in the unwelded condition (parent plate) and on specimens joined by welding, using the same process parameters as for the I-beam specimens. The notch was then machined to be in the HAZ, allowing typical growth rate data to be obtained. Closure measurements were made using a back-face strain gauge and incorporated an offset displacement circuit to increase the resolution of changes in compliance. K_{op} was estimated as the onset of linearity in the upper part of a load-displacement trace. Testing was carried out at 20 Hz on specimens $10 \times 30 \times 120$ mm, containing a 45° notch 5 mm deep.

CA testing was performed with either a constant K_{max} or at R values from 0.1 through to 0.7. VA growth rate data were acquired for a 1/20 ratio of high-to-low amplitude loads (maintaining $R = 0.1$), with a load amplitude increase of 150%. Other VA tests involved the application of a single high amplitude load or one block of 10 high amplitude loads. Growth rate and closure response were monitored in these tests as a function of the ratio of crack length to monotonic plastic zone size for the high amplitude load. The intention here was to examine the correspondence between growth rate and closure trends subsequent to an overload, and to see the effect of a change from a single spike to a block of overloads. Load amplitude increases of 25%, 75% and 150% were used.

Figure 6a and 6b show growth rate data obtained under a variety of experimental conditions from long cracks in the parent plate and HAZ, respectively. Two curves are shown for $R = 0.1$, representing two different heats of the aluminium alloy, and are included to indicate the level of scatter between individual tests performed under nominally similar conditions. Figure 7 shows closure data obtained from tests at $R = 0.1$ for both conditions of the alloy. Considering firstly the parent plate data in Figure 6a, it can be seen that the $K_{max} = \text{constant}$ curve is very similar to that obtained at $R = 0.7$. This can be interpreted as confirming that closure is not having an effect under these conditions, and implies that K_{max} in the fatigue cycle does not influence the threshold condition in this material (for a ΔK value of $2 \text{ MPa m}^{\sqrt{m}}$ and $R = 0.7$, $K_{max} = 6.67 \text{ MPa m}^{\sqrt{m}}$ compared with $K_{max} = 30 \text{ MPa m}^{\sqrt{m}}$ at $\Delta K \approx 2.5 \text{ MPa m}^{\sqrt{m}}$ in the $K_{max} = \text{constant}$ test). This is in contrast to the proposal of Vasudevan *et al.*¹¹ that near-threshold growth rate phenomena can be explained in terms of a relationship between K_{max} and ΔK . The ΔK_{eff} curve for $R = 0.1$ lies reasonably close to both the $R = 0.7$ and $K_{max} = \text{constant}$ curves and, in fact, the use of closure data affords a fairly good rationalisation of the growth rate data over the range of stress ratios considered.

The data for the two-level block loading test, with a 1/20 ratio of high-to-low amplitude cycles and a high load increase of 150%, lie considerably below the other curves. Note that the high amplitude ΔK values are being shown in this plot. Equivalent closure values, measured just prior to applying the high amplitude load, are shown in Figure 7. With a high load

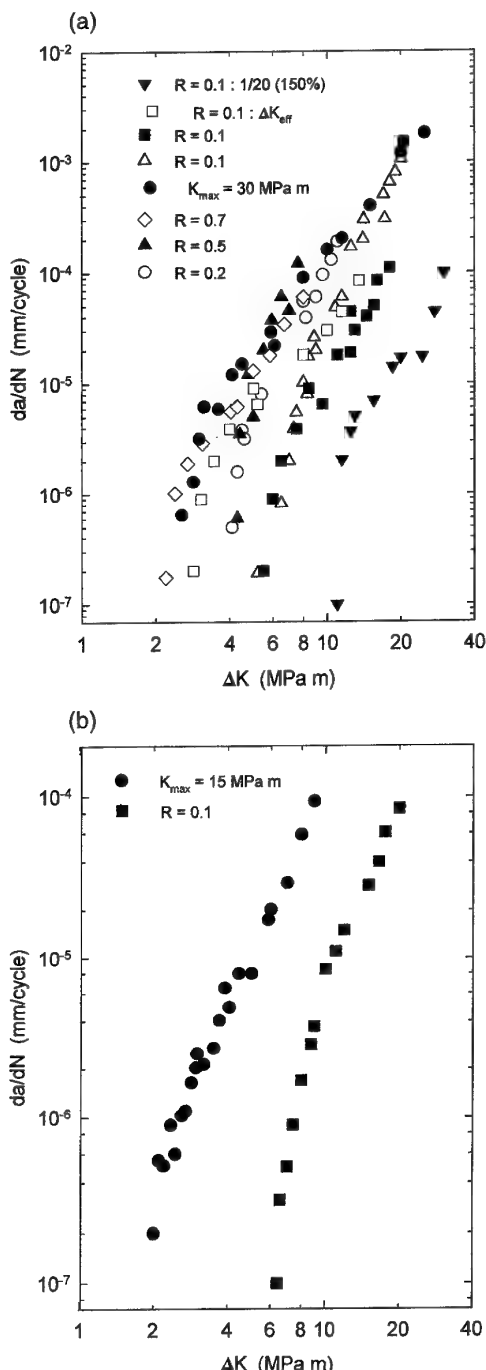


Figure 6 (a) Growth rate data for the unwelded SENB specimens of the 6261-T6 alloy, showing the influence of stress ratio, and comparing $K_{max} = \text{constant}$ testing with factoring out closure through use of ΔK_{eff} . (b) Typical growth rate data for the HAZ in the 6261 alloy

increase of 150% over the baseline load, other tests in this programme have shown the crack to arrest during the low amplitude cycling. If this effect is factored out of the growth rate data, i.e. only the high amplitude cycles are assumed to be contributing to growth, the data then fall within the likely scatter band of the $R = 0.1$ results.

The HAZ material appears to show similar growth

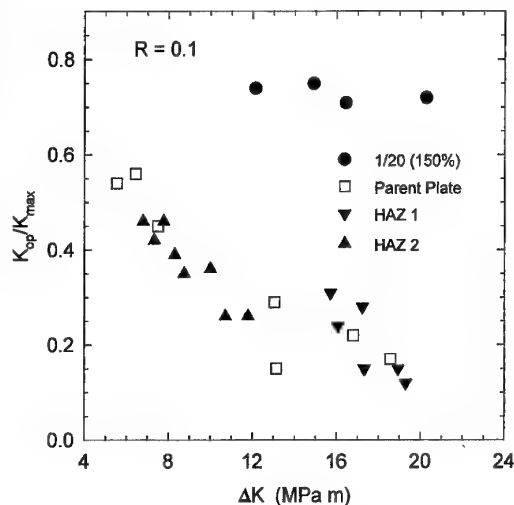


Figure 7 Closure data for parent alloy and the HAZ material. Data for the 1/20 ratio of high-to-low load amplitude (150% overload ratio) are also included

rate and closure trends to the parent plate under CA conditions (*Figure 6b*) although, as will be demonstrated shortly, both growth rate and closure response appear to be more variable than the parent plate under VA loading when a single high amplitude spike or single block of 10 high amplitude loads is applied.

In these latter tests, three levels of high load increase were considered, namely 25%, 75% and 150%, with a baseline $\Delta K = 10 \text{ MPa} \sqrt{\text{m}}$. In all cases, application of a 150% overload caused immediate arrest of the crack and the data are not shown in *Figures 8* and *9*, which present the results. *Figure 8* shows growth rate data as a function of the ratio of crack length (post-overload) to the high load monotonic plastic zone size. *Figure 9* gives the relevant closure information, plotted as K_{op}/K_{max} versus the same ratio as for *Figure 8*. Some observations can be made from these results, although larger data sets would be required to draw definitive conclusions. Firstly, there is, in general, a reasonable correspondence between trends in closure and trends in growth rate subsequent to an overload, although the use of closure alone would not adequately model the growth rate data. This can be seen, for instance, by comparing the closure data for the parent plate subject to a block of 75% overloads with the closure. Although there is an immediate, fairly sharp reduction in closure level after application of the high load block, there is not a concomitant increase in growth rate.

Secondly, a single 25% overload spike causes an immediate acceleration in crack growth rate in both HAZ and parent plate, which was not observed in any of the other tests. No other systematic differences between a single spike overload and a block of 10 overloads can be identified. All tests gave rise to growth rate retardation, although this was delayed in the case of the single 25% high load spike. When an immediate acceleration or retardation in growth rate followed the application of the high loads, this generally reached a peak value within a crack growth increment of about 0.5 times the high load monotonic plastic zone size. The only exception seen was for the case of a single block of 25% overloads applied to

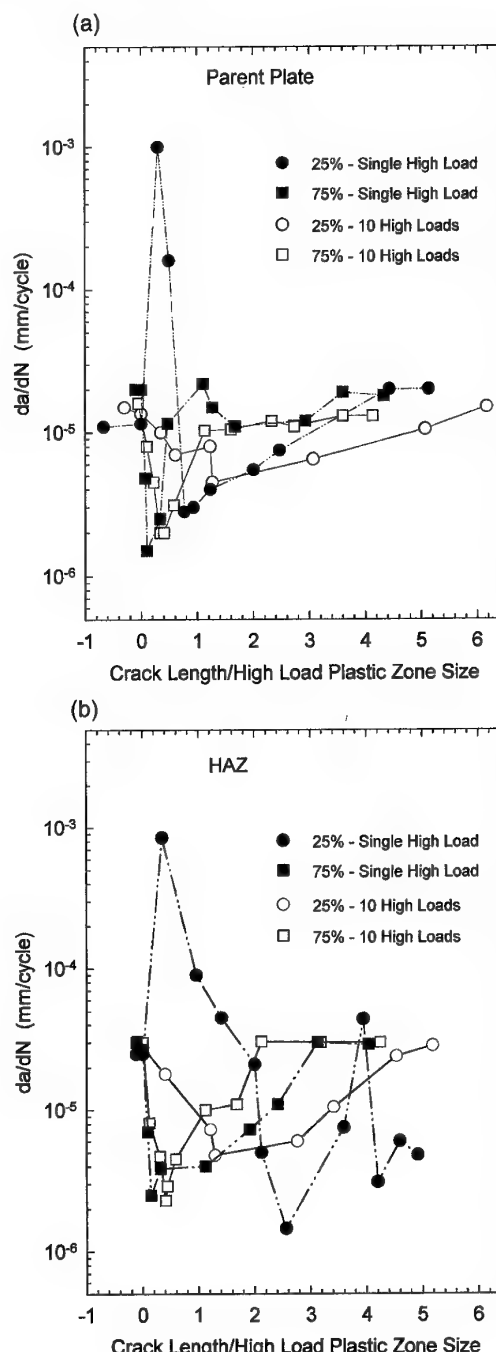


Figure 8 (a) Parent plate data – transients in crack growth rate as a function of the ratio of crack length increment (post-overload) to high load monotonic plastic zone size for 25% and 75% increases in load amplitude. (b) HAZ data – transients in crack growth rate as a function of the ratio of crack length increment (post-overload) to high load monotonic plastic zone size for 25% and 75% increases in load amplitude

the HAZ material. When delayed retardation occurred, this reached a peak at crack growth increments ≥ 1.0 of the high load monotonic plastic zone size. Variability in growth rate and closure data was higher for the HAZ material.

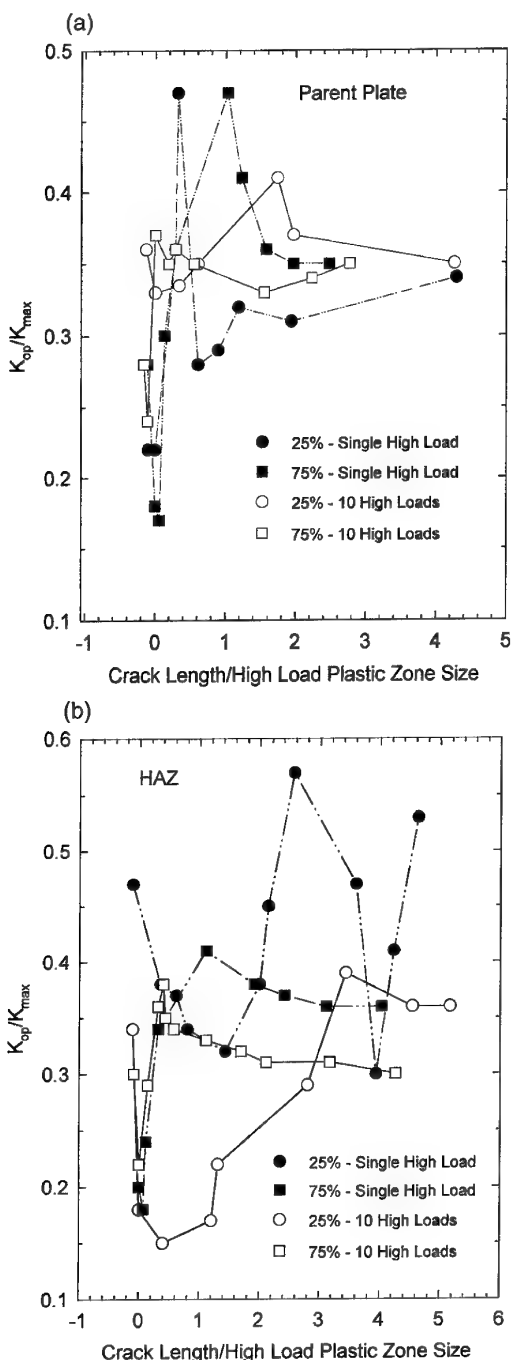


Figure 9 (a) Parent plate closure data – transients following the application of single and blocks of 10 high amplitude loads. (b) HAZ data – transients following the application of single and blocks of 10 high amplitude loads

SMALL CRACK GROWTH

If the cross-overs observed in the fatigue performance of the welded I-beams are related to events which occur in the crack initiation and small crack growth stage of life, clarification of relevant phenomena requires study of small fatigue cracks. The growth of such cracks at a weld toe is difficult to follow, so this part of the work used hourglass-shaped tension

specimens of the as-extruded 6261-T6 alloy, tested at 10 Hz with $R = 0.1$. Experimental details are given in Ref. ⁶.

One aim was to determine whether linear damage summation would be less accurate in the crack initiation phase (defined as detection of a crack with a surface length $< 20 \mu\text{m}$) compared with the early crack growth phase of fatigue life (surface lengths 20–500 μm). A second aim was to examine accelerations in growth rate during, and subsequent to, overload blocks applied when the crack size was comparable to grain size. The purpose here was to determine whether there exists a critical combination of overload, crack length and crack tip position relative to microstructural barriers. Such a combination might give rise to very high acceleration ratios, and subsequently to LDS values < 1 . Attention was directed also towards the case of relatively small load amplitude increases, which have been largely ignored in the literature to date.

Initially, CA growth rate data were acquired for stress amplitudes of 175, 200, 225 and 240 MPa, i.e. applied/proof stress ratios ($\sigma_{\max}/\sigma_{\text{proof}}$) of 0.55 to 0.75. VA block loading tests were performed using stress amplitudes of 175:240 MPa, 200:240 MPa and 225:240 MPa (i.e. load amplitude increases of 6.7%, 20% and 37%), with the lower stress always applied first. Figure 10⁶ shows growth rate acceleration ratios as a function of surface crack length for the various two-level VA block loading tests. Acceleration ratio is defined as growth rate during a high stress amplitude block over the growth rate in the previous low stress amplitude block. The acceleration ratio generally increases at a given crack length, with increase in ratio of high-to-low stress amplitude. A peak in this acceleration is evident in all three cases at a surface crack length between 80 and 130 μm , which could well correspond to an interaction with the first grain boundary in the depth direction. Acceleration ratios appear to become reasonably constant as the crack becomes longer.

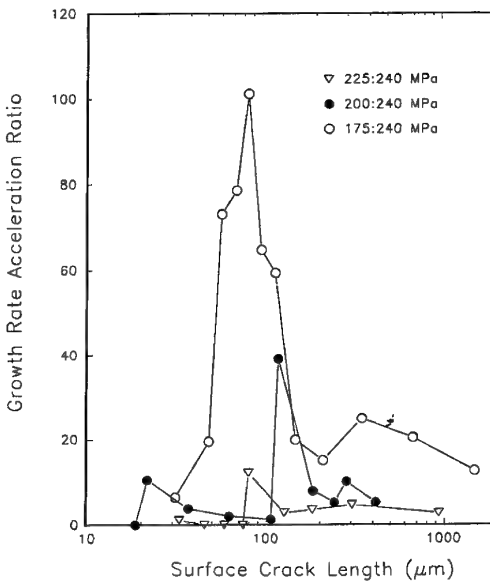


Figure 10 Small crack growth rate acceleration ratio as a function of surface crack length, for the three different high-to-low stress amplitudes

It was interesting to observe that when the surface crack length was less than $\approx 80 \mu\text{m}$ (where any closure effects would be limited) and the high load amplitude was small (225:240 MPa loading – a 6.7% overload), crack growth retardation sometimes occurred *during* the overload block (1000 cycles). This possibly represents a situation where interaction between blunting of the crack tip and its position with respect to the microstructure offset any gain from increase in crack tip stresses. Retardation *subsequent* to overload blocks occurred in the 200:240 MPa and 175:240 MPa tests, and appeared to be maximised in the 50–150 μm surface crack range, indicating again a possible interaction with the first grain boundary.

Miner's rule appears to a poor indicator of the number of cycles to develop a 20 μm surface length crack in this 6261-T6 alloy, as indicated in *Table 2*. The variability in life to develop such a crack, from 3.11 times greater than predicted for the case of 200:240 MPa block loading to 4.07 times lower than predicted for 175:240 MPa loading, appears likely to be explicable in terms of position of the crack tip relative to important microstructural influences (initiating defect size, second phase particles, etc.) during application of overload blocks. In contrast, predicted and actual lives to grow a crack from 20–500 μm are very similar. All that this implies, however, is that the net effect of growth rate accelerations and retardations is neutral for the particular two-step load blocks used.

Hence these data support the hypothesis advanced earlier that, where crack initiation and small crack growth are important to life, VA loading could potentially lead to nonconservative Miner's rule predictions. This effect would be expected to be variable, and most noticeable in situations where significant differences can occur in local geometry, hardness, microstructure and residual stresses, between nominally similar specimens. One example of this, as indicated in this programme, should be the case of aluminium weldments.

CONCLUSIONS

This relatively wide ranging programme of work has shed some light on an interesting area of life prediction for weldments, namely the reasons for observed cross-overs in fatigue performance for nominally similar specimens, and the influence they may have on linear damage summation modelling of fatigue life. The reasons are believed to relate to events which occur during crack initiation and growth to a size $\sim 500 \mu\text{m}$. This is of some practical relevance as a number of statutory design codes incorporate linear damage

assessment in handling VA loading. The main points can be summarised as follows.

1. Different cover plate terminations (geometry and whether welded or not) give rise to cross-overs in fatigue performance.
2. Changing the scale of I-beam and cover plate specimens leads to cross-overs occurring in fatigue performance.
3. Weld 'quality' differences between I-beam specimens from two fabricators, as quantified by weld profile and grain size/hardness in the HAZ, led to a cross-over occurring in the constant amplitude *S-N* data at a life $\sim 5 \times 10^4$ cycles. Welds made with a poorer profile, but smaller and harder HAZ (Fabricator 1), performed better at longer lives ($> 10^5$ cycles). Welds made with a better profile but with a softer, larger grained and more extensive HAZ (Fabricator 2) performed better at short lives ($< 10^4$ cycles). Two-level block loading of Fabricator 1 specimens led to nonconservative Miner's rule predictions.
4. Miner's rule predictions of life, based on constant amplitude *S-N* data, were found to be nonconservative under two-level block loading for the welded I-beam specimens which had been subjected to vibratory stress relief (VSR).
5. Miner's rule appears to be a poor indicator of the number of cycles to develop a 20 μm surface length crack in this 6261-T6 alloy under the specific block loading conditions used. Acceleration and retardation events cancel each other out during growth between 20 and 500 μm .
6. Growth rate acceleration and retardation during two-level block loading of small fatigue cracks is dependent on the ratio of high-to-low amplitude loads, and the crack size relative to important microstructural dimensions.

ACKNOWLEDGEMENTS

The assistance of Rick Lambrecht and Neil Sutcliffe with the experimental work, and financial assistance from the Aluminium Federation of South Africa, together with the assistance of Hulett Aluminium and Woma Flow Jet SA is gratefully acknowledged.

REFERENCES

- 1 BSI Code of Practice CP 118, *The Structural Use of Aluminium*. British Standards Institution, 1969.
- 2 BSI BS 8118, *The Structural Use of Aluminium, Part 1: Code of Practice for Design*. British Standards Institution, 1991.

Table 2 Comparison between actual life and predicted life (Miner's rule)

Stress ratio (MPa)	Cyclic life to initiate 20 μm crack		Cyclic life to grow from 20 to 500 μm	
	Predicted (Miner's rule)	Actual	Predicted (Miner's rule)	Actual
225:240	17149	26531*	36157	30868
		9179		41467
200:240	56535	176105	95697	101209
175:240	172120	42289	259480	248129

* Data from two different cracks in one specimen.

- 3 Gurney, T. R. *Fatigue of Welded Structures*, 2nd edn. Cambridge University Press, Cambridge, 1979.
- 4 Ibrahim, M. F. E. and Miller, K. J., Determination of fatigue crack initiation life. *Fatigue and Fracture of Engineering Materials and Structures*, 1980, **2**, 351–360.
- 5 Grimshaw, C. S., Miller, K. J. and Rees, J. M., Short fatigue crack growth under variable amplitude loading: a theoretical approach. In *Short Fatigue Cracks*, eds K. J. Miller and E. R. de Los Rios. Mechanical Engineering Publications, 1992, pp. 449–465.
- 6 James, M. N. and De Los Rios, E. R., Variable amplitude loading of small fatigue cracks in 6261-T6 aluminium alloy. *Fatigue and Fracture of Engineering Materials and Structures*, 1996, **19**(4), 413–426.
- 7 Maddox, S. J., Fatigue design of welded aluminium structures.
- 8 2nd International Conference on Aluminium Weldments, Munich, Germany, 24–26 May, 1982.
- 9 James, M. N., Lambrecht, H. O. and Paterson, A. E., Fatigue strength of welded cover plates on 6261 aluminium alloy I-beams. *International Journal of Fatigue*, 1993, **15**(6), 519–524.
- 10 James, M. N., Paterson, A. E. and Sutcliffe, N., Constant and variable amplitude loading of 6261 aluminium alloy I-beams with welded cover plates – influence of weld quality and stress relief. *International Journal of Fatigue*, 1996, in press.
- 11 Armstrong, R. A., Design and fatigue life prediction techniques for welded aluminium joints. 3rd International Conference on Aluminium Weldments, Munich, Germany, 15–17 April, 1985.
- Vasudevan, A. K., Sadananda, K. and Louat, N., Two critical stress intensities for threshold fatigue crack propagation. *Scripta Metallurgica et Materialia*, 1993, **28**, 65–70.

PII: S0142-1123(97)00033-9

Fatigue growth of small corner cracks in aluminum 6061-T651

R.L. Carlson, D.L. Steadman, D.S. Dancila and G.A. Kardomateas

School of Aerospace Engineering, Georgia Institute of Technology, Atlanta, GA 30332-0150, USA

Results of an experimental investigation of the fatigue growth of small corner cracks emanating from small flaws are presented. A three-point bending state of loading was used and, by virtue of the orientation of the square cross-section of the specimen, the maximum tensile stress was developed at the middle of the gage section and on a corner edge. A growth-arrest behavior was observed and increases in crack length during growth periods were of the order of the transverse grain size, so it is inferred that grain boundaries act as barriers to continuing growth. © 1998 Elsevier Science Ltd.

(Keywords: small cracks; anomalous growth; corner cracks; intermittent growth; grain boundary wall barriers)

INTRODUCTION

The discovery by Pearson¹ that the growth of 'small' fatigue cracks differed from that of 'long' cracks has served as an impetus for the initiation of many subsequent research investigations. Early papers by Miller², Suresh³, Lankford and Davison⁴ and Suresh and Ritchie⁵ identified some of the important parameters and provided classification schemes which emphasized the importance of crack size scale relative to microstructural features. The importance of microstructural features has been established further in research conducted by Chan and Lankford⁶, Navarro and de Los Rios⁷, Tanaka and Akinawa⁸, and Halliday⁹. Some of the investigations conducted have focused on the development of analytical methods for predicting growth histories. Edwards and Newman¹⁰ have suggested that the 'anomalous' growth of small cracks is caused by either an absence or a reduction in obstruction to closure. They have proposed the use of an effective range of stress intensity factors formulated to account for a reduction in closure obstruction.

EXPERIMENTAL DETAILS

Specimens

The objective of the study presented here was to introduce a new experimental procedure for investigating small corner crack growth. In contrast to surface cracks, corner cracks provide a capability for measuring crack depth. Also, cracks are often observed to be initiated at corners in service, and should be of concern for the development of predictive codes.

The specimen used in the present investigation is shown in *Figure 1a*. The specimen had circular cross-sections at the ends and a gage cross-section which

was square. The loading state applied to the specimen is shown in *Figure 1b*. By virtue of the orientation of the square cross-section of the specimen, and the application of three-point bending, the maximum tensile stress is developed at the middle of the gage section and on a corner edge, i.e. the neutral axis of bending coincides with a diagonal of the square cross-section. Since the region of high tensile stress is localized, the specimen should be suitable for the development of 'natural' cracks in a reasonably predictable location. Initially, of course, multiple cracking could be expected, but ultimately a dominant crack could be expected to develop. Swain¹¹ has suggested criteria for evaluating data for which multiple surface cracks occur.

For the initial tests, using the specimen and loading state described in *Figure 1a* and *1b*, a small corner notch was introduced at the location of maximum tensile stress to serve as a site for crack initiation. The test material for the investigation was the aluminum alloy 6061-T651, and specimens were machined from 16 mm diameter bar stock. The 0.2% offset yield strength was 283 MPa and the ultimate strength was 293 MPa. The average transverse grain size was 200 µm. The longitudinal grains were elongated and varied widely about an average of 350 µm.

Corner notches with a 60° included angle were cut at the midpoint of the specimen cross-section by use of a digitally controlled slitting saw. The faces adjacent to the notch were then polished with five grades of abrasive paper, ranging from 600 to 2000 grit. Final polishing was performed by use of a 3 µm and then a 1 µm diamond paste. By polishing after notching, it is possible to obtain very small notches.

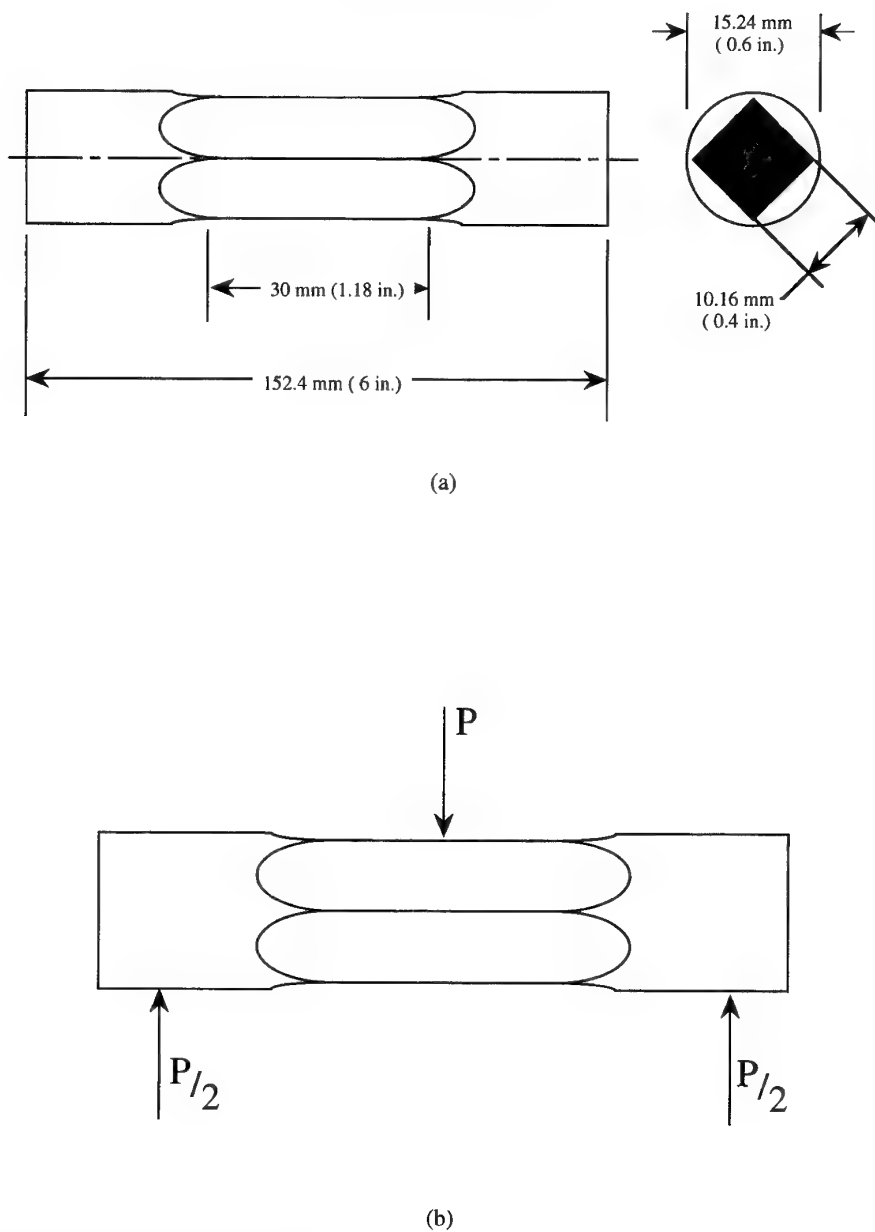


Figure 1 (a) Test specimen used; (b) loading state used

Test procedure

Experiments were conducted on an Instron servohydraulic testing machine which applied sinusoidal loading at 10 Hz. For the data reported the load ratio was $R = 0.0625$. A telemicroscope with a video camera and a monitor were used to measure crack length growth. Details of this system have been described previously¹². Crack lengths were measured at fixed intervals to obtain data for records of crack length versus loading cycle.

Cracks which started from notches were initiated by the application of a nominal maximum stress which was 0.9 of the yield strength. Small cracks were initiated after about 200,000 cycles of loading. The load was then reduced to produce a maximum stress of about 0.5 of the yield strength. Two types of experiments were conducted. In one test the growth of

a moderately long crack was monitored. Notch depths for these tests were about 150 μm .

Although the use of the stress intensity factor as a correlation parameter for small crack growth has been questioned, its use does provide a means of comparing long and small crack growth. It is, therefore, used for that purpose here. Its incorporation as a parameter for design for small crack growth is another issue which is discussed in a subsequent section. The stress intensity factor used is based on results for a corner crack in a bar with rectangular cross-section in the NASA/FLAGRO¹³ computer program.

Test results

Results for a long crack test are presented in the log-log plot of *Figure 2* for the near threshold region.

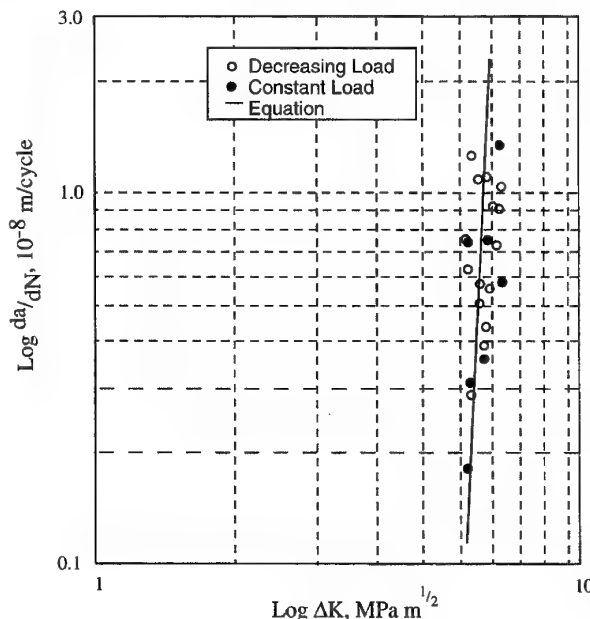


Figure 2 Growth rate in the near threshold region

A straight line through the data points can be represented by the equation

$$da/dN = 10^{-8}[\Delta K/6.7]^{28} \quad (1)$$

The exponent in Equation (1) is not to be confused with the exponent of the Paris equation for region II growth rate behavior. The large value of this exponent is the result of the fact that the da/dN vs. ΔK curve in region I, the threshold region, is much steeper than that for region II.

Data obtained from small crack experiments are presented in Figure 3a and 3b. The load applied at the midpoint of the test specimens was 854 N, and crack length values shown include the notch depth. The growth-arrest behavior which has been reported previously by other investigators is clearly evident. In addition to the crack lengths not being initially the same on the two corner faces, the directions of the crack paths were not always normal to the specimen axis and branching was sometimes observed. When branching occurred, one branch eventually became dominant.

Miller² has given a qualitative description of crack growth history by using the crack length on a left-hand ordinate and sizes of microstructural features on a right-hand ordinate. This provides a perspective for comparing the length of a growing crack with such features as inclusions and grain size. If, for the corner crack, it is assumed that the arc of the crack front is circular and centered at the crack corner, the number of grains, on average, along a crack front for a given crack length can be determined from the equation

$$n = \pi a/2D \quad (2)$$

where a is the crack length (or radius to the crack front from the corner), n is the number of grains along the crack front, and D is the transverse grain size. Equation (2) has been used to determine the scale of the right-hand ordinates of Figure 3a and 3b. Comparisons of the two ordinates then indicates the number of

grains encountered, on average, for a given crack length.

An examination of the initial growth-arrest features in Figure 3a would indicate that an elaborate scheme for computing growth rates is not warranted. Nevertheless, continuing growth is occurring and a growth trend is indicated. A simple method for representing the growth rates has been adopted. A trend curve has been developed by connecting successive inner corners of the steps. The rates so determined are represented by round data points on the Cartesian coordinate plot of Figure 4 for both faces of the corner. The small crack growth data are to the left of the near threshold curve of Equation (2). Thus, for a given ΔK , the small crack growth rates are greater than those for long cracks.

Data for a second small crack growth experiment are presented in Figure 2b, and they reveal that the crack length versus cycles histories for the two tests are not reproducible. The data of Figure 3b also exhibit an abrupt increase in crack length at a value of about 420,000 cycles. This may be attributed to the nature of crack initiation for this test. Cracks were initiated at the intersection of the root surface of the notch and the outer faces. On each face the direction of the initial crack deviated from a normal to the corner edge by about 40°. The crack on one face was about a plane normal to the corner edge, whereas the crack on the other face was below the normal plane. It has been inferred from this observation, and from the abrupt crack length increase, that the initial microcrack planes associated with the observed surface cracks were distinct and not connected, i.e. they were separated by an uncracked ligament which introduced a bridging mechanism. It is suggested that when this ligament was fractured, the observed sudden increase in crack length occurred. The development of multiple microcracking and subsequent coalescence has been observed and discussed by Swain¹¹ for surface cracks.

In view of the initial behavior indicated in Figure 3b, no attempt was made to calculate growth rates for this phase of growth, since the use of a stress intensity factor here is not considered reasonable. Growth rates beyond 420,000 cycles were, however, calculated, and these results are represented on the growth rate versus range of stress intensity factor plot of Figure 4 by square data points. Clearly, a comparison of these data with those for the growth data from Figure 3a again indicates a lack of reproducibility. The crack lengths used for this latter computation ranged from about 800 to 1300 μm . These crack lengths may appear to exceed limits used to define small cracks. It has, however, been observed¹⁴ that small crack behavior may extend to crack lengths which are about 10 times the grain size. Since the grain size in the plane of crack growth is about 200 μm , the growth range for which the calculations were made is within this size limitation. Consequently, the results reaffirm the importance of grain size.

DISCUSSION OF RESULTS

Two distinct features of small fatigue crack growth distinguish it from long crack growth. One is the observation that early growth for small cracks is intermittent, i.e. periods of growth and arrest are observed. The second is that if long crack methods of analysis

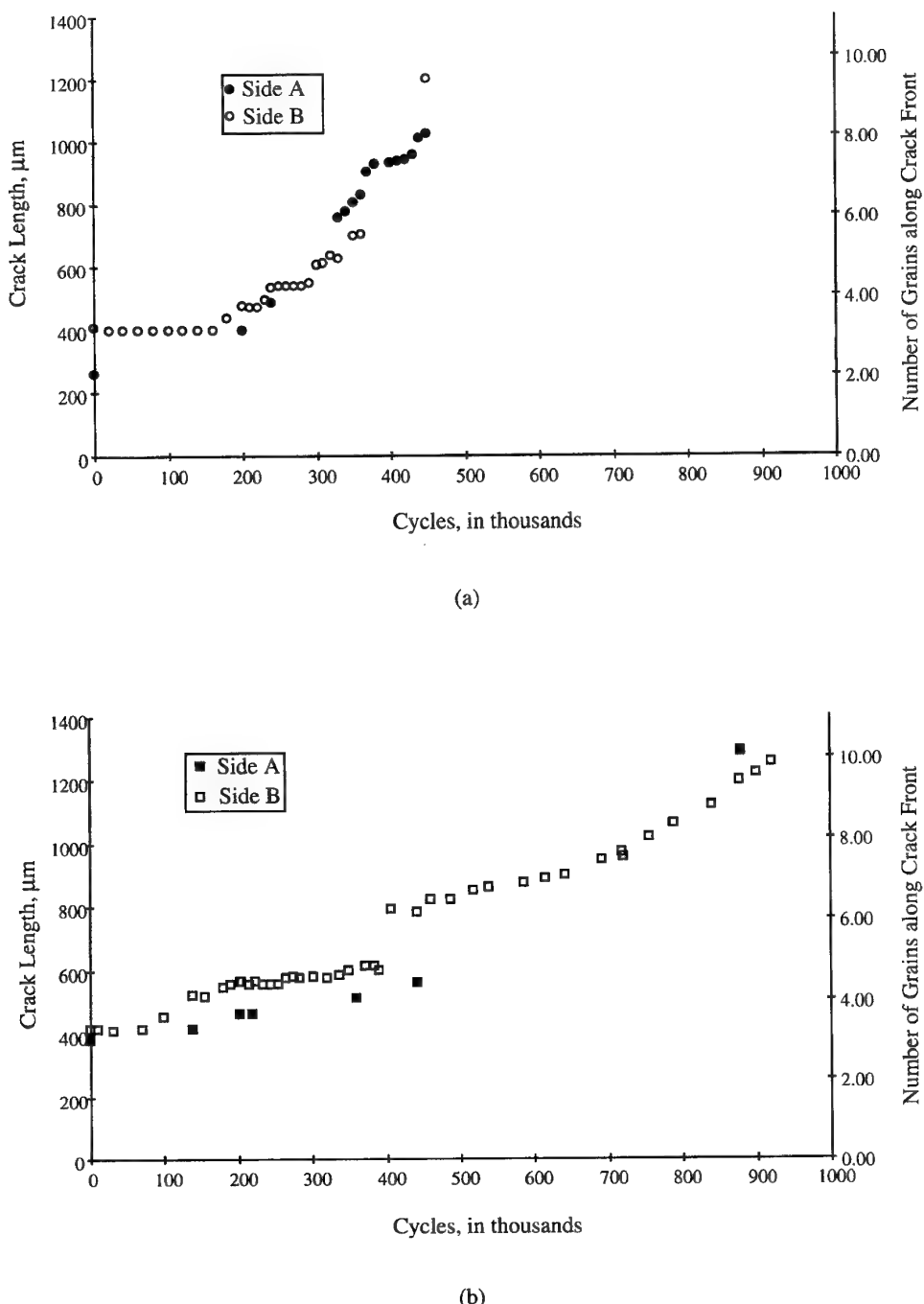


Figure 3 Growth data for small cracks: (a) first test; (b) second test

are used, the small crack growth rate can be greater than would be predicted. The use of the term 'anomalous' was introduced to describe this latter behavior. The so-called anomalous growth rate behavior will be discussed first.

Anomalous growth rate behavior

Results from a number of investigations have indicated that low load ratio tests on small cracks appear to correlate well with long crack data for high load ratio tests. It has been suggested¹⁰ that either an absence or a reduction in obstruction to closure for these test conditions provides an explanation for the

anomalous small crack behavior. The early deviations observed here from planar growth, however, could promote obstruction to closure for small cracks. Also, Halliday⁹ found evidence that substantial levels of closure can also occur for small surface cracks. The difference observed here between the orientations of the initial microcrack planes on the two adjacent corner surfaces suggests that initially there can be an internal, unfractured ligament. This could introduce a bridging mechanism which would result in an effort which would be counter to the absence or reduction of closure obstruction hypotheses. It is also of interest to note that Vasudevan and Sadananda^{15,16} maintain that the

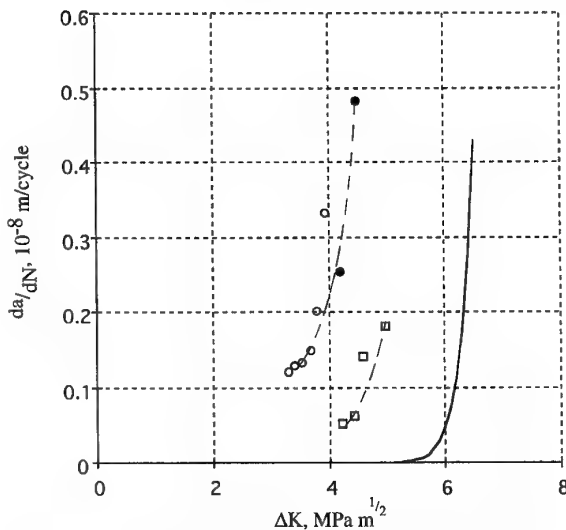


Figure 4 Cartesian plot of long and small crack results in the near threshold region

effects of obstruction to closure need not be invoked to explain fatigue crack growth behavior. They have presented results which suggest that the growth can be correlated by the use of two parameters, ΔK and K_{\max} .

Just after crack initiation a crack front encounters a small number of grains. Microstructural features such as grain size, grain orientation and inclusions may then be expected to affect the mechanics of crack growth.^{2,4,6-9,17,18}

For corner and surface cracks the number of grains increases with increasing crack depth, i.e. as the small crack grows and becomes a long crack. An examination of Figure 3 indicates that over the range for which growth-arrest behavior has occurred, the number of grains encountered by the crack front is small. Thus, when four grains are encountered, two, or half, of the grains have free surfaces. Thus, only the two internal grains are completely surrounded and constrained. It has been suggested¹⁹ that when the number of grains is small, the effect of the surface grain contributions to crack extension may be expected to be greater than when the surface grains are a small fraction of the total number of grains along the crack front. If this conjecture is correct, there could be, for the same alloy and crack depth, differences in crack growth rates for small corner cracks, small thumbnail cracks and short cracks. The thickness of a sheet with a short, through-edge crack would have to be very thin for the crack front to encounter a small number of grains. For the alloy tested the sheet would be about 0.6 mm thick for the crack front to encounter only three grains. The crack front of a 5 mm thick sheet would cross about 25 grains. Note also that whereas the crack front lengths of corner and thumbnail cracks increase with increasing crack length, the crack front lengths for through-edge cracks remain the same. Since the stress intensity factor is insensitive to these details, it cannot be expected to account for behaviors which may result from these differences.

Some of the proposals which have been offered to account for small crack growth are based on the introduction of an 'effective' range of stress intensity factors which, by being increased, yields predictions which

provide increases in crack growth rate. They do not, however, explicitly account for microstructural features.

It has been suggested here that the anomalous small crack growth behavior may be due at least in part to the fact that the ratio of the total number of grains on the crack front to the number of partially constrained, surface grains is small. This ratio increases, of course, with increasing crack size or decreasing grain size. An alternative to previous proposals for crack growth rate could be to introduce a function of this ratio. Thus let

$$\frac{da}{dN} = f[n_t/n_s]F[\Delta K, \Delta K_{th}, R, K_{IC}] \quad (3)$$

where n_t is the total number of grains intersected by the crack front, and n_s is the number of surface grains crossed by the crack front. The value of n_s will here be taken as 2.

A form of f which could be used is

$$f = [1 + g(n_t/2)] \quad (4)$$

where the function g should be constructed so that f is large for small cracks and approaches unity for long cracks. A function g which satisfies these requirements is

$$g = C_1 \exp[-C_2(n_t/2)] \quad (5)$$

Note that since the number of grains on a crack front depends upon the size of the grains, grain size is explicitly included in Equation (3). Also, it distinguishes, through the ratio n_t/n_s , the difference between small corner cracks and surface cracks of the same depth, i.e. n_t for a surface crack is twice that for a corner crack.

The total number of grains along a crack front depends on crack geometry and crack depth. The growth rate modification introduced in Equation (3) merely illustrates how the feature of grain size could be introduced, and it provides an example of how microstructural features may be included in analyses of very small crack growth.

Growth-Arrest behavior

The data of Figure 3 indicate that the increases in crack length during the growth periods were of the order of the grain size. This supports the contention²⁰⁻²³ that grain boundaries introduce barriers to continuing growth. Since it may be inferred that the use of 'grain boundary' describes a two-dimensional encounter, it may be more descriptive to visualize a three-dimensional geometry in which the advancing crack encounters a 'grain boundary wall'.

When there are only a few grains on the crack front, the growth-arrest phenomenon can be expected to be readily detectable. This is illustrated in Figure 5a, in which a hexagonal array has been chosen to represent grains on the crack plane. The size of the hexagons corresponds to the transverse grain size of the 6061-T651 aluminum alloy tested. When the crack is passing through the first few grains near the corner, the grain size is a large percentage of the crack length and few grains are encountered by the crack front. If crack lengths of this order are detectable, the role of grain boundary barriers to growth could easily be detected. When the crack front reaches a depth along which there are more than, for example, eight grains, the grain boundaries can still act as barriers to growth, but continuing growth can be expected to be smoothed

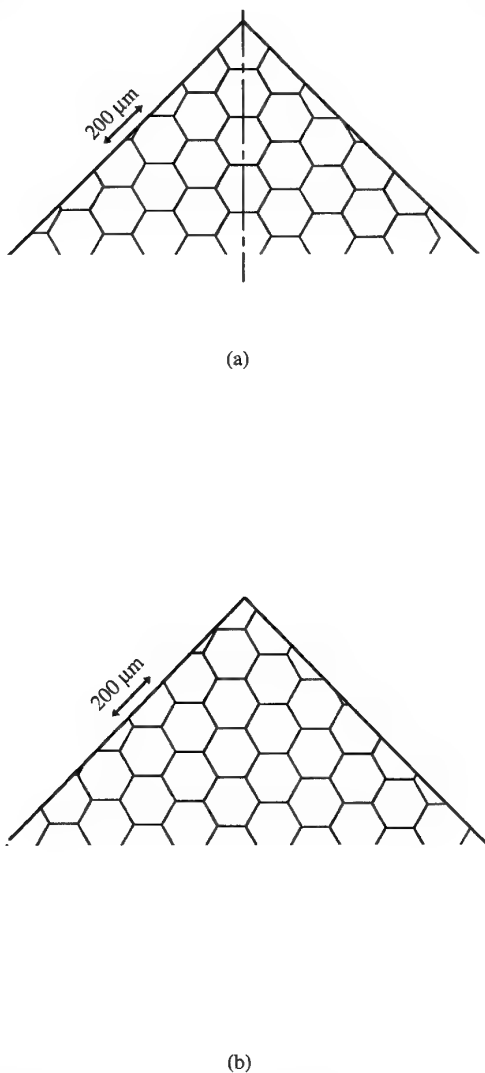


Figure 5 Models of grains on the crack plane

out. This probably occurs as the size of grains becomes a small fraction of the crack front length. Thus, although the crack front may have a local waviness, the amplitudes of the waves may be of the order of the grain size, and they in turn are also a small fraction of the measured crack depth.

The consequences of a wavy crack front have been examined by Rice²⁴. He performed an analysis for a wavy crack front in a homogeneous, isotropic material and obtained conditions for the stability of a given front, i.e. would the amplitude of the waves increase or decrease. The driving force for crack advance was the stress intensity factor which varied along the front. For the small crack problem the individual grains are anisotropic and a grain boundary wall represents a transition zone between grains of different crystallographic orientation. The introduction of local barriers and localized regions of anisotropy may provide an analytical basis for extending the analysis presented by Rice. An extension of Rice's research has been presented by Bower and Ortiz²⁵. They performed an analysis in which the crack front in a brittle material is locally retarded by the presence of particles. Although the encounter of a crack front with a small

particle differs from that of a crack front with the wall of a grain which is large compared to a particle, the crack growth barrier mechanism is common to the two cases.

The grain pattern of Figure 5a is symmetric with respect to a line which bisects the corner angle. Figure 5b represents a somewhat more realistic, nonsymmetric arrangement of grains, and it can be seen that initially crack growth on the right side of the top corner grain could be retarded by the inclined grain boundary. Again, however, when the crack depth is large compared to the grain size, the crack front would encounter a relatively large number of grains, and differences in growth rates could be expected to diminish, i.e. although local differences in crack advance may persist, the dimensions of the differences become a small fraction of the crack length.

CONCLUSIONS

1. Crack extensions during the growth periods of the growth-arrest behavior of the small corner cracks were of the order of the grain size for the 6061-T651 aluminum alloy tested. This supports the contention that grain boundary walls may introduce local barriers to continuing growth.
2. Small cracks were observed to grow below the threshold for the small load ratio R used.
3. The data obtained indicate that even for relatively well-controlled test conditions, the initial growth phase of the small fatigue cracks is not reproducible.
4. The initial crack growth behaviors of small cracks and short cracks may differ because of the large difference in grains along their crack fronts. Also, since small thumbnail cracks can, for the same crack depth, be expected to have about twice as many grains along their fronts as small corner cracks, their growth behaviors may differ. The stress intensity factor is insensitive to these differences.
5. The 'anomalous' growth rate observed for small cracks may be due in part to the fact that surface grains, which are a large fraction of the total number of grains along the crack front of a small crack, do not have the complete constraint that interior grains have. The form of a modified crack growth rate equation illustrates how the effects of a difference in internal and surface grain constraints may be introduced.

REFERENCES

- 1 Pearson, S., *Engineering Fracture Mechanics*, 1975, **8**, 235–247.
- 2 Miller, K. J., *Journal of Fatigue and Fracture of Engineering Materials and Structures*, 1982, **5**, 223–232.
- 3 Suresh, S., *Metallurgical Transactions*, 1983, **14A**, 2375–2385.
- 4 Lankford, J. and Davidson, D. L. *Fatigue Crack Growth Threshold Concepts*, eds D. L. Davidson and S. Suresh. Metallurgical Society of the American Institute of Mining and Mineral Petroleum Engineers, Warrendale, PA, 1984, pp. 447–463.
- 5 Suresh, S. and Ritchie, R. O., *International Metals Reviews*, 1984, **29**, 445–476.
- 6 Chan, L. S. and Lankford, J., *Acta Metallurgica*, 1988, **36**, 193–206.
- 7 Navarro, A. and De Los Rios, E. R., *The Philosophical Magazine*, 1988, **57**, 15–36.
- 8 Tanaka, K. and Akiniwa, Y. In *Advances in Fracture Research*, Proceedings of ICF 7, Vol. 2, 1989, pp. 869–889.

- 9 Halliday, M. D. *Journal of Fatigue and Fracture of Engineering Materials and Structures*, 1996, in press.
- 10 Edwards, P. R. and Newman, J. C. Short-crack growth in various aircraft materials. AGARD Report 767, 1990.
- 11 Swain, M. H. *Short Crack Test Methods*, eds J. M. Larsen and J. E. Allison. ASTM STP 1149, American Society for Testing and Materials, 1991, pp. 34–56.
- 12 Carlson, R. L., Dancila, D. S. and Kardomateas, G. A. In *Proceedings of the 6th International Fatigue Congress*, eds G. Lütjering and H. Nowack. Pergamon Press, Oxford, 1996, pp. 289–293.
- 13 NASA/FLAGRO Fatigue Crack Growth Computer Program, 1989.
- 14 Taylor, D. and Knott, J. F. *Fatigue Engineering Materials and Structures*, 1981, **4**, 147–155.
- 15 Vasudevan, A. K. and Sadananda, K. In *Proceedings of the 6th International Fatigue Congress*, eds G. Lütjering and H. Nowack. Pergamon Press, Oxford, 1996, pp. 473–478.
- 16 Sadananda, K. J. and Vasudevan, A. K. In *Proceedings of the 6th International Fatigue Congress*, eds G. Lütjering and H. Nowack. Pergamon Press, Oxford, 1996, pp. 375–380.
- 17 Miller, K. J., *Metals Science and Technology*, 1993, **9**, 453–462.
- 18 Hussain, K., De Los Rios, E. R. and Navarro, A., *Engineering Fracture Mechanics*, 1993, **44**, 426–436.
- 19 Leis, B. N., Topper, A. T., Ahmad, J., Brock, D. and Kanninen, M. F., *Engineering Fracture Mechanics*, 1986, **23**, 883–898.
- 20 Morris, W. L., *Metallurgical Transactions*, 1979, **10A**, 5–11.
- 21 Tanaka, K., Nakai, Y. and Yamashita, M., *International Journal of Fracture*, 1981, **17**, 519–533.
- 22 Sheldon, G. P., Cook, T. S., Jones, T. W. and Lankford, J., *Fatigue of Engineering Materials and Structures*, 1981, **3**, 219–228.
- 23 Lankford, J., *Fatigue of Engineering Materials and Structures*, 1982, **5**, 233–248.
- 24 Rice, J., *Journal of Applied Mechanics*, 1985, **52**, 571–579.
- 25 Bower, A. F. and Ortiz, M., *Journal of Mechanics and Physics of Solids*, 1991, **93**, 815–858.

PII: S0142-1123(97)00014-5

Multiaxial small fatigue crack growth in metals

David L. McDowell

G.W. Woodruff School of Mechanical Engineering, School of Materials Science and Engineering, Georgia Institute of Technology, Atlanta, GA 30332-0405, USA

Observations related to the formation and growth of small cracks ranging from subgrain dimension up to the order of 1 mm are summarized for amplitudes ranging from low cycle fatigue (LCF) to high cycle fatigue (HCF) conditions for polycrystalline metals. Further efforts to improve the accuracy of life estimation which address LCF, HCF and LCF-HCF interactions must consider various factors that are not presently addressed by conventional elastic-plastic fracture mechanics (EPFM) or linear elastic fracture mechanics (LEFM) approaches based on long, self-similar cracks in homogeneous, isotropic materials, nor by conventional HCF design tools such as the ϵ - N curve, the S - N curve, modified Goodman diagram and fatigue limit.

Development of microstructure-sensitive fatigue crack propagation relations relies on deeper understanding of small crack behavior, including (a) interactions with microstructure and lack of constraint for microstructurally small cracks, (b) heterogeneity and anisotropy of cyclic slip processes associated with the orientation distribution of grains, and (c) local mode mixity effects on small crack growth. The basic technology is not yet sufficiently advanced in these areas to implement robust damage tolerant design for HCF. This paper introduces an engineering model which approximates the results of slip transfer calculations related to crack blockage by microstructure barriers; the model is consistent with critical plane concepts for Stage I growth of small cracks, standard cyclic stress-strain and strain-life equations above threshold, and the Kitagawa diagram for HCF threshold behaviors. It is able to correlate the most relevant trends of small crack growth behavior, including crack arrest at the fatigue limit, load sequence effects, and stress state effects. © 1998 Published by Elsevier Science Ltd. All rights reserved

(Keywords: small cracks; multiaxial fatigue; high cycle fatigue)

INTRODUCTION

The formation and growth of microstructurally and physically small cracks in fatigue must be adequately addressed by a realistic model of the so-called 'crack initiation' regime under both low cycle fatigue (LCF) and high cycle fatigue (HCF) conditions. It is convenient and physically consistent to consider the growth of small cracks in polycrystalline metals to be subject to several characteristic regimes¹⁻⁶, shown in *Figure 1*. As discussed by Miller⁴, microstructurally small cracks are subject to strong interactions with microstructural barriers. The solid line in *Figure 1* illustrates typical results from a distributed dislocation model which characterizes small crack growth in terms of a series of periodic activations of slip in adjacent grains of different orientation, followed by dislocation blockage by grain boundaries and associated deceleration of da/dN ^{2,3}. Oscillatory da/dN behavior is commonly observed for microstructurally small cracks; it is experimentally well-established that this behavior is linked to small crack interactions with microstructure features

such as grain or phase boundaries^{1,3,5,7}. Typically, the experimentally observed spacing for the strongest barrier, d , is somewhat higher than the characteristic grain size, δ . If the applied stress is insufficient to produce cyclic slip in grains adjacent to the crack tip, then small cracks will decelerate and arrest at this length scale ($a \approx d$), giving rise to a fatigue limit. In general, d depends on the particular composition and arrangement of microstructures, and does not simply correspond to optical identification⁵. If cracks propagate past the strongest barrier, they continue to be subject to a diminishing influence of microstructure for several multiples of this length scale ($a < kd$, $k \approx 2$ to 7)^{1,2,6}. Finally, the propagation rate is only slightly affected by microstructure for $a > kd$. The dashed line in *Figure 1* represents the idealization of this oscillatory slip transfer model offered by the model originally proposed by Hobson^{4,8,9}.

Application of the class of linear elastic fracture mechanics (LEFM) or elastic-plastic fracture mechanics (EPFM) solutions which presume material isotropy, homogeneity and (often) self-similar crack exten-

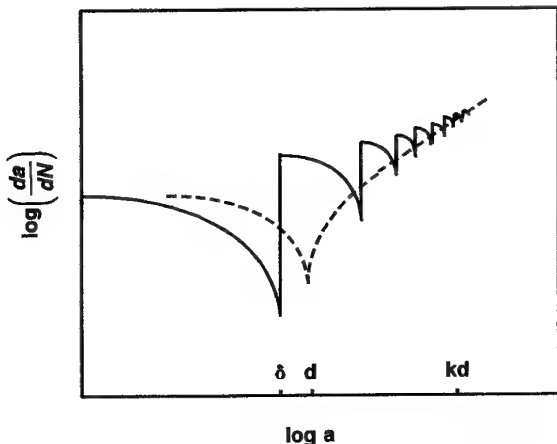


Figure 1 Schematic of typical progression of crack growth rate behavior as a function of crack length and stress amplitude for microstructurally small ($a < d$) and physically small ($a > kd$) cracks, with the transition regime between

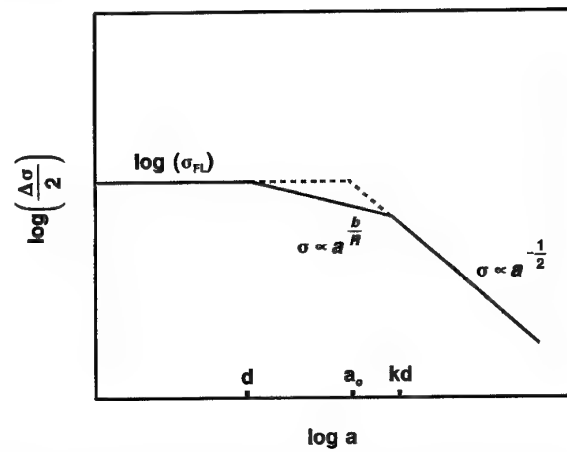


Figure 2 Schematic of Kitagawa diagram for HCF thresholds, separating into Regime I ($a < d$), Regime II ($a \approx d$ to $a = kd$) and Regime III ($a \geq kd$), with the LEFM threshold applicable to Regime III

sion to small fatigue cracks involves strong assumptions. First, microstructure affects the fatigue crack growth rate (FCGR) of small cracks very substantially, whereas long crack LEFM solutions for isotropic, homogeneous materials lack incorporation of appropriate length scales and arrest mechanisms. Second, the assumptions of planarity and self-similarity of crack growth often made in LEFM solutions applied to growth of long fatigue cracks is generally far from reality as small cracks meander among slip systems across grains. Third, the intrinsic nature of mixed mode crack tip opening and sliding displacements, distinct from remote load mixity, is most often neglected in the application of conventional LEFM solutions for long cracks to fatigue crack growth. Fourth, the ratio of the cyclic plastic zone or fatigue damage process zone to crack length for small cracks is often too large for small scale crack tip damage arguments to hold; this represents a potential fundamental limitation of singularity-based fracture mechanics. Although both plasticity and roughness-induced closure have been argued to affect growth of small cracks, the incorporation of these phenomena into fracture mechanics-based growth laws is often accompanied by quite simplified assumptions, such as the applicability of LEFM solutions for long, planar cracks in homogeneous materials. Comprehensive reviews of the mechanics challenges in developing fatigue crack growth laws for small cracks are available in the literature^{10,11}.

In addition to the behavior shown in *Figure 1*, several other phenomena should be recognized in the development of small crack propagation models.

(i) The observation of threshold behavior under HCF conditions is important. For cracks on the order of microstructural dimension, a smooth specimen fatigue limit is sometimes observed, while conventional long crack LEFM threshold conditions prevail for somewhat longer cracks ($a > kd$) that are apparently less sensitive to the influence of microstructure, as shown in the Kitagawa diagram^{1,4,6} of *Figure 2* for the completely reversed, uniaxial loading case. Crack length a_0 represents the intersection of the smooth specimen fatigue limit, σ_{FL} , and the long crack LEFM curve, i.e.

$$a_0 = \frac{1}{\pi} \left(\frac{\Delta K_{th}}{\sigma_{FL}} \right)^2 \quad (1)$$

where ΔK_{th} is the long crack LEFM threshold. These two limiting threshold conditions differ in the scale of crack length relative to microstructure; the fatigue limit represents the remote stress level for arrest of small cracks with length on the order of the spacing of strong microstructural barriers, whereas the LEFM threshold ΔK_{th} is associated with the material resistance to crack driving force for cracks which extend over a number of microstructural units^{4,6}.

(ii) For microstructurally small cracks, above threshold conditions, the strain-life relations form the basis for empirical description of combined crack nucleation/propagation lifetime to a predetermined crack length within the physically small crack regime, typically on the order of 0.5 to 1 mm.

(iii) A useful engineering model for small crack behavior in fatigue of metallic polycrystals should have predictive capability (or at least correlative capability) of the ubiquitous empirical observations (i) and (ii); of course, some materials do not adhere to the strain-life or cyclic stress-strain relations as typically written. It is essential to characterize Stage I and Stage I-II transition behavior of small crack growth in terms of mixed mode local conditions, regardless of remote loading mode, in view of the role of crystallographic anisotropy and the slip-driven nature of the fatigue process, as well as mixity induced by microstructure interactions. To this end, critical plane models for multiaxial fatigue offer a framework in which characteristic behaviors of small cracks under various stress states are catalogued.

This paper introduces an engineering model for small fatigue crack propagation which reflects crack interaction with microstructural barriers and is in accordance with HCF thresholds at different length scales. The crack growth law is a nondimensionalized generalization of a previously proposed critical plane-based small crack growth law^{12,13} which obeys the cyclic stress-strain and strain-life equations in uniaxial and torsional fatigue above threshold.

A THREE-REGIME SMALL CRACK PROPAGATION LAW

Here, we generalize microstructurally small crack propagation approximations based on slip transfer^{4,5,8,9} within the context of the multiaxial critical plane approach set forth by McDowell and Bennett¹³, assuming completely reversed loading. Identifying Regimes I, II and III as the microstructurally small crack regime (MSC), transition from microstructure sensitivity to relative insensitivity, and then to the physically or mechanically small crack regime (PSC), respectively, we introduce the normalized propagation relations

$$\left(\frac{da}{dN}\right)_I = D_{aN} \psi A \psi^B \left(1 - \frac{a}{d}\right) \quad (2)$$

$$\left(\frac{da}{dN}\right)_{II} = D_{aN} \psi <\psi^r\left(\frac{a}{kd}\right) - D> \quad (3)$$

$$\left(\frac{da}{dN}\right)_{III} = D_{aN} \psi <\psi^r\left(\frac{a}{kd}\right) - D\left(\frac{a}{kd}\right)^{1-Mr}> \quad (4)$$

and require that

$$\frac{da}{dN} = \max \left(\left(\frac{da}{dN}\right)_I, \left(\frac{da}{dN}\right)_{II} \right) \text{ for } a < kd \quad (5)$$

$$\frac{da}{dN} = \left(\frac{da}{dN}\right)_{III} \text{ for } a \geq kd \quad (6)$$

where A , r , d , k and D are constants and B is a parameter that depends on amplitude and stress state; D_{aN} is used to normalize the relations to the observed strain-life law, as discussed later. We define $\langle g \rangle = g$ if $g \geq 0$; $g = 0$ otherwise. Parameter ψ is defined as¹³

$$\psi = R_e C_e (\Psi_e)^M + (1 - R_e) C_p (\Psi_p)^m \quad (7)$$

where

$$\Psi_e = (1 + \mu\rho)(\beta_e R_n + 1) \left(\frac{\Delta\tau_n}{2} \frac{\Delta\gamma_{max}^e}{2} \right) \quad (8)$$

$$\Psi_p = (1 + \mu\rho)(\beta_p R_n + 1) \left(\frac{\Delta\tau_n}{2} \frac{\Delta\gamma_{max}^p}{2} \right) \quad (9)$$

and R_e is the ratio of the maximum elastic shear strain range to the maximum total shear strain range ($0 < R_e \leq 1$), i.e.

$$R_e = \frac{\Delta\gamma_{max}^e}{\Delta\gamma_{max}} \quad (10)$$

Here, $R_n = (\Delta\sigma_n/2)/(\Delta\tau_n/2)$, where σ_n and τ_n are the normal and shear stresses, respectively, on the plane of maximum range of shear strain. Parameter R_n varies from zero for completely reversed torsional fatigue to unity for uniaxial or biaxial loading conditions. Parameter ρ takes the form

$$\rho = \frac{\Delta\sigma_{kk}/2}{2\Delta\tau_n/2} - R_n \quad (11)$$

to model additional constraint effects on small crack propagation in a biaxial/triaxial stress field, and constant μ governs this influence^{12,13}. The terms involving β_e and β_p reflect mode mixity (modes I-II) of the crack tip opening and sliding displacements¹². The ψ parameter has previously been shown¹² to provide accurate correlation of fatigue life over a full range of stress states. Appendix A lists the forms for β_e , β_p , C_e , C_p , m and M necessary for accordance with the experimentally measured strain-life relations for a given final crack length in the finite life regime.

Equation (2) is a generalized multiaxial form of the Hobson model^{8,9} for slip transfer to adjacent, misoriented grains, which itself serves as an approximation to more detailed distributed dislocation models^{2,3}. The growth law in Equation (3) essentially defines the smooth specimen fatigue limit, when coupled with Equation (2), and further embodies the observation that da/dN is approximately linear in crack length through the transition from microstructure-sensitive to insensitive growth^{4,5}. This transition regime is commonly observed in plots of experimental data in the Kitagawa diagram^{1,6} (cf. Figure 2) which lie below the intersection of the smooth specimen fatigue limit and the backward extrapolation of the LEFM threshold limit for mechanically long cracks. Finally, the Regime III growth law in Equation (4) expresses the LEFM threshold limit for long cracks, while still adhering to the observation that da/dN is nearly linear with crack length for conditions well in excess of the threshold.

The transition at $a = kd$ is continuous in crack growth rate, $(da/dN)_{II} = (da/dN)_{III}$. The intersection $(da/dN)_I = (da/dN)_{II}$ occurs at the crack length a^* , given by

$$\frac{a^*}{d} = \frac{\left(1 + \frac{D}{A} \psi^{-B}\right)}{\left(1 + \frac{\psi^{-B}}{kA}\right)} \quad (12)$$

Two distinct types of threshold behavior are evident in Equations (3) and (4). First, the fatigue limit is introduced via the threshold constant D . Under HCF conditions for $a < d$ and stress levels below the fatigue limit, $(da/dN)_{II} = 0$ implies that

$$(\psi_{th})_I = (kD)^{1/r} \quad (13)$$

since $(da/dN)_I \rightarrow 0$ as $a/d \rightarrow 1$. For uniaxial loading conditions, Equation (13) may be restated as

$$(\psi_{th})_I = \left(\frac{\sigma_{FL}}{\sigma_f'} \right)^{2M} \Rightarrow (\sigma_{th})_I = \sigma_{FL} = \sigma_f' (kD)^{1/2Mr} \quad (14)$$

where $2M = -1/b$ (see Appendix A), and σ_{FL} is the completely reversed fatigue limit in HCF. If a fatigue limit does not exist, then $D = 0$ and the equations are still valid. In Equation (14), $(\sigma_{th})_I$ designates the uniaxial stress amplitude at threshold in Regime I.

It is also noted that if $a > d$ due to prior loading above the fatigue limit, then the nonpropagating crack threshold is decreased from the smooth specimen fatigue limit, in accordance with the Kitagawa diagram^{1,4,6}. For $d < a < kd$, the threshold value of ψ transitions from the smooth specimen limit in Equation (13) to the LEFM threshold which is valid for mechanically small cracks⁶. In this regime $(da/dN)_{II} = 0$ gives

$$(\psi_{\text{th}})_{\text{II}} = D^{1/r} \left(\frac{a}{kd} \right)^{-1/r} \quad (15)$$

Finally, for $a \geq kd$, the mechanically long crack LEFM threshold is obtained from $(da/dN)_{\text{III}} = 0$ as

$$(\psi_{\text{th}})_{\text{III}} = D^{1/r} \left(\frac{a}{kd} \right)^{-M} \quad (16)$$

For the uniaxial case, Equations (15) and (16) result in the threshold stress amplitude versus crack length relations

$$(\sigma_{\text{th}})_{\text{II}} = \sigma_f' D^{-b/r} \left(\frac{a}{kd} \right)^{b/r}, \quad (\sigma_{\text{th}})_{\text{III}} = \sigma_f' D^{-b/r} \left(\frac{a}{kd} \right)^{-1/2} \quad (17)$$

which are in accordance with the Kitagawa diagram. We can relate $(\sigma_{\text{th}})_{\text{III}}$ directly to the LEFM long crack threshold, ΔK_{th} .

In the finite life regime (above thresholds), it is very useful to normalize the crack growth relations to the classical strain-life relations corresponding to a given surface crack length in uniaxial and shear cases by defining D_{aN} as

$$\begin{aligned} D_{aN} &= 2 \int_{a_i}^{a_f} g^{-1}(a) da \quad (18) \\ &= 2 \int_{a_i}^{a^*} g_I^{-1}(a) da + 2 \int_{a^*}^{kd} g_{\text{II}}^{-1}(a) da \\ &\quad + 2 \int_{kd}^{a_f} g_{\text{III}}^{-1}(a) da \end{aligned}$$

$$\begin{aligned} D_{aN} &= 2 \frac{d}{A\psi^B} \ln \left[\frac{d - a_i}{d - a^*} \right] \quad (19) \\ &\quad + 2 \frac{kd}{\psi^r} \ln \left[\frac{\psi^r - D}{\psi^r \left(\frac{a^*}{kd} \right) - D} \right] \\ &\quad - 2 \frac{kd}{\psi^r M r} \ln \left[\frac{\left(\frac{a_f}{kd} \right)^{-Mr} (\psi^r - D)}{\psi^r - D \left(\frac{a_f}{kd} \right)^{-Mr}} \right] \end{aligned}$$

where g_I , g_{II} and g_{III} are respectively given by the right-hand sides of Equations (2), (3) and (4) upon dividing each by $D_{aN}\psi$, and a_i and a_f are initial and final crack lengths. It is assumed here that $a_i < d$ and that a_f lies within the physically small crack regime. As the threshold $(\psi_{\text{th}})_I$ is approached from above, D_{aN} rapidly increases; D_{aN} is no longer defined below the threshold in the crack arrest regime. It is therefore necessary to release the constraint of conformity to the strain-life relations just above the threshold. This may be achieved by assuming that D_{aN} is fixed, for values of $\psi < \xi(\psi_{\text{th}})_I$, at the value corresponding to $\xi(\psi_{\text{th}})_I$.

a value of $\xi = 2$ is reasonable, representing a life half that of the intersection of the stress-life curve with the fatigue limit. The relations Equations (2), (3) and (4) are then no longer normalized to the strain-life relations for $\psi < \xi(\psi_{\text{th}})_I$, and the coefficients of the FCGR equations become fixed.

For transition to either EPFM or LEFM relations in Regime III, we assume that

$$\frac{da}{dN} = \max \left(\left(\frac{da}{dN} \right)_{\text{III}}, \left(\frac{da}{dN} \right)_{\text{FM}} \right) \text{ for } a > kd \quad (20)$$

where $(da/dN)_{\text{FM}}$ is the long crack fatigue crack growth rate from the appropriate fracture mechanics relation, based on either EPFM (ΔJ_{eff}) or LEFM (ΔK_{eff}) concepts¹⁴. Hence, the growth relations in Equations (2), (3) and (4) apply to the regime where the FCGR is elevated above that associated with long crack LEFM conditions.

In this framework, the fatigue limit can be eradicated due to overload events which propagate the small cracks beyond primary barrier spacing, $a > d$. Then, the cracks can only be arrested if the stress amplitude is further decreased to conform to either the transition (Equation (15)) or LEFM (Equation (16)) thresholds.

Identification of constants

A deliberate feature of the present formulation is that most of the constants are obtained from standard data including cyclic stress-strain and strain-life relations, the long crack threshold, ΔK_{th} , the smooth specimen fatigue limit, σ_{FL} , and the characteristic shape of the Kitagawa diagram.

Beyond these constants, the model constants/parameters include the following.

- $r - b/r$ is the slope of the transition regime in the uniaxial Kitagawa diagram (see Figure 2), with typical values of r in the range 0.2 to 0.5 for typical values of fatigue strength exponent $b \approx -0.1$.
- d – discerned from minima of FCGR data for microstructurally small cracks⁵. Typically on the order of δ though somewhat larger, but less than a_o .
- k and D – once r , d and ΔK_{th} are selected, k and D are established by intersection points on the Kitagawa diagram for completely reversed uniaxial loading, i.e.

$$k = \left(\frac{\Delta K_{\text{th}}}{\sigma_{\text{FL}}} \frac{1}{\sqrt{\pi d}} \right)^{\frac{2Mr}{Mr - 1}}, \quad D = \left(\frac{\Delta K_{\text{th}}}{\sigma_f'} \frac{1}{\sqrt{\pi kd}} \right)^{2Mr} \quad (21)$$

where M and σ_f' are from strain-life relations (see Appendix A). Threshold D may also depend on the stress state (e.g. R_n) since the ψ parameter may not fully describe the stress state influence on the fatigue limit, but this possibility is not considered here.

- A and B – coefficient A and exponent B control the growth rate of microstructurally small cracks in Regime I relative to Regimes II–III, and must therefore be based on small crack FCGR data. For

example, if the relative fraction of life necessary to propagate initial cracks to some intermediate length over a range of stress amplitudes is available, then B can be adjusted to calibrate the model, once A is selected. The value of A affects the value of exponent B in the HCF limit ($R_e \rightarrow 1$), which in turn affects the FCGR below threshold since D_{aN} is fixed there; if only the behavior above threshold is considered, the value of A is more or less arbitrary and is selected to facilitate ease of identification of B . In the absence of detailed small crack FCGR data, nonlinear sequence effect fatigue data of the type embedded in damage curve approaches¹⁵ can serve as the basis for selecting A and B . In general, B depends on both stress state and amplitude, i.e. $B = B(R_n, R_e)$ for completely reversed loading. Data reported by Socie¹⁶ indicate the similarity of the small crack relative Regime I and II-III behaviors for two very different alloys, suggesting that a characteristic functional form of B might be representative of typical alloys.

The value of the normalization in Equations (2), (3) and (4) becomes apparent. Only the value of the constants d , A , r and parameter B need be determined from detailed small crack growth rate data. All other constants are reliably estimated from standard strain-life, smooth specimen fatigue limit and long crack threshold data which are relatively abundant in the literature. Even if estimates of d , A and B are used in the absence of sufficient small crack data, the normalization results in an accurate correlation of combined fatigue life across all three regimes above threshold. Variation of d will primarily affect the location of the minimum of the FCGR for small cracks, whereas B can be chosen to reflect observed amplitude and stress state sequence effects in fatigue tests conducted to some reference surface crack length, e.g. 1 mm. These type of data are fairly common for many alloys¹⁵.

ILLUSTRATION: SMALL CRACK GROWTH BEHAVIOR ABOVE THRESHOLD

The intent of this section is to illustrate the model performance under constant amplitude, completely reversed loading for reasonably realistic material parameter values for a given structural alloy. Due to its rather exhaustive strain-life and small crack growth characterization^{16,17}, 1045 steel is selected. The constants of the standard relations in equations for uniaxial and torsional fatigue (Appendix A) of both materials are presented in Table I¹⁷. For the axial-torsional loading case considered here, the value of μ is irre-

levant. We will only consider loading above the fatigue limit threshold in this particular work.

The values of d and ΔK_{th} selected for 1045 steel are $d = 0.12$ mm and $\Delta K_{th} = 6$ MPa/m. The value of d can be varied somewhat without fundamentally altering the behavior of the model; values from $d = 0.08$ to 0.15 mm led to similar behavior of the calibrated model, just shifting the minimum of FCGR to some degree. Specific FCGR data to assess the 'trough' of da/dN for microstructurally small cracks are not available for this material, but would provide a more precise value for d . The value of ΔK_{th} is representative of the completely reversed threshold for long cracks subject to $R = 0$ loading conditions¹⁸. With these values, we compute $k \approx 4$ and $D \approx 7 \times 10^{-5}$ from Equation (21), allowing for slight variation of k and D since M varies somewhat as a function of stress state (see Appendix A). The uniaxial fatigue limit is estimated as $\sigma_{FL} = 202$ MPa, corresponding to a fatigue life of 10^7 cycles, as suggested by the data of Socie¹⁶. The value of σ_{FL} may vary somewhat among different data sets. The value $r = 0.5$ is selected as reasonably representative of the slope (b/r) of the Kitagawa diagram in Regime II for alloys in this strength range⁶.

Socie¹⁶ reported experimental data for surface crack length versus number of cycles for constant amplitude loading of 1045 steel in tension-compression and in torsion. He introduced a graphical format which permits distinction of several important regimes, including the number of cycles for nucleation and growth to a 0.1 mm surface crack and number of cycles of growth to a 1 mm surface crack. Those data were used to fit parameter B through an iterative process. Equations (2), (3) and (4) have the attractive feature of closed form integrability for constant amplitude loading conditions, avoiding the need for numerical integration in iterative evaluation of B for a given loading amplitude, stress state, crack length and cycle count. With A arbitrarily selected as 10^5 , B was found to monotonically decrease according to

$$B = 1.95e^{-12R_e} + e^{-(2.6 + 6.4R_n)R_e} + 0.37R_n + 1.18 \quad (22)$$

The present model does not explicitly consider coalescence of small distributed cracks noted by Socie¹⁶ for 1045 steel, but this coalescence phenomenon is of primary significance in the latter stages of crack growth. The initial crack length was assumed as 10 μm ¹⁹, somewhat less than δ for this material ($\delta \sim 35-40 \mu\text{m}$ for fine-grained pearlite and ferrite¹⁷), while the final crack length was taken as 1 mm, in accordance with the failure definition adopted in the Socie data and the corresponding strain-life relations.

Figure 3 shows the predicted evolution of crack length versus cycles for uniaxial and torsional fatigue. Stress amplitudes in these plots range from 248 to 582 MPa in the uniaxial case, and from 124 to 304 MPa in shear, all significantly above the fatigue limit threshold. The highly nonlinear dependence of crack growth on amplitude in uniaxial fatigue is striking, whereas it is only slight in the case of torsional fatigue. Accordingly, it would be expected that sequence effects and departure from Miner's rule would be much more pronounced in the former case. In both

Table 1 Strain-life and cyclic stress-strain constants¹⁷

1045 Steel Uniaxial	Torsional
$c = -0.445$	$c_o = -0.445$
$\epsilon'_r = 0.26$	$\gamma'_r = 0.413$
$n' = 0.208$	$n'_o = 0.217$
$K' = 1258$ MPa	$K'_o = 614$ MPa
$b = -0.092$	$b_o = -0.097$
$\sigma_t' = 948$ MPa	$\tau_t' = 505$ MPa

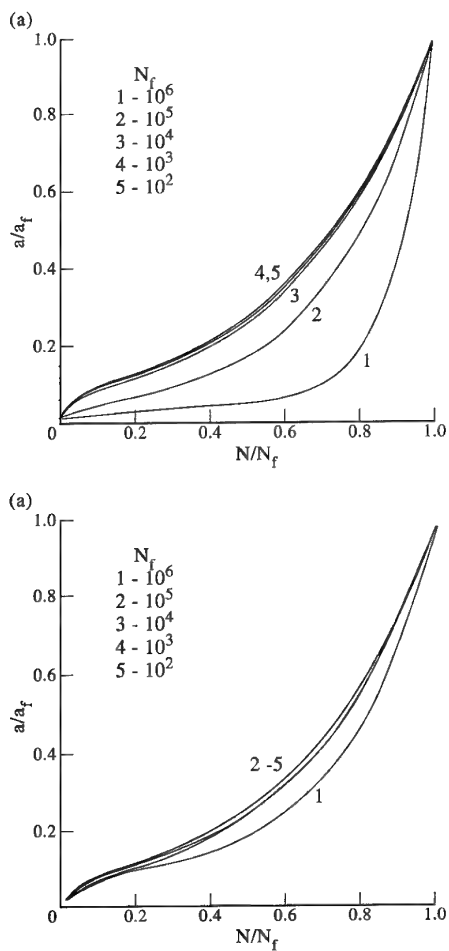


Figure 3 Predicted nonlinear growth of small cracks for 1045 steel in completely reversed (a) uniaxial fatigue and (b) torsional fatigue for a range of constant amplitude fatigue lives

cases, it is noted that the N_f values conform to the experimentally observed strain-life relations for a 1 mm surface crack. McDowell and Bennett¹³ have previously considered the ramifications of these sorts of amplitude and stress state dependencies in terms of modeling sequence effects.

Plots of predicted da/dN versus crack length appear in *Figure 4* for uniaxial and torsional fatigue. The transition from Regime I deceleration to Regime II is clear in each case, and occurs on the order of 70 to 100 μm . The Regime II-III FCGR is linear in crack length for amplitudes well above threshold, in accordance with trends of data for small cracks^{3,5}.

In *Figure 5* we plot the predicted FCGR under uniaxial loading for cracks growing from 10 μm initial length up to 1 mm in a manner that will be familiar to practitioners of LEFM and EPFM. An equivalent stress intensity factor range, ΔK_J , is defined based on the ΔJ -integral^{14,20} according to

$$\Delta K_J = \sqrt{E\Delta J} = \sqrt{E(\Delta J_e + \Delta J_p)} \quad (23)$$

$$= \Delta\sigma\sqrt{\pi a}\sqrt{\frac{1}{\pi}\left(1.6 + \frac{4.25E}{K'(1+n')}\left(\frac{\Delta\sigma}{2K'}\right)^{\frac{1}{n'}-1}\right)}$$

As distinguished from $\Delta K = Y\Delta\sigma(\pi a)^{1/2}$, ΔK_J

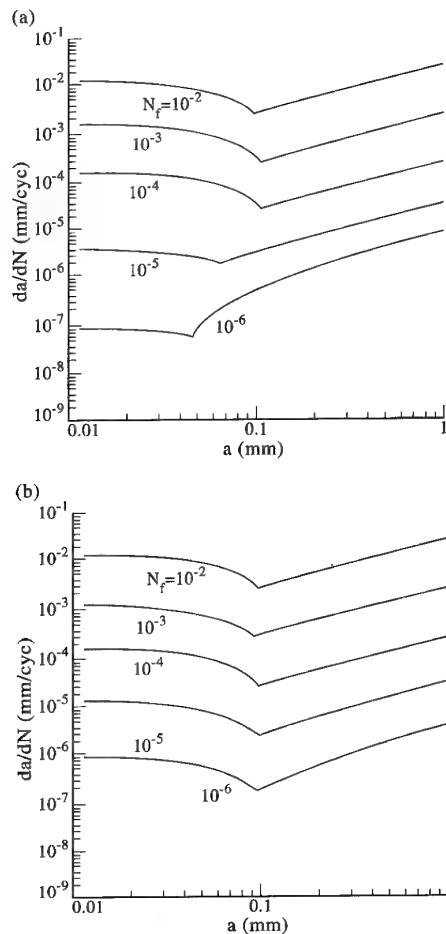


Figure 4 Predicted da/dN versus crack length for growth of small cracks for 1045 steel in completely reversed (a) uniaxial fatigue and (b) torsional fatigue for a range of constant amplitude fatigue lives

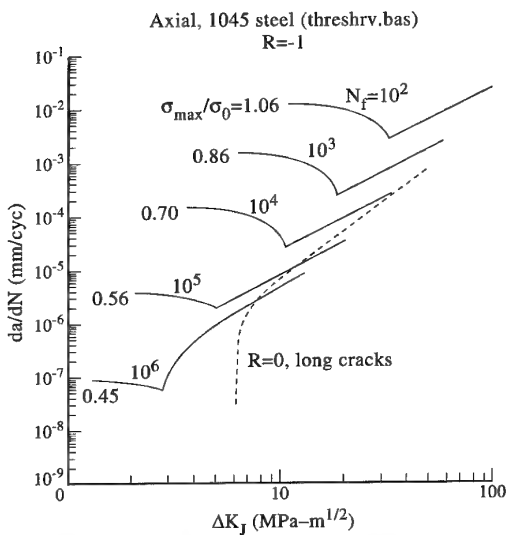


Figure 5 Predicted da/dN vs. ΔK_J for small cracks in 1045 steel for a range of completely reversed uniaxial stress amplitudes ($R = -1$); $\sigma_0 = 548$ MPa is the mean flow stress¹⁴ in the cyclic plastic regime. Long crack data for $R = 0$ appears as a dashed line¹⁸. Note that crack deceleration and arrest occur for a stress amplitude below the fatigue limit

includes a contribution from plasticity which may be very significant in the case of small cracks subjected to moderate to high remote stress amplitudes in the LCF regime. The calculated values of ΔK_J are based only on the fraction of the stress range (coefficient in Equation (23)) which is tensile, since closure effects are not explicitly considered. The characteristic dip in da/dN is evident in these model calculations, as is a wide range of Regime I da/dN levels for different amplitudes; this dip is a characteristic experimental observation, and has also been predicted by plasticity-induced closure models which consider initially fully open small cracks growing from initial defects²¹, analogous to short cracks growing from notches. The predicted da/dN vs ΔK_J trajectories generally approach the long crack $R = 0$ data from the left. Of course, for $\psi < (\psi_{th})_I$ the cracks would arrest at $a = d$. The typical scatter for small crack behavior observed for moderate amplitudes to HCF can therefore be understood, at least in part, to arise from deterministic amplitude dependence, as is also evident in the plasticity-induced closure modeling of Newman²¹. The non-uniqueness of growth behavior in *Figure 5* illustrates the apparent anomalies that can arise when interpreting small crack behavior in terms of standard long crack fracture mechanics parameters.

CONCLUSIONS

This work extends the critical plane multiaxial fatigue model of McDowell and coworkers^{12,13} to reflect basic mechanisms which have been observed to influence the growth of microstructurally and physically small cracks. We have focused here on representing the well-documented deceleration of microstructurally small cracks as they approach microstructural barriers such as a boundary with a misoriented grain with a lower resolved shear stress^{1,6,7} and crack arrest (threshold) conditions¹ associated with lack of slip transfer to adjacent grains. Of course, there are several relevant physical aspects of this problem of microstructure sensitivity, including shielding or intensification of the crack driving force due to interactions with microstructure features, local anisotropic plasticity-induced closure transients that develop with crack extension, and crack surface asperity interactions; models for slip transfer offer but one idealization of what is indeed a very complex set of mechanisms that potentially contribute to dependence of crack opening and sliding displacements on applied loading and crack length at microstructural scales. Correlations with experimental data indicate that slip transfer models exhibit significant predictive capability^{2,3} to describe microstructure interactions and naturally involve microstructural length scales which are observed to correlate with periodic crack growth deceleration and acceleration events^{1,7}. This indicates that to first order this mechanism is among the more influential of the set of microstructure interactions.

Modeling concepts based on microslip transfer to adjacent grains and dislocation blockage by grain boundaries^{2,5} are approximated by a form of the Hobson model^{4,8,9} for Stage I propagation generalized to multiaxial conditions using critical plane propagation concepts; the model is augmented by HCF considerations of transition to the long crack LEFM threshold

conditions to describe a complete, stress state-dependent Kitagawa diagram. Crack growth rate relations are introduced in three regimes – microstructurally small (Regime I), transition from microstructure-sensitive to microstructure-insensitive growth (Regime II), and physically small (Regime III) – in nondimensionalized form with dependence on applied stress and crack length to facilitate weighting of the regimes in accordance with the strain-life relations above threshold conditions. The model makes use of standard fatigue data formats such as cyclic stress-strain, strain-life, smooth specimen fatigue limits, and ΔK_{th} . Essentially, a few more parameters are introduced, including d , r , A , and weighting exponent, B ; ideally, these parameters rely on small crack growth data (preferably in the MSC Regime I or Regime I-II interface), but may be estimated to match observed sequence effects in the absence of such data. Amplitude dependence of the FCGR is also incorporated in the nonlinear growth law. In this work we have exercised the model above threshold conditions to demonstrate its general features. We have also neglected the crack incubation or nucleation stage, instead assuming the pre-existence of cracks. Although this assumption is reasonable for many polycrystalline alloys, inclusion of a nucleation stage is possible⁵ and indeed necessary in some cases (e.g. ductile, coarse grain alloys).

Due to the complexity of microstructure interactions with individual cracks and the degree of idealization necessary to address the combined effects of crack face roughness interference, plasticity-induced closure and mode mixity in an FCGR description, these effects have been implicitly embedded within the present model; accordingly, it must be calibrated to (albeit limited) experimental data. The model is an idealization based on slip transfer processes from grain-to-grain and grain boundary blockage of dislocations in a polycrystal^{2-4,8,9} which differs fundamentally from a crack closure idealization. Still, essential features of the transient nature of da/dN with crack length are captured, and trends are very similar to those of a plasticity-induced closure model²¹. We contend that a model based on slip transfer and microstructure barrier interaction with slip is first order relevant to the physics of microstructurally small crack growth, respecting as well supplementary and perhaps inseparable effects of plasticity-induced closure (particularly above threshold) and roughness-induced closure/interference (particularly in the vicinity of threshold or subthreshold). The latter effects are considered as intrinsic components of the fatigue crack growth process in the present model. Of course, they may be quite significant; for small cracks on the order of the grain size, a plasticity-induced closure transient arises not only from a change of constraint as a crack grows away from a nucleating defect, but potentially from strong surface gradients of dislocation density²² (constraint) which hitherto have only been implicitly considered through experimentally-based small crack closure modifications¹. For physically long cracks ($a > kd$), for which the apparent sensitivity of the FCGR to microstructure has diminished, the more classical LEFM/EPFM and associated closure modifications are practically applicable and can be experimentally verified; planarity and self-similarity assumptions which enable simplified analysis procedures are also often valid for longer cracks.

For simplicity, the present model presumes that transients of local stress redistribution and asperity contact are relatively short-lived, with the behavior accommodating the amplitude and stress state of interest for a given crack length. This assumption may be increasingly suspect for longer cracks where the usual LEFM solutions based on assumptions of homogeneity and isotropy become more strictly applicable, practical and robust. Of course, such effects may be explicitly included in the framework, if necessary. As it stands, this type of model reflects nonlinear load amplitude and stress state sequence effects for small cracks which are very similar to those observed experimentally¹³. Moreover, due to the closed form integrability of propagation relations (2)–(4) for a given amplitude, it is straightforward to assess the increment of crack length for a given block of loading in a complex loading history, without the need to consider increased resolution to capture transient effects as in closure models. This is desirable for robust, efficient engineering modeling schemes for evaluation of nonlinear growth of small cracks in LCF/HCF.

ACKNOWLEDGEMENTS

The author is grateful for the support of the Office of Naval Research MURI Program in Integrated Diagnostics (ONR N00149510539) in conducting this research.

REFERENCES

- 1 Tanaka, K. and Akiniwa, Y., Propagation and non-propagation of small fatigue cracks. In *Advances in Fracture Research*, Proceedings of ICF7, Vol. 2, Houston, TX, 20–24 March 1989, pp. 869–887.
- 2 Hussain, K., De Los Rios, E. R. and Navarro, A., A two-stage micromechanics model for short fatigue cracks. *Engineering Fracture Mechanics*, 1993, **44**(3), 425–436.
- 3 Wang, C. H., Effect of stress ratio on short crack fatigue growth. *ASME Journal of Engineering Materials Technology*, 1996, **118**, 362–367.
- 4 Miller, K. J., The two thresholds of fatigue behaviour. *Fatigue and Fracture of Engineering Materials and Structures*, 1993, **16**(9), 931–939.
- 5 Wang, C. H. and Miller, K. J., The effects of mean and alternating shear stresses on short fatigue crack growth rates. *Fatigue and Fracture of Engineering Materials and Structures*, 1992, **15**(12), 1223–1236.
- 6 Tanaka, K., Short-crack fracture mechanics in fatigue conditions. In *Current Research on Fatigue Cracks*, Vol. 1, eds T. Tanaka, M. Jono and K. Komai. Current Japanese Materials Research, Elsevier, 1987, Hong Kong, pp. 93–117.
- 7 Nisitani, H., Behavior of small cracks in fatigue and relating phenomena. In *Current Research on Fatigue Cracks*, Vol. 1, eds T. Tanaka, M. Jono and K. Komai. Current Japanese Materials Research, Elsevier, 1987, pp. 1–26.
- 8 Hobson, P. D., The growth of short fatigue cracks in a medium carbon steel. Ph.D. Thesis, University of Sheffield, Sheffield, 1985.
- 9 Hobson, P. D., Brown, M. W. and de los Rios, E. R., Two phases of short crack growth in a medium carbon steel. In *The Behaviour of Short Fatigue Cracks*, eds K. J. Miller and E. R. de los Rios. EGF Publication 1, Institute of Mechanical Engineers, London, 1986, pp. 441–459.
- 10 Leis, B. N., Hopper, A. T., Ahmad, J., Broek, D. and Kanninen, M. F., Critical review of the fatigue growth of short cracks. *Engineering Fracture Mechanics*, 1986, **23**(5), 883–898.
- 11 McDowell, D. L., Basic issues in the mechanics of high cycle fatigue. *International Journal of Fracture*, 1996, **80**, 103–145.
- 12 McDowell, D. L. and Berard, J.-Y., A ΔJ-based approach to biaxial fatigue. *Fatigue and Fracture of Engineering Materials and Structures*, 1992, **15**(8), 719–741.
- 13 McDowell, D. L. and Bennett, V. P., A microcrack growth law for multiaxial fatigue. *Fatigue and Fracture of Engineering Materials and Structures*, 1996, **19**(7), 821–837.
- 14 McDowell, D. L., An engineering model for propagation of small cracks in fatigue. *Engineering Fracture Mechanics*, in press.
- 15 Manson, S. S. and Halford, G. R., Re-examination of cumulative fatigue damage analysis – An engineering perspective. *Engineering Fracture Mechanics*, 1986, **25**(5–6), 539–571.
- 16 Socie, D. F., Critical plane approaches for multiaxial fatigue damage assessment. In *Advances in Multiaxial Fatigue*, eds D. L. McDowell and R. Ellis. ASTM STP 1191, ASTM, Philadelphia, 1993, pp. 7–36.
- 17 Fatemi, A. and Kurath, P., Multiaxial fatigue life predictions under the influence of mean-stresses. *ASME Journal of Engineering Materials Technology*, 1988, **110**, 380–388.
- 18 Hua, C. T. and Socie, D. F., Fatigue damage in 1045 steel under variable amplitude biaxial loading. *Fatigue and Fracture of Engineering Materials and Structures*, 1985, **8**(2), 101–114.
- 19 Murakami, Y., Correlation between strain singularity at crack tip under overall plastic deformation and the exponent of the Coffin–Manson law. In *Low Cycle Fatigue*, eds H. D. Solomon, G. R. Halford, L. R. Kaisand and B. N. Leis. ASTM STP 942, ASTM, Philadelphia, 1988, pp. 1048–1065.
- 20 Dowling, N. E., Crack growth during low-cycle fatigue of smooth axial specimens. In *Cyclic Stress–Strain and Plastic Deformation Aspects of Fatigue Crack Growth*. ASTM STP 637, ASTM, Philadelphia, 1977, pp. 97–121.
- 21 Newman, J. C., A review of modelling small-crack behavior and fatigue-life predictions for aluminum alloys. *Fatigue and Fracture of Engineering Materials and Structures*, 1994, **17**(4), 429–439.
- 22 Harvey, S. E., Marsh, P. G. and Gerberich, W. W., Atomic force microscopy and modeling of fatigue crack initiation in metals. *Acta Metallurgica et Materialia*, 1994, **42**(10), 3493–3502.

APPENDIX A

Normalization to strain-life expressions

Assuming that torsional and uniaxial strain-life and stress–strain relations of the form

$$\frac{\Delta\gamma}{2} = \frac{\tau_f'}{G} (2N_f)^{b_o} + \gamma_f' (2N_f)^{c_o}, \quad (A1)$$

$$\frac{\Delta\epsilon}{2} = \frac{\sigma_f'}{E} (2N_f)^b + \epsilon_f' (2N_f)^c$$

$$\frac{\Delta\tau}{2} = K_o' \left(\frac{\Delta\gamma'}{2} \right)^{n_o'}, \quad \frac{\Delta\sigma}{2} = K' \left(\frac{\Delta\epsilon'}{2} \right)^{n'} \quad (A2)$$

are obeyed for completely reversed uniaxial and torsional loading from a given initial to final crack length under predominately HCF and LCF conditions, respectively, we assign

$$\beta_e = \left[4 \left(\frac{\tau_f'}{\sigma_f'} \right)^2 - 1 \right] (R_n)^{j_e} \quad (A3)$$

$$\beta_p = \left[\frac{4}{3} \frac{K_o' (\gamma_f')^{(1+n_o')}}{K' (\epsilon_f')^{(1+n')}} - 1 \right] (R_n)^{j_p} \quad (A4)$$

in addition to the forms for C_e and C_p given by

$$C_e = \left(\frac{G}{\tau_f'^2} \right)^M, \quad C_p = (K_o' \gamma_f'^{(1+n_o')})^{-m} \quad (A5)$$

Homogeneous dependence on R_n is assumed in Equation (A3) and Equation (A4), so that $\beta_e = \beta_p = 0$ for pure torsion. Exponents j_e and j_p may differ, in general¹². Both uniaxial and torsional tests are required to

characterize most of the constants of this approach (except for μ), since no universal relationship is known to exist which uniquely relates fatigue under these two states of stress. No assumptions are made here regarding equivalent relationships between uniaxial and pure torsional behavior. To recover Equations (A1) and (A2) for torsional and uniaxial fatigue, we may assign exponents m and M ^{12,13} as

$$m = \frac{-1}{c(R_n)(1 + n'(R_n))}, M = \frac{-1}{2b(R_n)} \quad (\text{A6})$$

where the R_n -dependent parameters are defined by interpolation between torsional and uniaxial cases, i.e.

$$\begin{aligned} b(R_n) &= b_o + R_n(b - b_o), c(R_n) = c_o \\ &+ R_n(c - c_o), n'(R_n) = n'_o + R_n(n' - n'_o) \end{aligned}$$

Material constant μ in Equations (8) and (9) can only be assessed from fatigue experiments involving cyclic normal stresses on orthogonal planes, e.g. biaxial tension-compression, since $\rho = 0$ for the case of combined cyclic tension-compression and torsion¹².

PII: S0142-1123(97)00013-3

Effective strain-fatigue life data for variable amplitude fatigue

T.H. Topper and T.S. Lam

*Department of Civil Engineering, University of Waterloo, Waterloo, N2L 3G1,
 Canada*

The usual analysis procedure for variable amplitude fatigue calculates fatigue damage based on constant amplitude strain controlled fatigue tests of smooth specimens. The resulting predictions are typically nonconservative due to a load interaction effect in variable amplitude fatigue. This paper reviews recent work which shows that large loads in a service load history decrease the crack opening stress and as a result increase the effective strain range for subsequent small cycles. A new strain-life fatigue test is introduced in which periodic large strain cycles reduce the crack opening stress for subsequent smaller cycles. The overloads are applied frequently enough that closure free fully open crack growth is achieved for the small cycles in the long life regime. An effective strain-life curve is derived and a crack opening stress equation calibrated by comparison of constant amplitude and effective strain ranges at given fatigue lives. The use of the effective strain-life curve in predicting fatigue lives is illustrated for service strain histories and for a variable amplitude load sequence applied to notched specimens. The predictions are good but somewhat conservative. © 1998 Elsevier Science Ltd.

(Keywords: overloads; variable amplitude fatigue; effective strain)

NOMENCLATURE

<i>A</i>	Material constant defining the strain based damage parameter
<i>b</i>	Material constant defining the strain based damage parameter
<i>E</i>	Modulus of elasticity
<i>K_t</i>	Constant relating the notch root stress to the nominal stress
<i>N_f</i>	Number of cycles to failure
<i>N_{eq}</i>	Equivalent number of cycles to failure
<i>S_{max}</i>	Maximum stress
<i>S_{min}</i>	Minimum stress
<i>S_{op}</i>	Crack opening stress
<i>S_y</i>	Material constant related to the yield stress
α	Material constant defining the crack opening stress
β	Material constant defining the crack opening stress
$\Delta\epsilon$	Local strain range
$\Delta\epsilon^*$	Strain based damage parameter
$\Delta\epsilon_{CA}$	Constant amplitude strain range
$\Delta\epsilon_{eff}$	Effective local strain range
$\Delta\epsilon_i$	Intrinsic strain range at which crack does not propagate
$\Delta\sigma$	Local stress range
ΔS	Nominal stress range
$\Delta\epsilon_{min}$	Minimum local strain
$\Delta\epsilon_{op}$	Local crack opening strain

INTRODUCTION

Reference fatigue life data for the design of notched structural components are currently obtained from constant amplitude stress or strain controlled tests. However, numerous investigations¹⁻⁴ have shown that for variable amplitude loading experimental fatigue lives can be lower than the fatigue lives predicted using this data by factors of as great as 10. The reason for the greater than predicted severity of variable amplitude loading is that the large load cycles which cause local notch stresses of the order of the yield stress reduce the crack opening stress and increase the effective stress for subsequent smaller cycles^{5,6}. As a result, the crack growth rate and "damage" for the smaller cycles is increased and even small cycles below the constant amplitude fatigue limit can cause a significant amount of damage.

Researchers in our laboratory have proposed an effective strain-life curve for use in fatigue damage calculations. The effective strain range, $\Delta\epsilon_{eff}$, the range of strain for which a fatigue crack is open during a cycle, is given by the difference between the maximum strain and the greater of the minimum strain or the crack opening strain. A damage parameter $E\Delta\epsilon^*$ is introduced:

$$E\Delta\epsilon^* = E\Delta\epsilon_{eff} - E\Delta\epsilon_i \quad (1)$$

where E is the elastic modulus and $\Delta\epsilon_i$ is a material's intrinsic fatigue limit strain range below which a fully open crack will not cause fatigue damage. The strain

range $\Delta\epsilon^*$ is the part of the strain range which causes fatigue crack growth and damage. This parameter was found to be related to fatigue life by a power law

$$E\Delta\epsilon^* = AN_f^b \quad (2)$$

where A and b are material constants.

Previous studies⁷ have shown that the parameter $E\Delta\epsilon^*$ adequately accounts for mean stress effects in constant amplitude loading and gives good fatigue life predictions for variable amplitude loading for a variety of metals and load histories.

This paper describes a test program to obtain an effective strain-life curve and estimates of crack opening stress levels after overloads with a minimum amount of testing effort. Examples are given of the use of the data obtained to make life predictions for variable amplitude fatigue of smooth and notched components.

THE EFFECTIVE STRAIN-LIFE CURVE

When steady crack opening strain levels for constant amplitude straining are available, the effective strain in a cycle can be calculated directly as the difference between the maximum and crack opening strain. In this case, an effective strain-life curve can be constructed from the conventional fully reversed constant amplitude strain-life data. However, measuring crack opening stresses at the high local stress levels and short crack lengths associated with the growth of cracks from stress raisers is time consuming and requires equipment not found in many laboratories⁸.

Analytical⁹ and experimental studies^{5,8,10} have shown that if the maximum stress level in a fatigue test is equal to the cyclic yield stress, the crack opening stress falls below zero for many metals, fatigue cracks are fully open at all positive stress ratios and the applied strain range is fully effective. The range of strains which are fully effective can be extended by combining periodic large compression-tension overload cycles with smaller constant amplitude cycles having approximately the same peak stress as the large cycles^{5,11}. The type of stress time histories employed in such tests together with the resulting crack opening stress variation is shown in Figure 1. Each overload cycle decreases the crack opening stress which then increases

toward the steady state crack opening stress of the smaller cycles⁸.

An equivalent fatigue life for the smaller constant amplitude cycles, N_{eq} , is obtained by (a) subtracting the damage due to the overloads from unity to obtain the damage due to the constant amplitude cycles, (b) dividing by the number of constant amplitude cycles in the fatigue test to obtain the damage per constant amplitude cycle, and (c) taking the reciprocal of this value to obtain the equivalent life for the constant amplitude cycles.

Figure 2 gives fatigue data for fully reversed constant amplitude strain controlled fatigue tests and equivalent fatigue life data¹⁰ for tests with stress time histories of the type shown in Figure 1 for 2024 T351 aluminium. The $E\Delta\epsilon_{eff}$ vs life curve shown was derived from a curve fitted to the constant amplitude fully reversed strain-life data by subtracting the strain below the crack opening strain in a stress-strain loop from the strain range at given fatigue lives. The $E\Delta\epsilon_{eff}$ curve gives a good fit to the long life portion of the overload data. In this region, the crack opening stress is below the minimum stress and the strain range is fully effective. Crack opening stress levels were measured with a 1000 \times optical microscope⁸. The data were used to obtain the constants in the empirical equation of Du Quesnay *et al.*, which gives the steady state crack opening stress S_{op} as

$$S_{op} = \alpha S_{max} \left(1 - \left(\frac{S_{max}}{S_y} \right)^2 \right) - \beta S_{min} \quad (3)$$

where S_{max} and S_{min} are the maximum and minimum stresses in a stress-strain cycle, S_y is the cyclic yield stress and α and β are material constants. At very high strain levels with large plastic strains, Equation (3) gives a crack opening stress that is too low. Experience with a number of metals suggests that the crack opening stress level be taken as half the minimum stress when Equation (3) gives a lower value. This gives reasonably accurate values of the effective strain range for high strain levels in the metals examined to date.

The curves of $E\Delta\epsilon^*$ vs N_f and $E\Delta\epsilon_i$ vs N_f shown in Figure 2 were obtained by choosing a value of $E\Delta\epsilon_i$ which gave the best log-log linear fit of the

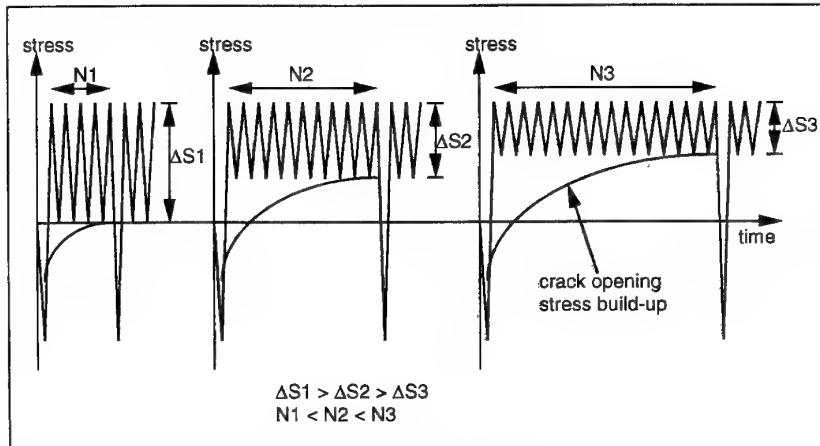


Figure 1 The stress-time histories used to construct the effective strain-life curve

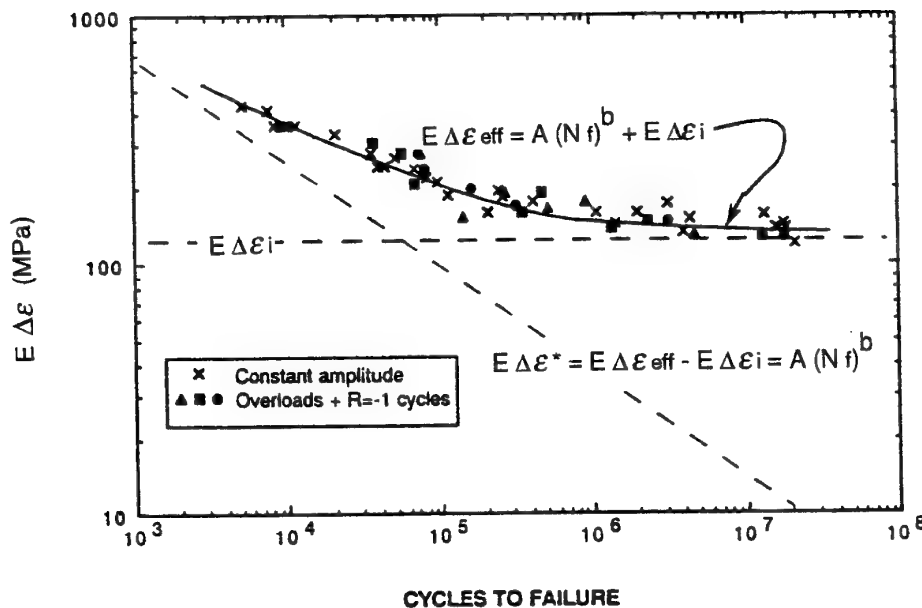


Figure 2 Fatigue life data for fully reversed constant amplitude and overload tests of 2024 T351 aluminium alloy

$E\Delta\epsilon^*$ values calculated from Equation (1) vs N_f . A plot of $E\Delta\epsilon^*$ vs N_f corresponding to the chosen $E\Delta\epsilon_i$ is shown in Figure 3². The linear curve shown gives a good fit to the $E\Delta\epsilon^*$ vs N_f data.

TESTS TO OBTAIN AN EFFECTIVE STRAIN-LIFE CURVE

In Figure 2, it is evident that at high strains the effective strain-life curve approaches the constant amplitude strain-life curve as the fraction of the stress-strain cycle that is closed becomes small. As noted earlier, the effective strain range at high strains calculated assuming that the crack opens at one half the minimum stress gives a good estimate of the small

fraction of the strain range between the minimum and crack opening stresses. A strain history such as that shown in Figure 1 gives effective strain-life data directly for low strain ranges and long lives. In using a strain time history such as that in Figure 1, the application of large overloads at frequent intervals maintains a very low crack opening stress so that even quite large subsequent cycles are fully open. When they are too large, however, the overloads do most of the damage and estimates of small cycle damage become inaccurate because, when small cycle damage is estimated by subtracting the overload damage from unity, the usual scatter in fatigue is magnified.

After experimenting with a variety of overload levels and frequencies of application^{10,12}, we have found

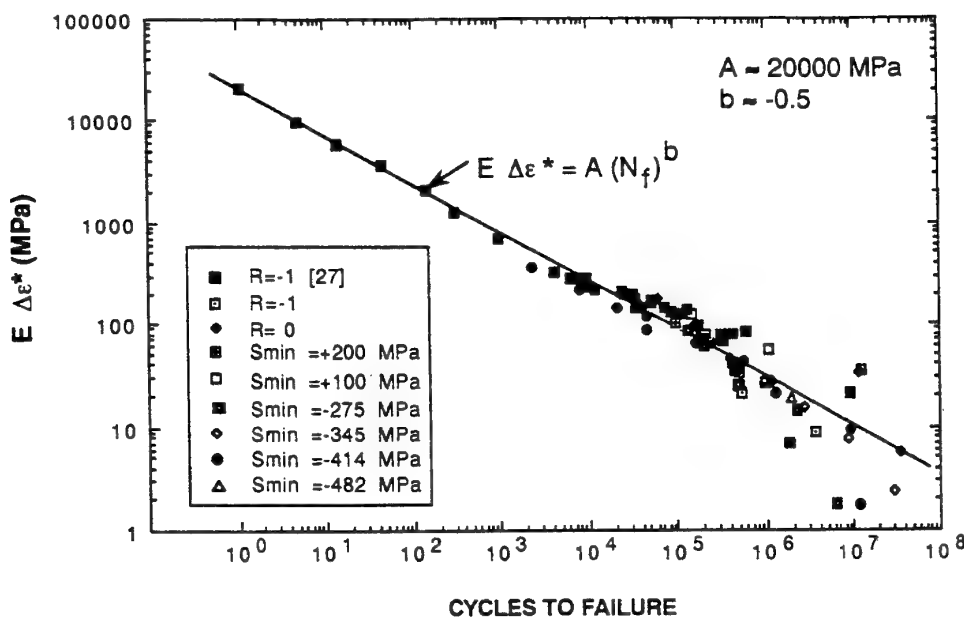


Figure 3 $E\Delta\epsilon^*$ vs fatigue life for 2024 T351 aluminium alloy

that using a fully reversed overload level that applied continuously would cause failure in 10^4 cycles, and adjusting the number of small cycles per block so that they do 80 to 90% of the damage per block, is satisfactory for a variety of metals. For very soft metals in which the amount of plastic strain is large at 10^4 cycles a smaller overload is used to allow load controlled testing which permits high test frequencies.

Figure 4 gives fully reversed constant amplitude strain-life data and equivalent life data obtained from tests using the load history of Figure 1 with an overload strain amplitude chosen to match the strain range at 10^4 cycles in the constant amplitude data for SAE 1045 steel¹³. The number of small cycles per block, η , for each test was chosen to give an estimated small cycle damage of 80% of the total damage.

An estimate of the effective strain range at a total strain range of 2% was made by subtracting one half the minimum stress divided by the modulus of elasticity from the total strain range. This corresponds to the previously noted observation that the crack opening stress can be taken to be one half the minimum stress at high strain levels. This data and the long life overstrain data for which the fatigue crack is expected to remain open throughout the stress-strain cycle are used to obtain an $E\Delta\epsilon^*$ vs N_f curve. A value of $E\Delta\epsilon_i$ which causes $E\Delta\epsilon^*$ values calculated from Equation (1) to fall on a log-log linear curve when plotted versus N_f is obtained by trial and error. The resulting linear $E\Delta\epsilon^*$ vs N_f curve, shown in Figure 5, gives a good fit to the data. The effective strain-life curve, established by summing $E\Delta\epsilon_i$ and $E\Delta\epsilon^*$ values at given fatigue lives, is shown in Figure 4. The long life fatigue data as expected fall on the curve.

The difference between the strain range for a fully reversed constant amplitude life curve $\Delta\epsilon_{CA}$ and that for the effective strain range life curve $\Delta\epsilon_{eff}$ at a given life is equal to the difference between the minimum strain, ϵ_{min} , and the crack opening strain, ϵ_{op} , in the constant amplitude stress-strain loop.

$$\Delta\epsilon_{CA} - \Delta\epsilon_{eff} = \epsilon_{op} - \epsilon_{min} = (S_{op} - S_{min})/E \quad (4a)$$

or

$$S_{op} = S_{min} + E(\Delta\epsilon_{CA} - \Delta\epsilon_{eff}) \quad (4b)$$

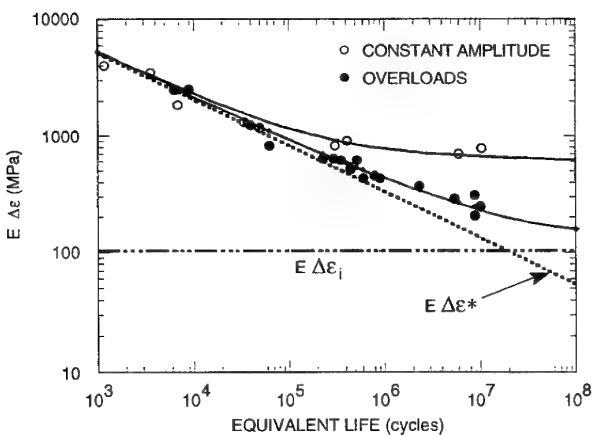


Figure 4 Fatigue life data for fully reversed constant amplitude and overload tests of SAE 1045 steel

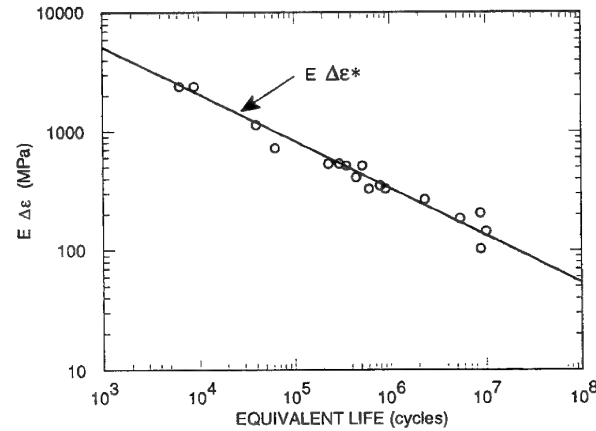


Figure 5 $E\Delta\epsilon^*$ vs fatigue life for SAE 1045 steel

Values of S_{op} obtained from the constant amplitude and effective strain-life curves of Figure 4 using Equations (4a) and (4b), together with a curve of Equation (3) fitted to the data and measured crack opening stress measurements¹³ are shown in Figure 6. The curve obtained from the present procedure gives crack opening stress values very close to the experimental values. Values of 0.75 and 0.23 were obtained for α and β , respectively. The value of S_y for this material obtained from an incremental step test is 400 MPa.

FATIGUE LIFE PREDICTIONS FOR SERVICE STRAIN HISTORIES

The authors' coworkers² have used equivalent strain-life curves and the $\Delta\epsilon^*$ damage parameter to predict fatigue lives for smooth specimens of a variety of metals subjected to measured service strain histories. In the examples given below, a log-skidder history consisting of 31,344 cycles and a grapple-skidder history consisting of 18,380 cycles were used. Each history was scaled to give various maximum strain ranges and applied to smooth specimens under strain control.

In performing the fatigue calculations, a block of the stress-strain history was rainflow counted for each test and the value of S_{op} calculated for the largest cycle in the test using Equation (3). The conservative

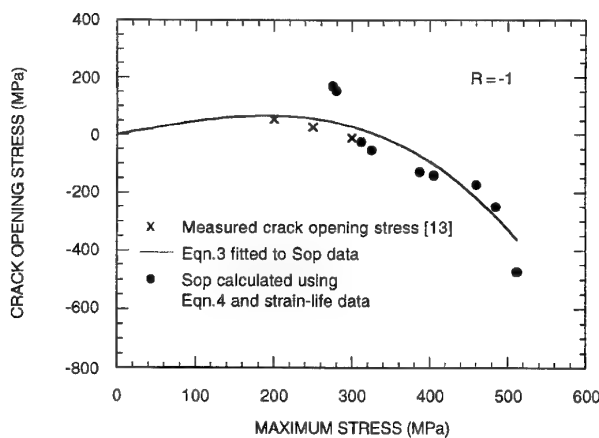


Figure 6 Equation (3) fitted to crack opening stress data

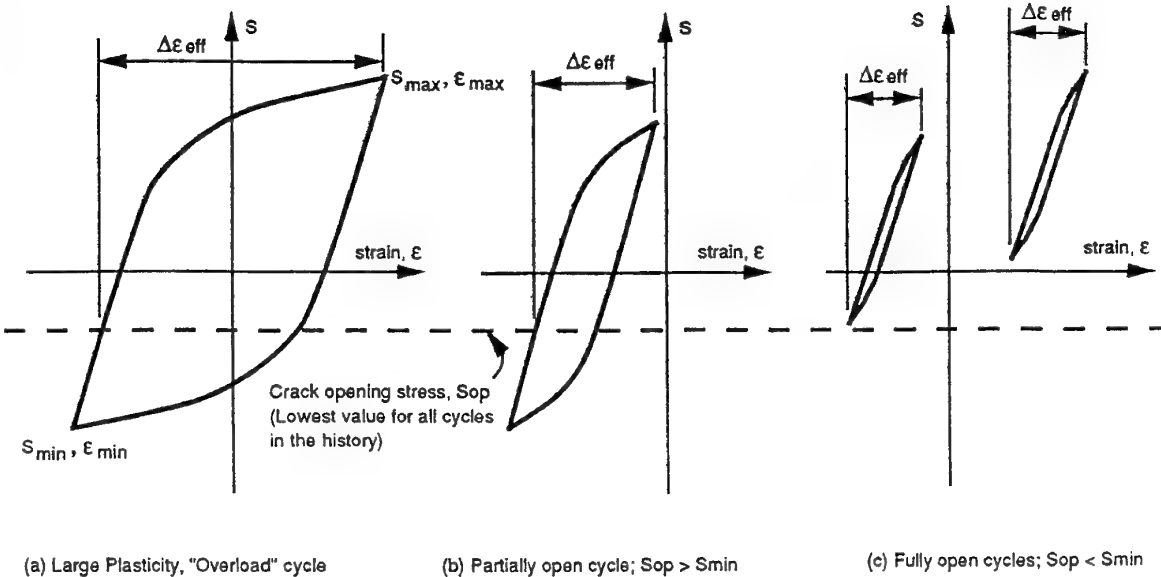


Figure 7 Typical rainflow counted cycles and crack opening stress approximation in a variable amplitude service history applied to specimens of a ductile material

assumption was made that this crack opening stress prevailed throughout the test and the value was used to calculate $\Delta\epsilon_{eff}$ for all the closed loops in the test as shown in *Figure 7*. The damage for all the cycles in a block was summed linearly and the number of blocks to failure was obtained as the reciprocal of the damage per block.

Experimental and predicted fatigue lives for an SAE 1045 steel tested using the grapple-skidder history³ and a 2024 T351 aluminium tested using the log-skidder history² are shown in *Figures 8* and *9*. Dashed curves in the figures indicate predictions made using the conventional constant amplitude reference fatigue data and a popular mean stress parameter¹⁴. The effective strain-life parameter gives predictions that follow the trend of the data well and tend to be conservative. It is assumed that the reason for the conservative predictions is the assumption that there is no recovery in the S_{op} from its lowest level following the largest strain cycle in the history. The predictions made using constant amplitude strain-life data signifi-

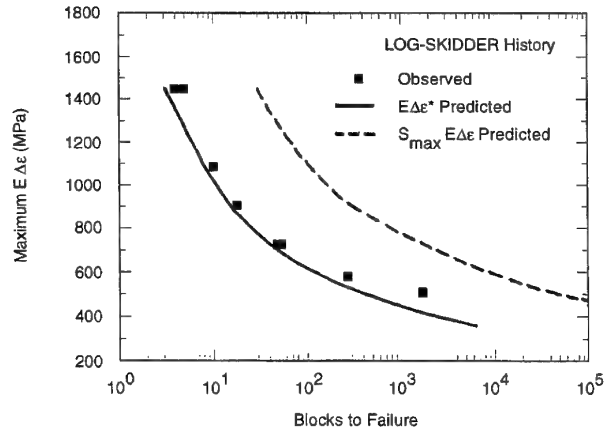


Figure 9 Experimental and predicted fatigue lives for 2024 T351 aluminium alloy² tested using the log-skidder history

cantly overestimate fatigue life. The reason is that steady state S_{op} levels are higher and effective strain ranges are smaller for small cycles in the constant amplitude reference tests and in the constant amplitude mean stress tests that were used to establish mean stress parameters than they are in the service strain histories.

FATIGUE LIFE PREDICTIONS FOR VARIABLE AMPLITUDE LOADING OF NOTCHED PLATES

Fatigue tests using overload histories similar to those of *Figure 1* were performed on plates of 2024 T351 aluminium having circular centre notches. The maximum nominal stress of the smaller cycles was equal to the maximum stress of the overload cycle. The overload cycle was selected so that the notch root stress cycle was equal to the cyclic yield stress of the metal, ± 350 MPa. Loading blocks consisted of an overload followed by 1000 cycles of the small cycle

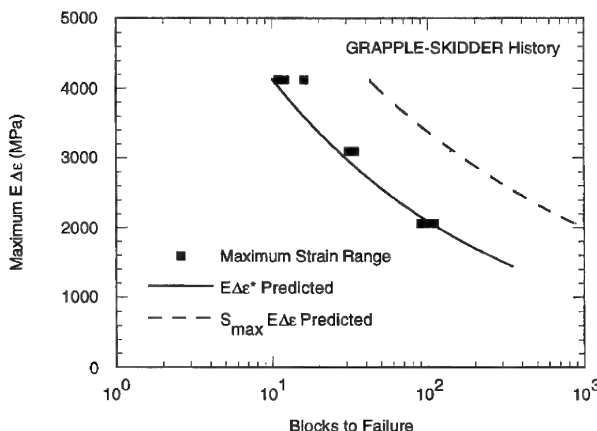


Figure 8 Experimental and predicted fatigue lives for SAE 1045 steel³ tested using the grapple-skidder history

selected for the test. Test data for notch diameters of 3, 1 and 0.24 mm are shown in *Figure 10*.

Fatigue lives were predicted using effective strain-life and $E\Delta\epsilon^*$ -life data such as that of *Figures 2* and *3*, obtained as outlined earlier, from smooth specimen constant amplitude and overload tests given in Ref. ⁶. Constants for Equation (3) were again obtained from the constant amplitude and overstrain data. Notch root strains were calculated using Neuber's rule ¹⁵ for inelastic strains:

$$K_t \Delta S = (\Delta\sigma \Delta\epsilon E)^{1/2} \quad (5)$$

where K_t is the theoretical stress concentration factor, ΔS is the nominal stress range, E is the modulus of elasticity, and $\Delta\sigma$ and $\Delta\epsilon$ are the local stress and strain ranges, respectively. A block of the notch root stress-strain history was then rainflow counted and $\Delta\epsilon_{\text{eff}}$ values were obtained as shown in *Figure 7*. In this case the value of S_{op} used was the value calculated for the overload cycle using Equation (3).

The predictions are shown as the solid curve in *Figure 10*. They are conservative. It is of interest to note here that no allowance has been made in these predictions for a reduced stress concentration factor for small notch sizes, even though previous work ¹⁶ has shown this metal to have a reduced fatigue notch factor for the two smaller notch sizes in constant amplitude fatigue. Although there is considerable scatter in the data for the two smaller notch sizes, the lower bound of these data at long lives is approximately the same as for the largest notch. Other work ⁶ has also shown that there is a smaller reduction in the effectiveness of a notch in fatigue with decreasing size in variable amplitude than in constant amplitude fatigue. It is believed that the reduced notch sensitivity in constant amplitude fatigue is due to cracks being stopped by an increase in crack opening stress. The large cycles in variable amplitude fatigue do not allow the crack opening stress to increase.

At short lives the predictions become increasingly conservative, since the use of notch root stresses and strains ignores the decrease in stress and strain as a crack grows out of the notch. As a result, the smooth specimen fatigue data obtained from a specimen with

a uniform stress and strain across the test specimen is conservative.

Predictions based on constant amplitude fatigue data plus a mean stress correction given by the dashed curve are nonconservative.

DISCUSSION

The test procedure suggested gives good effective strain-life data and a reasonable estimate of steady state crack opening stresses with a reasonable amount of testing. An improved estimate of crack opening stress levels for non-fully reversed stress cycles can be obtained if long life fatigue data is generated for a second stress ratio, such as zero to maximum loading, and S_y as well as α and β is taken to be a variable in Equation (3). However, since large stress-strain cycles have almost fully reversed stresses due to inelastic material stress-strain response, little improvement in the estimated S_{op} is expected for the largest cycle in a load history which is used in damage calculations. The additional test effort would add little to the accuracy of fatigue life predictions.

The effective strain-life curve has been found to adequately account for the effects of overloads and mean stresses on fatigue life. The assumption that the crack opening stress level remained at the level following the largest cycle in a block of load history gave fatigue life predictions that were conservative, but not unduly so in smooth specimens. More conservative predictions were obtained for notched plates at short lives. Here the constant stress field in the smooth specimens is more severe than the decaying stress field at a notch, so that the crack driving stresses as a crack grows from a notch are less severe than those in a smooth specimen. At long lives, where most of the fatigue life is spent in the initial part of crack growth close to the notch root, predictions fall closer to the lower boundary of the data for the notch sizes examined.

The prediction procedure used with the effective strain-life curve follows almost the same methodology as existing fatigue life prediction procedures using constant amplitude strain-life data. These procedures can relatively easily be modified by replacing the strain-life curve with the effective strain-life curve and using the effective strain range calculated as shown in *Figure 7* in place of the strain range for rainflow counted stress-strain loops ³.

CONCLUSIONS

1. A fatigue test program including fully reversed constant amplitude strain tests and tests in which a fully reversed overload cycle is followed by smaller constant amplitude cycles with the same maximum stress as the overload generates data for an effective strain-fatigue life curve and a crack opening stress curve with a reasonable test effort.
2. The effective strain-fatigue life curve together with a crack opening stress estimated using the data gave conservative fatigue life estimates for variable amplitude loading of smooth and notched specimens.

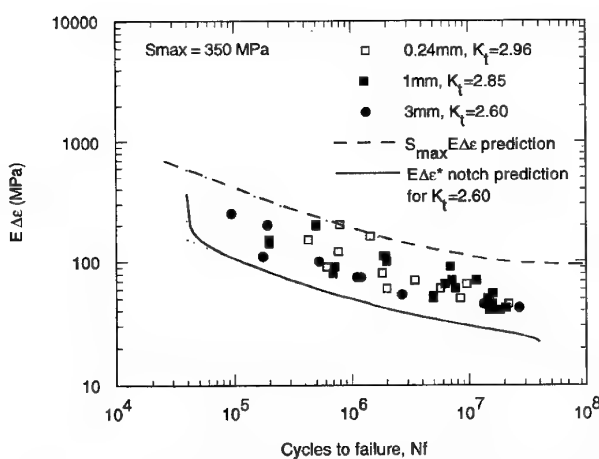


Figure 10 Strain-life predictions for notched 2024 T351 aluminium alloy specimens

REFERENCES

- 1 Conle, F. A. and Topper, T. H., Overstrain effects during variable amplitude service history testing. *International Journal of Fatigue*, 1980, **3**, 130–136.
- 2 Du Quesnay, D. L., Topper, T. H. and Jurcevic, R., A new fatigue life prediction model for variable amplitude loading. In *Localized Damage II*, eds M. H. Aliabadi, D. J. Cartwright and H. Nisitani. Computational Mechanics Publications, Southampton, 1992, pp. 103–120.
- 3 Du Quesnay, D. L., Pompetzki, M. A. and Topper, T. H., Fatigue life predictions for variable amplitude strain histories. SAE Technical Paper Series No. 930400. Society of Automotive Engineers, Warrendale, PA, 1993.
- 4 Dowling, N. E., Estimation and correlation of fatigue lives for random loading. *International Journal of Fatigue*, 1988, **10**(3), 179–185.
- 5 Vormwald, M. and Seeger, T., The consequences of short crack closure on fatigue crack growth under variable amplitude loading. *Fatigue and Fracture of Engineering Materials and Structures*, 1991, **14**(2,3), 205–225.
- 6 Du Quesnay, D. L., MacDougall, C., Dabayeh, A. A. and Topper, T. H., Notch fatigue behaviour as influenced by periodic overloads. *International Journal of Fatigue*, 1995, **17**(2), 91–99.
- 7 Topper, T. H., Du Quesnay, D. L., Pompetzki, M. A. and Jurcevic, R., A crack closure based model for mean stress and overload effects on fatigue damage. International Symposium on Fatigue Damage Measurement and Evaluation Under Complex Loadings, Fukuoka, Japan, July 1991.
- 8 Dabayeh, A. A. and Topper, T. H., Changes in crack-opening stress after underloads and overloads in 2024-T351 aluminum alloy. *International Journal of Fatigue*, 1995, **17**(4), 261–269.
- 9 Newman, J. C., A crack opening stress equation for fatigue crack growth. *International Journal of Fracture*, 1984, **24**, R131–R135.
- 10 Du Quesnay, D. L., Fatigue damage accumulation in metals subjected to high mean stress and overload cycles. Ph.D. Thesis, University of Waterloo, Waterloo, Ont., Canada, 1991.
- 11 Du Quesnay, D. L., Pompetzki, M. A., Topper, T. H. and Yu, M. T., The effects of compression and compressive overloads on the fatigue behaviour of a 2024-T351 aluminum alloy and a SAE 1045 steel. American Society of Testing and Materials, ASTM STP 942, pp. 173–183.
- 12 Pompetzki, M. A., Topper, T. H., Du Quesnay, D. L. and Yu, M. T., Effect of compressive underloads and tensile overloads on fatigue damage accumulation in 2024-T351 aluminum. *Journal of Testing and Evaluation, JTEVA*, 1990, **18**(1), 53–61.
- 13 MacDougall, C. and Topper, T. H., The influence of variable amplitude loading on crack closure and notch fatigue behaviour. *International Journal of Fatigue*, in press.
- 14 Smith, K. N., Watson, P. and Topper, T. H., A stress-strain function for the fatigue of metals. *Journal of Materials, JMLSA*, 1970, **5**(4), 767–778.
- 15 Neuber, H., Theory of stress concentration for shear-strained prismatic bodies with arbitrary non-linear stress-strain laws. *Journal of Applied Mechanics, Transactions ASME*, 1961, **E28**, 544.
- 16 Abdel-Raouf, H., Du Quesnay, D. L., Topper, T. H. and Plumtree, A., Notch size effects in fatigue based on surface strain redistribution and crack closure. *International Journal of Fatigue*, 1992, **14**(1), 57–62.

PII: S0142-1123(97)00058-3

Fatigue crack growth threshold: implications, determination and data evaluation

H. Döker

*DLR, German Aerospace Research Establishment, Institute of Materials Research,
 D-51170 Köln, Germany*

In standard test procedures the determination of fatigue crack growth threshold values is part of $da/dN-\Delta K$ -curve determinations, and with one specimen only one threshold value can be determined. Thus, the complete characterization of the threshold behaviour of a certain material, for example, by $\Delta K_{th}-R$ -curves, is extremely time consuming, specimen consuming and expensive. Based on experimental experience, a procedure is described which allows a complete $\Delta K_{th}-R$ -curve determination with a single specimen. The threshold behaviour of a material can be described by four constants, which can easily be determined. A very simple analytical description of the threshold behaviour of materials is given, by which even quite complicated appearing $\Delta K_{th}-R$ -curves can be represented. © 1998 Elsevier Science Ltd.

(Keywords: fatigue crack propagation; crack growth threshold; threshold determination; test methods; data evaluation; load ratio; standardization)

INTRODUCTION

According to ASTM standard E 647¹ the fatigue crack growth threshold ΔK_{th} is defined as the asymptotic value of the stress-intensity factor range ΔK at which the fatigue crack growth rate da/dN of long cracks approaches zero. Though fatigue crack growth threshold values have been determined for at least 30 years, no self-sufficient standard for the determination of threshold values independent from da/dN -curve determinations, could be established up to now. According to standard test procedures like ASTM E 647, the determination of fatigue crack growth threshold values is part of da/dN -curve determinations, and with one specimen only one threshold value can be determined. Thus, the complete characterization of the threshold behaviour of a certain material in accordance with existing standards, for example, by a $\Delta K_{th}-R$ -curve, is extremely time consuming, specimen consuming and expensive. Therefore, in many cases where threshold data seems to be indispensable, only isolated values are determined, and sometimes, the threshold behaviour of a material is judged on the basis of a ΔK_{th} -value determination at a load ratio, R , of 0.1.

This procedure is very questionable and it seems desirable to develop an independent and more economical procedure for the characterization of the threshold behaviour of materials. Based on the now 30 years of experience with threshold determinations, it is possible to propose such a procedure. First of all, threshold determination has to be decoupled from the da/dN -curve determination. This makes 10 or more threshold

determinations possible with one $C(T)$ -specimen, if the specimen width is large enough. Then, by analysing the threshold data it is possible to reduce the number of threshold determinations necessary to completely characterize a material.

GENERAL THRESHOLD BEHAVIOUR

The threshold behaviour of a material is usually described by a $\Delta K_{th}-R$ -curve, which may be influenced by environment and temperature. In many cases, ΔK_{th} decreases with increasing positive R -ratio as shown in Figure 1(a). In Figure 1(b) the curve of Figure 1(a) is presented as a $K_{max, th}-R$ -diagram according to Schmidt and Paris². $K_{max, th}$ is the K_{max} value at threshold. In Figure 1(c) the same curve is shown as a $\Delta K_{th}-K_{max}$ -diagram according to Döker *et al.*³.

The threshold behaviour of Figure 1(a) and (b) was interpreted by Schmidt and Paris² as a crack closure phenomenon according to Figure 1(d). To propagate a crack, it is thought that a stress-intensity factor range $\Delta K > \Delta K_0$ is necessary. As long as K_{min} of the loading cycle remains lower than the crack opening load K_{op} , ΔK_{th} decreases linearly with increasing positive R according to:

$$\Delta K_{th} = K_{max, 0}(1-R) \text{ for } 0 \leq R \leq R_c \quad (1)$$

with $K_{max, 0}$ being K_{max} at threshold for $R = 0$. The effective threshold, ΔK_0 , is:

$$\Delta K_0 = K_{max} - K_{op} = K_{max, 0} - K_{op} \quad (2)$$

For $R > R_c$, K_{min} is higher than K_{op} , and $\Delta K_{th} = \Delta K_0$.

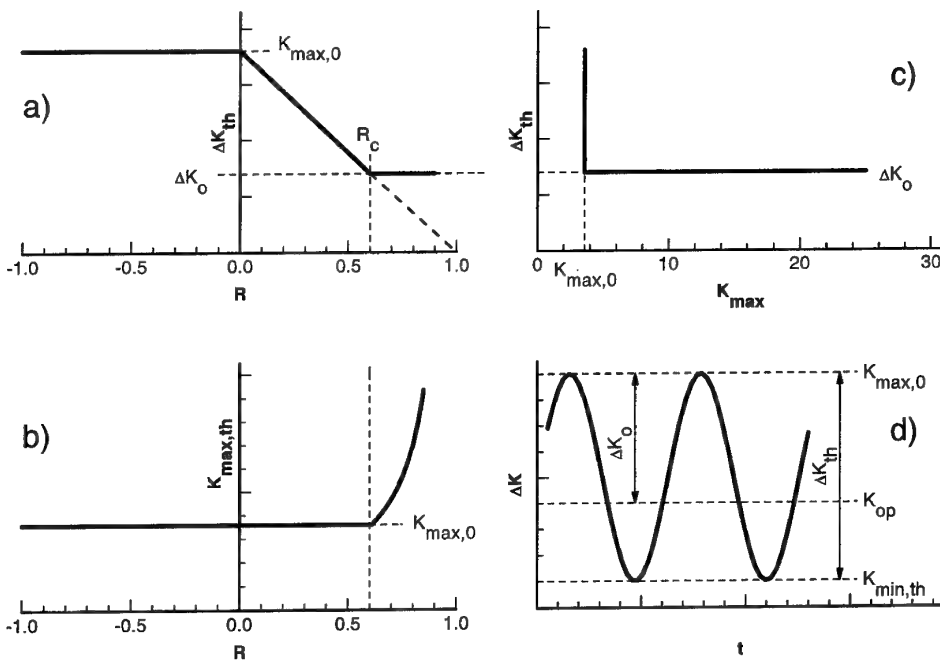


Figure 1 (a–c) Fundamental threshold behaviour of metallic materials in different graphical presentations and (d) presentation of the crack closure threshold model of Schmidt and Paris²

For negative R -ratios ΔK_{th} remains constant according to the definition of ΔK in ASTM E 647 and equals $K_{\max,0}$.

The two diagrams in *Figure 1(b)* and *1(c)* are much better suited to represent and understand the threshold behaviour of a corresponding material than the traditionally used $\Delta K_{\text{th}}-R$ -diagram. *Figure 1(b)* and *1(c)* show clearly, that under constant amplitude conditions a crack will grow, if at the same time $K_{\max} > K_{\max,0}$ and $\Delta K > \Delta K_0$. Thus, the threshold behaviour can be described by two independent constants only, namely $K_{\max,0}$ and ΔK_0 (see also Vasudevan *et al.*⁴). Experience shows that ΔK_0 is mainly determined by the base material of an alloy, and that the variation within one alloy group is very small. ΔK_0 values for different base materials are proportional to their elastic moduli⁵ while $K_{\max,0}$ can be strongly influenced by microstructure and environment.

$\Delta K_{\text{th}}-R$ -curves of the type shown in *Figure 1(a)* are often observed for steels and Al-alloys. In many cases, however, the observed $\Delta K_{\text{th}}-R$ -curves deviate considerably from the behaviour shown in *Figure 1(a)*. Neither is the decrease for low R -ratios linear nor is ΔK_{th} constant for high R -ratios. *Figure 2(a)* shows the $K_{\max,\text{th}}-R$ - and *Figure 2(b)* the $\Delta K_{\text{th}}-K_{\max}$ -diagram of such a material, a X 2 Cr-Ni-Mo-17-12 steel at 550°C⁶ (tests performed at DLR). It can be seen, that the $K_{\max,\text{th}}-R$ -curve at low R -ratios and the $\Delta K_{\text{th}}-K_{\max}$ -curve for higher K_{\max} -values can be represented by straight lines with the mathematical equations

$$K_{\max,\text{th}} = K_{\max,0} + \beta R \quad \text{with } \beta \geq 0 \quad (3)$$

$$\Delta K_{\text{th}} = \Delta K_0 + \alpha K_{\max} \quad \text{with } \alpha \leq 0 \quad (4)$$

with $K_{\max,0}$ and ΔK_0 being the intersection points of the two straight lines with the vertical axes, and α and β the respective slopes. Based on the simple relations

$R = K_{\min}/K_{\max}$ and $\Delta K = K_{\max}-K_{\min}$ applied to the threshold situation the $\Delta K_{\text{th}}-R$ -curve can be calculated by

$$\Delta K_{\text{th}} = (K_{\max,0} + \beta R)(1-R) \quad \text{from Equation (3)} \quad (5)$$

and

$$\Delta K_{\text{th}} = \frac{1-R}{1-R-\alpha} \Delta K_0 \quad \text{from Equation (4)} \\ \text{with } R < 1 \quad (6)$$

Equation (5) represents a downward oriented parabola, which intersects with the positive R -axis at $R = 1$ and with the ΔK_{th} -axis at $\Delta K_{\text{th}} = K_{\max,0}$ (see *Figure 3*). The curve of *Equation (6)* crosses the R -axis also at $R = 1$ and increases asymptotically to ΔK_0 . Now only four independent constants ($K_{\max,0}$, ΔK_0 , α and β) are necessary to describe the threshold behaviour of a material. Compared to the original understanding of Schmidt and Paris, Equations (5) and (6) give a first order approximation of the behaviour of a real material.

Figure 3(a) shows the construction of the $\Delta K_{\text{th}}-R$ -curve. The real ΔK_{th} -value is the maximum value of Equations (5) and (6). In region I of *Figure 3(a)* the threshold behaviour is controlled by *Equation (6)*. For a real material, ΔK_{th} can not decrease to 0, as the curve breaks off when K_{\max} reaches K_{lc} , that is, R reaches $(K_{\text{lc}}-\Delta K_{\text{th}})/K_{\text{lc}}$. In region II ΔK_{th} is controlled by *Equation (5)*. This means that $K_{\max,\text{th}}$ or, in the interpretation of Schmidt and Paris, that the crack opening load is influenced by K_{\min} . The transition point between region I and region II can be calculated by comparison of Equations (5) and (6).

For negative R -ratios ΔK_{th} decreases with decreasing R according to *Equation (3)*, as for negative R -ratios ΔK is defined as K_{\max} according to ASTM E 647 [region III in *Figure 3(a)*]. In region IV *Equation (6)* becomes relevant again and ΔK_{th} remains nearly con-

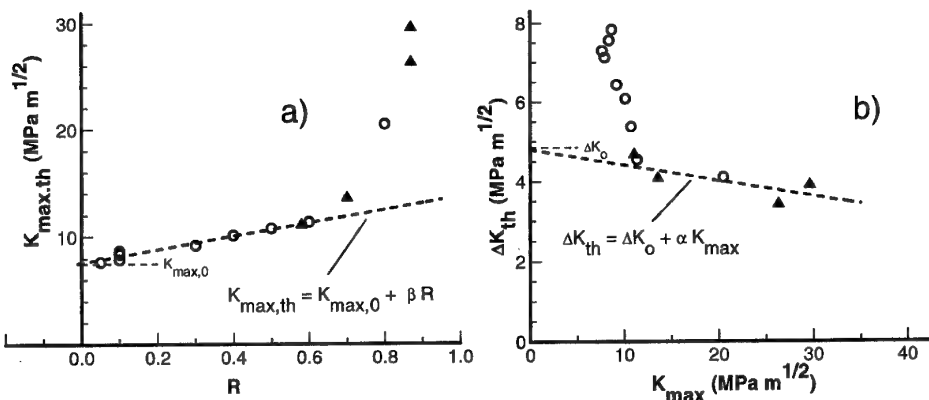


Figure 2 (a) $K_{\max,th}$ -R-diagram and (b) ΔK_{th} - K_{\max} -diagram for a high temperature steel at 550°C; ○, measured at constant R ; ▲, measured at constant K_{\max} (Huthmann and Gossman⁶)

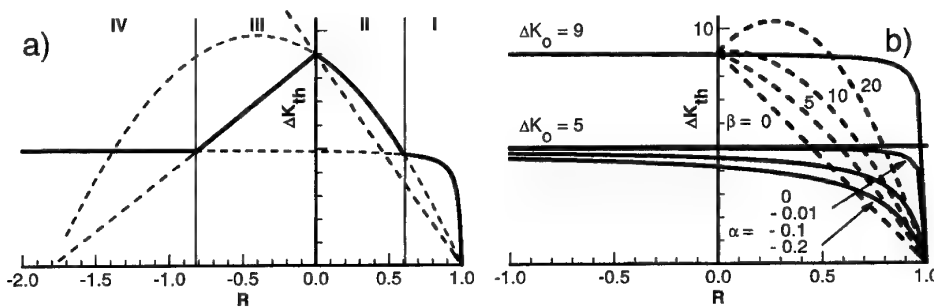


Figure 3 Construction of (a) a ΔK_{th} -R-curve and (b) the influence of a variation of the parameters α , β and ΔK_0 on the ΔK_{th} -R-curve

stant. An additional decrease of K_{\min} has no influence on ΔK_{th} .

In Figure 3(b) the influence of the magnitude of the four parameters $K_{\max,0}$, ΔK_0 , α and β is demonstrated. It is obvious that very different appearing ΔK_{th} -R-curves can be described. R -independent threshold behaviour is observed, if ΔK_0 has nearly the same magnitude as $K_{\max,0}$. If $K_{\max,0}$ is much higher than ΔK_0 , the threshold behaviour is mainly K_{\max} controlled and the deviation at high R -ratios cannot be observed during threshold determinations with constant R -ratio, unless extremely high R -ratios are used.

There are very few sources of threshold data in the negative and high positive R -ratio ranges. The data of Kemper *et al.*⁷ correlate very well with the curve shown in Figure 3(a). For positive R -ratios numerous data sets are available, and all checked data could be described according to Equations (3) and (4). This was for instance shown³ for data of Schmidt and Paris². Figure 4 shows the ΔK_{th} -R-curve for the data from Figure 2⁶. Data of Davenport and Brook exhibit the same behaviour⁸.

EXPERIMENTAL THRESHOLD DETERMINATION

As shown in the preceding paragraph, four independent constant values ($K_{\max,0}$, ΔK_0 , α and β) can describe the threshold behaviour of a material. These constants are well hidden in the ΔK_{th} -R-curve, but can be easily accessed via the $K_{\max,th}$ -R- and the ΔK_{th} - K_{\max} -diagrams. According to Figure 2, about five threshold values have to be determined at low R -ratio (e.g. 0.1

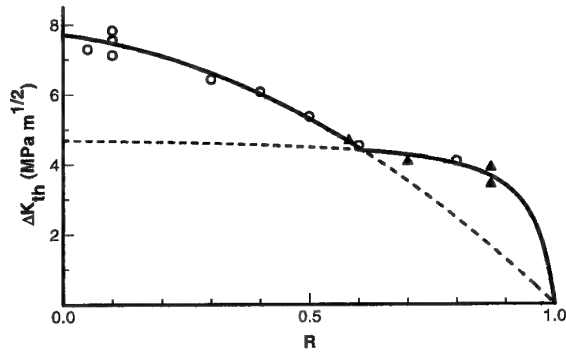


Figure 4 ΔK_{th} -R-diagram for the data from Figure 2⁶; ○, measured at constant R ; ▲, measured at constant K_{\max}

$\leq R \leq 0.5 \dots 0.7$) and about the same number at very high R -ratios, or better, at constant K_{\max} ⁹. The R -ratios and the K_{\max} -values should be evenly distributed in the relevant R - and K_{\max} -regions. The lowest K_{\max} -value should be chosen ca 20% higher than K_{\max} at threshold for the highest R -ratio of the constant R tests. The highest K_{\max} -value has to be lower than the limit for crack growth under constant load for the investigated material in the applied environment. In Figure 2 the values corresponding to the open circles were determined at constant R , whereas the values corresponding to the closed symbols were determined at constant K_{\max} . It can be seen that the result of a threshold determination is independent of the applied method. By calculating the regression lines through the data



Figure 5 Fracture surface of a 50 mm-C(T) specimen after ΔK_{th} -determinations

points, the four relevant constants to describe the threshold behaviour can be determined.

For the low R -ratio tests the load shedding procedure of ASTM E 647 may be applied. In our laboratory we use the d.c.-potential drop technique to measure the crack length, and use the crack length signal to control K_{max} and K_{min} applied to the specimen. After pre-cracking the specimen at low crack growth rates ($\sim 10^{-5}$ mm cycle $^{-1}$) for *ca* 1 mm, the applied ΔK is decreased by 5% every 0.1 mm until it takes more than 1 or 2 million cycles to pass the next 0.1 mm. This means that $da/dN < 10^{-7}$ mm cycle $^{-1}$ or 5×10^{-8} mm cycle $^{-1}$ has been reached. After this, the procedure is repeated (pre-cracking and load shedding) for the next R - or K_{max} -value. Figure 5 shows the fracture surface of such a specimen. The nice crack growth markings allow a post-mortem re-evaluation of the specimen. In order to avoid load interaction effects, it is recommended that for the single threshold determinations with one specimen R and K_{max} increase with increasing crack length.

According to ASTM E 647 the single threshold value is determined via an extrapolation procedure. The crack growth rates (equally spaced between 10^{-6} and 10^{-7} mm cycle $^{-1}$) are plotted in a log da/dN -log ΔK -diagram, and are extrapolated to 10^{-7} mm cycle $^{-1}$. The corresponding ΔK -value is taken as ΔK_{th} . This evaluation procedure is simply based on the tradition of plotting da/dN -curves in log-log-diagrams. Figure 6 shows that it could be better to use a linear plot of the da/dN -data to determine ΔK_{th} -values. The straight line in Figure 6(a) looks, transferred to the log-log-diagram, starting similar to the low crack growth region of a log da/dN -log ΔK -diagram. Vice versa the crack growth data points of Figure 6(b) taken from a real threshold measurement arrange on a straight line in Figure 6(a). The regression line through the data points can be easily extrapolated to $da/dN = 0$. The second advantage of the linear presentation of low crack growth rate data is, that it

is possible to determine an initial gradient of the da/dN - ΔK -curve, which is of interest for crack growth calculations. From the experience of numerous threshold determinations at the DLR laboratory one can state, that the crack growth rates for a valid extrapolation should lie between 2×10^{-7} and 5×10^{-8} mm cycle $^{-1}$.

It is clear from this procedure, that the crack growth rates measured during the single load shedding steps cannot be used as constant amplitude crack growth rates. Nevertheless, especially for the very low crack growth rates, the crack growth values corresponded well with correctly determined da/dN -curves.

If an unknown alloy is to be characterized with respect to threshold behaviour and the region of low R -ratio behaviour is unknown, the following procedure can be useful for making a rough estimate of the threshold behaviour of this material (Figure 7): one threshold value at low R -ratio (~ 0.1) is determined or is taken from a da/dN -curve, and is entered into a ΔK_{th} - R -diagram. Then, a straight line (line a in Figure

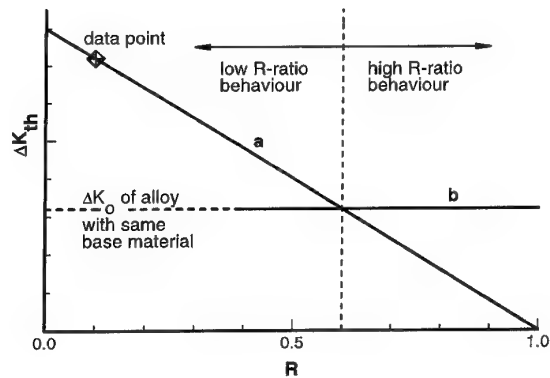


Figure 7 Diagram for the estimation of the threshold behaviour of an uncharacterized alloy from one data point and the known behaviour of an alloy with the same base material

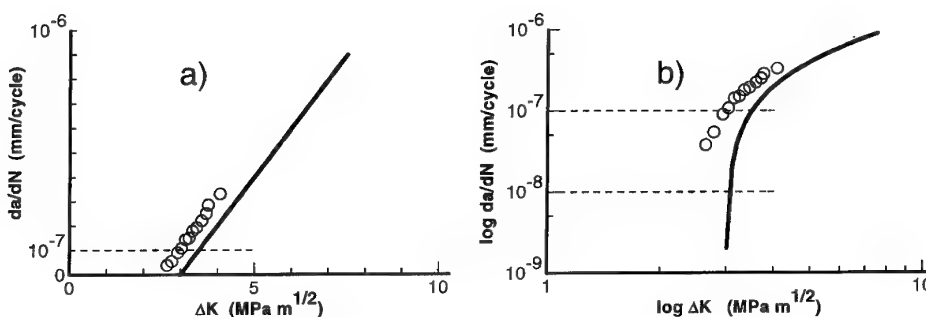


Figure 6 4(a) Linear plot and (b) log-log plot of da/dN -data of a single threshold determination

7) is drawn through this data point and the point $\{R = 1; \Delta K_{th} = 0\}$. A second line (line b) is drawn parallel to the R -axis in a distance corresponding to ΔK_0 or to a ΔK_{th} -value at high R -ratio of an alloy with the same base metal as the unknown alloy. Then, the region of low R -ratio behaviour is between $R = 0$ and R corresponding to the intersection point of these two lines. For metals, at positive R -ratios, line a can be expected to be the lower limit of threshold values of the unknown material.

SUMMARY

The fatigue crack growth threshold behaviour of metallic materials can be characterized to a first order approximation by two linear equations with four independent constants. The constants $K_{max,0}$ and α can be easily determined from a $K_{max,th}$ - R -curve derived from threshold determinations at low R -ratios. The constants ΔK_0 and β , which describe the intrinsic cyclic threshold behaviour, can be derived from a ΔK_{th} - K_{max} -curve from ΔK_{th} -determinations at high R -ratios or at constant K_{max} in the same manner.

The single threshold determination should render crack growth data between 2×10^{-7} and 5×10^{-8} mm cycle $^{-1}$. These da/dN -data should be plotted in a da/dN - ΔK -diagram with linear axes. Then ΔK_{th} should be determined as the intersection point between the regression line through the data points and the abscissa, which means an extrapolation to $da/dN = 0$.

Several threshold determinations can be performed with one specimen. In order to avoid interaction effects

between the single threshold determinations these should be performed in a sequence with increasing R and increasing K_{max} . Between the single threshold determinations the crack should be propagated at the R -ratio or the K_{max} -value of the next threshold determination at moderate crack growth rates for a distance that guarantees crack propagation along the whole crack front.

A new effort should be undertaken to establish an autonomous crack growth threshold standard.

REFERENCES

- 1 ASTM E 647, *Annual Book of ASTM Standards*, Section 3, Vol. 03.01. American Society of Testing and Materials, Philadelphia, PA, 1995, pp. 578–614.
- 2 Schmidt, R.A. and Paris, P.C., *Progress in Flaw Growth and Fracture Toughness Testing*. ASTM STP 536. American Society of Testing and Materials, Philadelphia, PA, 1973, pp. 79–94.
- 3 Döker, H., Bachmann, V., Castro, D. E. and Marci, G., *Zeitschrift für Werkstofftechnik*, 1987, **18**, 323.
- 4 Vasudevan, A. K., Sandananda, K. and Louat, N., *Materials Science and Engineering*, 1994, **A188**, 1.
- 5 Liaw, P. K., Leax, T. R. and Logsdon, W. A., *Acta Metallurgica*, 1983, **31**, 1581.
- 6 Huthmann, H. and Gossmann, O., In 23. *Vortragsveranstaltung des DVM-Arbeitskreises Bruchvorgänge*. Deutscher Verband für Materialforschung und -prüfung, Berlin, 1981, pp. 271–284.
- 7 Kemper, H., Weiss, B. and Stickler, R., In *Fatigue '87*, Vol. II, ed. R.O. Ritchie and E.A. Starke. EMAS, Cradley Heath, 1987, pp. 789–799.
- 8 Davenport, R. T. and Brook, R., *Fatigue of Engineering Materials and Structures*, 1979, **1**, 151.
- 9 Döker, H., Bachmann, V. and Marci, G., In *Fatigue Thresholds*, Vol. I, ed. J. Bäcklund, A. Blom and J. C. Beevers. EMAS, Cradley Heath, 1982, pp. 45–57.

PII: S0142-1123(97)00027-3

Role of microstructures on the growth of long fatigue cracks

A.K. Vasudevan*, K. Sadanand† and K. Rajan‡

*Office of Naval Research, Code-332, Arlington, VA 22217, USA

†Naval Research Laboratories, Code-6323, Washington, DC 20375, USA

‡Rensselaer Polytechnic Institute, Troy, NY 12180, USA

An analysis is presented to understand the role of microstructures on the two crack growth driving force parameters, K_{max}^* and ΔK_{th}^* , without invoking the extrinsic crack closure concepts. Microstructural variables considered are: grain size, precipitates and stacking fault energy. It is shown that K_{max}^* is strongly affected by the scale of the microstructure, such as grain size or precipitate spacing. For each case, the mode of slip deformation and environment affects the fatigue resistance as represented by K_{max}^* . However, the microstructures seem to have a smaller effect on ΔK_{th}^* . Also, the enhanced planarity of slip from the reduction in stacking fault energy has a pronounced effect on K_{max}^* when compared with the materials deforming under homogeneous slip. © 1998 Elsevier Science Ltd.

(Keywords: threshold fatigue crack growth; two threshold parameters K_{max}^* and ΔK_{th}^* ; microstructure – grain size and precipitate spacing; slip mode; crack deflection; stacking fault; pure iron; steel alloys; nickel-base; aluminum-base and copper-base alloys)

BACKGROUND

Experimentally, it has been observed that microstructures in a material have stronger or weaker effects on the near-threshold fatigue crack growth resistance. The three main types of microstructural parameters that contribute to the effect are: grain and precipitate size/distribution; and stacking fault energy. The size scales of these two microstructural features can span from $\sim 5 \mu\text{m}$ for grains (macro) to $< 0.01 \mu\text{m}$ for precipitates (micro). In all cases, it is the spacing of these blocking microstructural features from the advancing crack that governs the resistance to crack growth. Composite effects are observed when the spacing of one obstacle type differs from another. For instance, the precipitation effects on crack advance can override the grain size effect if the precipitates are not easily penetrable by the cracks. Similarly, reducing the stacking fault energy can accentuate the planarity of slip in a grain and hence restrict the cracks to grow along slip facets inducing significant crack deflection or crack path tortuosity. Other factors that can influence the planarity of slip would be antiphase boundary energy in order-disorder systems or in ordered intermetallics alloys.

We have shown that quantification of fatigue crack growth involves two *independent* driving force components, ΔK (cyclic) and K_{max} (static), which are *intrinsic* to a material in a given environment¹⁻⁶. Such a consideration differs from the *extrinsic crack closure* requirement that manifests itself behind the crack-tip

and which has been used to explain the effects of metallurgical and environmental variables^{3,4}. The two-parameter concept is self-consistent, does not require any extraneous factors to account for the effects of load-ratio R , overload crack retardation or short crack growth phenomena, etc. It fully describes the experimental trends for various materials and is applicable over the entire crack growth regime. Such an analysis leads to a broad classification of the entire fatigue crack growth behavior into five different classes based on $\Delta K-R$ data to provide a basis for understanding the synergistic effects of the mechanical and chemical crack growth driving forces with microstructure. We have observed that the two-parametric concept has wide applicability to various types of materials and for different environments^{2,5,6}. As an example, *Figure 1* shows the variation in $\Delta K_{th}-K_{max}$ for various types of alloys and composites at room and elevated temperatures. One can observe that for each material there are two critical stress intensity thresholds (ΔK_{th}^* and K_{max}^*) that depend on the material behavior in a given environment.

In the present article, we discuss the role of grain size, precipitate microstructure and stacking fault energy on the two driving forces for crack growth at the near threshold region. The effects at higher growth rates are minimized where the microstructural scales are smaller than the plastic zone size. We give selected examples from each of these microstructural groups to show their relative importance in governing the fatigue resistance. In all these systems, the aqueous environ-

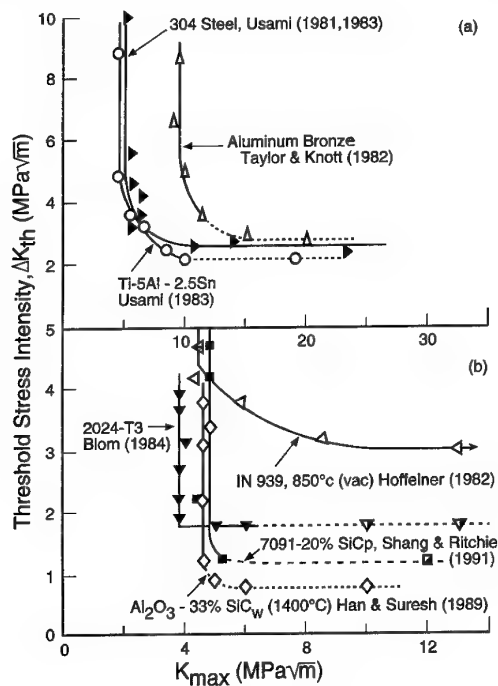


Figure 1 Fatigue map of ΔK_{th} vs K_{max} for several types of alloy at room and elevated temperature

mental effects are important, but are not considered due to lack of data⁵ in vacuum. All the discussions are presented in terms of the threshold critical stress intensities, K_{max}^* and ΔK_{th}^* , where the observed effects are significant.

GRAIN SIZE

K_{max}^* increasing with grain size

In most planar slip materials, the critical threshold stress intensity, K_{max}^* , increases with grain size. Here, the grain boundaries provide the extended topological obstacles to the slip. The effectiveness of these boundaries then depends on the degree of planar slip. In materials with homogeneous slip or easy cross slip, the grain size effect on K_{max}^* is relatively small. Figure 2 describes schematically the grain size (L) effect on K_{max}^* and ΔK_{th}^* when the material is deforming under planar or homogeneous slip modes. In the planar slip condition, the increase in K_{max}^* with grain size comes from the mechanism of crack deflection along crystallographic planes (see inset to Figure 2), giving rise to a faceted mode of crack growth. Here, K_{max}^* increases proportionally with the grain size, L . In contrast, the crack can grow by a plastic blunting process under homogeneous slip resulting in a smaller grain size effect. Thus, the factors that can govern the K_{max}^* dependence on grain size L are: (1) plasticity, (2) mode of slip, and (3) crack path tortuosity. To support the description in Figure 2, examples are given below for the case of, (a) pure iron, (b) mild steel alloys (homogeneous slip), for precipitation hardened aluminum-lithium and nickel-base superalloys (planar slip), and (c) solid solution Cu-Al alloy (with varying degree of planar slip). Planar slip alloys show two contrasting behaviors: (1) K_{max}^* increasing with grain size, and (2) K_{max}^* decreasing with grain size.

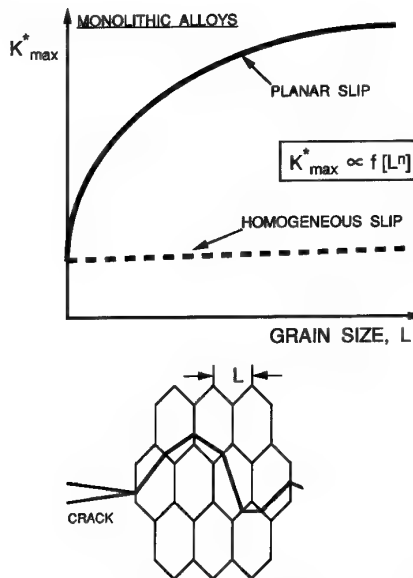


Figure 2 Schematic plot showing K_{max}^* variation with grain size L (linear scale) for planar and homogeneous slip alloys

(a) *Armco iron*. The first example is taken from an Armco iron⁷ that deforms under a homogeneous slip mode. Here the grain size was systematically varied from 3 μm to 3 mm. The critical threshold stress intensity values K_{max}^* , ΔK_{th}^* and the yield strengths were catalogued as a function of grain size. ΔK_{th}^* was estimated by extrapolating the $R = 0.1$ and 0.7 data to $R = 0.9$. The results of grain size (L) effect on K_{max}^* and ΔK_{th}^* are plotted in Figure 3a. Over a span of four orders of magnitude variation in L , K_{max}^* shows a modest increase with L . In comparison, the dependence of ΔK_{th}^* on L is even less. The slope of K_{max}^* vs L was ~ 0.2 on a log-log plot. The yield strength of iron decreased with the grain size, saturating at higher grain sizes. Interestingly, the yield strength did not follow the typical Hall-Petch relation. The average yield stress vs grain size exponent was ~ -0.3 instead of the usual -0.5 . The results seem to show that the yield stress has no direct relation to K_{max}^* .

From Figure 3a one observes that the yield stress decreases with grain size L . Whereas K_{max}^* increases linearly with L , suggesting that K_{max}^* is not directly affected by the yield stress. If plasticity (as represented by yield stress) is not contributing to K_{max}^* , then one needs to assess whether the role of crack path tortuosity is important. This can be done by analyzing the crack deflections in optical metallographs⁷ for each grain size. Estimated values of the amplitude and wavelength of crack meandering as a function of grain size are shown in Figure 3b. The amplitude and wavelengths are representative of the degree of tortuosity of a crack. It is interesting to note that both these factors increase with grain size up to $\sim 100 \mu\text{m}$ and then level off. The initial slope is consistent with one suggestion that crack deflection can take place at each grain boundary. At $L > 100 \mu\text{m}$, the slope is reduced significantly with a smaller grain size effect on K_{max}^* . This may mean that the amplitude and wavelength are less than the grain size, such that the crack deflections may be occurring at scales less than L . The deflection angle varies from about 40° to 90° as the grain size varies

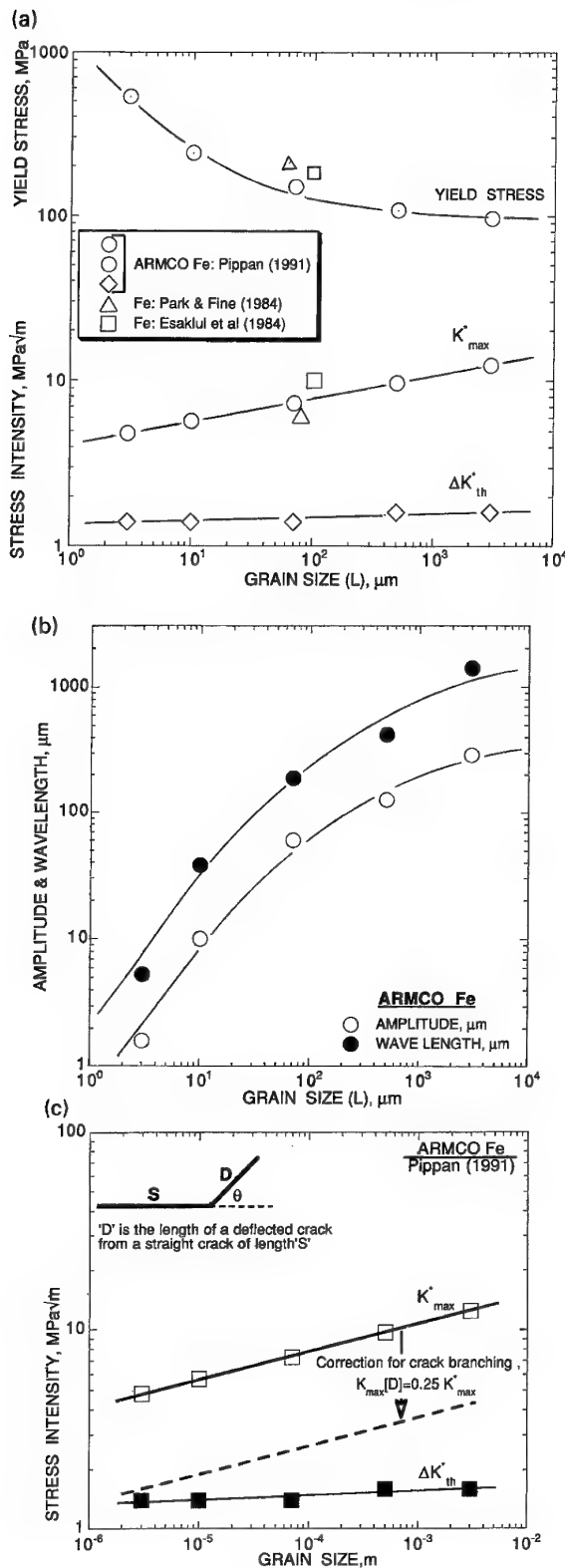


Figure 3 (a) Yield stress and K_{\max}^* variation with grain size for Armco Fe, (b) amplitude and wavelength variations with grain size for Armco Fe, and (c) contribution of crack deflection to K_{\max} .

from $3 \mu\text{m}$ to 3 mm . Crack deflection was observed within a large grain and is probably the result of some combination of $\{110\}$ slip bands intersecting in the iron lattice. There were also some cracks along the grain boundaries that branched onto slip bands. In such cases, the angle between branched cracks was $\sim 90^\circ$, suggesting that the crack deflections may be occurring along the $\langle 100 \rangle$ cleavage planes of iron. Thus the slope of the grain size effect on K_{\max}^* may indicate that: (1) the amplitude and wavelength of deflected cracks are less than the grain size; (2) cracks are deflecting at some specific angles; and (3) the angle of deflection changes from about 40° to 90° . When the deflections do occur within the grains, then secondary barriers to crack advance have become more important than the grain boundary itself. These secondary barriers could be $\{110\}$ type slip bands where the crack intersects.

Crack deflection. One can examine the role of crack deflection further by following the analysis given by Suresh⁸. We consider here only the deflection contribution, ignoring the role of crack closure. This is done by modifying his equation to give

$$K_{\max}[D] = \{D \cos^2(\theta/2) + S\}/(D + S)\}K_{\max}[\text{expt.}] \quad (1)$$

Here, $K_{\max}[D]$ is the stress intensity for a deflected crack, $K_{\max}[\text{expt.}]$ is the experimental value computed for a straight crack for a mode I loading, D is the length of a deflected crack at an angle θ with respect to a linear segment S of a crack (see inset to Figure 3c). The term in brackets is the crack deflection contribution for a mode I crack. Pippin⁷ has calculated the contribution from crack deflection using his fractographic data that showed a variation from 0.2 to 0.3 for the term in Equation (1) over the range of grain sizes studied. Assuming an average of 0.25, we can replot K_{\max}^* values in Figure 3a into those in Figure 3c. Here, K_{\max}^* is the same as $K_{\max}[\text{expt.}]$ since the experimental values represent mode I stress intensity. Then, $K_{\max}[D]$ can be estimated by including the correction factor of 0.25 in K_{\max} to give the dotted line curve in Figure 3c. One can observe that this corrected curve is still a function of grain size, about 25% lower in magnitude. Since the deflection term in Equation (1) did not become dependent on grain size, the functional dependence of K_{\max}^* on grain size remained the same. The analysis indicates that: (1) crack deflection enhanced K_{\max}^* by a factor of about 20%–30% in comparison to a linear crack, this factor essentially remains constant with grain size as the amplitude and wavelength are proportionally changing (see Figure 3b); (2) the slope of ~ 0.2 in Figure 3c remains the same even after correcting for deflection, and thus, in addition to deflection, other factors must be contributing to the K_{\max}^* dependence on grain size.

Thus crack deflection is not the only factor contributing to the K_{\max}^* variation with grain size, and some other factors play a role, as concluded by Pippin⁷. He points out that change in the shear stress field at the crack tip is an important contribution, and the value can increase when the deflected crack length $D > S$.

(b) Steels. A similar trend in K_{\max}^* vs L was observed in ferritic and low carbon¹⁰ steels, Figure 4. Here the slopes were about 0.2, similar to Armco

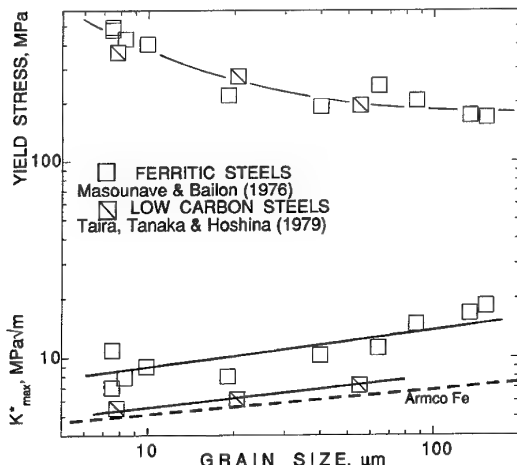


Figure 4 Yield stress and K_{\max}^* variation with grain size for steels

iron. As before, the yield stress of the alloy steels decreased nonlinearly with L . The threshold K_{\max}^* variation with grain size was related more to the change in grain size than the attendant change in yield strength. This lack of yield strength relationship to fatigue threshold behavior was analyzed by Yoder *et al.*¹² for steels. They observed that the yield strength was related more to fatigue at a transition ΔK which is slightly below the Paris region than at the near threshold ΔK . The transition $\Delta K \alpha \sqrt{L}$. Similar observations were also made on several alloys, including steels¹³. It was observed that K_{\max}^* was more dependent on the lamellar packet size than the prior austenitic grain size¹³. Taira *et al.*¹¹ have performed a detailed study on low carbon steel with grain sizes varying from 7.8 to 55 μm at various R ratios, -1.0, 0 and 0.5. They have concluded that the threshold stress intensity followed a Hall-Petch type relation with threshold $\Delta K \alpha \sqrt{L}$ at all R ratios, similar to the results of others^{11,13}.

(c) Nickel-base alloys. For a planar slip deforming material, we have chosen some examples from nickel-base superalloy 901¹⁴⁻¹⁷ and Astroloy¹⁸. Here the grain size effect on K_{\max}^* was large. The planarity of slip comes from the presence of high volume fraction of ordered γ' precipitate in the matrix. There were two sets of data for the 901 alloy with different heat treatments. The grain size effect is plotted in Figure 5 for the two cases in terms of K_{\max}^* and ΔK_{th}^* . The K_{\max}^* increased with L for both heat treated conditions, while ΔK_{th}^* remained nearly constant. The slope of the K_{\max}^* variation with grain size for the 901 alloys was about 1.0. The slope for the Astroloy was about 2.0. These high values of slopes can be due to: (1) size of γ' ; (2) size distribution of γ' ; and (3) mixture of fine and coarse grain structures. In a Waspalloy¹⁹ a factor of five reduction in threshold stress intensity at $R = 0.05$ has been observed when the γ' size was reduced from about 100 nm to about 10 nm for a constant grain size of about 130 μm . The increase in K_{\max}^* with L is probably due to crack deflections along crystallographic crack facets in these alloys. The slopes are higher than the Fe and Fe-base alloys shown in Figures 3 and 4. The yield strength and crack profile results were not reported for further analysis.

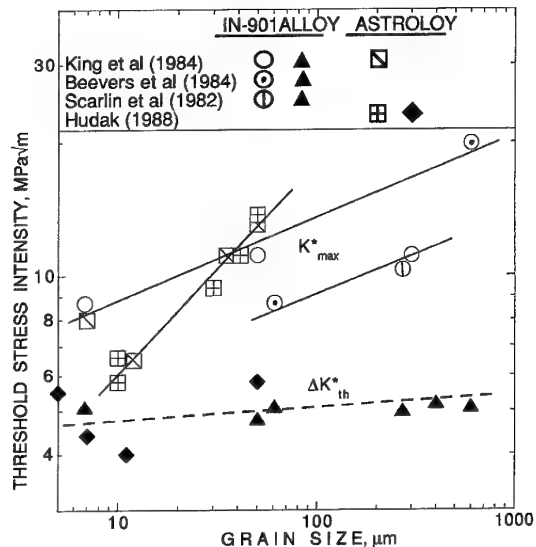


Figure 5 K_{\max}^* and ΔK_{th}^* variation with grain size for several Ni-base superalloys

Note that for both planar as well as homogeneous slip alloys, ΔK_{th}^* is relatively less sensitive to grain size L compared to K_{\max}^* .

K_{\max}^* decreasing with grain size

There are some alloys whose behavior can be different from the ones described above. Here, K_{\max}^* can decrease (instead of increasing) with grain size L . One such case is a Cu-Al alloy where addition of Al in solid solution decreases the stacking fault energy of Cu to change its slip deformation from homogeneous to planar mode.

Figure 6 illustrates the K_{\max}^* variation with grain size for Cu and various Cu-Al alloys^{20,21}. Here, K_{\max}^* decreases with grain size with two different slopes. The first decreasing slope is about -0.2 while the second is about -0.05. It is not clear why such variations in slope occur; probably due to change in the fracture mode. Figure 6 shows that the change in slope occurs around 15–50 μm as the Al content is increased from 2%–8%. The first reduction in K_{\max}^*

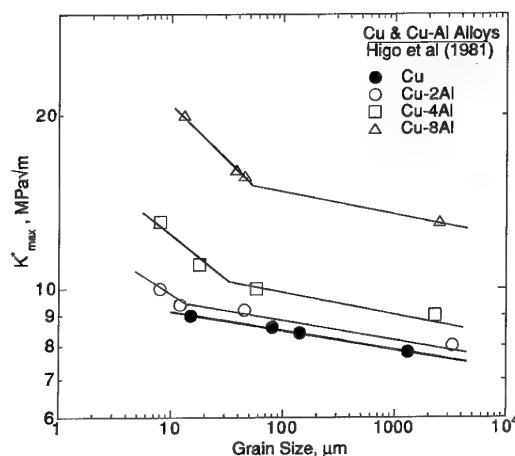


Figure 6 K_{\max}^* variation with grain size for Cu and Cu-Al alloys

begins from a transgranular fracture process and slowly changes toward an intergranular mode²⁰. At smaller grain sizes the fracture appears to be predominantly transgranular, while at larger sizes it is intergranular. The change in the fracture mechanism seems to occur at near the finer grain sizes. Such a reduction in threshold K_{max}^* with grain size has also been observed in α -brass²². Most of the Cu-base alloys and also pure Cu showed intergranular fracture and faceted fracture surfaces at the threshold region. Higher grain sizes showed large amounts of intergranular fracture. These observations indicate that the decrease in K_{max}^* could be due to some impurity effect on the grain boundary. If some grain boundary impurities are present in these alloys, then the fatigue threshold can decrease with stacking fault energy. Cu-base alloys are commonly prone to impurity effects such as bismuth. In the higher Al-containing alloys, such as Cu-8Al, this trend is maintained even at five orders of magnitude higher growth rates than at threshold. But this trend reverses as the Al content is lowered. At lower Al contents, K_{max}^* increases with grain size at higher crack growth rates.

PRECIPITATES

In most precipitation hardened alloys the matrix can form several precipitates within the grains during aging treatments. The spacing of these precipitates is significantly smaller than the grain size of the alloy. The precipitates can range in shape, size and spacing, and can form with or without habit planes. They can be coherent, semi-coherent or incoherent. Planar slip can result in these alloys by the presence of coherent and semi-coherent precipitates. In the case of incoherent precipitates, slip becomes more homogeneous, enabling plastic blunting at the crack tip. If the incoherent precipitates are platelets (with larger aspect ratios) and are present amidst coherent ones, they can curtail the planar slip distances, forcing the dislocations to cross slip. Under these conditions, the spacing of platelet shaped precipitates would become more effective than the spacing of spherical ones in affecting the crack advance. When the platelet spacing gets comparable to the grain size of the alloy, the role of precipitates would be diminished and the grain size effect would dominate the fatigue behavior. Figure 7 shows a schematic trend of K_{max}^* varying strongly with precipitate size λ_p until it becomes comparable to the grain size L . The illustration shows the nature of crack deflection that can occur due to the presence of only the platelet precipitates.

To show the trend in Figure 7, a precipitation hardenable Al-Li-Cu alloy system was chosen as an example. There are three major precipitate types in this system: δ' , θ' and T_1 . While θ' [on (100) habit plane] and T_1 [on (111) habit plane] are platelet precipitates that show coherence on the plate face, δ' is an ordered coherent spherical precipitate. δ' precipitates induce planar slip deformation via dislocation cutting. θ' and T_1 platelets reduce the planarity by inducing cross slip. If one maintains the δ' precipitate size constant in the alloy, then the planar slip mode would be constant. Then, by varying the platelet precipitate spacing one could change the planar slip distances and study their effects on fatigue crack resistance similar

to that described under the grain size section earlier. Now, in addition to grain boundaries as barriers, we have T_1 precipitates. These variations can be achieved by a combination of adjusting the alloying elements, [Li/Cu], and heat treatments²³⁻²⁵. Such a combination can vary the relative amounts of the platelet precipitates, while maintaining a constant δ' precipitate size. Here, we observed that T_1 precipitates were more effective than θ' , because T_1 forms on the same crystallographic habit plane {111} as the dislocation glide planes of the alloy. Transmission electron micrographs showing the two types of precipitates in the Al-2Li-3Cu alloy are shown in Figures 8a and 8b. Figure 8a shows the dark field image of δ' precipitate, while Figure 8b shows the bright field image of T_1 . From the electron micrographs for each individual alloy and heat treatment, the average T_1 spacing and average size of δ' were quantitatively measured and related to K_{max}^* . The volume fraction of θ' was significantly smaller compared to T_1 , and hence was not recorded. It should be pointed out that both θ' and T_1 form on the dislocations; but T_1 can also form on subgrain boundaries²⁵.

Figure 9 illustrates the variation in K_{max}^* with the spacing (λ_p) of T_1 . The slope due to T_1 spacing is ~0.5, while that due to grain size is ~0.1. Here, we observe that K_{max}^* increased dramatically with λ_p up to about 0.2 μm and the slope reduced thereafter. At $\lambda_p > 0.2 \mu\text{m}$, the effect of grain size L sets in. The K_{max}^* data was obtained in laboratory air which had relative humidity of about 40%. The far right of the figure indicates the binary Al-Li alloy data having only the δ' precipitate (with no T_1), showing only the grain size effects on K_{max}^* . The role of T_1 is similar to that of the grain size effect, except that the effect of T_1 is greater than grain boundaries. Since T_1 forms on the crystallographic habit plane {111} the same as the dislocation glide plane, an advancing crack on such a plane appears to interact with T_1 effectively deflecting at T_1 . For small T_1 spacing of less than ~0.3 μm the K_{max}^* values scale with λ_p . At larger T_1 spacing the K_{max}^* scales with the grain size L . *In situ* fatigue deformation experiments conducted in the electron microscope²⁶ indicated a crack deflection at T_1 precipitate sites.

In order to understand the variations in slopes in Figure 9 due to T_1 and grain size, one must characterize the basic microstructures in these Al-Li-Cu-Zr alloys. These are unique alloys which exhibit highly pancake-shaped unrecrystallized grain structures having large aspect ratio, that is, the longitudinal grain dimension is of the order of a few millimeters with respect to the transverse dimension of ~100 μm . In addition, there are subgrains that can form within or adjacent to the large grains. It is observed that T_1 precipitates form both within the grains on dislocations and on the subgrain boundaries. On the subgrain boundaries T_1 has one of its four variants shared with those in the adjacent grains. Thus, there are three obstacle spacings for a crack growing along the transverse direction; while a crack along the longitudinal direction will encounter two obstacles. As a result, the longitudinal threshold stress intensity value would be affected less than the transverse; even though the grain size along the longitudinal direction is the largest. This was observed in two different compositions of Al-Li-Cu-

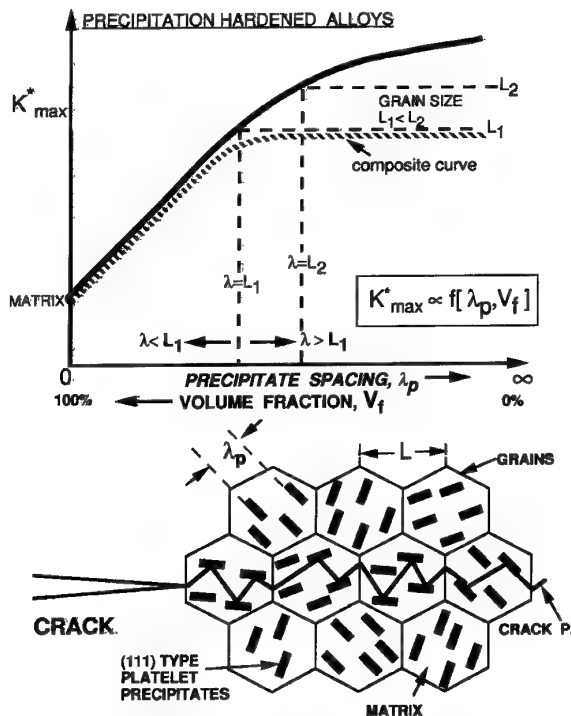


Figure 7 Schematic illustration of the effects of precipitate spacing (λ_p) and grain size (L) on K^*_max (linear scale). When $\lambda_p < L$, the precipitate spacing has a dominant effect on K^*_max

Zr alloys²⁷; where the threshold values along the longitudinal direction were lower by about a factor of 3 to 5 with respect to the transverse. This is contrary to common observations where the largest grain size exhibits higher thresholds. Thus, in *Figure 9* as the data was obtained along the transverse direction, the resistance to crack growth may be coming from the T₁ obstacle spacing within the grains and at subgrain boundaries decorated with T₁ and the high angle grain boundaries. One needs to conduct systematic studies to sort out the relative effects of these three obstacles on K^*_max .

Crack energy

The above discussion on K^*_max variation with grain size (*Figure 3*) can also be rationalized in the following manner. Assuming that the crack follows the slip band in iron, which can deflect at each of the grain boundaries, one can estimate the pile-up energy as a function of grain length. The energy of a pile-up per unit length of n dislocations can be written as

$$W = c_1 n^2 b^2 \quad (2)$$

where c_1 is a constant. The number of dislocations in the pile-up is related to its length l and the back stress σ_b on the dislocation:

$$n = c_2 l \sigma_b \quad (3)$$

where c_2 is another constant. The yield stress of an alloy, σ_{ys} , can be written as a Hall-Petch relation:

$$\sigma_{ys} = \sigma_o + kL^{-0.5} \quad (4)$$

where σ_o is the lattice friction stress, L is the grain size, and k is the Hall-Petch constant. Assuming that the pile-up length l is related by a power law to L by

$$l = L^p \quad (5)$$

when $\sigma_o = \sigma_{ys}$ the stored energy in the pile-up can be written by substitution of Equations (3), (4) and (5) into Equation (2) as

$$W = [c_1 c_2 b^2] L^p [\sigma_o + kL^{-0.5}] \quad (6)$$

Since the crack driving force $G = K^2_{max}$, which is proportional to W , then

$$K_{max} = (\text{constant}) L^p [\sigma_o + kL^{-0.5}] \quad (7)$$

The slope of the plot from Equation (7), K_{max} vs L on a log-log scale, can lie between +2 and -1. A slope of less than 1 indicates that the pile-up length has a less than linear dependence on grain size L , that is $p < 1$ in Equation (5). When $p = 1$, the pile-up length is comparable to the grain dimensions. In a more general sense, one can write Equation (7) in the form

$$K_{max} = (\text{constant}) L^p [\sigma_o + kL^m] \quad (8)$$

where p and m are constants. The second term in Equation (8) is related to the pile-up, while the third term to Hall-Petch. If $m = -0.5$ then Equation (8) reduces to Equation (7), complying with the Hall-Petch relationship. Equation (8) indicates that K_{max} should increase with L , in accordance with the experimental result shown in *Figures 3, 4 and 5*, which can be written as

$$K_{max}^* = \alpha L^\beta \quad (9)$$

where α is a constant that is related to the resistance of crack extension from one grain to the next and β

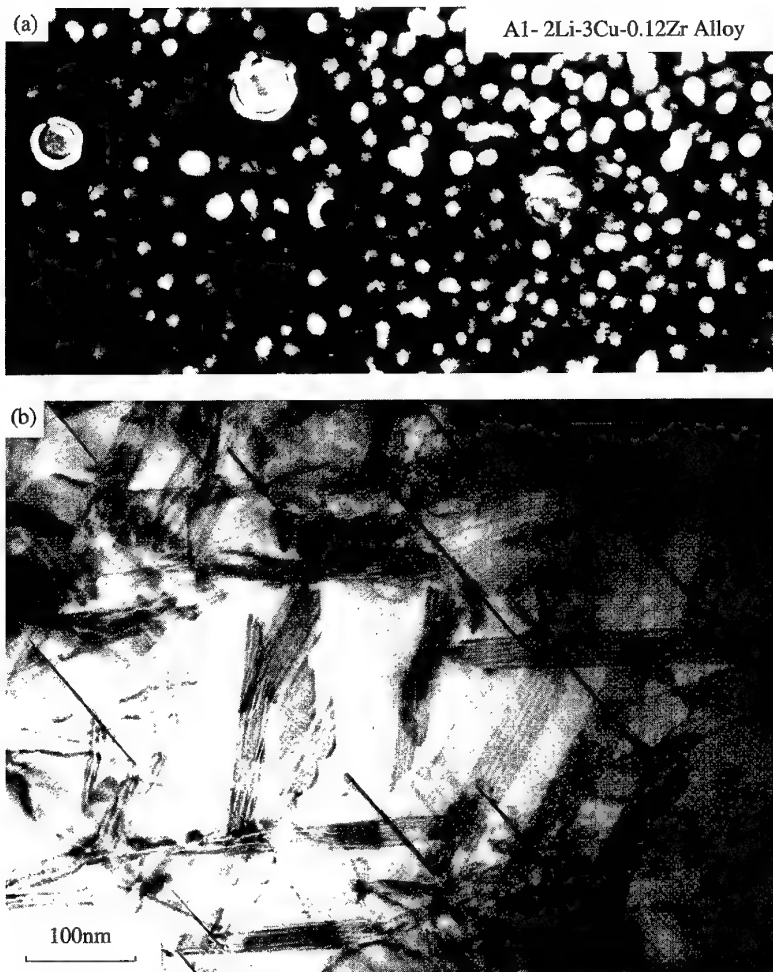


Figure 8 Transmission electron micrograph of Al-2Li-3Cu alloy showing: (a) the spherical δ' precipitates under dark field and (b) platelet T_1 precipitates under bright field

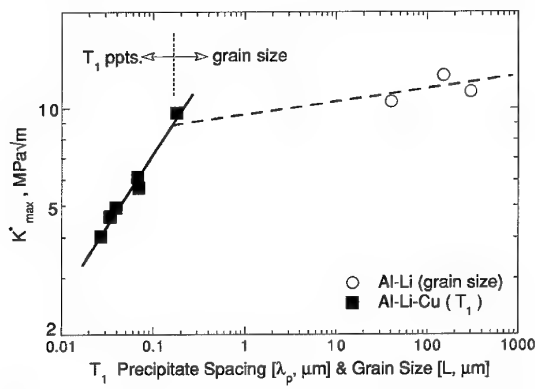


Figure 9 K_{\max}^* variation with T_1 precipitate spacing in Al-Li-Cu alloys and grain size in binary Al-Li alloys

is the exponent that can vary with alloy conditions. The linear slope β can vary depending on the mode of slip. Equation (7) indicates that the critical threshold stress intensity K_{\max}^* calculated from pile-up energy increases with grain size, with a slope larger than the experimental curves in Figure 3a. Equation (9) is also valid for the Cu-Al alloys in Figure 6, except that the constants α and β have negative values.

Current state of understanding

The analysis indicates that: (1) grain size dependence on K_{\max} seems to be pronounced in materials that exhibit planarity of slip deformation; (2) the relation between K_{\max} and obstacle spacing such as grain size or precipitate spacing varies with β values ranging from -0.05 , to $+0.05$, $+0.1$, to $+0.5$, $+1.0$ to $+2.0$, see Figure 10; (3) in several cases, crack deflection occurs at or near the microstructural obstacles. The corrected K_{\max} for the deflection, based on simple linear elastic analysis, do not seem to eliminate its dependence on grain size; and (4) while K_{\max} increases with obstacle spacing, an attendant decrease in yield stress suggests that the two variations appear to have no direct relationship. This does not exclude that the K_{\max} variation with obstacle spacing is not related to plasticity.

There have been several studies on the grain size dependence of fatigue thresholds in alloys.^{7,9-18} These studies conclude that the contribution from crack deflection is only about 20% and that the additional effects are coming from roughness-induced closure. Interestingly, the crack deflection itself does not seem to be related to the grain size. Suresh⁸ has analytically evaluated the combined effects of crack deflection and crack closure and arrived at an expression that involves the multiplication of two terms:

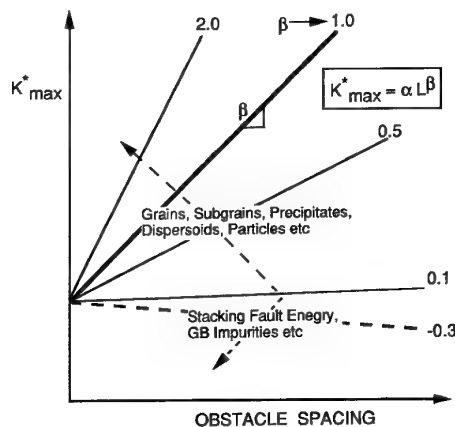


Figure 10 Schematic diagram (log-log scale) showing the effect of obstacle spacing on K_{\max}^*

$$\Delta K(\text{total}) = \Delta K[\text{deflection}] \Delta K[\text{closure}] \quad (10)$$

In this analysis, there is a closure contributing term U_{II} that characterizes the lateral sliding displacement of the mating fracture surfaces. U_{II} can presumably be determined from the microstructural observations. Unfortunately, the U_{II} term does not have a direct relation to crack deflection of the tortuosity of the crack path. On the other hand, Ravichandran and Dwarkadasa¹³ have deduced the combined effects of deflection and closure to be additive and not a product as in Equation (10):

$$\Delta K(\text{total}) = \Delta K[\text{deflection}] + \Delta K[\text{closure}] \quad (11)$$

In all these analyses, there is an implicit *assumption* that the ΔK dependence on obstacle spacing can be due to roughness-induced crack closure. The validity of such an assumption needs to be examined.

In analyzing these roughness-induced closure models in the light of the observed microstructural effects on K_{\max} outlined in this article, we find that (a) the roughness-induced closure models do not seem to have terms that can be directly related to the crack path tortuosity measured in terms of wavelength of the crack deflections, and (b) the models have some independent assumptions relating either to the point of contact of the hills and valleys or to the sliding displacements (like U_{II} in Ref.⁸) which do not correspond to the scales of the microstructural features. The grain size dependent exponent β in Equation (9) varies significantly under different conditions of microstructural scales (Figure 10) and is not a constant. Hence, we conclude that the systematic dependence of K_{\max} on obstacle spacing is not simply relatable to crack closure, since no closure model explains such slope variations observed by experiment.

STACKING FAULT ENERGY

In solid solution alloys containing no precipitates, one can change the alloy composition to alter the slip modes to vary from a homogeneous to a planar slip. As an example, the variation in slip mode can occur due to changes in stacking fault energy (SFE). Low SFE restricts the slip to a planar mode. In general, the

degree of planar slip in a given alloy can be affected either through lowering of SFE, or by choosing materials with crystal anisotropy (as in some low crystal symmetry HCP materials like Mg, Zn, Ti, Be) or with coherent ordered particles (as in Ni-base superalloys and Al-Li alloys).

In Cu-base alloys with Al additions varying from 0% to 14%, the SFE of the unalloyed Cu can be decreased^{28,29} from about 50 ergs cm⁻² to about 5 ergs cm⁻². The threshold fatigue crack resistance then increases with decrease in SFE through a process of crack deflection. Figure 11 illustrates the behavior in Cu-Al^{20,21} alloys. The Cu-Al alloy data was taken from two sources^{20,21}: at $R = 0.5$ and $R = 0.13$ respectively. K_{\max}^* values decrease with SFE, with a slope of about -0.3 . The corresponding yield stress also decreased with stacking fault energy with a slope of about -0.4 . The K_{\max}^* and yield stress data from Higo *et al.*²⁰ were taken at a grain size of $\sim 30 \mu\text{m}$ to match with the data from Saxena and Antolovich²¹. In the Cu-Al system, Higo *et al.*²⁰ have observed crystallographically rough fracture surfaces as the Al content was increased, which is a result of crack deflection. The observed trends indicate the important role that the degree of planar slip in an alloy can play on the near threshold stress intensity K_{\max}^* .

SUMMARY

Based on the analysis of the experimental fatigue crack propagation data from several classes of materials, one can draw the following conclusions.

- Fatigue damage is a two parametric problem to be described in terms of K_{\max}^* and ΔK_{th}^* that depend on the microstructural scales, slip mode and environment.
- At the threshold region of crack growth, K_{\max}^* depends strongly on the microstructural obstacle spacing such as grain size L and precipitate spacing λ_p : $K_{\max}^* = \alpha L^\beta$, where α is a constant relating to the crack growth resistance and β is another constant related to the alloy chemistry. When there are no other superimposed effects like impurities that can

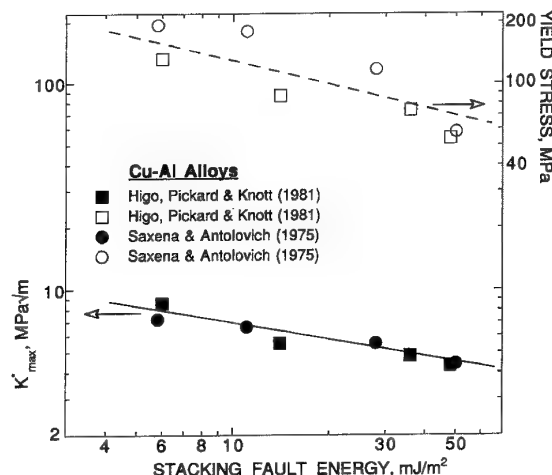


Figure 11 Yield stress and K_{\max}^* variation with stacking fault energy for Cu-Al alloys

Table 1 Summary of observations

$K_{max}^* = \alpha L^\beta$ Equation (9)	Slip mode	Material
$\beta = \sim 0.05\text{--}0.5$	Homogeneous Planar	Unalloyed Fe, Cu, Al, etc. steels, Al alloys, overaged alloys Al-Li-X, stainless steel, Ti-Al, α - β Ti alloys, underaged alloys
$\beta = \sim 1.0$	Planar	Ni-base superalloys, intermetallic alloys (?), low SFE alloys, unalloyed Ti, Mg, Zn, Be, etc.
$\beta = \sim 2.0$	Planar	Ni-base alloys, necklace grains Waspaloy
$\beta = \sim -0.05$ to -0.3	Planar	Low SFE Cu alloys

alter the fracture process, the overall effect appears to come in large part from crack deflection. In addition to the strength of the obstacle, the slip mode (homogeneous vs planar) plays a strong role in the effect of grain size on K_{max}^* . Yield strength seems to have a lesser effect on the fatigue damage process. *Table 1* is a summary of the observations with some examples of the alloys that fall into the category of slip mode that comply with Equation (9), where L can be grain size or particle spacing.

- At higher crack growth rates, like in the Paris regime, the microstructural effects on the stress intensities are small.
- ΔK_{th}^* is less sensitive to the grain size or precipitate spacing in a given alloy.

ACKNOWLEDGEMENTS

The authors wish to thank the reviewers for critical reading of the manuscript and helpful comments. We also sincerely acknowledge Dr M.S. Duesbery, FMR Inc., for the crack energy calculations. One of us (AKV) thanks Dr R. Pippin, Austria for sending his Fe data and for stimulating discussions.

REFERENCES

- Vasudevan, A. K., Sadananda, K. and Louat, N., *Scripta Metallurgica et Materialia*, 1993, **28**, 65.
- Vasudevan, A. K., Sadananda, K. and Louat, N., *Materials Science and Engineering A*, 1994, **188**, 1.
- Louat, N., Sadananda, K., Duesbery, M. S. and Vasudevan, A. K., *Metallurgical and Material Transactions*, 1993, **24A**, 2225.
- Sadananda, K. and Vasudevan, A. K. *ASTM STP-1220*, 1995, p. 484.
- Vasudevan, A. K. and Sadananda, K., *Metallurgical and Material Transactions*, 1995, **26A**, 1221.
- Vasudevan, A. K. and Sadananda, K., *Metallurgical and Material Transactions*, 1995, **26A**, 3199.
- Pippin, R., *Materials Science and Engineering A*, 1991, **138**, 1.
- Suresh, S., *Metallurgical Transactions*, 1985, **A16**, 249.
- Masounave, J. and Bailon, J.-P., *Scripta Metallurgica*, 1976, **10**, 165.
- Masounave, J. and Bailon, J.-P., *Scripta Metallurgica*, 1975, **9**, 723.
- Taira, S., Tanaka, K. and Hoshina, M. *ASTM STP-675*, 1979, p. 135.
- Yoder, G. R., Cooley, L. A. and Crooker, T. W. *ASTM STP-791*, 1983, pp. 1–348.
- Ravichandran, K. S. and Dwarakadasa, E. S., *Acta Metallurgica*, 1991, **39**, 1343.
- King, J. E., *Materials Science and Engineering*, 1987, **3**, 750.
- Francois, D. In *Advances in Fatigue Science and Technology*, eds C. Moura Branco and L. Guerra Rosa. Kluwer Academic, Dordrecht, 1989, p. 23.
- Beevers, C. J., Bell, K. and Carlson, R. L. In *Fatigue Crack Growth Threshold Concepts*, eds D. L. Davidson and S. Suresh. AIME, 1984, p. 327.
- Scarlin, R. B., Melton, K. N. and Hoffelner, W. In *Fracture and the Role of Microstructure*, Vol. 2, eds F. E. Matzer and K. L. Maurer. EMAS, 1982, p. 689.
- Hudak, S., Davidson, D. L., Chan, K. S., Hopland, A. C. and Walsch, M. J. AFWAL-TR-88-4090 Final Report, June 1988.
- Antalovich, S. D. and Jayaraman, N. In *Fatigue: Environment and Temperature Effects*, eds J. J. Burke and V. Weiss. Plenum, New York, 1983, p. 119.
- Higo, Y., Pickard, A. C. and Knott, J. F., *Metallurgical Science*, 1980, **14**, 233.
- Saxena, A. and Antalovich, S. D., *Metallurgical Transactions*, 1975, **6A**, 1809.
- Beevers, C. J., *Metallurgical Science*, 1980, **14**, 418.
- Vasudevan, A. K., Doherty, R. D. and Suresh, S. In *Aluminum Alloys – Contemporary Research and Applications*, Vol. 31, eds A. K. Vasudevan and R. D. Doherty. Academic Press, New York, 1989, p. 446.
- Tosten, M. H., Vasudevan, A. K. and Howell, P. R., *Metallurgical Transactions*, 1988, **19A**, 51.
- Williams, D. B. and Howell, P. R. In *Aluminum Alloys – Contemporary Research and Applications*, Vol. 31, eds A. K. Vasudevan and R. D. Doherty. Academic Press, New York, 1989, p. 365.
- Vechio, K. Personal communications, 1995; Ph.D. Thesis, Lehigh University, 1988.
- Stanzl-Tschegg, S. E., Konig, J. and Tschech, E. In *Fatigue '93*, Vol. I, eds J.-P. Bailon and J. I. Dickson. EMAS, 1993, p. 519.
- Carter, C. B. and Ray, I. L. F., *Philosophical Magazine*, 1977, **35**, 189.
- Gallagher, P. C. J., *Metallurgical Transactions*, 1970, **1**, 2429.

PII: S0142-1123(97)00040-6

Physical meaning of ΔK_{RP} and fatigue crack propagation in the residual stress distribution field

Masashiro Toyosada, Toshio Niwa and Junichi Sakai**Department of Naval Architecture and Marine Systems Engineering, Kyushu University, 6-10-1, Hakozaki, Higashi-ku Fukuoka, 812-81, Japan*

Previous papers have shown ΔK_{RP} to be a useful parameter describing fatigue crack propagation behavior, where ΔK_{RP} is an effective stress intensity factor range corresponding to the excess RPG load (re-tensile plastic zone's generated load) in which the retensile plastic zone appears under the loading process. In this paper, the relationship between ΔK_{RP} and the zone size ($\tilde{\omega}$) (which is smaller between the tensile plastic zone at maximum load and the compressive plastic zone at minimum load) was investigated using a crack opening/closing simulation model so as to consider a physical meaning of ΔK_{RP} . As a result, it becomes clear that ΔK_{RP} dominates the zone size $\tilde{\omega}$ where fatigue damage mostly occurs. This result supports the following crack propagation equation

$$\frac{da}{dN} = C(\tilde{\omega})^m$$

where C and m are material constants.

Simulation and fatigue crack propagation tests were then carried out for compact tension (CT), center cracked tension (CCT) and four points bend (4PB) specimens under constant amplitude loading to obtain C and m values for HT-50 steel. Fatigue crack propagation tests were also carried out under constant amplitude loading using CCT specimens with residual stress distribution due to flame gas heating at the center line or edge lines. The T specimen introduced tensile residual stress at the tip of a notch, and the C specimen introduced compressive residual stress. It therefore becomes clear that tensile residual stress leads to a decrease in RPG load, while compressive residual stress leads to increase in RPG load, and that the simulation results are in good agreement with the experimental RPG load. It also becomes clear that simulated crack growth curve using the simulated $\tilde{\omega}$ and the above equation is in good agreement with the experimental curve. It is understood that tensile residual stress creates only a slight increase in crack propagation rate and compressive residual stress create a big decrease a crack propagation rate. © 1998 Elsevier Science Ltd.

(Keywords: crack opening/closing phenomena; fatigue crack propagation; residual stress)

INTRODUCTION

In the previous paper¹, we showed that the logarithmic curve of $\Delta K_{RP} \sim da/dN$ was linear in stage I as well as stage II of a long crack, where ΔK_{RP} is an effective stress intensity factor corresponding to the excess RPG load (re-tensile plastic zone's generated load) where the re-tensile plastic zone appears under the loading process.

Newman's calculation model² was modified to solve the neglected effect of the change of stress distribution ahead of a crack under the loading process, to leave elastic plastic materials along the crack surface, and also to introduce plastic shrinkage with an immediate generation of new crack surfaces due to the emancipation of the internal force in the Dugdale model

during the unloading process³. By using the simulation model, the RPG load was simulated under a decreased maximum load while keeping the minimum load. As a result, the delayed retardation effect with a decreasing maximum load can be quantitatively assessed and the condition of stopping a crack can be presented by $\Delta K_{RP} \leq 0$.

In this paper, to study the physical meaning of ΔK_{RP} , the relationship between ΔK_{RP} and the zone size of the zone with fatigue damage ($\tilde{\omega}$) (which is a smaller size between the tensile plastic zone at maximum load and the compressive plastic zone at minimum load) was initially investigated using the crack opening/closing simulation program. From this result, a new fatigue crack propagation equation is introduced, which relates $\tilde{\omega}$. The values of the material

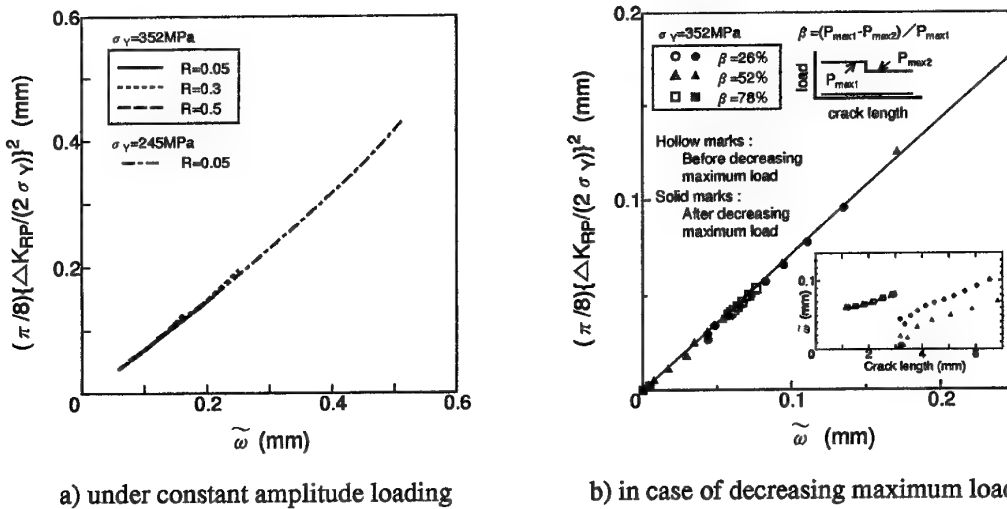


Figure 1 Relationship between ΔK_{RP} and $\tilde{\omega}$. (a) Under constant amplitude loading; (b) in the case of decreasing maximum load

constants were then obtained with fatigue crack propagation tests using center cracked tension (CCT), compact tension (CT) and four points bend (4PB) specimens.

Fatigue crack propagation tests were carried out using CCT specimens with tensile residual stress or

compressive residual stress at the tip of a notch so as to investigate the effect of the residual stress distribution on the fatigue crack propagation. The effectiveness of the newly proposed fatigue crack equation was then evaluated.

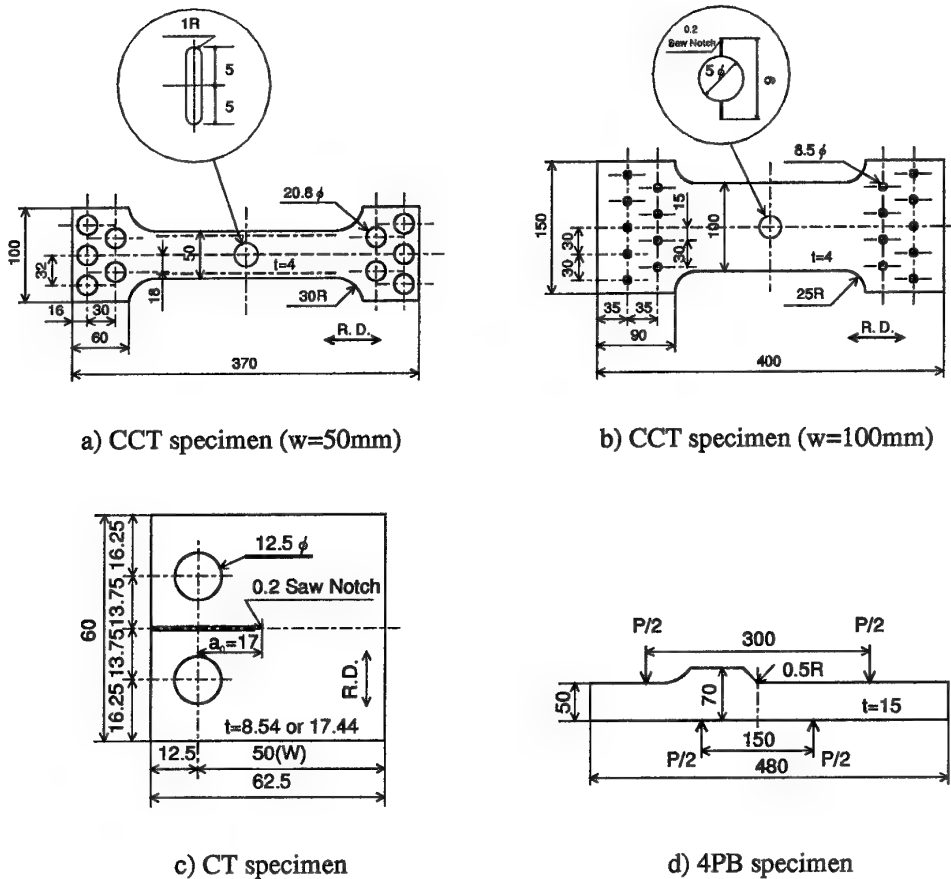


Figure 2 Configuration of specimens. (a) CCT specimen ($w = 50$ mm); (b) CCT specimen ($w = 100$ mm); (c) CT specimen; (d) 4PB specimen

RELATIONSHIP BETWEEN ΔK_{RP} AND THE ZONE SIZE EXPERIENCING FATIGUE DAMAGE AHEAD OF A CRACK

There is a region near a crack tip ahead of a crack where a tensile plastic zone appears under the loading process and a compressive plastic zone appears under the unloading process in one cyclic loading. Plastic works are consumed only in this region. A size of the region $\tilde{\omega}$ is defined by the smaller size between the tensile plastic zone at maximum load and the compressive plastic zone size at minimum load in one cyclic loading. The former is larger than the latter under constant amplitude loading, but not necessarily under random loading. From the previous paper, it is confirmed that the following equation is applicable not to stage II but also to stage I.

$$\frac{da}{dN} = C_1(\Delta K_{RP})^{m_1} \quad (1)$$

where C_1 and m_1 are material constants. The reason why ΔK_{RP} controls a fatigue crack propagation rate, however, is not yet understood.

For the purpose of understanding the physical meaning of ΔK_{RP} , we investigate the relationship between ΔK_{RP} and $\tilde{\omega}$ for CCT specimens using the simulation program of crack opening/closing phenomena developed in the previous paper³. The principle of the simulation model is that the COD in the imaginary crack (tensile plastic zone) for the Dugdale model is supposed to correspond to the elastic stress length receiving a magnitude of yield stress for the residual plastic deformed layer (element). The gauge length of these elements does not change during loading and unloading if the situation of the element keeps elastic. These elements are left at the real crack surfaces after dividing into two parts as a crack advances. The length of these elements also changes in accordance with the emancipation of cohesive stress just after the new crack surfaces are produced. The model is composed under an arbitrary stress distribution field³.

Figure 1 shows the results, where *Figure 1a* shows the relationship between ΔK_{RP} and $\tilde{\omega}$ under constant amplitude loading with various stress ratios, and *Figure 1b* shows a case where the maximum load is decreased. It is seen that the relationship between ΔK_{RP} and $\tilde{\omega}$ does not change even if the stress ratio changes (see *Figure 1a*). In *Figure 1b*, the open symbols show the data before the maximum load is decreased and the filled symbols show the data after decreasing the maximum load while keeping a minimum load. In the figure, a solid line shows the data for the constant amplitude loading. It is recognized that $\tilde{\omega}$ decreases discontinuously just after the maximum load is decreased as illustrated in *Figure 1b*. However, the relationship between ΔK_{RP} and $\tilde{\omega}$ remain on the constant amplitude loading curve. The vertical axis of the figure shows a plastic zone size (ω) under monotonic loading (maximum load-RPG load) with a yield stress of $2\sigma_Y$ in the case of small scale yielding conditions. In other words, ω shows a plastic zone size at a maximum load for a supposed condition where the K value in monotonic loading is equal to ΔK_{RP} and the yield strength of a material is $2\sigma_Y$. Because of an existing linear relationship between ω and $\tilde{\omega}$, it can

Table 1 Chemical composition and mechanical properties of HT-50 steel used

Chemical composition (%)	
C	0.15
Si	0.18
Mn	1.10
P	0.011
S	0.004
Cu	0.01
Ni	0.02
Cr	0.02
Mo	0.01
Sol Al	0.25
Mechanical properties	
Yield Strength (MPa):	406
Tensile Strength (MPa):	507
Elongation (%):	24

be said that Equation (1) represents the following equation indirectly.

$$\frac{da}{dN} = C(\tilde{\omega})^m \quad (2)$$

where C and m are material constants.

The above equation suggests that a fatigue crack propagation rate is dominated by the zone size of the zone receiving fatigue damage. In other words, Equation (2) is an intuitive way of expressing fatigue growth.

EXPERIMENTAL PROCEDURES AND THE MATERIAL CONSTANTS OF THE PLATE USED

Table 1 shows the chemical composition and mechanical properties of the HT-50 steel plate used. The CCT, CT and 4PB specimens as shown in *Figure 2* were made of the steel for the purpose of obtaining the values of C and m as detailed in Equation (2). These specimens are annealed at 620°C for 2.5 h so as to remove any residual stress before fatigue testing. Constant amplitude loading with a stress ratio of 0.05 was adapted to these specimens. $\tilde{\omega}$ for each specimen was calculated using the simulation program inputting the testing condition.

Figure 3 shows the relationship between ΔK and

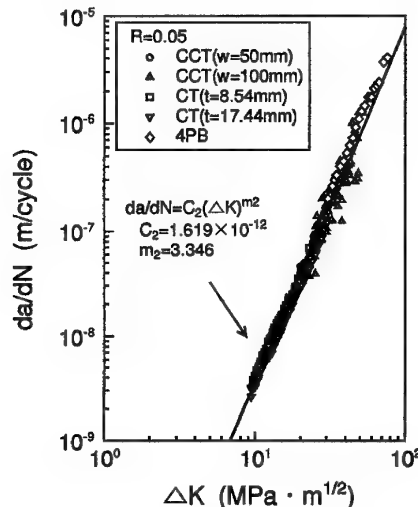


Figure 3 Relationship between crack propagation rate and ΔK

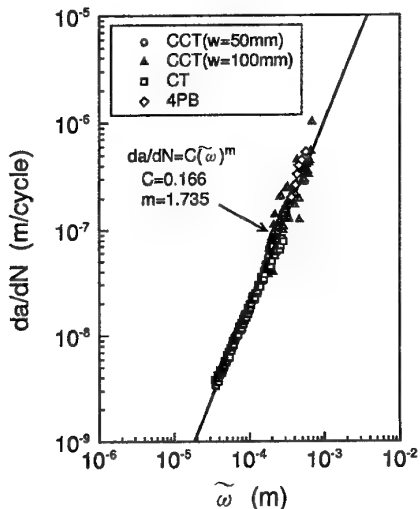


Figure 4 Relationship between crack propagation rate and $\tilde{\omega}$

da/dN for each test. On the other hand, Figure 4 shows the relationship between $\tilde{\omega}$ and da/dN . Fatigue propagation tests were carried out under the same stress ratio conditions for the different specimens. Almost the same $da/dN \sim \Delta K$ curves were, therefore, obtained regardless of the specimen configurations (Figure 3). It was also recognized that the differences of the $da/dN \sim \tilde{\omega}$ curves do not also appear as shown in Figure 4, this meant, therefore, that $\tilde{\omega}$ is proportional to $(\Delta K)^n$ where n is some constant value when $R \approx 0$. On the other hand, $\tilde{\omega}$ is proportional to $(\Delta K_{RP})^2$ because of the result of Figure 1.

For the purpose of studying the effect of residual stress on fatigue crack propagation, flame gas line heating at a center line (see the dashed line in Figure 2a: T specimen) or edge lines (see chain lines in Figure 2a: C specimen) was conducted on the CCT specimen. The former was to produce tensile residual stress at the tip of any cracks and the latter produces compressive residual stress. The flame gas heating was carried out at a peak temperature at the back surface

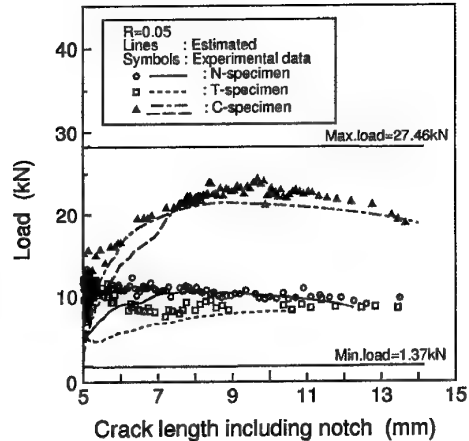


Figure 6 Comparison between measured RPG load and estimated ones

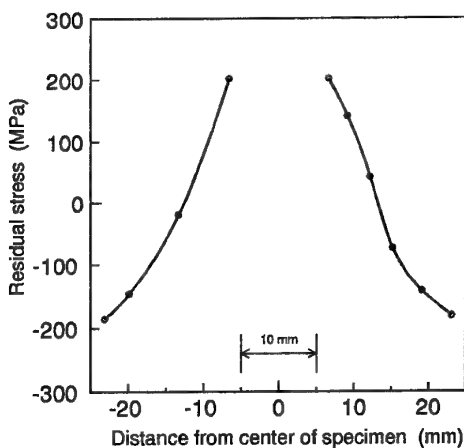
so as to reach 700°C which is mechanically the melting point of steel, giving lead to uniform residual stress in a thickness direction.

Residual stress distribution for the T and C specimens was measured by means of a relaxation method using strain gages placed on the front and back of the surfaces. Figure 5 shows the results, where the data show the average values of the front and back surfaces. It can be seen that the T specimen has a tensile residual stress at the tip of a crack and the C specimen a compressive residual stress.

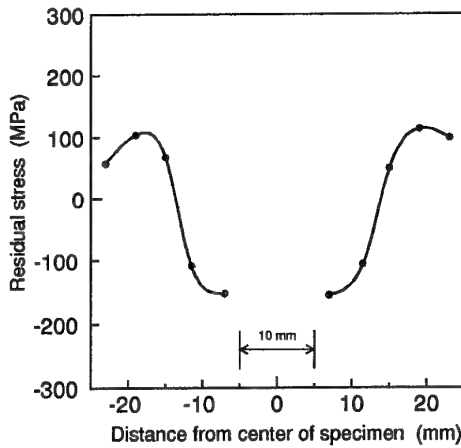
Fatigue crack propagation tests for T, C and N specimen (without residual stress) were carried out under constant amplitude loading with the same maximum and minimum loads for each specimen. During the tests, not only crack length and cycles but also RPG loads were measured by an automatical compliance measuring system¹.

EXPERIMENTAL RESULTS AND DISCUSSION

Figure 6 shows the change in the RPG load as a crack advances for each specimen. It can be understood that



a) T-specimen



b) C-specimen

Figure 5 Residual stress distribution after gas heating. (a) T specimen; (b) C specimen

tensile residual stress leads to a decrease in RPG load while compressive residual stress leads to an increase in RPG load (compare with the RPG load for the N specimen without residual stress). It can be expected, therefore, that tensile residual stress decreases fatigue crack growth life since an increase in effective loading amplitude and compressive residual stress extends fatigue crack growth life because of a decrease in amplitude ($=$ maximum load – RPG load). The simulation results of the RPG load, obtained by inputting the measured residual stress distribution as shown in Figure 5 into the program, are also shown in Figure 6 for each specimen. Two results are shown for the C specimen. The dotted line shows the RPG load which is defined at the generation of tensile yielding at a crack tip. On the contrary, the chain line also shows the RPG load which is defined by the load at a starting moment of the growing tensile plastic zone.

Figure 7 shows an example of detailed simulation testing under the loading process for the C specimen. It is understood that the fatigue crack closes at a minimum load (see Figure 7a). It can be seen that in

spite of reaching the tensile yield stress at the tip of a crack, the crack closes near a crack tip inside the crack (see Figure 7b). This phenomenon is considered to happen due to the compressive residual stress. The crack opens as the load increases. Figure 7c shows a crack configuration and a working stress distribution at a moment when the crack opens. However, it can be seen that the tensile plastic zone does not grow. This is understood to be because the increment of the load as shown in Figure 7b to Figure 7c contributes only when opening the crack and not for the growth of the tensile plastic zone because the compressive residual stress is sufficiently large to close a crack. The RPG load is then considered to coincide with the opening load in this case, although a RPG load is larger than a crack opening load in the case of no residual stress. The chain line in Figure 6 shows for the opening load, which corresponds to the RPG load defined by the load at a starting moment of a growing tensile plastic zone. It becomes clear from Figure 6 that the simulation results of the RPG load are in good agreement with the experimental ones even in a field with residual stress distribution.

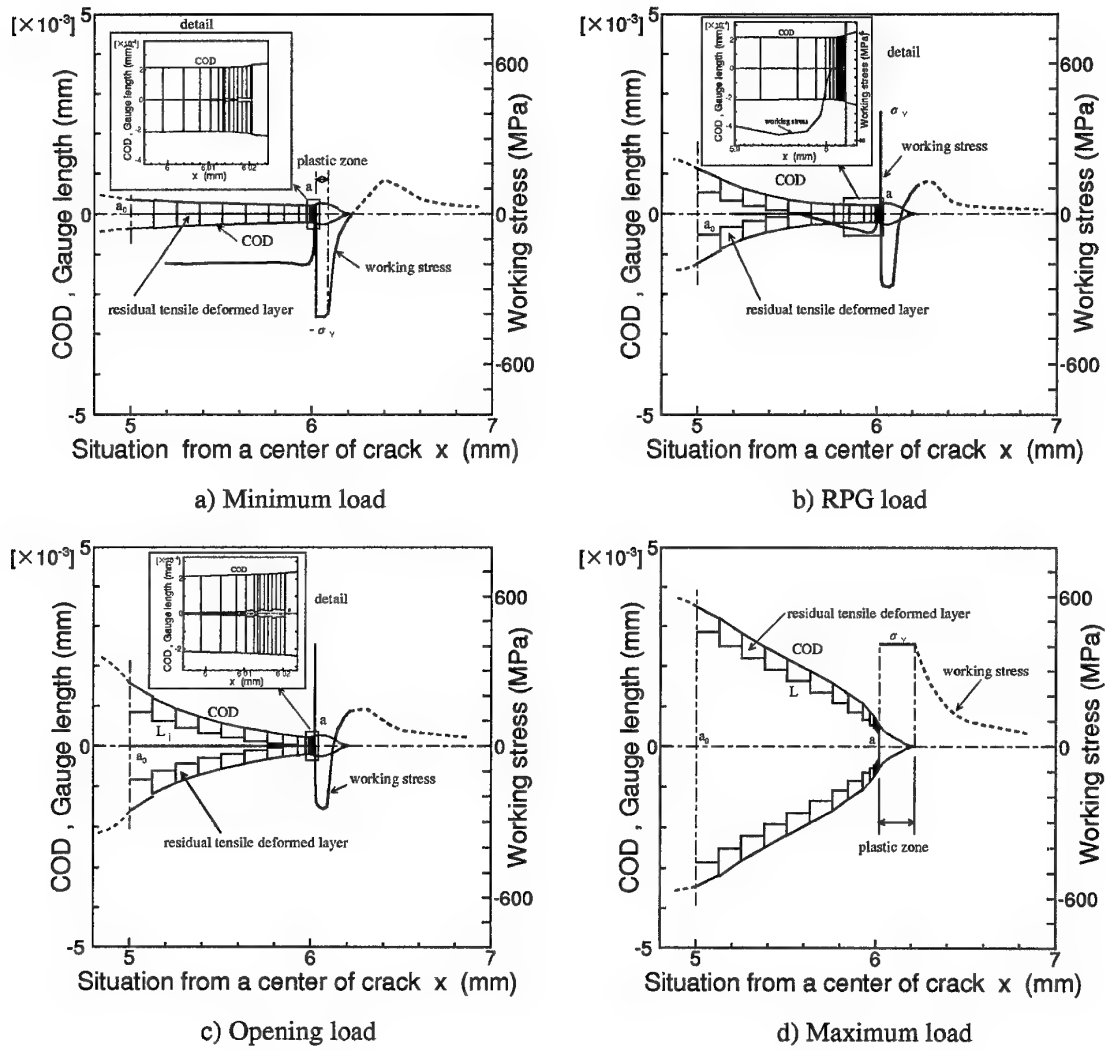


Figure 7 COD, residual tensile deformed layer and working stress distribution calculated for C specimen ($a = 6.02$ mm, fatigue crack length = 1.02 mm). (a) Minimum load; (b) RPG load; (c) opening load; (d) maximum load

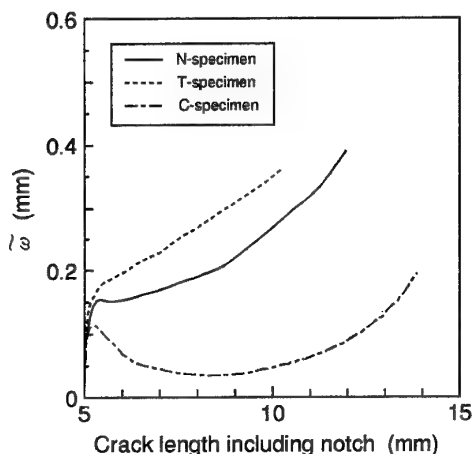


Figure 8 The change of $\bar{\omega}$ for the N, T and C specimens

Figure 8 shows the simulation results of $\bar{\omega}$ for each specimen. It is understood that $\bar{\omega}$ increases as cracks advance for the N and T specimens. However, $\bar{\omega}$ decreases as a crack advances up to a certain crack length and then reaches a minimum and increases again as a crack advances for the C specimen. This phenomena may originate due to the excessive growth of a crack closing region at the minimum load for the C specimen because of the compressive residual stress.

Figure 9 shows the measured fatigue crack growth curve for the T, N and C specimens which are loaded under the same loading conditions. It was understood that tensile residual stress shortens fatigue life slightly and, on the contrary, compressive residual stress leads greatly extends fatigue life. In the figure, the estimated fatigue crack growth curve is also shown using simulated $\bar{\omega}$ and material constants as obtained in Figure 4, where an initial crack length was calculated to be 2 mm. It can be concluded from the figure that Equation (2) is applicable even under the field of residual stress distribution.

CONCLUSIONS

For the purpose of studying the meaning of ΔK_{RP} , the zone size of a zone with plastic consumed ahead of a fatigue crack where fatigue damage mostly occurs in one cyclic loading was investigated using a crack opening/closing simulation program previously

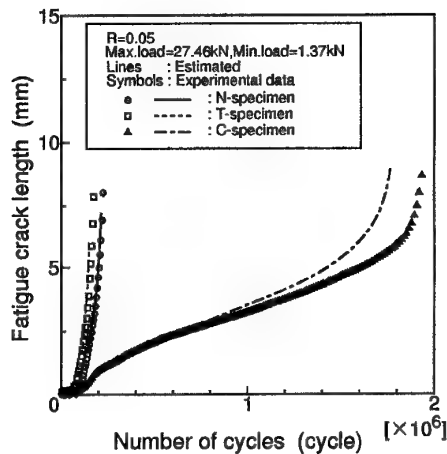


Figure 9 Comparison between the experimental crack growth curves and the estimated ones

developed. Fatigue crack propagation tests were carried so as to study the effect of residual stress distribution on fatigue crack propagation rate. The main results obtained in this study were:

1. ΔK_{RP} dominates the zone size of the zone receiving fatigue damage ahead of a crack.
2. Tensile residual stress lead to a decrease in RPG load and compressive residual stress lead to an increase in RPG load.
3. RPG load can be simulated quantitatively even in the field of residual stress distribution using a crack opening/closing simulation program previously developed.
4. Compressive residual stress greatly extend fatigue life.

REFERENCES

1. Toyosada, M. and Niwa, T., The significance of RPG load for fatigue crack propagation and the development of a compliance measuring system. *International Journal of Fracture*, 1994, **67**, 217–230.
2. Newman, J. C. Jr., A crack-closure model for predicting fatigue crack growth under aircraft spectrum loading. NASA Technical Memo No. 81941, NASA, 1981.
3. Toyosada, M., and Niwa, T., Simulation model of fatigue crack opening/closing phenomena for predicting RPG load under arbitrary stress distribution field. *Proceedings of the 5th ISOPE*, 1995, pp. 169–176.

PII: S0142-1123(97)00016-9

The growth of cracks in Ti-6Al-4V plate under combined high and low cycle fatigue

B.E. Powell*, M. Hawkyard* and L. Grabowskit

*Department of Mechanical and Manufacturing Engineering, University of Portsmouth, Anglesea Road, Portsmouth PO1 3DJ, UK

tRolls-Royce plc, Elton Road, P.O. Box 31, Derby DE24 8BJ, UK

The fatigue crack growth rates in cross-rolled Ti-6Al-4V plate subjected to combined major and minor stress cycles have been measured at room temperature. The concept of crack closure was used to model the data for a test sequence using 1000 minor cycles per major cycle, and the model validated by either the accurate or safe prediction of the crack growth rates for a second series of tests involving 10,000 minor cycles per major cycle. Fatigue threshold values for the minor cycles derived from the growth rate data for combined major and minor cycle loadings were lower than those determined by the conventional load shedding method. In comparison with the behaviour of Ti-6Al-4V disc material which had been forged, the cross-rolled plate material exhibited: first, a clearly defined bilinear growth rate curve under a separate major cycle loading; second, similar or lower derived threshold values with separate minor cycle loadings; and third, reduced crack propagation lives for loadings combining major and minor cycles. © 1998. Published by Elsevier Science Ltd.

(Keywords: fatigue crack growth; combined high and low cycle fatigue; major/minor cycles; Ti-6Al-4V; fatigue thresholds; life predictions)

INTRODUCTION

The design of critical rotating aero-engine components, and the demonstration of their structural integrity, must include an assessment of their fatigue lives in the presence of possible levels of vibration. In such components a low cycle fatigue (LCF) loading arises from the large cyclic variation of the conjoint centrifugal and thermal stresses. In the simplest case this major stress variation occurs once per flight. However, rotating engine components have also experienced high cycle fatigue (HCF) failures as a direct result of vibrations of small amplitude. When they occur these high frequency minor cycles will be superimposed on part of each major cycle. Consequently, the fatigue integrity assessment requires an evaluation of the behaviour of aero-engine materials under the conjoint action of LCF and HCF loadings. Furthermore, it is essential that there is confidence in both the life prediction method used in such an assessment and the fatigue and fracture mechanics data it requires.

Powell *et al.*¹ have shown that the fatigue crack growth curve for a loading combining major and minor cycles is characterised by two regimes of behaviour (*Figure 1*). These regimes are evident in the double logarithmic plot of the growth increment per loading block ($da/d\text{block}$) versus the total stress intensity (ΔK_{total}). At the lower values of ΔK_{total} (regime 1) the individual minor cycles do not contribute to the

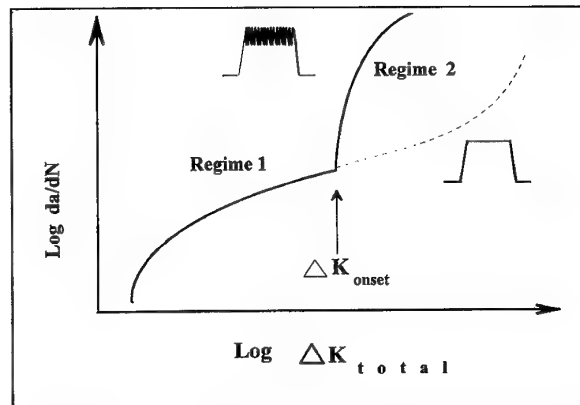


Figure 1 Form of fatigue crack growth rate curve for combined major and minor stress cycles

advance of the crack, and the growth rates and fractographic appearance correspond to those for an LCF loading yielding the same value of ΔK_{total} . At the higher values of ΔK_{total} (regime 2) the range of stress intensity associated with the minor cycles exceeds a threshold, and each minor cycle now contributes to the growth. This contribution may cause the growth rate to increase rapidly, so deviating from the response to the application of a separate LCF loading. The fracture surface may now exhibit 'block striations', that is to

say striation markings generated by each peak-to-peak cycle well separated by regions of growth due to the minor cycles²⁻⁴. The value of ΔK_{total} corresponding to the transition between these two regimes is labelled ΔK_{onset} . This transition has a substantial effect on the magnitude of crack propagation life under combined major and minor stress cycles, and its determination or estimation is the key to successful crack life predictions³.

The simplest model for the prediction of fatigue crack growth rates due to combined major and minor stress cycles assumes that there are no effects due to load history or load sequence. Thus the linear summation model adds the growth increments due to the total stress cycle (da/dN) and each minor cycle to give the growth rate for the combined loading block ($da/dblock$). Powell and coworkers^{3,5} have shown examples where the linear summation rule has been successful, and where, due to load interactions or short crack effects, it has not. Thus, for example, in Ti-5331S the striated crack growth due to the total cycle interferes with the faceted crack growth due to the minor cycles, so leading to a nonconformity with the predictions of the linear summation model³. Hawkyard *et al.*⁶ accounted for potential load interaction effects by associating them with the minor cycle component of HCF/LCF loadings. Satisfactory crack propagation life predictions were achieved for a wide range of HCF/LCF loadings applied to forged Ti-6Al-4V at room temperature by combining this approach with a model based on the concept of crack closure. A similar result was obtained by Claridge and Powell⁷ using a commercial software package whose algorithm for crack life predictions also employs the concept of crack closure in modelling the fatigue behaviour of materials. Significantly, Evans *et al.*⁸ have used closure corrected data to successfully predict the crack growth response of IMI 829 at 350°C for a range of major/minor cyclic combinations.

Thus, this paper first describes the fatigue crack growth behaviour of Ti-6Al-4V in rolled plate form when subjected to combined major and minor loadings; second employs the concept of crack closure to model the data for a given cycle ratio; and third validates the model by the prediction and measurement of crack growth rates for tests involving a greater number of minor cycles.

EXPERIMENTAL DETAILS

The material selected for testing was cross-rolled Ti-6Al-4V plate, as used in the construction of fan blades. Its manufacturing sequence consisted of: vacuum casting; forging first in the β and then in the $\alpha + \beta$ phase fields; cross-rolling in the $\alpha + \beta$ phase field; nondestructive testing; and finally applying a heat treatment simulating the production process of activated diffusion bonding. This treatment produced a microstructure of polyhedral grains of primary α , separated by colonies of transformed β , with some grain boundary precipitation of β . The grain size, determined by the linear intercept method, was 12 μm , with a volume fraction of the primary α of 75%. The cross-rolled texture was characterised by basal plane intensities on the transverse/short transverse plane and the longitudinal/short transverse plane of approximately ten

times and nine times random, respectively. Typical room temperature tensile properties, as measured in the longitudinal direction, consisted of a 0.2% proof stress of 870 MPa, a tensile strength of 980 MPa, and an elongation to fracture of 16%.

Corner notched testpieces (Figure 2) having a 7.071 \times 7.071 mm square cross-section at their gauge length have been cut from the Ti-6Al-4V plate. The specimen orientation, as defined by ASTM notation⁹, was longitudinal-short transverse (LS), which corresponded to the growth of a crack through the thickness of a fan blade in response to centrifugally induced stresses.

The specimens have been cyclically loaded in a special test facility which combines an electromagnetic vibrator with a servohydraulic fatigue machine. This hybrid machine could therefore apply low frequency major cycles and high frequency minor cycles either separately (Figure 3a and 3b) or conjointly (Figure 3c). The minor cycles were sinusoidal stress waves with a frequency of 150 Hz; whilst the major cycles were trapezoidal stress waves with 1 s rise and fall times and dwell periods of 6.8 s and 1.2 s at the maximum and minimum loads, giving a cyclic frequency of 0.1 Hz. A range of combined HCF/LCF loadings was generated by superimposing minor cycles, with a stress ratio of 0.7, 0.8, 0.85 or 0.9, on major cycles with a stress ratio of 0.01; the resulting amplitude ratios being 0.36, 0.22, 0.16 and 0.11, respectively. The superposition was limited to the dwell period at maximum load of the major cycles which produced an effective cycle ratio of 1000 minor cycle per major cycle. In the model validation tests a cycle ratio of 10,000 was used, which was achieved by simply extending the dwell period to 66.8 s.

Each specimen was precracked at room temperature using a stress ratio of 0.01 in order to generate a near quarter-circular crack with a radius of not less than 0.6 mm. The precise length of the precrack was determined with the aid of acetate replicas. Subsequently, room temperature crack growth rates were determined for separate major and combined major and minor cycles. A pulsed direct current potential difference system was used to monitor the crack growth as a function of the number of applied major cycles or combined cycle loading blocks; the output of the system being the ratio of the voltage across the mouth of the crack to that across reference probes. Each experiment was terminated at a crack length of approximately 3.5 mm and, following the breaking open of the specimen, the precise final crack length was determined using an optical microscope.

The test data was analysed by the three-point secant method, the input data consisting of paired values of voltage ratio and either cycles or loading blocks corresponding to equal increments in the voltage ratio. This procedure resulted in a ratio of crack increment to crack length measuring precision of 20. The linear relationship between voltage ratio and crack length established by Hicks and Pickard¹⁰, defined by the known values of voltage ratio and crack length at the start and end of the measurements, provided the calibration for the crack length monitoring system. The ranges of major, minor and total stress intensity factor were calculated using Pickard's¹¹ solution for the free surface position of a quarter-circular crack growing under remote tension.

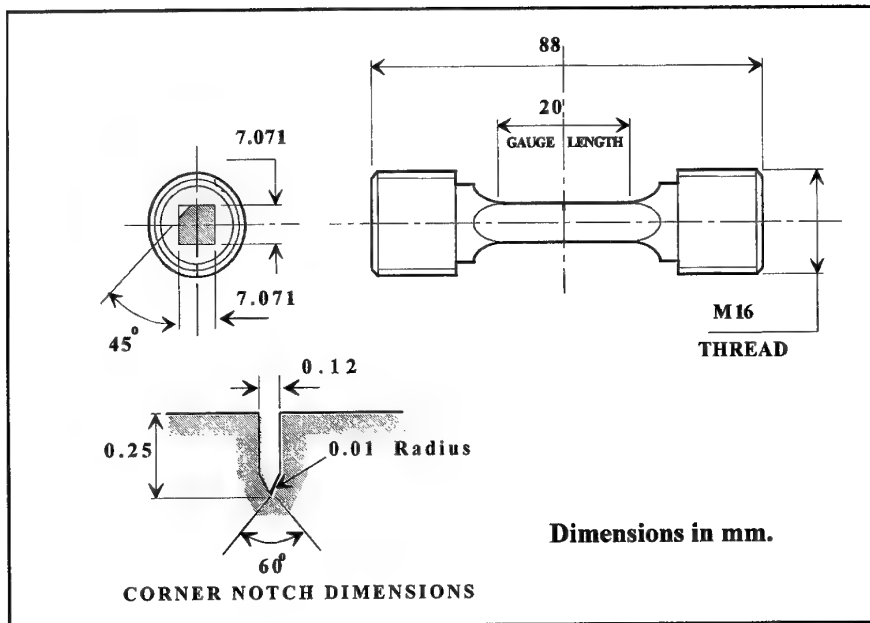


Figure 2 Specimen design

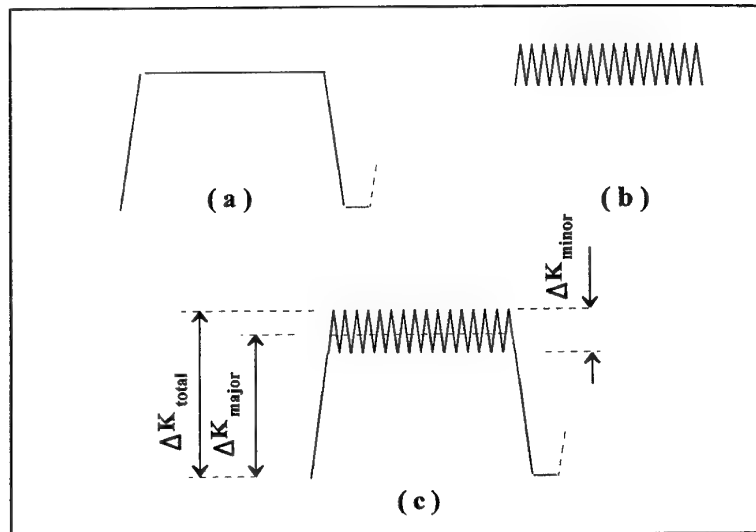


Figure 3 Loading waveforms: (a) separate major cycle, (b) separate minor cycles, (c) a major cycle and several minor stress cycles combined

In addition, the fatigue threshold values associated with separate minor cycle loadings (*Figure 3b*) were determined following a conventional load shedding sequence. Whilst maintaining the stress ratio constant, the maximum and minimum loads were systematically adjusted in order to establish and confirm the fatigue threshold value. The reductions in loads, which were never greater than 10%, were separated by crack growth increments of more than one monotonic, plane strain, plastic zone size. The fatigue threshold, which corresponded to a growth rate of $1 \times 10^{-8} \text{ mm cycle}^{-1}$, was bracketed by a 5% change.

RESULTS

Crack growth rate data for the separate application of a low frequency, major cycle loading exhibited a clearly

defined bilinear response, with the transition occurring at a value of ΔK of approximately $16 \text{ MPa}\sqrt{\text{m}}$ (*Figure 4*). The experimental data has been contained within scatter bands with the scatter band width corresponding to the variation in fatigue crack growth rate for a given value of ΔK . In the hypo-transitional region the data are characterised by slopes of 6.0 and a four-fold scatter band width. The fracture surface was faceted and fatigue striations were not observed (*Figure 5a*). By contrast, the hyper-transitional region was characterised by a slope of 2.2 and a two-fold scatter band width, whilst the fracture surface clearly showed the development of fatigue striations (*Figure 5b*).

Superimposing 1000 high frequency minor cycles with the chosen stress ratio on each major cycle gave growth rates which lay within or above the established scatter band for separate major cycles (*Figure 6*). As

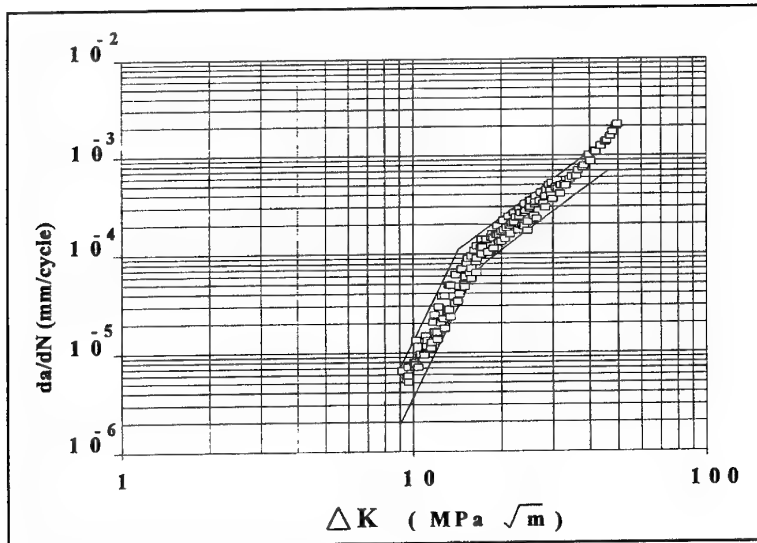


Figure 4 Fatigue crack growth rate curve for separate major cycles

the stress ratio of the minor cycles increased, the value of ΔK_{onset} , indicated by the divergence from the major cycle scatter band, also increased. Figure 5c shows the appearance of the block striations which are developed during regime 2 crack growth.

The contribution to crack growth associated with the superposition of high frequency cycles has been extracted from Figure 6. The procedure adopted assumes that the total stress cycles may affect the growth due to the minor cycles rather than the converse, and further, the growth due to the minor cycles within a given loading block is uniformly distributed. On this basis:

$$\frac{da}{dN}_{\text{minor}} = \frac{(da/dN_{\text{block}} - da/dN_{\text{total}})}{n} \quad (1)$$

where da/dN_{minor} , da/dN_{total} and da/dN_{block} are the crack advances associated with the application of a minor cycle, a total cycle, and a loading block; the latter consisting of a single major cycle and the appropriate number of superimposed minor cycles. Applying this procedure results in near-threshold growth rate curves for minor cycle loadings which have been periodically interrupted and underloaded by a low frequency cycle of large amplitude (Figure 7). Since these near-threshold growth rate curves extend down to a growth rate of 1×10^{-8} mm cycle $^{-1}$, threshold values for the HCF component of each combined loading can be established. These 'derived' threshold values were less than those obtained by a conventional test method using a constant amplitude loading (Figure 8), showing that the periodic introduction of the LCF loading has modified the growth due to the vibrational stress cycles. Moreover, it suggests that the prediction of growth rates for combined HCF and LCF loadings, based upon a knowledge of the growth rates from HCF and LCF loadings, when these are applied separately, would be nonconservative.

In this circumstance, it is preferable that the crack growth rate predictions utilise the derived minor cycle data, and that they are suitably modelled to account for the effect of stress ratio which stems from such phenomena as crack closure, crack tip blunting, or the

development of static fracture modes. For convenience, the model used to consolidate the derived minor cycle data by accounting for the effect of stress ratio will be presented in terms of the concepts of crack closure, since they are well known and have been found to be of value in achieving satisfactory predictions of the crack growth response to combined major and minor stress cycles^{6-8,12}, but this is not to imply that crack closure is the controlling mechanism. For a cyclic loading the effective stress intensity range (ΔK_{eff}) is given by

$$\Delta K_{\text{eff}} = K_{\text{max}} - K_{\text{op}} \quad (2)$$

where K_{max} and K_{op} are the maximum and crack opening stress intensity levels. Considering the case of a derived threshold value ($\Delta K_{\text{th R'}}$) for a given minor cycle stress ratio (R_{minor}), and further identifying the value of ΔK_{eff} with the derived threshold value for a stress ratio of 0.9 ($\Delta K_{\text{th 0.9'}}$), since it is reasonable to consider that this is closure free, yields the relationship

$$K_{\text{op}} = \{\Delta K_{\text{th R'}}/(1 - R_{\text{minor}})\} - \Delta K_{\text{th 0.9'}} \quad (3)$$

If it is assumed that the value of K_{op} is constant within the near-threshold regime, then for this region

$$\Delta K_{\text{eff}} = K_{\text{max}} - [\{\Delta K_{\text{th R'}}/(1 - R_{\text{minor}})\} - \Delta K_{\text{th 0.9'}}] \quad (4)$$

Plotting the growth rates as a function of the effective range of the applied stress intensity factor, as defined by Equation (4), has achieved a degree of unification of the near-threshold data for HCF loadings with stress ratios from 0.01 to 0.9. A single curve has been used to represent this data (Figure 9).

The fatigue crack growth rates resulting from the application of loading blocks containing 10,000 high frequency minor cycles per low frequency major cycle have been predicted. Having selected various values of the minor cycle stress intensity range (ΔK_{minor}) and R_{minor} , the minor cycle growth rates are estimated from the effective values of ΔK_{minor} calculated from Equation (4), and the single curve used to represent the HCF

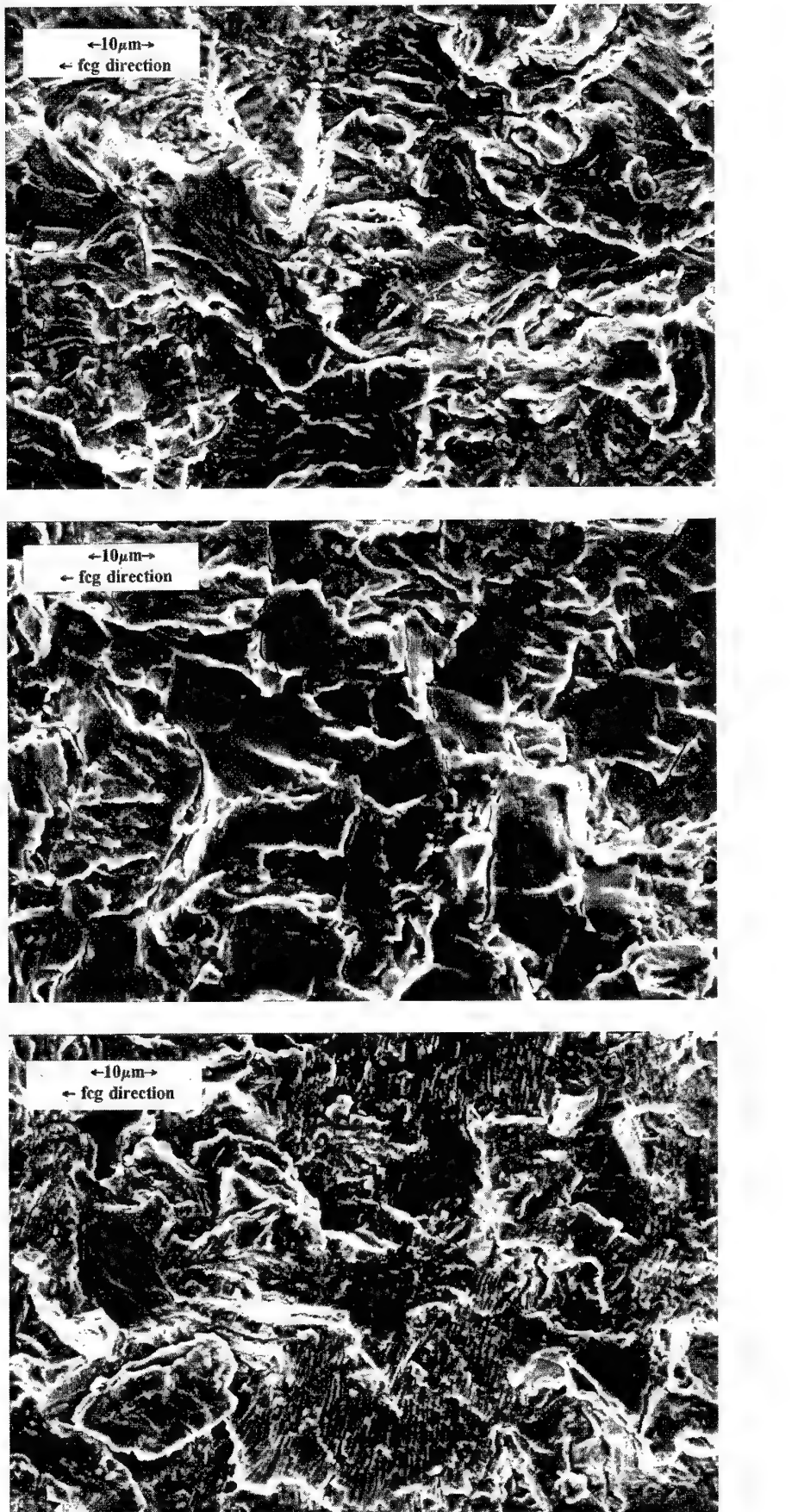


Figure 5 Dominant fracture processes: (a) cyclic cleavage resulting from major cycle growth at $\Delta K = 12.3 \text{ MPa}\sqrt{\text{m}}$, (b) ductile striations resulting from major cycle growth at $\Delta K = 23.2 \text{ MPa}\sqrt{\text{m}}$, (c) block striations resulting from combined major and minor cycle growth at $Q = 0.16$ and $n = 1000$ and $\Delta K_{\text{total}} = 19.5 \text{ MPa}\sqrt{\text{m}}$

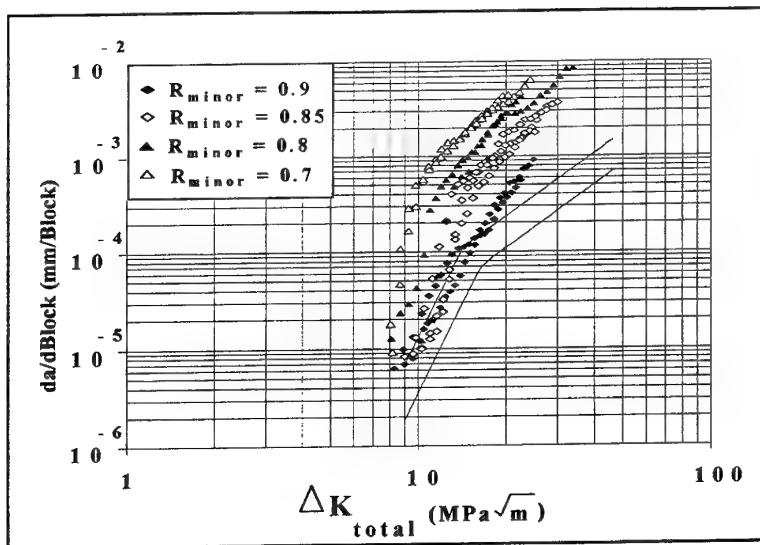


Figure 6 Fatigue crack growth rate curve for combined major and minor stress cycles

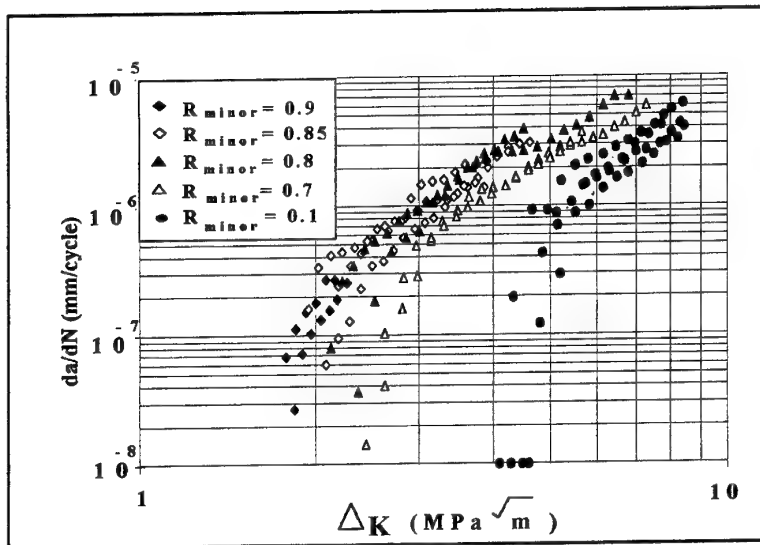


Figure 7 Derived minor cycle growth rate data

response (Figure 9). The total stress intensity range (ΔK_{total}) is then given by

$$\Delta K_{\text{total}} = \Delta K_{\text{minor}}[1 - R_{\text{total}}]/[1 - R_{\text{minor}}] \quad (5)$$

where the stress ratio for the total cycle (R_{total}) is related to that for the major (R_{major}) and minor (R_{minor}) cycles by the relationship

$$R_{\text{total}} = R_{\text{major}}[1 + R_{\text{minor}}]/2 \quad (6)$$

The corresponding values for the total cycle growth rates are then estimated from the upper bound to the LCF scatter band (Figure 4), respectively. These data are summed according to the relationship

$$da/dblock = da/dN_{\text{total}} + 10,000da/dN_{\text{minor}} \quad (7)$$

A subsequent series of experiments, using minor cycle stress ratios of 0.7, 0.8, 0.85 and 0.9, shows these predictions to be either accurate or safe (Figure 10).

DISCUSSION

In previous studies^{2,6,13} the crack growth behaviour of forged Ti-6Al-4V has been investigated using compact tension and corner notched specimens cut from forged discs. The crack growth planes in these specimens were radial/axial and axial/tangential, and the basal plane intensities were five times and two times random, respectively. The annealing process which followed forging favoured the development of an equiaxed morphology of phases, as described by Margolin¹⁴, but this was not carried to completion and consequently the primary α particles were elongated. The grain size of the microstructure, indicated by the linear intercept method, was 30 μm , whilst the volume fraction of primary α was approximately 45%.

In general terms, the fatigue crack growth behaviour of Ti-6Al-4V in the form of forged discs and cross-

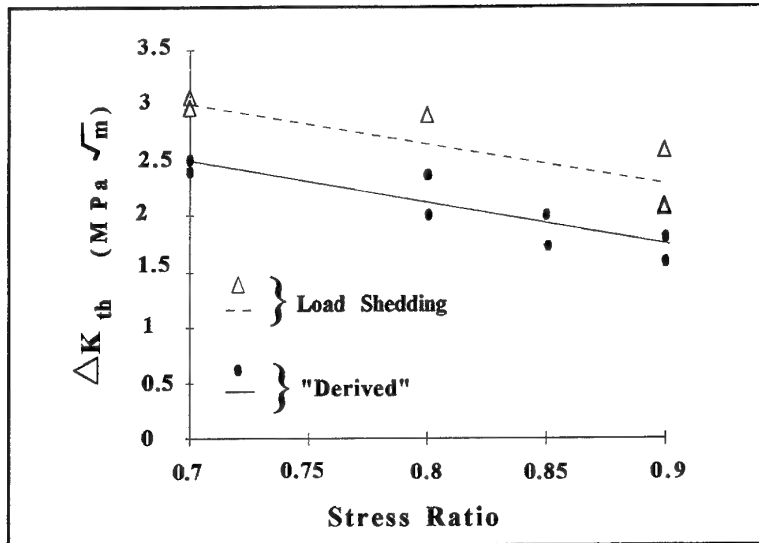


Figure 8 Threshold data for minor stress cycles

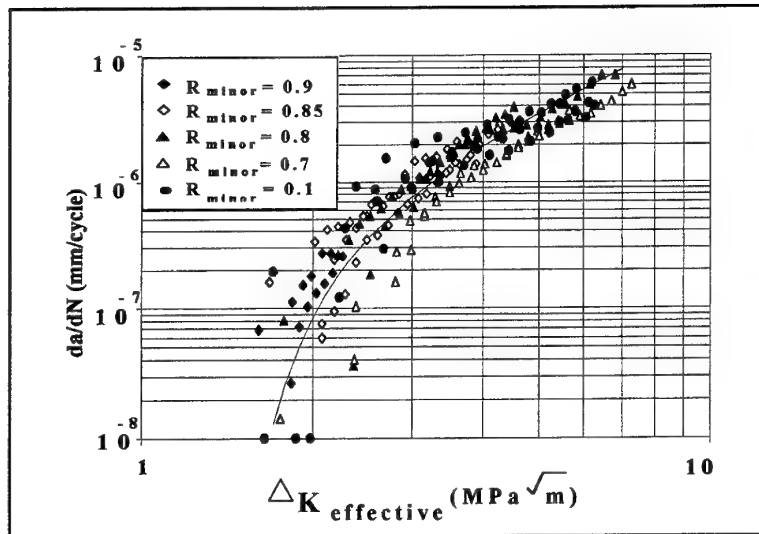


Figure 9 Consolidation of the derived minor cycle growth rate data

rolled plate are similar. However, cross-rolled plate exhibits a more sharply defined bilinear growth rate curve in response to the application of a separate LCF loading (*Figure 11*). Although derived threshold values for the two forms of Ti-6Al-4V are comparable at $R_{\text{minor}} = 0.7$, at $R_{\text{minor}} = 0.9$ the resistance to HCF growth in the presence of an LCF loading offered by the plate can be as low as 75% of that of the forged material (*Figure 12*).

The bilinear growth rate curves shown in *Figure 11* can be explained in terms of the concept proposed by Yoder *et al.*¹⁵ and the microstructure of the two materials. First, the effect of increasing the grain size is to shift the curve, and with it the transition point, to a higher value of ΔK . Thus, the reversed plastic zone size at the transition point has been identified with the mean grain size^{16,17}. Similarly, Yuen *et al.*¹⁸ identified the transition in growth mechanism from cyclic cleavage to striations with a cyclic plastic zone

size which approximated to the α grain size. The transitional ranges of stress intensity factor (ΔK_T) for the plate and forged materials are 16 and 20 MPa $\sqrt{\text{m}}$, respectively. Taking a value of 880 MPa as a representative value of the 0.2% proof stress (S_y) for the two materials, and calculating the reversed plastic zone (r_p) for plane stress conditions from the relationship

$$r_p = (1/8\pi)(\Delta K/S_y)^2 \quad (8)$$

yields plastic zone sizes of 13 and 21 μm , respectively. These compare favourably with the measured grain size of plate material of 12 μm , and the primary α grain size in the forged material of 23 μm .

Second, Yoder *et al.*¹⁵ suggested that the greater the clustering of the grain size distribution the sharper the transition. The primary α grains and the regions of transformed β in the plate material are of similar size and this material shows the sharper transition. A sharp transition will result in a low value of the hyper-

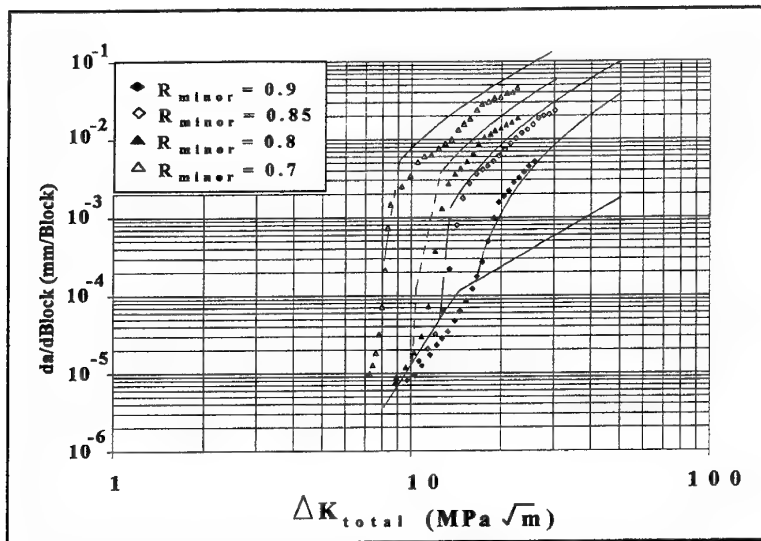


Figure 10 Experimental and predicted fatigue crack growth rates for combined major and minor cycles

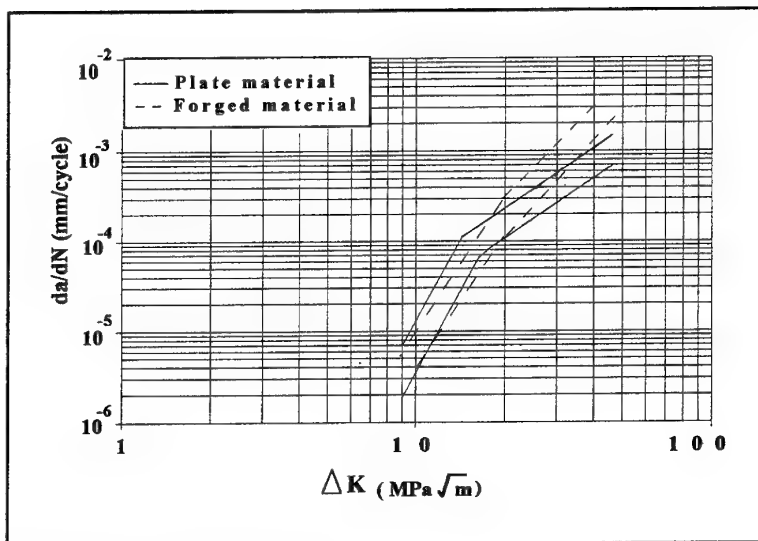


Figure 11 Major cycle growth rates in forged and plate material

transitional gradient. In the case of the plate material the hyper-transitional gradient was 2.2, that is to say close to the value of 2 which is associated with entirely striated growth.

The greatest difference in the derived threshold values of plate and forged materials is at $R = 0.9$, when the material's intrinsic resistance to crack advance prevails. Masounave and Baillon¹⁹ have suggested that a smaller range of stress intensity is required for crystallographic growth in fine-grained materials. The finer the grain size, the smaller the deviations of the crack path from the plane of maximum stress and the shorter the crack path. A finer grain size also gives a lower threshold value since there is a greater probability that an adjacent grain at the crack front is suitably orientated for further crack growth. Consequently, the finer grained plate material would be expected to have the lower threshold value. However, the two materials also differ in regard to

texture. Within the plane of the cracks, the plate material possesses an intensity of basal planes which is two to five times that of the forged material. The plate material has more planes suitably orientated for cyclic cleavage, this being the fracture mechanism at threshold²⁰.

In order that the practical significance of their different fatigue behaviours might be assessed, the crack propagation lives of plate and forged material have been compared. Corner cracks growing in a $25 \times 25 \text{ mm}^2$ section have been considered. The upper bound of the relevant fatigue crack growth curve has been numerically integrated²¹, from an initial crack size of 0.5 mm to a final crack size which was determined by the onset of minor cycle crack growth. The predicted lives are shown in Figure 13 as a function of the total applied stress range, for a combined loading in which $R_{\text{major}} = 0.01$ and $R_{\text{minor}} = 0.90$. It is apparent that the lower threshold values for plate material derived from

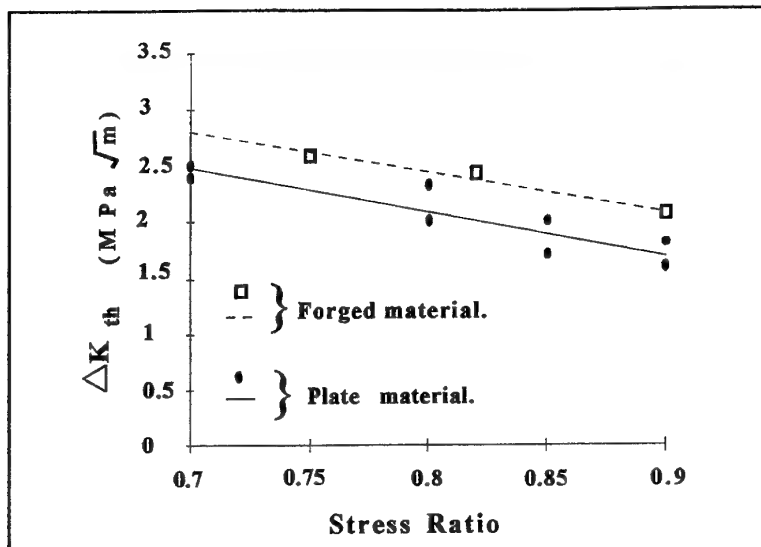


Figure 12 Derived minor cycle threshold data for forged and plate material

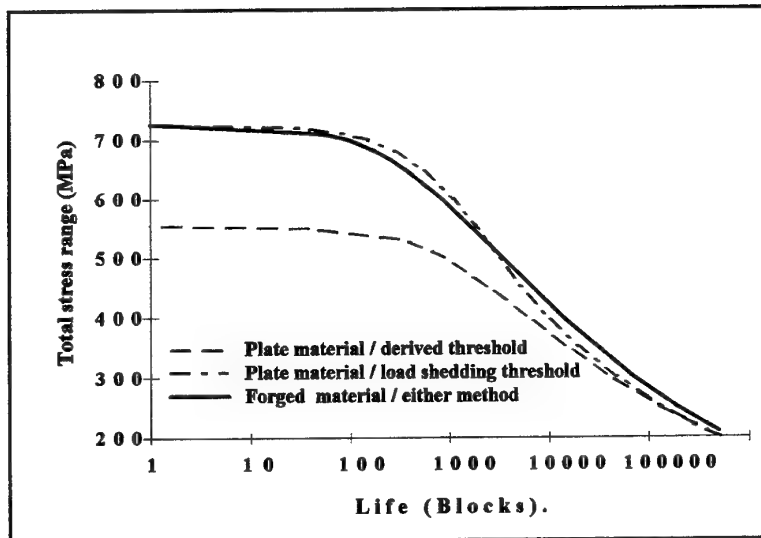


Figure 13 Fatigue crack propagation lives for corner cracks growing in forged and plate material

tests combining major and minor cycles lead to reduced lives, most markedly at the higher stress ranges.

CONCLUSIONS

For cross-rolled Ti-6Al-4V plate tested at room temperature:

1. the fatigue crack growth rates for combined HCF and LCF loadings are predicted by a model based on the concept of crack closure;
2. the growth rates for the LCF loading are characterised by a sharply defined bilinear growth rate curve, which contrasts with the behaviour of forged material;
3. the minor cycle threshold values derived from the growth rate data for combined HCF and LCF loadings are lower than those found by the load shedding

method, and in the case of a stress ratio of 0.9 lower than those for forged material.

REFERENCES

- 1 Powell, B. E., Hall, R. F. and Hawkyard, M., First International Conference on Structural Integrity Assessment, Manchester, 1992, p. 336.
- 2 Powell, B. E., *International Journal of Fatigue*, 1987, **9**, 195.
- 3 Powell, B. E., *International Journal of Fatigue*, 1995, **17**, 221.
- 4 Specht, J. U., Third International Conference on Low Cycle Fatigue and Elastoplastic Behaviour of Materials, Berlin, 1992, p. 19.
- 5 Powell, B. E., Henderson, I. and Duggan, T. V., *Second International Conference on Fatigue and Fatigue Thresholds*, Birmingham, Vol. 2. EMAS, Warley, UK, 1984, p. 893.
- 6 Hawkyard, M., Powell, B. E., Hussey, I. and Grabowski, L., *Fatigue and Fracture of Engineering Materials and Structures*, 1996, **19**, 217.

- 7 Claridge, S. P. and Powell, B. E., First International Conference on Computational Methods and Testing for Engineering Integrity Computational Mechanics Publications, Southampton, UK, 1996, p. 87.
- 8 Evans, W. J., Medwell, N. and Spence, S. H., *12th International Symposium on Air Breathing Engines*. Vol. 1. American Institute of Aeronautics and Astronautics, 1995, p. 185.
- 9 ASTM Standard E-399-90, 1990, **03.01**, 407.
- 10 Hicks, M. A. and Pickard, A. C., *International Journal of Fracture*, 1980, **20**, 91.
- 11 Pickard, A. C., *The Application of 3-Dimensional Finite Element Methods to Fracture Mechanics and Fatigue Life Predictions*. EMAS, Warley, UK, 1986.
- 12 Zhang, S. J., Doker, H., Schulte, K. and Trautmann, K.-H., *Advances in Fatigue Lifetime Prediction Techniques*, Vol. 2, eds M. R. Mitchell and R. W. Landgraf. ASTM STP 1122, ASTM, Philadelphia, 1993, p. 54.
- 13 Powell, B. E., Henderson, I. and Hall, R. F., The growth of corner cracks under the conjoint action of high and low cycle fatigue. Report AFWAL-TR-87-4130, Air Force Wright Aero-nautical Laboratories, Wright-Patterson Air Force Base, Ohio, 1988.
- 14 Margolin, H., *Titanium 80: Science and Technology*. Metallurgical Society AIME, New York, 1980, p. 1555.
- 15 Yoder, G. R., Cooley, L. A. and Crooker, T. W., *Titanium 80: Science and Technology*. Metallurgical Society AIME, New York, 1980, p. 1865.
- 16 Yoder, G. R., Cooley, L. A. and Crooker, T. W., *Engineering Fracture Mechanics*, 1979, **11**, 805.
- 17 Yoder, G. R., Cooley, L. A. and Crooker, T. W., *Metallurgical Transactions*, 1977, **8A**, 1737.
- 18 Yuen, A., Hopkins, S. W., Leverant, G. R. and Rau, C. A., *Metallurgical Transactions*, 1974, **5**, 1833.
- 19 Masounave, J. and Baillon, J. -P., *Scripta Metallurgica*, 1976, **10**, 165.
- 20 Wardclose, C. M. and Beevers, C. J., *Metallurgical Transactions*, 1980, **11A**, 1007.
- 21 Powell, B. E. and Hawkyard, M., *Third International Conference on Structural Integrity Assessment*, Cambridge. EMAS, Warley, UK, 1996, in press.

PII: S0142-1123(97)00035-2

Environmental interactions with fatigue crack growth in alpha/beta titanium alloys

W.J. Evans*, M.R. Bache*, M. McElhone† and L. Grabowskit

*IRC in Materials for High Performance Applications, University of Wales,
Swansea SA2 8PP, UK

†Rolls Royce plc, P.O Box 31, Derby DE2 8EJ, UK

The impact of different environments on the growth of short through cracks ($0.25 \text{ mm} < a < 3 \text{ mm}$) in thin section DEN test pieces ($t = 2 \text{ mm}$) is evaluated for the titanium alloy IMI318 (Ti-6Al-4V) at atmosphere. Both oxidising and reducing atmospheres have been considered in the form of air, chlorine and hydrogen gas at various levels of partial pressure. Data are presented for crack growth under cyclic and dwell waveforms and for R values of 0.01 and 0.625. It is demonstrated that the measured rates are extremely sensitive to the gaseous species. This sensitivity is reflected in fracture surface features and quasi-cleavage facetting in particular. The implications for engineering component life predictions are discussed. © 1998 Elsevier Science Ltd.

(Keywords: Fatigue crack growth; Ti)

INTRODUCTION

It is well established that the early stages of fatigue crack growth in alpha + beta titanium alloys are associated with the development of faceted regions on the fracture surface. These facets form as the crack front addresses the local microstructure, almost invariably have a basal plane orientation, and due to their flat appearance are often described as 'quasi-cleavage' in form. They have been attributed to the separation of intense slip bands under the action of a tensile stress normal to the band^{1,2}. Interestingly, similar features are also observed on stress corrosion fractures, implying that a cyclic variation of stress is not a prerequisite for their formation. Indeed, this latter observation has been taken to imply that a corrosive species such as hydrogen is involved in the fracture mechanism³. To some extent, this view is reinforced by the reported order of magnitude reductions in faceted fatigue crack growth rates when tests are carried out in high vacuum⁴. Clearly, since these early stages of crack development dominate the fatigue lives of many components, any uncertainty in understanding the mechanisms involved or imprecision in the life prediction calculations could have serious repercussions.

The objective of the present research programme was to quantify the impact of different environments on the rates of fatigue crack growth, and in particular to observe their effects on quasi-cleavage facet formation. To this end a series of experiments was carried out on the Ti-6Al-4V alloy at ambient temperatures.

The measurements were made on through thickness cracks in thin section (2 mm), double edge notch specimens. The test conditions encompassed a range of environments including atmospheric air, hydrogen gas (at a partial pressure of 1 torr) and chlorine gas (at 10^{-2} torr and 1 torr). The effects of load ratio (R) and wave shape were also evaluated.

The interaction between environment and short crack growth behaviour is shown to be highly dependent on the species present and their oxidising or reducing nature. The implications of the findings for engineering component life prediction and models for facet formation are discussed.

EXPERIMENTAL METHODS

Specimens were manufactured from cross rolled Ti-6Al-4V plate material of 18 mm thickness. The material was heat treated below the beta transus to produce a bimodal primary alpha/transformed beta microstructure. All the specimens were machined from the plate with a common orientation so that the fatigue cracks developed in an identical plane and direction for successive tests, i.e. growing parallel to one of the rolling directions and through the thickness of the plate. A thin section, double edge notched specimen (DEN) with a K_t factor of 1.9 was employed for the fatigue crack propagation testing, *Figure 1*. By introducing a narrow, surface slit (using a diamond tipped slitting wheel) along the root of one notch, the test piece generated a through section crack advancing from a stress raiser and through a diminishing stress

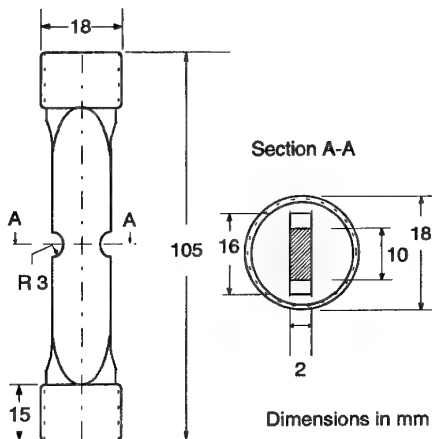


Figure 1 DEN specimen design

field. Pulsed d.c. potential monitoring of crack growth was facilitated by welding platinum wires (0.05 mm diameter) at diametrically opposed positions either side of the starter slit, *Figure 2*. A constant current power supply delivered 10 A through the specimen at predetermined sampling intervals during the test. To ensure accurate measurement of the voltage, the test cycle was interrupted at approximately 70% of the peak test stress condition for 8 s. Based on a previous analysis, a linear calibration was assumed between the voltage measured and the crack length⁵. The resultant crack length versus cycles data were used to calculate growth rates (da/dN) via a three-point secant method. Using a linear elastic fracture mechanics calibration of the test piece⁶, these rates were assessed as a function of the range of applied stress intensity factor (ΔK). Test data are reported for two loading waveforms: 1 Hz sine and a dwell cycle consisting of a linear rise and fall over

1 s with a hold at peak stress for 30 s, *Figure 3*. Two loading ratios of $R = 0.1$ and $R = 0.625$ were assessed. All testing was conducted under load control.

An environmental chamber encapsulated the specimen and loading rods of a servohydraulic testing machine. The chamber can be evacuated under an upstream pressure control loop which controls the flow of an inlet gas (or atmospheric air) to balance the pumping capability of the system. Vacuum control and pressure measurement are achieved by employing a Barocel capacitance manometer (range 2 to 10^{-2} torr) and an active inverted magnetron (AIM) gauge (range 10^{-2} to 10^{-8} torr). A schematic diagram representing the closed loop pressure control system is included in *Figure 4*. All testing in the current programme was conducted at 20°C.

Specific measures are not taken to control the degree of moisture in the chamber whilst testing is in progress, however, only high purity commercial gases with a minimal water content were employed for the controlled environments, detailed in *Table 1*. Prior to attaining the test condition, a repeated purging procedure using high purity argon was carried out in order to evacuate any gaseous species present in the chamber or supply lines. In the particular case of chlorine, certain tests were performed in a backfilled environment rather than under the controlled pressure conditions. For these backfilled tests, following the purging sequence the chamber was isolated from the evacuating line and a limited volume of chlorine gas admitted until the pressure increased to approximately 1 torr. The chamber was then sealed at the upstream end, trapping the chlorine in the chamber for the duration of the fatigue test.

The specimen fracture surfaces were examined using optical and scanning electron microscopes. In the case of one test piece evaluated in a controlled chlorine environment (TEN646), secondary ion mass spectroscopy (SIMS) provided qualitative measurements of the relative titanium to chlorine (Ti:Cl) ion concentration at selected points along the fracture path.

RESULTS

Fatigue crack growth rates measured from specimens tested under a 1 Hz sine waveform in atmospheric air are illustrated in *Figure 5*. Data for the two loading ratios, $R = 0.01$ and $R = 0.625$, are included. For comparison, a best fit line from a previously published database characterising the growth of corner cracks in similar cross rolled material is superimposed⁷. It is evident that through cracks in the DEN test piece

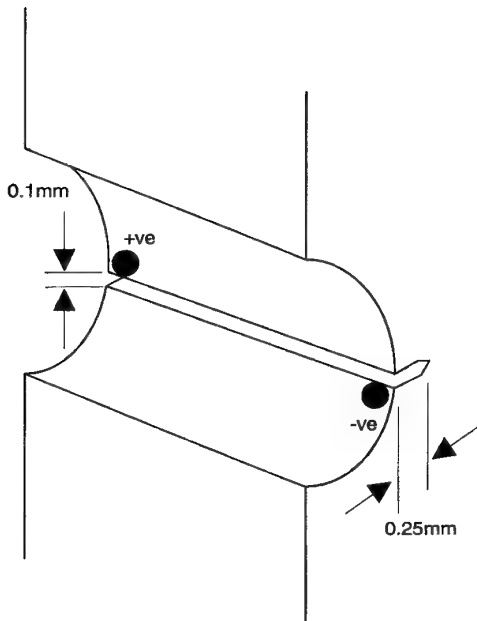


Figure 2 P.D. probe wire positioning with respect to starter slit

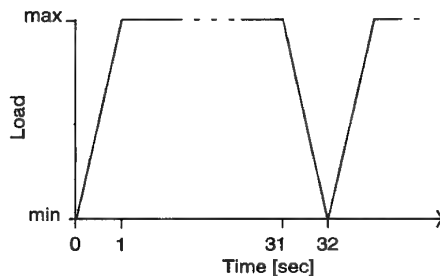


Figure 3 Dwell waveform

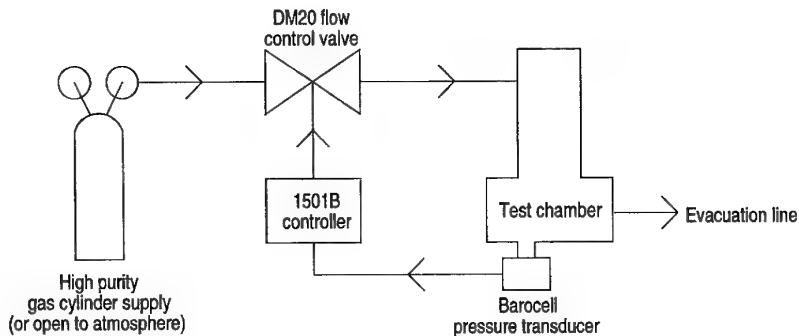


Figure 4 Schematic representation of environmental control

Table 1 Composition of commercial gases as specified by the suppliers

Gas	Relevant specification details
Pureshield argon	Ar 99.998% purity
High purity hydrogen	H ₂ 99.995% minimum purity
Chlorine 'electronic grade'	'Typical composition' Cl ₂ 120 ppm N ₂ 40 ppm O ₂ < 3 ppm hydrocarbons < 100 ppm CO ₂ < 3 ppm H ₂ O

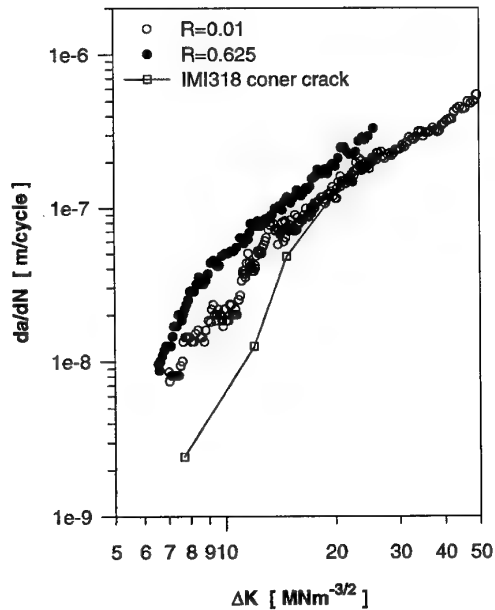


Figure 5 FCG in atmospheric air, 1 Hz sine waveform, various R

propagate at higher rates than the part through corner cracks, especially under low values of ΔK for the $R = 0.625$ condition.

The effects of different environments employing the same 1 Hz cycle are compared for the $R = 0.625$

condition in Figure 6. Chlorine, as a backfilled environment with an approximate pressure of 1 torr, causes a general increase in growth rates. This contrasts with the 1 torr hydrogen environment in which the growth rates are lower than atmospheric air.

The effects of R ratio and dwell in combination with a chlorine environment were explored in depth as illustrated in Figures 7 and 8. For comparative purposes, a best fit curve through the cyclic $R = 0.625/1$ Hz data in the chlorine environment has been superimposed from Figure 6. Two tests conducted in a controlled chlorine environment at 10^{-2} torr, both with the 30 s dwell waveform and at $R = 0.01$ but with different peak stresses (200 and 400 MPa, respectively), gave growth rate curves that are similar to the cyclic 1 Hz condition. In contrast, the same dwell period and pressure at the higher load ratio of $R = 0.625$ resulted in an extremely undulating growth rate response, Figure 8. At least two major episodes of acceleration followed by retardation can be identified for this specimen (designated TEN646). It is noticeable that the troughs in the growth rate appear to fall back to the equivalent 1 Hz sine test data. Finally, the same figure

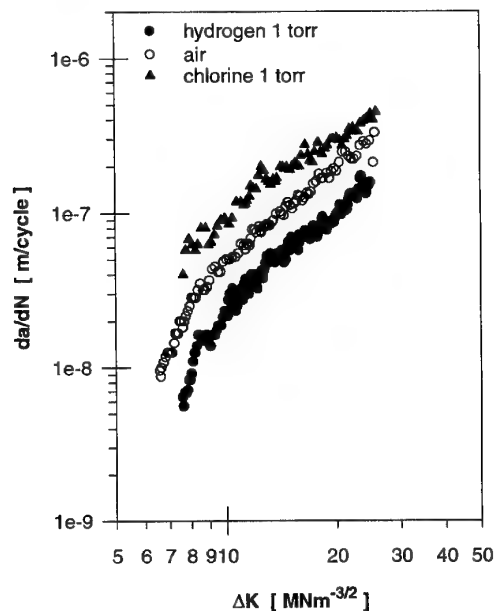


Figure 6 Effect of environment on 1 Hz sine tests at $R = 0.625$

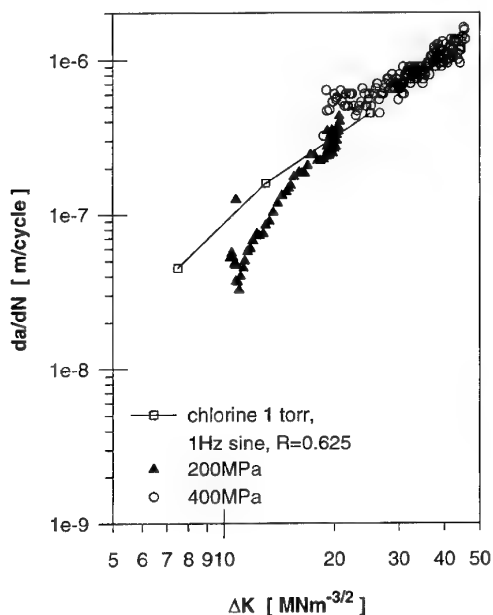


Figure 7 Effect of dwell loading in 1 torr chlorine, $R = 0.01$

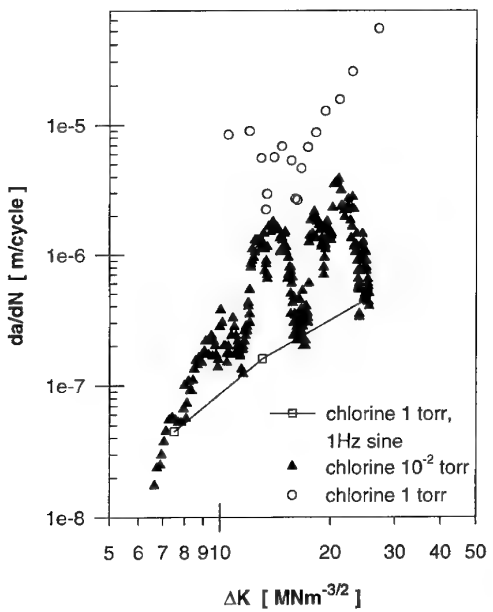


Figure 8 Accelerated rates in chlorine atmospheres under dwell loading at $R = 0.625$

also contains information on a high R , dwell test conducted in a backfilled chlorine environment at 1 torr pressure. The dramatic increase in growth rate is clearly evident, as are the further periods of relative retardation during the lifetime of the test.

The fracture surfaces of the specimens tested in air displayed the two types of features often reported in Ti-6Al-4V materials. The early stages of growth were associated with a region of quasi-cleavage facetting. In the later stages of fracture, however, fatigue striations start to dominate. These regimes were similar to those seen on corner crack specimens of identical material also tested in air⁷. Interestingly, the 1 torr hydrogen environment did not appear to alter the general pattern



Figure 9 Serrated fracture surface of specimen TEN646 ($R = 0.625/\text{dwell}/10^{-2}$ torr chlorine)

of behaviour. However, the tests in a chlorine atmosphere did induce a change, particularly with regard to an increase in the degree of facetting. Specimen TEN646 was examined in detail in view of the irregular crack growth rates defined above. The scanning electron macrograph shown in Figure 9 illustrates a serrated form of fracture surface with near linear ridges traversing the section. Facetting, illustrated in Figure 10, was dominant over the initial stages of crack growth up to an approximate crack length of 0.5 mm.

DISCUSSION

The research programme has highlighted a number of important characteristics in environmentally influenced fatigue crack growth of titanium alloys. Many of the issues raised by these short through cracks have not as yet been resolved in detail. However, it is relevant to review the trends found and to speculate on the likely mechanisms involved. In particular, it is evident that at the gas concentrations covered (1 torr maximum pressure), chlorine increases the rate of fatigue crack

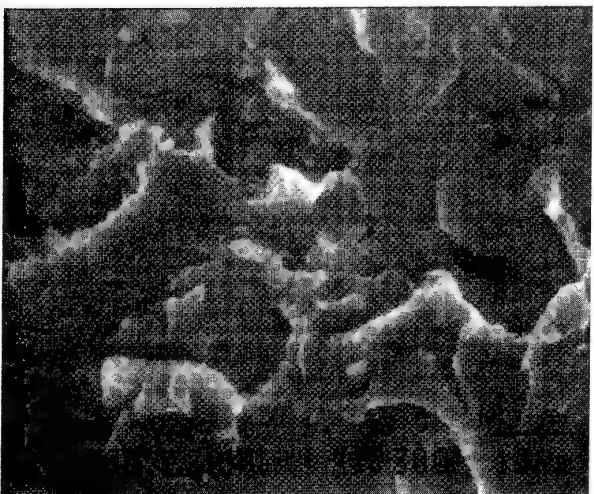


Figure 10 Dominant faceted region in early stages of chlorine assisted fracture

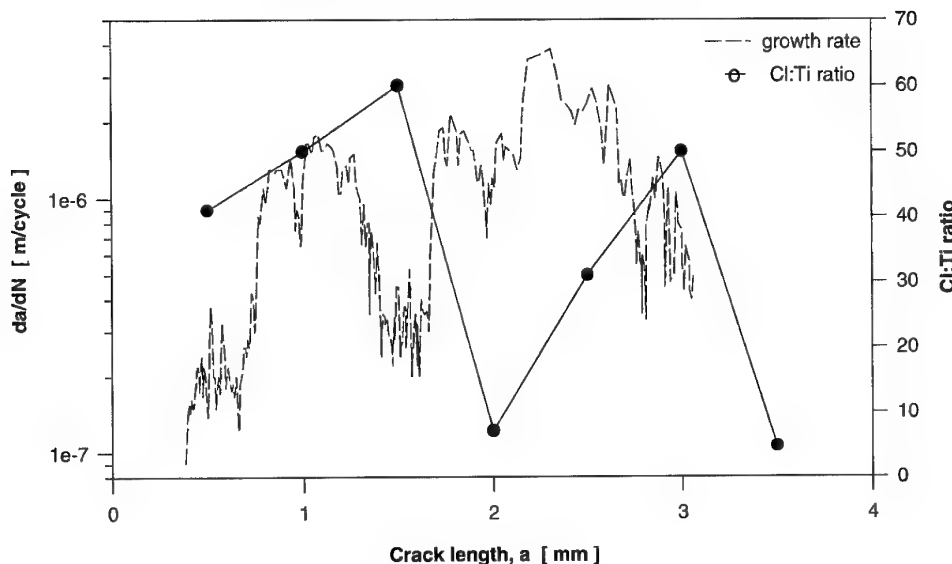


Figure 11 Comparison of FCG rates and chlorine assimilation for specimen TEN646

growth over air data whereas hydrogen is associated with a reduction in rate. The latter result was not entirely unexpected on the basis of a previous programme of work carried out by the authors on the near alpha titanium alloy Ti-6Al-5Zr-0.5Mo-0.25Si (IMI685). In that case, internal hydrogen concentrations did not affect growth behaviour until they exceeded 200 ppm, when hydride precipitation became possible. The same work showed that lower hydrogen concentrations affected fracture behaviour only by modifying the stress-strain response of the alloy⁸. It is suggested that hydrogen enters the crack tip plastic zone in the present situation causing an increase in yield strength and thereby making the formation of 'quasi-cleavage' facets more difficult. Such facets dominate the early stages of crack growth and have been attributed to the separation of slip bands under the action of a tensile stress normal to the band^{1,2}. In the alpha/beta titanium alloys, the facets typically have a basal plane orientation. It has been argued that their rate of formation is enhanced by oxygen⁹. The plasticity requirement is emphasised by the fact that the through cracks in plane stress/thin sections covered here grow faster than part-through cracks in thick sections⁷.

The wide range of experiments carried out in chlorine atmospheres suggests that at least three factors are important for accelerated growth. These are pressure, dwell time at peak stress and maximum stress or stress intensity factor. Other contributory factors are likely to be microstructural size, morphology and temperature, but these were not explored in the present work. It is clear that even at a pressure of 1 torr, both cyclic (1 Hz) and dwell (2 min) waveforms cause less than a two to three times increase in growth rate over air when the R value is 0.01. If R is increased to 0.625, however, the dwell cycle results in almost two orders of magnitude acceleration for the same pressure, although the cyclic response is similar to the $R = 0.01$ data. Reducing the pressure to 0.01 torr and maintaining R at 0.625 produces the interesting result that the growth rates fluctuate between an upper bound defined by the high pressure, high R dwell response

and a lower bound defined by the low R cyclic curve. It is interesting that the SIMS measurements of chlorine concentration from just below the fracture plane vary cyclically with crack length in a similar manner, Figure 11. It is also relevant that the fracture surfaces under all chlorine atmospheres are extensively faceted.

Chlorine, unlike hydrogen, is not soluble in titanium and will not therefore significantly influence the stress-strain characteristics of the alloy. Its effects are probably more related to the damage of surfaces in contact with the gas. On this basis, the lattice model of Fuller *et al.*¹⁰ appears to have some relevance. According to that approach, 'stretched' metallic bonds at the crack tip rupture under the action of chemical changes involving corrosive species. In the present situation, there are two possible ways in which this could occur in order to achieve the accelerated rates observed. Firstly, the bonds that fail could be associated with the basal plane so that the rupture process simply accelerates quasi-cleavage facet formation. Alternatively, the critical bonds are not at the sites of facet development. In that case, it is assumed that the initial failure event is the separation of favourably orientated basal planes at or ahead of the crack tip. This would occur irrespective of the external environment. It is then the response of the remaining unfavourably orientated regions or 'ligaments' to the environment which determines the macroscopic growth kinetics. Rupture of these ligaments through the ingress of chlorine would lead to a significant growth rate acceleration.

It is uncertain which of the two events is dominant in the present situation. However, the evidence available appears to support the latter model. The variable growth rates at $R = 0.625/0.01$ torr gas pressure plus the periodic variation of chlorine content on the fracture surface are consistent with this argument. The high R value is important in facilitating access to the crack tip. Under intermediate gas pressure, time is required for sufficient chlorine to gain entry whilst at higher pressures (1 torr) there is ample gas available for a continual advance of the crack. The periodic variation in chlorine content on the fracture surface of

the specimen tested at 0.01 torr suggests that the crack is held up until the ligaments surrounding the initial quasi-cleavage facets have ruptured. Whilst the ligaments remain load bearing they will restrict crack opening and thus reduce the peak stress intensity factor K_{\max} together with the subsequent rate of growth. Once a sufficient build up of chlorine has taken place, a rapid advance will then follow as the crack passes through the 'process zone' and its inherent basal plane damage. The cycle of facetting, chemical attack of the ligaments and accelerated rupture is then repeated.

CONCLUSIONS

It has been shown that the growth of through cracks in thin DEN test pieces (2 mm thickness) is significantly affected by chlorine gas. The extent of the induced acceleration in growth rates is affected by gas pressure, R value and length of the dwell period at peak stress. A mechanism for the chlorine enhancement is suggested. This involves the development of quasi-cleavage facets on basal planes by normal slip band processes and then the rupture of the surrounding ligaments through the ingress and chemical action of the chlorine molecules.

In contrast, hydrogen gas was found to reduce the rate of crack growth under equivalent conditions. The hydrogen is believed to act through modification of the stress-strain response in the plastic zone ahead of the crack tip.

ACKNOWLEDGEMENTS

Thanks go to Wayne Voice, Rolls Royce plc, for the results of the SIMS analysis and technical discussions concerning the technique. The supply of materials from Rolls Royce plc is also greatly appreciated.

REFERENCES

- 1 Evans, W. J. and Bache, M. R., *International Journal of Fatigue*, 1994, **16**, 443-452.
- 2 Davidson, D. L. and Eylon, D., *Metallurgical Transactions A*, 1980, **11A**, 837-843.
- 3 Birnbaum, H. K. In *Proceedings of Environment-induced Cracking of Metals*, eds R. P. Gangloff and M. B. Ives. NACE, 1989, pp. 21-29.
- 4 Evans, W. J. In *Titanium '95, Proceedings of 8th World Conference on Titanium*, Birmingham, UK, eds P. A. Blenkinsop, W. J. Evans and H. M. Flower. Institute of Materials, London, 1995, p. 1065.
- 5 Mom, A. J. A., Revised working document for the AGARD cooperative test programme on titanium alloy engine disc material. Report NLR TR 86019L, 1986.
- 6 Pickard, A. C., The application of 3-dimensional finite element methods to fracture mechanics and fatigue life prediction. EMAS, Cradley Heath, West Midlands, 1986.
- 7 Evans, W. J., Bache, M. R., Nicholas, P. J. and Grabowski, L. In *Proceedings of 12th International Symposium on Air Breathing Engines*, Melbourne, Australia, ed. F. S. Billig. American Institute of Aeronautics and Astronautics, Washington, DC, 1995, p. 229.
- 8 Evans, W. J. and Bache, M. R., *Scripta Metallurgica*, 1995, **32**, 1019.
- 9 Bache, M. R., Evans, W. J. and McElhone, M., The effects of environment and internal oxygen on fatigue crack propagation in Ti-6Al-4V. Proceedings of ICSMA-II, Prague, Czech Republic, August 25-29, 1997. In *Materials Science and Engineering A*, Vol A234-236, 1997, pp. 918-922.
- 10 Fuller, E. R., Lawn, B. R. and Thomson, R. M., *Acta Metallurgica*, 1980, **28**, 1407.

PII: S0142-1123(97)00028-5

Analysis of high temperature fatigue crack growth behavior

K. Sadananda* and A.K. Vasudevant

*Code 6323, Naval Research Laboratory, Washington, DC 20375, USA

*t*Code 332, Office of Naval Research, Arlington, VA 22217, USA

High temperature fatigue crack growth has been examined in the light of the new concepts developed by the authors. We observe that the high temperature crack growth behavior can be explained using the two intrinsic parameters ΔK and K_{\max} , without invoking crack closure concepts. The two-parameter requirement implies that two driving forces are required simultaneously to cause fatigue cracks to grow. This results in two thresholds that must be exceeded to initiate the growth. Of the two, the cyclic threshold part ΔK_{th}^* is related to the cyclic plasticity, while the static threshold K_{th}^* is related to the breaking of the crack tip bonds. It is experimentally observed that the latter is relatively more sensitive to temperature, crack tip environment and slip mode. With increasing test temperature, the cycle-dependent damage process becomes more time-dependent, with the effect that crack growth is dominated by K_{\max} . Thus, in all such fracture processes, whether it is an overload fracture or subcritical crack growth involving stress corrosion, sustained load, creep, fatigue or combinations thereof, K_{\max} (or an equivalent non-linear parameter such as J_{\max}) remains as one essential driving force contributing to the final material separation. Under fatigue conditions, cyclic amplitude ΔK (or an equivalent non-linear parameter like ΔJ) becomes the second necessary driving force needed to induce the characteristic cyclic damage for crack growth. Cyclic damage then reduces the role of K_{\max} required for crack growth at the expense of ΔK . © 1998 Elsevier Science Ltd.

(Keywords: high temperature fatigue; two loading parameters – ΔK and K_{\max} ; mild steels; nickel-base superalloys; titanium aluminides)

INTRODUCTION

The effect of high temperature on fatigue crack growth behavior has been studied extensively in the past¹; but the detailed systematic evaluation of threshold and near threshold crack growth behavior as a function of temperature, wave form, frequency, stress ratio, environment is limited. We examine some selected literature data to evaluate the effect of temperature on fatigue crack growth and its role in the two loading parameters, with particular reference to the threshold region². It is observed that temperature can affect all three stages of fatigue damage evolution: crack nucleation, short crack growth and long crack growth. In this report we limit our discussions mainly to the long fatigue crack growth behavior at high temperature, since the available data for short cracks as a function of stress ratio is limited.

TEMPERATURE AND ENVIRONMENT

When considering the effect of temperature on fatigue, we find that superimposed effects of creep and environment become important. These two time-dependent effects can vary with test temperature and material

properties. Figure 1 provides a general description of the role of environment and creep under cyclic loading¹. Regions of time- and cycle-dependent damage are illustrated in this figure. For clarity, we list the salient characteristics of the high temperature fatigue damage with some examples. (a) Fatigue is a damage resulting from cyclic loads; but cyclic loads do not necessarily cause fatigue damage alone, see Figure 1. For example,

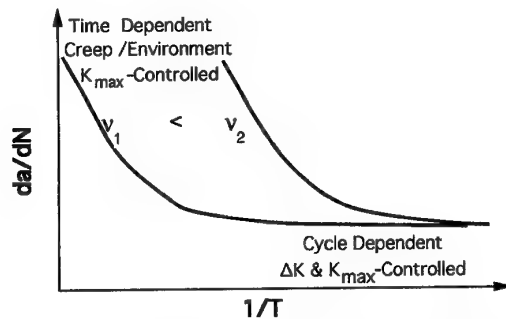


Figure 1 Schematic illustration of crack growth rate under cyclic loads as a function temperature and frequency; showing the regions of cycle-dependent and time-dependent processes

cyclic loads can accentuate the time-dependent damage (that includes environmental effects, creep or both) when the temperature is increased with an attendant decrease in frequency. Both creep and environmental damage are thermally activated processes. (b) Generally, increasing the strength of a material (high yield strength or creep strength) or decreasing its ductility increases the propensity of the material to the environmental effect (decreased K_{ISCC} ³) or to creep crack growth¹. (c) Increasing the stress intensity affects the two time-dependent processes differently, namely the creep and environmental contributions to damage. This is shown in the example from Alloy 718, Figure 2, where the effect of hold time (0, 1 and 10 min) at peak load and stress on the relative contributions of both creep and environment is shown. Crack growth rates in vacuum at zero hold time is used as a reference to compute the data to illustrate the effects. The figure shows that the creep contribution to crack growth rate increases with stress intensity and hold time at the peak load, while the environmental contribution decreases⁴ with stress intensity with lesser effects on hold time. The difference between the two time-dependent contributions arises since creep is more sensitive to the magnitude of the stress (particularly for materials with high creep rate exponents), while the environmental effects are more sensitive to the time of exposure. As the crack growth rates increase with ΔK , the time of environmental exposure at the crack tip [$1/(da/dt)$] decreases, thereby reducing the role of the environment. On the other hand, the creep contribution increases with increase in K_{max} , because of higher creep rates at higher stresses. (d) In all such analyses one must note that the intrinsic material properties can change with temperature due to instability of the alloy chemistry and/or microstructure. These microstructural changes with temperature can further result in (1) a change in slip character, (2) changes in strength (due to strain aging or dynamic aging), or (3) changes in ductility. All these changes can further affect the two thresholds ΔK and K_{max} for fatigue crack growth.

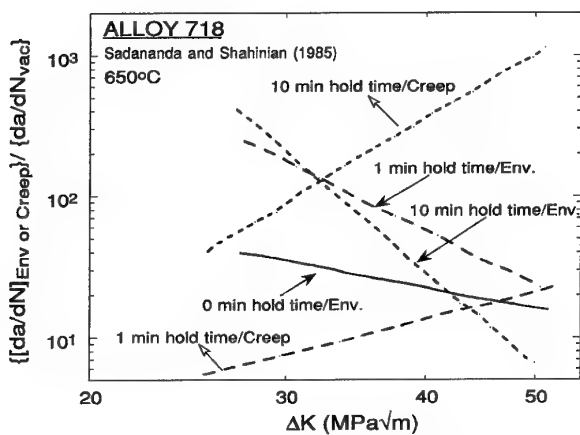


Figure 2 Effect of creep and environment processes on fatigue in Alloy 718 at 650°C. Zero hold time vacuum data is used as a reference to compute the data

TWO-PARAMETER DESCRIPTION OF DAMAGE

We have shown earlier^{2,5-7} that fatigue crack growth requires two independent loading parameters to uniquely describe a crack growth. Of these ΔK , an amplitude term, governs the cyclic plasticity contribution to the damage, and K_{max} governs the fracture process required for crack growth. The implication is that there must be two thresholds to simultaneously satisfy as a condition for fatigue cracks to grow; see Figure 3 for a summary of this process.

As the time-dependent contributions increase with rise in temperature, K_{max} becomes the dominating parameter. In the limit of purely time-dependent processes, the ΔK contribution goes to zero, leaving K_{max} as the main controlling parameter. Thus, as one progresses from cycle- to time-dependent processes, in the creep-fatigue domain, the parameter K_{max} becomes increasingly significant. In the past, we have noted that the creep-fatigue interactions were interpreted¹ by plotting the results either in the form (da/dN) vs. ΔK or (da/dt) vs. K_{max} . Since then we have realized the importance of the two driving force parameters for fatigue, and find that a correct description of creep-fatigue damage must also involve a three-dimensional representation² of (da/dN) or (da/dt) in terms of ΔK and K_{max} . With the reduction of the contribution from the cyclic damage component, the ΔK axis shrinks to zero, truncating the 3-D to a 2-D representation of (da/dt) with K_{max} .

Based on the two-parameter description, we have classified the overall fatigue crack growth behavior of materials into five groups⁵. Figure 4 provides a schematic description of Type I behavior characterizing the independence of ΔK from R . Type III characterizes a normal behavior with the extrapolated $\Delta K-R$ line intersecting at zero for $R = 1$. This curve gives a perfect L-shaped behavior, defining clearly the two critical thresholds as seen in the corresponding $\Delta K-K_{max}$ curves to the right of Figure 4. Type II is between Type I and III, with corresponding concave curvature in the $\Delta K-K_{max}$ curve. This is believed to be characteristic of materials where crack tip blunting can occur easily. Type IV is characteristic of environmentally sensitive materials, where static modes of environmental crack growth are superimposed on fatigue. Type V has been seen in some polymers where increased mean stress contributes to increased stiffness, thereby increasing ΔK with R . Using this kind of framework, we can analyze the effect of temperatures and load ratio on fatigue thresholds of several materials (a) to demonstrate that the existence of two threshold parameters is universally applicable, and (b) to examine how and possibly why each of the two parameters is affected by changes in temperature. The following examples are taken from mild steel, titanium and nickel aluminides to illustrate the role of the two loading parameters on fatigue damage at high temperatures.

TEMPERATURE AND LOAD RATIO

Although there has been extensive work on the characterization of high temperature crack growth, there has been very little effort to study the crack growth rates at near thresholds as a function of temperature and stress ratio. Part of the reason lies in the experimental difficulty of getting high temperature data for long

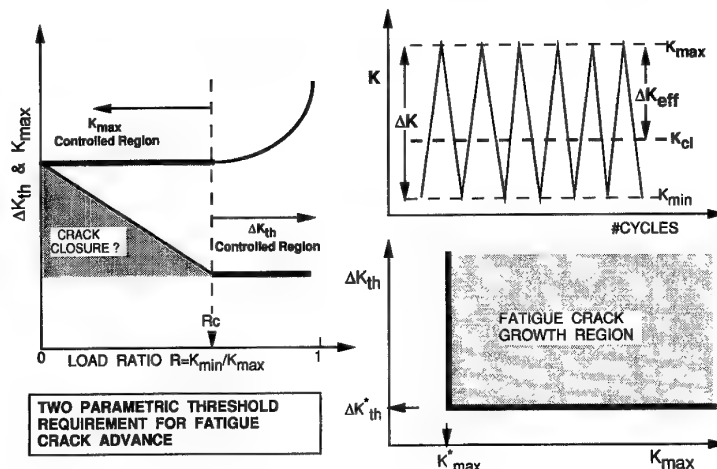


Figure 3 Schematic representation of the two parametric crack driving force requirement for fatigue damage, with respective definitions of the parameters

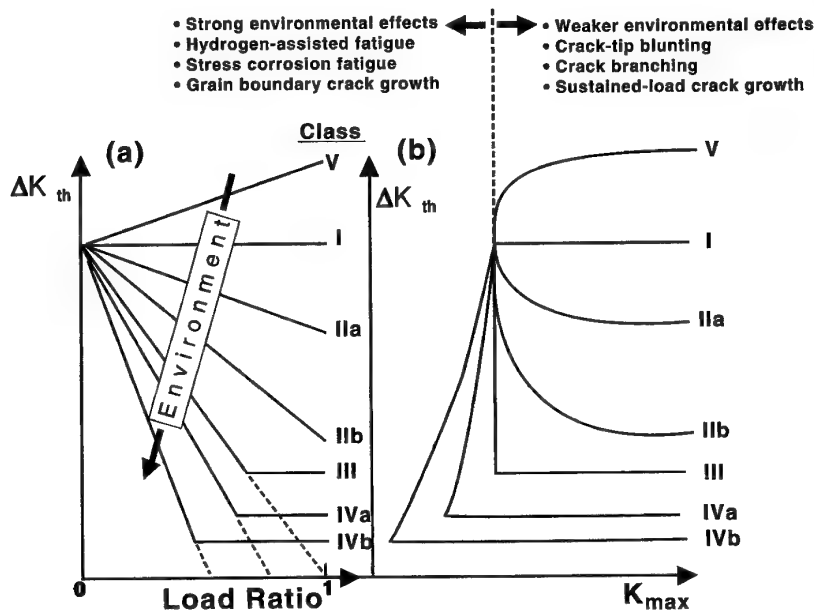


Figure 4 Schematic description of the overall fatigue deformations represented in terms of five classes of behavior, showing the important factors that can affect each region

periods of time. Needless to say, there is a need for such data to evaluate the relative roles of these two parameters as a function of temperature, frequency and hold time.

Figure 5a shows the threshold ΔK as a function of R -ratio for a mild steel and a weld metal; data taken from Priddle⁸ at 25°C and at a high temperature of 360°C. When ΔK_{th} is plotted against K_{max} it is evident that there exist two critical thresholds, ΔK_{th}^* and K_{max}^* , for fatigue crack growth, as shown in *Figure 5b* at 360°C for mild steel and a weld metal in *Figure 5a*. This represents a universal plot, defining the two asymptotic values along the ΔK and K_{max} axes, indicating the two critical threshold parameters. It also defines a complete threshold fatigue crack growth map for each material under a given test condition; see *Figure 3*. These fatigue maps define the limiting conditions above which fatigue crack growth is permissible.

Interestingly, within experimental error the threshold ΔK_{th} in vacuum for weld metal shows very little dependence on the R -ratio (*Figure 5a*) or on K_{max} (*Figure 5b*). In this case, K_{max}^* will equal ΔK_{th}^* at $R = 0$. To determine the complete L-shaped curve, test results at $R < 0$ are needed⁶. The ΔK_{th} independence of the R -ratio in vacuum confirms the absence of plasticity-induced crack closure, since in vacuum all other 'asperity' type contributions to closure are minimized⁵.

Figure 6a shows the crack growth data in titanium aluminides at 650°C from Haake *et al.*⁹. At threshold, ΔK_{th} is independent of R -ratio, similarly to vacuum data. ΔK begins to show a decrease with R at higher crack growth rates. The extrapolated lines of $\Delta K-R$ intersect the $R = 1$ axis at a positive ΔK value, reflecting a Type II behavior. Such a behavior will result in a concave shaped $\Delta K-K_{max}$ curve at both 25

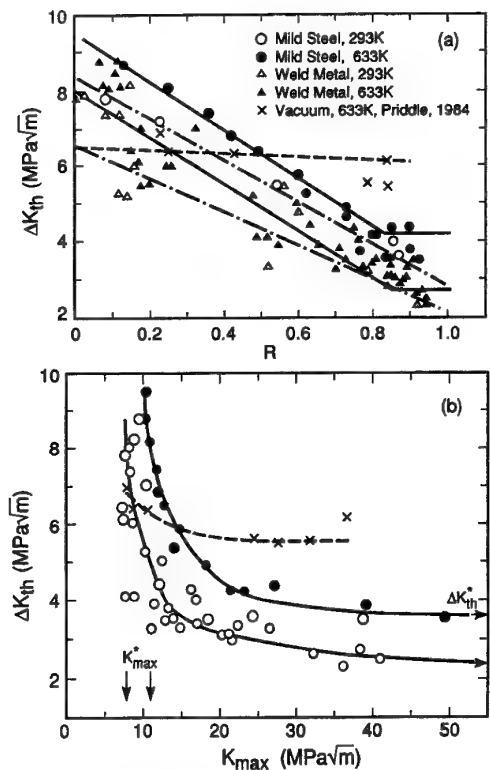


Figure 5 Fatigue threshold behavior in a mild steel and a weld metal: (a) load ratio effects on ΔK_{th} at room and elevated temperature; (b) high temperature ΔK_{th} - K_{max} for mild steel and the weld metal

and 650°C, *Figure 6b*. The effect is more pronounced at room temperature than at high temperature, even though more data at low and high R is needed to define the asymptotes in the curves. This shape represents an effect from a crack blunting type of damage process⁵.

High temperature fatigue crack growth behavior in Ni₃Al is shown in *Figures 7 and 8* at 600 and 800°C. The data was collected from Matuszyk *et al.*¹⁰. Since the experiments were performed only at two R values, $R = 0.1$ and $R = 0.6$, the data at intermediate R values were interpolated assuming a linear behavior of ΔK vs. R , see *Figure 4* for example. The existence of two thresholds ΔK and K_{max} is evident in both *Figures 7* and *8*. An interesting aspect of *Figure 8* at 800°C is the ΔK - K_{max} curve showing an upward curvature. Thus, as the crack growth rates increase or as the stress intensity increases, the concave curvature changes to a zero curvature at $1 \times 10^{-7}(\text{da}/\text{dN})$ and at a still higher crack growth rate it changes to a convex curvature. It appears to be difficult to use closure as an explanation for this type of fatigue behavior. We have classified this convex curvature behavior where ΔK increases with K_{max} as Type V, *Figure 4*. This type of behavior has been observed mostly in polymeric materials. Interestingly, a creep damaged metallic system also exhibits such Type V behavior. In the polymer case, as the mean stress or R -ratio increases, the stiffness of the material can increase by realignment of the molecular chains, causing an increase in fatigue strength. For Ni₃Al, creep deformation increases with mean stress or R -ratio with temperature. With increased deformation, stress severity at the crack tip can decrease,

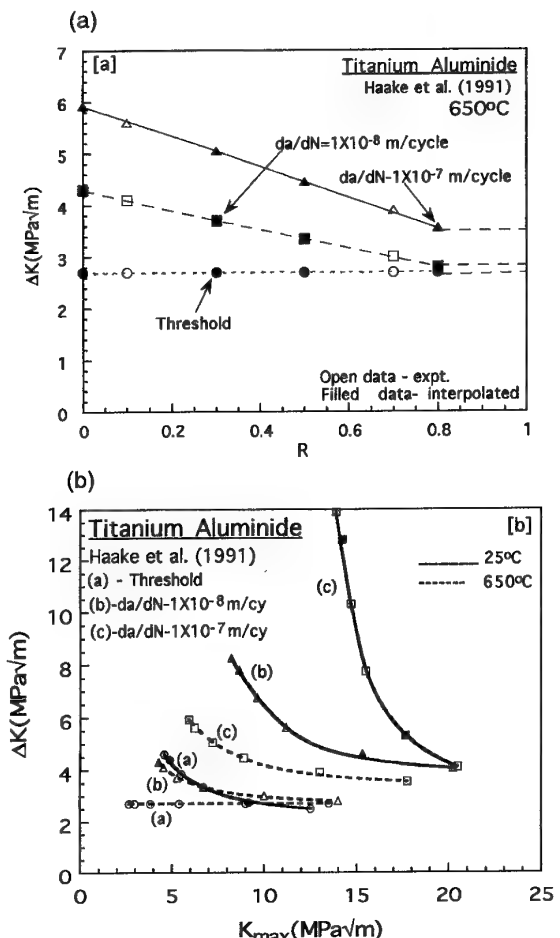


Figure 6 Fatigue results of a titanium aluminide at 650°C: (a) load ratio effects on ΔK at various growth rates; (b) corresponding ΔK_{th} - K_{max} at 25 and 650°C

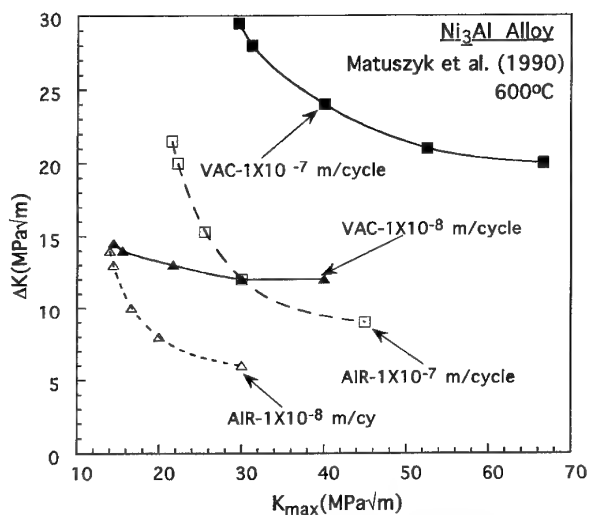


Figure 7 Fatigue crack growth behavior of a nickel aluminide at 600°C under vacuum and air at different growth rates

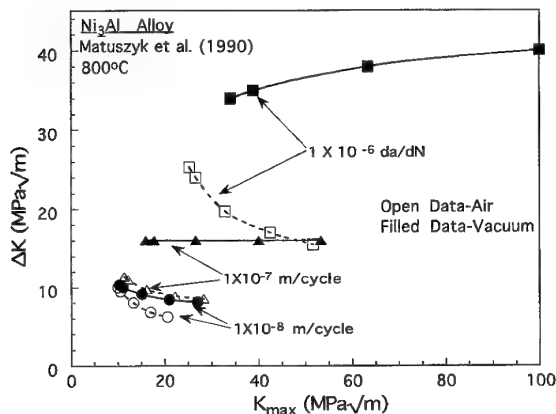


Figure 8 Fatigue crack growth behavior of a nickel aluminide at 800°C under vacuum and air at different growth rates

requiring a higher ΔK to induce crack growth. Thus ΔK can increase with mean stress or K_{max} , showing a convex curvature in the $\Delta K-K_{max}$ curve.

Figure 9a–c shows the crack growth behavior in a MARM-M002 nickel-base superalloy at 950°C, data from Webster.¹¹ Figure 9a shows the experimental data, (da/dN) vs. ΔK at three R -ratios: 0.1, 0.7 and 0.9. In Figure 9a a marked increase in crack growth rate is observed as R is increased from 0.7 to 0.9. Figure 9b is the relationship between ΔK and R near threshold growth rates. It can be seen that the decrease in ΔK is essentially linear, with no tendency to level off even at high $R \approx 1$. K_{max} is nearly constant with R . This trend is in contrast to the observation at low temperatures where the R effects on ΔK tend to converge to a plateau for $R > 0.6$ with the growth behavior controlled by ΔK_{th}^* (see Figure 3). The $\Delta K-K_{max}$ plot in Figure 9c shows a behavior similar to Type IV (Figure 4) but with $\Delta K_{th}^* \approx 0$. This implies that the fatigue damage contribution to (da/dN) is negligible, and the damage is predominantly controlled by K_{max} . Type IV behavior is generally observed when environmental contributions are dominant.⁵ For some other nickel-base alloys, such as Alloy 718, Rene 95, etc. the crack growth is also quite sensitive to the environment. As these test temperatures are high (950°C), crack growth can occur under pure creep deformation. Therefore tests under high vacuum must be done to separate the creep effects from environmental effects such as oxidation, as carried out for Alloy 718.^{1,4}

The behavior shown in Figure 10a–c is for data from Al-Abed and Webster¹² on another nickel-base alloy, IN6203. The tests were performed at somewhat lower temperature, 850°C, at $R = 0.1, 0.4$ and 0.7. Interestingly, the alloy seems to show a change in behavior from a cycle-dependent process to a time-dependent process with increase in R and with an increase in crack growth rates. Figure 10b shows the corresponding ΔK and K_{max} as a function of R -ratio at 3×10^{-3} mm cycle $^{-1}$ (open points are interpolated points used in Figure 10c). Figure 10b shows that there is a transition, indicating bilinear behavior. Although the data is limited, there seems to be a break in both ΔK and K_{max} with R . A purely K_{max} controlled time-dependent process should result in a straight line

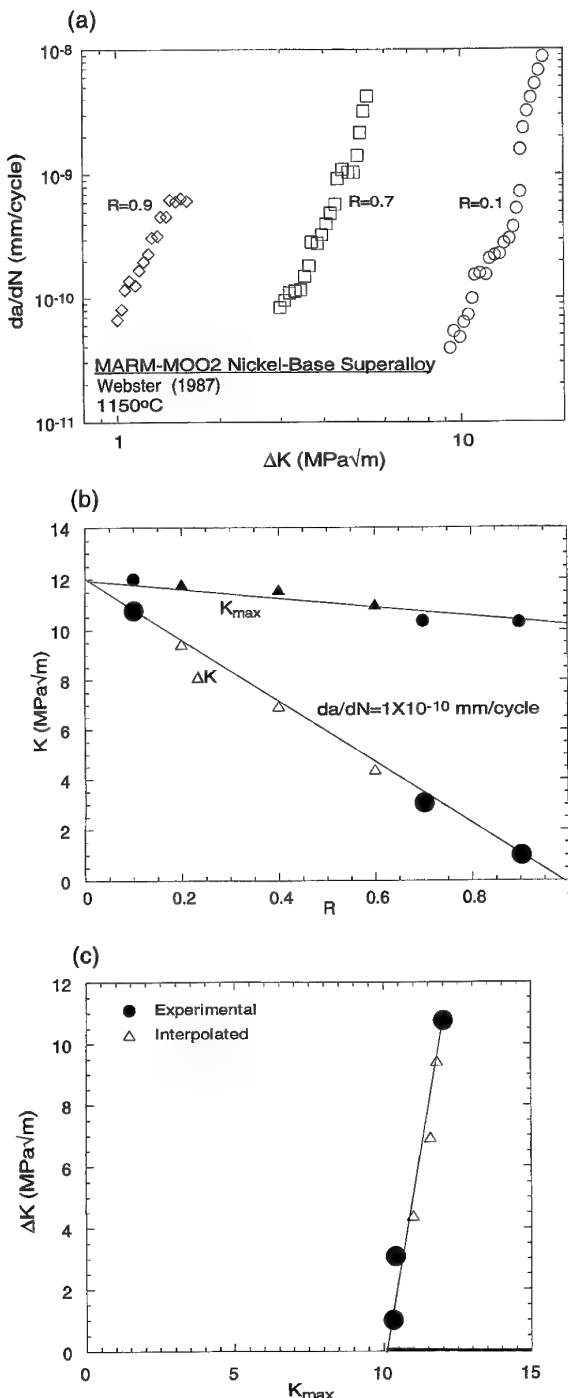


Figure 9 Fatigue results of MARM-M002 superalloy at 1150°C: (a) crack growth behavior at three different R -ratios; (b) R effects on ΔK and K_{max} at 10^{-10} mm cycle $^{-1}$; (c) fatigue map $\Delta K_{th}-K_{max}$ showing the K_{max} controlled process

$\Delta K-R$ curve passing through zero at $R = 1$. As discussed earlier, the cycle-dependent process has both ΔK and K_{max} controlled regimes, which is different from a time-dependent process. Figure 10b shows the extrapolation of low R data to high R data (dashed line) intersecting the $R = 1$ axis at $\Delta K > 0$, characteristic of Type II behavior (refer to Figure 4). This positive intercept is a clear indication that there is some minimum ΔK , corresponding to ΔK_{th}^* , required for the

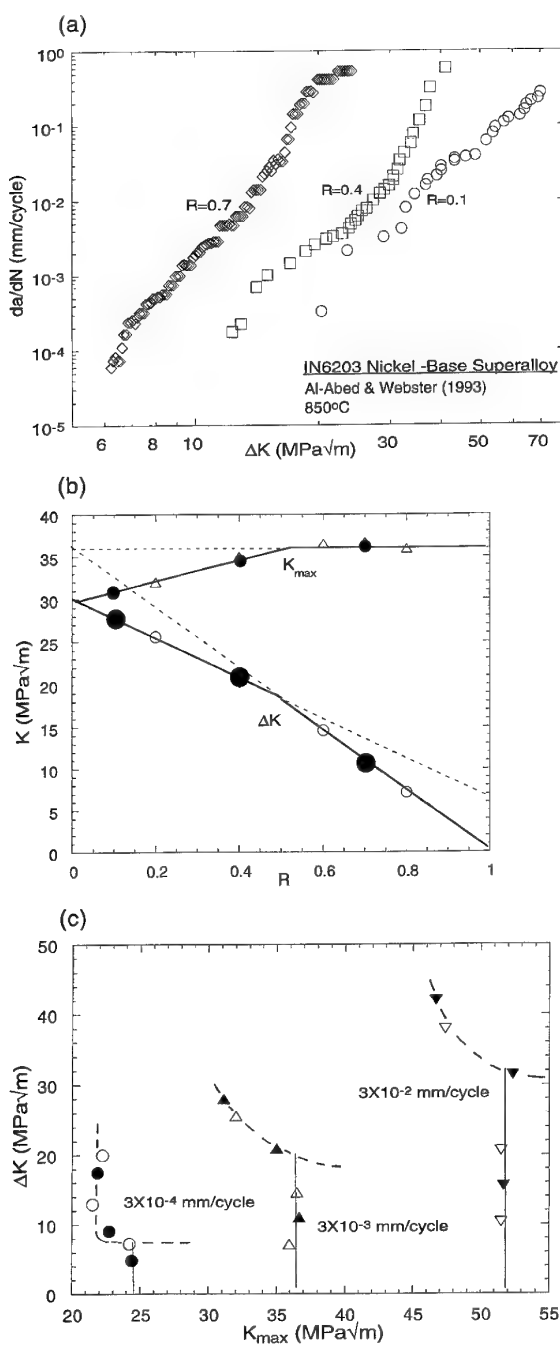


Figure 10 Fatigue results of IN6203 superalloy at 850°C: (a) crack growth behavior at three different R -ratios; (b) R effects on ΔK and K_{\max} at $3 \times 10^{-3} \text{ mm cycle}^{-1}$; (c) fatigue map $\Delta K_{\text{th}}-K_{\max}$ showing the transition from a ΔK to K_{\max} controlled process at various crack growth rates

cycle-dependent damage. Thus, the break in the line in *Figure 10b* is indicative of a transition from a cycle-dependent damage process at low R to a time-dependent process at high R (high K_{\max}). This can be seen in the extrapolation (dotted line) of the high R data (time-dependent process) to low R region, showing the need for higher K_{\max} for the time-dependent process to continue at low R -ratios. On the other hand, a cycle-dependent process requires lower K_{\max} . *Figure 10b* thus indicates that the cyclic damage helps in lowering

K_{\max} , that is otherwise required to cause a subcritical crack growth. At high R -ratios, the transition to a time-dependent process occurs, since the required K_{\max} to accomplish the task is now lower than that required for a cycle-dependent process.

These points are illustrated in *Figure 10c*, showing transitions in the $\Delta K-K_{\max}$ plots at different crack growth rates. At low crack growth rates, the cycle-dependent process, with a characteristic L-type shape, indicates the presence of both ΔK and K_{\max} thresholds for the fatigue crack growth. A sudden drop in the curves converging to a constant K_{\max} with ΔK approaching zero is indicative of the process change to purely K_{\max} controlled phenomena. The critical K_{\max} occurs at about 24, 36 and 52 MPa $\sqrt{\text{m}}$ respectively as the growth rate increases from 3×10^{-4} to $3 \times 10^{-2} \text{ mm cycle}^{-1}$ [see *Figure 10c*]. The time-dependent process could be a combination of both environmental and creep processes. To discriminate between the individual processes and observe which one is dominant can only be possible if test results from an inert environment are available.

SUMMARY

From the analysis of limited systematic high temperature fatigue data as a function of R -ratio, we observe that the two loading parameters ΔK and K_{\max} do apply to characterize the high temperature crack growth. In general, the temperature affects both these parameters, but K_{\max}^* more strongly. With increasing temperature, the contribution from the time-dependent process increases at the expense of the cycle-dependent process. The time-dependent damage processes include both environmental and creep, but if tests conducted under an inert environment are available one can delineate the relative role of these two contributions.

Analysis indicates the importance of the two-parameter requirement for fatigue, showing how these two parameters can naturally converge to one when the cycle-dependent process transitions to a time-dependent process at high temperatures and high stresses. One can also observe how these transitions are reflected in both $\Delta K-R$ and $\Delta K-K_{\max}$ plots. Similarly, at lower frequencies, transition from a cycle- to a time-dependent process can occur at a lower temperature. Such frequency effects can also be manifested to show transitions in both $\Delta K-R$ and $\Delta K-K_{\max}$ plots. Based on the current analysis, one can expect similar trends in the behavior under corrosion fatigue at ambient temperatures.

Finally, in all subcritical crack growth processes, K_{\max} (or its equivalent J_{\max}) is always an essential load parameter. Under fatigue conditions, damage being amplitude-dependent, an additional parameter ΔK (or its equivalent ΔJ) enters into the picture. In principle, this would reduce the role of K_{\max} that is otherwise required for a subcritical crack growth. Thus, fatigue becomes a natural subset of the subcritical crack growth phenomenon, under the umbrella of the two driving force parameters with the corresponding two thresholds.

REFERENCES

- 1 Sadananda, K. and Shahinian, P. In *Cavities and Cracks in Creep and Fatigue*, ed. J. Gittus. Applied Science Publishers, London, 1981, p. 109.
- 2 Vasudevan, A. K., Sadananda, K. and Louat, N., *Materials Science and Engineering A*, 1994, **188**, 1–22.
- 3 Sandoz, G., *Metallurgical Transactions*, 1972, **3**, 1169–1176.
- 4 Sadananda, K. and Shahinian, P. In *Corrosion in Nickel Base Alloys*. American Society of Metals, Cleveland, OH, 1985, pp. 101–116.
- 5 Vasudevan, A. K. and Sadananda, K., *Metallurgical Transactions*, 1995, **26A**, 1221–2134.
- 6 Sadananda, K. and Vasudevan, A. K., *Materials Science and Engineering A*, 1995, **192/193**, 490.
- 7 Sadananda, K. and Vasudevan, A. K. *Fatigue and Fracture Mechanics: 27th Volume*, ASTM STP-1296, 1997, 301–316.
- 8 Priddle, E. K. In *Fatigue Thresholds*, Vol. 1, eds J. Backlund, A. F. Blom and C. J. Beavers. Engineering Materials Advisory Services, West Midlands, UK, 1981, pp. 581–600.
- 9 Haake, F. K., Deluca, D. P., Holland, K. P. and Salivar, G. C. Pratt and Whitney Technical Report No. P.W/ED/FR/18997-8, October 1988.
- 10 Matuszyk, W., Camus, G., Duquette, D. J. and Stoloff, N. S., *Metallurgical Transactions*, 1990, **21**, 2967–2976.
- 11 Webster, G. A., *Materials Science and Technology*, 1987, **3**, 716–725.
- 12 Al-Abed, B. and Webster, G. A. In *Creep and Fracture of Engineering Materials and Structures*, eds B. Wilshire and R. W. Evans. Institute of Materials, London, 1993, p. 491.

PII: S0142-1123(97)00024-8

Introducing the compliance ratio concept for determining effective stress intensity

J. Keith Donald

Fracture Technology Associates, 2001 Stonesthrow Road, Bethlehem, PA 18015,
USA

Local crack tip strain measurements show that the conventional determination of ΔK effective may be misleading, especially when opening loads are relatively high as is often the case in the near-threshold regime. The conventional method assumes that K -opening can be directly related to a deviation in the linearity of a load vs crack mouth displacement curve ('compliance offset method'). Although this deviation in linearity can be attributed to closure, local strain measurements show that significant crack tip strain can occur below the K -opening load. The redistribution of stresses associated with a partially open crack and the effect of this redistribution on the stress field in front of the crack cannot be determined simply on the basis of a change in the slope of the load-displacement curve. However, a recent addition to ASTM E-647 (*Recommended Practice for Determination of Fatigue Crack Opening Load from Compliance*) implies that it can. An alternative 'compliance ratio' technique based on local crack tip strain is presented. A modification of this technique allowing the use of remote compliance measurements to account for crack tip strain below the opening load is suggested. © 1998 Elsevier Science Ltd.

(Keywords: fatigue; threshold; crack closure)

INTRODUCTION

Since the concept of crack closure was introduced by Elber in 1970¹ much controversy has surrounded the significance and the application of this concept. For example, Hertzberg *et al.*² observed a lack of correlation between conventionally measured effective stress intensities using remote displacement measurements and observed crack growth rates. The results of two ASTM 'round robin' programs^{3,4} on opening load measurement showed significant scatter, although this scatter was reduced when the data were subjected to a rigorous accept/reject criterion. More recently, Sadananda and Vasudevan^{5,6} have suggested that no elaborate crack closure measurements are either necessary or sufficient to account for the threshold behavior as a function of load ratio R . Finally, Chen *et al.*⁷ have provided supporting evidence that the contribution to the crack driving force below the opening load should be taken into account, resulting in a larger effective driving force compared with the conventional closure evaluation.

The author's contribution to crack closure measurement techniques began in 1986 with a presentation at the *Fatigue Crack Closure Symposium* (ASTM STP 982, eds J. C. Newman Jr. and W. Elber) recommending a method of standardizing the measurement technique⁸. This method served as the foundation for the current annex to ASTM E-647 (*Recommended*

Practice for Determination of Fatigue Crack Opening Load from Compliance). Standardization of the process was needed because measurements being reported in the literature were not necessarily consistent. However, another more fundamental concern regarding interpretation of the K -opening data still needs to be addressed. As it stands today, the 'ASTM technique' may provide misleading crack closure information in the near-threshold regime.

COMPLIANCE RATIO TECHNIQUE

A common interpretation of the closure mechanism visualizes a crack as 'peeling open' as stress is applied. Such an interpretation can lead to the assumption that the cyclic stress intensity is applied only when the crack tip is open (above K -opening). This places tremendous significance on the elusive K -opening level. However, if the closure mechanism were instead to be visualized as a stress redistribution (or load transfer) on a relatively compliant crack wake, then the concept of a local strain contribution below K -opening is not difficult to accept. What may be surprising is the large error that can result in the determination of ΔK effective if this contribution is ignored.

In the simplified case of a single element contributing to crack tip shielding (*Figure 1a*), the point of first contact or opening load at point 2 might not be as important in determining ΔK effective as the relative

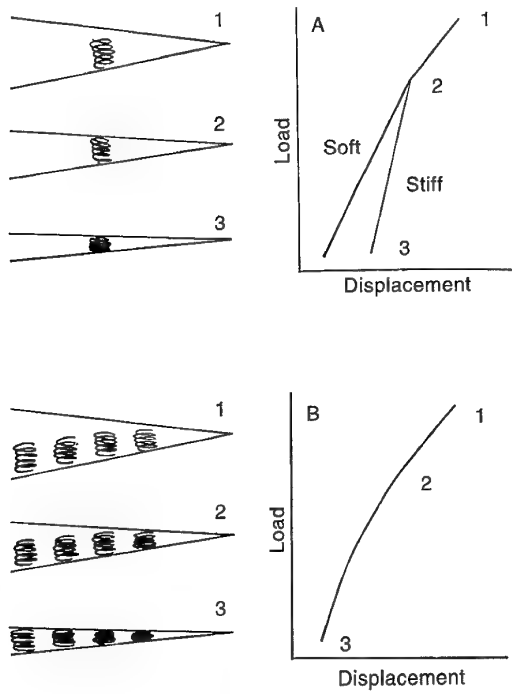


Figure 1 (a) Simplified case of single element contributing to crack tip shielding. First contact is indicated by point 2. The relative compliance of this element influences crack tip shielding. (b) In reality, a large number of elements makes the point of first contact difficult to distinguish

compliance of this element and the extent to which the crack tip is shielded from the driving force below the opening load (point 2 to point 3). At high opening loads, this contribution below K -opening cannot be ignored. In reality, a large number of elements makes the point of first contact difficult to distinguish on a standard load-displacement trace (*Figure 1b*). However, it is the compliance and distribution of the bulk shielding mechanism in the wake of the crack, and how this affects the cyclic strain immediately in front of the crack, that counts. In fact, it will be shown that ΔK effective can be determined without any direct measurement of the opening load.

To illustrate this point, a 2219-T851 aluminum alloy was tested to obtain low R data (ΔK applied and ΔK effective, 2% offset) and high R data (*Figure 2*). Despite a good correlation between closure-free data (ΔK applied, K_{max} of 11.0 MPa \sqrt{m} (10.0 ksi \sqrt{in})) and ΔK effective data using the ASTM 2% offset method, the lack of correlation in the near-threshold regime is astonishing. This is unexpected behavior since the ΔK effective data have a lower threshold than the high R data. Depending on the influence of K_{max} , the near-threshold ΔK effective data should have either the same or a higher value of threshold than the high R data. A crack tip strain contribution below the opening load could be responsible for this observation.

To test this concept, the same material was retested at a constant K_{max} of 3.3 MPa \sqrt{m} (3.0 ksi \sqrt{in}) and a stress ratio of 0.1. These constant K steady-state data compare well with data previously generated using decreasing K techniques as shown in *Figure 2*. Two miniature strain gages (0.38 mm \times 0.38 mm (0.015 in \times 0.015 in)) were then mounted (one on each surface)

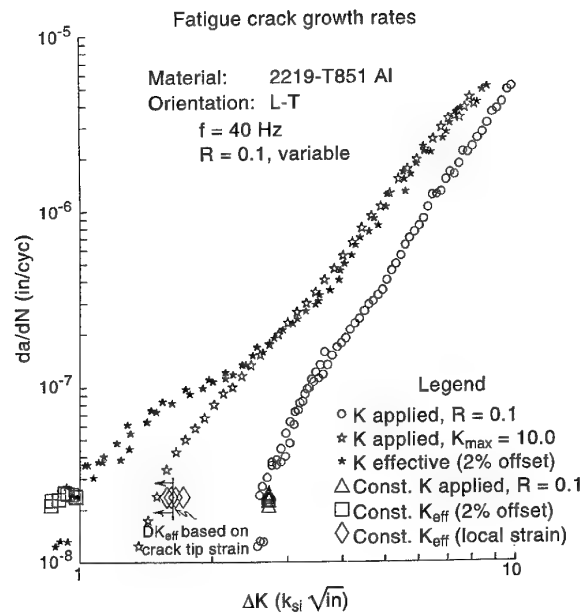


Figure 2 Crack growth rate response showing ΔK applied data at a stress ratio of 0.1, ΔK applied data at a K_{max} of 10 ksi \sqrt{in} and ΔK effective data based on the compliance offset method and the local strain compliance ratio method

directly in the path of the crack. Several load vs strain plots were made as the crack grew up to and through the gages. One of these plots is shown in *Figure 3*. As might be expected, the loading and unloading traces are identical, demonstrating that the cyclic plastic zone is too small to detect with strain gages at the crack tip. Therefore, plane-strain conditions prevail: the non-linearity is elastic in behavior and is strictly the result of crack tip shielding (crack closure). K -opening measurements based on a deviation from linearity of the load-displacement curve ignore Δ strain contributions below K -opening caused by the compliance of the crack closure mechanism. However, the crack driving force should be proportional to the crack tip strain field magnitude, not to the point of deviation in lin-

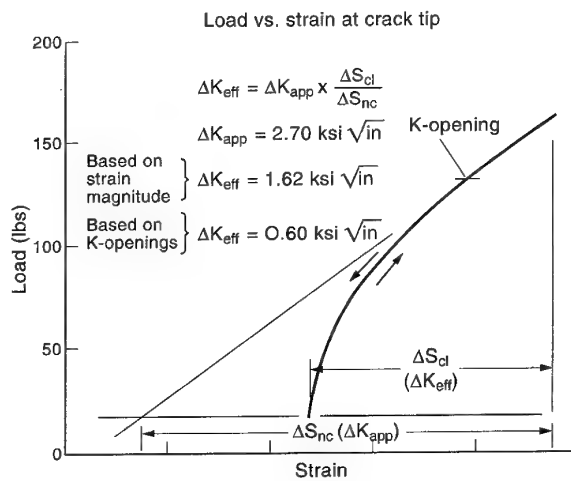


Figure 3 Plot of applied load vs local strain illustrating the compliance ratio technique for determining ΔK effective

earity between local strain and applied load. How, then, can ΔK effective be measured? A simple way of accomplishing this is illustrated in *Figure 3*. The calculation of the effective stress intensity is based on the ratio of the measured strain magnitude (ΔS_{cl}) to that which would have occurred in the absence of closure (ΔS_{nc}). This ratio is then multiplied by ΔK applied to determine ΔK effective and is referred to as the 'compliance ratio' technique.

Figure 4 illustrates the same calculation of ΔK effective based on the ratio of the secant compliance (C_s) divided by the compliance above the opening load (C_o) as follows:

$$CR = \frac{C_s}{C_o} \quad (1)$$

where CR = compliance ratio; $C_s = V_s/P$ (inverse slope of secant drawn between minimum load-displacement and maximum load-displacement); $C_o = V_o/P$ (inverse slope of load-displacement above opening load).

The constant ΔK effective data using both the local strain measurements and the 'compliance ratio' technique also appear in *Figure 2* and show excellent agreement with closure-free data at a high stress ratio ($R \approx 0.85$). Local strain measurements are not the only solution to meaningful crack closure measurements, particularly since they are not practical for most fatigue crack growth applications. Instead, the interpretation of load-displacement curves using remote measurements should be re-examined. Correct application of the 'compliance ratio' technique using remote compliance measurements (no direct measurement of crack tip strain) is suggested below.

ADJUSTED COMPLIANCE RATIO TECHNIQUE

Based on the above observations, it was decided to pursue an experimental technique with the following objectives.

1. To develop a crack closure measurement technique that accounts for the contribution to the cyclic stress intensity below the opening load.

2. To achieve the above objective without the direct measurement of the local crack tip strain.
3. To develop a method that does not require an arbitrary definition (such as a 2% offset).
4. To develop a method that is independent of gage location, specimen geometry, crack length, stress intensity and material.
5. To verify results with closure-free crack growth rate data at higher stress ratios recognizing the influence of K_{max} .

The 'adjusted compliance ratio' (ACR) is determined by subtracting the compliance prior to the initiation of a crack (C_i) from both the secant compliance (C_s) and the compliance above the opening load (C_o) as follows:

$$ACR = \frac{C_s - C_i}{C_o - C_i} \quad (2)$$

where ACR = adjusted compliance ratio; $C_i = V_i/P_i$ (inverse slope of load-displacement prior to initiation of a crack).

This results in a compliance that is due solely to the presence of the crack. The resulting ratio appears to be independent of measurement location and can be used to directly calculate the effective cyclic stress intensity. It is this ratio that accounts for the bulk shielding mechanism in the wake of the crack and how this affects the cyclic strain field immediately in front of the crack. The ACR may be normalized (ACR_n) to account for a bias in the secant compliance (C_s) or slope compliance (C_o) measurement due to noise or nonlinearity as follows:

$$ACR_n = \frac{C_{oi}}{C_{si}} \cdot \frac{C_s - C_i}{C_o - C_i} \quad (3)$$

where ACR_n = normalized adjusted compliance ratio; $C_{oi} = V_{oi}/P_{oi}$ (inverse slope of load-displacement above opening load prior to initiation of a crack); $C_{si} = V_{si}/P_{si}$ (inverse slope of secant drawn between minimum load-displacement and maximum load-displacement prior to initiation of a crack).

Finally, the effective stress intensity may be determined directly by multiplying the applied stress intensity by ACR_n :

$$\Delta K_{eff} = ACR_n \cdot \Delta K_{app} \quad (4)$$

where ΔK_{eff} = effective stress intensity; ΔK_{app} = applied stress intensity.

To evaluate this proposed method, a standard compact tension specimen as shown in *Figure 5* was machined from 2024-T351 aluminum plate. Two clip gage locations (G1 and G2) were used to demonstrate the gage location dependency of the various techniques. The first test consisted of generating fatigue crack growth rate data and periodic closure measurements at a constant ΔK of 5.9 MPa/m (5.4 ksi/in) and a stress ratio of 0.1. A frequency of 30 Hz was selected for the fatigue crack growth data with 2 Hz selected for the closure measurements. For each clip gage location, closure measurements and the corresponding determination of the effective stress intensity were based on the ASTM 2% offset method, the compliance ratio method and the adjusted compliance ratio method. The second test on the same sample consisted of a series of constant K_{max} , decreasing ΔK tests at stress ratios

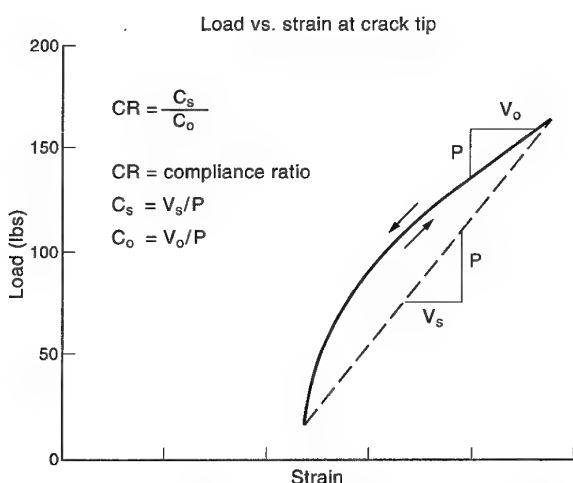


Figure 4 Plot of applied load vs local strain illustrating an alternative representation of the compliance ratio technique

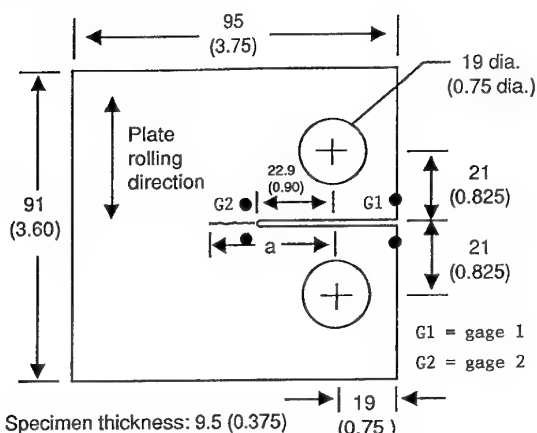


Figure 5 Diagram of compact tension specimen showing two clip gage locations (G1 and G2). Dimensions in millimeters (inches)

above observable closure levels to verify the proposed technique with closure-free crack growth data. Figure 6 shows the crack growth rate response of the constant ΔK segment followed by the series of constant K_{\max} segments as a function of crack length.

Figure 7 shows the effect of the three types of closure measurement techniques using two different displacement measurement locations. For a direct comparison of techniques, the K -opening values determined from the ASTM 2% offset method were converted to the equivalent ΔK effective factors. The compliance ratio and adjusted compliance ratio do not require conversion. As expected, the 'compliance offset' method shows strong sensitivity to measurement location and crack length. The 'compliance ratio' method also shows measurement location and crack length sensitivity, which is expected since the technique is intended only for local crack tip strain measurements. However, when the uncracked compliance is subtracted from the measurement, the resulting factor is inde-

pendent of the measurement location and somewhat independent of the crack length.

To see if the ΔK effectively determined by the 'adjusted compliance ratio' method makes sense, average values of the various methods are also shown in Figure 7 and compared with predictions based on closure-free crack growth rate data at higher stress ratios. A straight line fit of the constant ΔK data at a stress ratio of 0.1 (test 1) reveals an average crack growth rate of $5.217 \times 10^{-6} \text{ mm cycle}^{-1}$ ($2.054 \times 10^{-7} \text{ in cycle}^{-1}$). A straight line fit of the closure-free higher stress ratio data (test 2) is used to determine ΔK applied at growth rates equivalent to test 1. This procedure is repeated at four different values of K_{\max} and plotted in Figure 8. The effect of K_{\max} in the absence of closure is clearly indicated. It is also clear that extrapolation of closure-free data at a higher stress ratio gives the best agreement with the 'adjusted compliance ratio' technique at equivalent growth rates. However, more data are required to determine if these observations are statistically significant.

STATUS OF RESEARCH EFFORT

In cooperation with the Alcoa Technical Center, suggestions for further research have been identified and are currently in progress. Test software has been modified to handle more than one clip gage simultaneously. This will improve the data collection process and will allow continuous data acquisition without test interruptions. All crack closure measurements will be made using both clip gage locations and both the 'compliance offset' and 'compliance ratio' methods without stopping the test.

A full evaluation of the procedure is planned using the results of testing samples of 2324, 7055 and 6013 series aluminum plate using both the compact tension, $C(T)$, and center crack tension, $M(T)$, specimen geometry. In all cases, a comparison with the current ASTM method will be provided. The test methodology will include closure-free crack growth data at higher stress ratios on the same sample to verify the technique. The emphasis will be on near-threshold crack growth rate behavior under predominantly plane-strain conditions. It is important to determine the degree to which the technique is independent of crack length, closure mechanism, specimen geometry and material. It is hoped that improvements in the measurement procedure will lead to a better understanding of the role of K_{\max} in the near-threshold process.

SUMMARY AND CONCLUSIONS

The advantages of the 'adjusted compliance ratio' method are as follows.

1. The technique does not require an estimate of the opening load.
2. The measurement is independent of gage location and somewhat independent of crack length.
3. It is anticipated that the technique is independent of the closure mechanism, specimen geometry and material.
4. Scatter is reduced to acceptable levels.
5. The technique is fundamentally sound since it accounts for the cyclic stress intensity below the opening load.

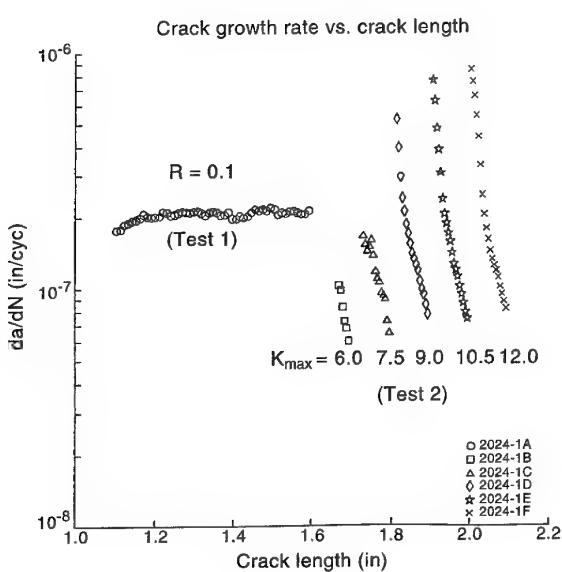


Figure 6 Crack growth rate response of constant ΔK segment (test 1) followed by a series of constant K_{\max} , decreasing ΔK tests (test 2)

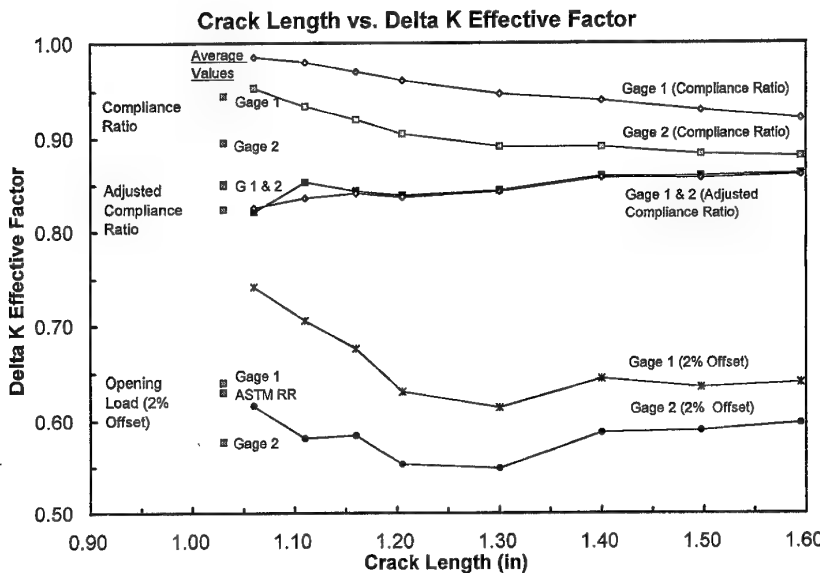


Figure 7 Three types of closure measurement techniques displayed using two different measurement locations

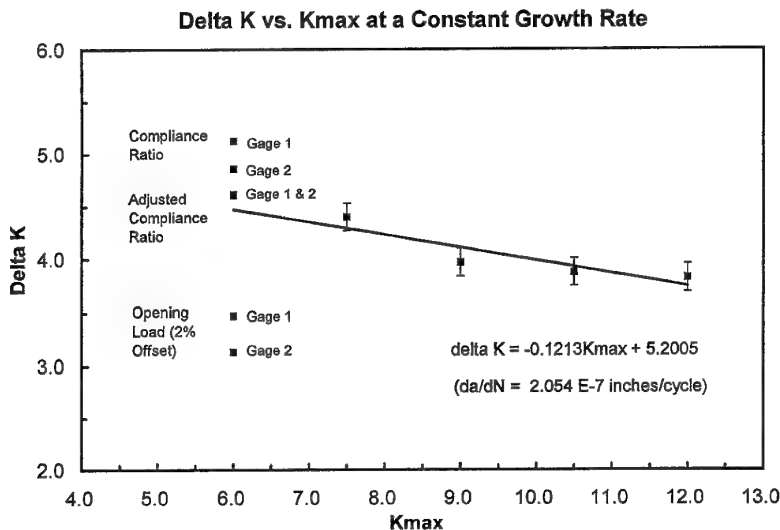


Figure 8 Plot of closure-free data as a function of K_{\max} at equivalent growth rates. Extrapolation of data gives best agreement with 'adjusted compliance ratio' technique

Although this appears to be a promising concept, much remains to be done. Obviously instrumentation noise, sensitivity and linearity are important issues. It is likely that the technique is not entirely independent of crack length, so this effect needs to be investigated as well. The work in progress mentioned in the STATUS OF RESEARCH EFFORT section should provide additional insight.

REFERENCES

- 1 Elber, W., ASTM STP-486. American Society of Testing and Materials, Philadelphia, PA, 1970, p. 230.
- 2 Hertzberg, R. W., Newton, C. H. and Jaccard, R., Crack closure: correlation and confusion. In *Mechanics of Fatigue Crack Closure*, ASTM 982. American Society for Testing and Materials, Philadelphia, PA, 1988, pp. 139-148.
- 3 Phillips, E. P., Results of the round robin on opening-load measurement. NASA Technical Memorandum 101601, Langley Research Center, Hampton, VA, 1989.
- 4 Phillips, E. P., Results of the second round robin on opening-load measurement. NASA Technical Memorandum 109032, Langley Research Center, Hampton, VA, 1993.
- 5 Sadananda, K. and Vasudevan, A. K. *Analysis of Fatigue Crack Closure and Thresholds*, ASTM STP-1220. American Society of Testing and Materials, Philadelphia, PA, 1995.
- 6 Sadananda, K. and Vasudevan, A. K. *Short Crack Growth Behavior*, ASTM STP-1296. American Society of Testing and Materials, Philadelphia, PA, 1996.
- 7 Chen, D. L., Weiss, B. and Stickler, R., Contribution of the cyclic loading portion below the opening load to fatigue crack growth. *Materials Science and Engineering A*, 1996, **208**, 181-187.
- 8 Donald, J. K., A procedure for standardizing crack closure levels. In *Mechanics of Fatigue Crack Closure*, ASTM 982. American Society for Testing and Materials, Philadelphia, PA, 1988, pp. 222-229.



PII: S0142-1123(97)00017-0

Fatigue crack growth from stage I to stage II in a corrosive environment

Ryuichi Hamano

National Research Institute for Metals, Tsukuba-shi, 1-2-1, Sengen, Ibaraki-ken 305,
Japan

How a corrosive environment such as a 3.5% NaCl aqueous solution would affect the transition of fatigue crack initiation mode from stage I (shear mode) cracking to stage II (normal mode) cracking was investigated, using notched specimens of HT80 and SNCM439 steels (corresponding to AISI 4340 steel).

The experimental result that the transition of fatigue crack growth from stage I to stage II was accelerated in a hydrogen-related environment was discussed in terms of hydrogen induced dislocation multiplication near a crack tip. The microstructures immune to environmental damage were examined, using a precipitate-hardened steel. © 1998. Published by Elsevier Science Ltd. All rights reserved

(Keywords: stage I and II fatigue crack; corrosion fatigue life; hydrogen-related environment; iron-based alloys)

INTRODUCTION

To improve the resistance to corrosion fatigue cracking in stage I and near a stress intensity factor of a threshold sensitive to microstructures, we must clarify the mechanisms of corrosive environment assistance of fatigue damage in processes such as cyclic deformation and microstructure-sensitive crack initiation with early growth.

A fatigue crack is nucleated along the persistent slip bands (PSBs)¹, persistent Luders bands (PLBs)², or grain boundaries where slip bands impinge. The nucleated fatigue crack propagates over two successive stages – stage I (shear mode) and stage II (normal mode).

The transition of the fatigue crack growth from stage I to stage II has been investigated in monocrystals and polycrystals as a function of strain amplitude³, crystallographic orientation^{4,5}, slip behavior such as planar or wavy slip deformation^{6,7}, and grain boundaries⁸. The crack in stage I fatigue continues to grow along a primary slip plane⁹. Further growth of the crack activates several slip systems ahead of the crack by turbulent deformation or impedance of grain boundaries⁸. The crack deviates from the primary slip plane and grows perpendicular to the stress axis. Then, the secondary slip plays an important part in the transition of the fatigue crack growth from stage I to stage II¹⁰⁻¹². The past data on the effect of environment on crack growth in the stage II fatigue region have been summarized in a previous work¹³. Meanwhile, little attention has been paid to the effect of hydrogen-related environments on stage I crack propagation and the transition of crack growth from stage I to stage II.

The present work was also concerned with determining the crystallography of cyclic deformation of iron single crystals in air and in a 3.5% NaCl aqueous solution. The experiment is to make sure how cyclic deformation in a corrosive environment is associated with the earlier transition of fatigue crack growth from stage I to stage II.

EXPERIMENTAL PROCEDURES

Transition of fatigue crack growth from stage I to stage II

Commercially produced HT80 and SNCM439 steels were used in the study. The chemical compositions of the materials are as follows (in wt%). HT80: C – 0.11, Ni – 0.77, Cr – 0.68, Mo – 0.44, Mn – 1.01, Si – 0.19, P, S < 0.003, and balance Fe; SNCM439: C – 0.39, Ni – 1.78, Cr – 0.81, Mo – 0.26, Mn – 0.71, Si – 0.25, P, S < 0.003, and balance Fe. SNCM439 steels were austenitized for 3.6 ks at 1473 K, oil quenched, and tempered for 13.2 ks at 753 K, followed by machining. HT80 specimens were machined from as-received plates. The grain sizes of the HT80 and SNCM439 steels were 30.6 and 294.0 μm, respectively. The values of tensile strength of the HT80 and SNCM439 steels were 852 and 1264 MPa, respectively. Sheet test specimens (length 200.0 mm, width 50.0 mm, thickness 5.0 mm) were machined. A 12.5 mm deep U notch with a root radius of 0.65 mm was spark-machined in each specimen. The U notched specimens were electrolytically polished in a chilled solution of 90 vol% acetic acid and 10 vol% perchloric acid.

Fatigue tests were performed on a closed loop ser-

servohydraulic machine, using a sinusoidal wave and a load ratio of 0.1. The cyclic loads were set up to produce a crack extension of about 2.0 mm from the notch root after about 10^5 cycles. The details of test conditions are given in *Table 1*. The testing temperature was 295 ± 1 K. A frequency of 15 Hz in laboratory air with a relative humidity of about 50%, and a frequency of 1 Hz in a 3.5% NaCl aqueous solution, were employed. A cathodic potential of -1.2 V against a silver-silver chloride reference electrode (saturated with KCl), which is converted to -0.98 V against the standard hydrogen electrode, was applied with a potentiostat. The specimens were immersed for 86.4 ks in a 3.5% NaCl aqueous solution at the cathodic potential, before loading. The values of free corrosion potential for the HT80 and SNCM439 steels were -413 and -405 mV, respectively.

The early hydrogen-related transition of fatigue crack growth from stage I to stage II is considered to be dependent on hydrogen charging methods. Two types of hydrogen charging were carried out with a galvanostat. (1) Specimens were precharged with hydrogen for 86.4 ks at a cathodic current density of 22 A m^{-2} and fatigue tests were carried out in air after completion of precharging. At a cathodic current density of 22 A m^{-2} , no blistering occurred after charging. (2) Specimens were fatigued in a 3.5% NaCl aqueous solution at a cathodic current density of 22 A m^{-2} after completion of precharging for 86.4 ks at a cathodic current density of 22 A m^{-2} . Fatigue tests were performed with a load amplitude of 350 MPa. The other fatigue test conditions were the same as mentioned above. After fatigue tests, fatigue cracks were observed with a scanning electron microscope (SEM).

Single crystal experiment

The specimens of gauge section 2.0 mm in thickness \times 4.0 mm in width \times 6.0 mm in length, oriented for two-fold slip deformation, were cut from a sheet of single crystals of iron. The axis of the specimen was close to [013]. The chemical composition of the as-grown crystal (in wt%) is: C, O, P, S < 0.002, Ni, Cu < 0.005, Si, Mn < 0.002, and balance Fe. After mechanical polishing with emery papers, the surface of the gauge section 6 mm in length was electrolytically polished by 50 μm in a chilled solution of 90 vol% acetic acid and 10 vol% perchloric acid. A closed loop servohydraulic machine was used under grip distance control. The grip distance was measured by a Shimazu differential transformer. The total strain means the relative displacement of the grips divided by the gauge length of the specimen. Fatigue tests were carried out in air and in a 3.5% NaCl aqueous solution at a

cathodic potential of -1.1 V against Ag/AgCl reference electrode (saturated with KCl) at 295 ± 1 K, using a sinusoidal wave with a frequency of 1 Hz, a load ratio of -1 , and a total strain of 5×10^{-3} . Specimens were immersed for 86.4 ks at a cathodic potential of -1.1 V against Ag/AgCl without applied load, before being fatigued in a 3.5% NaCl aqueous solution. After being cycled to 130, the slip band configuration was observed with a Carl Zeiss interference optical microscope.

EXPERIMENTAL RESULTS

Transition of fatigue crack growth from stage I to stage II

Figures 1a and 1b show the fatigue crack initiation of the SNCM439 steel in air on the plane at a depth of about half the thickness of the specimen¹⁴. The fatigue crack initiated at the notch root and grew in a direction of 45° to the applied load axis. Upon further growth, the crack branched into two cracks with one branch eventually ceasing and the second inclined normally to the applied load direction. *Figure 1b* shows the characteristic slip line field for a circular notch. The slip lines of α (defined as slip lines having an acute angle against the load axis in the clockwise direction) and β are logarithmic spirals and represent the directions of maximum shear stress and of pure shear strain in the plastic zone near a circular notch¹⁶. Comparing *Figure 1a* with *Figure 1b* shows that the fatigue crack was initiated at the notch surface and propagated in stage I along the traces of the characteristic slip lines until it reached a distance of about one grain size inward from the notch root surface. As the crack grew longer, it deviated from the characteristic slip lines, resulting in the transition to stage II cracking roughly normal to the applied stress axis.

The fracture surface of the SNCM439 steel is shown in *Figure 2*. *Figure 2b* shows etch pits corresponding to ridge patterns on the fracture surface of *Figure 2a*. *Figure 2c* shows schematically the etch pit as a six-sided angular figure based on the proposition that the (011) slip plane and $\langle 111 \rangle$ slip direction are parallel to the crack plane in the stage I region. In stage I fatigue, the fracture surface showed ridge patterns. The presence of these fine ridge patterns was consistent with the observation of Otsuka *et al.*¹⁷ on the fatigue crack initiation of the polycrystalline mild steel in air, where the direction of the parallel lines (ridges) in the shear mode fatigue crack coincided with the slip direction of $\langle 111 \rangle$ in b.c.c. iron. In the present paper, the fatigue crack which initiated on the activated slip

Table 1 Fatigue test conditions for SEM observations

	Laboratory air			3.5% NaCl solution		
	Stress amplitude (MPa)	Number of cycles	Crack length (mm)	Stress amplitude (MPa)	Number of cycles	Crack length (mm)
HT80	59.2*	12.2×10^4	2.65	47.7	7.1×10^4	2.40
SNCM439	103.8†	9.2×10^4	2.00	52.5	3.4×10^4	1.68

*[,] † Given as fatigue limits divided by an elastic stress concentration factor of 5.3¹⁵ of the present specimen. Fatigue limits for HT80 and SNCM439 steels are 314 and 550 MPa, respectively.

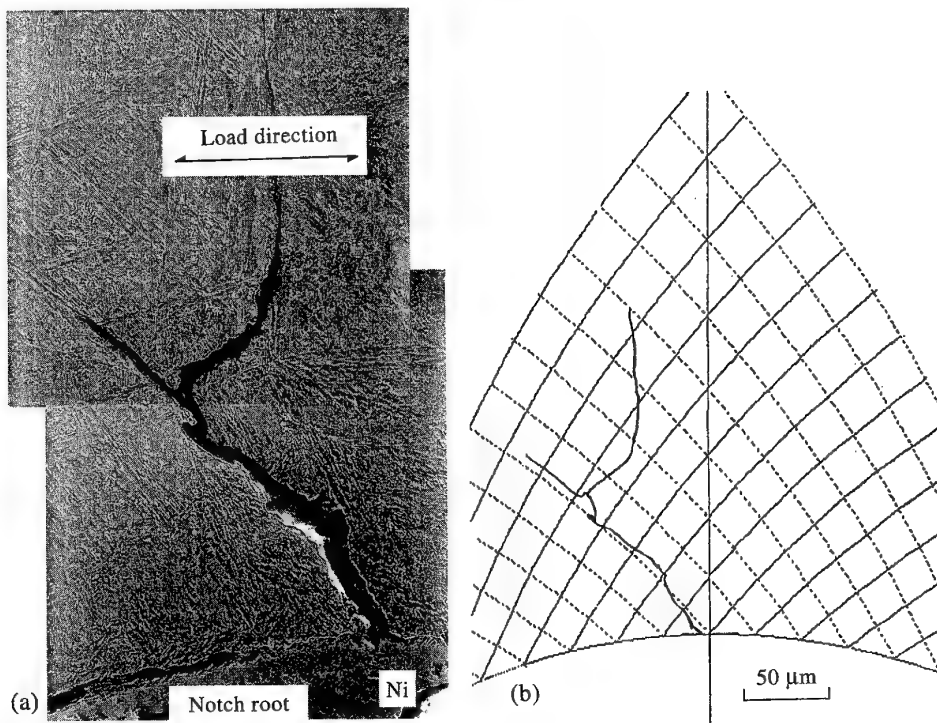


Figure 1 Scanning electron micrograph showing the fatigue crack growth on the plane at a depth of about half the thickness of SNCM439 steel specimen tested in laboratory air (a) and characteristic slip line fields for a circular notch (b). The dotted and real lines of (b) are the slip lines of α and β , respectively

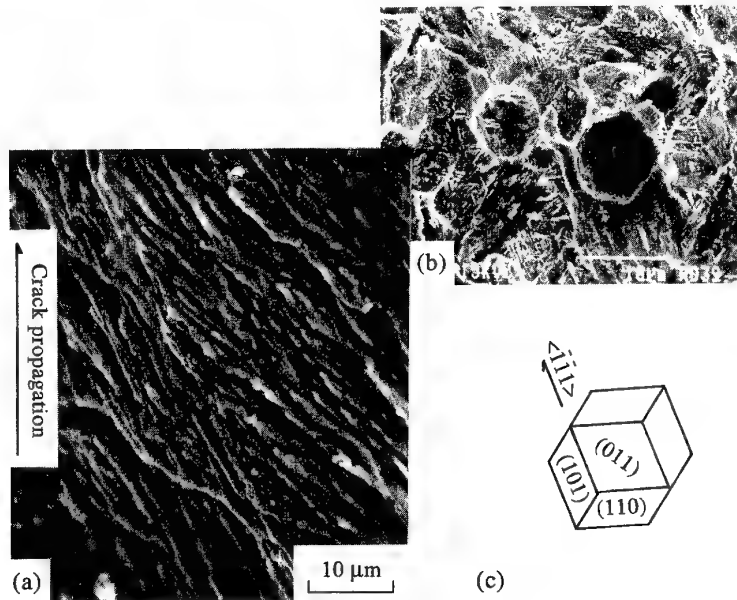


Figure 2 Scanning electron micrograph showing (a) the fracture surface in stage I cracking of the fatigue specimen of SNCM439 steel tested in laboratory air, (b) etch pitting figure, and (c) the schematic diagram consisting of (011) planes in the stage I fracture region near the notch root

planes with slip direction $\langle 111 \rangle$ was observed macroscopically to grow along the characteristic slip line.

Figures 3a and 3b show the fatigue crack initiation of the SNCM439 steel in a 3.5% NaCl aqueous solution on the plane at a depth of about half the thickness of the specimen. Figure 3b shows the fatigue crack of Figure 3a superimposed on the characteristic slip line field. Figures 2 and 3 show that the fatigue crack

initiation and subsequent earlier crack growth of the specimen in a 3.5% NaCl aqueous solution differed from specimens tested in air in the earlier transition of the crack propagation stage from shear mode to normal mode fatigue.

The fracture surface of transgranular cracking of the SNCM439 steel in a 3.5% aqueous solution is shown in Figure 4. The linear marks on the fracture surface

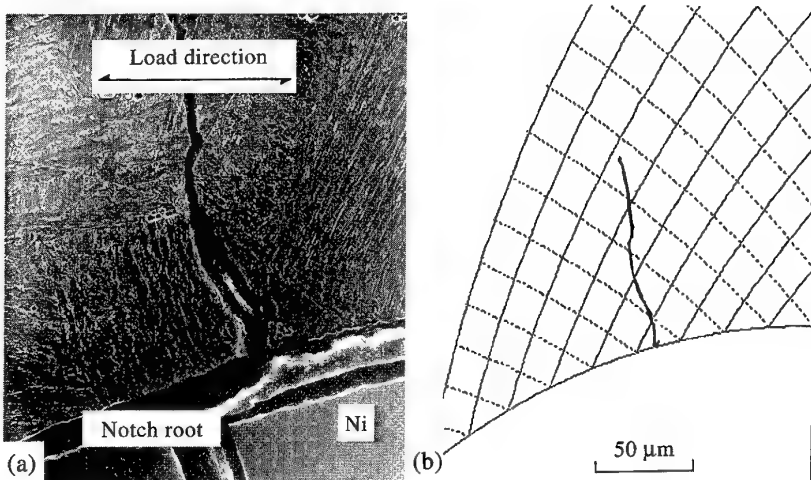


Figure 3 Scanning electron micrograph showing the fatigue crack growth on the plane at a depth of about half the thickness of SNCM439 steel specimen tested in a 3.5% NaCl aqueous solution (a) and characteristic slip line fields for a circular notch (b). The dotted and real lines of (b) are the slip lines of α and β , respectively

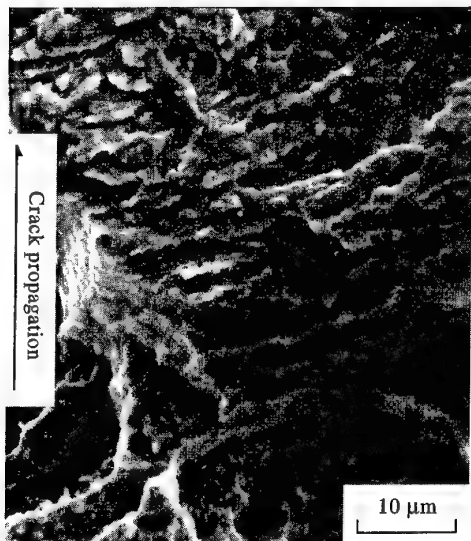


Figure 4 Scanning electron micrograph showing the fatigue fracture surface of SNCM439 steel near the notch root, tested in a 3.5% NaCl aqueous solution

which characterize stage I crack growth did not exist and the striations which characterize the fracture surface of stage II were observed. The fatigue crack in the SNCM439 steel in a 3.5% NaCl aqueous solution was initiated and grew normally to the applied stress axis.

The fracture surfaces of the HT80 steel on the planes at a depth of about half the thickness of the specimens in air and in a 3.5% NaCl aqueous solution are shown in *Figure 5*. The crack length in stage I fatigue in a 3.5% NaCl aqueous solution was obviously shorter than that in air and less than the mean grain size. *Table 2* shows the length of stage I crack from the notch root on the planes at various depths of specimens tested in air and a 3.5% NaCl aqueous solution for the HT80 and SNCM439 steels. As shown in *Table 2*, the crack length in the stage I fatigue region in a

3.5% NaCl aqueous solution was less than the mean grain size.

Figures 6a and 6b show the fatigue crack initiation of the SNCM439 steel charged with hydrogen by two methods. *Figure 6a* shows that the fatigue cracking of the specimen, which was precharged and dynamically charged, initiated at the notch root and grew normally to the applied load direction. *Figure 6b* shows that the fatigue crack of the specimen, which was precharged and fatigued in air, initiated at the notch root and grew in a direction of 45° to the applied load axis. Hence, the early transition of fatigue crack propagation to stage II fracture for the dynamically charged specimen is related to the sensitivity of the specimen to hydrogen-related embrittlement in fatigue cracking.

Figure 7 shows the fracture surface near the notch root of the fatigue specimen of the SNCM439 steel, precharged for 86.4 ks at a cathodic current density of 22 A m^{-2} and fatigue tested in laboratory air. The linear marks (ridge patterns) on the fracture surface characterize stage I fatigue like the above-mentioned specimen in air tests (*Figure 2a*). The direction of the linear marks in a stage I fatigue crack coincides with the slip direction of $\langle 111 \rangle$ in b.c.c. iron (*Figure 2a*).

Single crystal behavior

Figure 8 shows the interference optical microscopy of slip band configuration on the surface of $(0\bar{3}1)$. After 130 cycles in air, the slip planes of (101) and $(\bar{1}01)$ appeared on the surface. The surface in a 3.5% NaCl aqueous solution was smooth. Fine slip lines were observed. It is suggested that hydrogen-related environments affect the dislocation distribution of single crystal iron. The present result seems to correspond with the observation of highly dense dislocations of hydrogen-charged Fe-3.5% Si single crystals¹⁸.

DISCUSSION

When fatigued in a 3.5% NaCl aqueous solution, the earlier transition of fatigue crack growth from stage I to stage II took place, compared with being fatigued

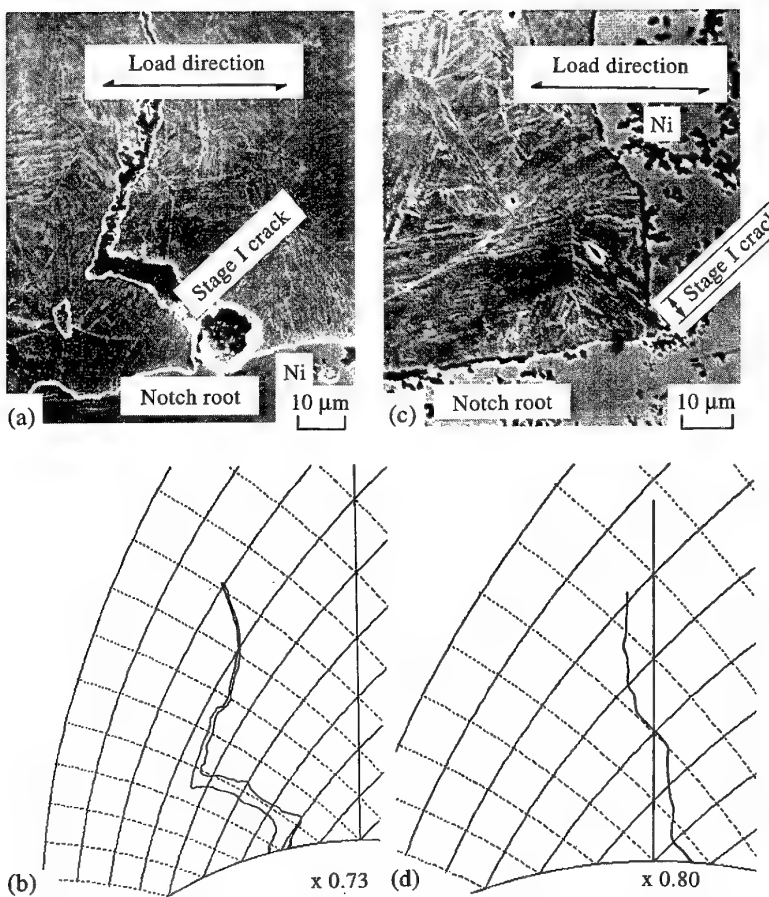


Figure 5 Scanning electron micrograph showing the fatigue crack profile of HT80 steel on the plane at a depth of about half the thickness of the specimen tested in air (a and b) and in a 3.5% NaCl aqueous solution (c and d). (b) and (c) show characteristic slip line fields with the dotted and real lines as the slip lines of α and β , respectively

Table 2 The length of stage I crack from notch root on planes at the depth from top surfaces of specimens tested in air and in a 3.5% NaCl aqueous solution for HT80 and SNCM439 steels

HT80	Depth (mm)	0.2	0.9	2.0
	Crack length (μm)	3.8	12.8	10.4 (56.8*)
SNCM439	Depth (mm)	0.2	0.6	2.0
	Crack length (μm)	0.0	0.0	0.0 (275*)

* Tested in air.

in air. As shown in *Table 2*, the length of shear mode cracking in an aqueous solution was dependent on the materials. In stage I fatigue, the fracture surface ridges were observed. The direction of fracture surface ridges was the same as the [111] direction of the primary slip vector generated by crossing of primary slip and cross slip planes (*Figure 2c*). The crack growth direction on the fracture surface is considered to be microscopically the direction of fracture surface ridges, which are coplanar with the fracture surface. Macroscopically, the stage I fatigue crack initiated at a notch root and grew along the characteristic slip lines having the maximum shear stress and strain. In other words, the stage I fatigue crack initiation and early growth took place on activated slip planes in the primary slip direction which is macroscopically in the planes of the maximum shear strain. As suggested by Koss and Chan¹⁹, coplanar slip band cracking as seen in stage I fatigue cracking creates large normal stress or hydro-

static stress near a crack tip. As pointed out by DeLange *et al.*²⁰, the higher internal normal stress in the shear bands such as PSBs or PLBs could also activate secondary dislocations^{20,21}. Therefore, how the deformation near a crack tip is affected by the presence of hydrogen invading from a corrosive environment during fatigue testing (*Figure 8*) should be considered.

The explanation for the present results being induced by the decohesion mechanism²² seems unlikely for hydrogen-induced embrittlement. The proposal that hydrogen enhanced the localization of plasticity^{23,24} is attractive from slip line traces and fractographic observations in the present study.

When the brittle mechanism is based on hydrogen-assisted, localized plasticity, and the stress required for plastic deformation is locally decreased by the presence of hydrogen, highly localized ductile rupture is probable, and the total macroscopic deformation remains

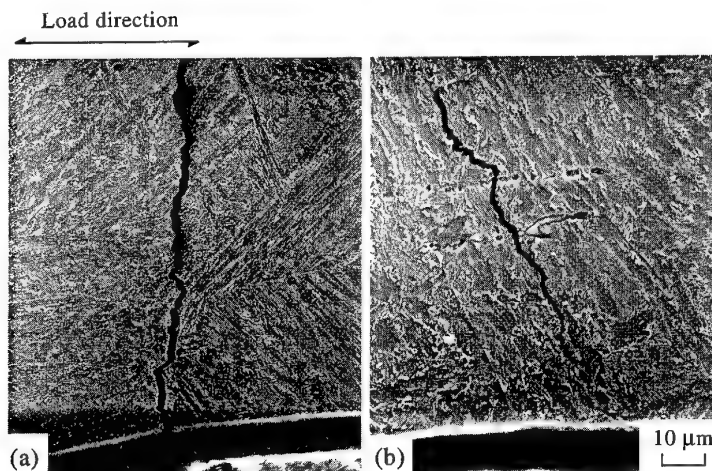


Figure 6 Scanning electron micrograph showing the fatigue crack initiation near the notch root of SNCM439 steel specimen hydrogen-charged in the two modes: (a) precharged for 86.4 ks at a cathodic current density of 22 A m^{-2} and fatigued in air, (b) precharged for 86.4 ks and kept on charging during fatigue test at a cathodic current of 22 A m^{-2}

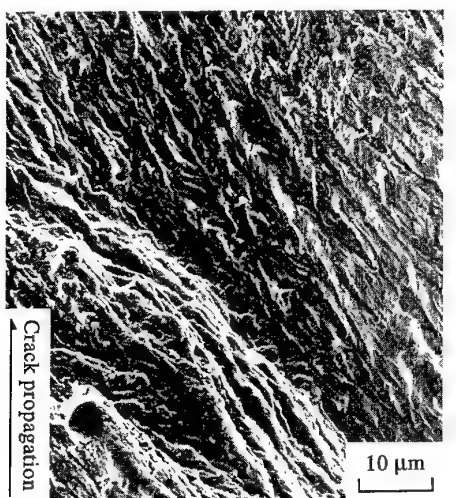


Figure 7 Scanning electron micrograph showing the fracture surface in the stage I fatigue cracking of SNCM439 steel precharged for 86.4 ks at a cathodic current of 22 A m^{-2} tested in laboratory air

small. When such strain localization occurs along primary slip planes and fatigue cracking advances on the primary slip planes, fatigue crack growth leads to premature and accelerated stage I fracture, as pointed out by Dollar *et al.*²⁴ on cyclically deformed CMSX-2 in hydrogen, which differs from the present results.

In the present study, the observation of the earlier transition of fatigue crack growth from stage I to stage II and the appearance of striations on the fracture surfaces in a 3.5% NaCl aqueous solution suggest: (1) the secondary slip plays an important role in the transition of fatigue crack growth; (2) the fatigue crack grows by the operation of more than two slip systems leading to macroscopically brittle (transcrystalline) fractures bisecting the two active slip planes^{25,26}. It seems reasonable to propose that the dominant cause of hydrogen-related fatigue cracking is hydrogen-assisted strain localization ahead of the notch root, creating subsequent crack propagation in more than two slip systems and hence explaining the suppression of stage

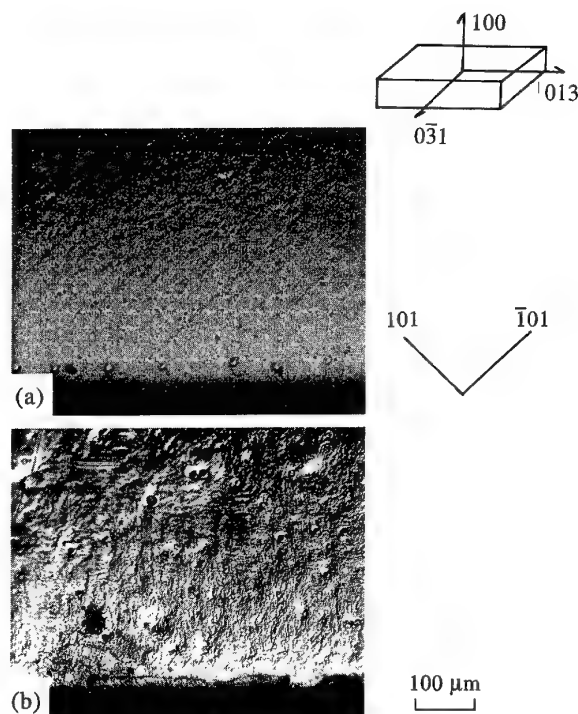


Figure 8 Interference optical micrograph showing the slip band configuration of [013] iron single crystal on (0̄31) surface after 130 cycles with a total strain of 0.5%, (a) in air and (b) in a 3.5% NaCl aqueous solution

I growth. The present results suggest an alternative interpretation. From the point of view of a shorter shear mode crack in a 3.5% NaCl aqueous solution than in laboratory air, and the existence of ridges on the fracture surfaces at the notch root of the SNCM439 steel which was precharged with hydrogen and fatigued in air, it is suggested that the hydrogen diffused to the triaxial stress field at the tip of the fatigue crack induced the earlier transition of fatigue crack growth modes. As described in the previous section, the stage I fatigue crack advanced along the inhomogeneous

shear bands of characteristic slip lines. By restricting the crack growth to the shear band, hydrostatic or normal stress increases along the band and behind the tip of the band¹⁹. The combination of intense shear and large hydrostatic stress accelerates the diffusion of hydrogen to the triaxial stress sites. The triaxial stress state is more enhanced in materials of inhomogeneous deformation¹⁹, as well as in ones of high strength, or large grain size²⁷ during shear mode cracking. Therefore, as mentioned above, it is considered that the hydrogen diffused to inhomogeneous shear bands promotes slip multiplication or fine distribution of dislocations near the inhomogeneous shear band, leading to an earlier transition of cracking from stage I to stage II (*Table 2*). The observation of slip band configuration on the iron single crystal specimen suggests that a hydrogen-related environment affects the dislocation distribution of the specimen (*Figure 8*).

Finally, the reason why the existence of hydrogen occluded in materials changes the distribution of dislocations might be considered to be due to: the decrease of the external stress necessary to operate the dislocation source; anisotropy of the core of edge and screw dislocations¹⁸; and increase of mobility of screw dislocations^{28,29}.

APPLICATION TO THE IMPROVEMENT OF CORROSION FATIGUE LIFE

In this section, microstructures immune to environmental damage were examined using a precipitate-hardened steel, based on the above-mentioned concept.

As described in the previous section, stage I fatigue crack initiated and advanced along the intense shear bands. It is suggested that the triaxial stress field at the tip of the stage I fatigue crack was more enhanced by the materials of inhomogeneous slip deformation. Hydrogen diffused to the triaxial stress field accelerated the transition of fatigue cracking from stage I to stage II, leading to premature failure. To improve the resistance to fatigue cracking of high strength materials in a hydrogen-related environment, it is desirable that the slip deformation of materials is not concentrated in a particular slip band.

Previous work³⁰ showed that high strength steels hardened with coherent precipitates with the matrix have a tendency for inhomogeneous slip deformation. Strain concentration is increased when the coherent precipitates are easily cut by moving dislocations (slip channeling)³¹. Coherent precipitates change to incoherent with the matrix with aging.

The bimodal distribution of the coherent precipitates for strengthening the matrix and incoherent precipitates for preventing slip channeling can be expected to improve fatigue life in a corrosive environment³⁰. Thus, it is necessary to investigate whether or not the introduction of incoherent precipitates into the matrix would be able to improve both the strength and fatigue life of the specimens in a 3.5% NaCl aqueous solution.

The fatigue life experiments were conducted on the precipitate-hardened steels that had nominal chemical compositions (in wt%) of Ni - 5.07, Al - 1.94, Cr - 1.73, Mo - 1.55, Mn - 0.19, C - 0.14, and balance Fe. The test pieces were round bars of 3.5 mm in diameter and 16 mm gauge length. They were melted in a vacuum induction furnace. The heat treatment is

available elsewhere³⁰. They were austenitized at 1373 K for 1.8 ks, water quenched, and then aged at 783 K for 2.4 ks (abbreviated as 1373) or aged at 923 K for 86.4 ks (abbreviated as 923) or aged at 953 K for 86.4 ks accompanied by 783 K aging for 2.4 ks (abbreviated as 953). After aging at 783 K for 2.4 ks, the specimens were hardened due to the precipitation of NiAl or/and M₂C coherent with the matrix (underaged condition). Meanwhile, after aging at 923 or 953 K for 86.4 ks, the precipitates consisted of M₂C and NiAl both of which lost coherency with the matrix (overaged condition). After aging at 953 K for 86.4 ks followed by 783 K for 2.4 ks, the matrix is hardened by the bimodal precipitation of coherent (NiAl) and incoherent precipitates. The room temperature tensile 0.2% offset stress was as follows: 878 MPa for specimen 923, 1011 MPa for specimen 953, 1498 MPa for specimen 1373. Subsequent fatigue tests were carried out at a temperature of 295 ± 1 K, using a sinusoidal wave with a load ratio of 0.1 in air or in a 3.5% NaCl aqueous solution on a closed loop servohydraulic machine. A frequency of 20 Hz in air or 1 Hz in aqueous solution was employed.

The fatigue lives of specimens 1373, 953, and 923 are shown in *Figure 9*. The fatigue lives in air were on the order of 0.2% offset stress at the same number of cycles. In a 3.5% NaCl aqueous solution, the fatigue lives of the three kinds of materials decreased. Specimen 1373 exhibited the worst fatigue.

The three kinds of materials are different in strength. Thus, *Figure 10* shows the fatigue lives obtained from *Figure 9* by normalizing the stress amplitude by half of the 0.2% offset stress. As shown in *Figure 10*, the corrosion fatigue life of specimen 1373 is extremely low. The corrosion fatigue life of specimen 953 is restored to close to that of specimen 923. It is concluded that the coexistence of coherent and incoherent precipitates increases homogeneous deformation, thus improving the resistance to hydrogen-related corrosion fatigue cracking.

CONCLUSIONS

Corrosive fatigue tests were carried out in air and in a 3.5% NaCl aqueous solution at a temperature of 295

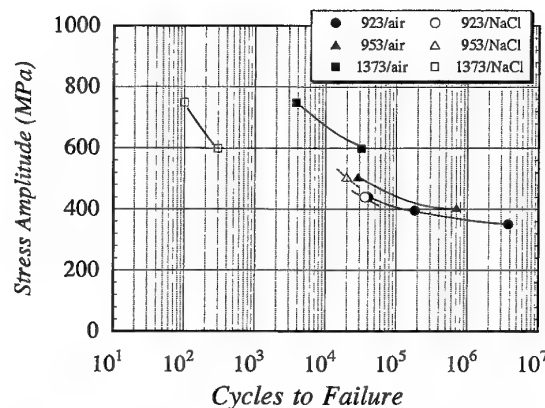


Figure 9 Fatigue lives of specimens 1373, 953 and 923 fatigued in air and in a 3.5% NaCl aqueous solution. The stress amplitude means half the difference between the maximum and minimum stresses

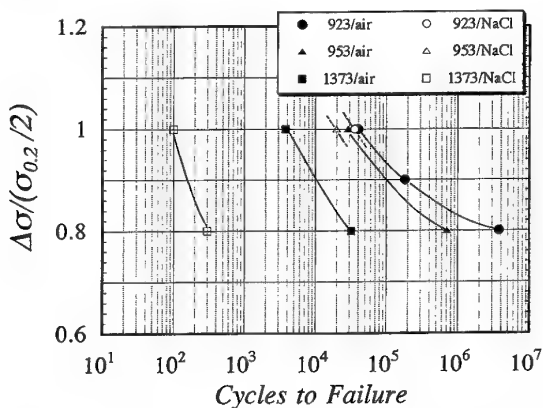


Figure 10 Fatigue lives of specimens 1373, 953 and 923 obtained by plotting *Figure 9* by normalizing the stress amplitude ($\Delta\sigma$) by half of the 0.2% offset stress ($\sigma_{0.2}$)

± 1 K with a load ratio of 0.1 and a sinusoidal wave, using notched specimens of HT80 and SNCM439 (corresponding to AISI 4340) steels. The experimental result was that the transition of fatigue crack growth from stage I to stage II is accelerated in a hydrogen-related environment, discussed in terms of hydrogen-induced dislocation multiplication near a crack tip. Microstructures immune to environmental damage were shown using precipitation-hardened steel.

REFERENCES

- 1 Mughrabi, H., Herz, K. and Stark, X., *International Journal of Fracture*, 1981, **17**, 193–220.
- 2 Hong, S. I. and Laird, C., *Materials Science and Engineering A*, 1990, **128**, 55–75.
- 3 Hong, S. I. and Laird, C., *Metallurgical Transactions*, 1991, **22A**, 415–425.
- 4 Tabata, T., Fujita, H. and Hiraoka, M., *Philosophical Magazine*, 1983, **47**, 841–857.
- 5 Ikeda, S., *Transactions JIM*, 1979, **20**, 235–243.
- 6 Sanders, T. H. and Starke, E. A., *Acta Metallurgica*, 1982, **30**, 927–939.
- 7 Iwatani, T., Katagiri, K. and Koyanagi, K., *Metallurgical Transactions*, 1979, **10A**, 503–507.
- 8 Li, C., *Metallurgical Transactions*, 1992, **23A**, 3293–3301.
- 9 Chan, K. S., Hack, J. E. and Leverant, G. R., *Metallurgical Transactions*, 1987, **18A**, 581–591.
- 10 Li, C. and Bretheau, T., *Acta Metallurgica*, 1989, **37**, 2645–2650.
- 11 Wojcik, J. S., Chan, K. S. and Koss, D. A., *Acta Metallurgica*, 1988, **36**, 1261–1270.
- 12 Chan, K. S. and Leverant, G. R., *Metallurgical Transactions*, 1987, **8A**, 593–602.
- 13 Hamano, R., *Metallurgical Transactions*, 1988, **19A**, 1461–1469.
- 14 Hamano, R., *Metallurgical and Materials Transactions*, 1995, **26A**, 1–6.
- 15 Peterson, R. E. *Stress Concentration Design Factors*. John Wiley, New York, 1965.
- 16 Rice, J. R., *Transactions AIME, Journal of Applied Mechanics*, 1968, **6**, 379–386.
- 17 Otsuka, A., Mori, K. and Kawamura, T., *ZAIRYOU*, 1977, **27**, 49–53.
- 18 Wang, Y. B., Chu, W. Y. and Hsiao, C. M., *Scripta Metallurgica*, 1985, **19**, 1161–1164.
- 19 Koss, D. A. and Chan, K. S., *Acta Metallurgica*, 1980, **28**, 1245–1252.
- 20 De Lange, O. L., Jackson, P. J. and Nathanson, P. D. K., *Acta Metallurgica*, 1980, **28**, 833–839.
- 21 Hong, S. I. and Laird, C., *Fatigue and Fracture of Engineering Materials and Structures*, 1991, **14**, 143–169.
- 22 Oriani, R. A. and Josephic, P. H., *Acta Metallurgica*, 1974, **22**, 1065–1074.
- 23 Robertson, I. M. and Birnbaum, H. K., *Acta Metallurgica*, 1986, **34**, 353–366.
- 24 Dollar, M., Bernstein, I. M., Domnanovich, A., Kromp, W. and Pinkolits, H., *Metallurgical Transactions*, 1991, **22A**, 2597–2603.
- 25 Lynch, S. P., *Acta Metallurgica*, 1988, **36**, 2639–2661.
- 26 Ulmer, D. G. and Altstetter, C. J., *Acta Metallurgica et Materialia*, 1991, **39**, 1237–1248.
- 27 Gray, G. T., Williams, J. C. and Thompson, A. W., *Metallurgical Transactions*, 1983, **14A**, 421–433.
- 28 Tabata, T. and Birnbaum, H. K., *Metallurgical Transactions*, 1984, **18**, 231–236.
- 29 Lynch, S. P. *Fatigue Mechanisms*. STP 675, ASTM, Philadelphia, 1979, pp. 174–213.
- 30 Hamano, R., *Metallurgical Transactions*, 1993, **24A**, 127–139.
- 31 Worhem, D. W., Robertson, I. M., Leckie, F. A., Socie, D. and Altstetter, C., *Metallurgical Transactions*, 1990, **21A**, 3215–3220.

PII: S0142-1123(97)00019-4

Characterization of crack tip and geometry induced closure

W.J. Evans* and **S.H. Spencer†**

*IRC in Materials for High Performance Applications, University of Wales,
Swansea SA2 8PP, UK

†British Aerospace, Warton, Preston, Lancashire, UK

The paper presents a comprehensive series of closure measurements on a coarse grained near alpha titanium alloy. The work at room temperature involved three different monitoring techniques: DCPD, strain gauge and replicas. The information generated on part-through cracks at several stresses and over a range of crack lengths is used to assess the '3D' nature of the closure process. Particular attention is given to the cracked area in contact at each condition and crack peeling on loading. Application of the observations to a notch geometry is discussed. © 1998 Elsevier Science Ltd.

(Keywords: titanium alloy; DCPD technique; replica method; strain gauge measurements; 3D closure relations)

INTRODUCTION

The last 20 years have witnessed significant advances in the measurement and modelling of crack tip closure. This work has identified a number of contributory factors to the closure process, including plastic deformation, surface roughness and environmental debris¹⁻³. The plasticity mechanism, in which both the current crack tip plastic zone and the residual plastic wake from previous crack front positions play a part, has been a dominant consideration. One important observation is that there are significantly larger levels of closure associated with plane stress compared with plane strain loading conditions⁴. Measured values have been used to account for observed discrepancies in crack growth rates, including R value effects, threshold behaviour and differences between geometrically small cracks and much larger or 'long' cracks. It is now well understood that closure effects must be incorporated in component life prediction algorithms if these are to be reliable and efficient in establishing in-service behaviour.

Much of the published work focuses on large, through section crack geometries situated in essentially uniform stress fields. In contrast most cracks of engineering interest have a part-through nature and are usually found in the vicinity of stress concentration features. Furthermore, many of the techniques for experimentally characterising closure are either limited in the sense that they focus on conditions at the surface, such as strain gauge⁵ and *in situ* SEM⁶ measurements, or are destructive, requiring detailed sectioning or hole drilling⁷.

An objective of the present programme was to

explore ways of overcoming these limitations which could then form the basis of a '3D' view of closure. On this basis, particular attention was given to the development of quarter circular and elliptical cracks growing in both uniform and notch stress fields. Closure characterisation involved the collection and amalgamation of data obtained from PD, strain gauge and replica monitoring techniques. Although the principal aim was to evaluate plasticity induced closure, the work was carried out on a coarse grained near alpha titanium alloy so that the relative contributions from plasticity and roughness mechanisms could be assessed. It is anticipated that the measurements obtained will provide support for the progress being made in advanced numerical modelling activities.

EXPERIMENTAL DETAILS

Baseline fatigue crack propagation behaviour was characterised through a standard square section corner crack (CC) testpiece, *Figure 1*. The specimen had a 0.1 mm thick machined starter slit at one edge with a radius of 0.25 mm. The slit allowed quarter circular cracks to develop which then grew to a maximum depth of 4 mm. The CC geometry was subjected to uniform stresses of 450 and 600 MPa. The majority of the tests were conducted at 1 Hz and $R = 0.1$, although a small number were carried out at $R = 0.5$.

Crack development in a non-uniform stress field was evaluated through a specifically designed double edge notch (DEN) design, *Figure 2*. The notch root radius was 3 mm and the reduced cross-section at the notch was 10 mm × 10 mm, which is equivalent in size to the CC testpiece. The resultant elastic stress concentration

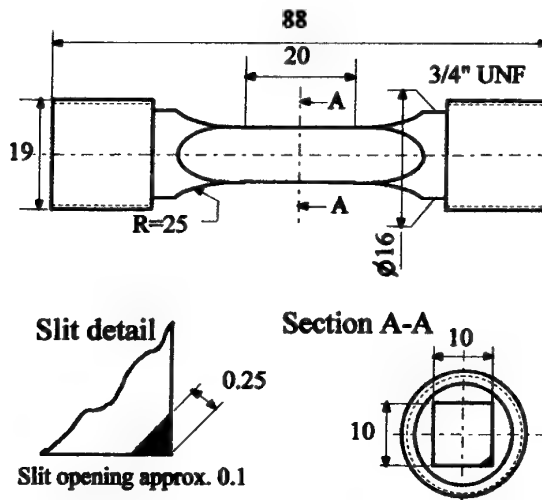


Figure 1 Corner crack testpiece

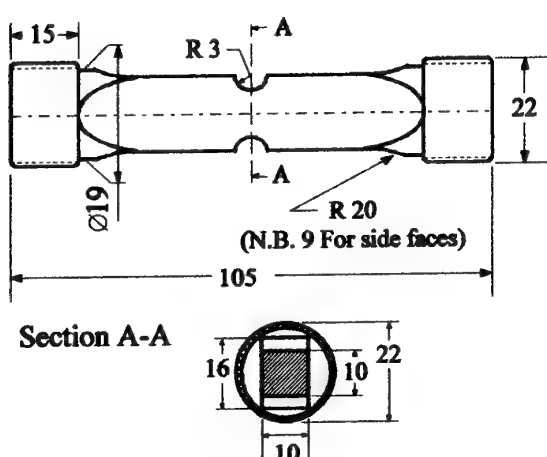


Figure 2 Double edge notch testpiece

factor, K_t , was 1.9 with respect to the net section. The testpiece was given a similar edge starter slit to the CC specimen. The notch programme was carried out at 1 Hz and nominal applied stresses of 350 and 550 MPa.

Crack growth in both CC and DEN specimens was monitored by means of a direct current potential drop (DCPD) system in which the comparatively high current of 30 A was pulsed to minimise any heating effects. The probe wires were attached immediately adjacent to the starter slit in order to enhance the sensitivity and resolution of the measurements, *Figure 3*. The PD equipment was linked via a computer to an optical system that was triggered at appropriate intervals to provide photographic records of surface crack lengths.

Closure measurements were obtained by three different methods. The most comprehensive set of values was obtained from the DCPD technique. They involved the current being applied continuously during selected cycles and the voltage change monitored in terms of the cyclic variation in load. A series of control experiments

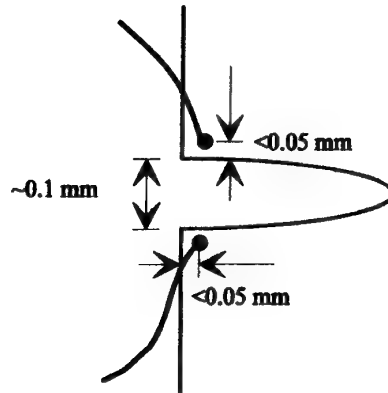


Figure 3 Positions of the DCPD probe wires

confirmed that the longer exposure to the electric current for these measurements did not adversely influence the crack growth response. To facilitate the acquisition of the DCPD closure measurements, a triangular waveform of 100 s duration was applied for the cycle in which data were collected. By its nature, the DCPD technique records information for the area of cross-section of the crack. Replicas on the other hand provide data for the surfaces only. They required the fatigue tests to be interrupted so that the acetate sheets could be applied in the vicinity of the crack tip. Information on closure response in general, and the length of crack closed at a given stress level in particular, was obtained by examining the replicas in an optical microscope. The third method involved small strain gauges. The active gauge size was 0.38 mm and using cyanoacrylate these were bonded to the specimens adjacent to the crack plane and fractionally behind the crack tip. The coarse grained nature of the alloy used for this programme resulted in highly jagged crack paths. Consequently, it was necessary to introduce some prior crack growth before positioning the gauges. *Figure 4* illustrates a typical strain gauge location.

The closure experiments were carried out on a near alpha titanium alloy. The IMI 829 (Ti-5.5Al-3.5Sn-4Zr-2Mo-0.2Mo-0.3Si) has been widely used for high temperature and high toughness applications. For this work, it was heat treated above the beta transus at 1050°C for 30 min before air cooling and ageing at 625°C for 2 h. The microstructure consisted of a mixed basket weave/aligned alpha morphology in a compara-

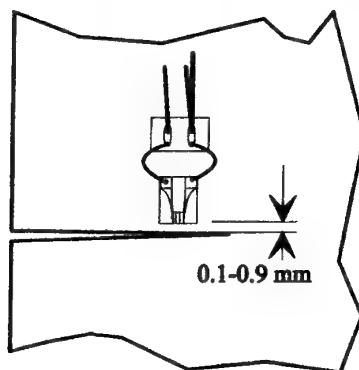


Figure 4 Strain gauge location

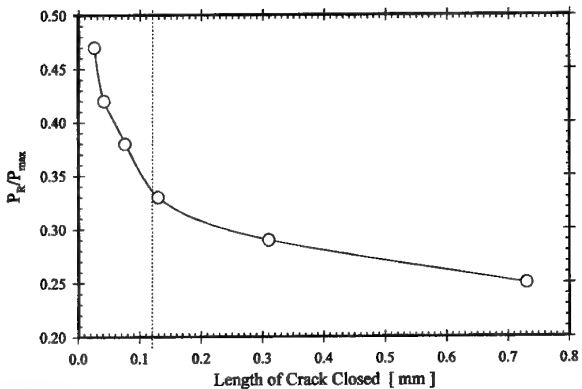


Figure 5 Dependence of crack length closed from replicas on applied load

tively large prior beta large grain size (~ 0.5 mm). This microstructure results in an irregular crack path with an enhanced tendency for roughness induced closure.

DATA ANALYSIS

The results from the surface dominated replica measurements are recorded in *Figure 5*. The graph relates applied load as a fraction of the maximum load (P_R/P_{\max}) to the measured length of crack closed at the same load. The data in *Figure 5* are for a crack with a nominal length of approximately 2 mm. Similar results were obtained for other crack lengths. They are consistent with the SEM stereo-imaging work of Davidson⁶ on an aluminium alloy and, as in that case, the length of the closed crack, d , can be related to (P_R/P_{\max}) by the expression $(P_R/P_{\max}) = 1 - m \log(d + 1)$ with $m = 0.15$ for the data in *Figure 5*.

The variation in measured voltage change, ΔV , with applied load is illustrated for one loading cycle in *Figure 6*. The voltage change $\Delta V = V_P - V_0$ with V_P the voltage at load P and V_0 the voltage at P_{\min} , the minimum load. On increasing the load from P_{\min} the voltage initially varies linearly with P . A comparison with the replica measurements in *Figure 5*, which were made on an equivalent testpiece, suggests that the linear response corresponds to the initial rapid unpeeling of the crack from the outer surface with a consider-

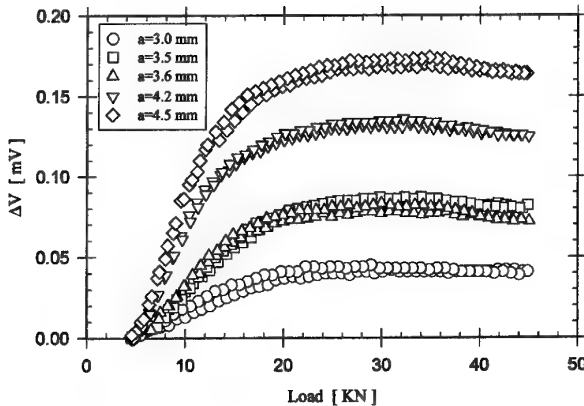


Figure 7 Dependence of voltage change per cycle on crack length

able length opening for a relatively small increase in load. The position P_A is approximately equivalent to a point in the replica data where opening becomes more difficult and the load increases significantly for a comparatively small change in open crack length. The changeover point is represented on the replica graph by a dotted line, *Figure 5*. During the subsequent phase of opening, ΔV varies nonlinearly with load until the upper transition point P_B is attained. P_B is the load at which the crack becomes fully open and, in many cases, ΔV remains virtually constant for further increases in load. In practice, measurement of P_A and P_B can be difficult and imprecise. For this reason, an intercept value P_C is defined for correlation purposes on the basis of the initial and final linear regimes, *Figure 6*. A typical dependence of the ΔV - P relationship on crack length is given in *Figure 7*. It is evident that the change in voltage increases as the cracks become larger, even though the adoption of the ($V_P - V_0$) criterion normalises out any changes in voltage due to crack growth.

The strain gauge approach was intended to characterise variations in local strain behind the crack tip during the opening/closing process. To allow comparison of data for different crack lengths, the strain values were expressed in the form $\Delta\epsilon = \epsilon_P - \epsilon_0$ with ϵ_P the strain at load P and ϵ_0 the strain at P_{\min} . Typical dependences of $\Delta\epsilon$ in microstrain on applied load per cycle and on crack length are shown in *Figure 8* for a gauge situated about 2 mm from the starter slit at which growth

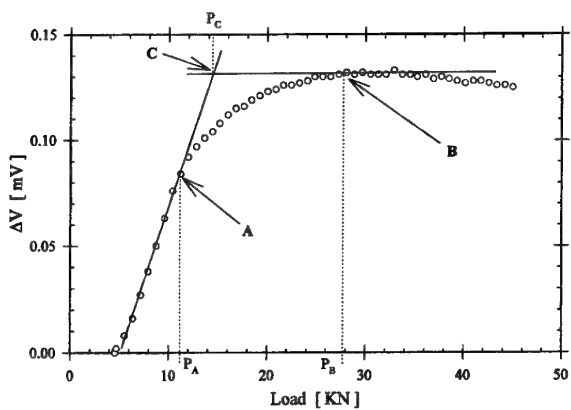


Figure 6 Significant transition loads (P_A , P_B , P_C) for the DCPD closure measurement

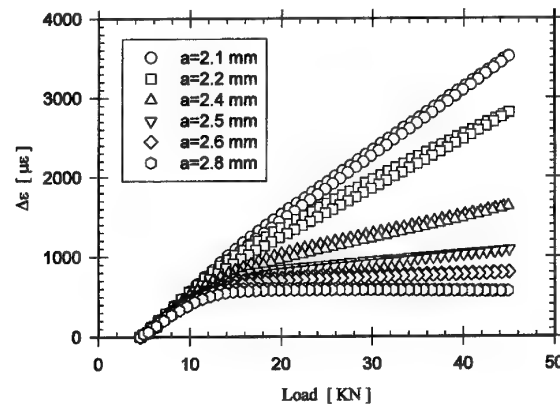


Figure 8 Dependence of microstrain per cycle on crack length

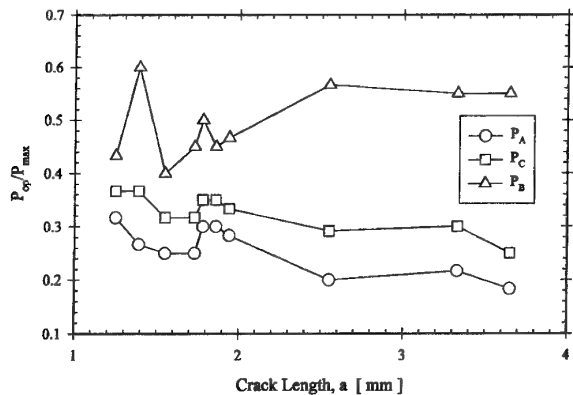


Figure 9 Variation of DCPD closure parameters with crack length

commenced (i.e. $a = 2$ mm). It is clear that the shape of the gauge signal is strongly dependent on the crack length. Thus, there is a tendency for the upper regime to 'fall over' more as the crack tip moves further away from the gauge position. As in the case of the DCPD measurements, it was convenient to represent strain gauge closure by an intercept value, P_G , obtained by drawing straight lines through the initial and final linear regimes.

CRACK TIP CLOSURE IN UNIFORM STRESS FIELDS

The variation of the three DCPD closure parameters, P_A , P_B and P_C , with crack length is illustrated for CC test data at 600 MPa in Figure 9. It is instructive to focus initially on the upper, P_B , value and, to this end, a more detailed presentation is made for a 450 MPa test in Figure 10. The highly serrated nature is typical and is a reflection of the fact that the material is coarse grained and that there are significant deviations in the crack path. The variations in voltage readings therefore represent point-to-point contacts which will vary as the crack grows. The line through the data in Figure 10 is an average value for P_B . Similar values were obtained from other CC tests and a comparison made with replica measurements of the load at which the crack tip opens or closes. The good correlation between the two sets of information is evident from

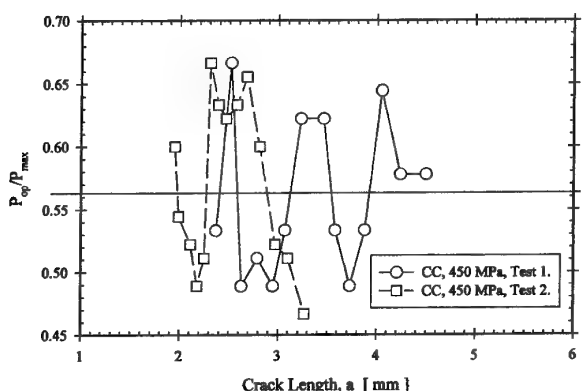


Figure 10 Wide variations in first contact load (P_B) with crack length

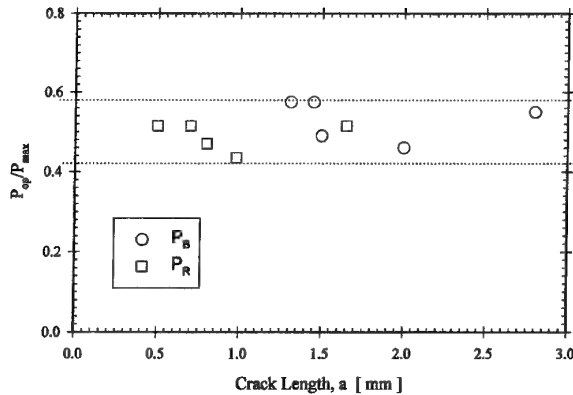


Figure 11 Comparison of first contact loads from PD (P_B) and replicas ($P_R - \max$)

the comparison in Figure 11. It is apparent also from this amalgamation that the first contact load is similar for cracks as small as 0.5 mm, which is approximately the size of the prior beta grains.

The principal purpose of the DCPD technique is the measurement of crack length. Although the monitoring systems are generally calibrated in terms of length, they actually respond to changes in cracked area. For this programme, detailed finite element and empirical calibrations were carried out on an area basis. It was shown that a general calibration curve was appropriate irrespective of the range of quarter circular and elliptical crack shapes encountered. Using this calibration, the voltage changes during the closure experiments were expressed as cracked area in contact. Figure 12 illustrates how the area in contact changes with the cyclic variation in load for a series of crack lengths in a CC testpiece. Even for the longest crack lengths studied at 450 MPa ($\Delta K = 40 \text{ MPa}\sqrt{\text{m}}$), only 11% of the crack face comes into contact at minimum load. The change in this minimum percentage with crack length is given in Figure 13. It is clear that the contact area increases as the stress increases from 450 to 600 MPa. It is also apparent from the data at 450 MPa that for crack lengths up to 2 mm the contact area is virtually constant at approximately 1.5%. The K_{\max} at the transition point where contact area begins to increase is 26 MPa $\sqrt{\text{m}}$. Using this value, the equation $r_p = 1/\pi(K_{\max}/\sigma_{ys})^2$ can be used to calculate the plane

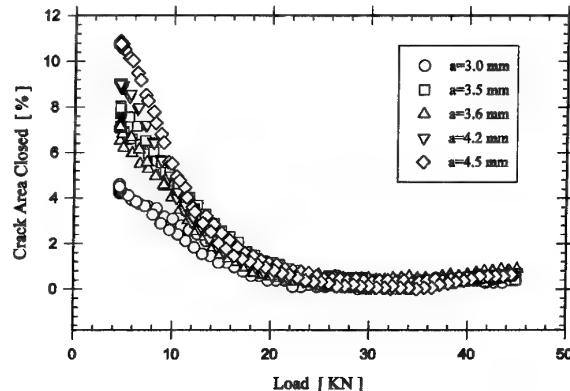


Figure 12 Change in closure contact area with load per cycle and crack length

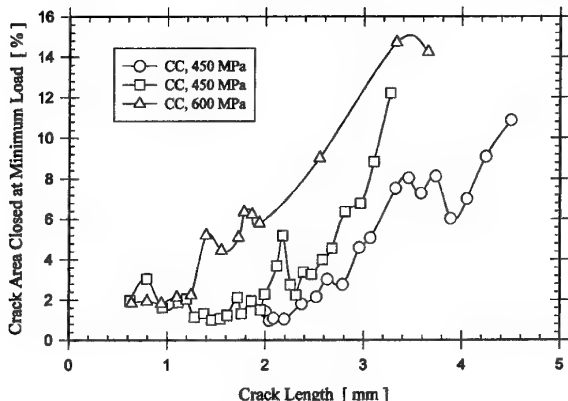


Figure 13 Dependence of cracked area closed at minimum load on crack length

stress crack tip plastic zone size, r_p . If the cyclic yield strength, σ_{ys} , is 620 MPa⁸ then $r_p = 560 \mu\text{m}$. This is similar to the average prior beta grain size ($\sim 0.5 \text{ mm}$), suggesting that the transition point is related to the development of plane stress plasticity that is greater than the microstructural unit size. A further observation on crack tip plasticity can be made from the data in Figure 9. The P_A and P_C measurements suggest that the closure load initially falls with crack length, but at $a = 1.8 \text{ mm}$ there is a minor reversion in this trend so that the closure level increases before falling away again at larger a . For this crack length at 600 MPa, K_{max} is $39 \text{ MPa}\sqrt{\text{m}}$. Feeding this into the equation $r_p = 1/3\pi(K_{max}/\sigma_{ys})^2$, a value of $420 \mu\text{m}$ is obtained for the plane strain plastic zone size, strongly suggesting that this is the point at which the plastic zone dimensions exceed the microstructural unit size along the entire crack front.

GEOMETRY INDUCED CLOSURE

The final issue relates to the strain gauge measurements. Strictly speaking, the only valid values are at the points where the crack tip just passes beyond the gauge position. These quantities, defined earlier as the intercepts P_G , were found to have a similar magnitude to the DCPD intercepts, P_C . It is now argued, however, that the strain gauge signals contain valuable information even when the crack tip has passed well beyond the gauge position. In essence, the gauge only responds when the faces adjacent to it have contacted to an extent that the local load can be supported. Thus, if the crack has grown 2 mm (say) beyond the gauge, a signal will be generated only when there has been 2 mm of closure back from the tip on unloading. Effectively, the fixed gauge provides equivalent information to the replica measurements in Figure 5. This view is reinforced by Figure 14, which compares strain gauge and replica data for cracks of a similar size in CC specimens. Working from this basis, it is interesting to explore strain gauge information for the $K_t = 1.9$ DEN. Figure 15 compares notch root and side face gauges for a crack growing from the corner starter slit. DCPD data (P_C) are included for comparison. It is clear that the gauges do not give the same response as those on the CC specimen in Figure 14. In all cases, the indicated closure level increases after the

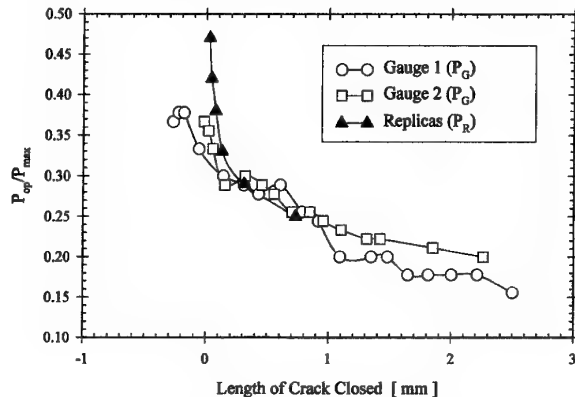


Figure 14 Comparison of replica and strain gauge measurements of crack 'peeling'

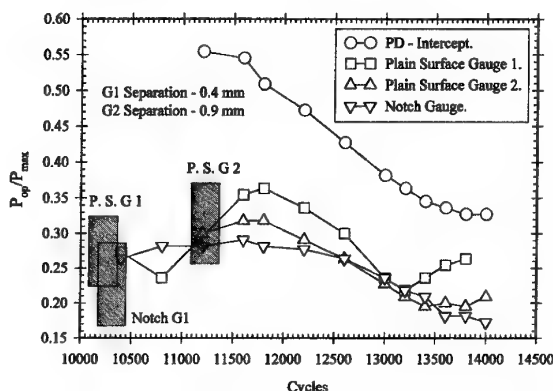


Figure 15 Closure measurements at notch root and plain side face

crack is well past the gauge positions. Furthermore, the notch root gauge indicates a lower level of closure than both side face gauges. Both pieces of information are consistent with stress redistribution due to plasticity at the notch root, causing the local surface to experience a negative R cycle. McClung¹ has shown how closure levels fall for $R = -1$ compared to $R = 0$ cycles. The subsequent rise in measured closure values can thus be attributed to the 'internal' crack front experiencing enhanced closure inboard of the surface. This interpretation is consistent with previously reported life prediction anomalies and crack shape variations in the same DEN⁸.

CONCLUSIONS

The research programme has clearly demonstrated important correlations between DCPD, strain gauge and replica techniques for characterising crack closure. When amalgamated, these methods provide a valuable database for modelling 3D closure effects. Important differences for cracks experiencing geometry induced closure at notches are highlighted. These have implications for life prediction calculations.

REFERENCES

- 1 McClung, R. C., *Metallurgical Transactions*, 1991, **22A**, 1559–1571.
- 2 Llorca, J. and Sanchez Galvez, V., *Engineering Fracture Mechanics*, 1990, **37**, 185–196.

- 3 Llorca, J., *Fatigue and Fracture of Engineering Materials and Structures*, 1992, **15**, 655–669.
- 4 Sehitoglu, H. and Wei, S. In *Fatigue Under Biaxial and Multiaxial Loading*, eds K. Kussmaul, D. McDiarmid and D. Socie. ESIS10, MEP, London, 1991, pp. 1–21.
- 5 Vormwald, M. and Seeger, T., *Fatigue and Fracture of Engineering Materials and Structures*, 1992, **14**, 205–226.
- 6 Davidson, D. L., *Engineering Fracture Mechanics*, 1991, **38**, 393–402.
- 7 Fleck, N. A., Smith, I. F. C. and Smith, R. A., *Fatigue and Fracture of Engineering Materials and Structures*, 1983, **6**, 225–239.
- 8 Evans, W. J., Nicholas, P. J. and Spence, H. S. In *Advances in Fatigue Lifetime Predictive Techniques*, Vol. 3, eds M. R. Mitchell and R. W. Landgraf. ASTM STP 1292, ASTM, Philadelphia, 1996, pp. 201–219.

PII: S0142-1123(97)00043-1

The effect of stress ratio on fatigue crack growth rate in the absence of closure

R. Sunder*, J. Portert and N.E. Ashbaught

*BiSS Research, 99, 14A Cross, Malleswaram, Bangalore 560 003, India

*t*University of Dayton Research Institute, 300 College Park, Dayton, OH 45469,
USA

A fractographic study† was performed on Al-alloy fatigue fracture surfaces produced by programmed load sequences. The load sequences included steps of constant amplitude cycles at three different stress ratios, each step is preceded by a small number of high amplitude cycles designed to avoid the influence of crack closure and to serve as fractographic markers. The experiments were conducted on different specimen geometries to produce conditions associated with a long crack under *fully elastic* conditions and a short crack in a notched coupon seeing *high local post yield* stress conditions. Crack sizes covered in the study ranged from 0.02 to 12 mm, and growth rates ranged from 2×10^{-7} to 4×10^{-5} mm cycle $^{-1}$. Fractographic evidence from the study suggests that the crack growth rate can vary by up to a factor of five with applied stress ratio change from 0.64 to 0.73. In the case of the long crack, the effect is less noticeable or totally absent. In the case of naturally initiating notch root cracks, the effect is more pronounced at higher stress level and lower crack growth rate. © 1998. Published by Elsevier Science Ltd.

(Keywords: fractography; fatigue crack growth; stress ratio; crack closure; small cracks)

INTRODUCTION

Load history effects in metal fatigue under random service loading are closely linked with mean stress effects in crack formation and stress ratio effects in fatigue crack growth. Most predictive models would indicate that in the absence of mean stress or stress ratio effects, cumulative fatigue damage will be load sequence (history) insensitive. In general, stress ratio effects in fatigue crack growth have been associated with fatigue crack closure¹. Crack growth rate (da/dN) equations also account for the rapid increase in da/dN as K_{max} approaches K_{1c} ^{2,3}.

Several mechanisms may be responsible for the stress ratio effect on fatigue crack growth rate⁴⁻⁶. Of these, fatigue crack closure has emerged as by far the most 'popular' to explain the effect in terms of truncation of applied stress intensity range, ΔK , to an effective range, ΔK_{eff} . This reduction in ΔK is a consequence of closure in the wake of the crack, effectively working like a wedge, that does not allow stress intensity to drop below a certain level. The closure of the fatigue crack can be attributed to one or more mechanisms – crack tip plasticity, roughness, asperities, oxide layer formation, etc.^{1,7}. The first three of these

are load history sensitive, making crack closure a widely accepted phenomenon to model load interaction effects in fatigue life prediction for random, service load conditions³. Oxide layer formation can have a major influence on stress ratio effects on threshold stress intensity, ΔK_{th} .

The objective of this study was to examine fractographically the effect of stress ratio on crack growth rate in the *absence* of fatigue crack closure. For ease of measurements, a 'fractography friendly' Al-alloy 2014-T6511 with an average grain size of approximately 15 µm was chosen for the study. The tests were conducted on different specimen types to cover a wide range of stress levels.

EXPERIMENTAL PROCEDURE

Two different coupons were tested. One was a 5 mm thick, 45 mm wide single edge tension, SE(T), coupon. The other was a specially designed 10 mm thick, 23 mm wide notched SE(T) coupon with $K_t = 2.5$. Figure 1 shows drawings of the two specimens used in testing.

The load sequence used in the experiments appears in Figure 2. Each block consists of three steps of 2000 load cycles, each step is preceded by 10 marker cycles. The stress range for each of the steps is the same. Step #1 is at applied stress ratio $R = 0.73$, Step #2 at $R = 0.69$ and Step #3 at $R = 0.64$. Thus, even at the

†This investigation was conducted at the Materials Directorate of Wright Laboratory at Wright-Patterson Air Force Base, OH, USA, under contract F33615-94-C-5200.

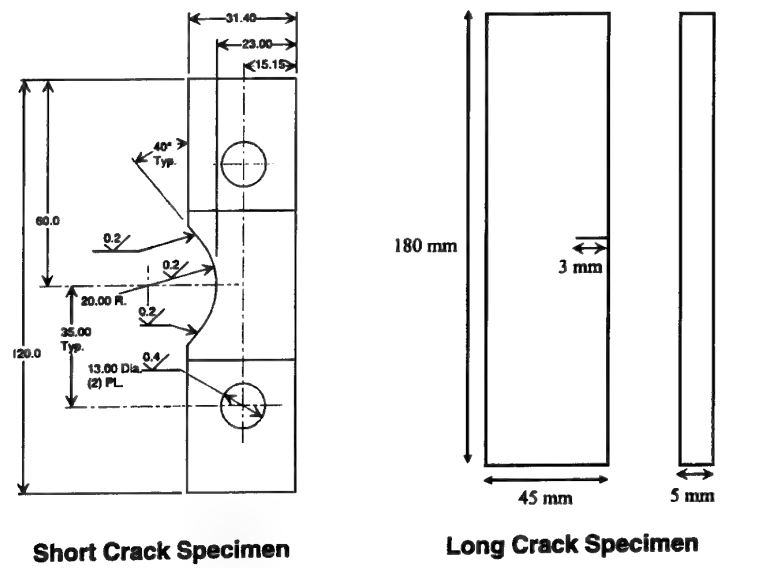


Figure 1 Test coupons used in experiments

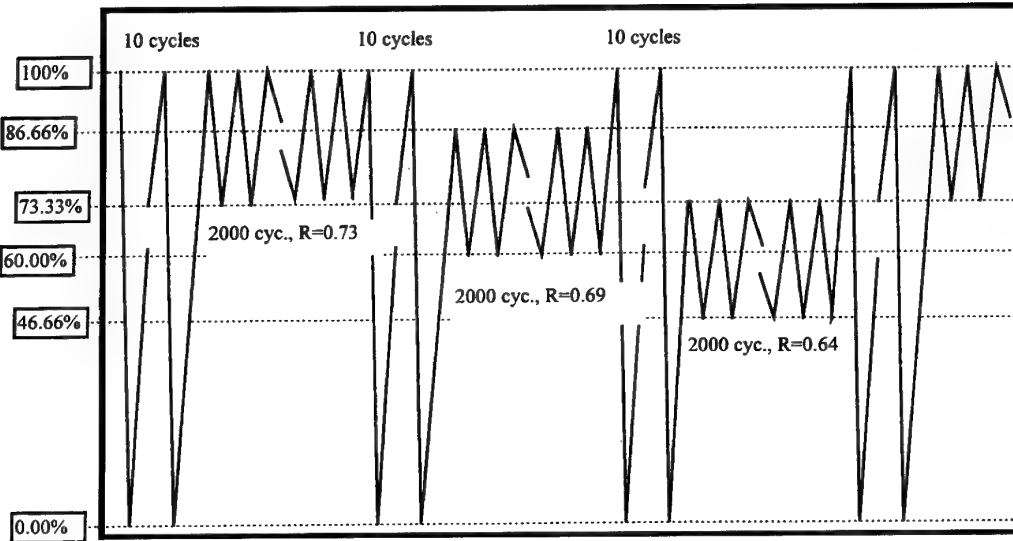


Figure 2 Schematic of load sequence used in testing

lowest of these stress ratios, the fatigue crack is unlikely to see any closure. As a further 'insurance' against closure, the marker cycles were applied with a much lower minimum stress, designed to take crack closure stress even lower. Repeated blocks of the sequence described above were applied to the test specimen through to failure. Due to potential backlash in the pin loading arrangement on the notched SE(T) specimen, minimum load in the block for that specimen was increased from 0% to 4.67% of maximum load.

Previous work had suggested that at $R = 0$, crack closure stress in this material varies between 0% and 50% of S_{max} and depends on net stress levels. S_{max} in the marker cycles is the same as S_{max} during the first step at $R = 0.73$. This precludes any load interaction effects associated with overloads. Even the cycles at the lowest stress ratio of $R = 0.64$ see an overload ratio of just 36% due to the markers. Overloads under 50% of baseline loading have generally been found to

cause only negligible retardation effects on crack growth.

Approximate calculations of plane strain plastic zone size suggest fatigue crack extension in a single step of 2000 cycles would be under 5% of the plastic zone size due to the preceding markers. This calculation also supports the possibility that plasticity induced retardation effects, if any, would apply uniformly to all three steps.

All three sets of marker loads contain 10 cycles. This number was selected to ensure discernible marker bands on the fracture surface even at very low crack growth rates of $10^{-5} \text{ mm cycle}^{-1}$ due to the marker cycles. The step size of 2000 cycles for each of the stress ratios was selected to improve chances of measurable crack extension even at growth rates as low as $10^{-7} \text{ mm cycle}^{-1}$. Step size serves as a 'resolution amplifier' in microscopy. At very low growth rates, individual striations may be too fine to

be picked up under the microscope. Ref.⁸ noted that striation spacings indicating crack growth rate under 10^{-4} mm cycle⁻¹ have not been observed. However, a band of multiple such striations is more readily identified when spaced with marker cycles that leave behind their own bands with contrasting morphology.

In the process of ensuring minimum load interaction effects and absence of fatigue crack closure, variation of applied stress ratio was restricted to between 0.64 and 0.73. It was assumed, however, that even this interval is wide enough to show any stress ratio effect on crack growth rate.

A total of three tests were conducted. Applied load levels and estimated stress responses are listed in *Table 1*. The da/dN measurements are shown in *Table 2*. A plot of these results is shown in *Figure 3*. The material constants on the same material from Ref.⁹ are given in *Table 3*. The constants E , S_f , and e_f are Young's modulus, tensile strength and failure strain, respectively. K' and n' are the cyclic strength coefficient and cyclic strain hardening exponent, respectively. For the K levels considered in *Table 2*, C and m are the coefficient and exponent, respectively, for the Paris crack growth law and K_c is the operational fracture toughness. These constants were used in analysis of inelastic specimen response and fatigue crack growth analysis. Due to inelastic response, the effective stress ratios in the tests on the notched SE(T) specimens were slightly different from applied stress ratios. When the material yields under tensile loading and subsequent stress reversal are totally elastic, the effective stress ratio will be less than the applied stress ratio.

Test 1 was on an SE(T) specimen with an edge crack. A 3 mm saw cut served as the crack initiator. The test was at $S_{max} = 100$ MPa to simulate long crack fully elastic conditions. Tests 2 and 3 were conducted on a specially designed notched coupon (see *Figure 1* for details) with $K_t = 2.5$. The purpose of these tests was to simulate the behavior of real engineering

components with stress raiser and associated stress gradient. The specimen was designed with a notch enforcing natural crack initiation under conditions of controlled local inelasticity. The maximum applied load (50 kN) in Test 2 was selected to induce notch root yield, with estimated notch root maximum stress reaching 515 MPa compared to a material yield stress of 420 MPa. This maximum load caused limited residual stresses upon unloading, thereby reducing the effective stress ratio from 0.73 to 0.72 in Step #1. Test 3 used a higher maximum applied load (75 kN), thereby producing considerable inelastic deformation of the notch root, leading to formation of noticeable residual stresses and associated reduction in effective stress ratio (see *Table 1*).

Table 1 summarizes the estimated stress response of the test coupon in the three tests. Stress levels for Tests 2 and 3 were estimated as notch surface local stresses after Neuber conversion. The maximum stress varied from 100 to 670 MPa to cover both fully elastic and inelastic loading conditions. As mentioned earlier, subsequent cycling after initial inelastic deformation produced a purely elastic response. As seen from *Table 1* and *Figure 2*, the programmed pattern of loading in all three tests was identical, though stress levels varied considerably. A minor difference was the minimum 4.67% tensile load component in the notched coupons to avoid loading pin backlash at zero load. The other difference was in crack initiation. The SE(T) specimen had a saw-cut crack initiator, while the notched coupons saw natural crack initiation.

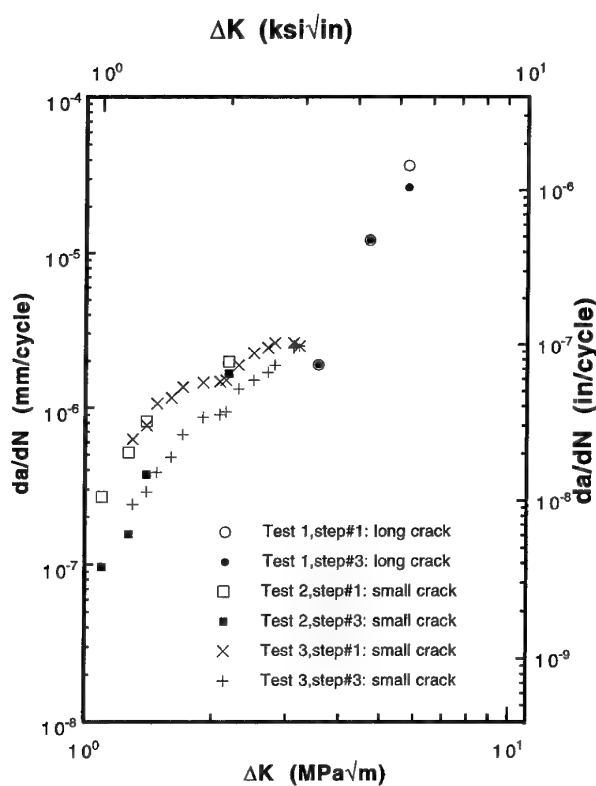
In all the tests, the specimen was cycled to failure through repeated cycling with the programmed load sequence shown in *Figure 2*. After the test, the fracture surface was trimmed for observation on a Leica Cambridge 360FE 0303 Scanning Electron Microscope.

Table 1 Loading conditions and estimated specimen response. Refer to *Figure 2* for load sequence

Test	1	2	3
Specimen geometry	SE(T) W45/T5 mm	Notched SE(T) ($K_t = 2.5$) W23/T10 mm	Notched SE(T) ($K_t = 2.5$) W23/T10 mm
Reference loading (100%)	100 MPa	50 kN	75 kN
Maximum net stress (MPa)	100	217	326
Maximum notch local stress (MPa)	—	515	670
Applied stress ratio		Step #1 (2000 cycles) $R = 0.73$	
Effective stress ratio	0.73	0.72	0.683
S_{max} (MPa)	100	515	670
ΔS (MPa)	26.67	145	217
Applied stress ratio		Step #2 (2000 cycles) $R = 0.69$	
Effective stress ratio	0.69	0.67	0.624
S_{max} (MPa)	86.66	442.5	564
ΔS (MPa)	26.67	145	217
Applied stress ratio		Step #3 (2000 cycles) $R = 0.64$	
Effective stress ratio	0.64	0.61	0.537
S_{max} (MPa)	73.33	370	458
ΔS (MPa)	26.67	145	217
Applied stress ratio		Step #4 (10 cycles)	
Effective stress ratio	0.00	$R = 0$	$R = 0.0467$
S_{max} (MPa)	100	0	— 0.16
ΔS (MPa)	100	515	670
		518	777

Table 2 da/dN data

a (mm)	ΔK (MPa \sqrt{m})	da/dN (mm cycle $^{-1}$)		Test
		Step #1	Step #3	
4.5	3.55	1.89×10^{-6}	1.89×10^{-6}	1
7.8	4.68	1.21×10^{-5}	1.21×10^{-5}	
11.9	5.77	3.68×10^{-5}	2.65×10^{-5}	
0.04	1.1	2.69×10^{-7}	9.6×10^{-8}	2
0.05	1.27	5.17×10^{-7}	1.55×10^{-7}	
0.065	1.4	8.18×10^{-7}	3.73×10^{-7}	
0.15	2.18	1.97×10^{-6}	1.64×10^{-6}	
0.024	1.3	6.25×10^{-7}	2.4×10^{-7}	3
0.028	1.4	7.69×10^{-7}	2.89×10^{-7}	
0.032	1.48	1.06×10^{-6}	3.85×10^{-7}	
0.037	1.6	1.15×10^{-6}	4.81×10^{-7}	
0.042	1.7	1.35×10^{-6}	6.73×10^{-7}	
0.049	1.9	1.44×10^{-6}	8.65×10^{-7}	
0.058	2.08	1.46×10^{-6}	9.0×10^{-7}	
0.066	2.15	1.49×10^{-6}	9.33×10^{-7}	
0.076	2.3	1.87×10^{-6}	1.31×10^{-6}	
0.087	2.5	2.24×10^{-6}	1.49×10^{-6}	
0.099	2.7	2.43×10^{-6}	1.68×10^{-6}	
0.11	2.8	2.61×10^{-6}	1.87×10^{-6}	
0.125	3.1	2.61×10^{-6}	2.43×10^{-6}	
0.136	3.2	2.49×10^{-6}	2.49×10^{-6}	

**Figure 3** Comparison of long and small crack growth rates

RESULTS AND DISCUSSION

Test 1: long crack under elastic loading

All the fractographs from this test show the fatigue crack growing from right to left. For consistency in measurements, they are all from the mid-thickness region, at least 1 mm from the specimen surfaces.

At crack size 4.5 mm ($\Delta K = 3.6$ MPa \sqrt{m}), the mid-thickness area largely shows uniformly spaced striation bands, that in fact make it difficult to identify the band corresponding to the highest stress ratio (see Figure 4). The crack growth rate over each of the 2000 cycle steps was estimated to be 1.891×10^{-6} mm cycle $^{-1}$. In Figure 4, we find crevices along some of the marker bands, indicating that the fatigue crack attempted to change direction during the 10 marker cycles. This was not apparent at lower crack growth rates and appears to indicate a point where the preferred plane of crack extension is no longer the same for the marker cycles and those in Steps #1–3.

Figure 5 shows equally spaced striation bands from all three steps. This fractograph is from a mid-thickness site corresponding to $a = 7.8$ mm. Towards the left end of the fractograph, we find an increasing contribution of the marker cycles to fatigue crack extension. The marker bands now show a width of their own. The growth rate in each of the 2000 cycle steps is 1.207×10^{-5} mm cycle $^{-1}$, while in the marker cycles it is 6.03×10^{-4} mm cycle $^{-1}$. These do not differ greatly from the computed values of 1.549×10^{-5} and 4.53×10^{-4} mm cycle $^{-1}$ from material constants. However, the marker cycle component is steadily

Table 3 Material constants 2014-T6511⁹

E (MPa)	S_f (MPa)	e_f	K' (MPa)	n'	C (mm(MPa \sqrt{m}) $^{-1}$)	m	K_c (MPa \sqrt{m})
70800	1075.0	0.25	1479	0.148	10^{-7}	3.27	60

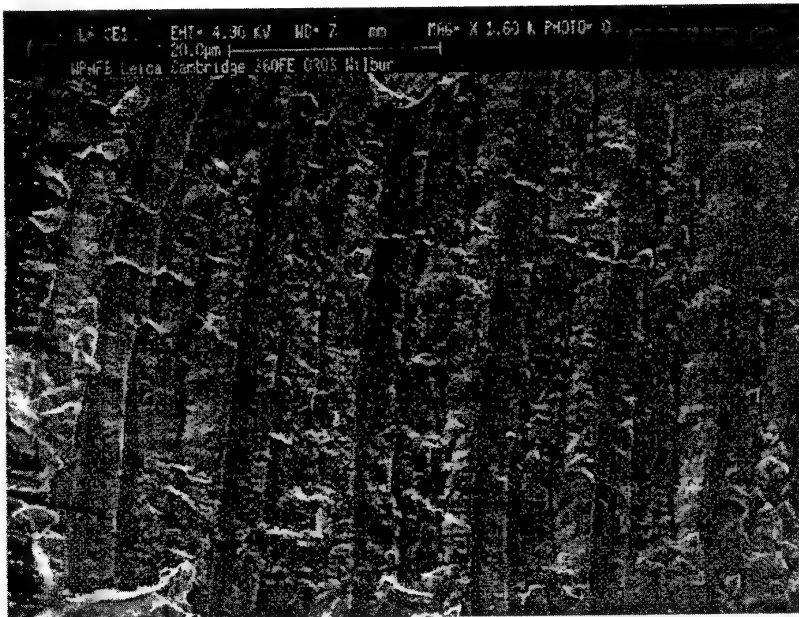


Figure 4 SE(T) specimen at $S_{\max} = 100$ MPa. Mid-thickness region. $a \sim 4.5$ mm. $\Delta K = 3.6 \text{ MPa} \sqrt{\text{m}}$ in Steps #1–3. $da/dN \sim 1.89 \times 10^{-6}$ mm cycle $^{-1}$ (Steps #1–3)

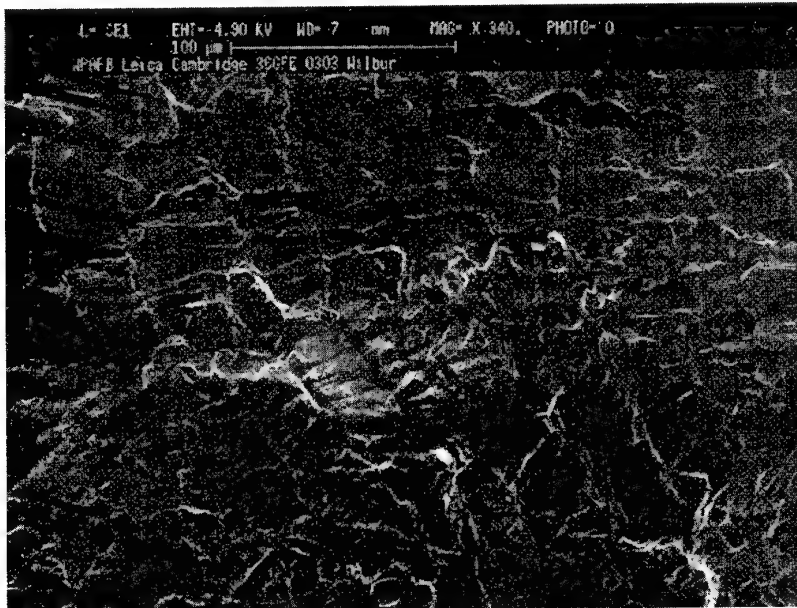


Figure 5 SE(T) specimen at $S_{\max} = 100$ MPa. Mid-thickness region. $a \sim 7.8$ mm. $\Delta K = 4.17 \text{ MPa} \sqrt{\text{m}}$ in Steps #1–3. $da/dN \sim 1.21 \times 10^{-5}$ mm cycle $^{-1}$ (Steps #1–3) and 6×10^{-4} mm cycle $^{-1}$ in marker cycles (Step #4)

increasing and appears to always exceed estimates from ΔK , while da/dN in the 2000 cycle steps is less than estimates. Schijve¹⁰ has observed that, due to crack front incompatibility, a crack grown in flat mode at low ΔK will show accelerated growth rate at high ΔK , until the new shear plane is established. Conversely, when a crack already in the shear plane is forced to grow in the flat plane, it will show reduced growth rates until the flat plane is re-established. The striation bands in the middle of the fractograph in Figure 5 clearly appear to reflect such incompatibility.

The fractograph in Figure 6 is from a site corresponding to crack length $a = 11.9$ mm in the mid-thickness area. The crack growth rate is identical in Steps #1 and #2 (from the right) at 3.55×10^{-5} mm cycle $^{-1}$ and somewhat less in Step #3 (2.65×10^{-5}). The growth rate during the marker cycles is 1.9×10^{-3} mm cycle $^{-1}$ or 70 times greater than in the smaller cycles. This is in contrast to the 50:1 ratio at $a = 7.8$ mm. Individual striations from the marker cycles are now clearly visible.

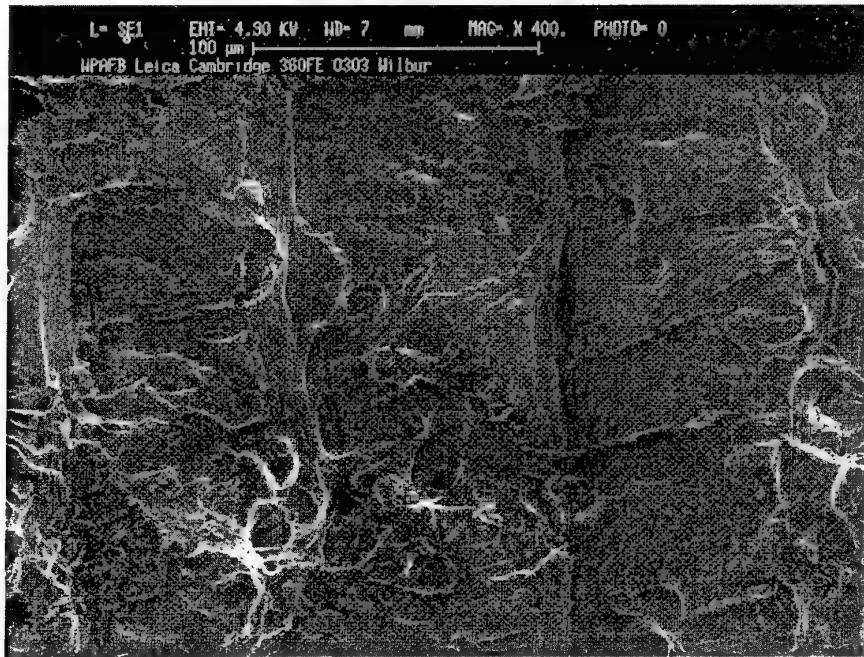


Figure 6 SE(T) specimen at $S_{\max} = 100$ MPa. Mid-thickness region. $a \sim 12$ mm. $\Delta K = 5.18$ MPa $\sqrt{\text{m}}$ in Steps #1–3. $da/dN \sim 3.55 \times 10^{-5}$ mm cycle $^{-1}$ (Steps #1 and 2), 2.65×10^{-5} mm cycle $^{-1}$ in Step #3, 1.9×10^{-3} mm cycle $^{-1}$ in Step #4

Test 2: notched coupon at 50 kN maximum loading

Figures 7–11 show fractographs from Test 2 covering crack growth from a size of 0.04 mm up to 3 mm. A single fatigue crack initiated at a point about 0.025 mm from the notch root and grew to failure.

Figure 7 shows the origin of the naturally initiating fatigue crack. After growing along a 45° plane over the first 10–15 μm , further growth occurs along the horizontal plane. Figure 8 shows the first discernible

striation patterns that appear at a crack depth of about 0.04 mm. As reasoned earlier, the gradual decrease in striation spacing appears to indicate non-closure related stress ratio effect. As K_{\max} at this point is under 15% of K_{Ic} , one would have to assume that the effect is local stress related. Notch root S_{\max} in the three steps reduces from a post yield value of 515 MPa in the first step, through a near yield value of 442 MPa in the second step, and down to a fully elastic 370 MPa

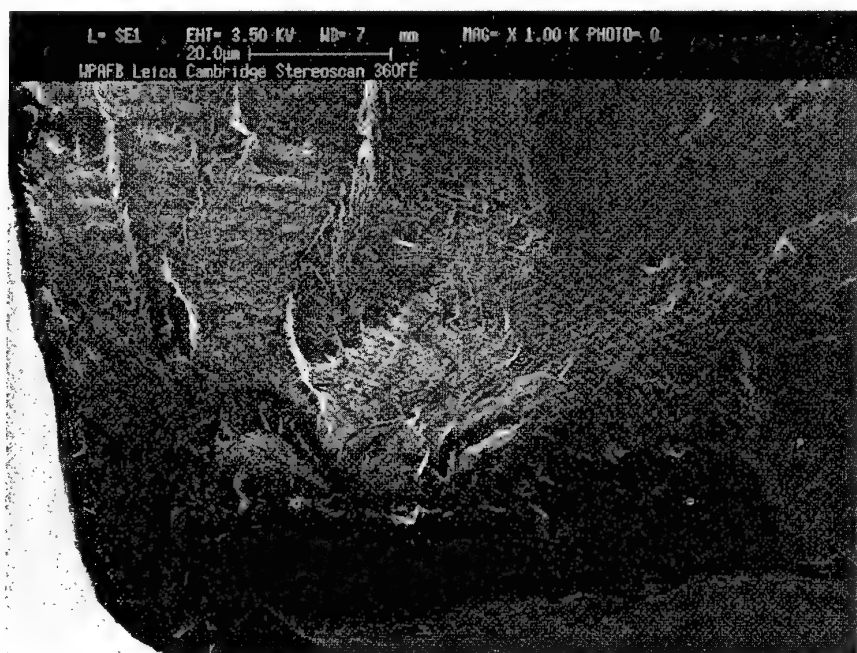


Figure 7 Notched SE(T) specimen tested at $P_{\max} = 50$ kN. Origin of naturally initiating fatigue crack on the notch surface about 0.02 mm from the specimen side

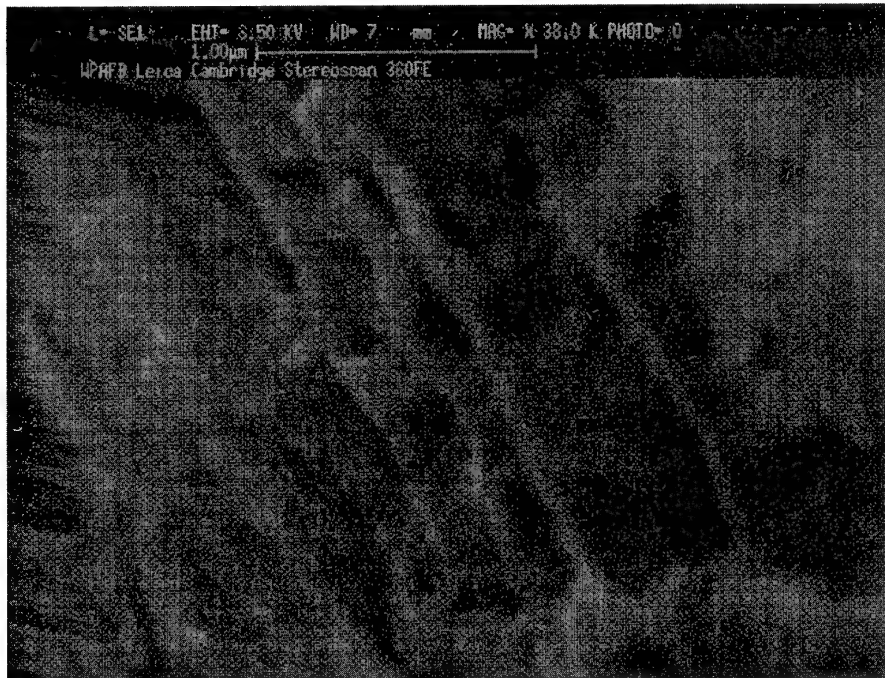


Figure 8 Notched SE(T) specimen tested at $P_{\max} = 50$ kN. First discernible striation bands at a crack depth of 0.04 mm. $\Delta K = 1.1 \text{ MPa} \sqrt{\text{m}}$ in Steps #1–3. $da/dN \sim 2.69 \times 10^{-7} \text{ mm cycle}^{-1}$ in Step #1 and $0.96 \times 10^{-7} \text{ mm cycle}^{-1}$ in Step #3

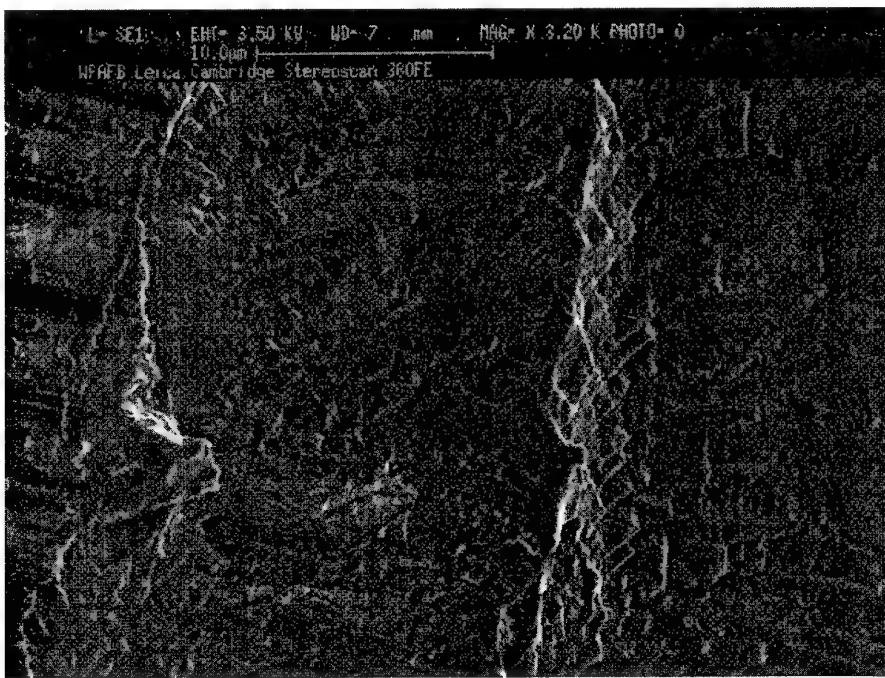


Figure 9 Notched SE(T) specimen tested at $P_{\max} = 50$ kN. Striation bands at a crack depth of 0.065 mm. $\Delta K = 1.1 \text{ MPa} \sqrt{\text{m}}$ in Steps #1–3. $da/dN \sim 2.69 \times 10^{-7} \text{ mm cycle}^{-1}$ in Step #1 and $0.96 \times 10^{-7} \text{ mm cycle}^{-1}$ in Step #3

in the third step. The crack growth rate in the first step was estimated from the striation band width to be $2.69 \times 10^{-7} \text{ mm cycle}^{-1}$, while in the third step it was 2.8 times less at $9.6 \times 10^{-8} \text{ mm cycle}^{-1}$, which is the lowest recorded crack growth rate in this study.

For the crack shown in *Figure 8*, the calculated ΔK value over Steps #1–3 is $1.1 \text{ MPa} \sqrt{\text{m}}$. Assuming the material constants in *Table 3* and the absence of a

threshold, $da/dN = 1.37 \times 10^{-7} \text{ mm cycle}^{-1}$. The long crack data described earlier always showed calculated growth rates to be in excess of observed striation spacings. This had been attributed to the retardation effect due to crack front incompatibility caused by the marker loads. In contrast, the data from *Figure 8* indicate that the crack growth rate in Step #1 is twice the estimated value. This may be attributed to the

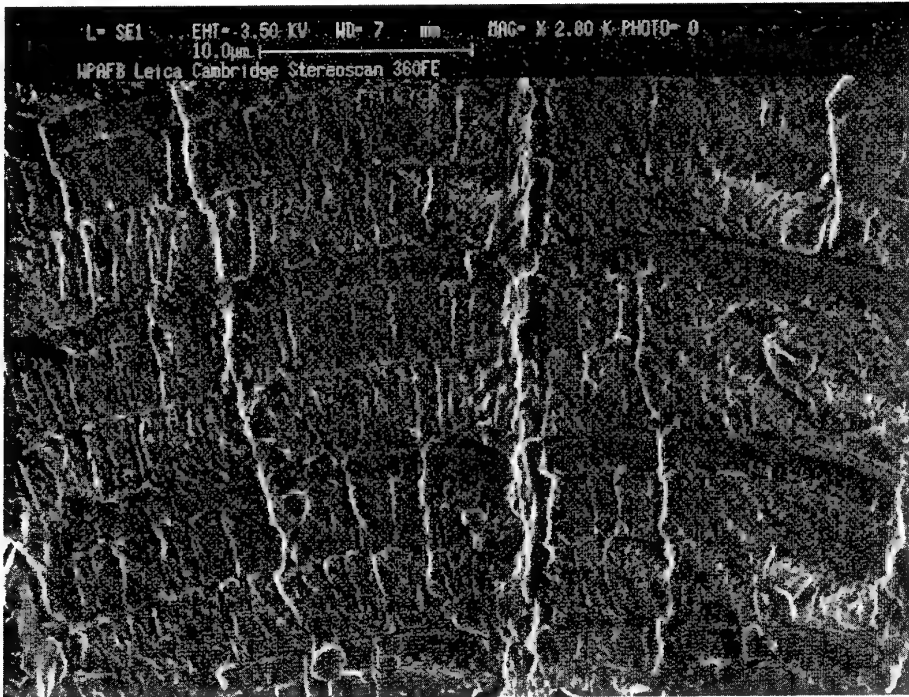


Figure 10 Notched SE(T) specimen tested at $P_{\max} = 50$ kN. Mid-thickness region. $a \sim 0.12$ mm



Figure 11 Notched SE(T) specimen tested at $P_{\max} = 50$ kN. $a = 3.5$ mm

small crack effect, and the local stresses that are close to yield and ultimate stress. As S_{\max} in Steps #2 and 3 recedes, the growth rate drops to even less than the estimate. *Figure 9* shows the fatigue crack extending across two planes at $a = 0.065$ mm, with a clear and consistent reduction in crack growth rate over the three steps.

Figure 10 shows a fractograph corresponding to $a = 0.12$ mm. At this particular point, we find the crack

growth rate to be identical in Steps #1 and 2, and down to a third in Step #3. The same argument advanced earlier may be suggested to apply with regard to the long crack under elastic conditions. Crack growth in Step #3 is retarded by closure in the crack extension mode that is currently active. Just 30 μ m away, at a crack size of 0.15 mm, crack growth rates over all three steps even out (see *Figure 11*). This trend continued right through to $a = 3.5$ mm, just before failure.

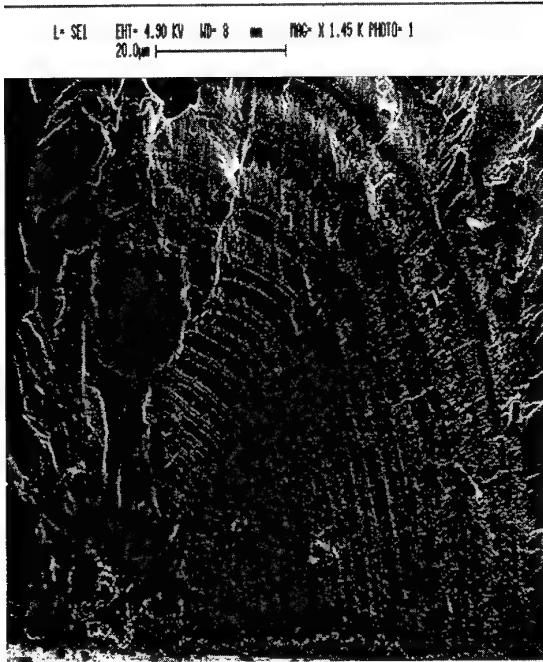


Figure 12 Notched SE(T) specimen tested at $P_{\max} = 75$ kN. Original initiation site of the seven identified on this sample

Test 3: notched coupon at 75 kN maximum loading

In contrast to Test 2 which initiated a single crack at the notch root, at least seven crack initiation sites were observed on the fracture surface from Test 3. Two of these sites appear in Figures 12–14. An enlarged local area from one of the sites is also shown to give a clear indication of crack growth rates.

It has been observed earlier¹¹ that under a given load spectrum the number of crack initiation sites will increase with applied stress level. As multiple crack

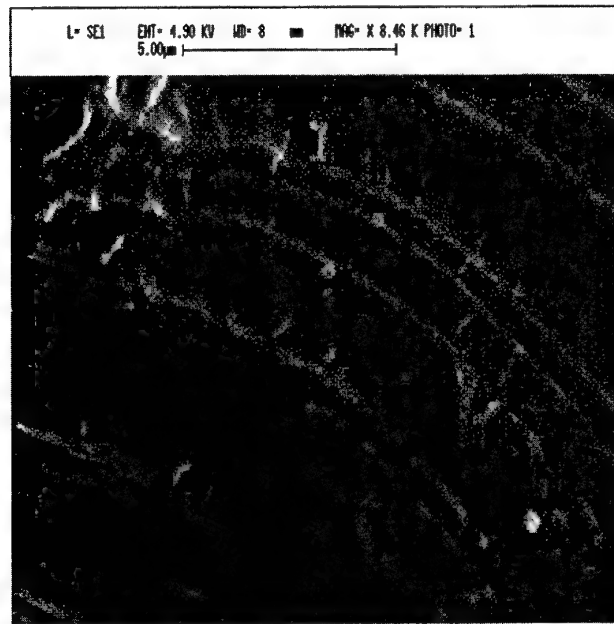


Figure 13 Notched SE(T) specimen tested at $P_{\max} = 75$ kN. $a = 0.06$ mm. Enlarged section from Figure 12

initiation would not have occurred simultaneously, one may expect to see differences in observed crack growth rates across multiple sites, given the same crack size. The site showing the lowest growth rate may be assumed to have initiated first¹¹. From these considerations, it would appear that the site shown in Figure 12 served as the first initiation site. The crack appears to have grown out of an inclusion site seen at bottom left as a semi-circular crack. The left half of the crack surface appears to have been obliterated due to rubbing. However, the right half has enough clear regions from which to measure the crack growth rate.

Figure 13 shows an enlarged segment of the fracture surface, clearly indicating gradual decrease in crack growth with decreasing stress ratio. The ratio of the largest to smallest striation band spacing is 4.33 at a crack size of about 0.06 mm. It may be recalled that the ratio had been 2.8 in Test 2 at a crack size of 0.04 mm. This more dramatic stress ratio effect may be attributed to the higher stress level in this test (see Table 1). The ratio may have been larger at smaller crack size. It diminishes with crack size and, as seen in Figure 14 from another site, appears to even out as the crack size exceeds 0.1 mm.

The crack size at which growth rates over the three different stress ratios evened out in Test 2 was about 0.15 mm, which may be explained by the reduced stress level in that test. In terms of notch root response to applied stress level, both these dimensions are negligible when viewed in terms of the stress gradient. It would follow that even at a crack size around 0.15 mm, local stresses would be of the same order as those estimated for the notch factor. Why then does the stress ratio cease to strongly influence crack growth rate? The answer may lie in growth rate sensitivity to stress ratio: one may argue that at lower (near threshold) stress intensity (and growth rate), when the fatigue crack barely extends in a single cycle, the effect of large cyclic applied stress levels will be significant. Over this interval the S_{\max}/S_f ratio may be crucial as indicated by the larger R effect in Test 3 as opposed to Test 2 (reduction in da/dN by a factor of 4.33 as opposed to 2.8 in Test 2). Indeed, the same trend would also be indicated by expressions for crack initiation life from LCF concepts^{12,13}. As crack driving force due to the ΔK component increases, the stress-related R -effect component diminishes and crack closure starts playing its well documented role. Further, as K_{\max} approaches K_c , the quasi-static component takes over and toughness-related stress ratio effects dominate (Forman equation in Refs^{2,3}).

CONCLUDING REMARKS

In summary, the results from the study suggest that in the process of fatigue damage over its different stages, fatigue crack growth rates will be dominated by both stress as well as stress intensity parameters. There is some analog in the way stress ratio affects fatigue damage in the early and late stages of fatigue. In both cases, the ratio of the maximum to ultimate (S_{\max}/S_f or K_{\max}/K_c) increases the damaging power of the driving variable (ΔS or ΔK) in a way that cannot be described from first principles. The effect is to be empirically established from testing. In contrast, the intermediate stage of ΔK -dominated damage accumulation is con-

L= SEI EHT= 4.90 KV WD= 12 mm MAG= X 778. PHOTO= 1
50.0µm



Figure 14 Notched SE(T) specimen tested at $P_{\max} = 75$ kN. $a \sim 0.1$ mm

trolled by crack closure that induces the stress ratio effect by directly controlling the range of the damaging parameter (ΔK_{eff}). The stress ratio effect over this stage can therefore be modeled analytically.

Specially designed load sequences permitted fractographic measurement of crack growth rates down to 10^{-7} mm cycle $^{-1}$ and up to 10^{-3} mm cycle $^{-1}$. Further modifications to the load program are likely to extend the capability of fractography to even lower crack growth rates and smaller crack sizes.

Fractographic evidence from this study indicates the possibility of noticeable stress ratio effects in the absence of fatigue crack closure. These effects will be more significant at lower crack growth rates and as applied and net (local) stress levels approach ultimate stress. Thus, fatigue thresholds are stress level sensitive. However, with increase in crack growth rate above near threshold levels ($\sim 2.10^{-6}$ mm cycle $^{-1}$), the stress ratio effect could be influenced more strongly by fatigue crack closure.

The present study was conducted using a very limited range of stress ratio variation ($R = 0.64$ – 0.73). Given a wider range of stress ratios, the above effects are likely to be more dramatic.

The techniques used in this study appear to hold the potential for more fundamental research work in the area of notch root fatigue crack initiation, stress ratio effects and notch sensitivity studies.

ACKNOWLEDGEMENTS

The authors would like to acknowledge the helpful technical guidance and support provided by Dr Ted Nicholas of the Materials Directorate, Wright-Patterson Air Force Base. The first author also appreciates useful discussions with Dr Raghu V. Prakash of the National Aerospace Laboratories, Bangalore, India. Excellent test support and guidance on SEM for the fractographs

have been provided by Mr Andy Lackey and Ms Luann Piazza, respectively.

REFERENCES

- 1 Elber, W., The significance of fatigue crack closure. In *Damage Tolerance in Aircraft Structures*. STP 486, American Society for Testing and Materials, Philadelphia, 1971.
- 2 Forman, R. G., Kearney, V. E. and Engle, R. M., Numerical analysis of crack propagation in cyclic loaded structures. *Journal of Basic Engineering, Transactions ASME*, 1967, **39**, 459.
- 3 Newman, A., Crack-closure model for predicting fatigue crack growth under aircraft spectrum loading. In *Methods and Models for Predicting Fatigue Crack Growth under Random Loading*, eds J. B. Chang and C. M. Hudson. ASTM STP 748, American Society for Testing and Materials, Philadelphia, 1981, pp. 53–84.
- 4 Booth, G. S. and Maddox, S. J., Correlation of fatigue crack growth data obtained at different stress ratios. *Mechanics of Fatigue Crack Closure*, eds J. C. Newman Jr. and W. Elber. ASTM STP 982, American Society for Testing and Materials, Philadelphia, 1988, pp. 516–527.
- 5 Walker, K., The effect of stress ratio during crack propagation and fatigue for 2024-T3 and 7075-T6 aluminum. *Effects of Environment and Complex Load History on Fatigue Life*. STP 462, American Society for Testing and Materials, Philadelphia, 1970.
- 6 Maddox, S. J., The effect of mean stress on fatigue crack propagation: A literature review. *International Journal of Fracture*, 1975, **11**(3), 389–407.
- 7 Elber, W., Fatigue crack closure under cyclic tension. *Engineering Fracture Mechanics*, 1970, **2**, 37–45.
- 8 Davidson, D. L. and Lankford, J., Fatigue crack growth in metals and alloys: mechanisms and micromechanisms. *International Materials Reviews*, 1977, **37**(2), 45–76.
- 9 Sunder, R., Prakash, R. V. and Mitchenko, E. I., Calculation of spectrum load notch root crack growth rate under elastic and inelastic conditions. *Advances in Fatigue Lifetime Predictive Techniques*, Vol. 2, eds M. R. Mitchell and R. W. Landgraf. ASTM STP 1211, American Society for Testing and Materials, Philadelphia, 1993, pp. 30–44.
- 10 Schijve, J., Fatigue damage accumulation and incompatible crack front orientation. *Engineering Fracture Mechanics*, 1974, **6**, 245–252.
- 11 Prakash, R. V., Sunder, R. and Mitchenko, E. I., A study of naturally initiating notch root fatigue cracks under spectrum

- loading. In *Advances in Fatigue Lifetime Predictive Techniques*, Vol. 3, eds M. R. Mitchell and R. W. Landgraf. ASTM STP 1292, American Society for Testing and Materials, Philadelphia, 1995, pp. 136–160.
- 12 Manson, S. S. and Muralidharan, U., A single expression formula for inverting strain-life and stress-strain relationships. *Fatigue and Fracture of Engineering Materials and Structures*, 1987, 9(5), 343–356.
- 13 Morrow, J. D., Fatigue properties of metals. In *Fatigue Design Handbook*, Section 3.2. Society of Automotive Engineers, 1968.

PII: S0142-1123(97)00023-6

Observation of fatigue damage in structural steel by scanning atomic force microscopy

Yoshikazu Nakai*, Seiichirou Fukuharat and Kenji Ohnishi†

*Department of Mechanical Engineering, Kobe University, 1-1, Rokkodai, Nada,
Kobe 657, Japan

†Graduate School, Kobe University, 1-1, Rokkodai, Nada, Kobe 657, Japan

Fatigue slip bands and plastic deformation around fatigue microcracks were observed by scanning atomic force microscopy. In fatigue slip bands, extrusions were observed but intrusions were not detected. Large extrusions were found in slip bands whose traces at specimen surface were almost perpendicular to the loading axis. Microcracks propagated under mixed mode condition of Mode I, Mode II, and Mode III. © 1998 Elsevier Science Ltd.

(Keywords: fatigue slip band; crack initiation; small crack growth; scanning atomic force microscopy)

INTRODUCTION

Since microscopic observation is the most useful method to clarify the mechanisms of fatigue processes in materials, the progress of metal fatigue study has strongly depended on the development of new microscopic observation methods such as optical microscopy (OM), transmission electron microscopy (TEM), and scanning electron microscopy (SEM). Recently, we developed a new method called 'scanning probe microscopy (SPM)', which gives three-dimensional images of solid surfaces on the atomic scale. It has excellent capabilities for analyzing the topographic nature of solid surfaces. SPM was first developed by Binning and Rohrer in 1982¹ from scanning tunneling microscopy (STM). Since their investigation, many types of scanning probe microscope have been developed, such as the scanning atomic force microscope (AFM), the scanning magnetic force microscope (MFM), and the scanning lateral force microscope (LFM). By using the STM and AFM, Komai *et al.*² observed the microcrack initiation and growth behavior in stress corrosion cracking. Ishii *et al.*³ observed fatigue slip bands by STM. Matsuoka *et al.*⁴ observed cleavage fracture surfaces. It was difficult to conduct continuous monitoring of the fracture processes in these studies because only small size samples could be inspected, and/or the area to inspect cannot be determined by optical microscopy at high magnification. In the present study, SPM was employed which was designed for large samples (maximum size 300 mm × 300 mm × 100 mm) with a high magnification optical microscope. The fatigue slip bands, fatigue crack initiation, and growth behavior of microcracks in structural steel were observed by SPM in AFM mode. The

main purpose of the present paper is to clarify what kind of fatigue phenomena can be understood more clearly by the SPM than by other microscopies.

MATERIAL AND EXPERIMENTAL PROCEDURES

The material for this study was a structural steel for ships, JIS KA32, which was provided by Sumitomo Metal Industries, Ltd. The chemical composition of this steel (in mass%) is as follows: 0.15C, 0.15Si, 1.10Mn, 0.011P, 0.004S, 0.01Cu, 0.02Ni, 0.02Cr, 0.01Mo, 0.25Al, and balance Fe. The yield strength of this material is 401 MPa, the tensile strength is 502 MPa, and the elongation is 25%. The material was heat treated at 620°C for 150 min before the specimens were machined. Prior to the fatigue tests, the surface of the specimens was polished by buffing.

The shape and dimensions of specimens are shown in *Figure 1*, where (a) is a specimen for tension test observation (Type A), (b) is a smooth specimen for fatigue slip band observation (Type B), and (c) (Type C) and (d) (Type D) are notched specimens for fatigue crack initiation and small crack propagation observations. To observe fatigue crack initiation processes at high magnification, the region for crack initiation should be limited to a small area. In the initial stage of our fatigue crack initiation study, Type C specimens were employed, but the crack initiation region was too large for the AFM observation, i.e. fatigue cracks initiated out of the observation region. Therefore, Type D specimens were employed for this study. Sharp surface notches were introduced at the tips of a blunt notch in the Type C specimen. The root radius of the sharp notch was 10 µm and the length was 500 µm.

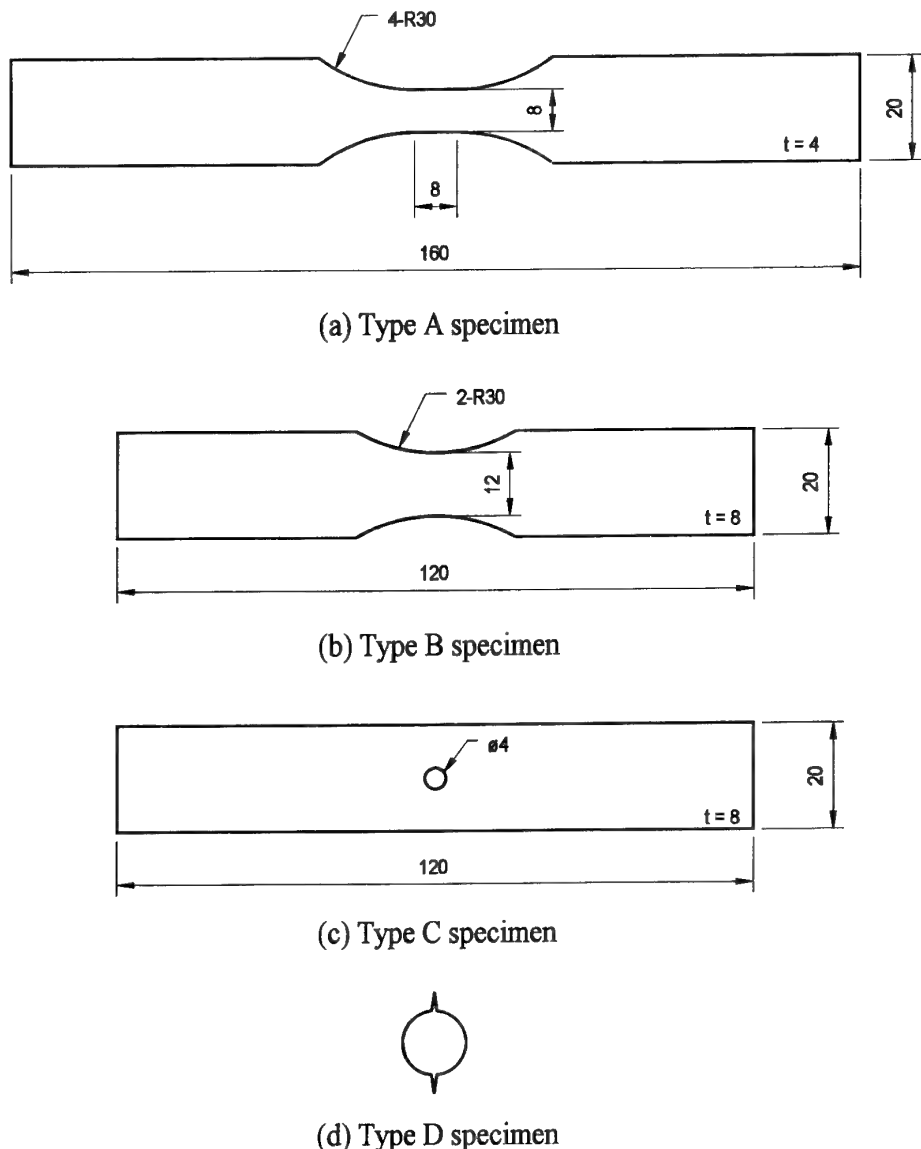


Figure 1 Shape and dimensions of specimens

The growth behavior of small cracks which initiated in Type C specimens were also observed by AFM.

The fatigue tests were carried out in a resonance type bending testing machine operated at a frequency of 33.3 Hz under fully reversed cyclic loading ($R=-1$).

The scanning probe microscope (Seiko Instruments Inc., SPA-350), which has a large stage unit, was employed for the present AFM observation. The resolution of the microscope is 0.5 nm in the surface direction and 0.1 nm in the vertical direction. The region for AFM observation was determined by optical microscopy at a magnification of 2000 on a CRT monitor. For most of the AFM observations, the scanning area was $20 \mu\text{m} \times 20 \mu\text{m}$.

EXPERIMENTAL RESULTS AND DISCUSSION

S-N curve

The fatigue life of the material was examined at several stress amplitudes using Type B specimens.

Figure 2 indicates the relation between the stress amplitude, σ_a , and the number of stress cycles to failure, N_f . The fatigue limit of the material was 235 MPa.

Slip bands

An example of slip bands formed in tension tests is shown in Figure 3 and those formed in fatigue tests are shown in Figure 4a and b. The slip bands in Figure 4a and b formed in the same specimen. The stress for Figure 3 was 500 MPa, which is just below the tensile strength, and the stress amplitude for Figure 4 was 216 MPa for 3.00×10^5 cycles, which is just below the fatigue limit. The scanning area of these observations was $20 \mu\text{m} \times 20 \mu\text{m}$. These figures clearly show the difference between surface morphology for monotonically loaded tension specimens and those in fatigued specimens. The slip band surfaces observed in the monotonically loaded tension specimen give the appearance of a sheared deck of cards. In fatigue tested

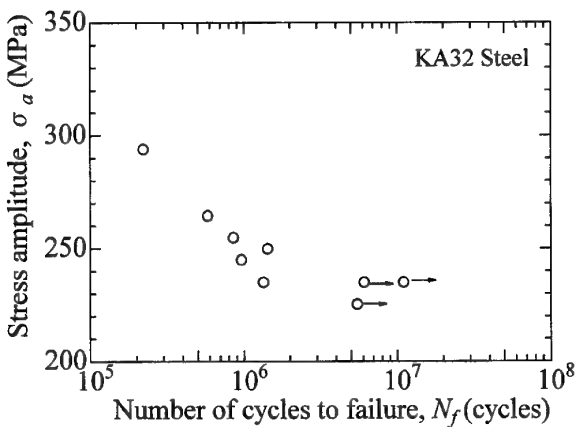


Figure 2 S-N curve

specimens, however, mountainous extrusions can be observed on an otherwise flat surface. Both figures show that slip bands are blocked by grain boundaries. For the slip bands shown in *Figure 4a*, the angle between the slip line at the surface and the loading direction was 82° , and the height of the slip bands is about 400 nm. For the slip bands shown in *Figure 4b*, the angle was 50° and the height of the slip bands is about 200 nm. These results suggest that the surface roughness induced by slip depends on the slip direction. The surface roughness induced by the slip system with a trace at the surface of about 90° from the loading direction is greater than that for an in-plane slip system that has a trace at the surface of about 45° from the loading direction.

Figure 5 explains the relation between surface roughness and slip direction, where the cube ABCDEFGO indicates a small region of a specimen that is located adjacent to the surface⁵. In the figure, plane ABCD represents the specimen surface, plane CKLM represents the slip plane, and the y-axis and arrow QH represent the loading direction. Line CK is the slip trace at the specimen surface and line ST is on the slip plane and parallel to line KC. Arrow HR is the slip direction on the slip plane, and arrow HP is the normal of the slip plane. The surface roughness induced by the slip is $s \sin \beta \cos \alpha'$, where s is the slip distance in the HR direction, α' is the angle between the normal to the surface and the trace of the slip band on the plane that is perpendicular to the surface and parallel to the loading axis, and β is the angle between the normal to the surface and the slip traces on the surface (see *Figure 5*). When $\angle QHR = \angle PHQ = 45^\circ$, the resolved shear stress along the slip direction takes the maximum value, and the following relation should be satisfied:

$$\cos \beta = \sqrt{2} \cos \alpha \quad (1)$$

For $\alpha = 90^\circ$, the value of β should be 90° , which gives the maximum roughness of the surface for a given slip distance. For $\alpha = 45^\circ$, the value of β should be 0° and no slip step forms on the specimen surface. These considerations are in agreement with the findings mentioned above.

Along the slip plane where the resolved shear stress takes the maximum value, the following equation should be satisfied:

$$\cot^2 \alpha + \tan^2 \alpha' = 1 \quad (2)$$

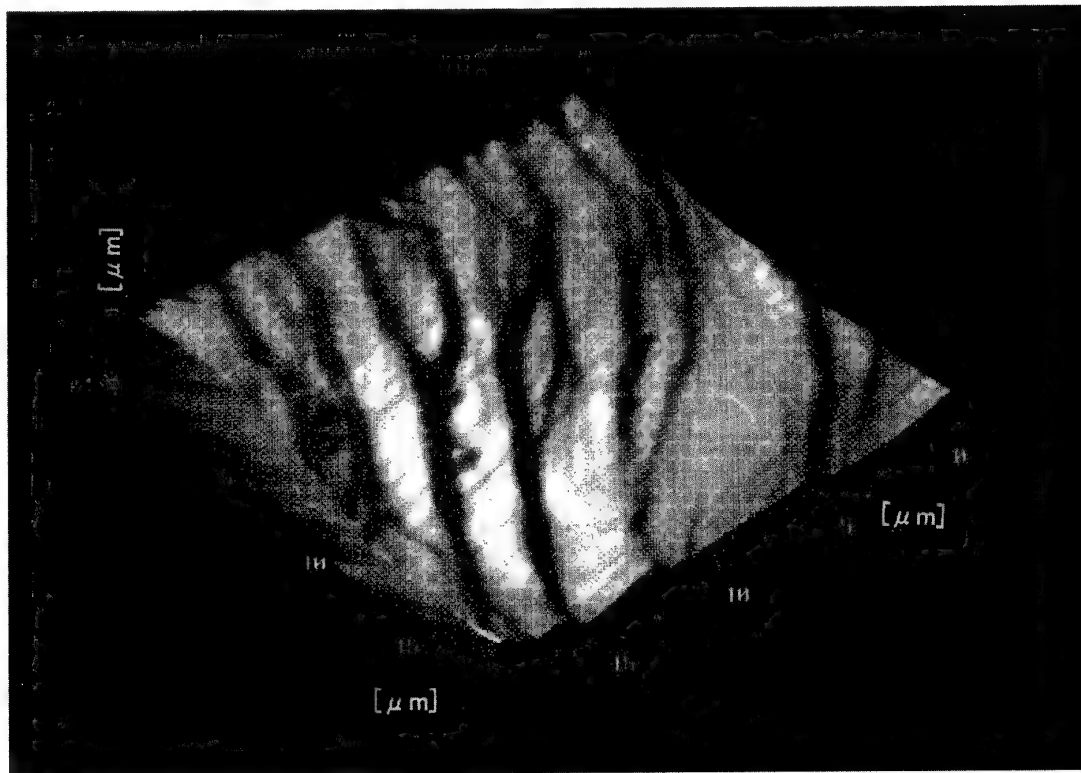
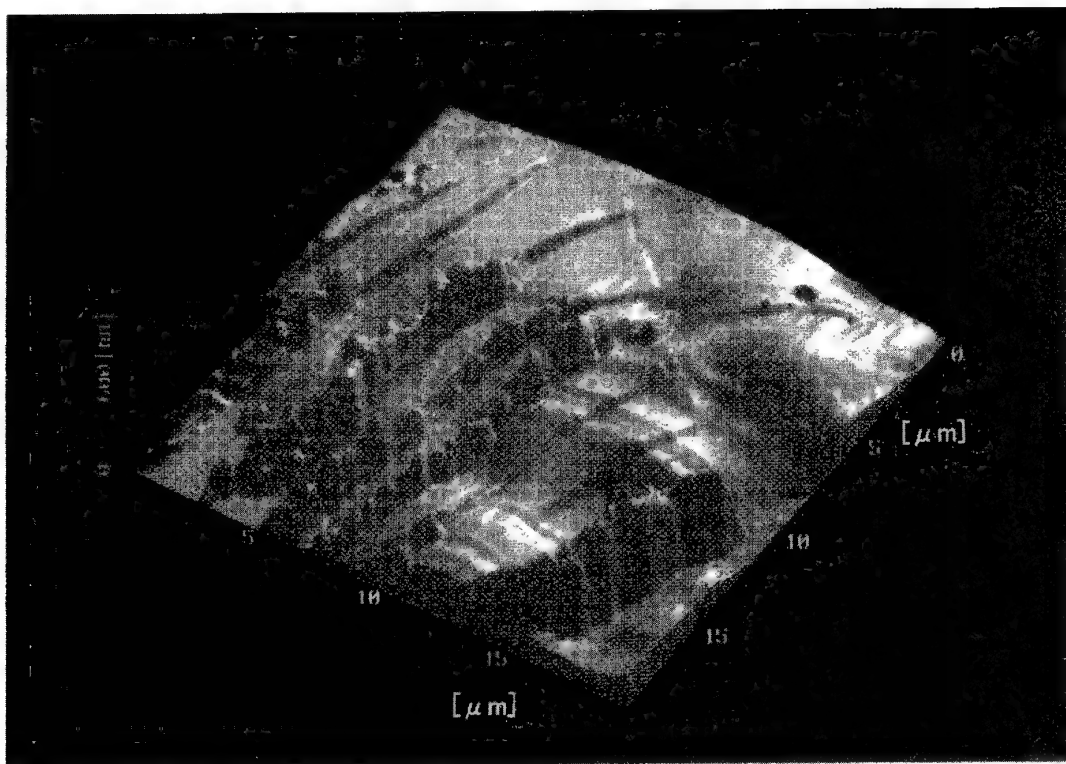
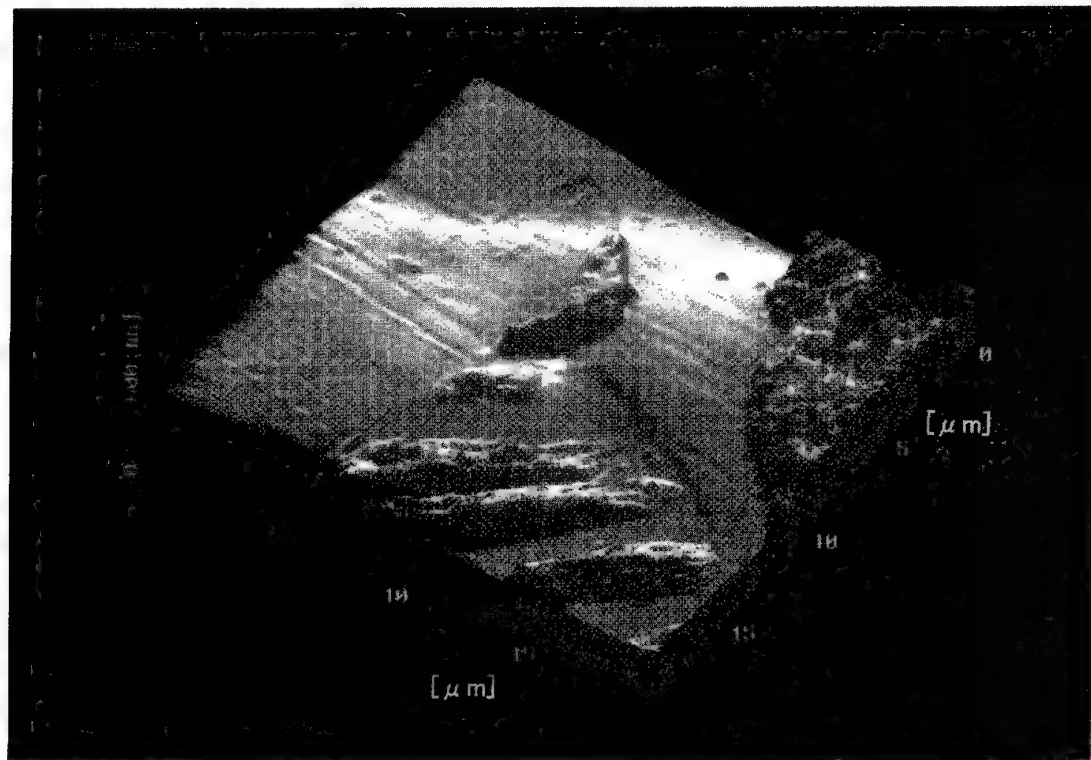


Figure 3 Slip bands observed in monotonically loaded tension specimens (area 20 μm \times 20 μm)



(a)



(b)

Figure 4 Fatigue slip bands (area $20 \mu\text{m} \times 20 \mu\text{m}$)

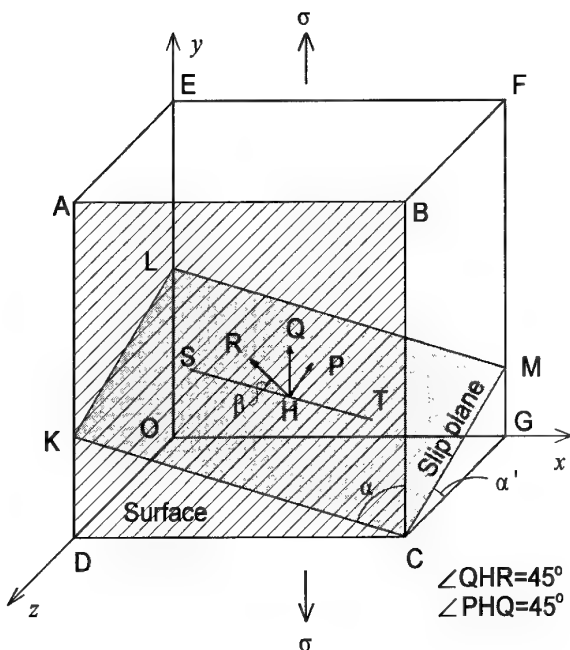


Figure 5 Slip plane and direction relative to stress axis and surface

By using 0.04%C steel, Tanaka *et al.* examined the relation between angles α and α' for microcracks just after initiation⁵. As seen in Figure 6, where σ_{wo} is the fatigue limit, their results agree with Equation (2), and show that fatigue cracks initiated along the slip

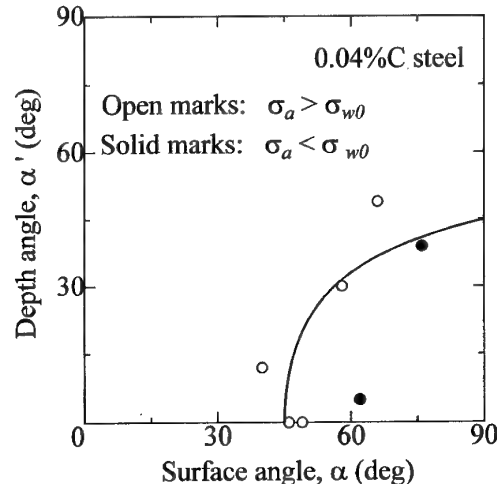


Figure 6 Crack angle relative to stress axis and surface normal

plane where the resolved shear stress took the maximum value but the angle between the crack trace on the surface and the loading axis was not necessarily 90° . Tanaka *et al.* reported the same relation for 3%Si-Fe⁶. These observations indicate that the stress concentration due to surface roughness is not responsible for the crack initiation.

It has been believed that intrusion and extrusion are formed at the same time⁷. In the present observation, however, extrusions are observed on the surface, but no intrusions were formed in the slip bands.

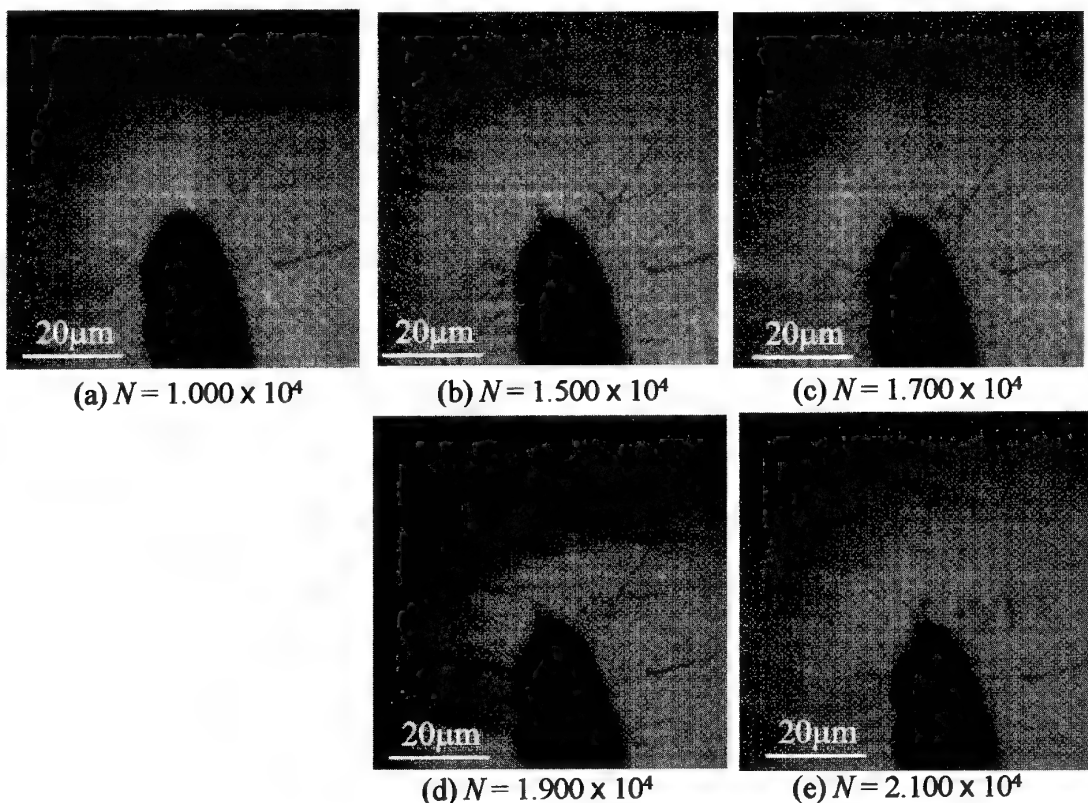


Figure 7 Optical micrographs of fatigue crack initiation process

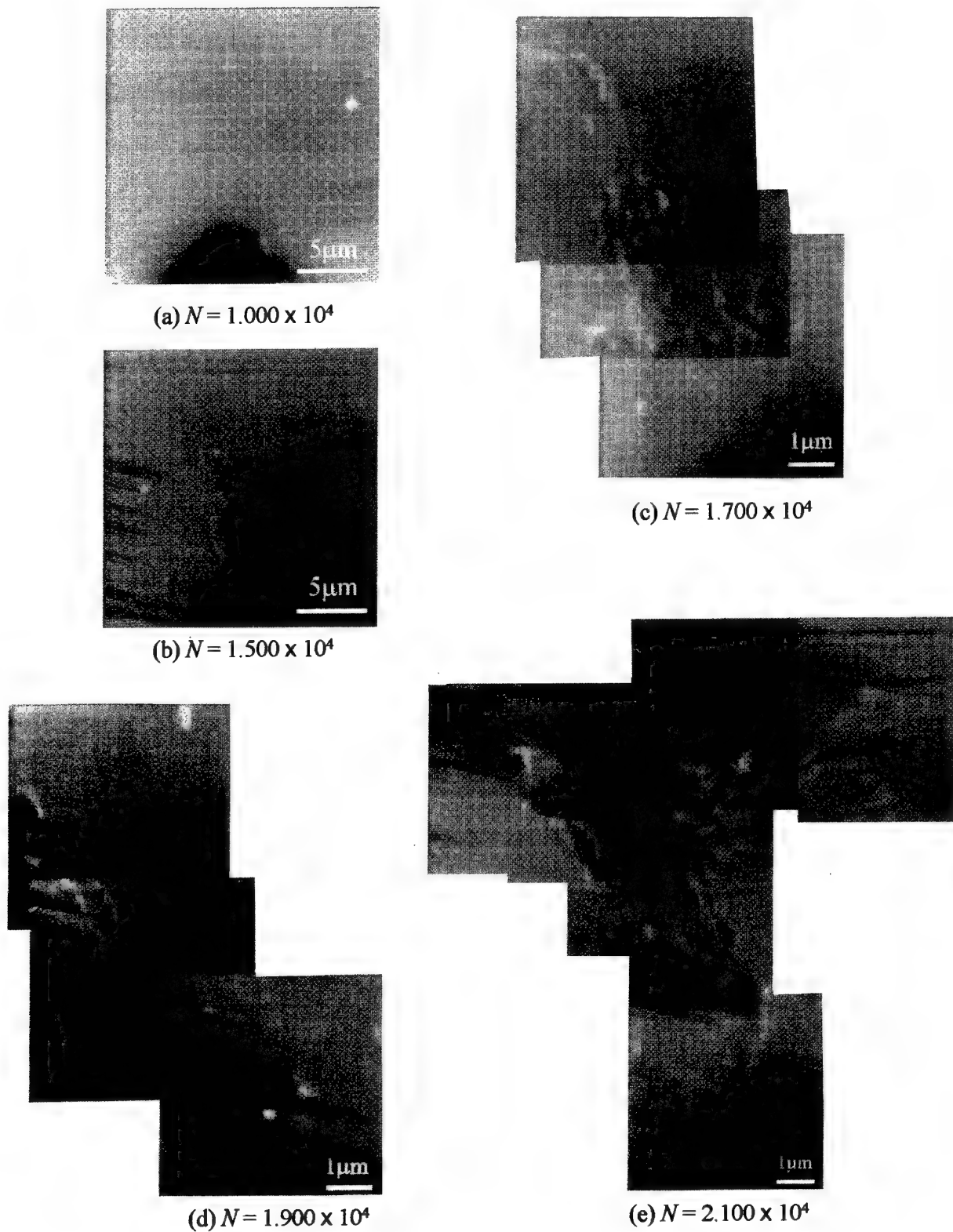


Figure 8 AFM images of fatigue crack initiation process

Microcrack initiation process

By using Type D specimen, the fatigue crack initiation process was observed at the nominal stress amplitude, σ_a , of 196 MPa. Figure 7 indicates the

process observed with an optical microscope, and Figures 8 and 9 show the same area observed by AFM. When the number of cycles, N , was 1.0×10^4 , no apparent indication of fatigue damage was observed by OM. By AFM, however, speckle type extrusions

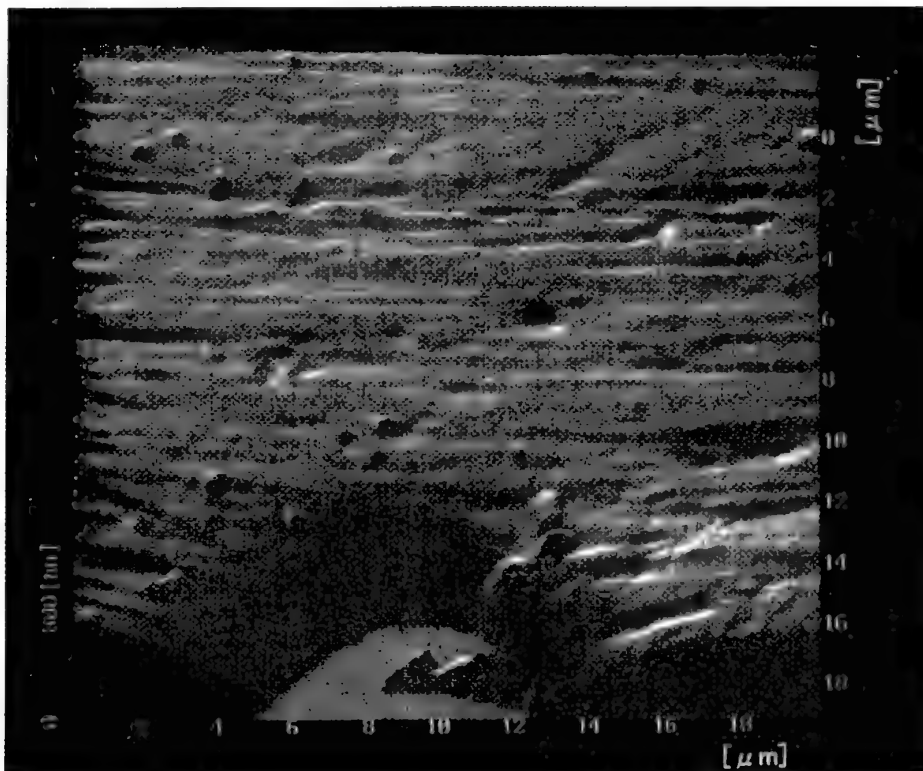
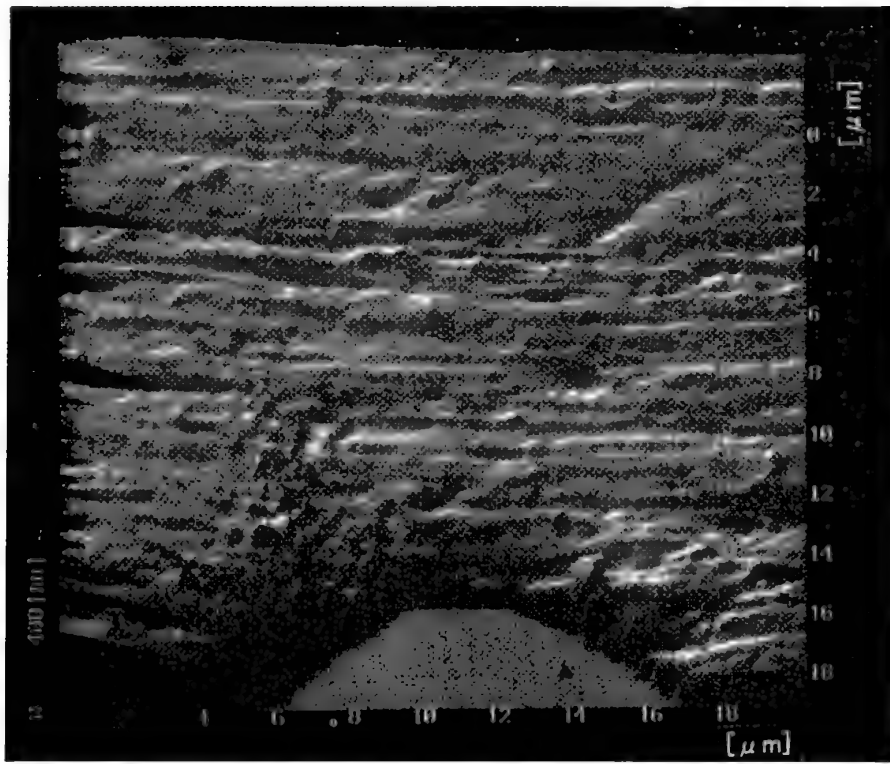
(a) $N=1.000\times 10^4$ (b) $N=1.500\times 10^4$

Figure 9 Axonometric view of AFM images of fatigue crack initiation process (area $20 \mu\text{m} \times 20 \mu\text{m}$)

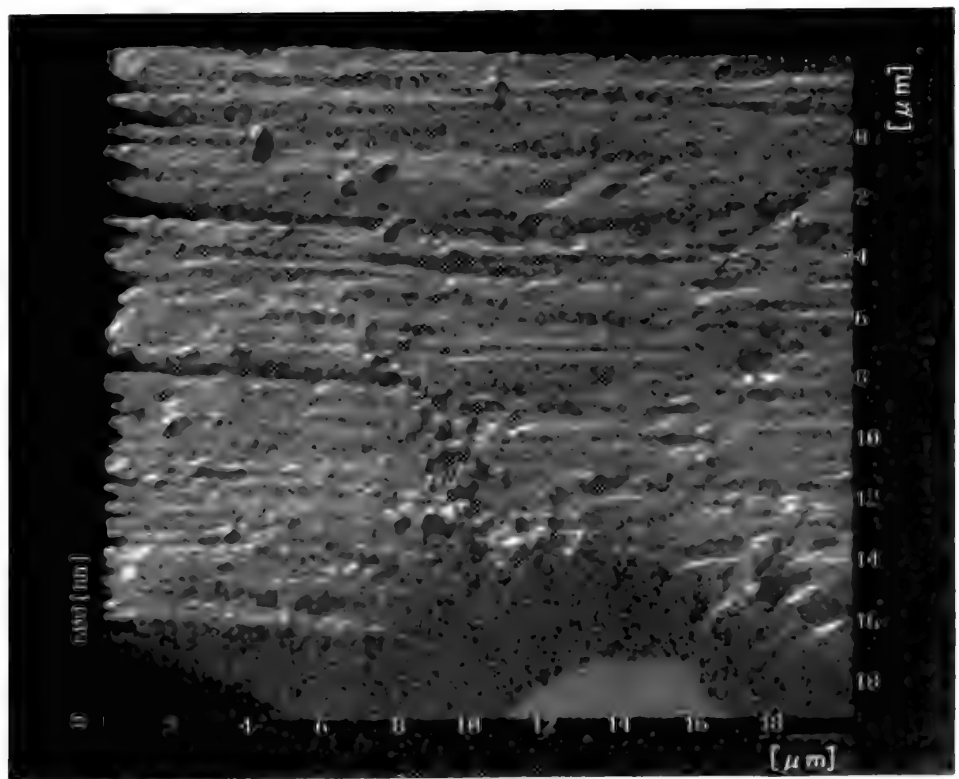
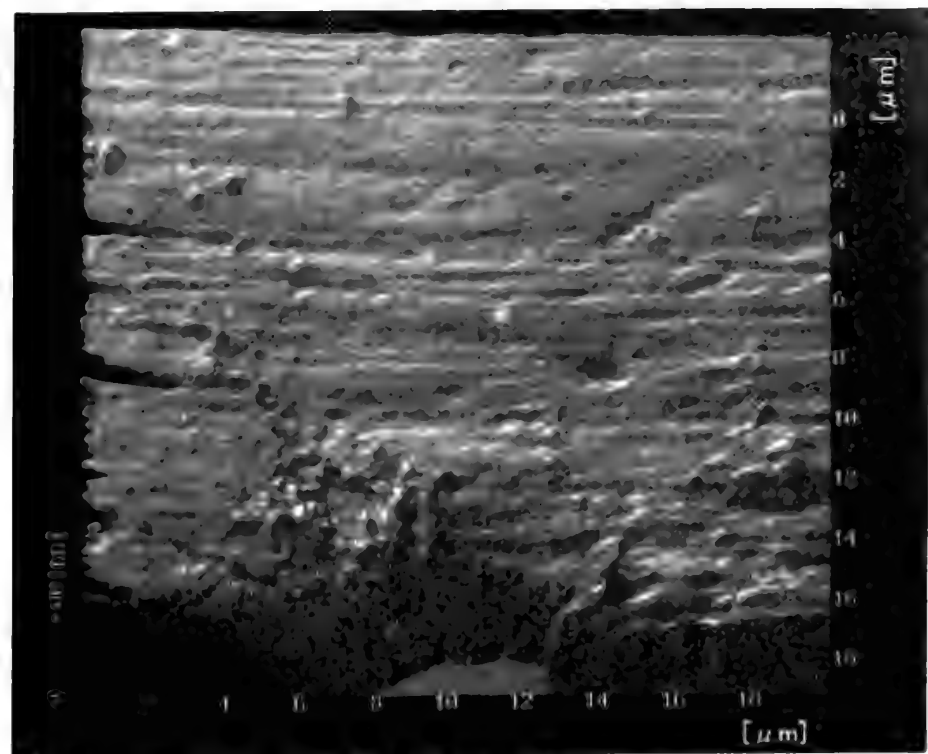
(c) $N=1.700\times 10^4$ (d) $N=1.900\times 10^4$

Figure 9 Continued

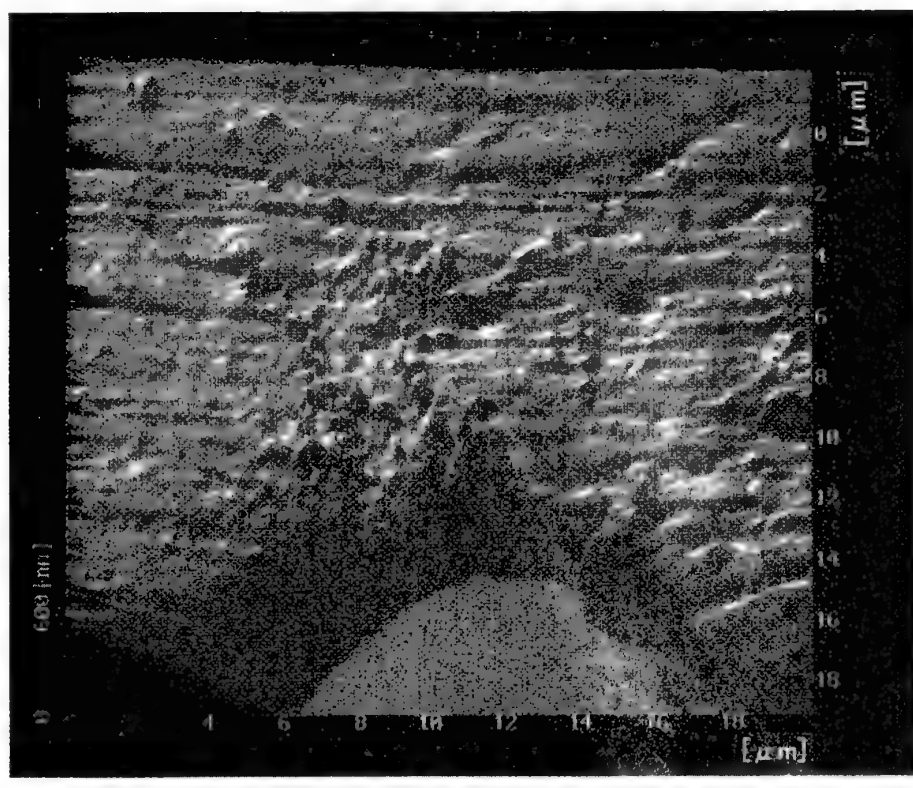
(e) $N=2.100 \times 10^4$

Figure 9 Continued

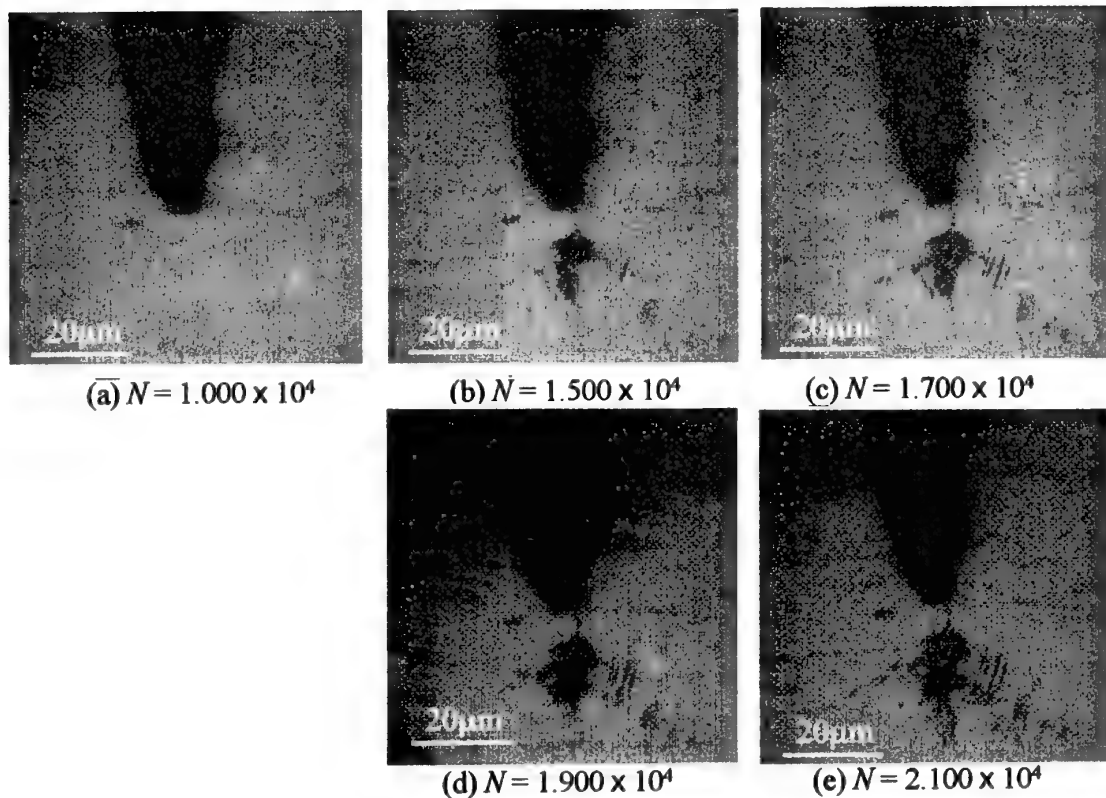


Figure 10 Optical micrographs of fatigue crack initiation process

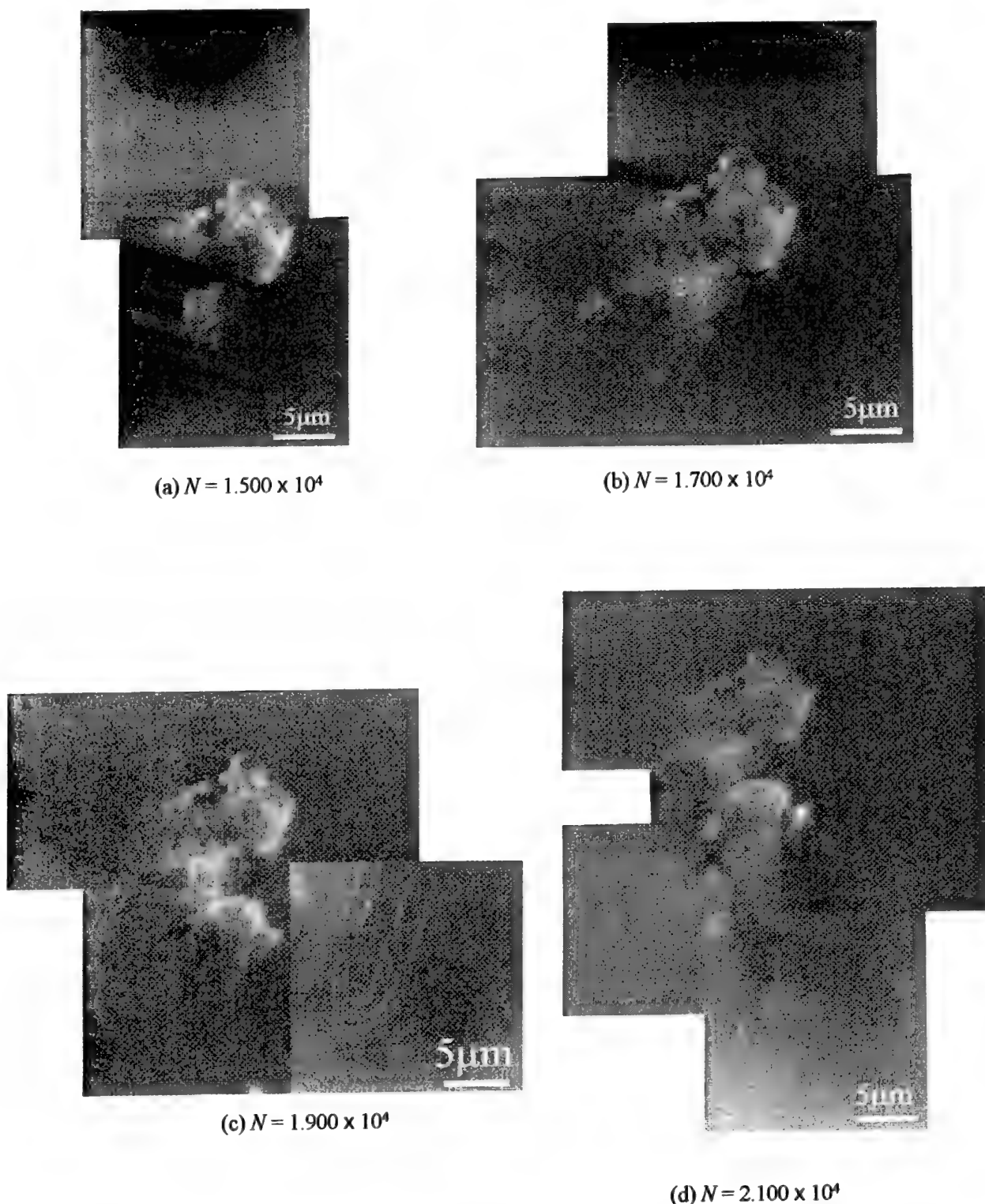


Figure 11 AFM images of fatigue crack initiation process

can be found, but it is not clear whether these speckles came from slip deformation or not. After $N = 1.5 \times 10^4$ cycles, the growth of slip bands can be observed by both OM and AFM, but it is difficult to distinguish between slip bands and cracks by OM, and it is also difficult to determine when cracks initiated. In the

AFM images, however, cracks can be distinguished from the slip bands. With the number of loading cycles increased, the number of speckle type extrusions increased, and they arranged along lines. These slip bands are not similar to those observed in a smooth specimen. It was reported that this kind of extrusion

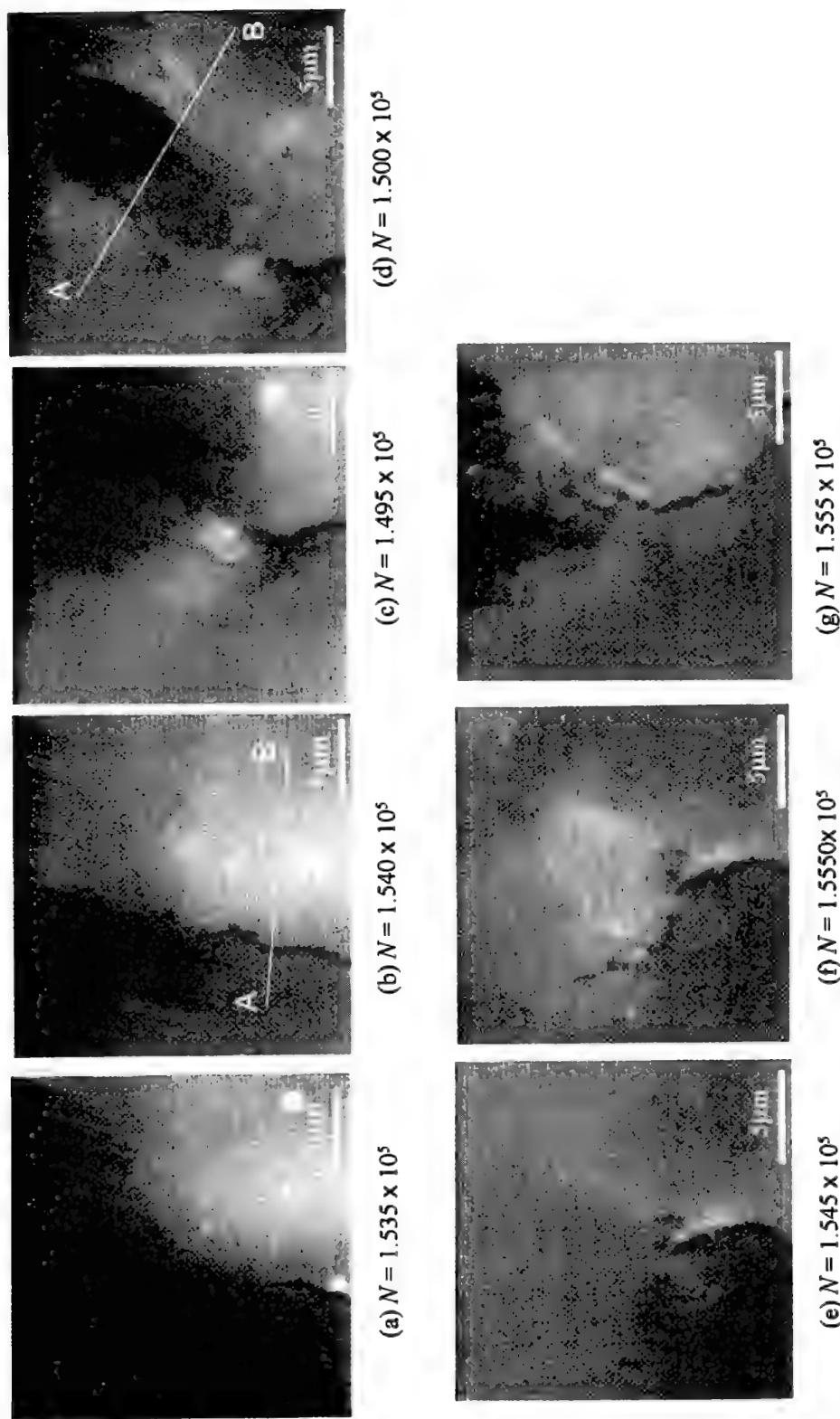
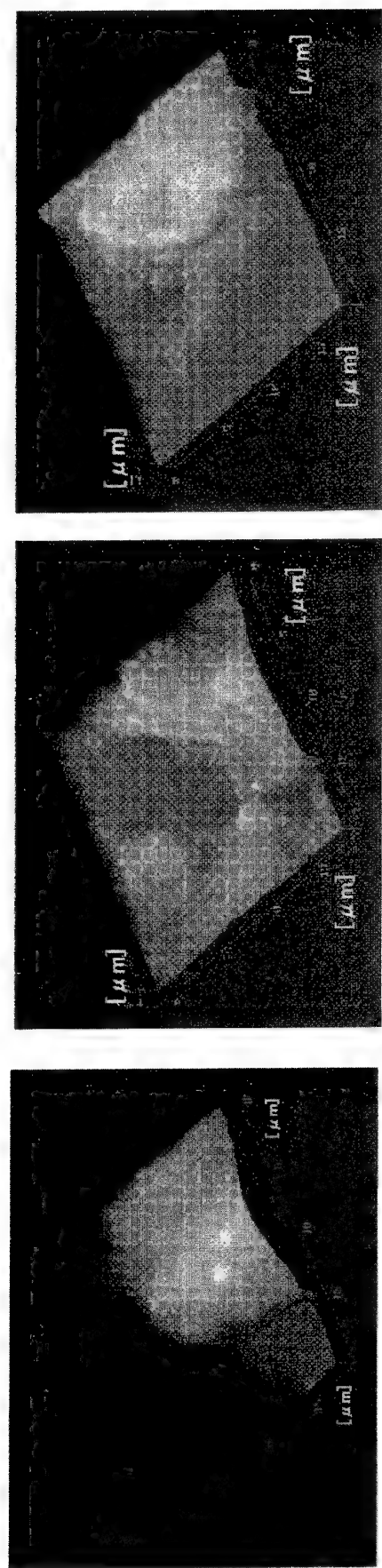
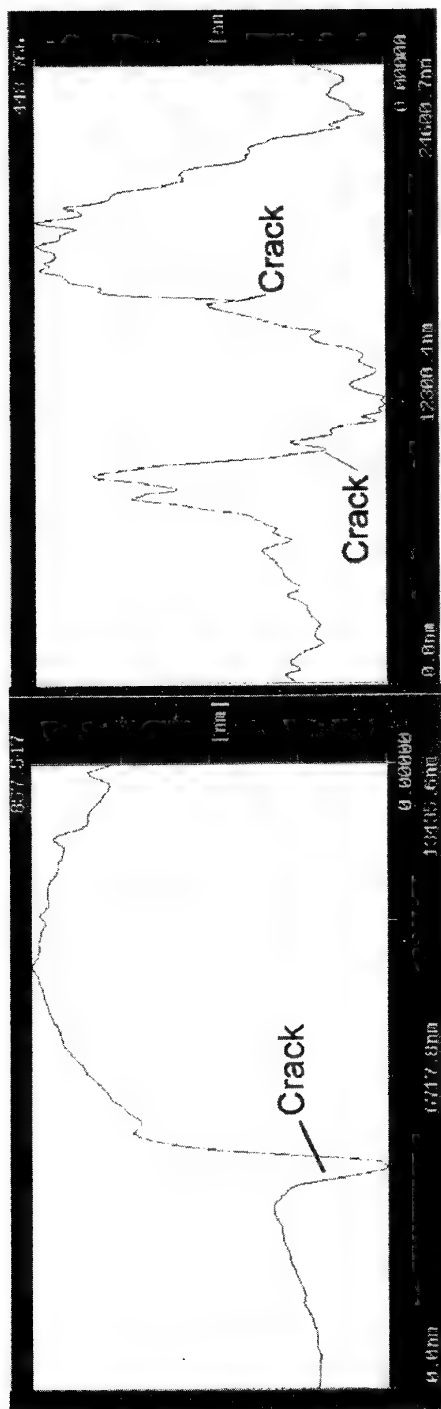


Figure 12 Deformation around microcracks



(a) $N = 1.540 \times 10^5$ (Fig. 12(b)) (b) $N = 1.500 \times 10^5$ (Fig. 12(d)) (c) $N = 1.555 \times 10^5$ (Fig. 12(g))

Figure 13 Axonometric view of AFM images of fatigue crack propagation process (area $20 \mu\text{m} \times 20 \mu\text{m}$)



(a) $N = 1.540 \times 10^5$ (A-B section in Fig. 12(b)) (b) $N = 1.500 \times 10^5$ (A-B section in Fig. 12(b))

Figure 14 Cross-sections of microcracks

was observed in torsion loaded fatigue test specimens where only in-plane slip can operate⁹. When the value of N was 1.7×10^4 , no crack was observed. A crack was found when the value of N was 1.9×10^4 .

The fatigue damage around the other tip of the notch is shown in Figures 10 and 11. In this case, no crack and slip bands were observed at $N = 1.0 \times 10^4$. At $N = 1.5 \times 10^4$, slip bands and a crack of grain size length were observed. The slip bands are considered to define the crack tip plastic zone. No indication of crack initiation was observed in the OM and AFM images.

In both cases, cracks much shorter than the grain size were not found. Even just after the initiation, every crack has length longer than the grain size. By considering the observation together with the direction of initiated cracks mentioned above, the damage accumulation model, for example, proposed by Tanaka and Mura⁸, is supported for the crack initiation process of the present material. The model proposes that fatigue cracks of grain size length may initiate when the strain energy accumulated along the slip bands reaches a critical value.

Microcrack propagation process

Growth behaviors of microcracks just after initiation observed by using Type C specimen are shown from Figures 12–14, where Figure 12 shows top views of the surface, Figure 13 shows axonometric views of the surface, and Figure 14 indicates the cross-sections at places shown by lines A–B in Figure 12b and d. It is clear that there are big differences in height across the crack, and this difference was also found around the crack tip. These figures indicate that microcracks propagate not only under combined conditions of Mode I and Mode II, but the Mode III component also exists for these cracks.

In Figures 12d and 13b, the crack branched to two cracks. Each crack tip propagated along the grain boundary. The cross-section of the crack is shown in Figure 14b. Side grains of the two cracks are subjected to high deformation, but the deformation of the grain between two cracks is small.

When the crack tip approaches the triple point of the grain boundary (Figure 12e), its growth rate decreases. After the crack tip passes through the triple point, it turns to the left (Figure 12f and 12g), and its growth rate approaches the steady state value. Figure 13c is an axonometric view of Figure 12g. In this case, the deformation of grains located on both sides of the cracks was small, but the right side grain moves up to form a plateau (see Figure 13c).

Practical application and future tasks

The observation of fatigue damage on an atomic scale may be useful not only for scientific research, but also for the inspection of structures and machine components because we can detect the very early

stages of fatigue damage by scanning atomic force microscopy. For this approach, stand-alone type SPMs, including AFMs, may be useful.

For further understanding, quantitative measurement of growth behavior in fatigue slip bands during fatigue processes, and the observation of slip motion in each fatigue cycle, will be carried out. We are planning to make a small fatigue testing machine which can be set in the SPM system.

CONCLUSIONS

The fatigue crack slip band, fatigue crack initiation process, and growth behavior of fatigue microcracks in structural steel were observed both by optical microscopy and scanning atomic force microscopy. The following results were obtained.

1. Scanning atomic force microscopy is more appropriate to detect fatigue crack initiation processes than optical microscopy.
2. In fatigue slip bands, extrusions were observed but intrusions were not detected. Large extrusions were found in slip bands with traces at the specimen surface almost perpendicular to the loading axis.
3. No microcracks smaller than the grain size were found. Their size just after initiation was comparable to the grain size. They propagated under mixed mode conditions of Mode I, Mode II, and Mode III.

ACKNOWLEDGEMENTS

Support of this work by Grant-in-Aid for Developmental Scientific Research (B) (Project No. 07555624) by the Japanese Ministry of Education, Science, Sports and Culture is gratefully acknowledged. The authors also express their appreciation to Sumitomo Metal Industries, Ltd for providing the material used in this study.

REFERENCES

- 1 Sakurai, T., Kobayashi, A. and Sakai, A., *Journal of Japan Institute of Metals*, 1986, **25**, 821–831.
- 2 Komai, K., Minoshima, K. and Itoh, M., *Journal of Materials Science, Japan*, 1994, **43**, 336–342.
- 3 Ishii, H., Yamanaka, S. and Tohgo, K. 7th International Conference on Mechanical Behaviour of Materials, 1995, pp. 367–368.
- 4 Matsuoka, S., Sumiyoshi, H. and Ishikawa, K., *Transactions of the Japan Society of Mechanical Engineers*, 1990, **56A**, 2091–2097.
- 5 Tanaka, K., Nakai, Y. and Maekawa, M., *Journal of Materials Science, Japan*, 1982, **31**, 376–382.
- 6 Tanaka, K., Hojo, M. and Nakai, Y. In *Fatigue Mechanisms: Advances in Quantitative Measurement of Physical Damage*, eds J. Lankford, D. L. Davidson, W. L. Morris, and R. P. Wei. ASTM STP 811 ASTM, Philadelphia, 1983, p. 207.
- 7 Forsyth, P. J. E., *Journal of the Institute of Metals*, 1958, **87**, 10.
- 8 Tanaka, K. and Mura, T., *Journal of Applied Mechanics, Transactions ASME*, 1981, **48**, 97–103.
- 9 Nakazawa, H. and Honma, H. *Fatigue Strength of Metals*, Yokendo, Tokyo, 1982, p. 10.



PII: S0142-1123(97)00025-X

Assessment of fatigue load spectrum from fracture surface topography

Takao Kobayashi, Donald A. Shockey, Charles G. Schmidt and Richard W. Klopp

Department of Metallurgy and Fracture Mechanics, SRI International, 333 Ravenswood Avenue, Menlo Park, CA 94025, USA

The possibility of deducing load spectrum parameters from fatigue failure surfaces is explored by applying innovative, three-dimensional topographic characterization and analysis techniques to failure surfaces in aluminum sheet. Precise, high-resolution elevation maps of fracture surfaces were obtained using confocal optics scanning laser microscopy. Elevation power spectral density curves resulting from a fast Fourier transform of the elevation data appear sensitive to stress intensity range and environment. A conjugate fracture surface matching procedure, FRASTA, can detect and may provide a way to quantify overloads. © 1998 Elsevier Science Ltd.

(Keywords: fractography; Fourier analysis; FRASTA)

INTRODUCTION

The growth history of a fatigue crack is governed in large part by load spectrum and environment. Thus, when a structural component fails under oscillatory loads, the failure analyst attempting to establish the cause of failure often seeks to learn the service conditions. Unfortunately, a record of load spectrum is not usually available.

The load spectrum experienced by aircraft, for example, depends on such things as pilot maneuvers and wind gust conditions, which are not easily monitored. Information from pilot reports, on-board load sensors, accelerometers, and strain gages is unreliable. Moreover, even if a flight spectrum could be measured for an aircraft, the load spectrum in the area where the failure occurred (such as around a rivet hole or joint) could be quite different and is not straightforwardly determinable by finite element computations¹.

However, it may be possible to deduce the load spectrum (in particular, the local load spectrum) by examining the fracture surfaces of the failed part or a part containing a crack, because the important loads in a spectrum are those that affect the crack process. By propagating the crack, by blunting the crack tip, or by retarding crack growth, these loads should manifest themselves somehow on the fracture surfaces. Fracture surfaces, therefore, may act as a load spectrum gage, providing details of the maximum and minimum loads, their frequency and sequence, and the occurrence and severity of overloads, as well as changes in environment.

However, a way is needed to read the fracture

surfaces and interpret the features in terms of the important parameters of the load. A procedure for deducing the stress intensity range, ΔK , already exists. When fatigue striations can be detected, striation spacing is sometimes correlated with crack growth rate^{2,3}, and growth rate is empirically related to ΔK by the Paris equation⁴. More recently, a relationship was reported between the striation height-to-spacing ratio and R , the ratio of minimum to maximum load in a load cycle^{5,6}. Combining these relationships suggests that the maximum and minimum loads of the spectrum are obtainable from the fracture surfaces.

In practice, however, the use of fatigue striations in failure analysis is often difficult⁷. In many cases, striations or regions containing enough uniform striations for meaningful analysis cannot be found. Moreover, the crack growth rate deduced from striations can differ significantly (by as much as a factor of 20) from the measured macrocrack growth rate. Nevertheless, it seems likely that valuable information regarding crack growth rate, load spectrum, and environmental conditions is encrypted in the topography of the fracture surfaces.

Better techniques are needed to extract this information. This paper explores several possibilities. We describe two techniques that can characterize fracture surface topography in three dimensions, at high-resolution, and with reasonable speed: a fast Fourier transform analysis of the topography for specifying a signature curve reflective of causative failure conditions; and a conjugate fracture surface matching procedure, FRASTA, for detecting and estimating the magnitude of overloads.

FATIGUE EXPERIMENTS AND FRACTURE SURFACE TOPOGRAPHY CHARACTERIZATION

To produce fracture surfaces for topographic analysis, we performed fatigue experiments on center-cracked panel specimens of 1 mm thick 2024-T3 aluminum sheet typical of that used for aircraft fuselage skin. To investigate the effect of stress intensity range, ΔK , and maximum stress intensity, K_{\max} , a fatigue test was performed in which the crack was propagated several millimeters at a ΔK of 4 MPa $\sqrt{\text{m}}$ and a K_{\max} of 10 MPa $\sqrt{\text{m}}$, and then an additional several millimeters at a ΔK of 8 MPa $\sqrt{\text{m}}$ and a K_{\max} of 20 MPa $\sqrt{\text{m}}$. To investigate the effect of environment, a specimen was loaded under conditions similar to those of the test performed under the low ΔK , low K_{\max} condition, but in vacuum until the crack grew about 1 mm, and then in air for the remainder of the crack growth. To investigate overload effects, a test was performed in which overloads of several magnitudes were applied during crack growth. In all cases, the stress ratio, R , was constant at 0.6 and the load cycle frequency was 5 Hz.

After specimen failure, elevation maps of selected areas of the conjugate fracture surfaces were made using the FRASTAscope, a system we developed consisting of a confocal optics scanning laser microscope[†] (COSLM), a precision, computer-controlled x - y - θ stage,[‡] and computer programs to control data acquisition, manipulation, and display. When a 50 \times objective is used, the FRASTAscope surveys a rectangular fracture surface area of 223 $\mu\text{m} \times$ 149 μm by optically scanning in the x -direction and mechanically stepping in the y -direction, recording the strength of the signal for each pixel in a 600 \times 400 pixel array. After completing the survey of the initial plane, the specimen is raised in the z -direction by 1/256 of the elevation range of the rectangular area and resurveyed to measure the new signal strength for each pixel in the array. The procedure of incrementally raising the specimen, surveying the area, and recording signal strength is repeated until the elevation range is traversed.

Because of the very short depth of focus of the confocal optics (60 nm), the strength of the signal from a pixel is very sensitive to the distance of the surface in the pixel from the focal plane. The height of the area in each pixel is the z -position at which the signal strength is maximum. Thus, the maximum signal strength position as a function of x and y provides an elevation map of the rectangular area. The x - y - z characterization requires between 10 and 100 s, depending upon the fracture surface topography and reflectivity. At the most sensitive setting, in-plane and out-of-plane resolution is 0.25 μm and 60 nm, respectively. Larger areas of fracture surfaces are characterized by abutting the elevation data from adjacent areas. Depending on the size of the area one desires to examine, the abutting operation (which is also software controlled) can take several hours.

An alternative procedure for characterizing fracture surface topography in three dimensions is stereoscopy, in which stereo views are taken with the SEM and the

digitized elevation data are evaluated with a software program[§]. The SEM procedure can characterize a fracture surface at higher magnification than the COSLM procedure and thus is useful for analyzing fracture surface details. Furthermore, by using low magnification, say 10 \times , larger areas (125 mm^2) can be analyzed at high data density in about 30 to 40 s.

Both methods capture the elevation data in digital form. The data can be displayed in gray-scale images and in three-dimensional perspective plots.

FOURIER ANALYSIS OF FRACTURE SURFACE TOPOGRAPHY

Figure 1 shows gray-scale images and perspective views of conjugate areas from the low and high ΔK and K_{\max} surfaces obtained with the COSLM-based FRASTAscope. The shades of gray indicate relative height – lighter areas are higher; darker areas are lower.

Figure 1 provides a physical representation of the topographies that is relatively easy to grasp. However, differences in the topographies arising from differences in ΔK and K_{\max} are not easily discerned. To obtain an alternative representation of the topography, a one-dimensional fast Fourier transform operation was applied, row by row, to 400 rows of 400 elevation data points. *Figure 2* shows the ‘power spectral density’ curve obtained by averaging the 400 rows. In the figure, the sum of the squares of the real and imaginary components of the elevation amplitudes normalized by a crack extension distance is presented as a function of spatial frequency or roughness wavelength, rather than as a function of position (as in *Figure 1*). The power spectral density curve (a name that has its origins in Fourier applications to electrical signals) might be more aptly called the elevation power spectral density (EPSD) when topographic information is analyzed.

The EPSD curves in *Figure 2* for the fracture surfaces produced under low ΔK and K_{\max} differ measurably from those produced at high ΔK and K_{\max} . Thus, EPSD characterization discriminates these important load parameters. Moreover, the EPSDs of conjugate surfaces are nearly identical, suggesting that topographies produced under identical conditions are unique and reproducible.

Figure 3 shows the EPSD curves for the specimen fatigued in vacuum and then in air. A small but distinct difference is apparent above a spatial frequency of 3 \times 10⁴ m^{-1} (or wavelength less than 30 μm). Furthermore, the EPSD curve for the area fatigued in air closely matches the curve for the low ΔK area obtained on the previous specimen, demonstrating specimen-to-specimen reproducibility of fracture surface topography generated under similar conditions.

Thus, fracture surface topography appears to be sensitive to loading and environment conditions, and the EPSD curve appears to be a characteristic signature of the topography that reflects these conditions. Moreover, the EPSD is obtained objectively and efficiently, and may be more representative of macrocrack behavior than fatigue striations.

COMPARISON OF CONJUGATE FRACTURE SURFACE TOPOGRAPHS

In a third fatigue experiment, overloads of 3.3, 5.8, 8.4, and 11.8 MPa $\sqrt{\text{m}}$ were applied during crack growth, as

[†]Model 1LM21W, Lasertec Corporation, Yokohama, Japan.

[‡]6 in \times 6 in HighLine Dual-Axis Stage, Pacific Precision Laboratories, Inc., Chatsworth, CA.

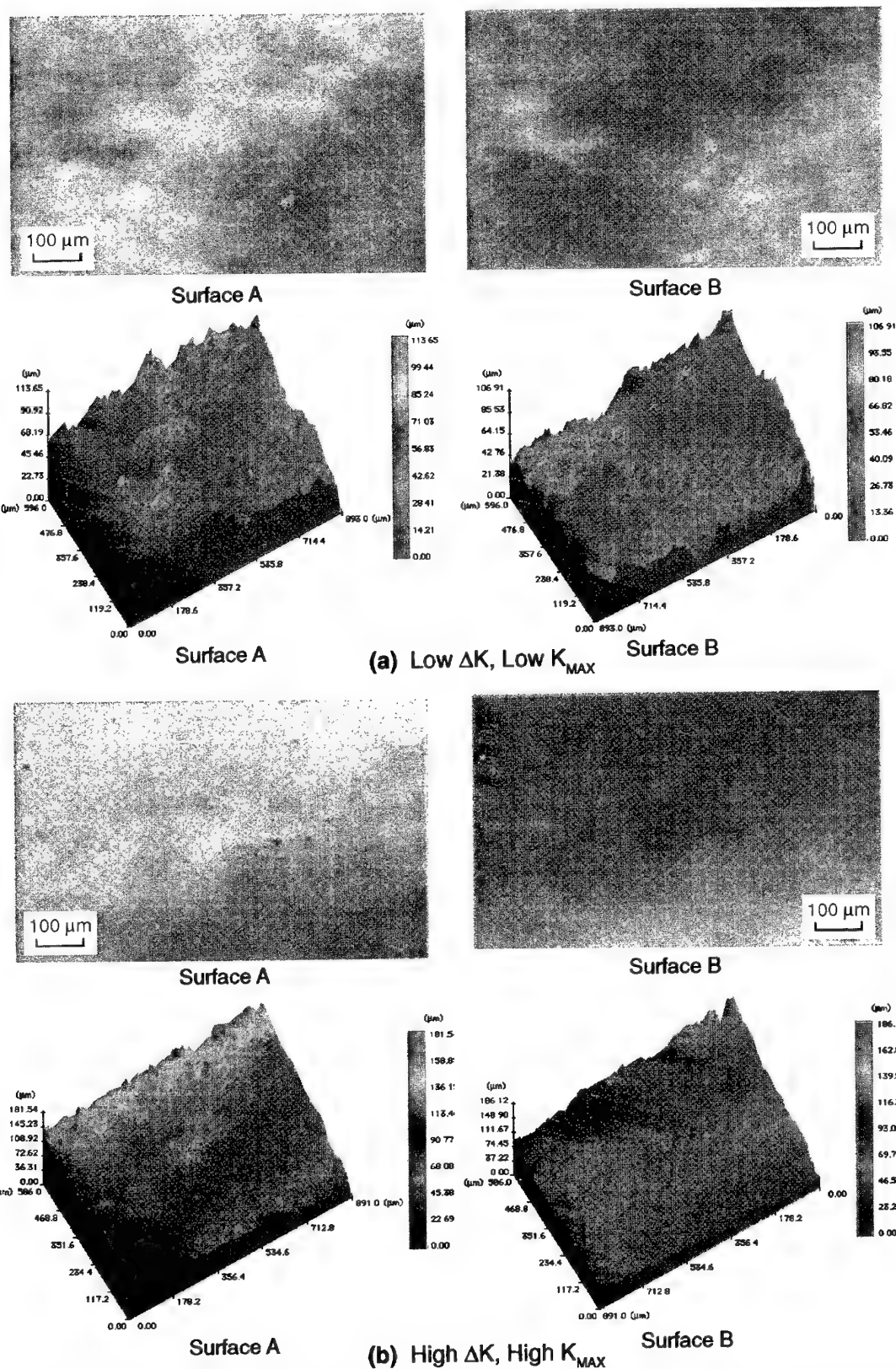


Figure 1 Gray-scale images and perspective views of the topographies of conjugate fracture surfaces produced under low and high ΔK and K_{max} fatigue conditions

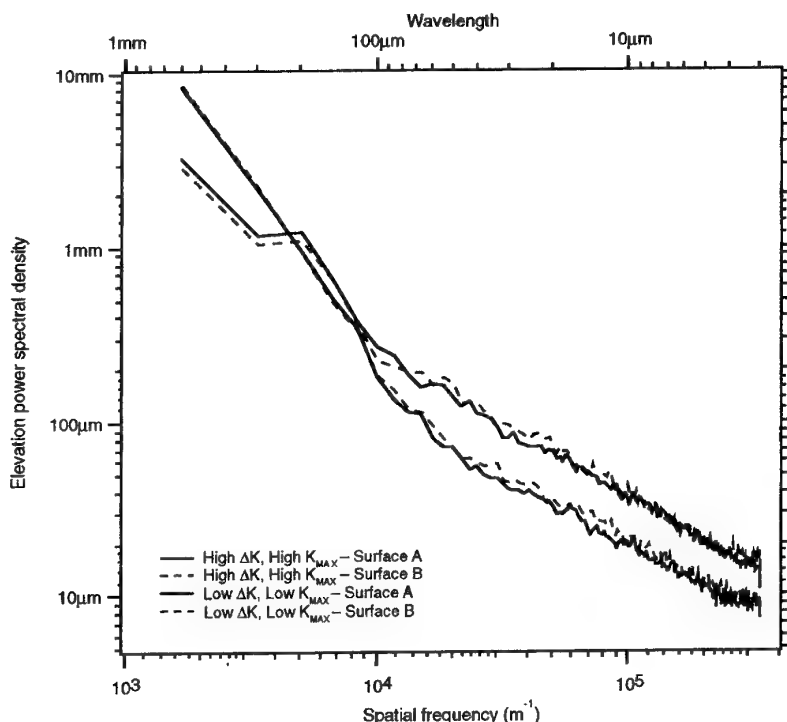


Figure 2 Fast Fourier transform elevation power spectral density curves for conjugate fatigue failure surfaces produced under high and low ΔK and K_{max} loading conditions

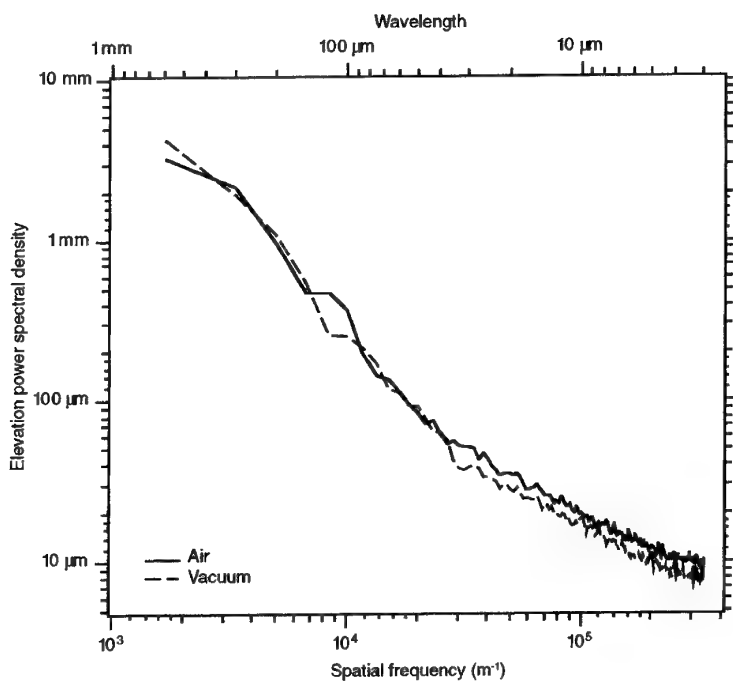


Figure 3 Elevation power spectral density curves for fatigue surfaces produced in air and vacuum

shown in *Figure 4*. The topographies of a 1.0 mm wide strip of the conjugate fracture surfaces in the center of the specimen were quantified with a COSLM in the crack growth direction. With the aid of computer software, the conjugate topographs were positioned and aligned with respect to each other to approximate the configuration of the fracture surfaces during the fatigue

test, as shown schematically in *Figure 5*. A cross-sectional view of the intersecting topographs depicts the crack in profile, while a projection of the crack front configuration is obtainable in a plan view. Damage in the process zone ahead of the crack front is depicted in both views. Areas where the topographs overlap are shown in black and are interpreted as

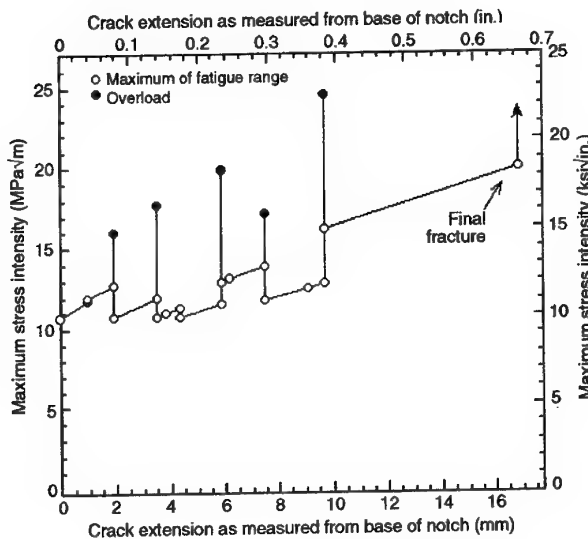


Figure 4 Maximum stress intensity versus crack length for fatigue experiment showing overloads

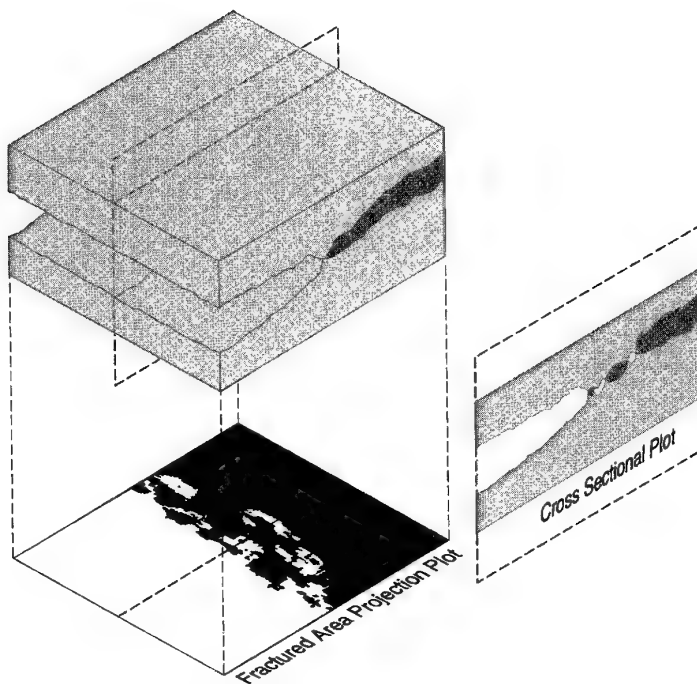


Figure 5 Reconstruction of the crack front configuration by superimposing fracture surface topographs

areas where the material is unbroken; areas where the topographs are separated are shown in white and are taken as fractured material. The procedure of comparing fracture surface topographs to analyze fractures is known as FRASTA (fracture surface topography analysis) and has been described elsewhere^{9,10}.

By displacing the topographs normal to the crack plane, the line of intersection moves and crack growth is simulated. Figure 6 is a series of plan projection views of the crack at increasing topograph displacements. The transition between the white area and the black area is a zone, rather than a line, and results from our choice of a large elevation range to characterize a large area of fracture surface. Better crack front defi-

nition can be obtained if a smaller area with a concomitant smaller elevation range is selected. Nevertheless, an average crack front can be defined by calculating the percentage of white (fractured) area in a plot and dividing by the plot height, and an effective crack growth rate (with respect to topograph displacement) can be obtained by plotting the percentage of fractured area against topograph displacement. This curve may be thought of as a fracture progression curve (FPC), indicating the relative (to crack opening displacement) growth history of a crack.

Results from the previous specimens showed that under steady state fatigue loading the area increase rate is constant and the FPC is linear. However, Figure

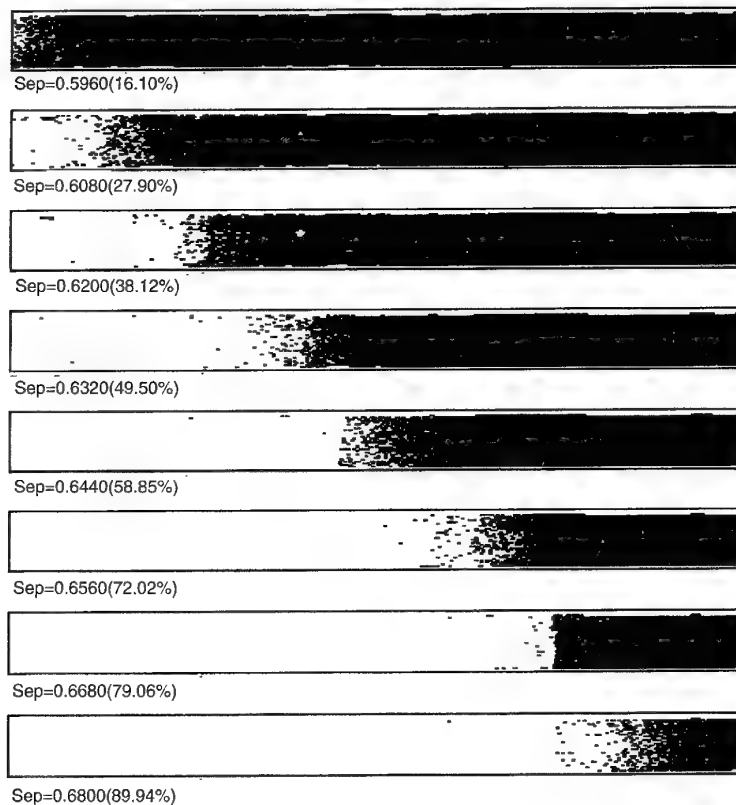


Figure 6 A series of plan views of a crack front at increasing topograph displacements (white areas indicate separated material; black areas indicate intact material)

7 shows that when an overload of above a certain magnitude is applied (above $3.3 \text{ MPa}\sqrt{\text{m}}$ in this case), a deviation from the steady state slope is produced. The slope initially decreases, then increases and attains the steady state slope. These deviations correlate with, but do not specify precisely, the crack lengths at which the overloads were applied. The degree of deviation increases with magnitude of the overload, suggesting

that overload magnitude can be computed from an analysis of the deviation geometry.

Figure 7 further shows that the deviation from the steady state line begins before the overload is applied. This could occur because the inelastic deformation produced by the overload results in a zone of compression around the crack tip, which tends to close the crack. Then when we match the conjugate surfaces we

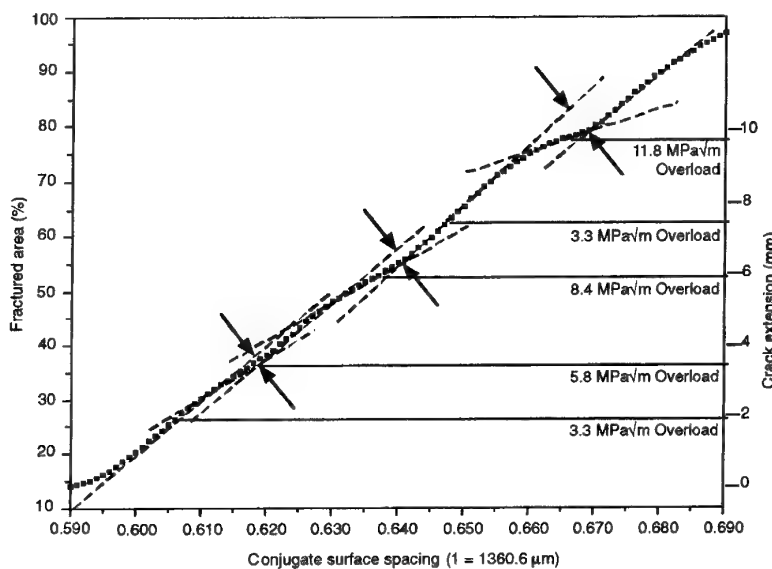


Figure 7 Fracture progression curve obtained from *Figure 6* and relation to overloads shown in *Figure 4*

observe an FPC slope change before overload application and (in *Figure 6*) an elongated transition zone of black and white.

Thus, the FPC appears to indicate the occurrence and location of overloads on a fracture surface and may provide the information needed to estimate the magnitude of overloads and define closure behavior. These promising prospects should be examined.

DISCUSSION OF THE RESULTS

These results show that certain parameters of the cyclic load spectrum, environment, and crack growth history may be obtainable from the fracture surfaces of a broken component. Additional investigations are required to confirm the observations and refine the procedures. If relationships can be established between fracture surface topography, crack growth characteristics, and load/environment parameters, fracture surfaces will be of much greater value in analyzing damage and failures in fixed wing and rotary wing aircraft, as well as in other structures subjected to cyclic loads. If relationships between elevation features and microstructure can be established, materials development efforts will be assisted.

Fundamental to success is a fast, accurate, high-resolution method for characterizing fracture surface topography. This prerequisite is fulfilled by software-automated stereoscopy and COSLM. Also necessary are three-dimensional analyses of the topography data: Fourier and FRASTA techniques provided promising preliminary results.

Passoja and Psioda¹¹ were the first to apply Fourier analysis to fracture surfaces. Using a one-dimensional transform, they determined the spatial frequency spectra of the roughness profile revealed on a cross-section. McSwain and coworker^{12,13} applied Fourier analysis to in-plane features of fracture surfaces. By calculating the two-dimensional power spectrum of a digitized SEM micrograph of a fatigue surface, they demonstrated that striation spacing could be determined quickly and accurately, even in cases where visual assessment was difficult or not possible. They further showed that Fourier analysis could classify and quantitatively characterize fracture surface patterns and distinguish among ductile rupture, cleavage, fatigue, and intergranular failure.

The results reported here suggest a greatly extended role of Fourier analysis to quantitative assessment of load and environment parameters. Application of a Fourier algorithm to three-dimensional fracture surface topography data produced EPSD curves that were sensitive to load parameters and environment, and fatigue surfaces produced under equivalent conditions produced nearly identical EPSD curves. This raises the exciting prospect of determining load and environment conditions that caused service failure by comparing EPSD curves from the field failure with EPSD curves from specimens fatigued under known conditions in laboratory tests.

The FRASTA technique of evaluating conjugate fracture surface topographs placed in the same relative configurations of the fracture surfaces during fatigue cracking also shows promise for extracting load information from fracture surfaces. FRASTA indicated the locations of overloads and changes of environment; the

amount of overload at these locations may be deducible from FPC slope deviations. Numerical computations are currently being performed to seek relationships between length and height of the deviations and the size of the zone of inelastic deformation and crack tip opening displacement.

CONCLUSIONS

- Important but previously unobtainable information regarding the conditions that produced fatigue failures can likely be obtained from fracture surfaces.
- Keys to extracting this information are a fast and accurate method for characterizing fracture surface topography and a three-dimensional analysis of the data.
- Fourier analyses of fracture surfaces may provide the basis for a library of reference curves useful in determining the load spectrum and environmental conditions that caused a service failure.
- Comparison of conjugate fracture surface topographs may indicate and quantify details of the overload spectrum experienced by a component that failed in fatigue.
- Shapes of striations may be quantifiable by stereoscopy or COSLM and provide a means to determine maximum and minimum values of the cyclic load spectrum.
- These expectations should be explored to seek advances in failure analysis technology.

ACKNOWLEDGEMENTS

This work was supported by the Federal Aviation Administration under Grant No. 93-G-065 and supervised by Dr Thomas H. Flournoy. The authors thank A.K. Vasudevan, J.T. Cammett, and C.L. Brooks for bringing the problem of load spectrum determination to our attention at the Fatigue Structural Reliability Workshop on 20–22 September 1995 at West Dennis, MA. We are also indebted to Y. Chuman and M. Yamauchi of Mitsubishi Heavy Industries, Ltd. for suggesting the use of Fourier analysis to characterize fracture surfaces.

REFERENCES

- 1 Brooks, C. L., Liu, K. and Eastin, R. G., Understanding fatigue failure analyses under random spectrum loading using a C-17 test article failure. In *Proceedings of the Aeronautical Structural Integrity Program Conference*, San Antonio, TX, November 1995; also in *Minutes of the International Conference on Aeronautical Fatigue*, Melbourne, Australia, 1–5 May 1995.
- 2 Pelloix, R. M. N., Crack extension by alternating shear. *Engineering Fracture Mechanics*, 1970, **1**, 697–704.
- 3 Bowles, C. Q. and Broek, D., On the formation of fatigue striations. *International Journal of Fracture*, 1972, **8**, 75–85.
- 4 Paris, P. C. and Erdogan, F., Critical analysis of crack propagation laws. *Transactions of the American Society of Mechanical Engineers*, 1963, **85D**, 528–534.
- 5 Murakami, Y., Shiraishi, N. and Furukawa, K., Estimation of service loading from the width and height of fatigue striations of 2017-T4 Al alloy. *Fatigue and Fracture of Engineering Materials and Structures*, 1991, **14**(9), 897–906.
- 6 Furukawa, K., Murakami, Y. and Nishida, S. -I., A method for predicting service load from the width and height of striation. *Journal of the Society of Materials Scientists, Japan*, 1996, **45**(3), 340–345.

- 7 McSwain, R. H. and Gould, R. W., Analysis of a helicopter blade fatigue fracture by digital fractographic imaging analysis. In *Proceedings of the International Conference and Exposition on Fatigue, Corrosion Cracking, Fracture Mechanics and Failure Analysis*, ed V. S. Goel. American Society for Metals, Salt Lake City, UT, December 1985, pp. 87–91.
- 8 Kobayashi, T. and Shockey, D. A., work in progress, SRI International, Menlo Park, CA, 1996.
- 9 Kobayashi, T. and Shockey, D. A., FRASTA: A new way to analyze fracture surfaces, Part 1: Reconstructing crack histories. *Advanced Materials and Processes*, 1991, **140**(5), 28–34.
- 10 Kobayashi, T. and Shockey, D. A., Fracture analysis via FRASTA, Part 2: Determining fracture mechanisms and parameters. *Advanced Materials and Processes*, 1991, **140**(6), 24–32.
- 11 Passoja, D. E. and Psioda, J. A., Fourier transform techniques – fracture and fatigue. In *Fractography and Materials Science*, ASTM STP 733, eds L. N. Gilbertson and R. D. Zipp. American Society for Testing and Materials, Philadelphia, PA, 1981, p. 355.
- 12 McSwain, R. H., Digitized fractographic image analysis. Ph.D. Thesis, University of Florida, Gainesville, FL, 1985.
- 13 Gould, R. W. and McSwain, R. H., Fractographic feature identification and characterization by digital image analysis. In *Fractography of Modern Engineering Materials: Composites and Metals*, ASTM STP 948. American Society for Testing and Materials, Philadelphia, PA, 1987, pp. 263–292.

PII: S0142-1123(97)00030-3

Cyclic relaxation in compression-dominated structures

Eric J. Tuegel and Craig L. Brooks

McDonnell Douglas Aerospace, P.O. Box 516, St. Louis, MO 63166-0516, USA

Cracks developed in two locations of a landing gear during full-scale fatigue testing. The two locations experienced compression-dominated loading during the test. The cracking could not be explained by conventional analysis methods. There was sufficient plasticity at these locations to allow the mean stress to relax under cyclic loading. Introducing cyclic relaxation of the mean stress into the analysis gave life estimates that correlated well with the full-scale fatigue test results. Subsequent coupon tests also demonstrated the need to account for cyclic relaxation of the mean stress. © 1998 Elsevier Science Ltd.

(Keywords: fatigue; cyclic relaxation; structures)

INTRODUCTION

During the full-scale fatigue test of a main landing gear, cracks were found at two locations: at the base of the upper aft strut door attach lug on the cylinder and at the base of the piston attach lug on the trailing arm (*Figure 1*). Multiple cracks with a combined length of 5 mm (0.2 in) were found at the strut door lug at slightly more than two test lifetimes. A test lifetime was equivalent to 14,400 flight hours for this test. A

5 mm (0.2 in) crack was found at the piston attach lug on the trailing arm at three test lifetimes.

A review of the normalized load spectra for these locations showed that loads were primarily compressive (*Figure 2*). The load spectra for one test lifetime at each location were developed using finite element models of the cylinder and trailing arm to construct stress transfer functions relating the applied loads to the local stresses. The theoretical elastic notch stress, $K_t\sigma$, for the reference condition was estimated to be 2177 MPa

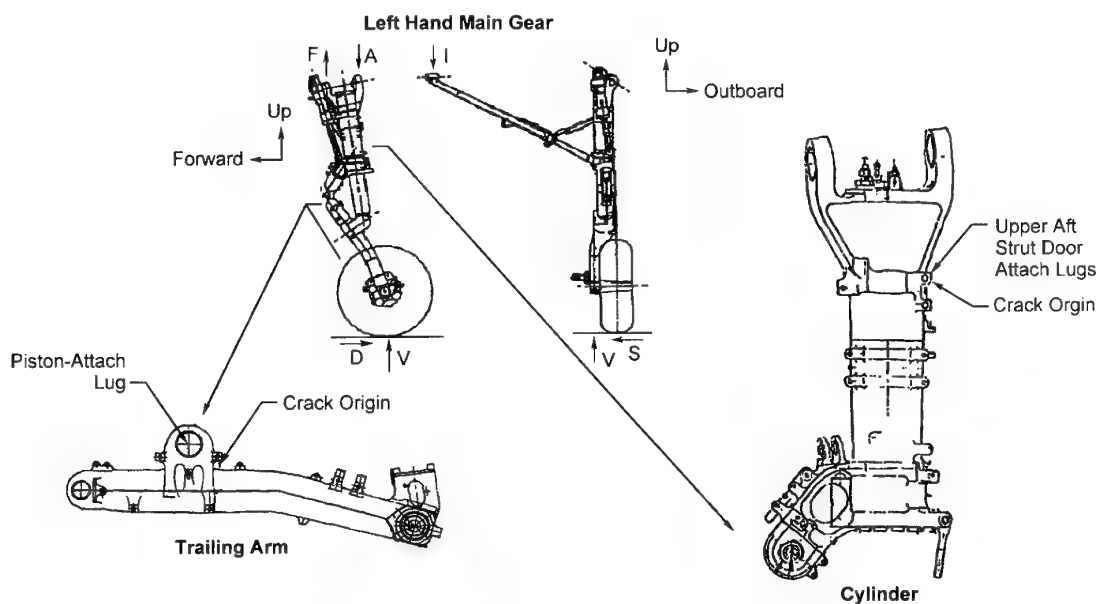


Figure 1 Main landing gear showing crack locations, primary loads and reactions

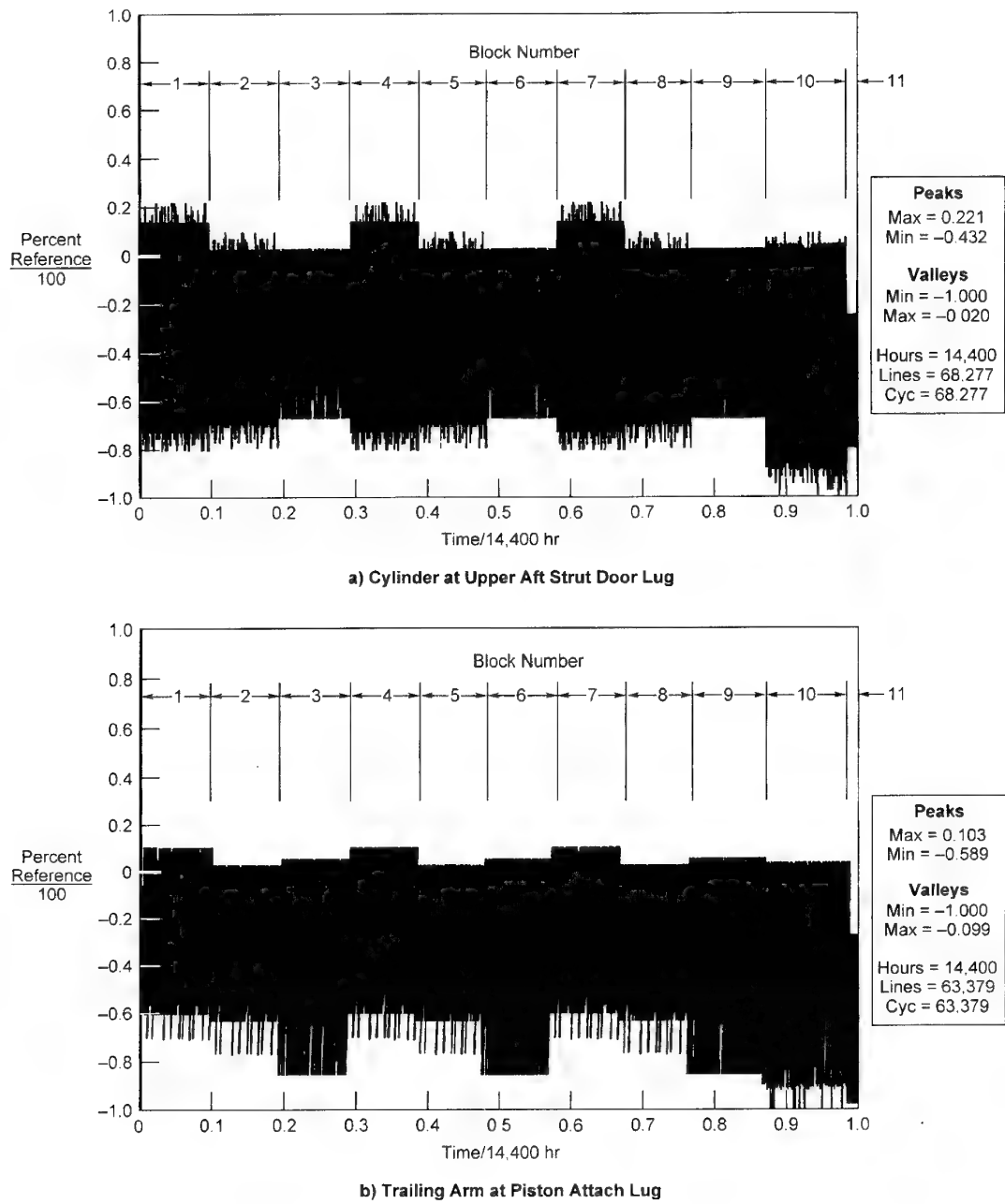


Figure 2 Applied loading spectra at critical locations: (a) cylinder at upper aft strut door lug; (b) trailing arm at piston attach lug

(316 ksi) at the strut door lug, and 2281 MPa (331 ksi) at the piston attach lug of the trailing arm, using the finite element models. Strain surveys of both areas using another gear confirmed these stresses. The cylinder and trailing arm were both made from Hy-Tuf steel, heat treated to an ultimate strength between 1516 MPa (220 ksi) and 1654 MPa (240 ksi). Conventional crack initiation predictions using the local strain approach with the cyclic stress-strain and strain-life curves in *Figure 3* gave estimates of approximately 3.5 lifetimes until cracking at the strut door lug, and 10 lifetimes at the piston attach lug. The observed cracking could not be explained with the current life prediction methods.

Many of the loading blocks had a stress range sufficient to cause repeated yielding in both tension

and compression. The maximum load excursions in each block of the loading spectra are analyzed in *Table 1* for both locations. The theoretical elastic notch stress range, $\Delta K_t \sigma$, is found by multiplying the difference between the peak and the valley by the reference $K_t \sigma$. The notch stress amplitude and strain amplitude, $\Delta \sigma_n/2$ and $\Delta \epsilon_n/2$ respectively, are then found using Neuber notch analysis. The plastic strain amplitudes, $\Delta \epsilon_p/2$, in *Table 1* for each block were calculated using the Ramberg-Osgood equation relating cyclic stress amplitude to cyclic plastic strain amplitude for Hy-Tuf steel, $\Delta \sigma/2 = 2881.4 \text{ MPa } (\Delta \epsilon_p/2)^{0.141}$.

For non-zero plastic strain amplitudes, smooth specimens of many polycrystalline metals exhibit cyclic relaxation of the mean stress¹⁻⁶. Thus, the repeating large cycles in the spectra should become completely

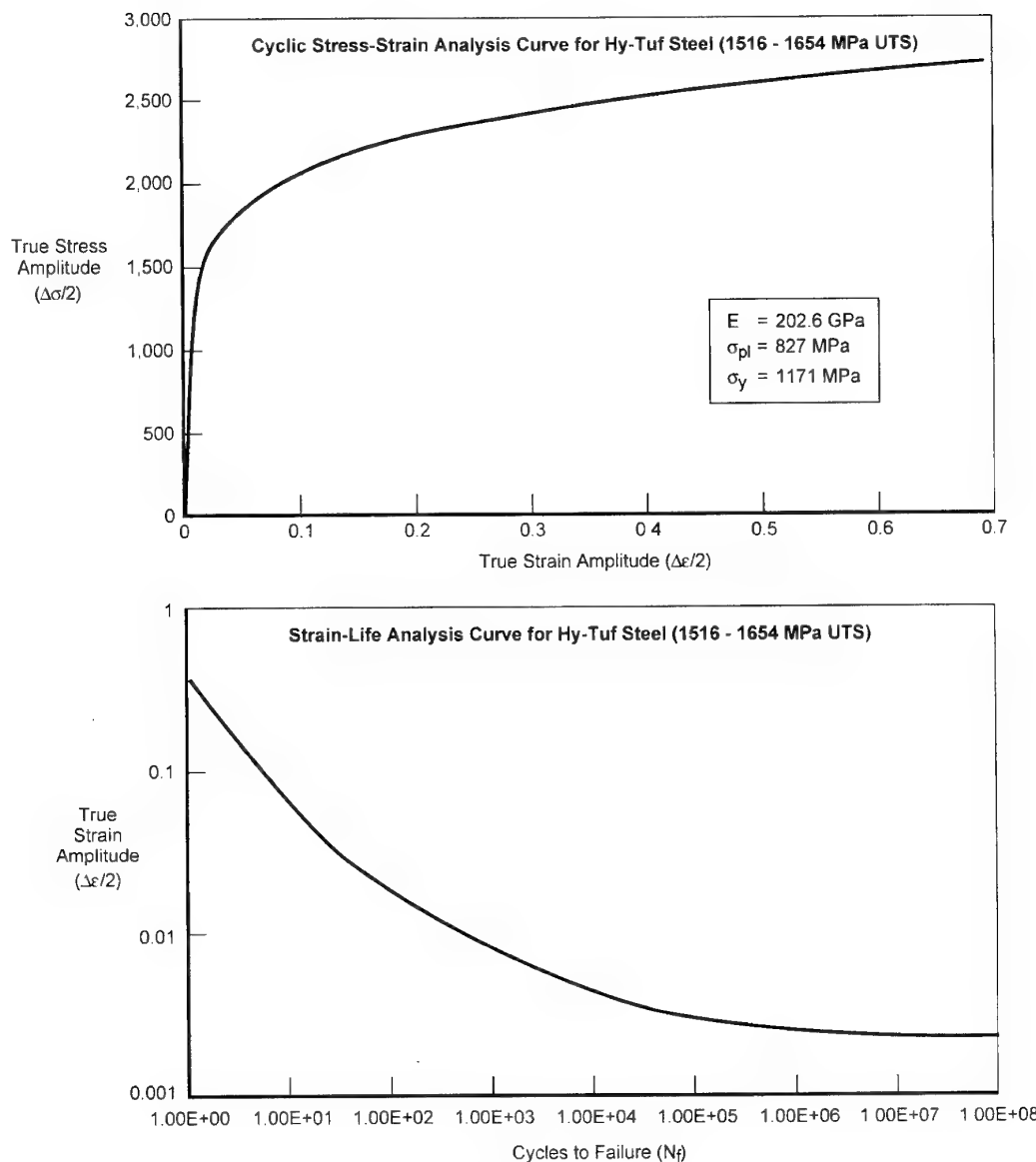


Figure 3 Hy-Tuf material curves used in the main landing gear failure analysis

reversed ($R = -1$), as indicated in *Figure 4*. The notch root stresses and strains for the small and intermediate load cycles would move with the hysteresis loops of the larger load cycles. Thus, the effective stresses at the notch root would be more tensile than the applied loading would indicate, and thus would be more damaging than anticipated.

Lacking detailed data on the cyclic relaxation of Hy-Tuf steel, an engineering approach was used. The spectra were already blocked as a result of testing the landing gear with different cylinder extensions (or stroke lengths). Each block of the spectrum was examined separately to see if there were enough cycles with significant plasticity to allow relaxation. The rules for cyclic relaxation in the analysis were as follows.

1. If $\Delta\epsilon_{pl}/2 > 0.0001 \text{ mm mm}^{-1}$ and $N > 10$ cycles, then the mean stress relaxed to zero. The block was shifted so that the mean of the cycles under consideration became zero.
2. If $\Delta\epsilon_{pl}/2 \leq 0.0001 \text{ mm mm}^{-1}$ or $N \leq 10$ cycles,

then the mean stress does not relax. However, the block must shift the same amount as the most recent prior block in which relaxation occurred.

How much each block of the spectra could shift, when considered individually, based on these rules is tabulated in the last column of *Table 1*.

The modified trailing arm spectra for analysis of the first lifetime of testing, and for the second and all subsequent lifetimes of testing, are shown in *Figure 5*. The trailing arm spectrum for the first lifetime was different from all the subsequent lifetimes because the first and second blocks were not candidates for relaxation under the above rules. After the first lifetime, the first and second blocks shifted the same amount as block 10, the most recent prior block in which relaxation was possible. Using the relaxed spectrum, the analysis gave an estimate of 2.2 test lifetimes for cracking at the piston attach lug.

The first block of the strut door lug relaxed under the above rules during the first lifetime of testing. So

Table 1 Determination of cyclic relaxation potential in each spectrum

Block	Peak	Valley	$\Delta K_c \sigma$ (MPa)	$\Delta \sigma_n/2$ (MPa)	$\Delta \epsilon_n/2$ (mm mm^{-1})	$\Delta \epsilon_{pl}/2$ (mm mm^{-1})	Shift amount
<i>Strut door lug spectrum</i>							
1, 4 and 7	0.22 (12 ×)	- 0.80 (12 ×)	2221	1038	0.0059	0.0007	0.29*
	0.13 (typ)	- 0.75 (typ)	1916	924	0.0049	0.0003	0.31*
2, 5 and 8	0.05 (10 ×)	- 0.75 (10 ×)	1742	857	0.0044	0.0002	0
	0.02 (typ)	- 0.70 (typ)	1568	673	0.0033	0.0000	0
3, 6 and 9	0.02	- 0.65	1459	654	0.0032	0.0000	0
10	0.05	- 1.0 (4 ×)	2286	1059	0.0061	0.0008	0
		- 0.9 (typ)	2068	984	0.0054	0.0005	0.425
11	- 0.25	- 0.79	1176	470	0.0023	0.0000	0
<i>Trailing arm lug spectrum</i>							
1, 4 and 7	0.10	- 0.70 (10 ×)	1824	889	0.0046	0.0002	0
		- 0.60 (typ)	1596	679	0.0034	0.0000	0
2, 5 and 8	0.02	- 0.76 (9 ×)	1779	872	0.0045	0.0002	0
		- 0.63 (typ)	1551	670	0.0033	0.0000	0
3, 6 and 9	0.05	- 0.86	2075	987	0.0054	0.0005	0.405
10	0.04	- 1.0 (10 ×)	2372	1087	0.0064	0.0010	0
		- 0.9 (typ)	2144	1011	0.0056	0.0006	0.43
11	- 0.30	- 0.98	1551	670	0.0033	0.0000	0

* Used average of 0.30.

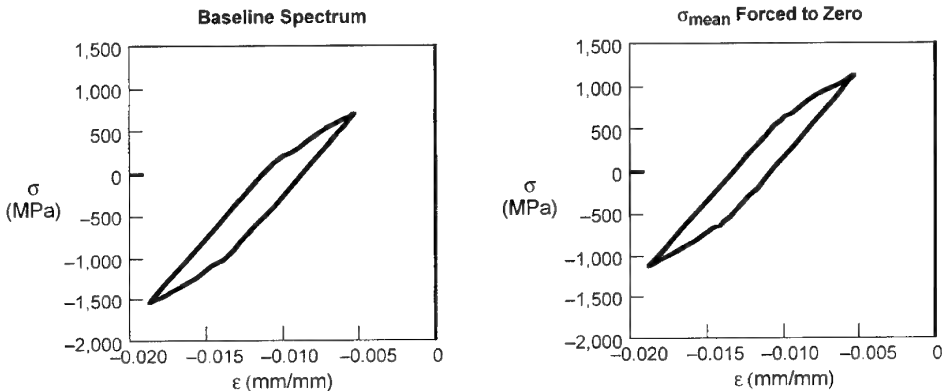


Figure 4 Schematic of mean stress shift due to cyclic relaxation using the largest hysteresis loop in strut door lug spectrum

the modified strut door lug spectrum shown in *Figure 6* was used for all lifetimes of testing. With the modified spectrum, cracking at the strut door lug was predicted at 1.2 test lifetimes. Thus, cyclic relaxation provided an explanation for why cracks developed in these two locations.

FOLLOW-ON TESTING

A follow-on coupon test program was conducted to demonstrate and validate a redesign of the strut door lug fillet. This test program provided more data with which to further test the hypothesis of cyclic relaxation. Fillet specimens (*Figure 7*) fabricated from Hy-Tuf steel were tested back-to-back in a servohydraulic test machine. Two specimens loaded back-to-back in the test machine gave a symmetric geometry for the tests, reducing concern about bending in the specimens. Teflon tape was placed between the two specimens to avoid friction load transfer and fretting.

The baseline loading spectrum for the strut door lug fillet (*Figure 2a*) was used as the command signal for the test. Crack initiation was monitored by removing the specimens from the test machine at regular intervals and using dye penetrant to find cracks. The results of the tests and the crack initiation predictions, with both

the baseline and relaxed spectra, are shown in *Figure 7*. Even with the considerable scatter in test results, the prediction made by assuming cyclic relaxation of the mean stress correlated better with the data than the baseline prediction using the applied loading spectrum. However, shifting the spectrum to account for cyclic relaxation does not seem to have captured everything happening at the notch root.

AREAS FOR FURTHER INVESTIGATION

Shifting the spectrum in the analysis changes the computed mean strain as well as the mean stress. This has no effect on the predictions here since the analysis used the Smith-Watson-Topper equation, $\Delta \epsilon_{eq}/2 = [(\sigma_{max}/E)(\Delta \epsilon/2)]^{1/2}$, which only involves the strain amplitude. However, if the absolute strain values at the notches influence the time to cracking, then shifting the spectrum will not yield good life predictions.

Consideration of the cyclic relaxation phenomenon raises the question of whether significant relaxation can occur when the material yields on the initial loading but remains elastic on all subsequent loading cycles. Stress relaxation is observed when monotonic tension loading is stopped after the material yields and the specimen is held at a constant extension. But the

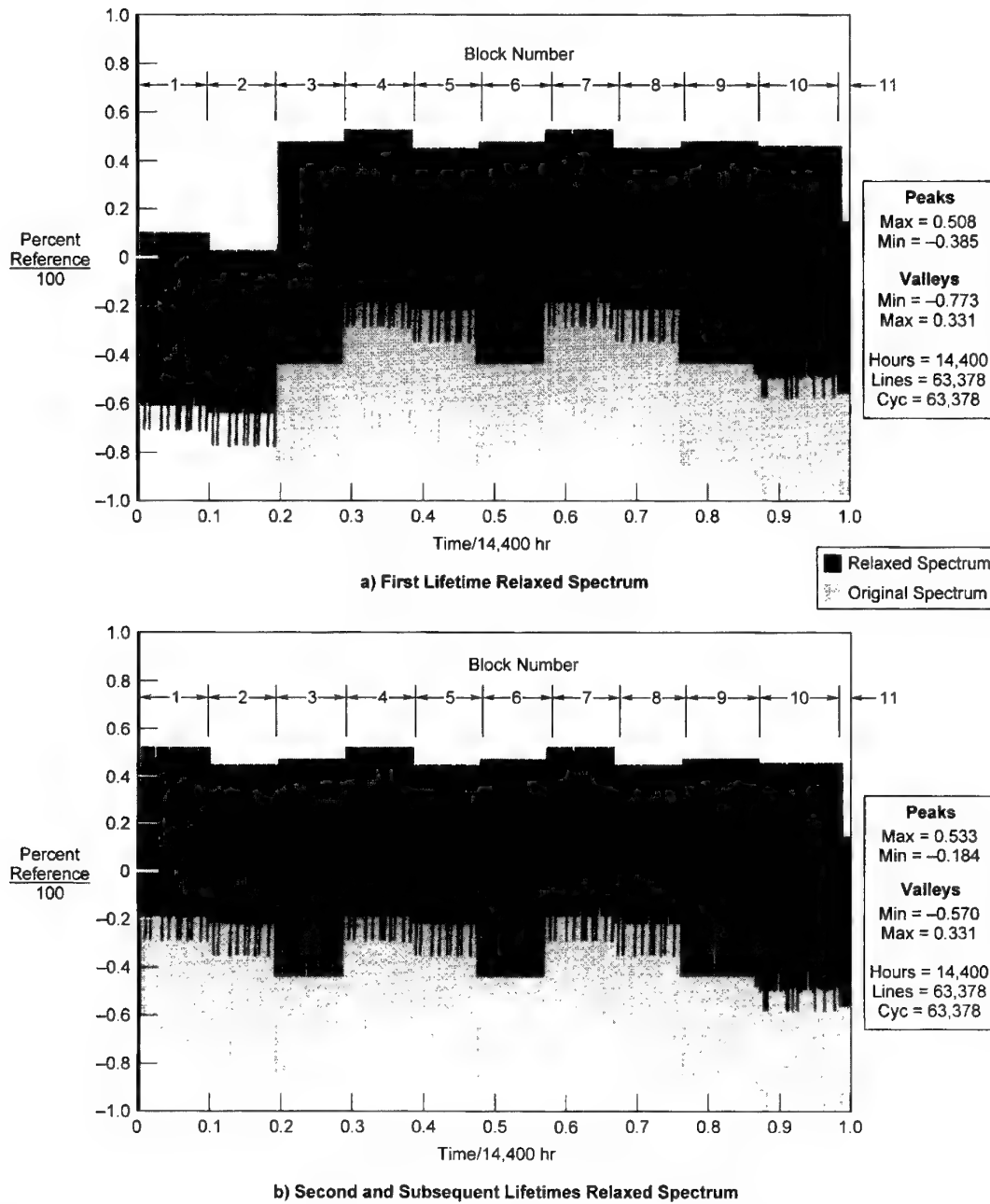


Figure 5 Relaxed trailing arm spectra: (a) first lifetime relaxed spectra; (b) second and subsequent lifetimes relaxed spectra

amount of relaxation is not enough to be detected in a fatigue life estimate. However, small oscillatory loading has been reported to relax residual stresses^{7,8}. Will mean stresses behave in the same way as residual stresses? Is cyclic fatigue loading of a form that would cause the same relaxation observed in Refs 7, 8? Just as important, will some types of fatigue loading cause relaxation of the compressive residual stresses from life enhancement processes such as coldworking holes and interference fit fasteners? The authors are not aware of sufficient data to provide validated answers to these questions.

Another area of interest is the influence that cyclic relaxation has on crack growth. It must occur within the crack tip plastic zone, but its effect on long crack growth is already included in the crack growth rate

data. However, the effects of cyclic relaxation in the plastic zone may be more significant for short cracks where the plastic zone size has the same magnitude as the crack length. The effective loading on a short crack may not be appropriately characterized by the far-field elastic loading. Cyclic relaxation ahead of the crack tip might be part of the reason why long crack growth data does not represent short crack observations.

These questions are posed so that others can also be challenged by these issues and possibly begin to investigate them.

SUMMARY

Two examples of seemingly inexplicable cracking in areas of compression-dominated loading were explained

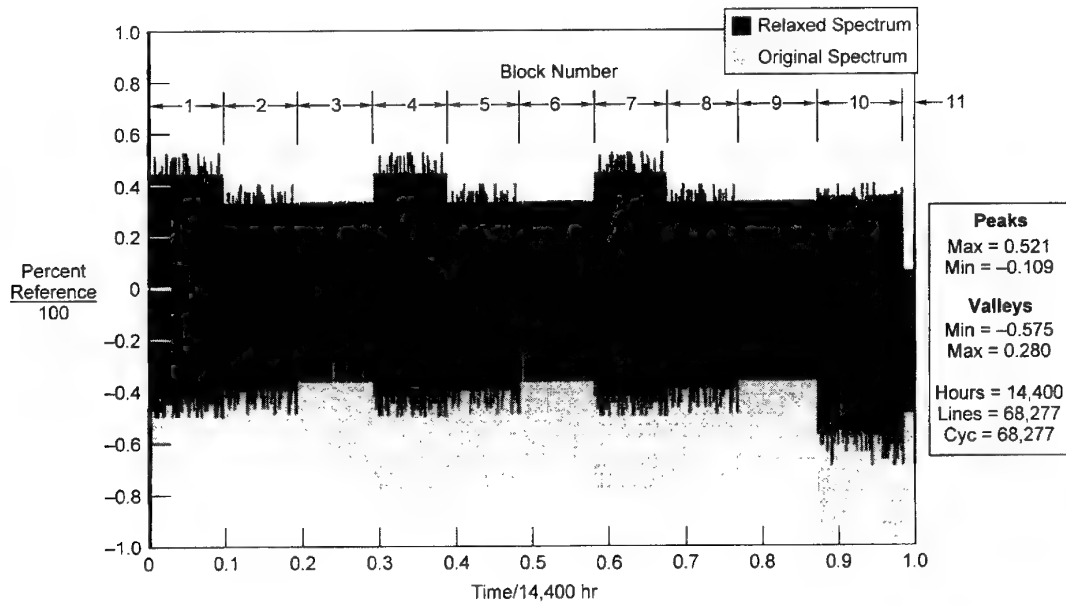


Figure 6 Relaxed aft strut door lug spectrum for all lifetimes of testing

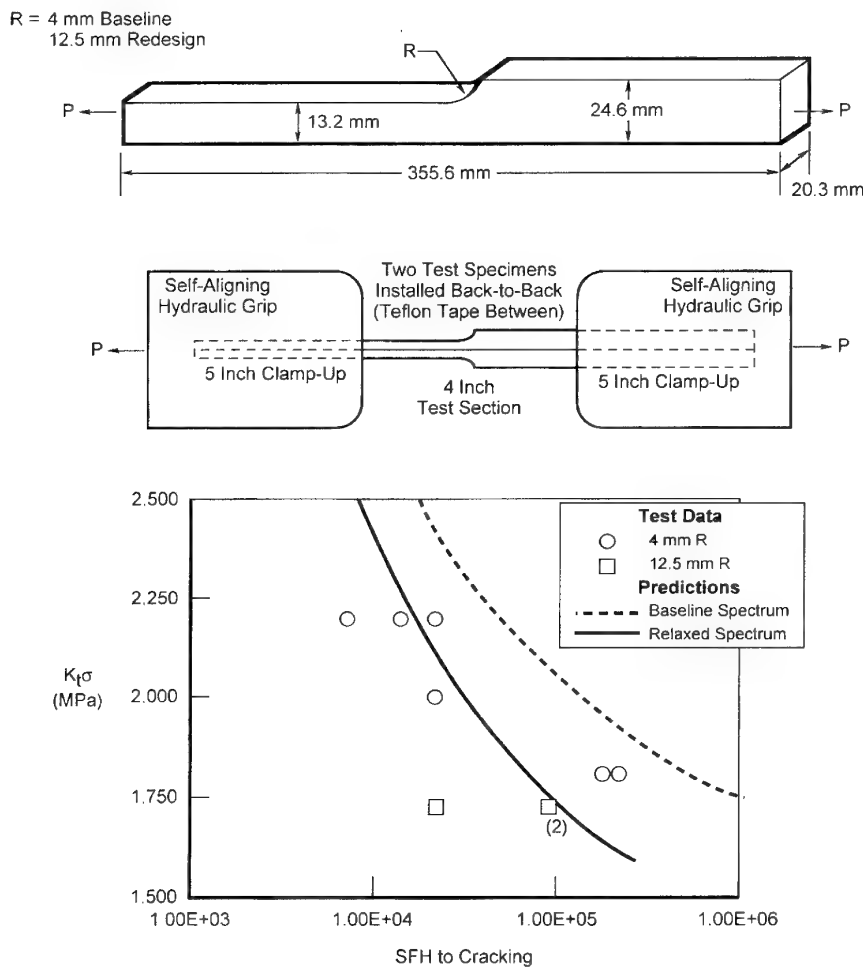


Figure 7 Correlation of predictions using the baseline spectrum (Figure 2a) and the relaxed spectrum (Figure 6) with fillet coupon test data

by accounting for the local cyclic relaxation of the compressive mean stress. An engineering approach to account for the relaxation was to shift the mean of the loading spectrum. The shifted spectrum was used in the local strain approach to predict the onset of cracking in the gear. A follow-on coupon test program further verified the analytical approach.

Additional refinements of the analysis method are needed to improve the correlation with test data. Data on the cyclic relaxation behavior of various materials are needed to develop material models within the analysis routines to automatically account for relaxation. There are numerous locations on aircraft where the loading is tension- or compression-dominated. This analysis method may be applicable for structures such as the upper and lower surfaces of the wings and horizontal tails, and the landing gear.

ACKNOWLEDGEMENTS

The authors would like to thank Dan Rich and Bill Nowak for providing the data from the follow-on testing.

REFERENCES

- 1 Morrow, J., Ross, A. S. and Sinclair, G. M., *Transactions, Society of Automotive Engineers*, 1960, **68**, 40–48.
- 2 Morrow, J. and Sinclair, G. M., Cycle-dependent stress relaxation. *Symposium on Basic Mechanism of Fatigue*. ASTM STP 237, 1958.
- 3 Topper, T. H., Sandor, B. and Morrow, J., *Journal of Materials*, 1969, **4**(1), pp. 189–199.
- 4 Morrow, J., Wetzel, R. M. and Topper, T. H., Laboratory simulation of structural fatigue behavior. *Effects of Environment and Complex Load History on Fatigue Life*. ASTM STP 462, 1970, pp. 74–91.
- 5 Conway, J. B. and Sjodahl, L. H., *Analysis and Representation of Fatigue Data*. ASM International, 1991.
- 6 SAE Fatigue Design Handbook, AE-10. Society of Automotive Engineers, 1988.
- 7 Ohol, R. D., Nagendra Kumar, B. V. and Noras, R. A., Measurement of vibration-induced stress relief in the heavy fabrication industry. *Mechanical Relaxation of Residual Stresses*. ASTM STP 993, 1988, pp. 45–57.
- 8 Bouhelier, C., Barbarin, P., Deville, J. P. and Miege, B., Vibratory stress relief of welded parts. *Mechanical Relaxation of Residual Stresses*. ASTM STP 993, 1988, pp. 58–71.



PII: S0142-1123(97)00048-0

Cumulative fatigue damage modeling—crack nucleation and early growth

Gary R. Halford

Senior Research Scientist, National Aeronautics and Space Administration, Lewis Research Center, Cleveland, OH 44135, USA

Prior research into linear and nonlinear fatigue damage accumulation in metals and alloys is briefly reviewed, and general trends are identified. Nonlinear damage rules offer substantially more accurate, and hence less unconservative, fatigue life predictions than the classical linear damage rule (LDR). Increased accuracy does not require excessive cost of analysis or additional databases. The nonlinear damage curve approach and its double linear damage rule (DLDR) equivalent are models that, at most, require only twice the effort of the classic LDR. These models require no increase in complexity of use, nor do they require additional material property or mission loading information to achieve the improved accuracy. Greatest improvements (factors of 5–10 or more in mission lifetime) accrue when missions include considerable high-cycle fatigue with some severe low-cycle fatigue loadings. Criteria are proposed for judging those severe mission loading circumstances when the classical LDR becomes unacceptably nonconservative. © 1998 Elsevier Science Ltd.

(Keywords: fatigue (metal); low-cycle fatigue; high-cycle fatigue; cumulative damage)

INTRODUCTION

For many years, structural design engineers have used the simplistic notion that fatigue damage accumulates in a material linearly with usage—regardless of severity or sequencing of mission loads. The universally accepted damage assessment model is the classical linear damage rule (LDR), first proposed by SKF's Palmgren¹ in 1924 for application to the Swedish ball bearing industry. Some 15 years later, Langer², working for Westinghouse in the electric power generation area, independently proposed a similar linear rule for pressure vessel and piping components made of steel. Six years later, in 1945, Miner³ of Douglas Aircraft built upon Langer's work and applied the LDR to tension-tension axial fatigue data for an aircraft skin material (aluminum alloy 24S-T ALCLAD). Miner demonstrated excellent agreement between the LDR predictions and his experimental results. This success lead to the strong association between Miner and the LDR; so much so that many today refer to it as Miner's LDR. Closer scrutiny of Miner's cumulative fatigue results, however, reveals that none of the several combinations of loading levels (2, 3 and 4 levels were used) included fatigue lives exceeding an order of magnitude from one another. Hence, little opportunity was allowed by the experiments for interactions that could cause deviations from a LDR. In fact, application of a current nonlinear damage rule, the damage curve approach (DCA)^{4,5} to Miner's data will be shown to give essentially the same degree of accuracy as the LDR. Both the DCA and

LDR predict cycle fraction summations at failure to within factors of ± 1.5 of the experimental results. This is the same degree of deviation reported by Miner for his baseline constant amplitude fatigue tests. In short, Miner's data were not critical discriminating data. It is doubtful that these data could statistically distinguish any of the multitude of nonlinear cumulative damage models from the classical LDR.

Over the decades since Miner's work, the LDR has been demonstrated, under certain critical circumstances, to suffer limitations in accuracy. Life losses of five to ten times or more have been reported by many, including Richart and Newmark⁶, Webber and Levy⁷, Manson *et al.*⁸, Bizon *et al.*⁹ and McGaw *et al.*¹⁰. So compelling are the laboratory observations, that dozens of nonlinear cumulative fatigue damage models have been proposed. See for example, the thorough reviews of O'Neill¹¹ and Schijve¹², and a more modern review by Manson and Halford¹³.

The need arises for more complex rules under extreme conditions wherein the consequence of applying the LDR is serious nonconservatism. These effects have been shown experimentally many times over for a broad range of materials and regimes of fatigue life. The most severe interactions occur when there is an appropriate mixture of low-cycle fatigue (LCF) and high-cycle fatigue (HCF) loading. The further apart the lives in LCF and HCF, the greater the deviation from linearity of damage accumulation. It is this very trend that the cumulative fatigue damage models have attempted to emulate.

Despite the improved accuracies of the new models, they have not been used in structural design. Lack of use is partially due to the requirement for specific experimentally determined constants. Since fatigue damage analyses are seldom made until late in the design sequence, there is neither the time nor the incentive to generate the requisite laboratory fatigue data for analysis by any other technique than the classical LDR. This shortcoming lead to the evolution at NASA-Lewis in 1981^{4,5} of the DCA and its equivalent, a modification of the original 1961 double linear damage rule (DLDR) of Manson *et al.*¹⁴. No experimental constants have to be evaluated to apply either of the two interrelated models. As will be discussed, the models use a single universal constant that fortunately does not exert a sensitive influence on predicted cycle fraction summations. Hence, one of the major limitations impeding the use of nonlinear cumulative damage equations was surmounted with this advancement. The remaining major barrier to widespread acceptance is the lack of confidence due to lack of experience with use. To date, these two models have been applied to few complex mission loading profiles for structural components of practical concern¹⁵⁻¹⁷. Interest that had been sparked nearly two decades ago, however, is regaining popularity in the reusable space propulsion and aeronautical gas turbine industries. Concerns are being raised because of the cumulative damage-proneness of aging aircraft and of new component designs that feature unavoidable combinations of thermomechanical LCF loading and high-order, poorly-damped vibratory excitations of HCF. Increased use of nonlinear damage rules may take place in the future as needs intensify.

FEATURES OF THE DAMAGE CURVE APPROACH

The DCA is a simple empirical damage accumulation equation that recognizes two well-established observations. In LCF, damage in the form of cracking of initially smooth specimens begins very early in the life, whereas in HCF, cracking damage is not detectable until very late in life. The transition in behavior is not abrupt, but rather smooth and continuous across the entire range of fatigue lives. The DCA equation for damage (D) takes the form of a power-law equation of the applied cycle fraction (n/N_f), where n is the number of applied cycles of loading at a level that would give rise to a fatigue life of N_f cycles to failure. The power-law exponent is the function, $g(N_f)$, that is,

Damage curve approach.

$$\text{Damage, } D = (n/N_f)^{g(N_f)} \quad (1)$$

Equation (1) is displayed in *Figure 1*. It is appropriate to point out that Equation (1) is of identical form to the classical LDR. For the LDR, $g(N_f)$ is such a simple function that it is a constant and equal to unity. Hence,

Linear damage rule.

$$\text{Damage, } D = (n/N_f) \quad (2)$$

Equation (2) implies that damage accumulates linearly with applied cycle fraction, independent of *life level*,

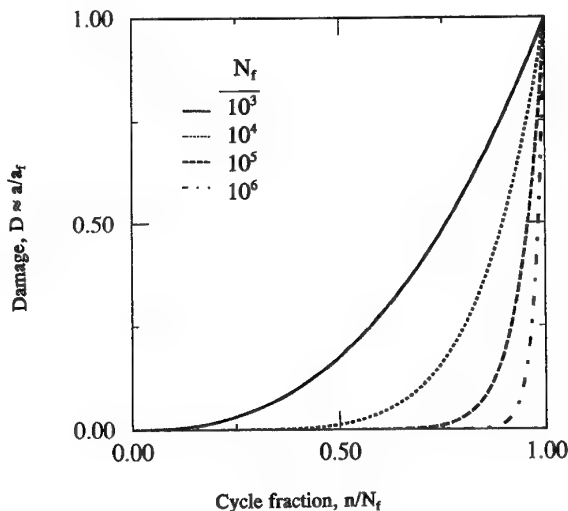


Figure 1 Schematic fatigue damage accrual—DCA

N_f . As discussed earlier, this implication is at odds with common knowledge among fatigue researchers who recognize that damage in LCF and HCF does not accrue at the same rate, nor does it accrue linearly with applied cycle fraction.

Neither Equations (1) nor (2) address the much more complex issue of the relationship of fatigue life to a loading parameter such as stress amplitude, mean stress, strain range, hysteresis energy, product of peak tensile stress and strain range, or any other measure of the magnitude of fatigue loading. These so-called 'damage accumulation equations' are concerned only with the magnitude (or level) of cyclic life and the applied cycle fractions at each fatigue life. Neither equation is capable of distinguishing how a given life is arrived at (i.e. strain-controlled, load-controlled, high or low *R*-ratio, degree of multiaxiality, etc.). Consequently, the presumption, in the event of no specific information to dictate otherwise, must be that the equations are applicable to any and all loading conditions. As will be pointed out in a later section, Miner's data³ involved *R*-ratios of stress of + 0.5, + 0.2 and - 0.2. In general, the LDR is applied with little regard to whether or not mean stresses are involved. The same degree of disregard for mean stresses would also be expected to apply to the DCA. However, few *R*-ratio data have been evaluated to date using the DCA.

In either Equations (1) or (2), the damage (D) could be interpreted physically as a dimensionless crack length (a/a_f). Note that (a/a_f) cannot become negative, nor can it decrease (without sintering of the crack faces). Experience on the development and early growth of cracks tells us that the exponent, $g(N_f)$, in Equation (1) is > 1 and increases as N_f increases. For reasons of cost and time it is impractical to determine the exact form of $g(N_f)$ from observations of tiny cracks at various fractions of the fatigue life. Instead, $g(N_f)$ is back-calculated on the basis of two-level loading cumulative fatigue damage tests. A subscript of 1 refers to the first loading level, 2 to the second. A rather large fatigue data base on engineering alloys (ferritic and austenitic steel, titanium, aluminum, etc.) was employed^{4,5} to evaluate $g(N_f)$. Initial evaluations were accomplished with room temperature data, how-

ever, subsequent evaluations have been made with elevated temperature fatigue data for stainless steels and nickel and cobalt-base superalloys. While most of the high temperature data were for rapid cycling conditions with little opportunity for creep-fatigue interactions, agreement between experiment and the DCA was comparable to that achieved with room temperature results. Some of the elevated temperature results included creep-fatigue and thermomechanical fatigue data. The equation evolving from these calibrations is

$$(n_2/N_{f,2}) = 1 - (n_1/N_{f,1})^{h(N_{f,1}/N_{f,2})} \quad (3)$$

where $h(N_{f,1}/N_{f,2}) = (N_{f,1}/N_{f,2})^{0.4}$. Equation (3), which merely reflects a large number of observations implies that the degree of cumulative damage interaction resulting from operating at two different loading (life) levels is dependent, not upon the *absolute* life levels, but only on the *relative* life levels, $(N_{f,1}/N_{f,2})$. This is a remarkably powerful observation. It leads to the notion that the mechanisms involved in damage accumulation during fatigue testing do not vary so much in kind (as the level of fatigue life increases), as they vary simply in magnitude. Furthermore, the variation in magnitude is of an exponential form. The greater the ratio of extremes lives, that is, $(N_{f,1}/N_{f,2})$ the more severe is the interaction or deviation from the LDR. Furthermore, the same degree of interaction occurs between 10^1 and 10^3 as occurs between 10^6 and 10^8 cycles to failure, as both conditions have two orders of magnitude separating the life levels. The end result is that the function $g(N_f)$ in Equation (1) becomes $K(N_f)^{0.4}$. The constant K is, somewhat surprisingly, an arbitrary constant. However, from physical observations of fatigue behavior, K is generally ≥ 1 . It is generally convenient to let $K = 1$ for the lowest fatigue life in a mission loading sequence being analyzed. The only material related constant in Equation (2) is the 0.4 power in the exponent. The numerical sensitivity to this constant is low. Deviations of $\pm 25\%$ from its value of 0.4 translate to errors in the final cycle fraction summations of $+49\%$ and -28% respectively for $(n/N_{f,1}) = 0.1$ and $(N_{f,1}/N_{f,2}) = 0.001$.

Another interesting feature of Equation (2) is that the algebra is such that the so-called 'loading order effect' in two-level fatigue loading is taken into account automatically. For loading first at an LCF life of $N_{f,1}$ followed by loading to failure at an HCF life of $N_{f,2}$, the cycle fraction summation, $\Sigma[(n_1/N_{f,1}) + (n_2/N_{f,2})]$ is < 1.0 , whereas, reversing the order, that is, loading first at $N_{f,1}$ of HCF, followed by loading at $N_{f,2}$ of LCF, gives a cycle fraction summation > 1.0 . Working through Equation (3) step-by-step illustrates this automatic feature. Start with an LCF life fraction, $n/N_{f,1}$ (a number < 1). Raising this fraction to a power of < 1 (i.e. $N_{f,1}/N_{f,2} < 1$ and hence raised to the power 0.4 is still < 1) results in a numerical value that is larger than the initial value of $n/N_{f,1}$. Thus, when this larger number is subtracted from unity, the calculated remaining life fraction for HCF, $(n_2/N_{f,2})$ is less than it would have been had the LCF life fraction been subtracted from unity (as would be done when applying the LDR). Thus, the end result is a total life fraction summation of < 1.0 . Now, if we start with the HCF cycle fraction (referred to as $n/N_{f,1}$ since it comes first in the sequence), the power $(N_{f,1}/N_{f,2})$ is > 1 , and the numerical value of

$(n_1/N_{f,1})\exp[(N_{f,1}/N_{f,2})^{0.4}]$ is smaller than $(n_1/N_{f,1})$. When this smaller numerical value is subtracted from unity, the resultant LCF cycle fraction is larger than it would have been had the HCF life fraction been subtracted from unity (as would be done when applying the LDR). The end result this time is a total life fraction summation of > 1.0 . Figure 2 illustrates this feature of Equation (2). Note that in the extreme with a very large difference between the LCF and HCF lives, the *maximum* cycle fraction summation approaches 2.0, but the *minimum* has no lower limit. Values as low as 0.01 or even 0.001, in theory, could be achieved. These observations lead to another feature of the DCA. Consider a multiply repeated loading pattern for which a very small fraction of LCF damage is followed by a small fraction of HCF loading (potential for deviating far below the LDR), followed by another small fraction of LCF (with potential for deviating above the LDR, but limited to a factor of 2), followed by more LCF, etc. Each shift from LCF to HCF produces a loss that is not bounded, but each shift from HCF to LCF is bounded by a gain of no more than a factor of 2. Calculations for single- and multiple-blocks of loading using Equation (2) have been performed and are shown in Figure 3. The proportions of applied damage at $N_{f,1}$ and $N_{f,2}$ have been selected to maximize the deviation from the LDR. The ordinate is the sum of the cycle fractions at predicted failure and the abscissa is the life, $N_{f,2}$, of the two levels. The lowest life, $N_{f,1}$, is held constant at 10^3 cycles to failure. Clearly, as $N_{f,2}$ increases relative to $N_{f,1}$, the total damage summation decreases. For blocks of alternate LCF and HCF loading, a net loss is predicted. However, the loss is not quite as severe (30% higher cycle fraction summation) as it would have been had the loading involved only a single block.

Application of the DCA to a cumulative fatigue damage evaluation of multiple steps in loading levels leads to a large number of forward and backward solutions of a power law equation. When damage levels

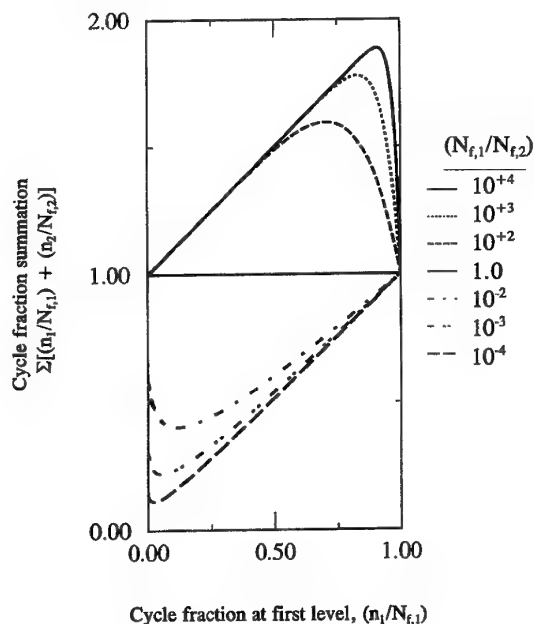


Figure 2 Loading order effects for single-step, two level loadings

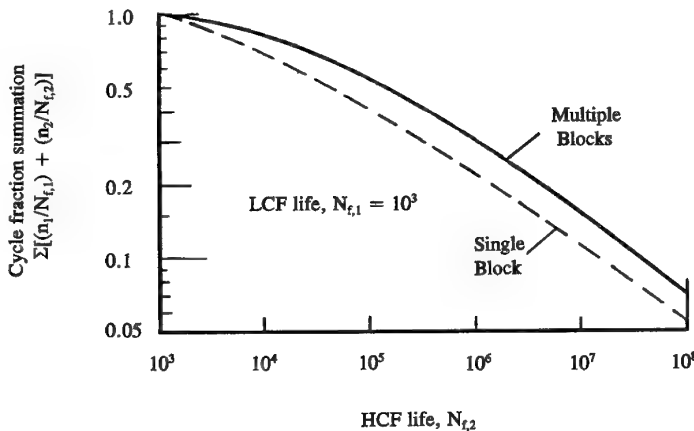


Figure 3 Multiple block loading less damaging than single block

are low, double and triple precision of calculation is necessary to avoid cumulative errors that could overshadow the desired result. Under these circumstances, there is considerable merit in adopting and modifying the DLDR method first proposed in 1961¹⁴.

DOUBLE LINEAR DAMAGE RULE

The computational disadvantages of the DCA for multiple changes in loading levels can be circumvented by approximating the curves of the DCA with bi-linear DLDR representations. Figure 4 shows four life levels according to each model. The straight line connecting the breakpoints of the bi-linear curves has been selected according to the rationale given by Manson and Halford⁴. The region to the lower left of the break points represents Phase I behavior of the material in fatigue, whereas Phase II behavior is to the upper right. Although not required, it may be convenient in the mind's eye to associate Phase I with 'microcrack initiation' and Phase II with 'microcrack' propagation, wherein the ultimate failure herein is best described as 'macrocrack' initiation. Macrocrack initiation precedes macrocrack propagation. This latter regime is more

readily described in terms of fracture mechanics principles developed for long-cracks.

Once the damage accumulation curves have been bilinearized, it becomes a simple matter to describe the fatigue process in terms of the two distinct phases. Since damage accumulates linearly in each phase, a LDR describes each phase. Thus, it becomes a simple matter to apply the classical LDR twice; first to Phase I damage, then starting over and applying the same rule to Phase II damage. The fatigue life used in these respective calculations is not the total life, N_f , but rather, N_I and N_{II} , respectively. Thus, failure is predicted once the two LDRs have been satisfied in sequence

$$\Sigma D_I = \Sigma(n/N_I) = 1.0 \quad (4a)$$

then

$$\Sigma D_{II} = \Sigma(n/N_{II}) = 1.0 \quad (4b)$$

It is now necessary to present the relations between N_I and N_f and N_{II} and N_f . From Manson and Halford⁴

$$N_I = N_f \exp(ZN_f)^{\Phi} \text{ and } N_{II} = N_f - N_I \quad (5a)$$

where

$$\Phi = [1/\ln(N_{f,1}/N_{f,2})] \ln[\ln(0.35Q)/\ln(1-0.65Q)] \quad (5b)$$

$$Z = \ln(0.35Q)/(N_{f,1})^{\Phi} \quad (5c)$$

and

$$Q = (N_{f,1}/N_{f,2})^{0.25} \quad (5d)$$

If the multiple loading pattern has only two life levels, $N_{f,1}$ (the lowest life level in this case) and $N_{f,2}$, Equation (4a) can be solved immediately for N_I and N_{II} . Manson and Halford^{4,13} show a large number of example comparisons of laboratory data with life predictions by the DLDR and the DCA. Either approach is in excellent agreement with the experimental results. However, when a spectrum of life levels is involved, a criterion must be invoked to select the minimum and the maximum total lives ($N_{f,1}$ and $N_{f,2}$) that contribute significant damage so as not to be ignored. Fortunately, because of compensating errors,

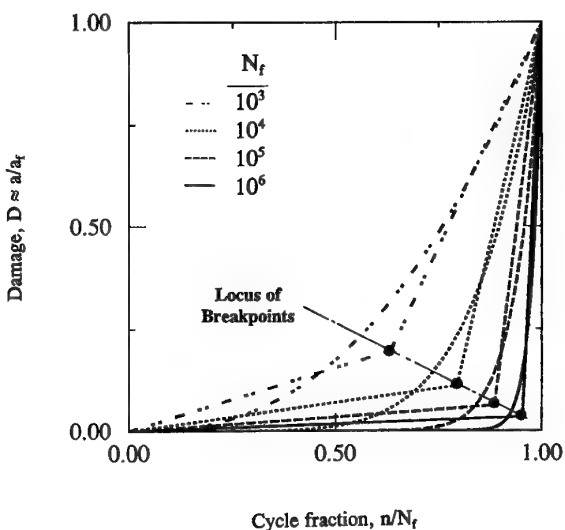


Figure 4 DLDR and DCA

this criterion need not be too precise. As a starting point, it is recommended that the minimum and maximum lives be associated with a cycle fraction n/N_f of at least 0.1% of the life fraction associated with the smallest repeating block.

The numerical example given by Manson and Halford⁴ for an aeronautical gas turbine engine compressor material, Ti-6Al-4V, at 77°C used $N_{f,1} = 2500$ and $N_{f,2} = 64\,000$. Thus

$$N_I = N_f \exp[-111.2(N_f)^{-0.523}] \quad (6a)$$

$$N_{II} = N_f \{1 - \exp[-111.2(N_f)^{-0.523}]\} \quad (6b)$$

While the equations appear complex, application of the DLDR is no more complicated than applying the LDR twice.

Presuming the applicability and hence eventual acceptance of nonlinear cumulative fatigue damage models, the next question facing designers who must project potential durability of their product, is, 'When should we apply a more complex, and slightly more costly, nonlinear damage analysis, and when can we get by with the simple LDR?' The answer to that query is the central issue of this paper. However, before stating the criteria for judging when to ignore the LDR, in favor of a nonlinear rule, the presentation of a couple of examples of mission loadings are instructive.

Perhaps the best illustration of when a nonlinear damage accumulation rule is not needed is the very data base used by Miner in his demonstration of the 'validity' of the LDR. Miner reported cumulative fatigue damage test results for a popular aluminum aircraft skin material of the time, 24S-T ALCLAD. Constant amplitude baseline fatigue tests were conducted at R stress ratios (min/max) of +0.5, +0.2 and -0.2 covering cyclic lives from 20 000 to 3 000 000 cycles to failure (complete separation). Twenty-two cumulative fatigue damage tests were then conducted within this life range using two, three or four levels of loading. Unfortunately, in any given cumulative damage test, the minimum and maximum fatigue life levels included in the loading sequence never exceed a factor of more than ca 10. Consequently, the potential for severe loading order interaction was precluded. The conditions selected were incapable of rendering the tests as critical discriminators. To illustrate this, Table I shows Miner's experimental cycle fraction sums based on a linear cycle fraction summation. The theoretical sum according to the LDR would always be 1.00. Maximum deviations of the experimental from the LDR predictions are 0.61 on the low side to 1.49 on the high side. Similarly, the maximum deviations of the DCA from the LDR are of the same order, 0.64–1.33. These values compare well with the maximum deviations of individual data points from the average fatigue curve of the baseline results³, that is, ca ± 1.5 . The average of the 22 experimental cycle fraction summations is 1.01 compared to the LDR prediction of 1.00 and the DCA prediction of 0.99. In this case, there is no reason to abandon the LDR in favor of a more sophisticated nonlinear damage rule. The extremes in life levels are simply not great enough to expect a nonconservative LDR prediction. Another factor that has limited the maximum deviations observed

Table 1 Comparison of Miner's³ cumulative fatigue damage data for 24S-T ALCLAD aluminum with the LDR and the DCA

Experiment ³ $\Sigma(n/N_f)$	Prediction LDR ¹⁻³ $\Sigma(n/N_f)$	Prediction DCA ^{4,5} $\Sigma(n/N_f)$
1.45	1.00	0.68
0.80	1.00	1.19
0.98	1.00	0.96
1.03	1.00	0.88
0.99	1.00	0.75
1.00	1.00	1.04
0.75	1.00	1.19
0.61	1.00	1.32
0.75	1.00	1.06
1.32	1.00	0.91
1.11	1.00	1.08
0.99	1.00	0.64
0.81	1.00	1.17
1.04	1.00	0.81
0.79	1.00	0.86
1.07	1.00	0.85
1.30	1.00	0.80
1.39	1.00	1.33
0.81	1.00	0.80
1.49	1.00	1.31
0.80	1.00	0.85
0.93	1.00	1.33
1.01 ave.	1.00 ave.	0.99 ave.

is the relative amount of damage imposed at the first loading level in two level tests. The smallest cycle fraction imposed was 0.40. Thus, if the life at the second loading level was unaffected by the first, the damage sum would have been 1.40. Similarly, had there been zero life left for the second loading level, the cycle fraction summation would have been 0.40. These summations could not have differed appreciably from the baseline data scatter, and hence cannot be used as discriminators.

With the subsequent recognition of nonlinear, cumulative damage loading order effects, better designed experiments have been performed. The results of Bizon *et al.*⁹ are an excellent example. A summary plot of their results (each solid symbol represents one LCF/HCF test) for Haynes 188, a cobalt base superalloy, is shown in Figure 5. Life levels used in the two

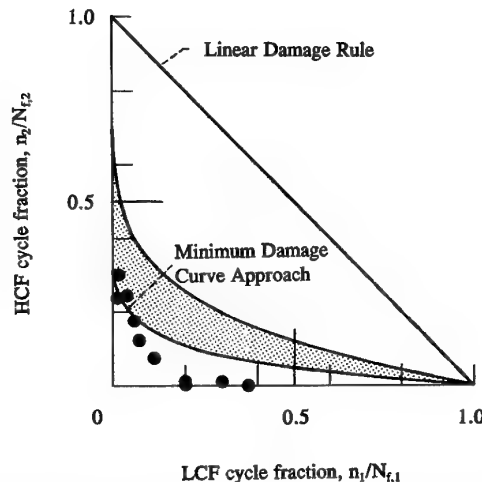


Figure 5 HCF/LCF interaction in single-step, two-level loading. Haynes 188, 760°C⁹

level tests covered four orders of magnitude (30–300 000). The greatest deviations from the LDR occurred at initial LCF life fractions in the vicinity of 0.1, giving rise to a total cycle fraction summation at failure of only 0.18. These results reinforce the two important considerations mentioned earlier for deciding when it may be important to consider a nonlinear damage rule, the range of life levels involved and the proportion of cycle fractions accumulated at each. The predictions of the experimental results by the DCA are not as good as might be desired, but nonetheless are far better than predictions by the LDR. Based upon total cycle fraction summation, the greatest deviations between prediction and experiment for the LDR is 1.0 vs 0.18, a factor of > 5 to 1, and for the DCA is 0.25 vs 0.18, a factor of only 1.4 to 1, a significant improvement in accuracy.

CRITERIA FOR ABANDONING THE LDR

Based upon analytic comparisons of the LDR, DCA and DLDR, the following guidelines can be used to judge when a nonlinear rule will contribute enough additional accuracy to make it worthwhile applying.

First, an assessment must be made of the minimum and maximum life levels to be considered in the cumulative fatigue damage analysis. For this purpose, it is necessary to identify the lowest life level, $N_{f,1}$, and the highest, $N_{f,2}$, in the mission loading spectrum having a cycle fraction, $n/N_f > 0.001$. Then

1. If $N_{f,1}$ and $N_{f,2}$ are less than two orders of magnitude apart, continue with the LDR, because the maximum deviation between the DCA and the LDR under these conditions will be less than a factor of 2 on the total predicted mission life. Since a factor of 2 is representative of reproducibility attainable in baseline fatigue testing, cumulative damage analyses cannot be expected to produce greater accuracy.
2. If $N_{f,1}$ and $N_{f,2}$ are greater than two orders of magnitude apart, a nonlinear damage rule is generally called for. However, the expected improved accuracy will depend upon the proportion of cycle fractions involved in the mission spectrum. Missions dominated ($> 50\%$) by LCF cycle fractions and hence relatively small HCF cycle fractions can continue to be analyzed with the LDR with little loss of accuracy. On the other hand, missions dominated by HCF cycle fractions, yet containing small LCF cycle fractions, should be analyzed with a nonlinear damage rule, since considerable deviation from the LDR would be expected.

EXTENUATING CIRCUMSTANCES

Cumulative fatigue damage analyses tacitly assume the material, while undergoing fatigue damage, retains its original mechanical, physical and thermal properties. Circumstances arise, however, wherein exposure to mission loading environments can cause significant changes to a material's properties. For extended high-temperature exposure, materials can soften due to annealing, harden due to precipitation phenomena, and embrittle due to oxidation or other environmental interactions. Similarly, depending upon the original state of the material entering service, LCF loading into the

plastic regime can cause cyclic strain hardening of initially soft materials and cyclic strain softening of initially cold-worked materials. Such changes alter both the cyclic stress-strain response of the material and its inherent strength and ductility. In essence, the original material has been altered into one with different fatigue properties. These changes should not be classified as fatigue damage *per se*. Mission loadings also can induce crack closure that alters subsequent small crack growth. Similarly, before cracks develop, large loads can alter residual and mean stress states within the material that can alter expected fatigue life, not due to damage, but rather due to changes in the local stress-strain cycling conditions. These latter effects are well known and are taken into consideration during cumulative damage analyses (see, for example, Tuegel and Brooks¹⁸ of this conference). However, only limited attempts have been devoted to developing a better understanding of hardening and softening effects in cumulative fatigue (see, for example, Manson and Hailu¹⁹).

SERVICE RELATED COMPLEXITIES

Structural hardware experiences numerous complexities that are not incorporated in the smooth, polished, axially-loaded, laboratory-sterile coupons used to develop the nonlinear fatigue damage models discussed herein. The question is: How is the DCA (or DLDR) applied to circumstances that differ significantly from those that formed the basis for its development†. To deal with all of the factors would require a sizable handbook. Space limitations dictate only cursory comments on two representative examples, notch effects and surface attack from damage mechanisms other than fatigue. What follows are logical extensions of how the nonlinear damage rules might be applied. In both cases discussed, the LDR would not have the same logical basis for dealing with the truly nonlinear effects. Unfortunately no experimental data are currently available to validate the ensuing suggestions.

Notch effects

The stress-strain concentrating effects of a notch give rise to a gradient of stress and strain at the notch root. The highest values are at the free surface where fatigue cracks would nucleate and begin their growth into a decreasing stress-strain field; a situation quite different from that found in smooth, axially-loaded coupons. For the same nominally applied stresses and strains, a notched specimen will nucleate a crack much sooner than a smooth specimen because of the higher values of local cyclic stress and strain. Once the crack has nucleated and grown for a distance that exceeds the notch depth, the notched specimen no longer perceives the presence of the notch and begins to behave the same as a smooth specimen with the same total crack depth (including the depth of the notch). To truly deal with this transient cracking behavior would require extensive analyses of the steadily decreasing driving forces on the crack. It would also require a

†The same question obviously should be asked of the classical LDR. However, the answer would not necessarily be the same as for the DCA (and DLDR).

far better description of small crack growth behavior than currently exists. However, if the concept of damage evolution based on the DLDR were applied to the notched specimen, a highly simplistic view could be adopted. Namely, the Phase I damage (microcrack initiation) could be based upon the maximum concentrated values of notch root stress and strain via application of the theoretical stress concentration factor (K_T) or if plasticity is involved, via application of the classical Neuber rule[†]. Once Phase I damage has reached unity, then Phase II damage is tracked. Phase II damage (microcrack propagation) would then be assessed on the basis of the nominal stresses and strains applied to the structural region surrounding the notch.

Another important aspect of stress-strain gradients at a notch is the susceptibility to plasticity induced residual stresses if local yielding occurs under high loads. These residual stresses act as fatigue mean stresses and can significantly alter the value of the fatigue life to be used in the DCA or the DLDR. To account for induced residual stresses at a notch root requires a local stress-strain analysis. Fortunately, a relatively simple mechanics of materials analysis approach is available for use, that is, the local Neuber notch analysis²⁰.

Surface attack

Surface attack by mechanisms other than fatigue are numerous. They include mechanically induced surface alterations such as frictional wear, fretting, galling, erosion or high velocity impact. Thermally or chemically induced surface changes include oxidation, sulfidation and corrosion phenomena. These effects may act as damage that can significantly alter the fatigue resistance of a material. Corrosion is selected as a single example for discussion purposes. Massive corrosive attack wherein surface material is lost at rapid rates will be dismissed immediately as being so overwhelming to fatigue resistance that interaction is not an issue. Of greater concern is highly localized corrosion wherein tiny corrosion pits or spikes take on features not totally unlike cracks. In the presence of cyclic stresses and strains, the stress concentrating characteristics of these environmentally induced defects serve to hasten the appearance of fatigue cracks long before initiation by classical fatigue damage mechanisms. In essence, the fatigue microcrack initiation processes can be nearly eliminated, or at least severely foreshortened by corrosive mechanisms. Furthermore, the fatigue microcrack propagation phase could also be shortened by chemically induced weakening of the material immediately ahead of a growing microcrack. The major hurdle to be surmounted seems to be quantification of the extent of corrosion induced damage in a form that is compatible with quantification of fatigue damage. A portion of the hurdle is the cycle dependency of fatigue and the time dependency of corrosion. Simultaneous assessment of these two damaging mechanisms under a variable amplitude loading mission (and perhaps even a variable corrosive environment mission) is a particularly complex task for which little guidance

is available. Yet, simultaneous damage by these two mechanisms occurs in a large number of practical structural applications ranging from naval vehicles and equipment of all types to aging aircraft structures and ground-based vehicles. This is an area of structural durability assessment that needs further research. However, as a first approximation, the microcrack initiation phase of the DLDR could be considered to be consumed entirely by corrosion. This over-approximation would help to account for some of the reduction in the microcrack propagation portion of the total cyclic lifetime.

SUMMARY

Nonlinear cumulative damage rules offer more accurate, and hence more conservative, fatigue life predictions than the LDR. The nonlinear DCA and the DLDR cumulative fatigue damage models require only twice the effort of the classic linear rule. Nor do they require additional material property or mission loading information to achieve the improved accuracy. Greatest improvements accrue when missions include HCF with some severe LCF loadings. Criteria are proposed for judging those severe mission loading circumstances when classical linear damage accumulation becomes unacceptably nonconservative. Extenuating circumstances are noted that should be dealt with prior to performing any cumulative fatigue damage analysis. Brief discussion was devoted to bridging the gap between damage models based on smooth, axially-loaded, laboratory coupons and the application of these models to service mission loading conditions that differ significantly from the sterile laboratory conditions.

ACKNOWLEDGEMENTS

Sponsored by the United States Navy, United States Air Force, Federal Aviation Administration, and Engineering Foundation, New York City.

REFERENCES

- 1 Palmgren, A., Die Lebensdauer von Kugellagern. *Zeitschrift des Vereinesdeutscher Ingenieure*, 1924, **68**(14), 339–341. See also, *The Service Life of Ball Bearings*. NASA technical translation of German text, NASA TT F-13460, Center for Aerospace Information, Linthicum Heights, Maryland, 1971.
- 2 Langer, B. F., Fatigue failure from stress cycles of varying amplitude. *Journal of Applied Mechanics*, 1937, **59**, A160–A162.
- 3 Miner, M. A., Cumulative damage in fatigue. *Journal of Applied Mechanics*, 1945, **67**, A159–A164.
- 4 Manson, S. S. and Halford, G. R., Practical implementation of the double linear damage rule and damage curve approach for treating cumulative fatigue damage. *International Journal of Fracture*, 1981, **17**, 169–192.
- 5 Manson, S. S. and Halford, G. R., Recent developments in practical implementation of the double linear damage rule. *International Journal of Fracture*, 1981, **17**, R35–R42.
- 6 Richart, F. E. and Newmark, N. M., An hypothesis for determination of cumulative damage in fatigue. *Proceedings, American Society for Testing and Materials*, 1948, **48**, 767–800.
- 7 Webber, D. and Levy, J.C., Cumulative damage in fatigue with reference to scatter of results. *Scientific and Technical Memorandum 15/58*. Ministry of Supply, London, UK, 1958.
- 8 Manson, S.S., Freche, J.C. and Ensign, C.R., Application of a double linear damage rule to cumulative fatigue. *Fatigue Crack Propagation*. ASTM STP 415. American Society for Testing and Materials, 1967, Philadelphia, PA. pp. 384–412.
- 9 Bizon, P.T., Thoma, D.J. and Halford, G.R., Interaction of high cycle and low cycle fatigue of Haynes 188 at 1400°F. *Structural*

[†] $(K_T)^2 = (K\sigma)(K\epsilon)$, where $K\sigma$ = actual stress concentration factor and $K\epsilon$ = actual strain concentration factor.

- Integrity and Durability of Reusable Space Propulsion Systems.* NASA CP-2381, 1985, Center for Aerospace Information, Linthicum Heights, Maryland, pp. 129–138.
- 10 McGaw, M.H., Kalluri, S., Moore, D. and Heine, J., The cumulative fatigue damage behavior of MAR-M 247 in air and high-pressure hydrogen. *Advances in Fatigue Lifetime Predictive Techniques*, second volume (Eds Mitchell, M.R. and Landgraf, R.W.). ASTM STP 1211. American Society for Testing and Materials, 1993, Philadelphia, PA, pp. 117–131.
- 11 O'Neill, M.J., *A Review of Some Cumulative Damage Theories.* ARL/SM-Report-326, Aeronautical Research Laboratories, Melbourne, Australia, 1970.
- 12 Schijve, J., The accumulation of fatigue damage in aircraft materials and structures. AGARD-AG-157, Advisory Group for Aerospace Research and Development, Paris, 1972.
- 13 Manson, S. S. and Halford, G. R., Re-examination of cumulative fatigue damage analysis—an engineering perspective. *Engineering Fracture Mechanics*, 1986, **25**, 539–571.
- 14 Manson, S. S., Nachtigall, A. J. and Freche, J. C., A proposed new relation for cumulative fatigue damage in bending. *Proceedings American Society for Testing and Materials*, 1961, **61**, 679–692.
- 15 Walcher, J., Gray, D. and Manson, S.S., Structural design analysis aspects of cold end rotating structures. AIAA Paper 79-1190, 16 American Institute of Aeronautics and Astronautics, Reston, VA, June 1970.
- 17 Halford, G.R. and Manson, S.S., Re-examination of cumulative fatigue damage laws. *Structural Integrity and Durability of Reusable Space Propulsion Systems.* NASA CP-2381, 1985, Center for Aerospace Information, Linthicum Heights, Maryland, pp. 139–145.
- 18 Halford, G.R., Over pressure proof factors for fatigue loaded pressure vessels. *Material Durability/Life Prediction Modeling—Materials for the 21st Century*, PVP-Vol. 290 (Eds Zamrik, S.Y. and Halford, G.R.). ASME, New York, 1994, pp. 49–56.
- 19 Tuegel, E. and Brooks, C., Cyclic relaxation in compression-dominated structures. Paper No. 34, *First International Conference on Fatigue Damage in Structural Materials*, Hyannis, MA, 22–27 September 1996. The Engineering Foundation, New York, 1996.
- 20 Manson, S.S. and Hailu, S., Maverick behavior of the irreversibly hardening 304 stainless steel in sequential loading. *Material Durability/Life Prediction Modeling—Materials for the 21st Century*, PVP-Vol. 290 (Eds Zamrik, S.Y. and Halford, G.R.). ASME, New York, 1994, pp. 1–9.
- Anon, *Fatigue Design Handbook*, Section 3.2, SAE, Advances in Engineering, Vol. 4, 1968, New York.

PII: S0142-1123(97)00031-5

Analytical modeling for life extension of aging equipment

R.A. Sire and S.W. Hopkins

Failure Analysis Associates, Inc., 149 Commonwealth Drive, Menlo Park, CA 94025,
USA

Rising replacement costs for all types of structures continue to pressure the technical community to find methods for reliably extending the useful lifetime of existing structures. Structures having significantly long remaining lives from reliably detectable levels of damage are the best candidates for lifetime extension. Methods for identifying the best candidates, methods for developing and validating analytical life prediction models, and areas which need improvement are discussed. © 1998 Elsevier Science Ltd.

(Keywords: life extension; nondestructive evaluation; analytical modeling)

INTRODUCTION

Not all aging structures are currently good candidates for reliable lifetime extension. In many cases, structures must be classified as poor candidates because of a lack of tools and techniques for reliably measuring damage.

Figure 1 shows a generic representation of damage accumulation with usage. Damage can be quantified using any measurable parameter that directly relates to remaining life. Crack length is a commonly used damage parameter for structures in which crack growth leads to failure. Loading can be either cyclic (i.e. fatigue) or constant (i.e. creep or stress corrosion). Structural wall thickness is another parameter that can be used to quantify general corrosion or erosion dam-

age. The usage parameter can be either exposure time, loading cycles, or a combination of both, depending on the dominant life-limiting damage mechanism. Selection of the most appropriate usage parameter is important for damage modeling, and the choice is not always obvious. An example of inappropriate usage parameter selection occurred in the aircraft industry when the number of operating hours was chosen to quantify both airframe life and engine life between inspections. However, in most cases both airframe and engine damage accumulates more directly with the number of operating cycles (take-off/landing, maneuvers) and not the amount of time in operation. Many years ago, aircraft averaged about 1 h per flight. Cumulative damage was typically assessed in terms of operating hours. Usage of today's commercial aircraft can range from commuter flights averaging less than 1 h per flight to international flights that can last in excess of 10 h. Therefore, the actual number of flights and not operating hours becomes very important in predicting damage accumulation in aircraft, especially for fatigue critical components in aircraft experiencing frequent ground-air-ground cycles.

The foregoing example is not intended to imply that exposure time is not an appropriate usage parameter in all cases. Damage accumulation in components for which life is limited by creep or corrosion mechanisms is best quantified in terms of exposure time. There are a number of articles and books that describe in detail the procedures for performing lifetime extension calculations¹⁻³.

Initial damage (crack size)

Classification of a specific component within the framework shown in Figure 1 helps to determine whether or not the component is a candidate for life

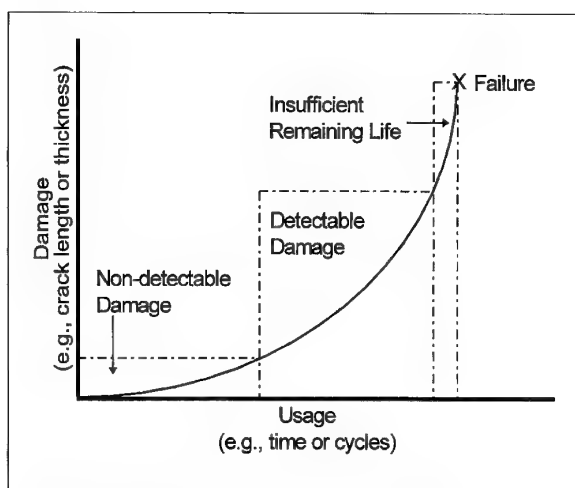


Figure 1 A generic case of damage accumulation with usage

extension. If a component expends only a small portion of its useful life developing *detectable* damage, then it is likely to be a good candidate. Conversely, if a component expends a relatively large fraction of its useful life developing detectable damage, then the component is not a good candidate for life extension. Therefore, there is a continuous effort to improve damage detection capabilities to locate and quantify smaller and smaller levels of damage.

Unfortunately, the reliability of detecting damage decreases with the magnitude of damage, as is shown for example in *Figure 2* for cracking. The bars in *Figure 2* represent detection reliability for a particular eddy-current inspection process used for turbine disk bolt holes⁴. The reliability of simply detecting a surface crack within the bolt hole (Criterion A) is only 35% if the actual crack is less than 0.010 in long, and improves to over 90% if the crack is 0.1 to 0.2 in long. This data also shows that reliability decreases when additional requirements are placed on the detection process. For example, the reliability decreases slightly if the inspector must also identify which side of the bolt hole is cracked, either radially inward or radially outward (Criterion B). If the inspector is also required to size the length of a surface crack within a factor of 2 (Criterion C), then the inspection reliability decreases even further. By imposing the additional requirement that the inspector correctly reports the position along the length of a bolt hole to within 1/8 of the bolt hole length (Criterion D), the reliability is further reduced to a small fraction of the initial 'detection only' level. These evaluations also showed a consistent trend toward lower reliability for smaller crack sizes.

A trade-off exists between accurate detection and sizing of smaller defects and inspection reliability. Even with large cracks in this example, 100% inspection reliability could not be achieved. This leads to the

most important question the analyst must ask the inspector.

What is the largest damage (crack) that will not be detected?

The answer to this question will determine the location of a component on the damage axis in *Figure 1*. In most cases, this must be treated probabilistically using the distribution of crack sizes that could go undetected for a particular inspection process.

Laboratory testing

Once a component has been identified as a candidate for lifetime extension, materials data characterizing damage progression as a function of usage must be obtained, either from an existing material database or through laboratory testing. In the following discussion, fatigue crack growth is used as a representative damage mechanism.

In the laboratory, fatigue crack growth rate testing is often done with constant amplitude loading, and crack length is measured as a function of the number of applied load cycles. *Figure 3* shows a schematic representation of typical laboratory specimen data for fatigue crack growth. Numerous tests may be conducted using different constant amplitude loads, different mean loads, and/or different initial crack sizes. The data from each specimen is then reduced to crack growth rate per cycle (da/dN) as a function of crack tip stress intensity factor range (ΔK), similar to the materials data⁵ shown in *Figure 4*. The data may further be curve-fit using any of a number of existing mathematical models developed to account for load ratio and/or crack closure effects on fatigue crack growth rate.

The analyst should then take the materials data or fitted growth rate model and numerically simulate the

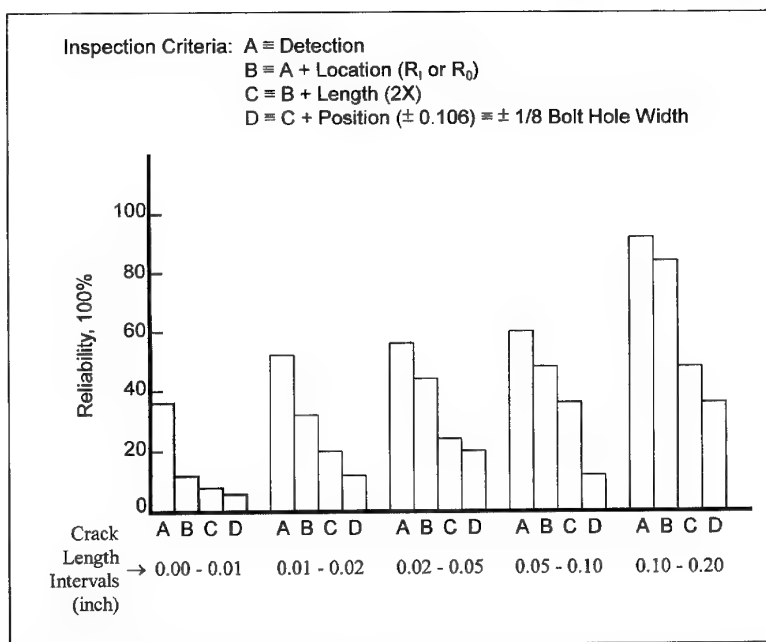


Figure 2 Inspection reliability for cracking in a bolt hole population as a function of inspection criteria and crack size. Selected surface crack length intervals are indicated

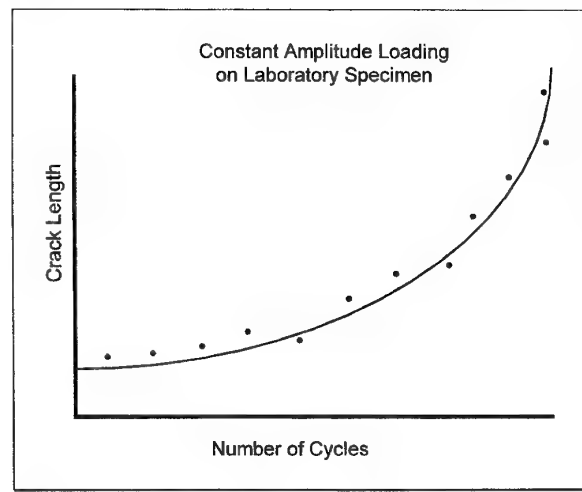


Figure 3 Schematic representation of typical laboratory data of fatigue crack length as a function of applied load cycles

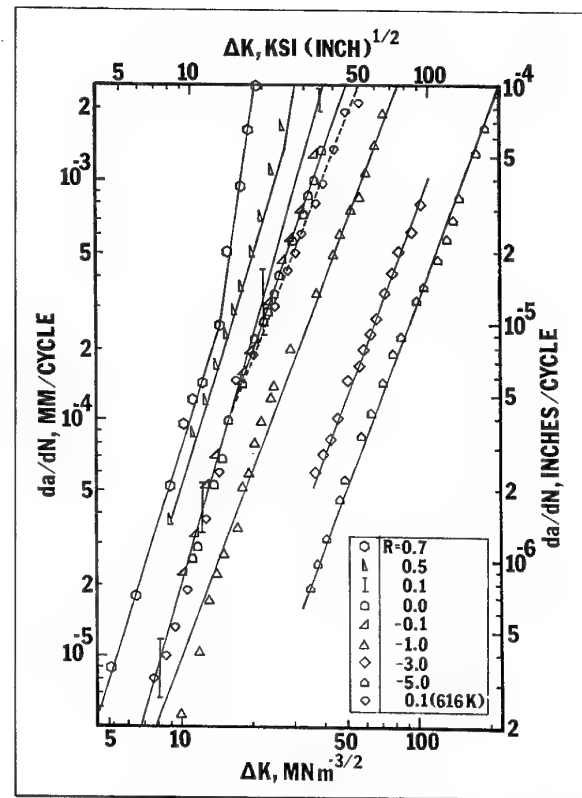


Figure 4 Crack growth rate as a function of stress intensity factor range for various R -ratios in a Ti-6Al-4V material tested at room temperature and 616 K

laboratory specimen performance to confirm the validity of the data reduction and the analytical model. The analyst must know the specimen size, loads, and initial crack size in order to simulate crack growth as a function of applied cycles (Figure 3). This is the most fundamental check on a lifetime prediction model. If the analyst cannot accurately predict the specimen results, then the laboratory data and the analytical model should be revisited to determine the source of

the discrepancy. The analyst should simulate every laboratory specimen test to ensure that both the model and the data reduction process are correct.

The next step in providing assurance that the lifetime prediction model is reliable involves predicting the fatigue crack growth behavior for a component level laboratory test under constant amplitude loading *prior* to testing. Any disagreement between the prediction and the subsequent outcome of the component test must be reconciled.

Variable amplitude or block loading laboratory testing at the component level is the next phase in building confidence in the lifetime prediction model. Variable amplitude cyclic loading requires that the lifetime prediction model have a means of accounting for various spectrum loadings. Most structures are subjected to spectrum loading and not constant amplitude loading. If a successful lifetime prediction can be made without having to generate materials data under spectrum loading, then there is no reason to conduct the additional specimen testing. If, on the other hand, the lifetime prediction model cannot successfully predict the component laboratory results, then additional laboratory testing and modeling are required. Figure 5 shows a flow chart that depicts the basic confirmation steps just described.

Field experience

Field experience should also be used for validation of any lifetime prediction model. Any service component that is being retired because of observed damage should be analyzed with the same lifetime prediction model. This should also be done for field failures.

By assuming that a crack or damage of a size just below the detectable limit existed at the time of the last inspection of a component, and knowing the number of cycles (usage) that the component experienced since the last inspection, does the lifetime prediction model yield a crack size equal to or larger than the currently observed crack size? Alternatively, the model could be used to back-calculate the size of damage that was missed during the last inspection by using the currently observed damage size. In this case, could the back-calculated size have been missed with a reasonable probability based on the currently perceived inspection reliability?

These types of comparisons with prior field experience represent a critical validation/calibration step for any predictive model. A model must be capable of accurately simulating past experience before being used to predict future performance.

Laboratory materials data

As discussed earlier, material property data generated in the laboratory is a very important input to any lifetime prediction model. However, generation of a wide range of data encompassing many influential variables can be very expensive. For this reason, utilization of existing data either from proprietary databases or the open literature can aid in the development of a robust analytical model for a particular damage mechanism. Existing data for several materials covering a broad range of independent variables can be used to validate a particular damage model at a fraction of the cost of generating such data for a specific material of interest. Once a damage model has been validated

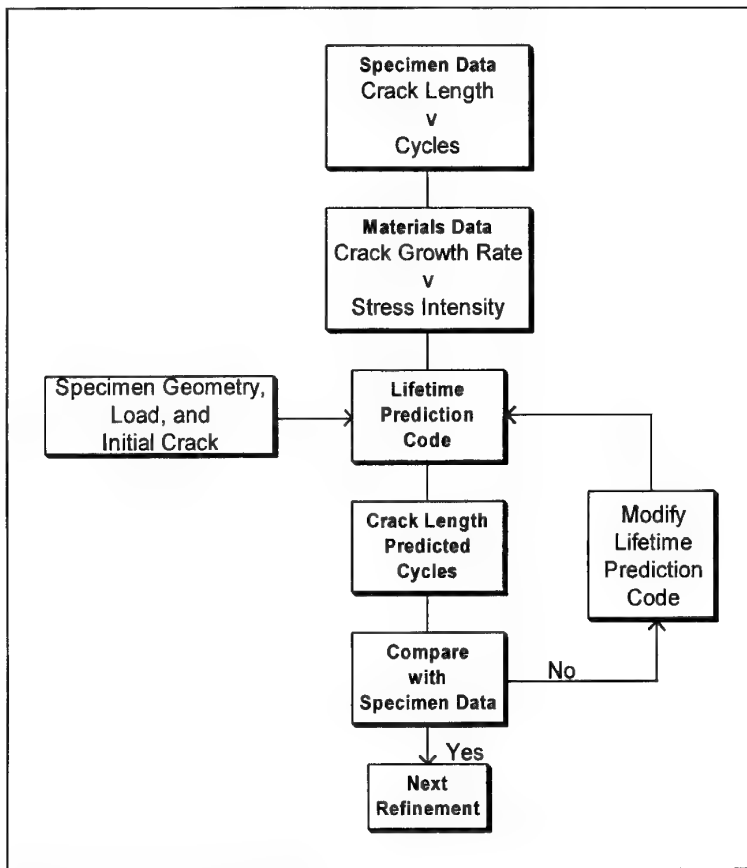


Figure 5 Representation of model validation process

using existing data (preferably for similar materials), then a much smaller number of tests are required to calibrate the model for a specific material for which existing data may not be available.

For example, the material data^{5,6} shown in Figures 4 and 6 provide sets of data for characterizing crack growth behavior in Ti-6Al-4V over a broad range of *R*-ratios. The exact dependence of growth rate on *R*-ratio for a different alloy will depend on the alloy. However, an analytical model capable of reproducing the *R*-ratio effects shown in Figures 4 and 6 could then be calibrated for another similar material by conducting two to three *R*-ratio tests at *R* values bracketing the range of interest. The validated and calibrated model then provides a means for interpolating growth rates at intermediate *R*-ratios.

Normalized material data for fatigue crack growth threshold following a single cycle overload⁶ on the previously presented materials is shown in Figure 7. For all of this work the fatigue crack growth threshold was defined at a crack growth rate of 10^{-10} in cycle⁻¹. Tests were first performed to measure the baseline threshold, without an overload, which is shown in Figure 6. Then additional tests were performed in which a single cycle overload (to a maximum stress intensity factor K_{OL}) was applied to the specimen before the threshold stress intensity factor was measured. In Figure 7, the baseline measurements have been identified by a subscript B for both the threshold stress intensity range (ΔK_{THB}) and the corresponding maximum stress intensity factor (K_B). The resulting

threshold stress intensity range (ΔK_{TH}) data after the single cycle overload was then normalized by the baseline data. Figure 7 shows that the normalized data is essentially independent of the applied *R*-ratio. All of the data presented in Figures 6 and 7 was generated using crack sizes commonly considered to be in the long crack regime.

For most lifetime prediction applications, the long crack regime is the only regime of interest due to nondestructive evaluation (NDE) limitations. Most commonly applied NDE inspection methods cannot reliably detect cracks (or damage) in the small crack regime. Initial defects and fatigue cracks that can be reliably detected are typically of a size where they will behave like long cracks. For this reason, most lifetime extension models are based on long crack behavior, and they use NDE results to assess current levels of damage.

The detection and sizing reliability of NDE inspection is continually improving. As improvements are made in NDE reliability, needs will increase for more accurate predictive models and more material crack growth rate data in the short crack regime.

SUMMARY

- Only components having significant remaining life from a *reliably detectable* level of damage are good candidates for lifetime extension.
- Tools are currently available to perform accurate lifetime predictions for components.

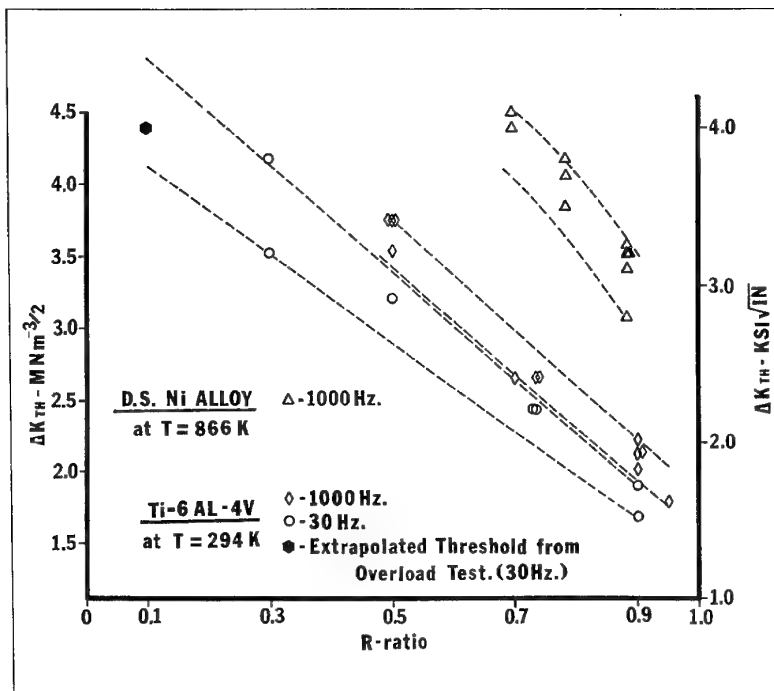


Figure 6 Threshold stress intensity factor range as a function of stress ratio for two alloys at 30 and 1000 Hz. The threshold is defined at a crack growth rate of 10^{-10} in cycle $^{-1}$

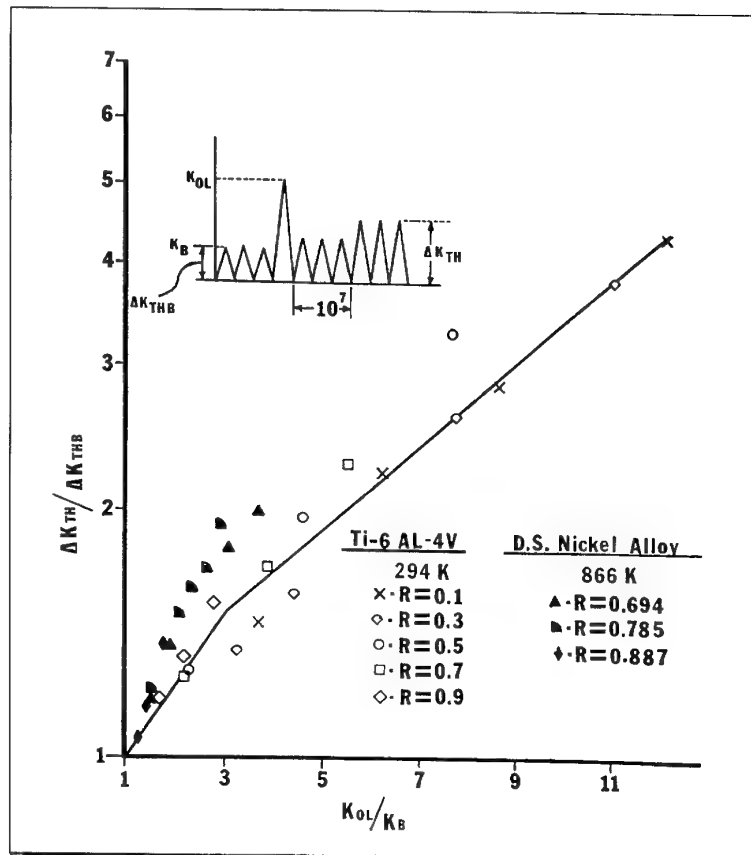


Figure 7 Relative change in fatigue threshold following single cycle overloads as a function of the relative overload for two alloys at various R-ratios. The threshold is defined at a crack growth rate of 10^{-10} in cycle $^{-1}$

- Improvement is needed in reliable NDE methods to find damage earlier in a component's lifetime.
- NDE improvements will expand the range of components to which lifetime extension techniques can be applied.

REFERENCES

- 1 Hopkins, S. W. and Rau Jr., C. A., Prediction of structural crack growth behavior under fatigue loading. *Fatigue Crack Growth Measurement and Data Analysis*, eds S. J. Hudak Jr. and R. J. Bucci. ASTM STP 738, American Society for Testing and Materials, 1981, pp. 255-270.
- 2 NASCRAC™, NASA CRack Analysis Code, Version 3.0. Failure Analysis Associates, Inc., Menlo Park, CA, 1996.
- 3 *Fatigue Design Handbook*, AE10. Society of Automotive Engineers, Inc., 1988.
- 4 Allison, D. E. et al., Cost/risk analysis for disk retirement. Air Force Wright Aeronautical Laboratory, AFWQAL-TR-83-4089, 1984.
- 5 Yuen, A., Hopkins, S. W., Leverant, G. R. and Rau, C. A., Correlations between fracture surface appearance and fracture mechanics parameters for stage II fatigue crack propagation in Ti-6Al-4V. *Metalurgical Transactions*, 1974, **5**, 1833-1842.
- 6 Hopkins, S. W., Rau Jr., C. A., Leverant, G. R. and Yuen, A., Effect of various programmed overloads on the threshold for high-frequency fatigue crack growth. *Fatigue Crack Growth Under Spectrum Loads*, eds R. P. Wei and R. I. Stephens. ASTM STP 595, American Society for Testing and Materials, 1976, pp. 125-141.

PII: S0142-1123(97)00022-4

Modeling of cyclic stress-strain behavior and damage mechanisms under thermomechanical fatigue conditions

H.J. Maier and H.-J. Christ

Institut für Werkstofftechnik, Universität-GH-Siegen, 57068 Siegen, Germany

A multi-component model was applied to predict the cyclic stress-strain response of different alloys under thermomechanical fatigue conditions based upon isothermal hysteresis loops. A ductile AISI 304 L-type stainless steel and two high strength alloys, the near- α titanium alloy IMI 834 and the nickel-base superalloy IN 100, were chosen as test materials. These represent alloys with rather different dislocation slip modes, stress-strain characteristics and damage mechanisms. Model predictions are compared with experiments and the differences in cyclic stress-strain response and damage mechanisms under isothermal and thermomechanical fatigue conditions, respectively, are discussed based upon microstructural observations. © 1998 Elsevier Science Ltd.

(Keywords: modeling of cyclic stress-strain response; thermomechanical fatigue; damage mechanisms)

INTRODUCTION

Ideally, fatigue life prediction methods should be based on laboratory data obtained in tests which resemble as closely as possible those experienced by the actual component. Many high-temperature components, such as turbine blades used in aero engines, are subjected to complex mechanical strain cycles in combination with thermal transients, and often thermomechanical fatigue (TMF) is the life-limiting degradation mode. As TMF testing requires expensive equipment and is time-consuming, fatigue life prediction is usually based on isothermal laboratory tests run at the maximum operating temperature experienced by the component. It is assumed that this test method leads to a conservative lifetime prediction. However, the cyclic stress-strain response, crack initiation and crack growth are often reported to be different in tests performed under isothermal and TMF conditions^{1,2}, respectively, which may lead to a non-conservative life prediction if only the isothermal case is considered³.

Advanced life prediction methods usually require an accurate knowledge of the cyclic stress-strain path. Further, there is increasing interest in the development of lifetime assessment methods based upon microstructural observations as these methods appear to have the potential for a reliable prediction of fatigue damage under service conditions. Multi-component models have been shown to be closely related to microstructure⁴ and to be applicable to both isothermal cyclic loading conditions^{5,6} as well as high-temperature creep deformation⁷.

In the present study a multi-component model was

used to calculate the cyclic stress-strain response under TMF conditions of three different alloys. The alloys studied were chosen so as to cover different cases of stress-strain characteristics and damage mechanisms.

EXPERIMENTAL DETAILS

In the present paper the cyclic stress-strain response of a near- α titanium alloy IMI 834, an AISI 304 L-type steel and a nickel-base superalloy IN 100 under isothermal and TMF conditions is modelled. The titanium alloy IMI 834 (5.8Al–4.0Sn–3.5Zr–0.7Nb–0.5Mo–0.35Si–0.06C, in wt%) was tested with both an equiaxed and bimodal microstructure. All fatigue tests on this alloy were run in symmetrical push–pull closed-loop plastic strain control using a triangular waveform. In the TMF tests the maximum temperature corresponded either to the maximum strain (in-phase tests) or to the minimum strain (out-of-phase tests). Cylindrical samples with a gauge length of 14 mm and a gauge diameter of 8 mm were used. Prior to testing the gauge section was electropolished. In all tests on IMI 834 reported here the plastic strain rate ($\dot{\epsilon}_{pl}$) was kept constant throughout the tests.

Data for the stainless steel were taken from Zauter *et al.*⁸. Those tests were run in a similar manner to the tests on IMI 834. For further details see Ref. ⁸. Modeling of the deformation behavior of the IN 100 alloy was done based upon isothermal data given in Mallet *et al.*⁹. The tests reported therein were all run in total strain control.

MODELING OF CYCLIC STRESS-STRAIN BEHAVIOR

In recent years there has been an increasing interest in multi-component or composite models as these are closely related to microstructure^{5,6}. Obviously, a microstructure such as the one shown in *Figure 1*, where phases with different mechanical properties are present, can be treated as a composite on a macroscopic level. However, composite models are also applicable to single-phase materials as cyclic deformation often results in the formation of a heterogeneous dislocation arrangement. Thus, even in a single-phase material the variation in the local dislocation density will cause a spatial variation of the yield stress within the microstructure. Further variations in local yield stress may arise from different grain orientations or when precipitates are present. Similar to the original model proposed by Masing¹⁰ in 1923, such a microstructure can be considered in a first approximation to be a composite consisting of elastic-perfectly plastic elements with different yield stresses that are strained in parallel, see e.g. Refs^{5,11-13}. As shown in various studies, composite models can describe kinematic hardening¹⁴, the Bauschinger effect and a memory of prior load history⁶. Furthermore, multi-component models are extended to three dimensions if the yield points are replaced by yield surfaces¹⁵.

Isothermal conditions

Under stabilized *isothermal* deformation conditions the microstructure does not change from cycle to cycle and also does not change within a given cycle¹⁶. Thus the distribution of the local yield stresses (σ_{yi}) of the elements i also remains unchanged. The distribution of σ_{yi} within the microstructure can be described by a normalized probability density function ($f_p(\sigma_{yi})$). The striking advantage of the composite model as used here is that this function can be calculated directly from the experimentally obtained stress-strain hysteresis loop as

$$f_p(\sigma_{yi}) = -\frac{2}{E} \frac{d^2\sigma_r}{d\epsilon_r^2} \quad (1)$$

where σ_r and ϵ_r refer to stress and total strain with respect to the last load-reversal point and E is the elastic modulus, see Ref.⁶. As a consequence of the parallel arrangement considered, $f_p(\sigma_{yi}^*)d\sigma_{yi}$ represents the area fraction of the elements that have a yield stress in the range from σ_{yi}^* to $\sigma_{yi}^* + d\sigma_{yi}$.

Figure 2 shows a stabilized hysteresis loop of the high-temperature titanium alloy IMI 834 fatigued at 500°C. Note that the hysteresis loop is plotted in relative coordinates. As this is a high strength alloy with a low elastic modulus, a nonlinear elastic behavior can be observed even at a relatively large plastic strain amplitude ($\Delta\epsilon_{pl}/2$), cf. *Figure 2*. At lower temperatures or in the low-temperature part of a TMF hysteresis loop the deviation from linear elasticity is even more pronounced. Thus, in the following the true plastic strain was calculated using a quadratic extension of

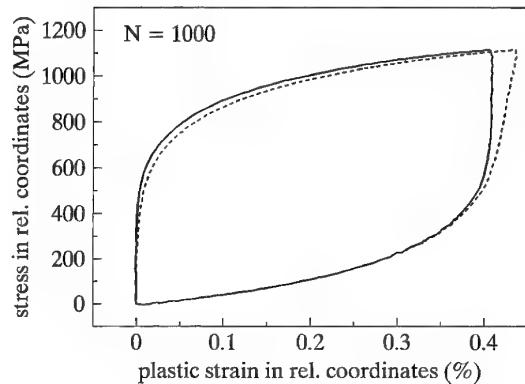


Figure 2 Experimentally obtained stabilized stress-strain hysteresis loop for equiaxed IMI 834 fatigued at $\Delta\epsilon_{pl}/2 = 0.2\%$, $\dot{\epsilon}_p = 1.6 \times 10^{-3} \text{ s}^{-1}$ and $T = 500^\circ\text{C}$. Dashed line: plastic strain calculated using Hooke's law; solid line: plastic strain corrected for nonlinear elasticity

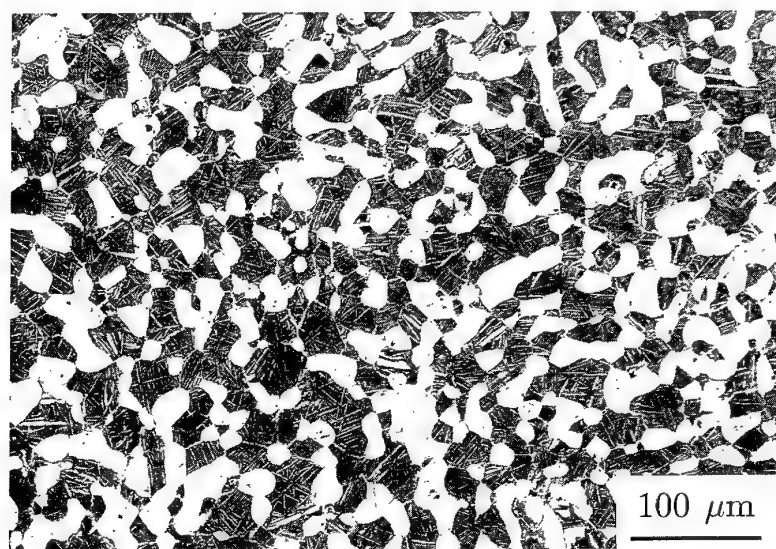


Figure 1 Optical micrograph of IMI 834 with bimodal microstructure showing bright etching primary α -phase and lamellar transformed prior β -phase

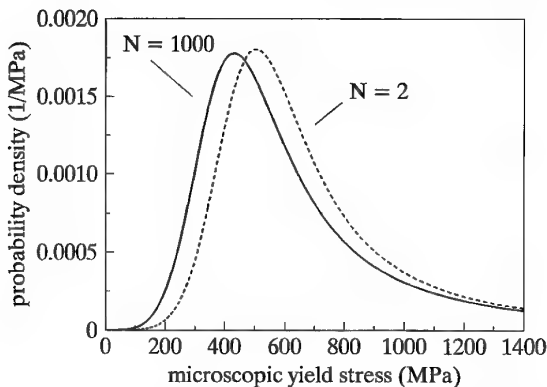


Figure 3 Probability density functions for equiaxed IMI 834 at $N = 2$ and $N = 1000$, respectively. Deformation conditions as in Figure 2

Hooke's law. For a detailed discussion of nonlinear elastic effects on cyclic stress-strain response see Ref. ¹⁷.

In Figure 3 the solid line represents the probability density function evaluated from the hysteresis loop shown in Figure 2, i.e. it represents stabilized deformation conditions. IMI 834 like other titanium alloys shows an initial cyclic softening as cyclic deformation involves strain localization as a result of shearing of ordered Ti_3Al precipitates. This change in microstructure affects the hysteresis loop shape. For comparison the probability density function evaluated from the second cycle is also included in Figure 3. However, the amount of cyclic softening in this alloy is relatively small as compared to the effects of temperature discussed in the next section, and cyclic saturation occurs quite rapidly. Therefore, only stabilized deformation conditions will be addressed in the following.

For calculation purposes it is convenient to replace the continuous distribution function given in Figure 3 by a discrete one with about 30 to 50 individual elements. Such a discrete distribution function is plotted in Figure 4. From this the stress-strain response of the material is calculated as illustrated for a simple two-element composite in the inset to Figure 4. In an iterative process all elements are strained by a small increment $\Delta\epsilon$ and the stresses acting on the individual elements are calculated assuming elastic-perfectly plas-

tic behavior of each element. This assumption is reasonable at least at intermediate (1×10^{-3} to 5×10^{-3}) plastic strain amplitudes ¹⁶. The total stress acting on the composite at point A in the inset to Figure 4 is given by the sum over the products of the stress acting in each individual element times the individual area fraction. Repeating this process, the stresses at points B, C and so on are determined. If smaller strain increments are chosen, the dashed stress-strain path plotted in the inset to Figure 4 results. If a complete discrete distribution function with about 30 to 50 elements is used instead of the simple two-element model just discussed, a smooth hysteresis loop will result. Note that as long as the microstructure does not change significantly during cycling the model accurately predicts the stress response for any given strain path from the analysis of a single hysteresis loop including the Bauschinger effect and memory of prior load history ⁶.

Non-Isothermal conditions

In a TMF test, the temperature changes continuously during cyclic deformation. Hence, the yield stress of the individual elements which are dependent on temperature will change within a cycle even if no further microstructure changes occur. For the sake of simplicity we will assume that the microstructure at any given temperature within a TMF cycle corresponds exactly to the microstructure obtained in an isothermal test at that specific temperature. In the following this will be termed pseudo-isothermal TMF behavior. If this assumption holds true, the stress-strain path is calculated iteratively, as in the isothermal case, but the probability density functions and the elastic modulus have to be determined for each temperature. For the details on the actual implementation of the model see Ref. ¹⁸. In most cases it is sufficient to use interpolated data from isothermal reference cycles obtained in intervals of about 100°C. Therefore, if pseudo-isothermal TMF behavior is assumed, the only input to the model required is isothermal hysteresis loops. These loops are also used to calculate the elastic modulus as a function of temperature and stress. In the next section the model predictions will be compared with TMF experiments and interpreted based on microscopic observations.

RESULTS AND DISCUSSION

High-Temperature titanium alloy IMI 834

In Figure 5 three probability density functions obtained from isothermal tests on equiaxed IMI 834 are shown. At the lowest temperature of 400°C a relatively broad distribution of microscopic yield levels is observed. As the temperature is increased the yield strength of all microscopic elements decreases, i.e. the distribution functions are shifted to the left. Furthermore, the distribution function obtained at 600°C is less broad than those obtained at lower temperatures, which indicates that the drop in yield stress with temperature is more pronounced for high yield level elements than for soft ones. From the three isothermal distribution functions plotted in Figure 5, a TMF hysteresis loop for in-phase cycling was predicted. The comparison between the computer-simulated hysteresis loop and the experimentally obtained one in Figure 6 demonstrates that the stress-strain response under TMF

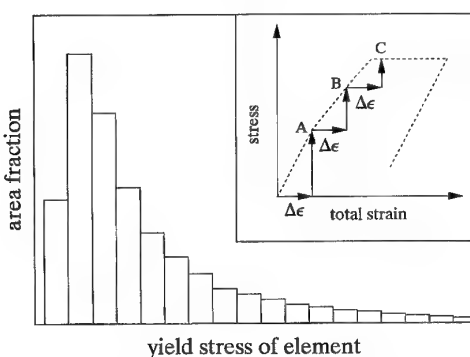


Figure 4 Discrete probability density function as used for modeling (schematic). The inset shows the iterative procedure used to calculate the stress-strain response of the material, see text for details

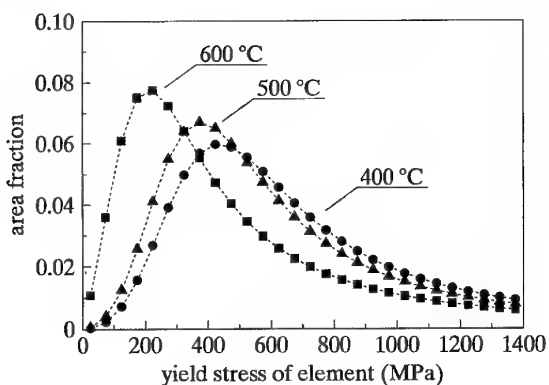


Figure 5 Probability density functions for different temperatures as calculated from isothermal test on IMI 834 fatigued at $\Delta\epsilon_p/2 = 0.2\%$ and $\dot{\epsilon}_p = 8 \times 10^{-5} \text{ s}^{-1}$

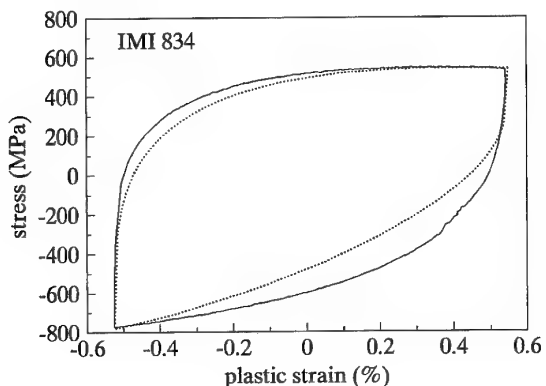


Figure 6 Experimentally obtained TMF hysteresis loop (solid line) of equiaxed IMI 834 and computer-simulated based hysteresis loop (dotted line). In-phase cycling between 400 and 600°C at $\Delta\epsilon_p/2 = 0.5\%$ and $\dot{\epsilon}_p = 2 \times 10^{-5} \text{ s}^{-1}$

conditions is predicted well in the low- and the high-temperature part of the hysteresis loop. At intermediate temperatures, especially in the descending part of the hysteresis loop, the magnitudes of the predicted stresses are significantly below the experimentally observed ones. Transmission electron microscopy (TEM) indicated that in all isothermal tests the precipitation of Ti_3Al promoted the formation of intense slip bands on basal planes, cf. *Figure 7*. The formation of subgrain structures was observed only occasionally in tests run at 600°C. In other words, the microstructure does not change significantly either between isothermal tests or during a TMF cycle, since shearing of Ti_3Al is the dominant mechanism operating over the whole temperature range. Hence, the changes in the probability density functions shown in *Figure 5* are mainly caused by changes in the yield level of the microscopic elements and not by significant changes in the dislocation arrangement. In other words, the assumption of pseudo-isothermal TMF behavior is reasonable and hysteresis loops predicted based on isothermal experiments and experimentally obtained TMF hysteresis loops should match well. As seen in *Figure 6*, this is the case in the low- and high-temperature part of the hysteresis loop. TMF tests run at higher mean temperatures¹⁹ indicated that dynamic strain aging

effects are more pronounced in TMF tests than in isothermal tests. Hence, since dynamic strain aging is not included in the model, the predicted stresses at intermediate temperatures are lower than the actual ones.

Microstructural changes are expected during long-term, high-temperature aging of a component under service conditions. These changes in microstructure affect the microscopic yield levels and thus the cyclic stress-strain response of the material is altered. For many high-temperature components like aero engine turbine blades that experience TMF loading conditions, start-up and shut-down times are short and operating times are relatively long. Therefore, it is often reasonable to assume that the microstructure in the real component is similar to the one established in a long-term isothermal test run at the maximum temperature of the TMF cycle. In silicon containing high-temperature titanium alloys like IMI 834, high-temperature aging for long periods results in the formation of incoherent silicide precipitations which nucleate preferentially on α platelet boundaries²⁰. In such a case probability density functions determined from *isothermal* hysteresis loops obtained from samples artificially aged at high temperature could be used to predict the cyclic stress-strain response of real components under long-term service conditions.

The fatigue lives of IMI 834 in isothermal tests run at 600°C and in-phase TMF tests run between 400 and 600°C were found to be almost identical within the experimental scatter. Out-of-phase testing was much more damaging and fatigue life was a factor of two to three lower than in the other test modes. This was observed for both equiaxed and bimodal microstructures¹⁹. Creep and fatigue tests showed that creep damage in both the isothermal fatigue tests run at 600°C and the TMF tests is negligible.

At high temperatures a non-protective oxide layer forms on titanium alloys. Oxygen can diffuse into the metal matrix and stabilizes and hardens the α -phase, thus a brittle subsurface layer (α -case) is formed. In isothermal tests the oxygen-penetrated zone is thicker than in a TMF test. However, in an out-of-phase TMF cycle the tensile stresses in the low-temperature part of the hysteresis loop are significantly higher than the tensile stresses generated in an isothermal test run at the maximum temperature of the TMF test. Indeed, scanning electron microscopy revealed that in out-of-phase tests quasi-cleavage along the basal planes occurred frequently in surface grains and in grains near to the surface. Thus, oxygen-penetration eases crack nucleation and enhances the growth rate of small cracks. In an isothermal test run at 400°C tensile stresses were quite high, however oxygen diffusion into the matrix was negligible. Thus, irrespective of the actual test temperature, isothermal testing will always result in *non-conservative* estimates of out-of-phase TMF fatigue life in this alloy. Again, isothermal tests of samples artificially aged at the maximum temperature expected during service, say 600°C, and then tested at lower temperatures and high stresses might give better estimates of fatigue life under TMF loading conditions than isothermal tests run at the maximum temperature of the TMF cycle.

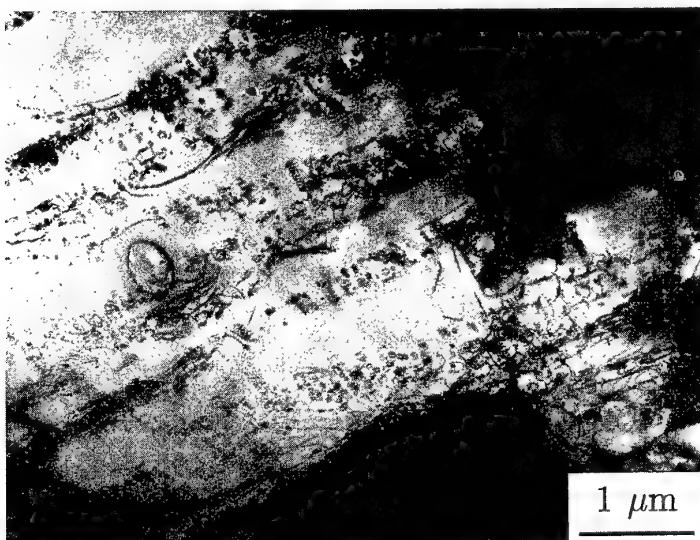


Figure 7 TEM micrograph showing formation of slip bands in primary α -phase in bimodal IMI 834 deformed at $\Delta\epsilon_p/2 = 0.2\%$ and $T = 500^\circ\text{C}$. Test interrupted at $N/N_f = 0.2$

Nickel-Base superalloy IN 100

In isothermal multiple step tests on IN 100 Skelton and Webster²¹ observed that the stress-strain hysteresis loops stabilized rapidly after each change in strain amplitude. Thus, only stabilized deformation conditions will be addressed in the following. Isothermal hysteresis loops were calculated from Ramberg-Osgood parameters given for IN 100 in Ref. ⁹. From these the probability density functions for any temperature can be evaluated as described in Appendix A. These functions were then used as input for the model to predict a complex TMF hysteresis loop obtained using the diamond-shaped strain-temperature cycle given in Ref. ⁹. In Figure 8 the TMF hysteresis loop calculated based upon isothermal data is compared with one obtained experimentally in Ref. ⁹. The model correctly predicts the main characteristics of the TMF hysteresis loop, i.e. the unequal peak compressive and tensile stresses, the mean compressive plastic strain and the observation that the maximum compressive stress precedes the minimum strain. The deviations between

model prediction and experiment are mainly due to the extrapolations of the Ramberg-Osgood parameters required, as isothermal data given in Ref. ⁹ cover only the temperature range from 650 to 1000°C, whereas the actual TMF tests were run between 600 and 1050°C. The close agreement between the model prediction and the TMF hysteresis loop obtained experimentally indicates that the assumption of pseudo-isothermal TMF behavior is reasonable in this case.

Data given in Ref. ²¹ indicated also little effect of strain rate on the cyclic stress-strain response of IN 100. Thus, the model presented in the current paper may be used to estimate stress-strain response during TMF loading of components under cooling rates higher than those possible in a TMF test using uniaxial bulk samples. Furthermore, it was shown that for many materials in isothermal tests the accumulated energy required to form a crack is essentially the same irrespective of the actual loading conditions²²⁻²⁴. For IN 100 the accumulated energy expenditure, i.e. the area of all the stress-strain hysteresis loops, gives a good estimate of the number of cycles to crack initiation even in TMF tests²¹. As the current model predicts the hysteresis loop area quite accurately, cf. Figure 8, the model may also be used to predict the number of cycles to crack initiation in this material.

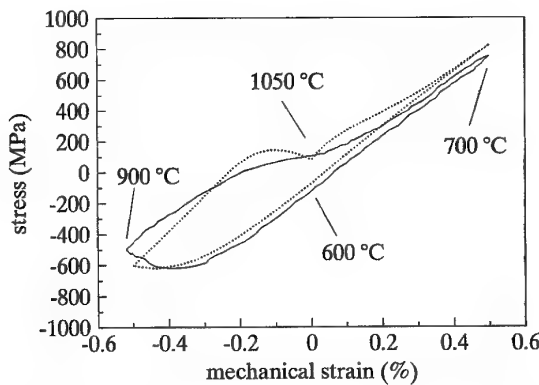


Figure 8 Experimentally obtained and computer-simulated TMF hysteresis loops for IN 100. Temperatures at selected points are indicated. Experimental data (solid line) from Mallet *et al.*⁹. A diamond-shaped temperature-strain cycle with temperature varying between 600 and 1050°C was used, see Ref. ⁹ for details

AISI 304 L-type stainless steel

In the preceding sections examples were given where the assumption of pseudo-isothermal TMF behavior of the material holds. This assumption is justified in two cases: (i) the microstructure does not change much with temperature during the TMF cycle and thus is similar to the isothermal tests, as shown before for IMI 834; (ii) the microstructure rapidly adapts to the new deformation conditions, as demonstrated for IN 100 by Skelton and Webster²¹. The AISI 304 L-type steel discussed in the following is an example where different microstructures are established during TMF loading than in isothermal tests.

In Figure 9 a computer-simulated hysteresis loop is compared to an experimentally obtained TMF hysteresis loop.

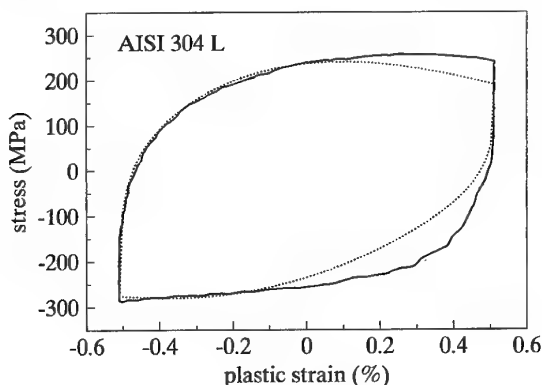


Figure 9 Comparison between computer-simulated TMF hysteresis loop (dotted line) and experimentally obtained hysteresis loop of AISI 304 L-type stainless steel. Experimental data was obtained from Zauter *et al.*⁸. In-phase cycling between 400 and 650°C at $\Delta\epsilon_{pl}/2 = 0.5\%$ and $\dot{\epsilon}_{pl} = 6.7 \times 10^{-5} \text{ s}^{-1}$

esis loop recorded from an in-phase test on AISI 304 L-type steel. The simulation mirrors the stress-strain response in the low-temperature part of the hysteresis loop almost perfectly, but predicts stresses in the high-temperature part of the hysteresis loop lower than those actually measured. The almost perfect simulation in one part of the hysteresis loop and the deviations seen at high temperatures result directly from the correlation of the model with microstructure. Figures 10a and 10b are TEM micrographs displaying the dislocation arrangement established in *isothermal* tests on AISI 304 L. At 650°C a subgrain structure is formed in isothermal tests (Figure 10a), whereas at 400°C a more planar dislocation arrangement is formed as a result of dynamic strain aging (Figure 10b). In a TMF test between 400 and 650°C the dislocation arrangement does not always change quickly enough to adapt to the extremely different microstructures shown in Figures 10a and 10b. In fact, TEM observations⁸ showed that in TMF tests the microstructure does not change significantly during the cycle. As seen in Figure 11 the dislocation arrangement formed in the TMF test is different from both of the isothermal microstructures shown in Figures 10a and 10b. In the high-temperature part of the TMF hysteresis loop the dislocation slip character becomes wavy²⁵ and dislocations are annihilated partially. However, this will only partially remove the microstructural contributions from the low-temperature part of the TMF cycle. In fact, it has been reported that the dislocation density in AISI 304 L is higher in a TMF test than in an isothermal test run at the maximum temperature of the TMF cycle⁸. Consequently, the stresses measured in the actual TMF cycle are larger in the high-temperature part of the TMF cycle than those predicted assuming pseudo-isothermal TMF behavior.

Fatigue tests on various materials have indicated that in materials showing planar dislocation slip, the dislocation arrangement and thus the stress-strain response does not depend strongly on the loading conditions²⁶. In the low-temperature part of the TMF cycle, temperatures are in the range where dynamic strain aging significantly affects the stress-strain response and this leads to a more planar dislocation slip mode. Thus, the stress-strain response in the low-

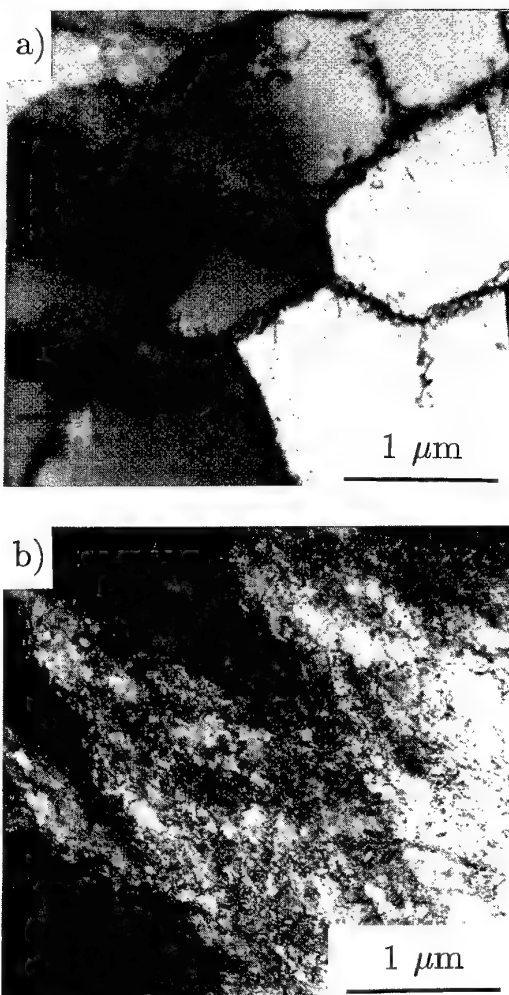


Figure 10 Bright-field TEM micrographs showing the dislocation arrangement of cyclic saturation formed in specimens deformed isothermally at $\Delta\epsilon_{pl}/2 = 0.5\%$ and $\dot{\epsilon}_{pl} = 5 \times 10^{-4} \text{ s}^{-1}$; (a) $T = 650^\circ\text{C}$ and (b) $T = 400^\circ\text{C}$. Courtesy of Zauter *et al.*⁸

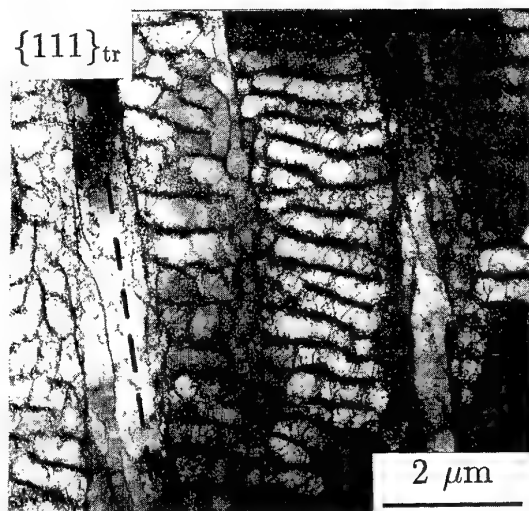


Figure 11 TEM bright-field micrograph⁸ showing the dislocation arrangement formed during TMF. Deformation conditions as indicated in Figure 9

temperature part of the cycle is very similar to that observed in an isothermal test at the corresponding temperature as planar dislocation slip modes prevail in both cases. Consequently, the model which is based on the isothermal microstructure correctly predicts the low-temperature part of the TMF cycle. An improved prediction of the stress-strain response in the high-temperature part of the TMF cycle requires that the kinetics of microstructural changes during the TMF cycle are properly accounted for. Within the framework of the current model microstructural changes are expressed as changes of the probability density functions. In other words, the isothermal probability functions shown in *Figure 5* have to be replaced by those representing the actual microstructure at the given temperature. It should be noted that the actual probability density function at any given temperature during a TMF cycle can be obtained directly by an analysis of the stress-strain response during an isothermal unloading experiment using Equation (1). Further work is underway to yield such information.

In contrast to IMI 834, in-phase testing of AISI 304 L is much more damaging than out-of-phase testing if temperatures are in the temperature range where creep mechanisms become important⁸. Various models have been proposed to estimate fatigue life in such cases based on isothermal creep and fatigue data, e.g. Ref.²⁷. Usually, the creep damage contribution is estimated from the measured or predicted stress-strain response during TMF loading. In isothermal tests on AISI 304 L the transition from low-temperature dislocation glide to creep-controlled deformation at high temperature is accompanied by a change from transgranular fatigue-dominated to intergranular creep-controlled failure. From this, the failure mode observed in TMF tests on AISI 304 L could be predicted from analysis of the TMF hysteresis loop shape²⁸. A detailed discussion of this, however, is beyond the scope of the present paper.

SUMMARY

A multi-component model which is closely related to microstructure was extended to address cyclic stress-strain response under thermomechanical fatigue conditions. Probability density functions describing the critical yield stresses of the elementary volumes are determined from isothermal hysteresis loops. Based upon these isothermal functions the TMF hysteresis loops were predicted assuming pseudo-isothermal TMF behavior. This represents the extreme case in that at any given temperature the microstructure established under TMF conditions always adapts to the microstructure in the corresponding isothermal test. The model was applied to high-temperature tests of the near- α titanium alloy IMI 834, the nickel-base superalloy IN 100 and an AISI 304 L-type stainless steel. A comparison between model predictions and experiments indicated that for the deformation conditions considered the cyclic stress-strain response of both the titanium alloy and the nickel-base superalloy could be predicted for complex TMF cycles. In contrast, in the stainless steel distinct differences between model predictions and experiment were observed. These are discussed based upon microstructural observations. If the maximum temperature of the TMF cycle is within the creep range, in-phase cycling is most damaging in

AISI 304 L-type steel. In contrast, as a result of environmental degradation the fatigue life of the high-temperature titanium alloy IMI 834 was observed to be the lowest in out-of-phase tests.

ACKNOWLEDGEMENTS

Financial support of this work by Deutsche Forschungsgemeinschaft is gratefully acknowledged. The assistance of R.P. Skelton in sharing data for IN 100 is greatly appreciated.

REFERENCES

- 1 Ellison, E. G. and Al-Zamly, A., *Fatigue and Fracture of Engineering Materials and Structures*, 1994, **17**, 39–51.
- 2 Miller, D. A. and Priest, R. H. In *High Temperature Fatigue: Properties and Life Prediction*, ed. R. P. Skelton. Elsevier Applied Science, London, 1987, p. 113–175.
- 3 Ellison, E. G. and Al-Zamly, A., *Fatigue and Fracture of Engineering Materials and Structures*, 1994, **17**, 53–67.
- 4 Mughrabi, H. In *Proceedings of 5th International Conference on the Strength of Metals and Alloys*, eds P. Haasen, V. Gerold and G. Kostorz. Pergamon, Oxford, 1980, pp. 1615–1638.
- 5 Mughrabi, H., *Acta Metallurgica*, 1983, **31**, 1367–1379.
- 6 Christ, H.-J. *Wechselverformung von Metallen*. Springer, Berlin, 1991.
- 7 Blum, W. In *Materials Science and Technology*, eds R. W. Cahn, P. Haasen and E. J. Kramer, Vol. 6, *Plastic Deformation of Materials*, ed H. Mughrabi. VCH, Weinheim, 1993, pp. 359–405.
- 8 Zauter, R., Petry, F., Christ, H.-J. and Mughrabi, H. In *Thermomechanical Fatigue Behavior of Materials*, ed. H. Schitoglu. ASTM STP 1186. ASTM, Philadelphia, 1993, pp. 70–90.
- 9 Mallet, O., Engler-Pinto, C. C., Rézal-Aria, F., Skelton, R. P., Nikbin, K. and Webster, G. A., *Materials at High Temperatures*, 1995, **13**, 47–54.
- 10 Masing, G., *Wissenschaftliche Veröffentl. aus dem Siemens-Konzern*, 1923, **3**, 231–239.
- 11 Burmeister, H. -J. and Holste, C., *Physica Status Solidi A*, 1981, **64**, 611–624.
- 12 Polak, J. and Klesnil, M., *Fatigue of Engineering Materials and Structures*, 1981, **5**, 19–32.
- 13 Christ, H.-J. In *Proceedings of 5th International Conference on Fatigue and Fatigue Thresholds, FATIGUE '93*, eds J.-P. Bailon and J. I. Dickson. EMAS Ltd., UK, 1993, pp. 115–120.
- 14 Asaro, R. J., *Acta Metallurgica*, 1975, **23**, 1255–1265.
- 15 Iwan, W. D., *Journal of Applied Mechanics, Transactions ASME*, 1967, **34**, 612–617.
- 16 Holste, C. and Burmeister, H. -J., *Physica Status Solidi A*, 1980, **57**, 269–280.
- 17 Sommer, C., Christ, H. -J. and Mughrabi, H., *Acta Metallurgica et Materialia*, 1991, **39**, 1177–1187.
- 18 Maier, H. J. and Christ, H. -J., *Scripta Materialia*, 1996, **34**, 609–615.
- 19 Pototzky, P., Hardt, S., Maier, H. J. and Christ, H.-J., in preparation.
- 20 Madsen, A., Andrieu, E. and Ghonem, H., *Materials Science and Engineering A*, 1993, **171**, 191–197.
- 21 Skelton, R. P. and Webster, G. A., *Materials Science and Engineering A*, 1996, **216**, 139–154.
- 22 Skelton, R. P., *Materials Science and Technology*, 1991, **7**, 427–439.
- 23 Skelton, R. P., *Materials Science and Technology*, 1994, **9**, 1001–1008.
- 24 Skelton, R. P., Rees, C. J. and Webster, G. A., *Fatigue and Fracture of Engineering Materials and Structures*, 1996, **19**, 287–297.
- 25 Erm, A. M. and Motteff, J., *Metallurgical Transactions*, 1982, **13A**, 1577–1588.
- 26 Christ, H. -J. and Mughrabi, H., *Fatigue and Fracture of Engineering Materials and Structures*, 1996, **19**, 335–348.
- 27 McGaw, M. A. In *Thermomechanical Fatigue Behavior of Materials*, ed. H. Schitoglu. ASTM STP 1186. ASTM, Philadelphia, 1993, pp. 144–156.
- 28 Zauter, R., Christ, H. -J. and Mughrabi, H., *Metallurgical and Materials Transactions*, 1994, **25A**, 401–406.

- 29 Skelton, R. P., Maier, H. J. and Christ, H.-J., submitted to
Materials Science and Engineering A.

APPENDIX A

In the literature the stress-strain relationship is often reported using the coefficients A and β of the Ramberg-Osgood law:

$$\sigma_r = A \epsilon_{pl,r}^\beta \quad (A1)$$

where σ_r and $\epsilon_{pl,r}$ refer to stress and plastic strain in relative coordinates. If the Ramberg-Osgood law describes the shape of the hysteresis loop satisfactorily, the probability density function (Equation (1)) can be directly evaluated as²⁹

$$f_p(\sigma_{y,i}) = -\frac{2}{E^2} \frac{A\beta(\beta-1)\epsilon_{pl,r}^{\beta-2}}{\left(1 + \frac{1}{E} A\beta\epsilon_{pl,r}^{\beta-1}\right)^3} \quad (A2)$$

The parameters A , β and the elastic modulus E are the only input parameters to the model, but are all dependent on temperature. Usually, isothermal tests are carried out at 50 or 100°C intervals. To model the TMF hysteresis loop, values in smaller temperature increments are necessary and therefore the parameters have to be interpolated. The elastic modulus for any given temperature can easily be calculated from a least-squares fit to the actual data. However, the parameters A and β do not change smoothly with temperature and thus should not be interpolated separately. A detailed description of an improved interpolation method is given in Ref. ²¹. For a detailed discussion of the relationship between the Ramberg-Osgood parameters and the probability density function, see Ref. ²⁹.



PII: S0142-1123(97)00044-3

Analysis and prediction of microstructural effects on long-term fatigue performance of an aluminum aerospace alloy

P.E. Magnusen, R.J. Bucci, A.J. Hinkle, J.R. Brockenbrough and H.J. Konish

Aluminum Company of America, Alcoa Laboratories, 100 Technical Drive, Alcoa Center, PA 15069-0001, USA

A program of experimental and analytical tasks has been conducted to define the linkage(s) between microstructural characteristics and fatigue performance in an aluminum alloy typically used for airframe structural applications. The first goal was to develop data for quantitatively linking measurable characteristics of material microstructure with long-term fatigue performance. The second goal was to develop models to predict fatigue performance based on the microstructural characteristics. The work focused on several process variants of aluminum alloy 7050-T7451 plate. This material was chosen because of its widespread use for flight-critical airframe structural components, and the particular characteristics associated with the manufacturing, service and maintenance of thick section components. Within the framework of this objective, life-limiting microstructural features have been identified and ranked by severity, and models to quantitatively describe the evolution and growth of macrostructural cracks from those features have been developed.

The modeling framework has been applied to predict the cyclic lifetime of the 7050 alloy process variants based on the populations of life-limiting microstructural features. In addition, the models have been used to show how changes in the material characteristics may affect the fatigue performance. This includes predictions of the effect of changing the life-limiting microfeature size and shape distributions, and the effect of changing material strength properties.

The use of this modeling approach to probabilistically describe the implications of changes in the microstructure has been demonstrated, thereby allowing the effects of material pedigree to be predictively linked with the structural integrity of end components. The modeling framework has potential applications in airframe design support processes, and as a tool for use in material and product form selection processes. © 1998 Elsevier Science Ltd.

(Keywords: aluminium alloy 7050; fatigue; aerospace; microstructure; life prediction modelling)

INTRODUCTION

Modern trends in aircraft design and maintenance aimed at reducing airframe manufacturing costs and extending service lifetimes of existing airframes require new capabilities to both limit and predict fatigue damage in structural materials. The economics of the airline industry are driving manufacturers to hold down acquisition costs by reducing the costs associated with airframe manufacture. In addition, airplane operators are extending the service lives of their aircraft far beyond those envisioned during the original design phase^{1,2}. While these two trends are distinctly different, they both require new material understanding, performance and predictive capabilities.

Widespread damage in aging aircraft is becoming an increasing concern as both civil and military fleet operators are extending the service lifetime of their aircraft. During extended service, the propensity for

aircraft to develop crack-like damage increases with time. The development of structural damage may be a consequence of either corrosion or the growth of multiple small fatigue cracks. The existence of widespread damage in a structure can impact the airworthiness of the aircraft, which previously have been only required to certify tolerance to discrete (large scale) cracks in an otherwise undamaged structure³⁻¹¹. However, when widespread fatigue damage is present, damage tolerance derived inspection intervals can be rendered non-conservative and/or component failure due to a main crack could occur at loads below the regulatory limit (those predicted by fracture mechanics)^{1,12}. Clearly there is a need to prevent widespread cracking in the first place.

The occurrence of widespread damage sites can be associated with the intrinsic characteristics of the material microstructure¹³. Material microstructural sites prone to the development of crack-like damage, attributable to corrosion or fatigue, can be associated with

particles, inclusions, pores, grain boundaries, etc.¹³⁻²¹. While these features are necessarily a part of the material, the character of these features can be altered through composition and process modifications while still meeting the required material strength performance characteristics. There currently exists no methodology for assessing the impact of these changes on preventing the development of widespread fatigue damage.

Low cost airframe manufacturing initiatives are aimed at reducing part count and assembly costs by machining complex parts from thicker starting material, thus reducing parts and costs of building up components from thinner material; producing integrally stiffened panels instead of fastening stiffeners onto thinner structural panels; and the use of net and near-net shaped parts. These manufacturing methods, however, can potentially affect certification requirements for assurance of structural safety. Single part replacements for traditional built-up structure removes some redundancy associated with the later structural assemblies, and eliminates the inherent crack stopping ability associated with interfaces between assembled parts. Therefore, there is increased need to develop methodologies which can be used to ensure safe life performance from single piece components, and to consider material process/microstructural effects on performance.

In response to the needs defined above, this program develops an approach to model damage evolution which originates from material microstructure. The model utilizes conventional fracture mechanics technology consistent with traditional aircraft design methodologies. The effects of crack-initiating microstructural features are incorporated into the life analysis through their effects on the crack driving force, and the statistical aspects of microfeature distribution are accounted for by incorporating a probabilistic sampling method. Probabilistic predictions of fatigue performance are made for several process variants of an aerospace aluminum alloy using knowledge of microstructural feature distributions. These predictions are then compared with lifetime data from multiple fatigue testing to demonstrate the capability of the predictive methods.

MATERIAL TESTING AND CHARACTERIZATION

This program selected aluminum alloy 7050-T7451 thick plate for evaluation. While the focus of this paper is on development of analytical techniques for lifetime assessment, the work relies heavily on microstructural characterization and fatigue test data for 7050. The details of the material characterization and testing work are reported in Ref. ²². Aluminum alloy 7050 is commonly used as a structural material in both civil and military aircraft, and has been chosen for use in the form of thick sections for replacement of traditional built-up structure to achieve part consolidation. Extensive evaluations of 7050 fatigue performance have been conducted previously²³⁻²⁸ which provide a basis for this program. Among the key findings from this prior work are that fatigue damage initiation occurs at microfeatures which are metallurgical in origin, and the lifetimes are controlled by the feature size and spatial distribution characteristics. Furthermore, micro-feature distribution is a function of alloy composition, pro-

cessing history and product form. Thus, for a given class of material, the fatigue lifetime can be influenced through process/composition history. These effects made it possible to utilize different processing routes to produce material with varying microstructures and different levels of fatigue performance for this program.

Three process variations of alloy 7050 thick (nominally 6") rolled plate and one of thin (1") were characterized and tested. The material variants and the key life-limiting microstructural features of each are listed in *Table 1*. The alloy variants are referred to as *old* material, *now* material, *low porosity* material and *thin* material, and the key features are microporosity, constituent particles and grain structure. For each material, extensive fatigue testing was performed to characterize the inherent material performance. Both smooth round specimens and flat bar specimens with two open holes were tested. The smooth specimen test allowed quantification of microstructural influences because the test section is uniformly stressed and is sensitive to the largest inhomogeneity in the test section. The open hole specimen, on the other hand, has a notch stress concentration at the holes, and the volume of material seeing the highest stress is much smaller. This makes the latter specimen more sensitive to the frequency distribution of microstructural features. The understanding of the effects of micro-feature type, size and distribution are important if the life assessment methods are to transfer from laboratory coupon to end component scale.

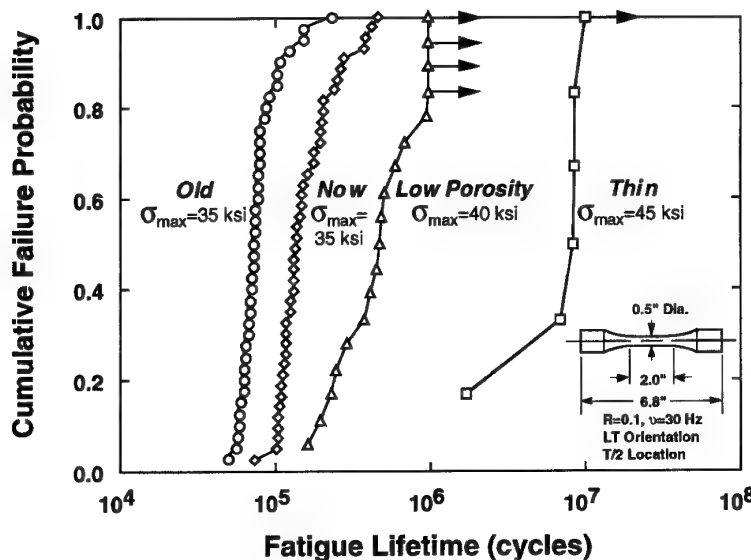
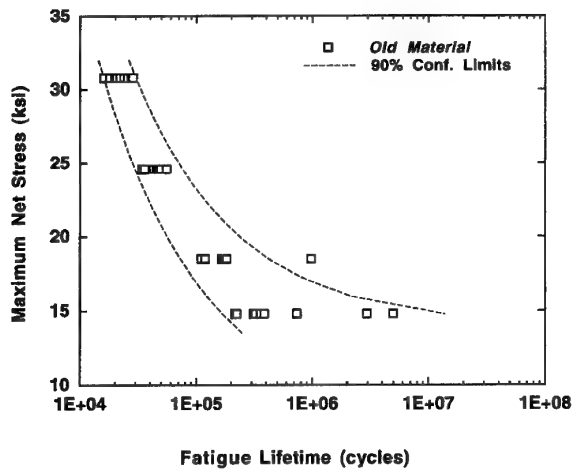
The smooth fatigue test specimens were machined with the long (or axial load) dimension parallel to the long transverse direction of the parent material (LT test direction) and centered about the midplane of the starting plate material. The tests were conducted in laboratory air with a stress ratio of 0.1, with maximum cyclic stresses of 35 ksi for the *old* and *now* materials, 40 ksi for the *low porosity* material, and 45 ksi for the *thin* material. The stresses were increased for the *low porosity* and *thin* variants because the lifetimes would have been excessively long at a lower maximum cyclic stress. The cumulative smooth fatigue lifetime distributions for each of the materials are shown in *Figure 1*. Despite the differences in cyclic stress for two of the variants, the data show the ranking of fatigue performance to be *old* material, *now* material, *low porosity* material and *thin* material.

Open-hole specimen fatigue specimens were also machined in the LT direction and taken from the midplane of the parent material. The tests were conducted in laboratory air with a stress ratio of 0.1. For each of the material variants, several stress levels were tested to generate stress vs lifetime (*S/N*) curves. The open hole *S/N* curves for the *old*, *now*, *low porosity* and *thin* materials are shown in *Figures 2-5*, respectively. Also shown are bounds around the data which represent the 90% confidence limits. The results from the open-hole specimen tests gave the same relative ranking of materials, except that the *now* and *low porosity* materials had similar lifetimes.

Fractography of failed smooth and open hole fatigue specimens for the four variants of 7050 was conducted. The purpose was to identify the controlling microstructural feature which limit the lifetime, and provide quantification of the controlling feature size distri-

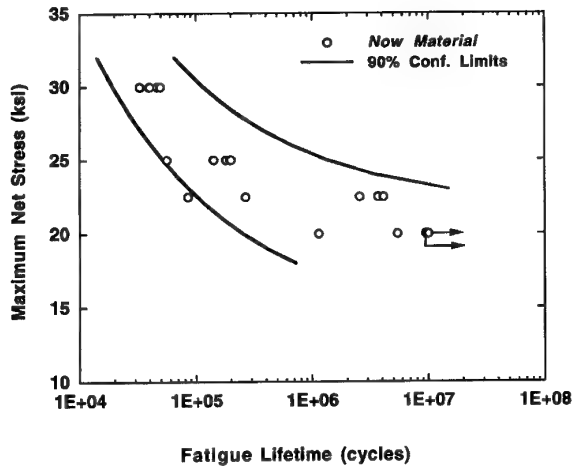
Table 1 Key microstructural features of the materials used for this study

Material	Product thickness (")	Key microstructural feature
Old material	5.7	Coarse porosity
Now material	5.7	Porosity
Low porosity material	6.0	Small porosity, constituent particles
Thin material	1.0	Constituent particles, refined grain size

**Figure 1** Cumulative fatigue lifetime distributions for the four microstructural variants**Figure 2** Open hole fatigue stress vs lifetime plot for the *old* material variant. Tests conducted at $R = 0.1$, 30 Hz, LT orientation, lab air

butions for use as input into fatigue lifetime prediction models. The fractographic data are reported in Ref. ²².

Random plane metallographic characterizations of the particle populations for each material variant was conducted. While microporosity is generally regarded to be more degrading to fatigue performance than particles, the spatial and frequency distributions of the two feature types are vastly different and affected by material pedigree. In contrast to microporosity which

**Figure 3** Open hole fatigue stress vs lifetime plot for the *now* material variant. Tests conducted at $R = 0.1$, 30 Hz, LT orientation, lab air

is sparse, and largely confined to the centerline region of thick plate, constituent particles are copious and more evenly distributed throughout the volume of the material. Thus, highly localized geometric stress concentrations, such as at the corner of holes, will always have particles associated with them, whereas the likelihood of encountering a micropore within a small volume of material is more remote. These data on constituent particle distribution also provide input to the

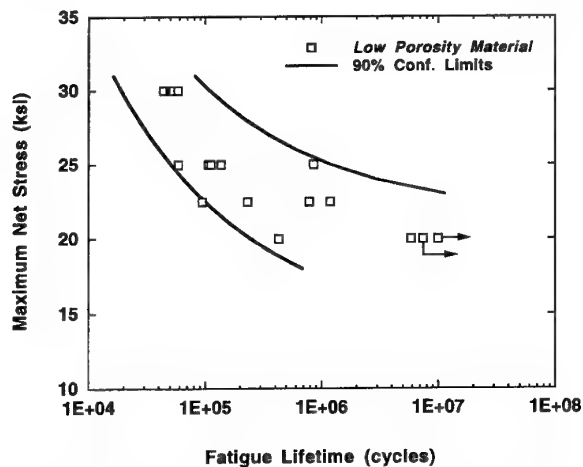


Figure 4 Open hole fatigue stress vs lifetime plot for the low porosity material variant. Tests conducted at $R = 0.1$, 30 Hz, LT orientation, lab air

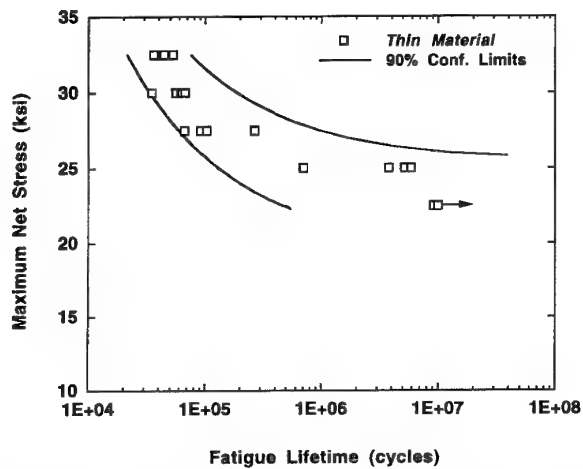


Figure 5 Open hole fatigue stress vs lifetime plot for the thin material variant. Tests conducted at $R = 0.1$, 30 Hz, LT orientation, lab air

development of modeling methods which account for microstructural influences on lifetime. The metallographic characterization data are reported in Ref. ²².

LIFE PREDICTION MODELING

The modeling approach taken assumes that fatigue life is composed entirely of crack growth from critical (life-limiting) microfeatures which are modeled as pre-existing cracks, whose size is equivalent to the size of the microfeature. This equivalent initial flaw size (EIFS) distribution can be viewed as a material characteristic, and serves as a starting point for fracture mechanics analysis. This distribution of crack-initiating features represents an extreme value distribution or high-end tail of the total population of like features within the material. This extreme value distribution is obtained from fractography of the failed smooth specimens. It has also been shown for a population of constituent particles that the extreme value distribution can be approximately calculated based on quantitative metallographic results and specimen geometry effects²².

The fracture mechanics based approach to fatigue life modeling employed here is based on a fracture mechanics program on crack coalescence from Grandt *et al.*²⁹⁻³¹. The original numerical algorithm calculated the fatigue life of an open hole fatigue specimen containing one or more elliptical cracks which are subject to remote cyclic loading. The Newman–Raju stress intensity factor solutions^{32,33} were used to describe the crack driving force using the assumption of elliptical initial cracks to represent the intrinsic life-limiting microfeatures.

Crack growth prediction with accrued cycles entails the standard ΔK -rate integration process of linear elastic fracture mechanics, beginning with the growth of small, naturally forming cracks at a size scale below typical fracture mechanics application (typically $< 0.05''$). In this study, ΔK -rate data obtained from long-crack specimens are employed. Small crack growth below the long-crack ΔK threshold is approximated by a simple linear extrapolation of the intermediate $da/dN - \Delta K$ region to low growth rates. While the small crack effect is an important aspect of understanding, the present investigation placed emphasis on the analytical protocols enabling utilization of well established (handbook) fatigue databases. The crack growth relationship for the all material variants was the same and the data are represented by the Paris equation³⁴:

$$da/dN = C\Delta K^m$$

Where the constants $C = 3.9 \times 10^{-10}$ and $m = 4.175$.

To incorporate the effect of microfeature type (in particular micropores and particles), a modification of the Newman and Raju stress intensity factor solution is required. Trantina and Barishpolsky³⁵ examined the stress intensity factor solution of an ellipsoidal micropore or particle of diameter $2R$ and height h , which contains an equatorial crack of length b . A remote stress σ is applied perpendicular to the plane of the crack. An effective stress intensity factor K for this flaw geometry is:

$$K_{T-B} = \beta\sigma\sqrt{\pi b}$$

Where the dimensionless geometric term β is given by:

$$\beta = 2/\pi + B(1.12k_t - 2/\pi - 1)(R/(b + R))^{10} + (R/(b + R))^{1.8}$$

Here k_t is the elastic stress concentration factor for the ellipsoidal microfeature which depends on the aspect ratio $h/2R$. The value of k_t can be obtained from standard fracture mechanics handbooks. The constant B is 1.0 for a micropore, and 2.0 for a bonded cracked particle, and 0.3 for an unbonded particle. The ratio of the Trantina–Barishpolsky stress intensity factor to the stress intensity factor of a penny shaped crack is used to modify the Newman–Raju stress intensity factor to account for the type of crack-initiating feature.

Two main failure limit states control the termination of the crack growth model: net section strength and fast fracture of the material. If the net section stress exceeds the limit stress (taken here as the material static yield strength), the calculation is terminated. The fast fracture limit state can be controlled in either of two ways: exceedance of a crack growth rate or exceedance of the material fracture toughness. The model software checks whether either of these criteria are met after each incremental cyclic crack growth step.

Microfeature distribution effects are incorporated in the model using a probabilistic approach which relies on the statistical microstructural feature distribution information. Using the general purpose probabilistic software program PROBAN³⁶, the effects of microfeature size, location and type are treated as random variables. With the measured distributions as input, a stratified Monte Carlo sampling method, Latin Hypercube sampling, was used to randomly sample the distribution variables and calculate the fatigue lifetime distributions. By altering the input stress used in the model, an entire probabilistic stress-life curve can be developed.

MODEL CALCULATIONS OF FATIGUE DATA

The smooth axial fatigue lifetime data were calculated deterministically from an equivalent initial flaw (EIF) representation of the life-limiting microfeature size population measured from the fatigue fracture surfaces. The lifetime calculations were performed for the *old*, *now* and *low porosity* materials. Many of the failures for the *thin* variant exhibited slip induced fatigue cracking, and were not associated with an identifiable microstructural inhomogeneity. The current approach does not consider slip induced cracking in the model, and therefore the lifetime data for the *thin* variant are not predicted. The calculated fatigue lifetime distributions for the *old*, *now* and *low porosity* materials are plotted along with the actual lifetime distribution in Figures 6–8, respectively. There is good agreement between the predicted and actual distributions for the *old* and *now* variants, while the prediction for the *low porosity* material is conservative.

The crack-initiating microfeature type and extreme value size, shape and location distributions obtained from open-hole specimen fracture surfaces were used as the EIF input to the model to calculate fatigue life curves for each material variant. The growth model was linked to PROBAN program treating the microfeature distributions as random variables. Also required for the model calculations is an estimate of the local stress

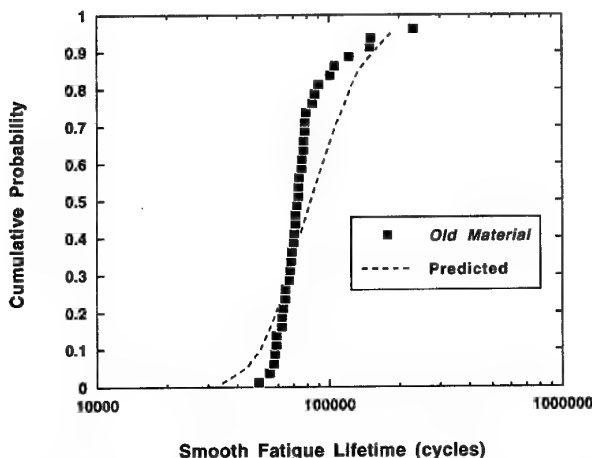


Figure 6 Comparison between the actual smooth fatigue lifetime distribution and the predicted lifetime distribution based on the input extreme value distribution parameters for the *old* material. Tests conducted at 35 ksi max. stress, $R = 0.1$, LT orientation, T/2 location, 30 Hz in lab air

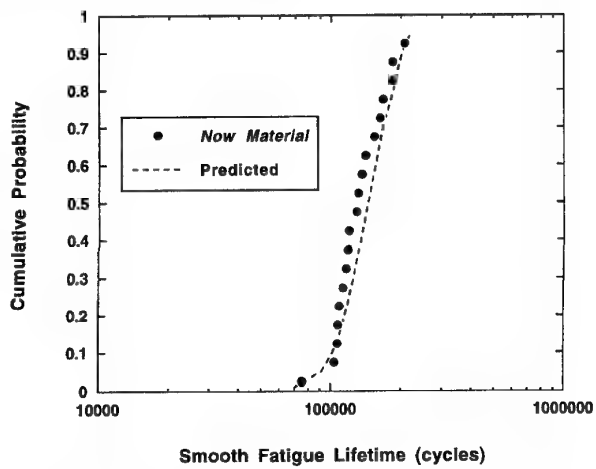


Figure 7 Comparison between the actual smooth fatigue lifetime distribution and the predicted lifetime distribution based on the input extreme value distribution parameters for the *now* material. Tests conducted at 35 ksi max. stress, $R = 0.1$, LT orientation, T/2 location, 30 Hz in lab air

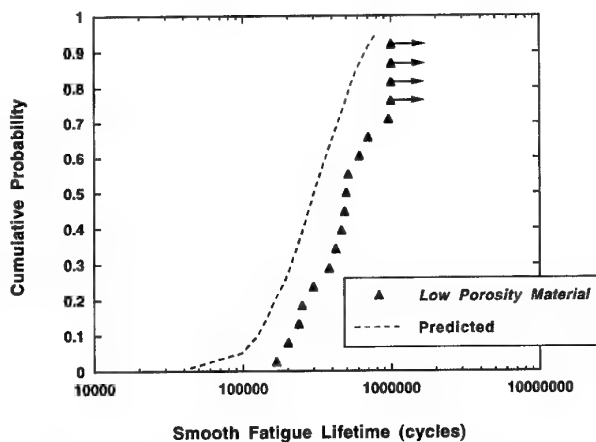


Figure 8 Comparison between the actual smooth fatigue lifetime distribution and the predicted lifetime distribution based on the input extreme value distribution parameters for the *low porosity* material. Tests conducted at 35 ksi max. stress, $R = 0.1$, LT orientation, T/2 location, 30 Hz in lab air

concentration factor, k_t , for the crack-initiating features in each of the material variants. This can be obtained from handbooks for regularly shaped crack-initiating features but needs to be estimated here for irregular micropores and particles. The values of k_t were estimated by fitting the model to the open hole S/N data at the stress level which resulted in infinite life (the fatigue limit) and using the value of k_t which gave the best fit. The input microfeature distribution parameters and the values of k_t obtained for each material are listed in Table 2.

The calculated open-hole specimen stress vs life curves for each material along with the fatigue test data are shown in Figures 9–12. The model was used to calculate the 5, 50 and 95% failure fractiles for each material. In general, the results of the model are in good agreement with the test data. Exceptions are the predicted lifetimes at high stresses in the *thin* material where the model tends to over-predict the lifetimes. This may be due in part to the 'short crack'

Table 2 Input parameters for each of the 7050 material variants used in the model calculations of fatigue performance. The depth and width parameters represent the extreme value distribution parameters for crack-initiating inhomogeneities

Variable	Old material	Now material	Low porosity material	Thin material
Crack-initiator type	Pore	Pore	Particle	Particle
Crack depth distribution parameters	Weibull	Weibull	Lognormal	Lognormal
	$m = 8.22E-3$	$m = 4.33E-3$	$m = 2.64E-3$	$m = 6.3E-4$
	$s = 4.05E-3$	$s = 1.42E-3$	$s = 2.41E-3$	$s = 2.3E-4$
	Lower bound = 1.35E-3	Lower bound = 0.0	Lower bound = 2.0E-4	Lower bound = 2.0E-4
Crack width distribution parameters	Lognormal	Lognormal	Lognormal	Lognormal
	$m = 4.08E-3$	$m = 2.1E-3$	$m = 1.76E-3$	$4.3E-4$
	$s = 1.62E-3$	$s = 9.0E-4$	$s = 1.83E-3$	$s = 1.8E-4$
	Lower bound = 5.0E-4	Lower bound = 5.0E-4	Lower bound = 2.0E-4	Lower bound = 1.0E-4
Crack growth rate Paris law	$C = 3.9E-10$	$C = 3.9E-10$	$C = 3.9E-10$	$C = 3.9E-10$
Yield stress	$m = 4.175$ Lognormal $m = 66.5$ $cov = 5.0E-2$ Lower bound = 60	$m = 4.175$ Lognormal $m = 66.5$ $cov = 5.0E-2$ Lower bound = 60	$m = 4.175$ Lognormal $m = 66.5$ $cov = 5.0E-2$ Lower bound = 60	$m = 4.175$ Lognormal $m = 66.5$ $cov = 5.0E-2$ Lower bound = 60
Local stress concentration factor, k_t	11.0	7.5	4.25	3.75

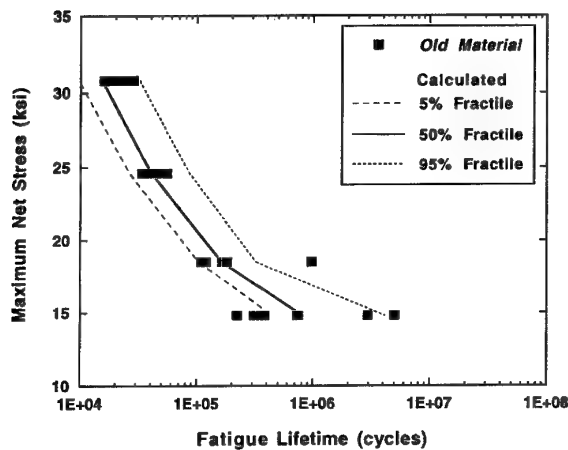


Figure 9 Comparison between the open hole fatigue life test data and the calculated S/N curve for the *old* material. The testing was done at $R = 0.1$, LT orientation, T/2 location, 30 Hz in lab air

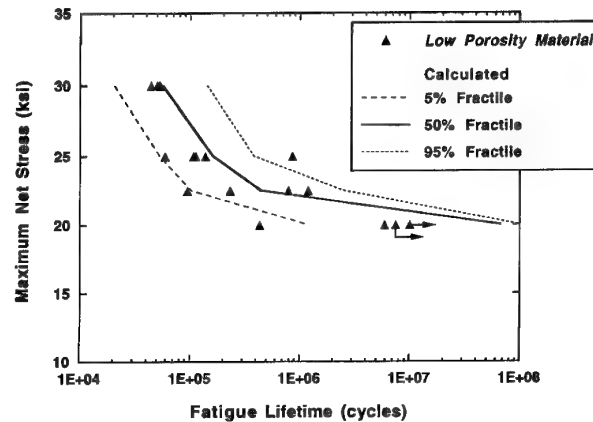


Figure 11 Comparison between the open hole fatigue life test data and the calculated S/N curve for the *low porosity* material. The testing was done at $R = 0.1$, LT orientation, T/2 location, 30 Hz in lab air

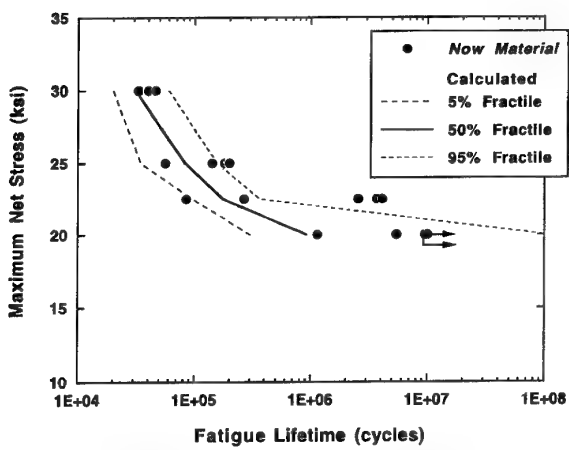


Figure 10 Comparison between the open hole fatigue life test data and the calculated S/N curve for the *now* material. The testing was done at $R = 0.1$, LT orientation, T/2 location, 30 Hz in lab air

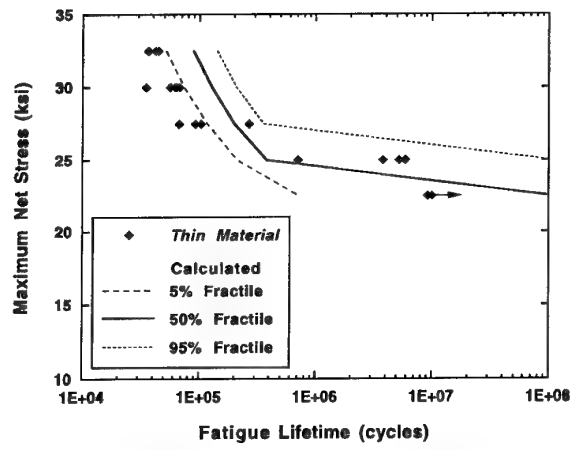


Figure 12 Comparison between the open hole fatigue life test data and the calculated S/N curve for the *thin* material. The testing was done at $R = 0.1$, LT orientation, T/2 location, 30 Hz in lab air

effect not being well represented by the input fatigue crack growth rate data at the smaller equivalent initial crack size in this material. Despite this difference, the data for the other variants are very well represented by the model results.

PARAMETRIC STUDIES

An analytical approach to assess effects of processing and composition on microstructure and material performance can greatly reduce material development costs and shorten the development time. As an illustration of the model utility, a parametric study was performed to assess impact of microstructural parameters on material performance. Specifically, the effects of particle size, shape and material yield strength on fatigue performance are evaluated.

The effect of changing the shape of crack-initiating features is evaluated through the effect of changing local stress concentration, k_t , on the stress level which yields infinite life. Figure 13 plots the ratio of the infinite life stress to the yield stress vs the local stress concentration for both micropores and particles. The data shows that micropores have a much more severe stress concentration than particles at equivalent aspect ratios. This suggests that particles must first crack before they have a significant effect on the infinite life stress. The sensitivity of the fatigue model to changing feature size is assessed by calculating the cyclic stress versus life curves for varying starting sizes. The influence of particle size on fatigue life is shown in Figure 14 for particle sizes ranging from 0.001 to 0.01" at a stress concentration k_t of 2. The effect of increasing particle size is to decrease the life throughout a range of stresses, but the infinite life stress is not affected by changes in the particle size. The sensitivity of fatigue life to the material yield strength has also been examined by calculating the cyclic S/N curves at different yield strengths. The data are shown in Figure 15 based on a fixed particle size of 0.005", and the yield strength is varied from 60 to 80 ksi. The figure shows fatigue life is almost independent of yield strength at stresses well above the infinite life stress, but the endurance limit increases with increasing yield strength. It should be noted that for aluminum alloys,

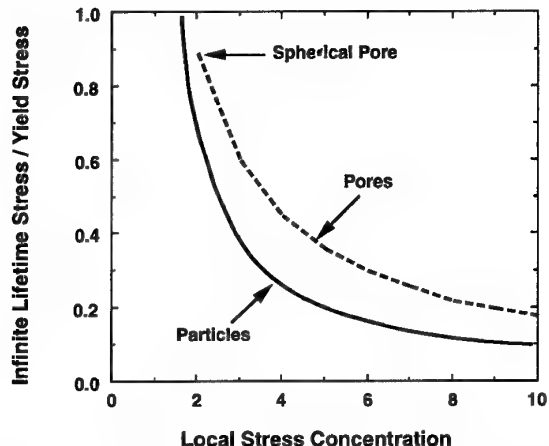


Figure 13 Plot of the sensitivity of the infinite life stress to the local stress concentration factor for both micropores and particles

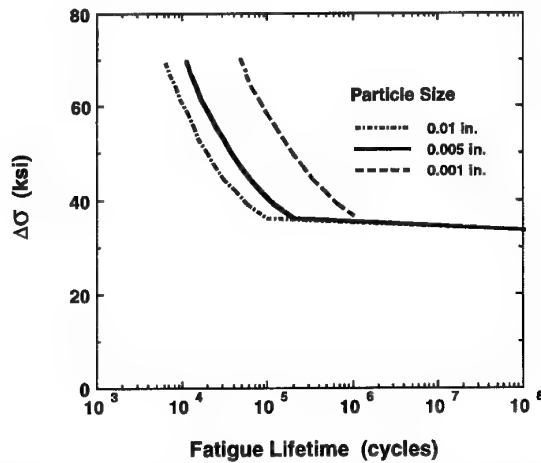


Figure 14 Sensitivity of fatigue stress vs lifetime (S/N) curve to particle size for a yield strength of 70 ksi

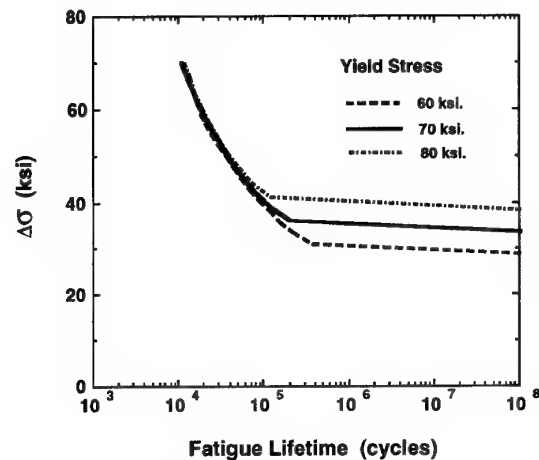


Figure 15 Sensitivity of fatigue stress vs lifetime (S/N) curve to yield stress for a particle size of 0.005" and local stress concentration $k_t = 2.0$

varyations in yield strength may be accompanied by microstructural variations which may exert influence on the fatigue behavior. The calculations here are only intended to show trends.

DISCUSSION

The analytical modeling task has provided a method to reasonably estimate the performance capabilities of a material based on the life-limiting microstructural feature populations. A significant aspect of the modeling is that fracture mechanics principles can be applied to the scale of the microstructural features which govern fatigue life. This enables fatigue life estimates to be made based on an understanding of the size distributions of crack-initiating microstructural features. Also, the effects of feature shape and location distribution, as well as material yield strength effects can be estimated. The modeling provides a set of analytical tools to translate understanding of life limiting features of material microstructure, known to emanate from the compositional and processing history of an aluminum

alloy product, into useful life-cycle guidance for airplane design/material trade studies.

The analytical tools developed in this program to predict evolution of damage emanating from material micro-features can have value when applied to current aviation industry needs. Much attention is given to the consequence of secondary widespread fatigue damage that in the presence of large scale accidental damage could compromise damage tolerance below acceptable limits. The analytical tools to predict the development of damage from intrinsic characteristics of the material microstructure provide new capabilities to aid in widespread fatigue damage prevention and control strategies. Though widespread damage sites may often be due to extrinsic sources such as manufacturing imperfections or traffic damage, significant fatigue failures in aircraft have been associated with intrinsic material characteristics¹³. The analytical methods can be applied to assess performance of existing materials based on an understanding of the microstructure and process history. Materials design for both retrofit and new applications can employ this analysis to rapidly assess manufacturing options for tighter control of life-limiting microfeature populations. Thus, optimum process, microstructure and performance options can be assessed faster and more cheaply than previously possible.

Analysis protocols are necessary to ensure that durability and damage tolerance are not compromised in efforts to reduce manufacturing costs. Potential benefit exists by applying the analysis methods to airplane parts which could be integrally machined instead of being built up from several components. Because some redundancy in structure is eliminated and due to the lack of inherent crack stopping ability which is present in built-up structure, greater demands are placed on thick section material performance. Traditionally, thicker section material ranks lower in fatigue durability performance than thinner material. The analysis methods provide a means for assessing material options and assessing effects of part consolidation on long-term structural durability. Material development efforts for increased thick section performance can also benefit from rapid assessment of process, microstructure and performance combinations.

SUMMARY

There are needs within the aviation industry for increased material understanding, material performance and predictive capabilities. The application of models which can predict evolution of fatigue damage starting from inherent microstructural feature populations hold promise for fulfilling these needs. The current work has demonstrated the feasibility of a practicable fracture mechanics based approach to modeling fatigue damage evolution from inherent microstructural feature populations in metallic high strength alloys commonly used in aircraft primary structure.

ACKNOWLEDGEMENTS

This work has been supported by funding from the Office of Naval Research through contract N00014-91-C-0128 and through Alcoa funding.

REFERENCES

- 1 *Proceedings of the FAA-NASA Symposium on Continued Airworthiness of Aircraft Structures*, Atlanta, GA, 28–30 August 1996, Federal Aviation Technical Center, Atlantic City International Airport, USA (in press).
- 2 Goranson, U.G., "Damage tolerance—fact and fiction", *Proceedings of the 17th Symposium of the International Committee on Aeronautical Fatigue (ICAF)*, A.F. Blom (Ed.), Engineering Materials Advisory Services, Ltd., Warley, U.K., June 1993.
- 3 Landy, M. A. and Smithers, O. L., Durability and damage tolerance control plans for U.S. Air Force aircraft. *Journal of Aircraft*, 1983, **20**(89), 689.
- 4 Goranson, U.G. and McGuire, J.F., Airworthiness. *Aerospace Engineering*, March 1994, 28–34.
- 5 Aircraft Structural Integrity Program Requirements, MIL-STD-1530, revision A. U.S. Department of Defense, Washington, DC, USA, 1988.
- 6 Berens, A.P., Morcock, D.S., Brown, K.E., Davis, J.C., Johnson, R.L., Larson, C.E. and White, D.J., *Handbook of Force Management Methods*. AFWAL-TR-81-3079, Flight Dynamics Laboratory, Air Force Wright Wright Aeronautical Laboratories, Air Force Systems Command, Wright-Patterson Air Force Base, OH, April 1981.
- 7 Manning, S.D. and Yang, J.N., *USAF Durability Design Handbook: Guidelines for the Analysis and Design of Durable Aircraft Structures*. AFWAL-TR-83-3027, Flight Dynamics Laboratory, Air Force Wright Wright Aeronautical Laboratories, Air Force Systems Command, Wright-Patterson Air Force Base, OH, August 1988.
- 8 Brussat, T.R., Ekwall, J.C. and Jauregui, J.A., *Documentation of the Navy Aircraft Structural Integrity Program (NASIP), Revision B*. Report No. NADC-87089-60, U.S. Naval Air Development Center, Warminster, PA, October 1988.
- 9 *Damage Tolerance Assessment Handbook, Volume II: Airframe Damage Tolerance Evaluation*. Final Report DOT-VNTSC-FAA-93-13.II, U.S. Department of Transportation, Volpe National Transportation Systems Center, Cambridge, MA, October 1993.
- 10 *Airworthiness Standards: Transport Category Airplanes*. 14 CFR part 25 of the Federal Aviation Regulations (FAR), U.S. Department of Transportation, Federal Aviation Administration, National Technical Information Service, Springfield, VA, USA.
- 11 Swift, T., Damage tolerance capability. *Fatigue of Aircraft Materials*, Proceedings of the Specialists' Conference dedicated to the 65th birthday of J. Schijve, Delft University Press, Delft, The Netherlands, 1992, pp. 351–387.
- 12 Swift, T., Widespread fatigue damage monitoring—issues and concerns. *5th International Conference on Structural Airworthiness of New and Aging Aircraft*, Hamburg, Germany, 16–18 June 1993.
- 13 Gran, R.J., Orazio, F.D. Jr., Paris, P.C., Irwin, G.R. and Hertzberg, R.W., *Investigation and Analysis Development of Early Life Aircraft Structural Failures*. AFFDL-TR-70-149, U.S. Air Force Flight Dynamics Laboratory, Wright Patterson AFB, OH, USA.
- 14 Kung, C. Y. and Fine, M. E., Fatigue-crack initiation and microcrack growth in 2024-T4 aluminum alloys. *Metallurgical Transactions A*, 1977, **10A**, 603–610.
- 15 Starke, E.A., Jr and Lutjering, G., Cyclic plastic deformation and microstructure. In *Fatigue and Microstructure*. American Society for Metals, Metals Park, OH, 1979, pp. 205–243.
- 16 Detert, K., Scheffel, R. and Stunkel, R., Influence of grain size and dispersion of small particles on crack initiation and growth during fatigue in age hardened Al-Mg-Si alloys. In *Strength of Metals and Alloys* (ICSMA7), Vol. 2, Pergamon, New York, 1985, pp. 1219–1224.
- 17 Richie, R.O. and Lankford, J., eds. *Small Fatigue Cracks*. TMS-AIME, Warrendale, PA, 1986.
- 18 Lankford, J., Effect of oxide inclusions on fatigue failure. *International Metals Reviews*, September 1987, p. 221.
- 19 Labarre, L.C., Angers, L.M., Bucci, R.J., Emptage, M.R., Leon, D.D. and Billman, F.R., CW67 P/M Alloy product improvements through statistical quality control. *ASM International ISTFA'87: Advanced Materials, Conference Proceedings*, ASM International, Metals Park, OH, USA, 1987, pp. 27–31.
- 20 Newman, J.C. Jr. and Edwards, P.R., Short crack growth behavior in an aluminum alloy, an AGARD Cooperative test programme. AGARD-R-767, North Atlantic Treaty Organization (NATO), 1988.
- 21 Julta, T., Nicholson, C.E. and Jolley, G., Nucleation of fatigue cracks by inclusions. *Fracture Control of Engineering Structures*

- 22 ECFT-6, 6th Biennial European Conference on Fracture, Amsterdam, The Netherlands, 15–20 June 1986, Engineering Materials Advisory Services, Ltd., Warley, U.K., 1988, p. 1609.
- 23 Magnusen, P.E., Bucci, R.J., Hinkle, A.J., Brockenbrough, J.R., Konish, H.J. and Miyasato, S.M., Final report: the role of microstructure on the fatigue durability of aluminum aircraft alloys. ONR Contract N00014-91-C-0128, U.S. Office of Naval Research, Arlington, VA, USA, November 1995.
- 24 Owen, C. R., Bucci, R. J. and Kegarise, R. J., An aluminum quality breakthrough for aircraft structural reliability. *Journal of Aircraft*, 1989, **26**, 178–184.
- 25 Hinkle, A.J., Magnusen, P.E., Rolf, R.L. and Bucci, R.J., Effect of microporosity on notched specimen fatigue life. *Structural Safety and Reliability*, Vol. 2, *Proceedings ICOSSAR'89, Fifth International Conference on Structural Safety and Reliability*. American Society of Civil Engineers, New York, 1989, pp. 1467–1474.
- 26 Magnusen, P.E., Bucci, R.J., Hinkle, A.J., Artley, M.E. and Rolf, R.L., The influence of metal quality on airframe structural durability. *Advances in Fracture Research*, Vol. 2, *Proceedings of the Seventh International Conference on Fracture (ICF 7)*, Houston TX, 20–24 March 1989, Permagon Press, New York, NY, USA, pp. 999–1006.
- 27 Magnusen, P. E., Hinkle, A. J., Kaiser, W., Bucci, R. J. and Rolf, R. L., Durability assessment based on initial material quality. *Journal of Testing and Evaluation*, 1990, **18**, 439–445.
- 28 Magnusen, P.E., Hinkle, A.J., Rolf, R.L., Bucci, R.J. and Lukasak, D.A., "Methodology for the assessment of material quality effects on airframe fatigue durability". *Fatigue 90, Vol. II, Proc. Fourth International Conference on Fatigue and Fatigue Thresholds*, Honolulu, HA, USA, Materials and Components Engineering Publications Ltd, Birmingham, U.K., 1990, pp. 2239–2244.
- 29 Grandt, A.F., Jr., Perez, R. and Tritsch, D.E., Modeling the influence of initial material inhomogeneities on the fatigue life of notched components. *Fatigue and Fracture of Engineering Materials and Structures*, 1993, **16**, 199–213.
- 30 Grandt, A.F. Jr., Perez, R. and Tritsch, D.E., Cyclic growth and coalescence of multiple fatigue cracks. *Advances in Fracture Research, 6th International Conference on Fracture*, New Delhi, India, December 1984, Vol. 3, Pergamon Press, New York, NY, USA, pp. 1571–1578.
- 31 Grandt, A.F., Jr., Thakker, A.B. and Tritsch, D.E., An experimental and numerical investigation of the growth and coalescence of multiple fatigue cracks at notches. *Fracture Mechanics*, Seventeenth Vol. ASTM STP 905. American Society for Testing and Materials, Philadelphia, PA, 1986, pp. 239–252.
- 32 McComb, J. C., Pope, J. E. and Grandt, A. F., Growth and coalescence of multiple fatigue cracks in polycarbonate test specimens. *Engineering Fracture Mechanics*, 1986, **24**, 601–608.
- 33 Newman, J.C. and Raju, I.S., Stress intensity factor equations for cracks in three-dimensional finite bodies. NASA Technical Memorandum 83200. Langley Research Center, Hampton, VA, August 1981.
- 34 Raju, I.S. and Newman, J.C., Jr., Stress-intensity factors for circumferential surface cracks in pipes and rods under tension and bending. *Fracture Mechanics*, Seventeenth Volume. ASTM STP 905. American Society for Testing and Materials, Philadelphia, PA, 1986, p. 789.
- 35 Paris, P.C., Fatigue—an interdisciplinary approach. *Proceedings 10th Sagamore Conference*. Syracuse University Press, Syracuse, NY, 1964, p. 107.
- 36 Trantina, G. G. and Barishpolsky, M., Elastic-plastic analysis of small defects—voids and inclusions. *Engineering Fracture Mechanics*, 1984, **20**, 1–10.
- 37 Det Norske Veritas, PROBAN: General Purpose Probabilistic Analysis Program. Veritas Sesam Systems, Hovik, Norway, January 1992.

PII: S0142-1123(97)00026-1

Microstructure based fatigue life predictions for thick plate 7050-T7451 airframe alloys

Marek A. Przystupa*, Robert J. Buccit, Paul E. Magnusent and Andrew J. Hinklet

*Department of Materials Science and Engineering, University of California at Los Angeles, Los Angeles, CA 90095-1595, USA

^tAlcoa Technical Center, 100 Technical Drive, Alcoa Center, PA 15069, USA

The purpose of this work was to test a microstructure based fatigue life prediction Monte-Carlo model for potential use in quantifying fatigue quality and reliability of metallic structural alloys. The model used was of the crack growth type with the sizes of crack initiating pores, local crack geometry and crack tip texture as random variables. The model was verified using data for 7050-T7451 plate alloy fatigue tested in smooth sample configuration at σ_{max} of 241 and 276 MPa and $R = 0.1$. The mechanical testing was supplemented with characterizations of the size distributions of the fatigue performance limiting bulk porosity and measurements of the actual sizes of the fatigue crack initiating pores. Predicted fatigue lives were in good agreement with the experimental results and the model identified the size distribution of the crack initiating pores as the dominant variable controlling fatigue performance. The distributions of those pores were predicted from the bulk pore size data using the statistics of extremes. The developed approach proved effective in incorporating microstructural information in modeling fatigue and could be used in ranking fatigue quality and reliability of materials based on microstructural data. © 1998. Published by Elsevier Science Ltd.

(Keywords: fatigue life predictions; airframe alloys, 7050 alloy; statistics of extremes)

INTRODUCTION

Most of the existing crack growth life prediction models are based on the Paris/Erdogan type growth laws. Since such laws are deterministic, these models are suitable for predicting the average fatigue life. Statistical variability can be introduced into them either through the stochastic multiplication factor or by replacing all parameters with stochastic variables¹. The latter approach allows for dynamic change of the crack tip environment with crack length, hence it is ideal for investigating microstructural effects using a Monte-Carlo (MC) method². The MC model used in this work incorporates microstructural changes on the crack path through the following crack growth law^{3,4}:

$$\frac{da}{dN} = C\Delta K^m = \mathcal{D} \frac{C'}{M^n} \Delta K^m \quad (1)$$

where C , C' , m and n are material constants, \mathcal{D} is a crack deflection correction coefficient, and M is a Taylor factor dependent on material crystallographic texture⁵. Integrating Equation (1) gives fatigue life equal to

$$N = N_o + \int_{a_o}^{a_{crit}} \frac{M^n}{\mathcal{D} C' \Delta K^m} da \quad (2)$$

where N_o is the number of nucleation cycles, a_o is an initial and a_{crit} a final crack length. The microstructure enters the model through (1) initial crack size a_o equal to the size of the microstructural crack initiating flaws, (2) Taylor factor M controlled by crystallographic texture, and (3) crack deflection correction \mathcal{D} related to the spatial distribution of the microstructural features. During MC simulations Equation (2) can be integrated numerically with random values of N_o , a_o and a_{crit} as input and with randomly selected values of M and \mathcal{D} for each integration step. The calculations are then repeated for various combinations of all variables, giving the distribution of fatigue lives. The model is extremely flexible and allows for simulation of the effects from each individual variable and from their combinations. In this work we investigated only the effects of the initial crack sizes a_o , texture and crack deflections on fatigue lives of the 7050-T7451 plate alloys. In these alloys the cracks initiate preferentially from large pores and it can be assumed that the nucleation stage is insignificant, e.g. $N_o = 0$ ⁶.

EXPERIMENTAL RESULTS

The test material used was 7050-T7451 thick (145 mm) plate alloy with yield strength of 455 MPa, tensile

strength 515 MPa, fracture toughness 32.3 MPa $\sqrt{\text{m}}$ and fatigue crack growth rate given by the relation⁷

$$\frac{da}{dN} = 7.5 \times 10^{-12} \Delta K^{4.175} \quad (3)$$

(results in m cycle^{-1} for ΔK in MPa $\sqrt{\text{m}}$). The L-T smooth fatigue samples used in testing were cut from the plate center and had gauge length 50.8 mm and diameter 12.7 mm. All tests were conducted at ambient atmosphere under constant amplitude loading with maximum stresses 241 MPa (45 samples) and 276 MPa (23 samples), $R = 0.1$ and at frequency 10 Hz. The results are summarized in Figure 1.

The microstructural characterizations included both metallography and fractography. The metallography focused on the measurement of the size distribution of the bulk porosity at the center of the plate. The magnification used was $900 \times$ and the data were collected from the LS, TL and ST planes. The obtained cumulative size distribution of pore maximum dimensions is shown in Figure 2. The average bulk pore maximum dimension was 23.8 mm, aspect ratio 1.52 and area density 76.1 mm^{-2} . Additional microstructural data on the same material have been reported in Ref.⁸. The fractographic examinations were limited to 20 samples tested at $\sigma_{\max} = 241 \text{ MPa}$. In all cases cracks initiated from large pores which had average maximum length of $153.2 \mu\text{m}$ and average aspect ratio of 1.80. The cumulative size distribution of the pore maximum dimensions is also shown in Figure 2.

RESULTS AND DISCUSSION

The results obtained were used in estimating both the magnitudes of the microstructural contributions to the scatter in fatigue lives and in testing the predictive capabilities of the microstructure based fatigue MC model. The former can be obtained from Equation (2) by integrating it with the upper and lower bound values of the microstructural variables and the latter by changing microstructural variables with crack length. To obtain bounds on the initial crack sizes, it

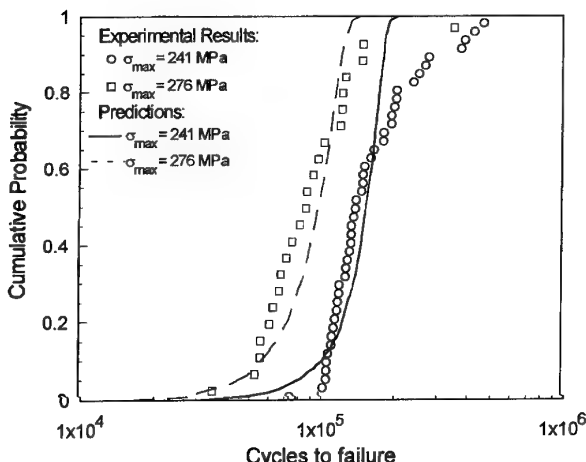


Figure 1 Comparison of the experimental S - N results with the predictions from the Monte-Carlo simulations for indicated σ_{\max} levels: 7050-T7451 plate alloy, L-T smooth fatigue samples, $R = 0.1$, 10 Hz

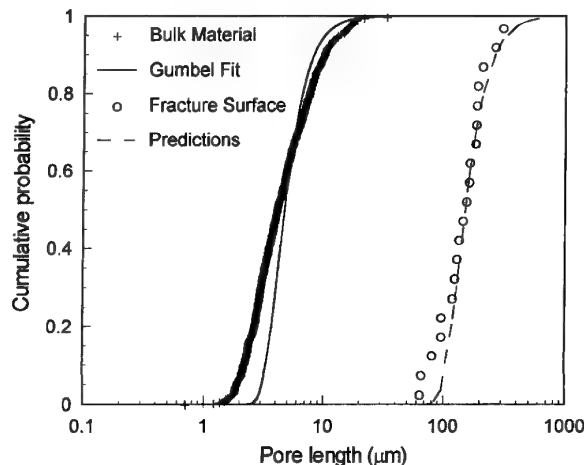


Figure 2 Distributions of the largest dimensions of the bulk and the actual crack initiating pores for 7050-T7451 plate alloy. The predicted crack initiating pore size distribution was obtained from the weighted Gumbel distribution fitted to the bulk data using a sample size of 1.54×10^5

was assumed that each pore acts as a microcrack and that the initial crack size is equal to the size of the largest pore intersecting the fatigue sample surface. The size distribution of such pores, one from each sample, constitutes an extreme value distribution of bulk pores (parent distribution) with the sample size, N_G , equal to the number of pores intersecting the sample surface⁹. To obtain the extreme value distribution, the bulk pore sizes were fitted with a Gumbel parent

$$F(\log d) = \exp \left(- \exp \left(- \frac{\log d - \mu}{\sigma} \right) \right) \quad (4)$$

where d is pore size and μ and σ are distribution parameters. The weight function used for each point had the following recommended form:

$$w_i = \frac{1}{1 - p_i} \quad (5)$$

where i is the ordered pore size number and p_i its empirical probability⁹. The Gumbel distribution was chosen because it described best the right tail of the parent and because of its utility in the extreme value calculations. For a Gumbel parent the extreme value distribution is also given by Equation (4), with the same dispersion σ but with μ equal to

$$\mu_N = \mu + \sigma \ln N_G \quad (6)$$

The investigated alloy had pore area density 76.1 mm^{-2} , hence the sample size, N_G , was 1.54×10^5 . The parameters of the parent and extreme distribution are compiled in Table 1 and both distributions are com-

Table 1 Parameters of the Gumbel distributions of pore largest dimensions

	μ	σ
Bulk pores (weighted fit)	1.450	0.290
Crack initiating pores ($N_G = 1.54 \times 10^5$)	4.913	0.290

pared with the experimental data in *Figure 2*. The predicted sizes of the crack initiating pores are in very good agreement with the actual fractographic data, indicating the correctness of the approach. The predicted crack initiating pore sizes corresponding to the 1 and 99 percentiles were 87.4 and 517 μm respectively. They were used as the initial crack sizes in Equation (2) to estimate the variability in fatigue life attributable to pores. Obtained crack growth curves, for $\sigma_{\max} = 240 \text{ MPa}$, are given in *Figure 3a*. They were generated using stress intensities from Raju and Newman¹⁰ and assuming an initial thumbnail crack with depth equal to the pore size and aspect ratio of the bulk pores. The predicted dispersion was 150,000 cycles, which is comparable to that of the experimental data.

The effects of the changes of the crystallographic texture along the crack path on fatigue life have been estimated from the expected changes of the resulting Taylor factors (M). For f.c.c. metals and alloys those changes can lead to local M between 2.5 and 4.5⁵. The crack growth curves obtained using these values are shown in *Figure 3c*. They were simulated for initial crack size 172 μm , the predicted extreme average, $n = 2^3$ and using the same loading conditions as for the pore size effect. The obtained range of fatigue lives was 165,000 cycles. It should, however, be kept

in mind that this represents the maximum one-sided effects. In reality the scatter will be smaller because the extreme conditions are not going to persist throughout the entire fatigue life. The realistic estimate of texture effect was obtained by varying M with crack length. For small cracks with plastic zone of the order of a few grains M was assumed to be uniformly distributed between 2.5 and 4.5. Since for longer cracks the plastic zone penetrates an increasing number of grains, the range of local M values can be progressively decreased. Eventually, for a critical number of grains, N_{crit} , of about 25, the crack tip samples the average texture, hence M can be assumed constant and equal to the average value¹¹, *Figure 4a*. Such changes of M used in 1000 MC simulations resulted in the predicted fatigue life range of only 5200 cycles, *Figure 3c*.

To evaluate the contribution from the changes of microstructural crack geometry on scatter, the reported fracture surface roughness data for 7050-T7451 alloy have been used¹². The profile roughness was incorporated into the crack growth model by assuming that the crack had idealized periodic profile shown in *Figure 4b*. For such profile the deflection correction factor in Equation (2) is equal to^{3,13}

$$\mathcal{D} = \frac{1}{R_L} \quad (7)$$

where R_L is the profile roughness parameter equal to the ratio of the crack true and projected lengths. The maximum reported value of the profile roughness for 7050-T7451 alloy is 1.54¹²; it gives the lower limit for \mathcal{D} . The upper limit corresponds to the straight crack without deflections, i.e. when both R_L and \mathcal{D} are one. Crack growth curves obtained for those limits are given in *Figure 3b*. The estimated fatigue life variability was 61,000 cycles, which is less than that for texture. This is again a one-sided overestimation. To obtain a realistic estimate of the range, the \mathcal{D} values were varied along the crack path uniformly between the upper and lower bounds. The resulting spread of fatigue lives was only 2200 cycles, *Figure 3b*.

The fatigue lives in the 7050-T7451 plate alloys

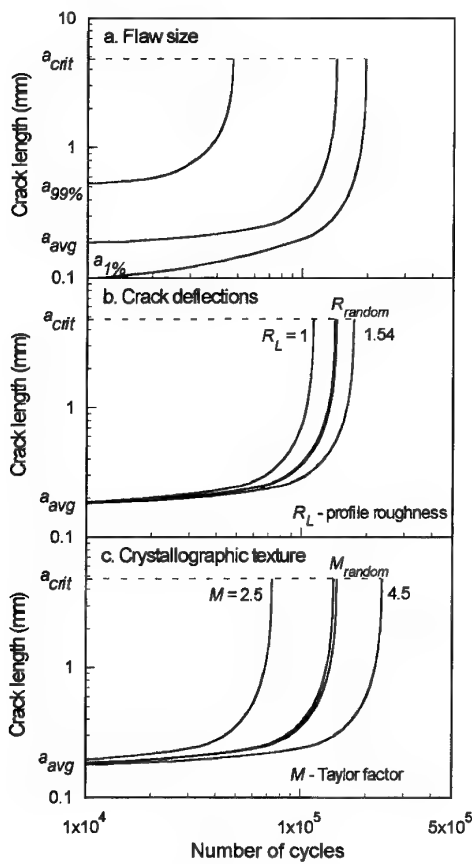


Figure 3 Effects of the extreme variation of (a) flaw sizes, (b) crack deflections, and (c) texture on fatigue life of the 7050-T7451 plate alloy fatigued at $\sigma_{\max} = 241 \text{ MPa}$ and $R = 0.1$. Random curves correspond to the random variations of deflections and texture along the crack path

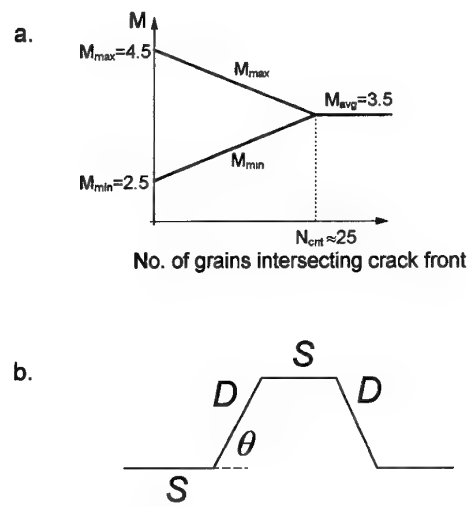


Figure 4 Schematics showing (a) change of the range of Taylor factor values with number of grains intersected by the crack tip and (b) idealized crack profile assumed during Monte-Carlo simulations

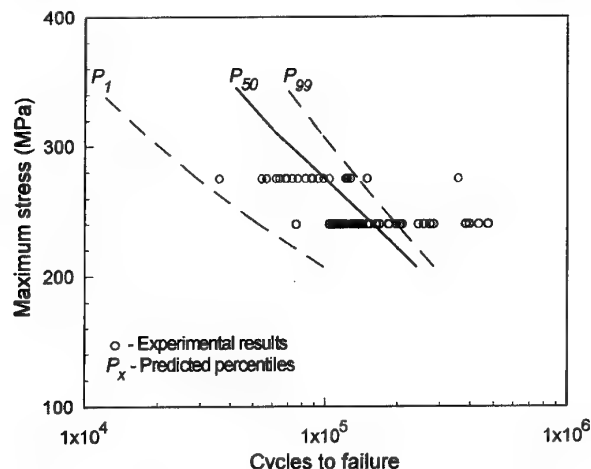


Figure 5 Comparison of the $S-N$ fatigue data for the 7050-T7451 plate alloys with the Monte-Carlo predictions obtained with initial crack sizes, texture and crack deflections as random variables

would then be expected to be controlled primarily by the size distribution of crack initiating pores, with other microstructural factors playing a secondary role. Figures 1 and 5 show a comparison of the experimental $S-N$ fatigue data with the MC results simulated with initial crack size, yield strength and crack deflections as random variables. The initial crack sizes were generated according to the predicted extreme value distribution, with aspect ratios equal to the bulk pore average. The yield strength and crack geometry fluctuations were incorporated into the model using the aforementioned distributions of Taylor factors and deflection corrections. The predictions compare favorably with the experimental data for both short and mid-range fatigue lives. For long lives the model underestimates the experimental results. Although this is desirable from the point of view of safe design, the underestimation is substantial. This error is due to the overestimation of the small crack initiating pore sizes by the extreme value procedure.

SUMMARY

- A Monte-Carlo crack growth model was used to estimate the magnitudes of microstructural effects on fatigue life of the 7050-T7451 thick plate alloys. The random variables used included crack initiating pore size, crystallographic texture and crack deflections.

- The model, with the initial crack sizes predicted from the bulk pore size distribution using statistics of extreme, shows good predictive capabilities for the low and mid-range fatigue lives.
- The size distributions of microstructural flaws, such as porosity, have been identified as the dominant variable controlling fatigue lives in 7050-T7451 plate alloys.

ACKNOWLEDGEMENTS

Work supported by the ONR under Grant N00014-91-J-1299 (UCLA) and Contract N00014-91-C-0128 (Alcoa). The authors would like to thank Dr J. Zhang and Ms A.J. Luévanos, formerly from UCLA, for performing some of the metallographic and fractographic examinations.

REFERENCES

- Provan, J. W. (ed) *Probabilistic Fracture Mechanics and Reliability*. Martinus Nijhoff, Dordrecht, 1987.
- Ang, A. H.-S. and Tang, W. H. *Probability Concepts in Engineering*, Vol. 2. Copyright by authors, 1990, pp. 274–325.
- Suresh, S. *Fatigue of Materials*. Cambridge University Press, Cambridge, 1991.
- Vasudevan, A. K., Sadananda, K. and Louat, N., A review of crack closure, fatigue crack threshold and related phenomena. *Materials Science and Engineering A*, 1994, **188**, 1–22.
- Bunge, H. J., Some applications of the Taylor theory of crystal plasticity. *Kristall und Technik*, 1970, **5**, 145–175.
- Grandt, A. F., Modeling the influence of initial material inhomogeneities on the fatigue life of notched components. *Fatigue and Fracture of Engineering Materials and Structures*, 1993, **162**, 199–213.
- Magnusen, P. E. et al., The role of microstructure on the fatigue durability of aluminum aircraft alloys. Final Report ONR Contract N00014-91-C-0128, Alcoa Technical Center, Alcoa Center, PA, 1995.
- Przystupa, M. A. et al., Development of the microstructure based stochastic fatigue life prediction models. Progress Report ONR Grant N00014-91-J-1299, UCLA, Los Angeles, CA, 1993.
- Castillo, E. *Extreme Value Theory in Engineering*. Academic Press, San Diego, 1988.
- Raju, I. S. and Newman, J. C. *Stress-Intensity Factors for Circumferential Surface Cracks in Pipes and Rods under Tension and Bending Loads*. ASTM STP 905, ASTM, Philadelphia, PA, 1986, pp. 789–805.
- Chan, K. S. and Lankford, J., The role of microstructural dissimilitude in fatigue and fracture of small cracks. *Acta Metallurgica*, 1988, **36**, 193–206.
- Luévanos, A. J., Przystupa, M. A. and Zhang, J., Accumulation of microstructural damage due to fatigue of high-strength aluminum alloys. *Journal of Materials Engineering and Performance*, 1994, **3**, 47–54.
- Vasudevan, A. K. and Suresh, S., Lithium-containing aluminum alloys: cyclic fracture. *Metallurgical Transactions*, 1985, **16A**, 475–477.

PII: S0142-1123(97)00032-7

The effects of load sequencing on the fatigue life of 2024-T3 aluminum alloy

Richard A. Everett Jr.

US Army Vehicle Technology Center, ARL, NASA Langley Research Center,
Hampton, VA 23681-0001 USA

Current fatigue life analysis of metallic rotorcraft dynamic components are based on a linear cumulative damage concept known as Miner's rule. This type of analysis assumes that there is no load sequence effect that occurs during the fatigue loading history. Past studies have shown that linear cumulative damage analysis of fatigue tests has produced life predictions that have been conservative as well as unconservative. Some of this uncertainty has been attributed to the fact that load sequence effects do exist in most fatigue load spectra. As a first phase the study reported herein was done to evaluate the load sequencing effects that could exist in commercial fixed-wing fatigue load spectra. To evaluate these effects a typical commercial wing spectra was reordered using a scheme that had previously been shown in fatigue block loading to produce the shortest fatigue lives. This scheme starts with the smallest load range in a load sequence and proceeds in ascending order until the largest load range is reached. Tests on open hole test specimens made of 2024-T3 aluminum alloy were conducted on the normal sequence of loads as well as the reordered scheme called lo-hi. Test results showed no significant differences between the fatigue lives of the normal load sequence and the reordered load sequence. A computer program called FASTRAN which calculates total fatigue life using only crack growth data was shown to predict the fatigue life of the spectrum tests with acceptable accuracy. © 1998 Elsevier Science Ltd.

(Keywords: aluminum; fatigue life prediction; spectrum tests)

INTRODUCTION

Current fatigue life analysis of metallic rotorcraft dynamic components is based on a linear cumulative damage concept known as Miner's rule. This type of analysis assumes that there is no load sequence effect that occurs during the fatigue loading history. In the past, studies have shown that linear cumulative damage analysis of fatigue tests has produced life predictions that have been conservative as well as unconservative¹. It has been suggested that some of this uncertainty is probably caused by the fact that load sequence effects do exist in many fatigue load spectra and that the linear cumulative damage analysis cannot account for these sequencing effects². The main objective of this work is to identify the load sequence effects that may exist in typical research and design fatigue load spectra.

The first phase of this work started with the study of a typical commercial transport design wing spectra. From previous studies it has been shown that in simple block sequences of loads, where the loading sequence was ordered from the smallest load ranges to the largest, the fatigue life from this type of sequence would give the shortest fatigue lives³. Since from an aircraft design perspective it is desired to underpredict

(conservative) the design life rather than overpredict, a reordering scheme was chosen that would produce a load sequence starting with the smallest load ranges in the commercial transport spectra, proceeding in an ascending order to the largest load ranges.

MATERIAL AND TEST SPECIMEN CONFIGURATION

The material used for this study was 2024-T3 aluminum sheet taken from a special stock of material at the NASA Langley Research Center which has been used for fatigue and fracture studies over several decades. The alloy 2024 has been used in the lower wing skin of many commercial transport aircraft. The material from the Langley stock has a yield strength of 52 ksi and an ultimate strength of 72 ksi⁴. The fatigue endurance limit for this material was shown to be approximately 8 ksi from a previous test program⁵. The nominal thickness is 0.090 in. The test specimens were machined to the configuration shown in Figure 1. The center hole diameter was 0.25 in, which resulted in an elastic stress concentration factor K_T of 3.02 based on gross section or 2.79 based on net section.

The fabrication of the center hole was done using a

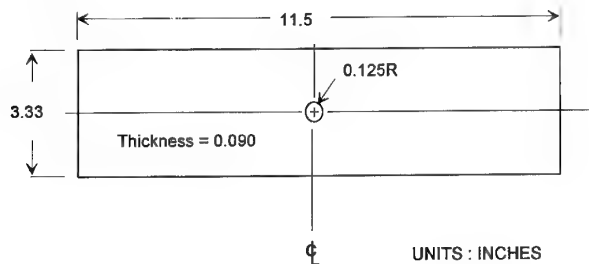


Figure 1 Test specimen geometry

procedure that produces a hole almost free of machining residual stresses⁶. First, a pilot hole is drilled about 0.01 in less than the final hole size with an aluminum backing plate to reduce burrs. A reamer is then used to produce the desired hole diameter. Each specimen is drilled individually. After the hole is drilled mechanically, the specimen is chemically polished. The chemical polish solution is 80% phosphoric acid, 5% nitric acid, 5% acetic acid, and 10% water, by volume⁴. The solution is heated to 220 F for 5 min. The chemical polishing procedure is designed to deburr the hole as well as to remove a layer of material that might contain machining residual stresses.

TEST SPECTRUM

The fatigue load spectrum chosen for phase 1 of this study was a test spectrum typical of that used in the design of fixed-wing commercial transport aircraft. In this paper the spectrum is referred to as commercial transport, type A. The loads in this spectrum are typical of those experienced on the lower wing surface of a commercial transport. Guide plates were used to prevent buckling under compressive loading. Tests were run in a servohydraulic, electronically controlled test stand using a software program that employs a procedure to control loads within 1%.

The spectrum used in this phase of the study consists of five different flight types. *Figure 2* shows flights number one and five. Flight number one is the most severe and occurs only once in 5000 flights, while flight number five is the least severe and occurs 3704 times in 5000 flights. Flight number two occurs 13 times, flight number three occurs 215 times, and flight number four occurs 1067 times, respectively, in the 5000 flight sequence. As stated previously, the method used in this study to evaluate load sequence effects was to reorder the normal flight sequence of loads in a low-to-high sequence and compare the fatigue life of the normal sequence to that of the reordered sequence. The sequence of loads in the two flights shown in *Figure 2* is the normal sequence. As a comparison, *Figure 3* shows flight number one as it appears in the low-to-high reordered sequence.

In the current work only the load sequence in each flight was reordered. The sequence of the flight types that makes up the 5000 flight sequence was not initially reordered. In the fatigue tests, when the initial 5000 flights have been applied, it is stated that one pass through the spectrum has been completed. One pass through the spectrum used herein was 208,022 cycles. In a spectrum fatigue test normally a test will run for

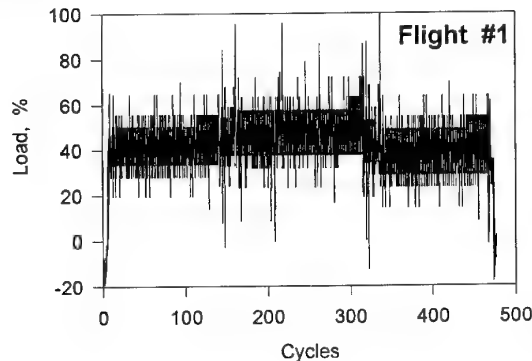


Figure 2 Flight number 1 and number 5 of the load spectrum

several passes through the spectrum before the test article fails.

DISCUSSION

To develop a reference point for the evaluation of the load sequence effects, fatigue spectrum tests were first run on the standard spectrum to establish the stress versus fatigue life curve (*S/N* curve). After the standard spectrum fatigue life data was established, fatigue tests were run on the reordered lo-hi spectrum at one of the stress levels used to establish the standard spectra *S/N* curve. Several tests were run at each stress level to assess the fatigue life scatter bands. The stress values shown in the following figures are based on the gross section of the test specimen. The maximum stress values shown on the *S/N* curves is the maximum stress in the spectrum. For the spectrum used in this work the maximum stress occurs only in flight number one and it occurs only once in this flight. Further, flight number one occurs only once in the 5000 flight spectrum.

Current test program

The *S/N* curve for the standard spectra tests is shown in *Figure 4* at the three stress levels tested where reasonable finite fatigue lives exist. Each symbol in the figure represents one fatigue test. If the stress level was decreased below the lowest stress shown in *Figure 4*, test lives would go beyond 10 million cycles which would require test times greater than 12 days for each individual test.

In order to keep the testing time at a reasonable length, a maximum stress of about 34 ksi was used to run the reordered lo-hi load sequence spectrum. At this stress level the shortest test life was almost 10

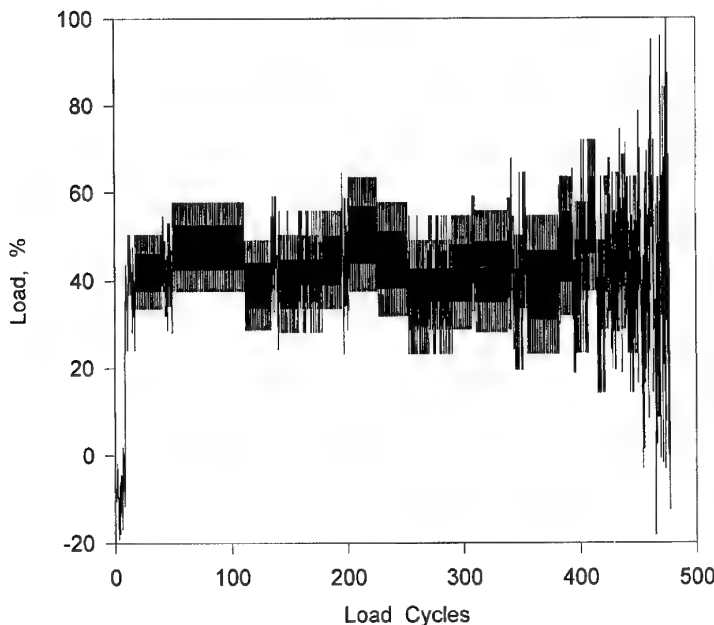


Figure 3 Flight number 1, reordered sequence, lo-hi

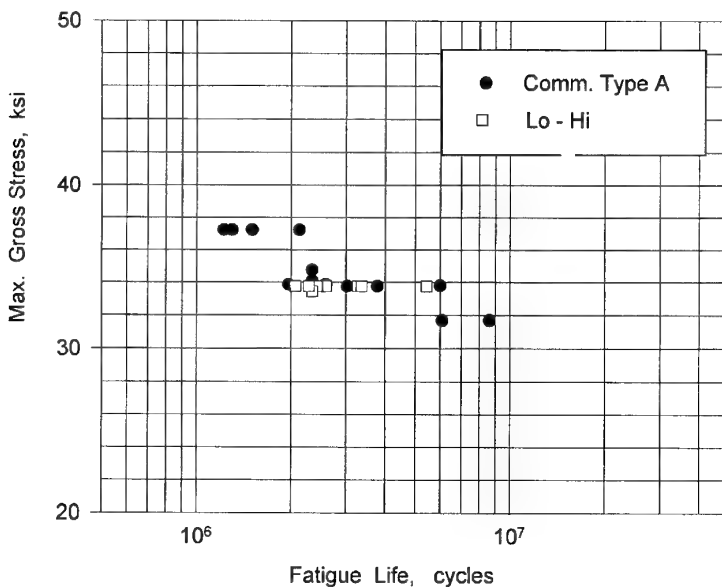


Figure 4 Spectrum fatigue tests, standard and lo-hi sequence

passes through the spectrum. *Figure 4* also shows the fatigue lives for the seven tests run on the reordered lo-hi spectrum.

As seen in *Figure 4*, the fatigue lives of the reordered lo-hi tests fall within the scatter band of the standard spectrum fatigue lives. These results would lead one to surmise that there is no load sequence effect in the commercial type A fatigue load spectrum used in this study. Further comments on the load sequence effect will be made later in this paper.

Life analysis of spectrum tests

As an analytical tool in helping to evaluate load sequence effects, a computer code called FASTRAN was used. This computer program was developed

almost two decades ago and was originally conceived as a crack growth analysis tool based on fatigue crack-closure concepts in fracture mechanics and was shown to help explain load interaction effects (herein called load sequence effects) in fatigue crack growth. This computer program was originally called FAST (Fatigue Crack Growth Analysis of Structures)⁷. Later the use of 'small-crack' concepts was incorporated into FASTRAN, and this analysis was shown to be very effective in calculating total fatigue life based solely on crack growth data⁸.

In *Figure 5* the FASTRAN analyses of the fatigue lives for the standard spectrum load sequence and the reordered lo-hi sequence are shown. As can be seen, the FASTRAN analysis of the standard spectrum shows

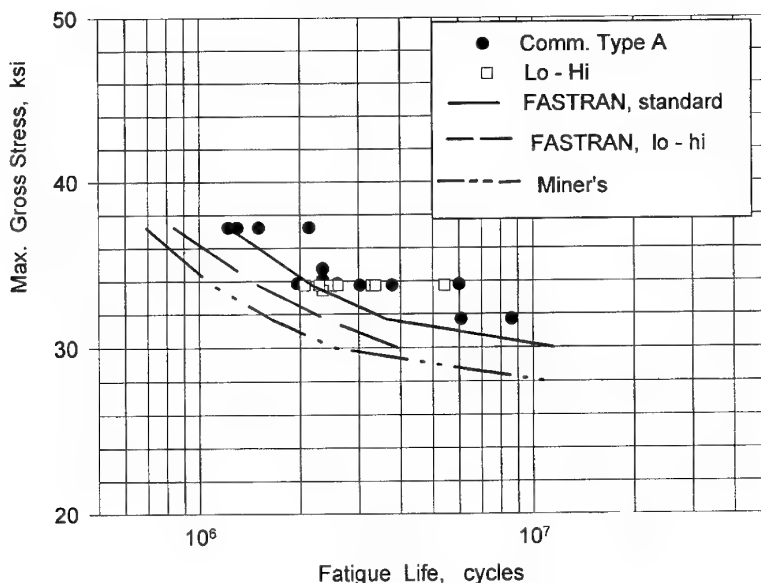


Figure 5 Spectrum fatigue tests compared to analysis

fatigue lives that are on the low side of the scatter of the test lives. FASTRAN also predicts a slight reduction in the fatigue lives of the reordered lo-hi spectrum.

At the three stress levels where spectrum tests were run, FASTRAN predicts a decrease in life of about 30% compared to the FASTRAN analysis of the standard load sequence. However, at a stress level of 30 ksi FASTRAN shows a 65% reduction in life. It has been surmised that a reduction in the stress levels will put more and more of the spectrum loads below the endurance limit of the material and hence only the higher loads are causing fatigue damage. This could in turn cause more of a load interaction effect since it is mostly the higher loads that cause the material to experience compressive residual stress fields near the 'damage' in the material, thus causing an 'increase' in the fatigue life². Future plans call for tests at the 30 ksi level to see if this more significant difference between the standard and the lo-hi fatigue lives is a fact.

As a further reference point, life analyses were also made using the classical Miner's analysis⁹. As is seen in Figure 5, the life predictions from the Miner's nominal stress analysis were a minimum of a factor of two less than those of the standard FASTRAN analysis. Since Miner's analysis is a linear cumulative damage analysis, it cannot predict a different life for the reordered lo-hi loading sequence.

Other related program results

In a similar study to the one reported herein, Perrett¹⁰ used five different reordering schemes on the standardized fighter spectrum called Falstaff. In this study one of the reordering schemes, called Diverge, was essentially the same as the lo-hi load sequence used herein. Another sequence in this work was a hi-lo sequence called Decay. Tests on open hole specimens with the Diverge (lo-hi) sequence showed an increase in life of about 40% when compared to Falstaff's normal loading sequence. Tests using Decay (hi-lo)

showed an increase in life by almost a factor of two. Neither of these increases were considered significant by the author. In much of the aircraft industry today a factor of two difference in fatigue lives is not considered very significant. It should be noted, however, that if one changes the specimen configuration opposite results can be found from the open hole test specimen. Tests in Ref. 10 also showed that on a specimen where holes are filled with a fastener, the Diverge (lo-hi) sequence gives longer lives than the standard Falstaff. However, for tests with the Decay (hi-lo) sequence, shorter lives were experienced. Results similar to these with joint specimens using fasteners were also reported in Ref. 11.

CONCLUDING REMARKS

The study reported herein was done to evaluate the load sequencing effects that could exist in commercial fixed-wing fatigue load spectra. To evaluate these effects a typical commercial wing spectrum was reordered using a scheme that had previously been shown in fatigue block loadings to produce the shortest fatigue lives. This scheme starts with the smallest load range in a load sequence and proceeds in ascending order until the largest load range is reached. Tests on open hole test specimens made of 2024-T3 aluminum alloy were conducted on the normal sequence of loads as well as the reordered scheme called lo-hi. Test results showed no significant differences between the fatigue lives of the normal load sequence and those of the reordered load sequence. A computer program called FASTRAN which calculates total fatigue life using only crack growth data was shown to predict the fatigue life of the spectrum tests with acceptable accuracy. This program has been shown to predict fatigue spectrum effects fairly accurately for several standardized loading spectra such as Falstaff, Twist, and Gaussian¹², as well as for 4340 steel specimens under the rotorcraft standardized spectra called Felix/28¹³.

Future work will explore the possible spectrum

effects in rotorcraft types of fatigue load spectra, compare the fatigue life of tests from actual spectra with a rainflow version of the same spectra, and with the use of FASTRAN explore what type of load sequences cause load interaction effects on fatigue life.

REFERENCES

- 1 Jacoby, G., Comparison of fatigue life estimation processes for irregularly varying loads. Proceedings of 3rd Conference on Dimensioning, Budapest, 1968.
- 2 Schijve, J., The accumulation of fatigue damage in aircraft materials and structures. AGARD Symposium on Random Load Fatigue, AGARD-CP-118, April 1972.
- 3 Naumann, E. C., Hardrath, H. F. and Guthrie, D. E., Axial load fatigue tests of 2024-T3 and 7075-T6 aluminum alloy sheet specimen under constant and variable amplitude loads. NASA Report TN D-212, 1959.
- 4 Newman Jr., J. C. and Edwards, P. R., Short-crack growth behavior in an aluminum alloy – AGARD cooperative test programme. AGARD-R-732, 1988.
- 5 Landers, C. B. and Hardrath, H. F., Results of axial-load fatigue tests on electropolished 2024-T3 and 7075-T6 aluminum-alloy-sheet specimens with central holes. NACA Report TN 3631, March 1956.
- 6 Everett Jr., R. A., The effect of hole quality on the fatigue life of 2024-T3 aluminum sheet. American Helicopter Society Technical Specialists Meeting on Rotorcraft Structures, Williamsburg, VA, October 1995.
- 7 Newman Jr., J. C., A crack-closure model for predicting fatigue crack growth under aircraft spectrum loading. In *Methods and Models For Predicting Fatigue Crack Growth Under Random Loading*, eds J. B. Chang and C. M. Hudson. ASTM STP 748, 1981, pp. 53–84.
- 8 Newman Jr., J. C., Swain, M. H. and Phillips, E. P., An assessment of the small-crack effect for 2024-T3 aluminum alloy. In *Small Fatigue Cracks*, eds R. O. Ritchie and J. Lankford. 1986, pp. 427–452.
- 9 Miner, M. A., Cumulative damage in fatigue. *Journal of Applied Mechanics, ASME*, 1945, **12**, A159–A164.
- 10 Perrett, B. H. E., An evaluation of a method of reconstituting fatigue loading from rainflow counting. 14th ICAF Symposium, Ottawa, June 1987.
- 11 Schijve, J., The endurance under program-fatigue testing. Full-scale fatigue testing of aircraft structures. 1st ICAF Symposium, Amsterdam, 1959.
- 12 Newman, J. C., Fatigue-life prediction methodology using a crack-closure model. *Journal of Engineering Materials and Technology*, 1995, **117**, 433–439.
- 13 Everett, R. A., A comparison of fatigue life prediction methodologies for rotorcraft. *Journal of the American Helicopter Society*, 1992, **37**(2), 54–60.

PII: S0142-1123(97)00021-2

Prediction uncertainties at variable amplitude fatigue

Thomas Svensson*Swedish National Testing and Research Institute, Box 857, S-501 15 Borås,
Sweden*

Predictions of variable amplitude fatigue life suffer from uncertainties originating from different sources. In this paper, important sources are discussed and estimated, by means of a variable amplitude fatigue model, based on level crossing counts and a version of the Palmgren-Miner cumulative damage rule. The influence of random material strength and parameter estimates is treated in certain detail. The use of simple mathematical models in the analysis introduces systematic errors, which are studied here in terms of the uncertainty regarding the crack opening level at variable amplitude. Additional uncertainties occurring in the fatigue design stage, such as load variation and structural component variability, are briefly discussed and exemplified. © 1998 Elsevier Science Ltd.

(Keywords: fatigue; prediction; statistics)

INTRODUCTION

The fatigue phenomenon shows a random behaviour. This fact has been established after many years of testing and analysis. Under service conditions also the fatigue load varies randomly, hence the overall uncertainty of fatigue life predictions increases.

The aim of this investigation is to give a rough estimate of how the overall fatigue prediction uncertainty is composed of contributions from different sources. Based on the results some conclusions can be drawn regarding the modelling of the variable amplitude fatigue behaviour. Interesting questions to be answered are: how detailed should the models be and how precise can we expect the obtained predictions to be?

Lifetime predictions at variable amplitude are usually based on the Palmgren-Miner law, i.e. the cumulative damage accumulation assumption. The damage caused by a certain load is predicted from constant amplitude tests summarized in a Wöhler curve or quantified by the Basquin equation

$$N = \alpha(\Delta\sigma)^{-\beta} \quad (1)$$

where N is the number of cycles to failure at the constant amplitude load range $\Delta\sigma$ while α and β are material dependent parameters, determined from test results.

Fatigue life at variable amplitude is affected by uncertainties regarding the following items.

- **Material properties.** Random material strength introduces uncertainties in the material properties. This

can be analysed by the introduction of random variables in the models.

- **Model errors.** The complexity of the fatigue phenomenon makes it necessary to use simplified models in order to predict fatigue life. A balance between simplicity and reliability is desirable and a comparison of model errors with other uncertainties can be useful.
 - **Parameter estimates.** Models are often parametric and the parameters are found by fitting the model to empirical data. The uncertainty of parameter estimates must be taken into account in the prediction situation.
 - **Load variation.** Fatigue in service is caused by load variations that show a random behaviour within certain limits. This will increase the overall uncertainty.
 - **Structural component properties.** Fatigue tests for material characterisation are often performed under highly controlled conditions in the laboratory. In engineering design problems the properties of structural components must be considered in a variety of environments. These components often show a greater variability than the laboratory test specimens and the uncertainty increases regarding material properties, geometric details, size effects, and environmental effects.
- In this paper we first investigate uncertainties in material properties and parameters, and the results are compared to the model errors in a specific laboratory investigation. Next, the additional uncertainties appearing at prediction of fatigue life in service are briefly discussed, i.e. uncertainties originating from the load

variation and the structural component property variation. Finally, we give a rough estimate of the overall uncertainty based on the specific example investigated.

RANDOM MODEL FOR FATIGUE LIFE

The Basquin equation (1) is an empirical relation, used in many different situations. The equation describes the average behaviour, and the life in different tests varies around this average life. In order to describe the variation we would like to randomize the Basquin equation, i.e. introduce random quantities into the equation. To do that it is desirable to use some physical considerations. However, fatigue is a complex phenomenon composed of different stages, each stage having specific features and physical explanations. In an attempt to get a randomization related to physics we choose here to consider the crack growth stage. This may not be relevant for cases containing a long initiation part, but it is applicable in many engineering situations where crack-like defects in welds and rough surfaces are present.

In the crack growth stage the damage is quantified as crack size and the damage accumulation is often described with a crack growth law. Load ratio effects and sequential effects are proposed by Elber¹ to be dependent on the crack closure, and we therefore consider the effective stress intensity factor, defined as

$$\Delta K_{\text{eff}} = \begin{cases} K_{\max} - K_{\text{op}}, & K_{\text{op}} \geq K_{\min} \\ K_{\max} - K_{\min}, & K_{\text{op}} < K_{\min} \end{cases} \quad (2)$$

where K_{\max} , K_{\min} , K_{op} are the maximum, minimum and opening stress intensity factors, respectively. Now consider the Paris law for the effective load at constant load amplitude:

$$da/dN = C'(\Delta K_{\text{eff}})^m = C(\Delta S_{\text{eff}})^m a^{m/2} \quad (3)$$

where ΔS_{eff} is the remote effective load range, defined analogously to ΔK_{eff} , a is the crack length, while C and C' are geometry dependent constants. This differential equation can be solved giving the number of cycles to failure, N_f , in terms of the final crack size:

$$N_f = \frac{1}{C(1 - m/2)} (a_0^{1 - m/2} - a_c^{1 - m/2}) (\Delta S_{\text{eff}})^{-m} \quad (4)$$

Since the ratio between the initial and the final crack sizes is small, and the exponent m is in the vicinity of 3, the influence of the final crack size a_c will be small. Based on this observation we assume that the random variation of fatigue life is determined essentially by the random initial crack size, a_0 . We rewrite Equation (4) as a randomized Basquin equation:

$$N = A(\Delta S_{\text{eff}})^{-\beta} \quad (5)$$

where A is regarded as the only random variable. The initial crack size for the specific crack, that eventually leads to fracture, should be the one that has the largest size of all initial cracks. This leads to the statistical assumption that a_0 approximately follows an extreme value distribution and A should have a similar distribution. Fatigue life test results are often well described by a log-normal distribution, and in many cases this distribution can approximate extreme value distri-

butions. We therefore let A be log-normally distributed, which is also convenient for the further analysis. One drawback with this simple model is that the distribution at different load levels only differs by a scale factor, giving a constant coefficient of variation (equal to the ratio between the standard deviation and the mean). In experiments this coefficient often increases with decreasing load level, but the influence of this drawback is assumed to be small in the present analysis.

UNCERTAINTIES IN THE CONSTANT AMPLITUDE CASE

We first consider lifetime predictions at constant amplitude based on constant amplitude tests. Bearing the crack growth stage in mind we use the Elber crack closure hypothesis. Assume that for a certain load ratio (the ratio between the minimum and the maximum load level) the opening load is a constant percentage (100c%) of the load range and can be described as

$$S_{\text{op}} = S_{\min} + c(S_{\max} - S_{\min}) \quad (6)$$

The effective load range then becomes

$$\Delta S_{\text{eff}} = S_{\max} - S_{\text{op}} = (1 - c)\Delta S \quad (7)$$

where $\Delta S = S_{\max} - S_{\min}$.

We take the logarithm of the Basquin equation (5) and introduce Equation (7):

$$\ln(N) = \ln(A) - \beta \ln[\Delta S(1 - c)] \quad (8)$$

The logarithmic transformation gives two convenient properties for the further analysis: (i) the logarithm of a log-normal random variable is normally distributed; and (ii) the variance of the transformed variable can be interpreted as the squared coefficient of variation for the original variable since Gauss's approximation formula (see for instance Ref.²) gives

$$\text{Var}(\ln N) \approx \text{Var}(N) \left(\frac{\partial \ln N}{\partial N} \Big|_{N=E[N]} \right)^2 = \frac{\text{Var}(N)}{E[N]^2} \quad (9)$$

We now want to make Equation (8) suitable for a standard linear regression model. Consider the lifetime results N_1, N_2, \dots, N_n from n fatigue tests at test levels $\Delta S_1, \Delta S_2, \dots, \Delta S_n$. Introduce the notation $Z = \ln(\Delta S(1 - c))$, let the mean value of the n transformed test levels be \bar{Z} and introduce the new variable $\alpha = E[\ln(A)] - \beta\bar{Z}$, where $E[\ln(A)]$ is the expected value of $\ln(A)$. We then obtain the standard linear regression model

$$\ln(N) = \alpha - \beta(Z - \bar{Z}) + X \quad (10)$$

where X is a normally distributed random variable with zero expectation and variance τ^2 . From the test results and the model (10), we can estimate α , β and τ . The crack opening related variable c cannot be estimated from this experiment alone. For the case when c is known, it is possible to predict lifetimes in new constant amplitude situations based on the estimates $\hat{\alpha}$, $\hat{\beta}$ and $\hat{\tau}$. Standard linear regression theory² gives the variance of the prediction as a sum of the variance contributions from X , $\hat{\alpha}$ and $\hat{\beta}$, respectively:

$$\tau_{\ln(N)|Z}^2 = \frac{\tau^2}{n} \left(n + 1 + \frac{(Z - \bar{Z})^2}{\frac{1}{n} \sum_{i=1}^n (Z_i - \bar{Z})^2} \right) \quad (11)$$

From formula (11) it can be concluded that if the load level is closer to the mean test level than the quadratic mean distance, then the third term is less than unity and the prediction variance is less than $\tau^2(n+2)/n$. For estimates of material properties based on a reasonable number of tests ($n > 10$), the prediction uncertainty is dominated by the uncertainty in the random variable A , i.e. not much is gained by increasing the number of tests.

The variable c represents the crack opening level. This level depends on a number of sources, and the model error caused by the wrong choice of c can be described by the bias t in $\ln N$ resulting from a change of c by an amount Δc . We obtain from Equation (8)

$$t \approx \Delta c \frac{\partial \ln N}{\partial c} = \Delta c \frac{\beta}{1 - c} \quad (12)$$

EXAMPLE

The results above will be illustrated by experimental results from a fatigue test programme on welded specimens^{3,4}. Each specimen consisted of a plate with a longitudinal attachment fillet welded to each edge and were fabricated from 12 mm thick steel plate to BS 4360, Grade 50. Constant amplitude tests have been made at two nominal load ratios ($R = 0$ and $R = -1$) for two different batches of specimens (1 and 2).

Assume that the load ratio effect can be modelled by the crack opening level. The model (7) then allows us to combine the two load ratio cases to one Wöhler curve. The specimens were not stress relieved, and one can therefore assume that they contain tensile residual stresses resulting in a local load ratio much higher than the nominal one. We therefore assume that in the pulsating load case ($R = 0$) the dominating crack is always open and the constant c is equal to zero. We can then estimate the c value in the alternating load case ($R = -1$) by the linear regression model

$$\ln(N_{i,j}) = \begin{cases} \ln(A_{i,j}) - \beta_j \ln[\Delta S_{i,j}] & i = 1, 2, \dots, m_j \text{ for } R = 0 \\ \ln(A_{i,j}) - \beta_j \ln[C\Delta S_{i,j}(1 - c_j)] & i = m_j + 1, \dots, n_j \text{ for } R = -1 \end{cases}$$

where j indicates the batch number. This model was applied for each of the two batches of specimens giving the two sets of material parameters with approximately 95% confidence limits:

$$\begin{aligned} \hat{\tau}_1^2 &= 0.034, \hat{\beta}_1 = 2.69 \pm 0.16, \hat{c}_1 = 0.06 \pm 0.05 \hat{\tau}_2^2 \\ &= 0.038, \hat{\beta}_2 = 3.01 \pm 0.21, \hat{c}_2 = 0.16 \pm 0.06 \end{aligned} \quad (14)$$

As can be seen in Figure 1, the two batches show slightly different properties.

UNCERTAINTIES AT VARIABLE AMPLITUDE LOAD

In the variable amplitude case the overall prediction uncertainty increases. Predictions based on constant amplitude data introduce new model errors and the load process itself can be of random nature. The influence of a variable amplitude load process is studied here with the aid of the modified level crossing model^{5,7}. This model is based on a version of the cumulative Palmgren–Miner rule and will be briefly described here.

Consider a load process with remote stress S and crack opening stress process S_{op} . Introduce the effective load process $\tilde{S} = (S - S_{op})_+$, where the + sign indicates the positive part. The accumulated damage D at a certain time T is then

$$D(T) = \int_0^\infty n_+(u; \tilde{S}, T) \tilde{g}(u) du \quad (15)$$

where $n_+(u; \tilde{S}, T)$ is the number of up-crossings of the effective load process at the stress level u , and $\tilde{g}(u)$ is a damage exhaustion function determined from constant amplitude tests expressed by the Basquin equation (1). One finds^{6,7} that the Basquin equation

$$N = A(\Delta S_{eff})^{-\beta} \text{ gives } \tilde{g}(u) = \frac{\beta}{A} u^{\beta-1} \quad (16)$$

In order to make a model in correspondence with the linear regression model (10), we again assume that there are n experimental results from constant amplitude tests available and rewrite Equation (16) as

$$N = A' \left(\frac{\Delta S_{eff}}{\Delta \tilde{S}_{eff}} \right)^{-\beta} \text{ giving } \tilde{g}(u) = \frac{\beta}{A'} \frac{u^{\beta-1}}{\Delta \tilde{S}_{eff}^\beta} \quad (17)$$

where $\Delta \tilde{S}_{eff}$ is the geometric mean of the n test levels and $A' = A(\Delta \tilde{S}_{eff})^{-\beta}$.

We first consider the case when the variable amplitude load process is deterministic. In order to make lifetime predictions we assume that the effective load process is periodic with period t , which implies

$$n_+(u; \tilde{S}, T) = \frac{T}{t} n_+(u; \tilde{S}, t) \quad (18)$$

where T is a multiple of t . Define a damage intensity ν

$$\nu = \frac{D(T)}{T} = \frac{\int_0^\infty n_+(u; \tilde{S}, t) \tilde{g}(u) du}{t} \quad (19)$$

The number of time units t until fracture N_t is found by letting D be equal to 1:

$$N_t = \frac{1}{\int_0^\infty n_+(u; \tilde{S}, t) \tilde{g}(u) du} = \frac{A'}{\frac{\beta}{\Delta \tilde{S}_{eff}^\beta} \int_0^\infty n_+(u; \tilde{S}, t) u^{\beta-1} du} \quad (20)$$

with the damage exhaustion function according to Equation (17).

PREDICTION UNCERTAINTIES

We want to find the uncertainties in the predicted lifetime N_t . From Equation (20) it can be seen that the distribution of the predicted lifetime at variable amplitude is similar to the constant amplitude case (5). The variance of the predicted lifetime can be studied from the logarithm of Equation (20):

$$\ln(N_t) = \alpha + X - \ln \left(\frac{\beta}{\Delta \tilde{S}_{eff}^\beta} \int_0^\infty n_+(u; \tilde{S}, t) u^{\beta-1} du \right)$$

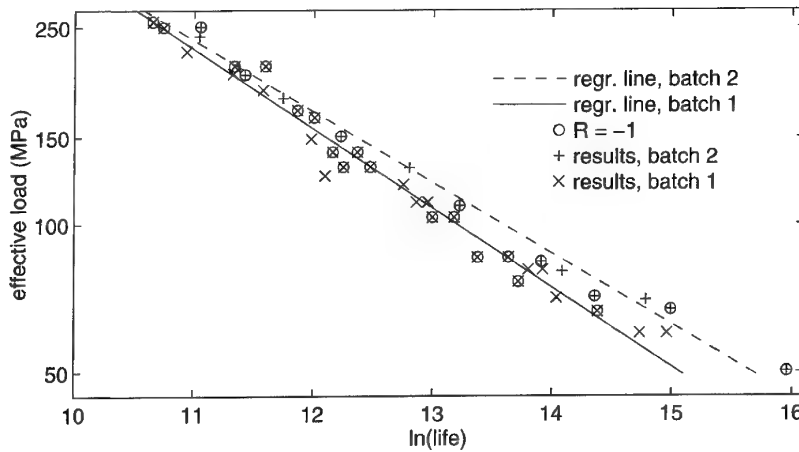


Figure 1 Results from constant amplitude tests plotted in a Wöhler diagram

(21)

where $\alpha = E[\ln(A')]$ and X is the random variable defined in Equation (10). We predict the log life

$$\hat{\mu}_t = \hat{\alpha} - \ln\left(\frac{\hat{\beta}}{\Delta \check{S}_{\text{eff}}^{\hat{\beta}}} \int_0^{\infty} n_+(u, \check{S}, t) u^{\hat{\beta}-1} du\right) \quad (22)$$

where $\mu_t = E[\ln(N_t)]$ and the prediction error can be written

$$\ln(N_t) - \hat{\mu}_t = \alpha - \hat{\alpha} + X \quad (23)$$

$$\begin{aligned} &+ \ln\left(\frac{\hat{\beta}}{\Delta \check{S}_{\text{eff}}^{\hat{\beta}}} \int_0^{\infty} n_+(u, \check{S}, t) u^{\hat{\beta}-1} du\right) \\ &- \ln\left(\frac{\beta}{\Delta \check{S}_{\text{eff}}^{\beta}} \int_0^{\infty} n_+(u, \check{S}, t) u^{\beta-1} du\right) \end{aligned}$$

For simplicity we call the property of the left hand side i Equation (23) Y , the three first terms at the right hand side U , and the last two terms at the right hand side V .

By the redefinition of A in Equation (17), the random variables U and V are independent. The variance of Y is then the sum of the variances of the two random variables U and V . The variance of U is the same as in the constant amplitude case, $\tau_U^2 = \tau^2(1 + 1/n)$, and the variance of V , τ_V^2 , can be calculated from the variance of the estimated exponent $\hat{\beta}$. Using Gauss's approximation formula we obtain

$$\begin{aligned} \tau_V^2 &\approx \text{Var}(\hat{\beta}) \left(\frac{\partial V}{\partial \hat{\beta}} \right)^2 = \\ &\text{Var}(\hat{\beta}) \left[\frac{1}{\hat{\beta}} \right. \\ &\left. + \frac{\int_0^{\infty} n_+(u, \check{S}, t) \ln(u) u^{\hat{\beta}-1} du}{\int_0^{\infty} n_+(u, \check{S}, t) u^{\hat{\beta}-1} du} - \ln(\Delta \check{S}_{\text{eff}}) \right]^2 \end{aligned} \quad (24)$$

In the constant amplitude case the result of Equation (24) simplifies to

$$\tau_V^2 \approx \text{Var}(\hat{\beta}) \left[\ln\left(\frac{\Delta S_{\text{eff}}}{\Delta \check{S}_{\text{eff}}}\right) \right]^2 \quad (25)$$

which is in accordance with the standard result (11).

EXAMPLE, CONTINUATION

The result (24) can be illustrated from the variable amplitude part of the experimental study^{3,4} treated above. Laboratory fatigue tests have been made at different deterministic variable amplitude load spectra. Four different types of spectra were used, all based on two sets of Rayleigh-distributed load ranges $\{\Delta S_{ij}; i = 1, 2, j = 1, 2, \dots, n_i\}$. The block lengths were $n_1 = 1024$ and $n_2 = 131,072$ cycles. The sets were applied (1) in random order, (2) in blocks with the cycles in an ordered sequence, (3) simulating a narrow band random process, and (4) simulating a broad band random process. Each spectrum was used with two load ratios ($R = 0$ and $R = -1$), here defined as the ratio between the global minimum and the global maximum of the process. In the first three spectra all individual cycles had the same stress ratio, while in the broad band case the stress ratio for individual cycles differed.

Based on the constant amplitude results (14), we will predict the life at variable amplitude with the modified level crossing model. To determine the effective load process we assume that the crack opening load stabilizes at a certain level. Let the opening level be expressed as in the constant amplitude case (6), but define equivalent \check{S}_{\min} and \check{S}_{\max} based on the root mean square (RMS) of the ranges, ΔS_{rms} . In the first three spectra with $R = 0$ all minima are equal to zero and we obtain, using Equation (6)

$$\check{S}_{\min} = 0, \check{S}_{\max} = \Delta S_{\text{rms}} \text{ giving } S_{\text{op}} = c \Delta S_{\text{rms}} \quad (26)$$

For the first three spectra with $R = -1$ all mean values are equal to zero, and we obtain

$$\begin{aligned} \check{S}_{\min} &= -\frac{\Delta S_{\text{rms}}}{2}, \\ \check{S}_{\max} &= \frac{\Delta S_{\text{rms}}}{2} \text{ giving } S_{\text{op}} = \Delta S_{\text{rms}} \left(c - \frac{1}{2} \right) \end{aligned} \quad (27)$$

where c is the crack opening coefficient in the constant amplitude case, i.e. $c = 0$ for $R = 0$ and $c = \hat{c}_1$ or \hat{c}_2 for $R = -1$. For the load spectrum 4 the stress ratio varies and we use the approximation

$$\tilde{S}_{\min} = \bar{S} - \frac{\Delta S_{\text{rms}}}{2}, \quad \tilde{S}_{\max} = \bar{S} + \frac{\Delta S_{\text{rms}}}{2}$$

giving $S_{\text{op}} = \bar{S} + \Delta S_{\text{rms}} \left(c - \frac{1}{2} \right)$ (28)

where \bar{S} is the mean value of the process.

Prediction intervals for the number of blocks to failure (based on uncertainties in material properties and parameter estimations) can be calculated according to the theory outlined above. The special linear regression model in this case (13) contains the additional variable c , and we must add the uncertainty originating from its estimation. With notation as above we obtain

$$\tau_{\ln N_t}^2 \approx \tau_U^2 + \tau_V^2 \approx \hat{\tau}^2 + \hat{\tau}_{\hat{c}}^2 + \hat{\tau}_{\hat{\beta}}^2 \left(\frac{\partial V}{\partial \hat{\beta}} \right)^2 + \hat{\tau}_{\hat{c}}^2 \left(\frac{\partial V}{\partial \hat{c}} \right)^2 \quad (29)$$

where the approximation marks are due to the fact that the estimated variables in this special case are not fully independent. The four estimated variances in (29) were calculated from the linear regression (13). The partial derivative with respect to \hat{c} was numerically calculated for the different load cases and found to be approximately equal to 3. The partial derivative factor with respect to $\hat{\beta}$ was calculated by numerical integration for each test condition, giving values ranging from 0 to 2.4, where the values vary depending on the difference between the spectrum severity and the severity of the geometrical mean, $\Delta \check{S}_{\text{eff}}$. Based on these results and an assumption of approximately normal distribution we obtain approximate 95% prediction limits for the logarithm of the number of blocks to failure:

$$\mu_t - 2\tau_{\ln N_t} < \ln N_t < \mu_t + 2\tau_{\ln N_t}, \quad (\approx 95\%) \quad (30)$$

The prediction theory is based on periodic processes. In this case we have periodic processes with periods equal to the block lengths. However, we do not know anything about the stationarity within the blocks and the prediction limits for the number of cycles to failure N must be extended as

$$\text{INT}(n_B \exp(E[Y] - 2\tau_{N_t})) < \text{NINT}(n_B \exp(E[Y] + 2\tau_{N_t})) + n_B \quad (31)$$

where n_B is the block length and the function INT stands for a truncation down to the nearest integer. Prediction results with prediction limits are plotted versus experimental results in Figures 2–5. The results show that the overall prediction errors exceed the variability represented by the prediction intervals, which means that the model errors are of considerable importance. The model errors will be estimated in terms of the crack opening level behaviour.

MODEL ERRORS

The use of the cumulative Palmgren–Miner law and the simple Basquin equation model are coarse simplifi-

cations of the real fatigue phenomenon. The resulting errors can only be estimated by comparison between prediction results and tests at variable amplitude. However, we can use the crack opening level in our example to illustrate the role of the model assumptions. As in the constant amplitude case (12), the c value influence on the lifetime prediction uncertainty can be found by the bias resulting from a change of c by an amount Δc :

$$t_c = \Delta c \partial Y / \partial c \quad (32)$$

Numerical calculations on the different spectra from our example show that this property can be estimated as $t_c \approx 3\Delta c$. A reasonable assumption of the error for the guessed c could be 0.1, which gives $t_c \approx 0.3$. This shows the sensitivity for the crack opening level when compared to the material related standard deviations estimated in our case to $\hat{\tau}_1 = 0.18$ and $\hat{\tau}_2 = 0.19$ (see Equation (14)).

STRUCTURAL COMPONENT PROPERTIES

Uncertainties regarding structural components in engineering design may in a few well-controlled applications be small, but should usually be of considerable influence. We will illustrate here the problem by means of the investigated results. In the example we had two batches of specimens. The two batches were both made of steel specified as BS 4360, Grade 50, but were manufactured by two different welders. The difference between the two batches at the constant amplitude tests can be seen in Figure 1, and we now investigate the influence on the variable amplitude predictions of mixing the two batches. This is made by using parameters from Batch 2 constant amplitude tests when predicting variable amplitude tests on specimens from Batch 1. Some of the results are shown in Table 1. Based on the results we estimate the batch-to-batch standard deviation as $|\ln \hat{N}_2 - \ln \hat{N}_1|/\sqrt{2}$. The variance contribution from this source is then in the interval 0.04–0.22 depending primarily on the maximum load level.

LOAD VARIATION

In the experimental study investigated here the variable amplitude loads were simulated and their level crossing properties were counted and known, when the predictions were made. The uncertainty in the load variation in this case was limited to the stationarity within the blocks. With block lengths being short compared to the lifetimes, this uncertainty was small in most experiments. In service, the load variation is not known beforehand, and variations caused by for instance different winds, roads or drivers can be of considerable importance for the prediction uncertainty.

In the simple case when the load process can be assumed to be a stationary and ergodic random process, it can be analysed. In that case we use the limit form of Equation (19):

$$\nu = \lim_{T \rightarrow \infty} \frac{D(T)}{T} = \lim_{T \rightarrow \infty} \frac{\int_0^\infty n_+(u, \tilde{S}, T) \tilde{g}(u) du}{T} \quad (33)$$

and the theory works as above. The variability of the

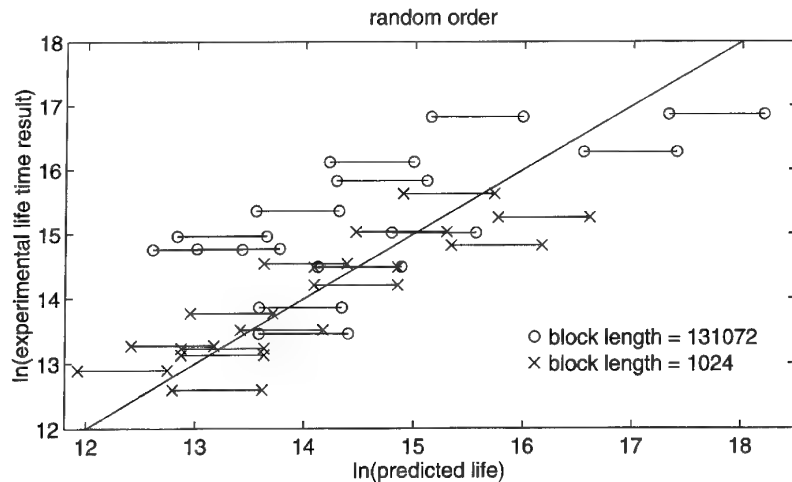


Figure 2 Predicted life with prediction limits versus experimental life for the random order load type

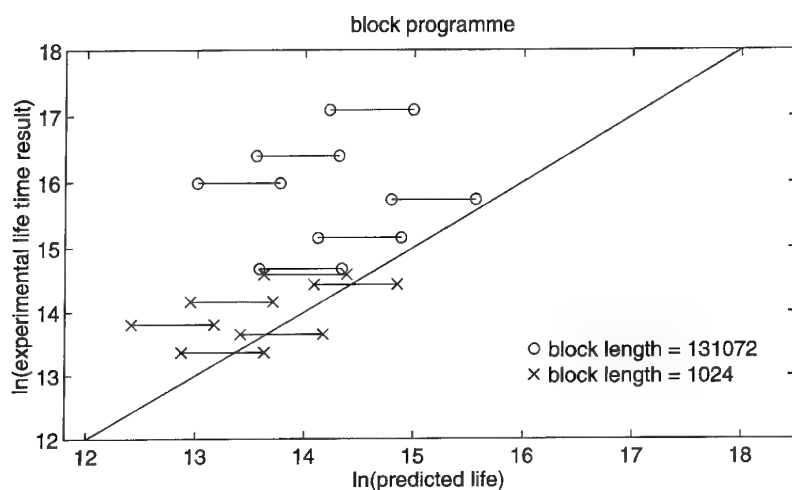


Figure 3 Predicted life with prediction limits versus experimental life for the block load type

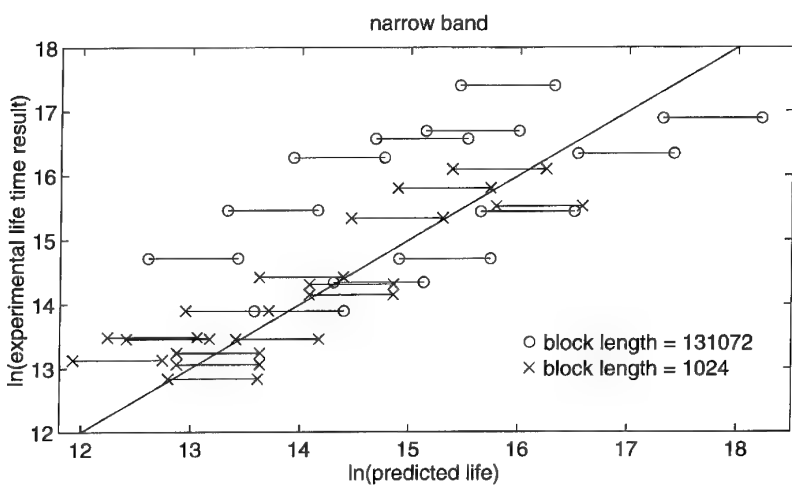


Figure 4 Predicted life with prediction limits versus experimental life for the narrow band load type

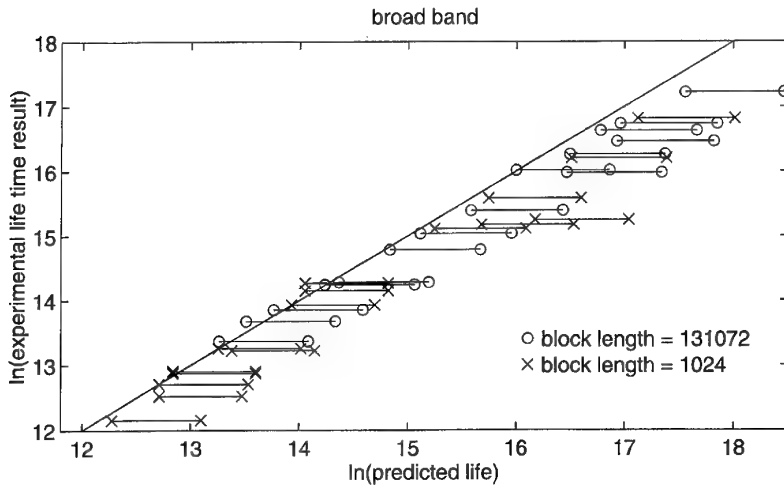


Figure 5 Predicted life with prediction limits versus experimental life for the broad band load type

Table 1 Prediction errors from mixing parameter sets:
 $|\ln \hat{N}_2 - \ln \hat{N}_1|$

	Maximum load	
	275	130
Random, block length 1024	0.27	0.51
Random, block length 131072	0.35	0.59
Narrow, block length 1024	0.37	0.61
Narrow, block length 131072	0.42	0.66

predicted lifetime caused by the variability of the load is highly dependent on the random process distribution. Here we estimate the variability for Gaussian processes with different irregularity factors. For each irregularity factor 100 processes, each containing 500,000 cycles, were simulated with an autoregressive filter method⁸. The variances of estimated $\ln(\text{life})$ are given in Table 2.

CONCLUSIONS

Prediction uncertainties at variable amplitude fatigue have contributions from a number of error sources. The contribution from each source has been estimated here using a simple log-normal model for the fatigue life distribution at constant amplitude and a level crossing method for lifetime prediction at variable amplitude. Under the assumption that the contributions are independent, the prediction squared error e_{\ln}^2 can be written as

Table 2 Variances of $\ln(N)$ for random Gaussian processes

Irregularity factor	Var($\ln(N)$)
0.3	0.0008
0.4	0.0002
0.8	0.00008
0.95	0.0003

$$e_{\ln N}^2 \approx \tau_X^2 + \tau_\alpha^2 + \tau_V^2 + t_M^2 + \tau_S^2 + \tau_L^2 + \epsilon^2 \quad (34)$$

where the variances originate from the random variables X , α and V as defined in Equation (21), the structural component uncertainties (S) and the load variation (L). The model bias contribution is approximated by its squared value t_M^2 , and ϵ contains additional unknown errors. The contribution from each source naturally varies for different applications, but from the examples outlined above we can get a picture of a possible distribution

$$\begin{array}{cccccccc} e_{\ln N}^2 & \approx & \tau_X^2 & + & \tau_\alpha^2 & + & \tau_V^2 & + t_M^2 + \tau_S^2 + \tau_L^2 \\ \underbrace{}_{0.25} & & \underbrace{}_{0.04} & & \underbrace{}_{0.003} & & \underbrace{}_{0.02} & \underbrace{}_{0.009} & \underbrace{}_{0.1} & \underbrace{}_{0.0008} \end{array} \quad (35)$$

where the numerical values are chosen within the limits found above. It can be concluded that the prediction error is dominated by structural component errors, model errors and material variability. The structural component errors, here illustrated by the batch-to-batch variation of specimens, seem to be of great importance. The model errors show that the used model is not sufficient for predicting lifetimes for such great variety of spectra. However, it seems not unrealistic that a better choice of crack opening levels could give reasonable results. Several studies have been made of the crack opening behaviour at single overloads and step changes of load levels. These studies have shown a dynamic effect of the crack opening level resulting in crack acceleration or deceleration. A more detailed study of the dynamics of the crack opening behaviour at more complicated types of variable amplitude loads is desirable, and may lead to better estimates of crack opening effects at service loads.

ACKNOWLEDGEMENTS

This work has been carried out in cooperation with Professor Jacques de Maré at the Division of Mathematical Statistics at Chalmers University of Technology, Sweden. The work is supported by the Swedish Research Council for Engineering Studies (TFR) through Contract 94-526 and by the Axel and Margaret Ax:son Johnson Foundation as a part of the project Risk Analysis for Building Structures.

REFERENCES

- 1 Elber, W., The significance of fatigue crack closure. In *Damage Tolerance in Aircraft Structures*. ASTM STP 486, American Society for Testing and Materials, 1973, pp. 230–242.
- 2 Rice, J. A. *Mathematical Statistics and Data Analysis*. Thomson, Belmont, CA, 1995.
- 3 Gurney, T. R., Comparative fatigue tests on fillet welded joints under various types of variable amplitude loading in air. In *Proceedings of the 12th International Offshore Mechanics and Arctic Engineering Conference*, Vol. III-B. American Society of Mechanical Engineers, 1993, pp. 537–542.
- 4 Gurney, T. R., Personal communication, 1995.
- 5 Holm, S., Josefsson, B. L., de Maré, J. and Svensson, T., Prediction of fatigue life based on level crossings and a state variable. *Fatigue and Fracture of Engineering Materials and Structures*, 1995, **18**(10), 1089–1100.
- 6 Svensson, T. and Holmgren, M., Numerical and experimental verification of a new model for fatigue life. *Fatigue and Fracture of Engineering Materials and Structures*, 1993, **16**(5), 481–494.
- 7 Svensson, T., Fatigue damage calculations on blocked load sequences. *Fatigue and Fracture of Engineering Materials and Structures*, 1996, **19**(2/3), 251–264.
- 8 Svensson, T., Fatigue testing with a discrete-time stochastic process. *Fatigue and Fracture of Engineering Materials and Structures*, 1994, **17**(6), 727–736.

PII: S0142-1123(97)00049-2

Unique fatigue threshold and growth properties of welded joints in a tensile residual stress field

Akihiko Ohta, Naoyuki Suzuki and Yoshio Maeda

National Research Institute for Metals 1-2-1 Sengen, Tsukuba-shi, Ibaraki 305,
Japan

The fatigue threshold and high growth rate region properties were investigated on several kinds of welded joints. These properties became unique in spite of the variation of steels (ferrite-pearlite, martensite, austenite), welding method, heat input and stress ratio. It was revealed that the unique properties occurred from the fully opened fatigue crack due to the tensile residual stresses. Based on these results, the equation of the fatigue crack growth curve for the design and inspection of welded structures was proposed. It is also suggested that the inducement of compressive residual stress at the fatigue critical zone is effective in improving the fatigue properties of welded structures. © 1998 Elsevier Science Ltd.

(Keywords: fatigue crack growth; welded joint; tensile residual stress)

INTRODUCTION

It is well known that the fatigue crack growth rate increases with the increase of stress ratio in a base metal specimen where the residual stress is non-existent¹⁻⁵. The acceleration or the retardation of fatigue crack growth also occurs in a base metal after overloads⁶⁻¹⁰. The variation of crack growth rates is well explained by fatigue crack closure¹¹.

Large structures, such as ships, bridges and energy plants are made by welding. The fatigue crack usually initiates in the welded part of the structure. It is important to know, therefore, the fatigue crack growth properties in welded joints where welding residual stress exists.

In this paper, the fatigue crack growth properties of welded joints are investigated from the threshold to the high rate region. The growth properties become unique in spite of the variation of materials, welding method, heat input, stress ratio and loading pattern. The unique properties are obtained due to the tensile residual stress which makes the fatigue crack always stay open.

EXPERIMENTAL

The materials used in this investigation were 20 mm thick ferrite-pearlite steels SB410, SM490, martensite steels SPV490, HT80 and austenitic stainless steel SUS304. The chemical composition and mechanical properties of these steels are given in Table 1. Welded plates were prepared according to the specifications given in Table 2. The weld line was perpendicular to

the rolling direction. Most of the specimens were center cracked, transverse butt welded joints, as shown in Figure 1, without any postweld heat treatment (as-welded joint). The crack was located at the center of weld metal or the heat affected zone. The specimens for the base metal were of the same configuration as the welded ones. A compact type specimen was also used to get the fatigue growth properties in a compressive residual stress field.

Some of the specimens received the postweld heat treatment at 630°C or 720°C to release the welding residual stress.

The welding residual stress parallel to the loading direction, σ_r , was measured with stacked rosette type strain gages and by mechanically cutting around them¹².

An axial pulsating load was applied to the specimen on electrohydraulic fatigue testing machines. The waveform was sinusoidal, and the test frequency varied from 10 to 40 Hz. The fatigue crack growth rate, da/dn , was measured by using two sets of travelling microscopes of $\times 20$ magnification with an accuracy of 0.02 mm. The half crack length, a , was determined as the average of values from both surfaces of the specimen.

In the case of random loading tests, the stress pattern was selected to follow the Rayleigh distribution. That is, the normalized probability density P' is expressed by the following equation¹³:

$$P' = 1.011 \times \exp(-X^2/2) \quad (1)$$

where $0 \leq X \leq 3$, $X = (\Delta K - \Delta K_{\min})/\Delta K_d$ (ΔK_m , ΔK_{\min}

Table 1 Chemical composition and mechanical properties of materials (plate thickness: 20 mm)

Material	Chemical composition (wt %)										Grain size number	Tensile properties			Bend (180)	Charpy absorbed energy (J)	Vickers hardness Hv(10) (J)
	C	Si	Mn	P	S	Ni	Cr	Mo	V	Ceq. ^a		Yield strength (N/mm ²)	Tensile strength (N/mm ²)	Elongation (%)			
SB410	0.17	0.19	0.81	0.015	0.007	0.01	0.02	0.001	0.001	0.32	7.5	284	441	35	Good	39 (at -20°C)	146
SM490	0.15	0.37	1.36	0.020	0.005	0.03	0.02	—	—	0.40	8.5	372	530	25	Good	126 (at 0°C)	152
SPV490	0.12	0.28	1.22	0.019	0.004	0.02	0.01	0.11	0.03	0.37	7.5 ^b	579	628	40	Good	289 (at -10°C)	207
HT80	0.12	0.32	0.85	0.013	0.003	0.80	0.48	0.41	0.040	0.49	7.5 ^b	784	824	31	Good	186 (at -150°C)	286
SUS304	0.06	0.45	0.81	0.029	0.006	8.64	18.19	—	—	0.052	4.2 ^b	275	618	68	Good	—	176

^aCeq = C + Mn/6 + Si/24 + Ni/40 + Cr/5 + Mo/4 + V/14^bAustenite**Table 2** Welding procedure and mechanical properties of the welded joints

Material	Welding method	Welding position	Shielding gas (%)	Heat input (kJ/cm)	Welding current (A)	Welding voltage (V)	Welding speed (cm/min)	Number of passes		Tensile strength (N/mm ²)	
								First weld side	Second weld side	As-welded	Stress relieved
SB410	Submerged arc	Flat	45	670	36	32	10	—	—	496	—
SM490	Manual arc	Flat	21	180	23	12	8	5	524	—	—
	Gas metal arc	Flat, 100% CO ₂	30	370	37	27	4	1	553	547	—
	Submerged arc	Flat	20	550	35	58	8	6	571	—	—
			45	700	36	34	3	1	552	—	—
			70	850	38	28	1	1	542	—	—
SPV490	Submerged arc	Flat	45	660	30	34	8	—	642	620	—
HT80	Manual arc	Flat	20	170	20–22	11	18	—	840	788	—
	Gas metal arc	Flat, 20% CO ₂ , 80% Ar	21	330	33	31	10	—	802	773	—
	Submerged arc	Flat	21	400	30	35	18	—	814	—	—
			32	500	32	30	12	—	807	742	—
			44	600	32	26	8	—	784	—	—
SUS304	Submerged arc	Flat	41	600	34	30	4	—	588	566	—

and ΔK_d are defined as shown in *Figure 2*). The distribution parameter, $s = \Delta K_d/\Delta K_m$, was selected to be 0.25, 0.5 and 1.0. The random loading was approximated by block loading. X was uniformly divided into 62, and the total number of loading cycles for each block Σn_i was 10 000 cycles. The sequence of X was randomized according to a random number table. The repeated number of blocks was 1–600. The equivalent range of stress intensity factor, ΔK_{eq} , and the mean fatigue crack growth rate, da/dn , were calculated using the following equations¹⁴:

$$\Delta K_{eq} = \{\sum \Delta K_i^m \cdot n_i / \sum n_i\}^{1/m} \quad (3)$$

$$\overline{da/dn} = \Delta a / \sum n_i \quad (4)$$

where Δa is the increment of the half crack length for the sequence of blocks, and $n_i = 0$ for $\Delta K_i \leq \Delta K_{th}$. ΔK_{th} is the fatigue threshold obtained by the constant amplitude test.

The stress intensity factor, K , was calculated using the following equation¹⁵:

$$K = P \sqrt{a} \{1.77 + 0.227(2a/W) - 0.51(2a/W)^2 + 2.7(2a/W)^3\} / BW \quad (5)$$

where P is the load, W is the width and B is the thickness of specimen.

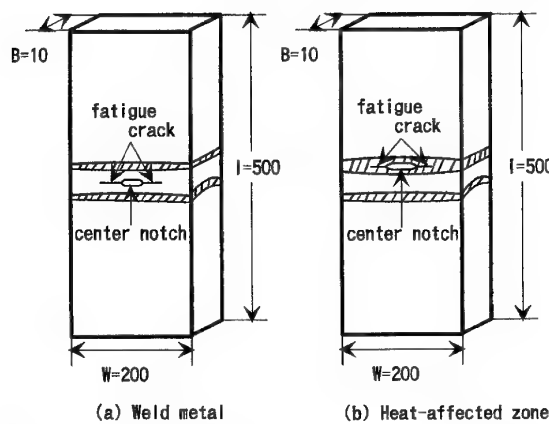


Figure 1 Specimen configuration

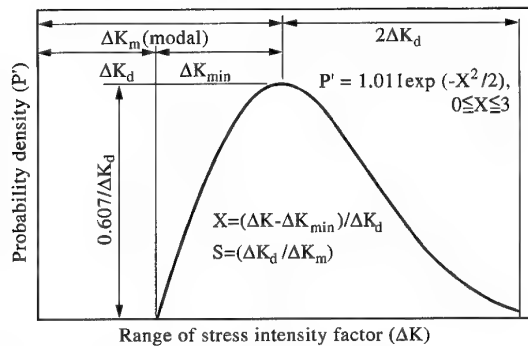


Figure 2 Rayleigh probability curve

The fatigue crack closure was observed using an extensometer mounted on the surface of specimen straddling the center notch¹⁶. The unloading elastic compliance method¹⁷ was applied to make the sensitivity high.

RESULTS AND DISCUSSION

Figure 3 shows the concept of the welding residual stress redistribution due to cutting or crack extension in the as-welded joint¹⁸. It is clear that the tensile residual stress is always induced at the crack tip.

The plots in Figure 4(a) shows the relationship between da/dn and ΔK at various stress ratios, R , for as-welded joints. It is clear that the properties do not change in spite of the difference of R . In this figure the solid curves are the proposed design curves for the fatigue crack grown in welded structures. The broken curves indicate the growth properties of the base metal. In the low growth rate region, the fatigue crack growth properties of welded joints are inferior to those of the base metal. The fatigue threshold for these welded joints is about a half of those for base metal at $R = 0$. The difference in the fatigue crack growth zone (weld metal and heat affective zone) in as-welded joints also gives no change¹⁸ as shown in Figure 4(b). The variation of parameters (five steels, three welding methods and three heat inputs) also gives no change in the observed crack growth rates as shown in Figure 4(c), (d) and (e). The fatigue crack growth properties of as-welded joints do not change in spite of the

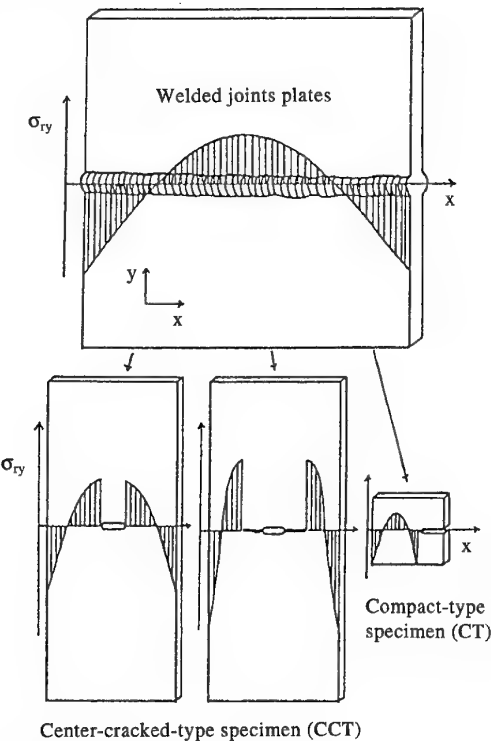


Figure 3 Welding residual stress distribution

microstructure and the mechanical properties. The reason will appear hereafter.

Figure 5 shows the variation of the fatigue crack growth properties of the base metal with stress ratio, R . The growth properties of the base metals with properties at a high stress ratio is similar to those of as-welded joints indicated with a hatched band. The similarity of the growth properties of as-welded joints and of the base metal at high R conditions suggest that the real stress ratio condition at the crack tip of welded joints is very high in spite of the applied stress ratio. That is, the tensile residual stress at the crack tip as shown in Figure 3 may increase the real stress ratio. The higher stress ratio condition makes the fatigue crack always open, and the effective range of the stress intensity factor, ΔK_{eff} , coincides with the applied range of the stress intensity factor, ΔK .

The records of fatigue crack closure are shown in Figure 6. The vertical line in this figure indicates that the fatigue crack is opened. It is clear that the fatigue crack of the as-welded joint is fully opened in the whole range of loading, while the fatigue crack of the base metal at $R = 0$ is partially closed¹⁹.

Another test to confirm the effect of welding residual stress on the fatigue growth properties of welded joints was carried out. Some specimens were tested after the postweld heat treatment. Figure 7 shows the results. The plots for the joints heat treated at 630°C are near the plots for the as-welded condition. However, the plots for the joints heat treated at 720°C (this is higher than the usual temperature given in industrial standard) are near those of base metal which received the same heat treatment. Thus, it is confirmed that sufficient relief of the tensile residual stress improves the fatigue growth properties up to those of the base metal. The

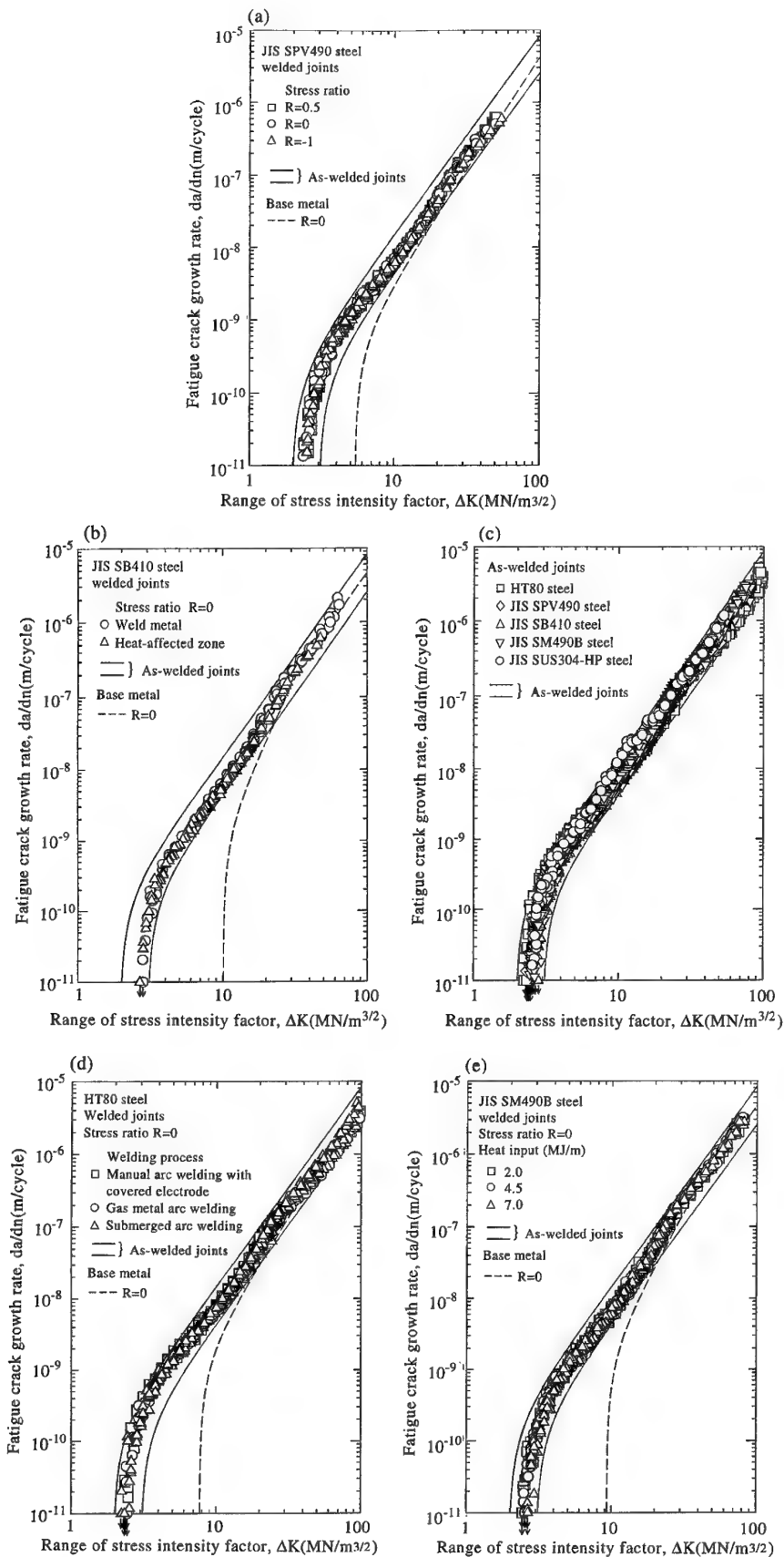


Figure 4 Fatigue crack growth properties of as-welded joints at various parameters. (a) Stress ratio, (b) crack growth zone, (c) steel, (d) welding method, (e) heat input

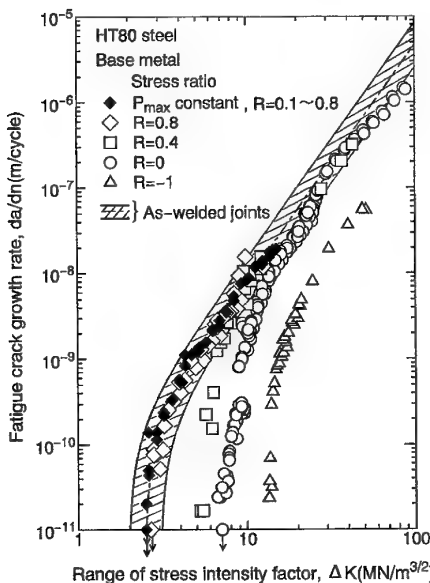


Figure 5 Fatigue crack growth properties of the base metal at various stress ratios

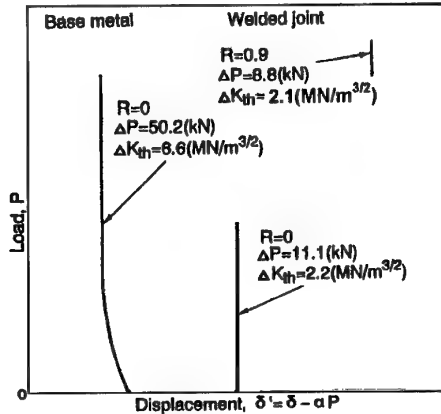


Figure 6 Records of crack closure

improved properties were obtained for the tensile residual stress of 5 MPa magnitude as shown in *Figure 8*.

The results under random loading testing are shown in *Figure 9*. It is clear that the growth properties under random loading coincide with those for the constant amplitude condition.

As stated above, the fatigue crack growth property of as-welded joints is unique in spite of the variation in materials, welding method, heat input, stress ratio and sequence of load pattern because the crack tip is fully opened due to the tensile residual stress. Thus, a unique design curve for fatigue crack growth of as-welded joints is given as shown in *Figure 10* by the statistical calculation on about 4000 plots. The safety side design curve is given as the 99.5% confidence limit represented by Equation (6).

$$da/dn = 2.60 \times 10^{-11}(\Delta K^{2.75} - 2.45^{2.75}) \quad (6)$$

The mean design curve is also given by Equation (7) which is used for calculating the fatigue crack

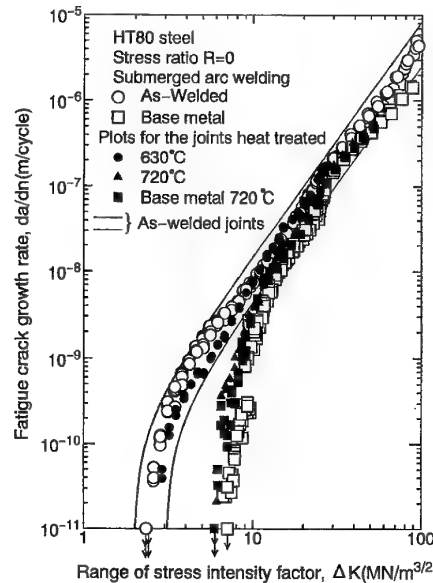


Figure 7 Fatigue crack growth properties of welded joints which received postweld heat treatment

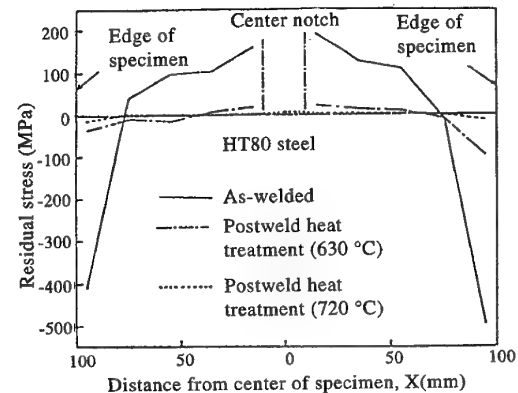


Figure 8 Variation of residual stress with postweld heat treatment

growth life when a fatigue crack is found at the inspection. The safety factor should be considered on the calculated growth life.

$$da/dn = 1.45 \times 10^{-11}(\Delta K^{2.75} - 2.00^{2.75}) \quad (7)$$

The use of the exponent of 3 as given in the guidance of BS PD6493 gives quite different trends with the plots as shown in *Figure 11*. In this guidance, it is pointed out that the stress for welded structures effectively fluctuates downwards from the yield strength so that the true value of R at a weld is independent of the value of R^{20} . This concept is analogous to the fact that the tensile welding residual stress makes the fatigue crack fully open.

The fatigue crack growth properties in synthetic sea water (ASTM D1141-52, 25°C, saturated with oxygen) is shown in *Figure 12*. In the higher rate region, the properties are similar to those in air. However, near the threshold region, the growth rate increases and the fatigue threshold is about half of that in air. The properties under random loading (Rayleigh distribution) coincide with those at constant amplitude.

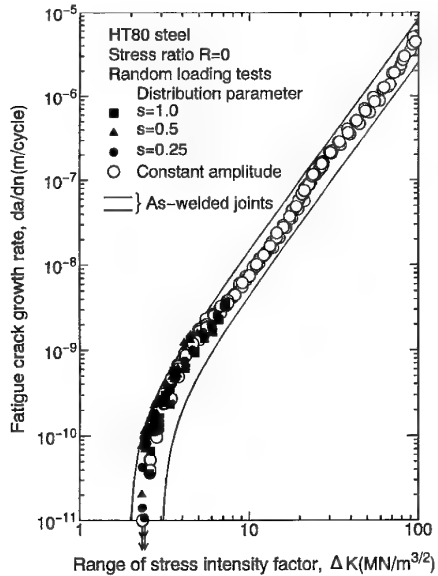


Figure 9 Fatigue crack growth properties of as-welded joints under random loading

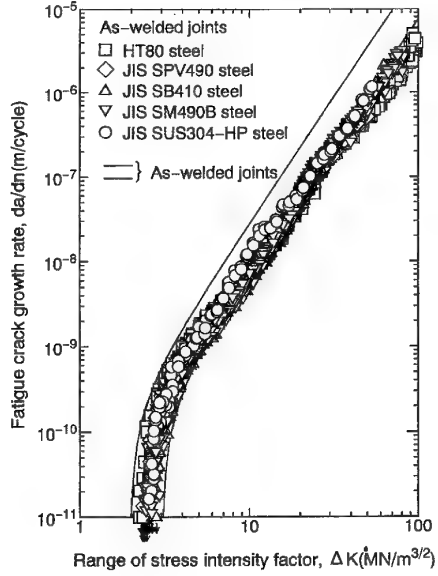


Figure 11 Quite different trends of data plots from exponent of 3

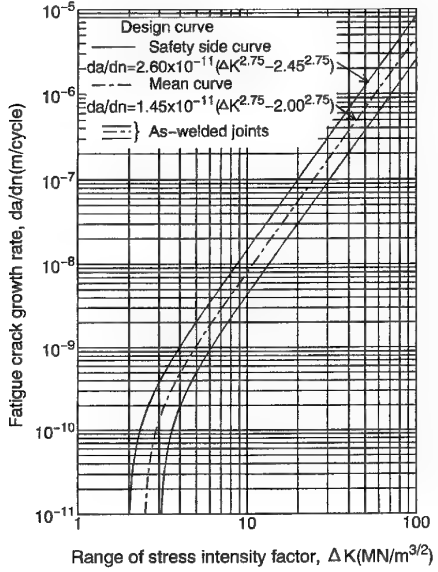


Figure 10 The design fatigue growth curve

The effect of dry and wet alternation which simulates the condition in the splash zone on the growth rate is shown in *Figure 13*. When the dry time is short, the growth rates are the same of those in the fully immersed condition. The coincidence of da/dn in these environments suggests that the narrow crack tip is hardly dried up except for a longer dry time even when the center hole and surface of specimen is dried. When the dry times becomes longer than a critical value, the crack tip might be dried up and the oxide debris, which is not carried out by the pumping motion of the synthetic sea water, is pushed to the fracture surface. Thus, the fatigue crack closure occurs in these conditions, and the fatigue crack growth rate decreases compare with those when fully immersed. As stated above, the fatigue crack growth properties in the splash

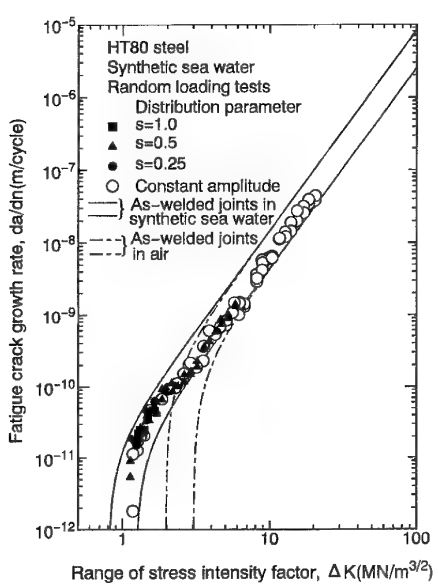


Figure 12 Fatigue crack growth properties in synthetic sea water under random loading

zone are conservative compared with those in the synthetic sea water.

The fatigue crack growth properties in a compressive residual stress field is shown in *Figure 14*. It is clear that the properties in the compressive residual stress field are superior to those of the base metal. This means that the fatigue crack growth properties could be improved by inducing the compressive residual stresses at the fatigue critical zone. An example is a compressive residual stress induced in the inner surface of a welded pipe by cooling the inner surface with water and heating the outer surface with an induction coil²¹.

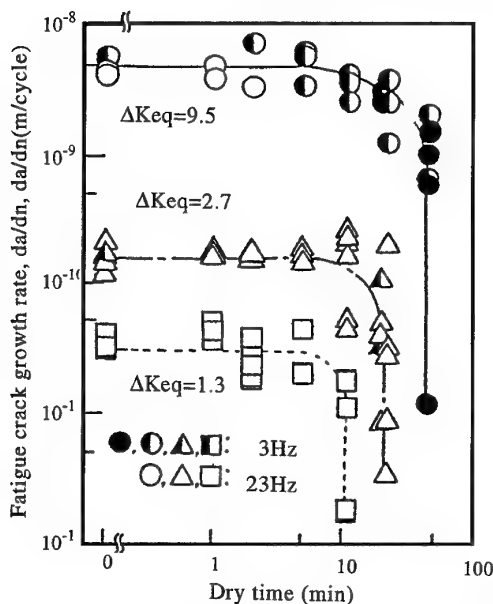


Figure 13 Variation of the fatigue crack growth rate with dry time in a modified splash zone environment

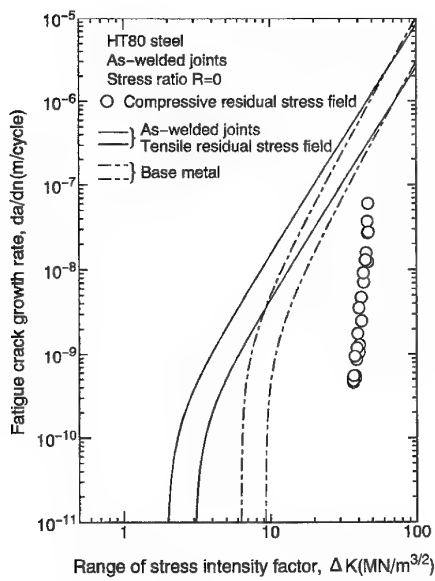


Figure 14 Superior fatigue crack growth properties in a compressive residual stress field

CONCLUSIONS

The fatigue crack growth properties of welded joints were investigated mainly by using center cracked specimens in which high tensile residual stress exists. The following conclusions were obtained.

1. The fatigue crack growth properties of as-welded joints becomes unique in spite of the difference in the crack growth zone (weld metal or heat affected zone), material (ferrite-pearlite, martensite, austenite), welding method, heat input, stress ratio and variation of the loading pattern.
2. The fatigue crack growth rates of as-welded center cracked specimens increase compared with those of

the base metal. The fatigue threshold of an as-welded specimen is about one-third of that of a base metal.

3. The increase of the fatigue crack growth rate and the low fatigue threshold of as-welded joints are obtained due to the tensile residual stress which makes the fatigue crack fully open.
4. Based on the above results, the design curve against fatigue crack growth are given as follows:

$$da/dn = 2.60 \times 10^{-11} (\Delta K^{2.75} - 2.45^{2.75})$$
 (safety side)

$$da/dn = 1.45 \times 10^{-11} (\Delta K^{2.75} - 2.00^{2.75})$$
 (mean curve)
5. The fatigue crack growth properties in synthetic sea water are inferior to those in air in the slow growth rate region. The fatigue threshold in synthetic sea water is about a half of that in air.
6. The induction of compressive residual stress near the fatigue critical zone is proposed to improve the fatigue crack growth properties.

REFERENCES

1. Paris, P. and Erdogan, F., A critical analysis of crack propagation laws. *Journal of Bas. Engineering, Trans. ASME*, 1963, **85**, 528-534.
2. Klesnil, M. and Lukas, P., Effect of stress cycle asymmetry of fatigue crack growth. *Materials Science Engineering*, 1972, **9**, 231-240.
3. Cooke, R. J. and Beevers, C. J., The effect of load ratio on the threshold stresses for Fatigue crack growth in medium carbon steels. *Engineering Fracture Mechanics*, 1973, **4**, 1061-1071.
4. Ohta, A. and Sasaki, E., Influence of stress ratio on the threshold level for fatigue crack propagation in high strength steels. *Engineering Fracture Mechanics*, 1977, **9**, 307-315.
5. Vosikovsky, O., The effect of stress ratio on fatigue crack growth rates in steels. *Engineering Fracture Mechanics*, 1979, **11**, 595-602.
6. Wheeler, O. E., Spectrum loading and crack growth. *Journal of Bas. Engineering, Trans. ASME*, 1972, **90**, 181.
7. Von Euw, E. F. J., Hertzberg, R. W. and Roberts, R., Delay effects in fatigue crack propagation. *ASTM STP*, 1972, **513**, 230.
8. Klesnil, M. and Lukas, P., Influence of strength and stress history on growth and stabilization of fatigue cracks. *Engineering Fracture Mechanics*, 1972, **4**, 77-92.
9. Wei, R. P. and Shih, T. T., Delay in fatigue crack growth. *International Journal of Fracture*, 1974, **10**, 77-85.
10. Matsuoka, S., Tanaka, K. and Kawahara, M., The retardation phenomenon of fatigue crack growth on HT80 steel. *Engineering Fracture Mechanics*, 1976, **8**, 507-523.
11. Elber, W., The significance of fatigue crack closure. *ASTM STP*, 1971, **486**, 230-242.
12. Ohta, A., McEvily, A. J. and Suzuki, N., Fatigue crack propagation in a tensile residual stress field under a two-step programmed test. *International Journal of Fatigue*, 1993, **15**, 9-12.
13. Klippstein, K. and Schilling, G. S., Stress spectrums for short-span steel bridges. *ASTM STP*, 1976, **595**, 203-216.
14. Ohta, A., Maeda, Y., Machida, S. and Yoshinari, H., Fatigue crack propagation in welded joints under random loadings in the splash zone. *Welding World*, 1995, **33**, 391-394.
15. Brown, W. F. and Srawley, J. E., Plain strain crack toughness of high metallic materials. *ASTM STP*, 1967, **410**, 1-66.
16. Ohta, A., Kosuge, M. and Sasaki, E., Fatigue crack closure over the range of stress ratios from -1 to 0.8 down to stress intensity threshold level in HT80 steel and SUS304 stainless steel. *International Journal of Fracture*, 1978, **14**, 251-264.
17. Kikukawa, M., Jono, M. and Tanaka, K.I., Fatigue crack closure behavior at low stress intensity level. In *Proceedings of the 2nd International Conference in Mechanical Behaviour of Materials*, 1976, pp. 254-277.
18. Ohta, A., Sasaki, E., Nihei, M., Kosuge, M. and Inagaki, M., Fatigue crack propagation rates and threshold stress intensity factor for welded joints of HT80 steel at several stress ratios. *International Journal of Fatigue*, 1982, **4**, 233-237.
19. Ohta, A., Sasaki, E., Kamakura, M., Nihei, M., Kosuge, M., Kanao, M. and Inagaki, M., Effect of residual tensile stresses

- on threshold level for fatigue crack propagation in welded joints of SM50B steel. *Transactions of the Japanese Welding Society*, 1981, **12**, 31-38.
- 20 Gurney, T. R., Fatigue design rules for welded steel joints. *Welding Institute Research Bulletin*, 1976, **17**, 115-124.
- 21 Ohta, A., Maeda, Y. and Kosuge, M., Significance of residual stress on fatigue properties of welded pipes. *International Journal of Pressure Ves. and Piping*, 1984, **15**, 229-240.

PII: S0142-1123(97)00041-8

Thickness effects on the fatigue strength of welded steel cruciforms

David P. Kihl* and Shahram Sarkani†

*Performance Evaluation Branch, David Taylor Model Basin CDNSWC, Bethesda, MD 20084-5000, USA

†Department of Civil, Mechanical and Environmental Engineering, The George Washington University, Washington, DC 20052, USA

Over 100 fatigue tests were conducted on high strength welded steel (HSLA-80) cruciforms of different thickness. Tests were conducted under both constant and random amplitude axial loads to characterize thickness effects on fatigue strength. Specimens were similar in size, except for the thickness which was varied between four nominal values. Examination of both experimental and analytical results (obtained using linear cumulative damage and Rayleigh approximation) indicates thicker specimens exhibit lower fatigue lives under both constant and random amplitude loadings. These results, when compared with the commonly used 'fourth root rule' thickness correction formula, indicate the latter to be generally conservative, particularly at low stress levels. © 1998 Elsevier Science Ltd.

(Keywords: stochastic fatigue; thickness effects; welded steel)

INTRODUCTION

The fatigue strength of many structures is based somehow on empirical data. Whether design *S/N* curves are used or allowable stress levels are prescribed, the fatigue strength of a structure can usually be traced back to fatigue tests performed on specimens of a given size, shape and configuration. Fatigue data are sometimes gathered from different sources and combined for analysis and generation of a representative *S/N* curve; sometimes combining different configurations that exhibit similar fatigue strength. An overall, or predominant, fatigue strength behavior is thereby obtained for a given group of details. If a specific application requires fabrication from a plate of single thickness, then the *S/N* curve may not reflect the proper fatigue behavior, depending on the thickness of the specimens used to generate the *S/N* curve. The following effort was therefore undertaken to empirically characterize the effect of plating thickness on the fatigue strength of welded steel. Both fully reversed constant amplitude and zero mean random amplitude loadings at various levels were considered in the characterization.

THICKNESS EFFECTS

Thickness effects on fatigue of steel joints are generally taken into account through the 'fourth root rule', which reduces the fatigue strength in an inversely proportional manner to the fourth root of the ratio of the plate thicknesses^{1,2}. The method uses fatigue behavior of

specimens of a given thickness and then describes the behavior of different thickness specimens relative to the reference thickness. A number of studies attribute thickness effects to changes in the stress concentration factor due to joint geometry^{3,4} and weld residual stresses⁵. Some researchers have suggested the fourth root rule is nonconservative and the exponent should be adjusted to provide for a more conservative fatigue strength estimate. Results of data analysis presented in this paper are compared to this commonly used relationship to address this notion.

TEST SPECIMEN CONFIGURATION AND FABRICATION

Test specimens were fabricated from high strength low alloy steel having a minimum yield strength of 80 ksi (552 MPa) (HSLA-80). The test specimens were cruciform shaped and were all welded using the same process (GMAW pulse) and welding consumable (100 s, 0.045 in (1 mm) diameter wire). Fabrication was carried out in a shipyard using standard welding procedures. Test specimens were all geometrically similar except that different plating thicknesses were used during fabrication, i.e. 1/4 in (6 mm), 7/16 in (11 mm), 3/4 in (19 mm) and 1 in (25 mm), as shown in Figure 1. A plating thickness of 7/16 in (11 mm) was chosen, instead of 1/2 in (13 mm), in order to compare with existing data⁶ of specimens fabricated in the laboratory. Fabrication was performed using a twin arc welding set-up to minimize distortion. Test plates were first

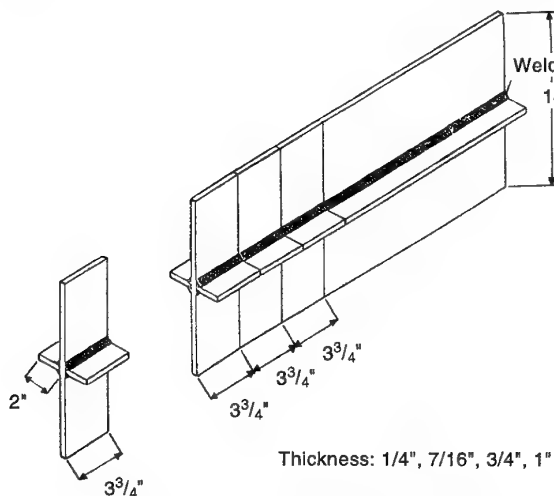


Figure 1 Test specimens cut from larger built-up test plate

fabricated by welding the 2 in (51 mm) side attachments to a plate nominally 14 in (356 mm) wide and 6 to 8 ft (1.8 to 2.4 m) long. Two weld passes were required to complete each fillet weld of the 1/4 in (6 mm) thick specimens, four passes for the 7/16 in (11 mm) thick specimens, six passes for the 3/4 in (19 mm) specimens, and eight passes for the 1 in (25 mm) thick specimens. Resulting weld profiles are shown in *Figure 2*. To produce test specimens, each test plate was then cut up into specimens 15/4 in (9.5 cm) wide to accommodate the hydraulic grips of the test machine, avoiding any sites which contained undesirable irregularities such as welding start/stop points. Yield strengths for the five plate thicknesses (batches of specimens) are 91.6 ksi (1/4 in) (632 MPa (6 mm)), 97.3 ksi (7/16 in) (671 MPa (11 mm)), 89.4 ksi (3/4 in) (616 MPa (19 mm)), 86.8 ksi (1 in) (598 MPa (25 mm)), and 92.5 ksi (7/16 in prior data) (638 MPa (11 mm)).

Attempts were also made to measure residual stresses in each of the four specimen configurations using both X-ray diffraction and sectioning. The results of this

effort were not entirely consistent and conclusive, but indicated that residual stresses as high as the yield stress of the base metal were present at the weld toe. Thinner specimens generally had much lower magnitude of residual stress than the thicker specimens. Although general trends were observed, the results were not consistent enough to include this effect in subsequent analysis of fatigue strength. Follow-on efforts are currently underway to further substantiate these values so that they may be incorporated in future studies.

TEST PROCEDURE

Tests were conducted in servohydraulic load machines, where the specimens were loaded by means of hydraulic grips and cycled axially. The applied load was determined based on the desired stress level and actual cross-sectional area measurements. The fatigue tests consisted of both fully reversed constant amplitude loadings and zero mean random loadings. Each test condition consisted of attempting to fail at least four specimens. Most conditions therefore contain four failures, a few low stress level conditions contain a mixture of failures and runouts due to a lack of extra specimens to try to obtain failures. If failure did not occur within 20 million cycles, the test was suspended. Cracks initiated at the weld toe near the middle of the specimen and grew through the thickness of the loaded plate and toward the edges of the specimen. Failure was said to occur when the compliance of the specimen at least doubled. Some specimens were completely separated into two pieces.

The random loads applied to the specimens represented seaway induced loads on ship structures that are predominantly narrowband Gaussian. Extrema of such loadings therefore closely follow a Rayleigh probability distribution. To develop a loading time history for testing purposes, a series of Rayleigh distributed extrema was generated on a computer using a first order autoregressive simulation procedure⁷. Simulation of 10,000 values (extrema) provided excellent agreement between the first 10 calculated and theoretical expected moments of the Rayleigh probability density function. The resulting Rayleigh distributed series of values had a correlation coefficient between successive values of 0.95 and unit RMS. For testing purposes the values were clipped to four times the unit RMS value. This clipping only affected four of the 10,000 values; changing them less than 10% from their simulated value. A series of peaks and valleys was then obtained by multiplying every other value by -1 to form a valley; unmodified values represented peaks. The peaks and valleys were then connected with smooth haversine curves to form a command signal for the load machine. The resulting time history represented 5000 cycles of unit RMS. Load histories were obtained by multiplying the unit RMS time history by the desired RMS stress and actual cross-sectional area. The load history was repeatedly applied to the test specimen until failure occurred. The matrix of test conditions, constant and random amplitude loadings, used in this characterization is provided in *Table 1*.

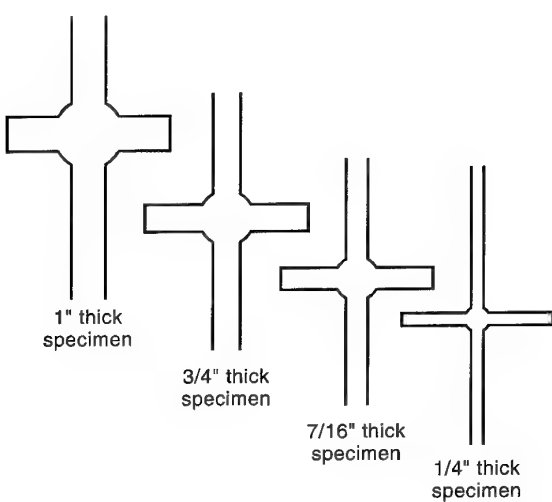


Figure 2 Weld profiles of typical test specimens

Table 1 Fatigue test matrix

Nominal specimen thickness	Constant amplitude, $R = -1$ (stress amplitude, ksi)	Random amplitude, zero mean (RMS stress, ksi)
1/4 in	12, 15, 30, 45	4, 5, 10, 15
7/16 in	12, 15, 30, 45	4, 5, 10, 15
3/4 in	12, 15, 30	4, 5, 10
1 in	12, 15, 30	4, 5, 10

DATA ANALYSIS

Results in the form of individual data points and calculated geometric means of the failed specimens are shown in *Tables 2* and *3*, for the constant and random amplitude loading conditions, respectively. The data show a fairly consistent trend, i.e. for a given stress, the thicker specimens generally exhibit lower fatigue lives than the thinner specimens. The trend is shown in *Figures 3* and *4*, where the geometric mean fatigue lives are plotted. The individual data were used to generate S/N curves for each of the four specimen thicknesses using the conventional power law relationship

$$N = 10^{\log(A)S^B} \quad (1)$$

Here the cycles to failure, N , and applied stress ampli-

tude, S , are related by parameters $\log(A)$ and B obtained from a regression analysis. The resulting S/N curves are shown in *Figure 5*. The S/N curve coefficients and associated statistics for each of the S/N curves are provided in *Table 4* for the constant amplitude loadings.

Having both constant and random amplitude test data provides an opportunity to predict the expected cycles to failure for the random amplitude loadings and compare these predictions with test results. Assuming a linear (in log-log space) S/N curve and linear cumulative damage⁸, the following relationship can be derived which predicts the expected cycles to failure⁹ for a loading process having Rayleigh distributed peaks:

$$N = \frac{A}{2^{-B/2}\sigma^{-B}\Gamma(1-B/2)} \quad (2)$$

Here, $\Gamma(x)$ denotes the Gamma function and σ is the RMS of the process.

This formulation, however, must be modified slightly to account for the clipped amplitudes. It should be noted that this expression gives essentially identical results to rainflow analysis, as would be expected for narrowband loadings.

$$N =$$

$$\frac{A}{2^{-B/2}\sigma^{-B}\left(\Gamma\left(1-\frac{B}{2}\right)-\Gamma\left(1-\frac{B}{2}, \frac{S_{max}^2}{2\sigma^2}\right)\right) + S_{max}^{-B}e^{-S_{max}^2/2\sigma^2}} \quad (3)$$

Table 2 Constant amplitude fatigue test results

Stress amplitude (ksi)	Cycles to failure				
	1/4 in	7/16 in	3/4 in	1 in	7/16 in (prior data)
12	3470000	1260000	1010000	333000	776000
	1240000	20200000*	625000	247000	3730000
	1290000	1590000	653000	227000	1120000
	10700000	20000000*	322000	342000	811000
	20100000*				1390000
	2070000				
Geometric mean†	2780000	1990000	604000	283000	1300000
	348000	1350000	214000	113000	572000
15	237000	487000	191000	167000	780000
	765000	513000	141000	157000	515000
	583000	1210000	145000	151000	229000
					1072000
Geometric mean	438000	799000	170000	145000	563000
30	168000	54800	36700	22200	66500
	123000	19600	26200	23700	61900
	47100	80600	24300	24700	70600
	61600	41400	30100	20600	82800
					79100
Geometric mean	88000	43500	29000	22700	71800
45	4130	9230	n/a	n/a	14500
	7390	16400			14800
	8160	11300			16300
	7510	18700			23200
					18000
Geometric mean	6580	13400	n/a	n/a	17100

* Indicates fatigue test was suspended without failure.

† Geometric mean is calculated using only failures.

Table 3 Random amplitude fatigue test results

RMS stress (ksi)	Cycles to failure				
	1/4 in	7/16 in	3/4 in	1 in	7/16 in (prior data)
4	6220000	18200000	3360000	2800000	16100000
	20000000*	20000000*	2860000	2360000	24200000
	20400000*	7240000	2410000	2910000	50500000*
	6390000	20000000*	3910000	2010000	4410000
Geometric mean†	6300000	11500000	3080000	2490000	12000000
5	2630000	4000000	1380000	1170000	2690000
	2030000	5830000	1250000	903000	5500000
	3090000	5100000	1290000	831000	7860000
	3910000	20000000*	1310000	1050000	4240000
Geometric mean	2830000	4830000	1310000	980000	4710000
10	229000	475000	148000	148000	488000
	519000	283000	138000	144000	687000
	531000	315000	133000	164000	902000
	858000	821000	179000	135000	463000
Geometric mean	482000	432000	149000	147000	612000
15	53400	93000	n/a	n/a	93600
	35200	63900			113000
	35100	53600			128000
	46000	103000			141000
Geometric mean	41700	75700	n/a	n/a	118000

* Indicates fatigue test was suspended without failure.

† Geometric mean is calculated using only failures.

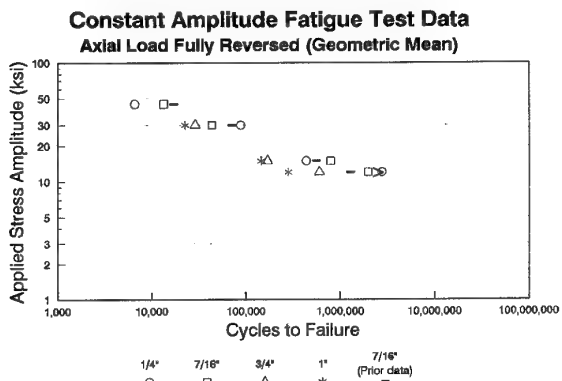


Figure 3 Geometric mean of constant amplitude data

Here, $\Gamma(x,y)$ denotes the incomplete Gamma function (evaluated from y to ∞), and S_{\max} is the maximum (clipped) value.

A comparison between fatigue life predictions using the above equation and the constant amplitude S/N curves with the geometric mean of the experimental data is shown in *Figure 6*. Excellent agreement is found for most of the random test conditions. At the low RMS loadings for the 1/4 in (6 mm) and 7/16 in (11 mm) specimen data, the predictions are slightly nonconservative. However, inclusion of runouts with failures, or allowing the suspended tests to run longer, may have produced failures which would have provided

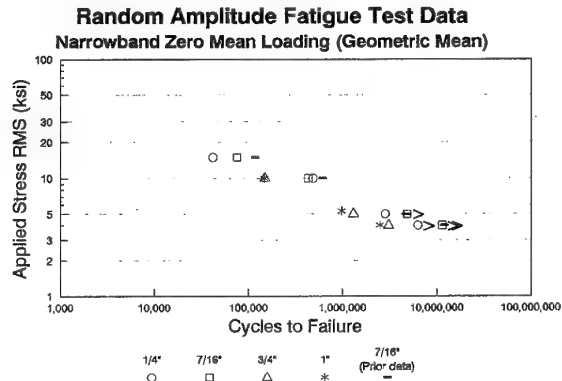


Figure 4 Geometric mean of random amplitude data

better agreement. The low cycle, high RMS loading for the 1/4 in (6 mm) specimen also showed predictions which were slightly nonconservative. Overall, the random fatigue data and predictions based on constant amplitude fatigue behavior are quite good.

COMPARISON WITH THE FOURTH ROOT RULE

As previously mentioned, the fourth root rule provides a method of accounting for thickness effects by determining the fatigue strength, S_t , of a given thickness specimen, t , relative to a reference thickness, t_{ref} , and associated fatigue strength, S_{ref} (at 10^6 cycles)¹:

Table 4 Coefficients of constant amplitude S/N curves (S/N curve of the form $\log(\text{life}) = \log(A) + B \log(\text{stress})$).

Specimen thickness	Stress amplitudes used* (ksi)	$\log(A)$	B	Correlation coefficient	Coefficient of variation	Standard estimation of error $\log(\text{life})$
1/4 in	12 15 30 45	10.7	-4.09	-0.944	0.554	0.350
7/16 in	12 15 30 45	10.4	-3.86	-0.976	0.383	0.210
3/4 in	12 15 30	9.06	-3.13	-0.959	0.328	0.172
1 in	12 15 30	8.39	-2.73	-0.991	0.145	0.068
7/16 in (prior data)	12 15 30 45	9.56	-3.21	-0.973	0.346	0.185

* Excluding runouts.

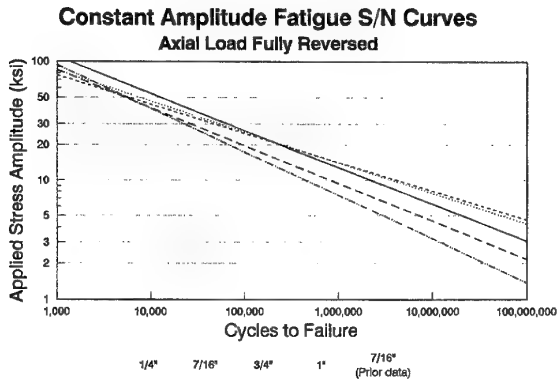


Figure 5 Constant amplitude S/N curves

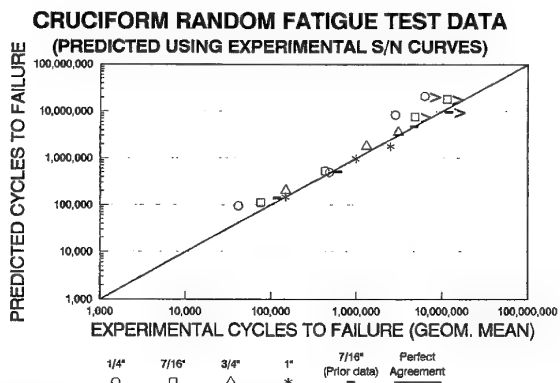


Figure 6 Fatigue lives predicted using actual constant amplitude S/N curves versus experimental fatigue lives

$$\frac{S}{S_{\text{ref}}} = \sqrt[4]{\frac{t_{\text{ref}}}{t}} \quad (4)$$

Typically for plate welded joints a reference thickness of 0.87 in (22 mm) is used, but other values may be used for other cases. This formulation appears to be based on both axial and bending tensile fatigue strength data ($R \sim 0$). When S/S_{ref} data at 1 million cycles were plotted against t/t_{ref} data on a log-log plot, the points were shown to generally follow a line with a slope of $-1/4$.

For purposes of comparison, fatigue strengths were determined from the four constant amplitude S/N curves derived from the test data presented in this paper. Using the 1 in (25 mm) thickness specimen data as a reference value, fatigue strengths associated with 10^3 , 10^4 , 10^5 , 10^6 and 10^7 cycles were determined for each

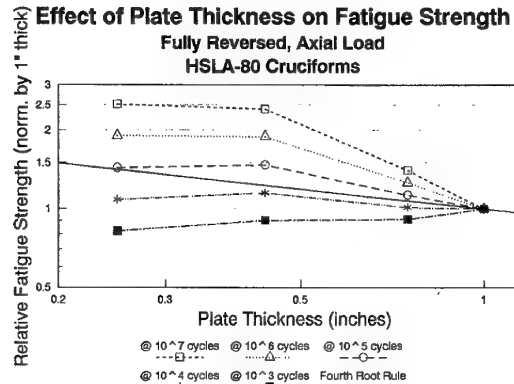


Figure 7 Normalized fatigue strength versus thickness

of the four specimen thicknesses and normalized by the reference values. A plot was then generated, as outlined above, and is shown in Figure 7.

The plot shows how well the fourth root rule predicts constant amplitude fatigue behavior for various plate thicknesses. As can be seen, better predictions are obtained for plating thicknesses that are closer to the reference plating thickness of 1 in (25 mm). In addition, better predictions are also obtained for fatigue lives in the range of 10^4 to 10^5 cycles.

Since many applications involve random loadings, it is of interest to examine the effectiveness of the fourth root rule in predicting random load fatigue behavior for the different plating thicknesses. Figure 8 shows predicted cycles to failure using the fourth root rule and Rayleigh approximation as modified in Equation (3). The fourth root rule is generally found to produce

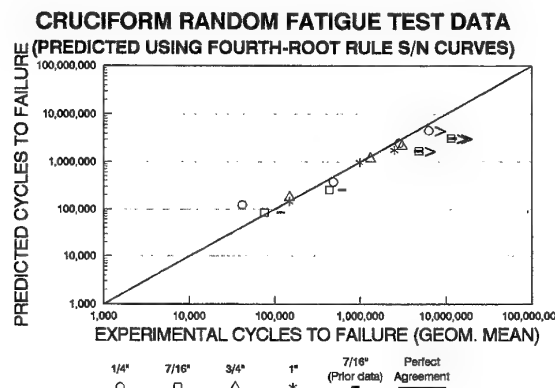


Figure 8 Fatigue lives predicted using fourth root rule constant amplitude S/N curves versus experimental fatigue lives

fairly good fatigue life estimates for the random loadings examined. However, at the lower RMS levels, the fourth root rule was found to predict conservative fatigue lives. This finding is even more significant considering that the experimental fatigue lives do not include runouts.

CONCLUSIONS

Constant and random amplitude fatigue tests were conducted on geometrically similar specimens to characterize the fatigue strength of welded steel joints as a function of specimen thickness (1/4 in (6 mm), 7/16 in (11 mm), 3/4 in (19 mm) and 1 in (25 mm)). From these data, constant amplitude S/N curves were generated and used to predict the random amplitude fatigue test results. The random loads represented a narrowband Gaussian process of various intensities defined by the RMS value. Results generally show good agreement between prediction and experiment. Predictions were obtained using linear cumulative fatigue damage accumulation and Rayleigh approximation.

Test results are then used to compare thickness effects with the commonly used fourth root rule. Comparison of these results with the fourth root rule indicates that the latter is conservative for low stress high cycle conditions (beyond about 10^5 cycles). Test results also indicate fatigue strength to be relatively insensitive

to thickness effects for specimen thicknesses less than 7/16 in (11 mm). One must be cautious in extending these findings to other welded joint configurations without further experimental confirmation.

REFERENCES

- 1 Maddox, S. J. *Fatigue Strength of Welded Structures*, 2nd edn. Abingdon Publishing, Cambridge, 1991.
- 2 *Offshore Installations: Guidance to Design and Construction*, Department of Energy, UK, 1984.
- 3 Kottgen, V. G., Olivier, R. and Seeger, T., The influence of thickness on fatigue strength of welded joints, a comparison of experiments with prediction by fatigue notch factors. In *Steel in Marine Structures*, 1987, pp. 303–313.
- 4 Orgasaeter, O. et al., Effect of plate thickness on the fatigue properties of a low carbon micro-alloyed steel. In *Steel in Marine Structures*, 1987, pp. 315–335.
- 5 Leirrade, H. P., Effect of residual stresses and stress ratio on the fatigue strength of welded components. *Welding in the World*, 1988, **26**(7/8), 158–187.
- 6 Sarkani, S., Kihl, D. P. and Beach, J. E., Fatigue of welded cruciforms subjected to narrow-band loadings. *Journal of Engineering Mechanics*, 1992, **118**(2), 296–311 (Erratum: 1993, **119**(2), 417).
- 7 Sarkani, S., Feasibility of auto-regressive simulation model for fatigue studies. *Journal of Structural Engineering Division, ASCE*, 1990, **116**(9), 2481–2495.
- 8 Miner, M. A., Cumulative damage in fatigue. *Journal of Applied Mechanics*, 1945, **12**, A159–A164.
- 9 Miles, J. W., On structural fatigue under random loading. *Journal of Aeronautical Science*, 1954, **21**, 753–762.

PII: S0142-1123(97)00045-5

Fatigue analysis and the local stress-strain approach in complex vehicular structures

F.A. Conle and C.-C. Chu*Ford Scientific Research Lab, Ford Motor Company, MD 3182, SRL, Dearborn, MI 48121-2053, USA*

In the last 20 years the 'strain-life' fatigue analysis philosophy has achieved the status of industry standard in the automotive, truck and earth moving industries in North America. Although the fundamental concepts of the method are quite simple, the recent massive computerization of the techniques, and their incorporation into large dynamically loaded body and chassis durability calculation models, has resulted in new capabilities and insights for engineers, but also has meant new challenges for the creators of fatigue simulation software.

This paper gives a brief history of the evolution of this type of calculation software in the vehicular industry from the observation of stress-strain hysteresis behavior, through the early development of computer versions of the stress-strain shape and memory models, to their evolution into routines that are closely linked to vehicle dynamics models that calculate loads in structures, finite element models that transform the loads into local stresses, and subsequent plasticity correction and damage evaluation routines which yield expected life color contour plots for vehicle body and chassis. © 1998 Elsevier Science Ltd.

(Keywords: fatigue analysis; stress-strain; strain-life; vehicular; vehicle dynamics models)

INTRODUCTION

The objective in the automotive industry is to test as few prototypes as possible; preferably only one of any finalized model. Although, at present, we have to create and verify several more software packages before we can get to this ideal, the objective now appears attainable. The usual economic forces of reducing numbers of prototypes, minimization of testing/design iterations, optimizing gages and weight, and shortened design cycle time are driving us toward this objective. But what is the vision? We would like to be able to 'drive' a computerized vehicle over a digital version of our proving grounds, observe the vehicle load responses, and 'watch' the stress histories on any or all of the elements that model the body and components of the vehicle. After geometry or thickness optimization the procedure is repeated until we achieve the design life standard at minimum weight. Although other design areas, such as crash design, or vibration/noise design are also involved, the emphasis in this paper is only on the durability aspects of the procedure.

Fatigue problems are generally solved by addressing the three major aspects of the phenomenon: material properties; the effects of geometry; and the input load histories. These ingredients are prerequisite for both simple components, such as suspension arms, springs, etc. and also for large components such as complete car or truck bodies, that are essentially an assemblage of smaller components.

MATERIAL PROPERTIES

Although the work of Bauschinger¹ is normally accredited with the observation of the change in compressive yield after tensile plasticity, what one observes upon plotting his data (*Figure 1*), are the two essential ingredients of modern cyclic deformation modeling: material memory effects and Masing³ behavior. The

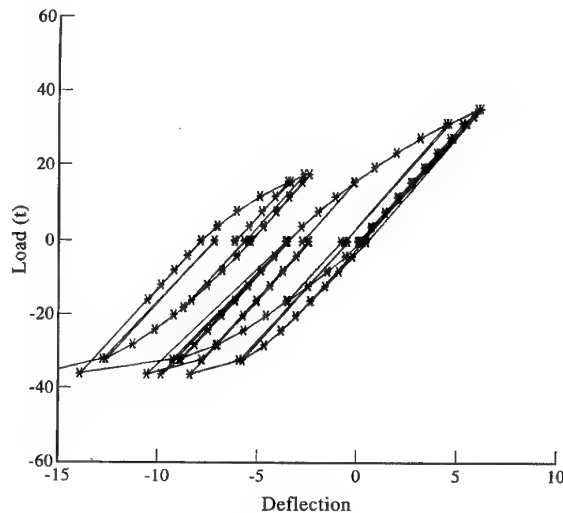


Figure 1 Stress-strain data plotted from Bauschinger, Ref 1

first model of cyclic stress-strain behavior was constructed by Jenkin (Ref. 2, *Figure 2*), and later translated into more theoretical terms in Refs 3–5. In the period between the introduction of these models and the present there was a long gap during which the models had only limited application because of the tedium of tracking the spring-slider values by hand calculation. The advent of computers enabled the concepts to be extended^{6–9} and the models were able to simulate the stress response of any variable amplitude stress history and produce the corresponding strain history, or vice versa. Although these models could follow a complex history, in the 1970s and even in the 1980s it was very difficult to digitize and store a service history of any significant length, and consequently there was little need for the abilities of these models on the desks of component engineers. Standard practice was to use a level crossing counted, or rainflow counted histogram to represent service loading. This considerably simplified the requirements for following the cyclic deformation history, and most of the programs, such as those sold by NCode™, PFatigue™ and Somat™ have adopted the principles described by Ref. 10, where the presence of an overall stress-strain hysteresis loop controls the placement of the smaller loops as taken from the histograms, as per *Figure 3*.

In the late 1980s computer disk space became much cheaper. This enabled long service histories, with multiple load or strain channels to be recorded and analyzed for everyday engineering problems. When the strains were observed using rosette gages, or loads in multiple channels, e.g. Refs 12–14 it became possible to predict the stress and strain tensor service histories. Presently this information is still commonly reduced to a single channel of stress or strain¹⁵, so that the uniaxial deformation and fatigue models can still be applied, but this compromise is now rapidly approaching its limits of applicability, and it has now become imperative to adopt the multiaxial deformation model

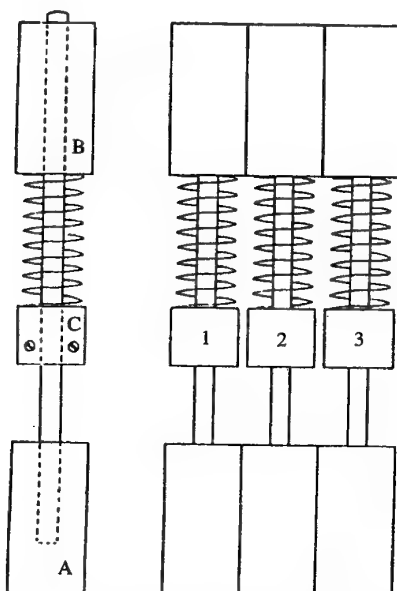


Figure 2 Mechanical analog of stress-strain hysteresis model by Jenkin, Ref. 2

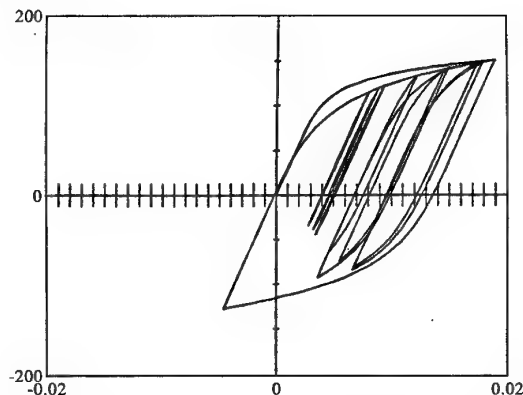


Figure 3 Example of a local stress-strain reconstruction from a range-mean rainflow history

theories^{16–20}. Of these the model proposed by Chu¹⁷ appears to be suitable for evaluation of cyclic deformation because of its computational speed, ability to simulate transient effects, and accurate management of multiaxial material memory events during variable amplitude deformation^{21,22}. *Figure 4* shows the simulated stress response due to an imposed biaxial strain history taken from a rosette gage. This multiaxial deformation model has now been added to the standard Ford Motor Co. fatigue analysis package for car and truck body durability analysis. At present it is switched on when the presence of multiaxial states of stress are detected. In the future when further improvements of the program logic and theory have been completed, it will replace the ‘uniaxial’ or single dimensional models used for the past 20 years.

DAMAGE ASSESSMENT

Aside from the stress-strain behavior of a material, the other important property is the measure of fatigue life. In the vehicular industry this has been characterized by the strain vs life curve, and the cyclic stress strain curve, which are derived from the stabilized deformation behavior during testing, and the ‘initiation’ life. *Figure 5* depicts the standard data sheet output for a typical file in the Ford materials fatigue database. The parameters passed to the calculation routines include: the elastic modulus; the cyclic fatigue strength coefficient and exponent; and the fatigue ductility coefficient and exponent. Actually, any equations that uniquely relate the stabilized values of stress, strain and life, provide sufficient information to calculate the popular damage parameters. In the various commercial and corporate packages the common parameters used to calculate fatigue life are:

- total strain vs life;
- Smith–Watson–Topper: $(\sigma_{\max} \epsilon_a)$ life;
- Morrow–Landgraf: replace σ'_f by $(\sigma'_f - \sigma_o)$;
- von Mises’ equivalent stress vs life;
- Brown–Miller: $(\gamma_a + K\epsilon_a)$ vs life;

Recent work^{22,23} has shown that the uniaxial parameters and the equivalent stress type parameters do not work well under multiaxial conditions. It is now recognized that an all encompassing damage algorithm must:

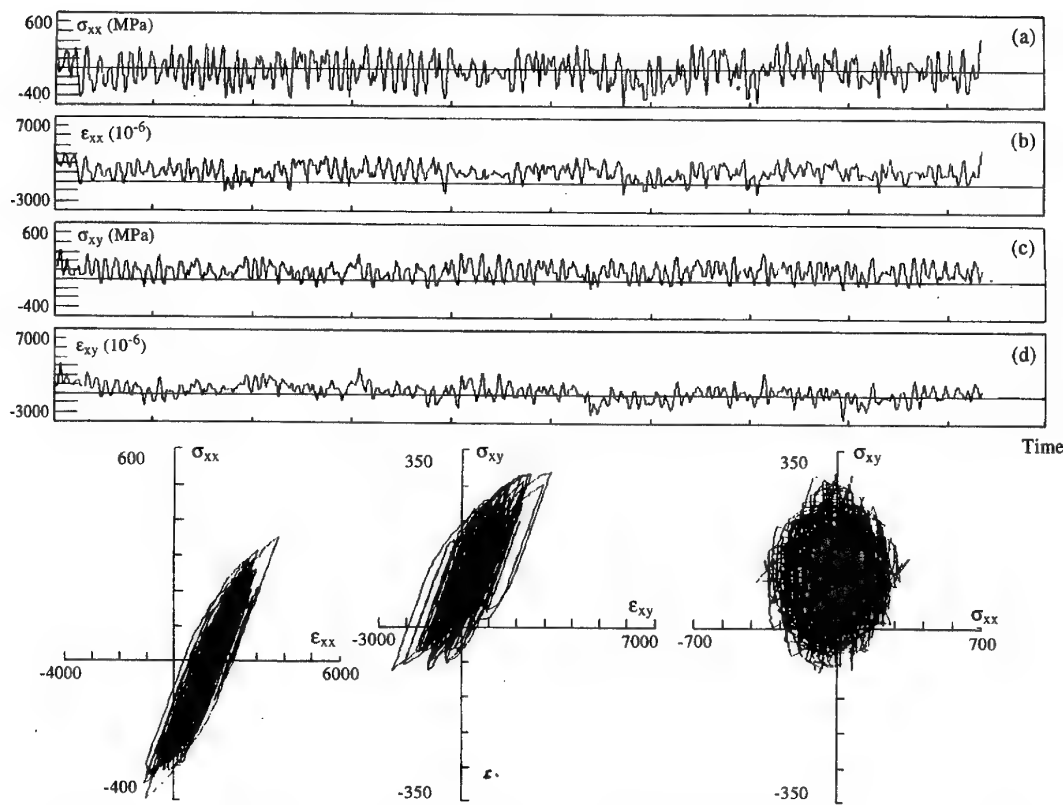


Figure 4 Multiaxial stress-strain simulation for SAE1045 steel showing ϵ_{xx} , ϵ_{xy} input histories and predicted σ_{xx} , σ_{xy} response

- search for the most damaging plane at the critical location: termed 'the critical plane approach';
- utilize terms that account for both normal stress and strain, and shear stress and strain on the critical plane.

Although the ultimate verdict has not been pronounced, given the present limited amount of experimental confirmation, the following parameters, when used with a critical plane approach, are the most universally effective:

- Brown-Miller;
- Fatemi-Socie-Kurath;
- Chu's modified Smith-Watson-Topper.

In the new versions of Ford corporate software all the parameters are calculated but greater confidence is attributed to the later three criteria listed above. The research on appropriate damage parameters appears to be drawing to a close. A more difficult problem in this area is the effect of overloads on amount of damage caused by subsequent cycles. The problem has a long history²⁴⁻²⁸, and substantial progress has been made, but at present the philosophy has not generally been incorporated into ground vehicle damage calculation software.

GEOMETRY

In a critical location approach applied to fatigue, geometric effects constitute the transformation of the external loads on the vehicle or component into the critical location's stress or strain. Most computerized techniques perform this task based on the methods shown

in Figure 6¹¹. The external load, be it force or moment, is translated into local strain by a curve, here termed ' P vs ϵ '. This curve can be defined by using the stress concentration factor approach, a measurement approach—used where a quick answer on an existing component is needed—or a computerized finite element analysis (FEA). The latter method also comes in two varieties; either a fully elastic analysis, which is the norm for most vehicular durability analysis done today, or a plastic FEA model which would compute the ' P vs ϵ ' curve directly; a method little used to date because of the expense and the general poor quality of FEA plasticity models when faced with reversals in loading direction. In cases where the nominal load to local transformation is done by means of an elastic analysis, a plasticity 'correction' is required to better approximate the behavior of the actual material. Reference 29 proposed a modification of Neuber's³⁰ analysis that is generally used presently throughout the vehicular industry. It basically finds the point on the material's stress-strain curve where the total energy matches that of the elastic analysis. In the early days of computerized analysis, this was achieved by scaling an appropriate load histogram with the worst case von Mises' equivalent stress, and then by applying the Neuber correction to each block of stress cycle in the history. In today's relatively complex FEA models similar techniques are still applied. After the complex load history is reduced to a uniaxial (elastic) stress history for each critical element, the Neuber correction is used to compute the local stress and strain. It should be noted here that this method only works well when the critical locations with plasticity are located within

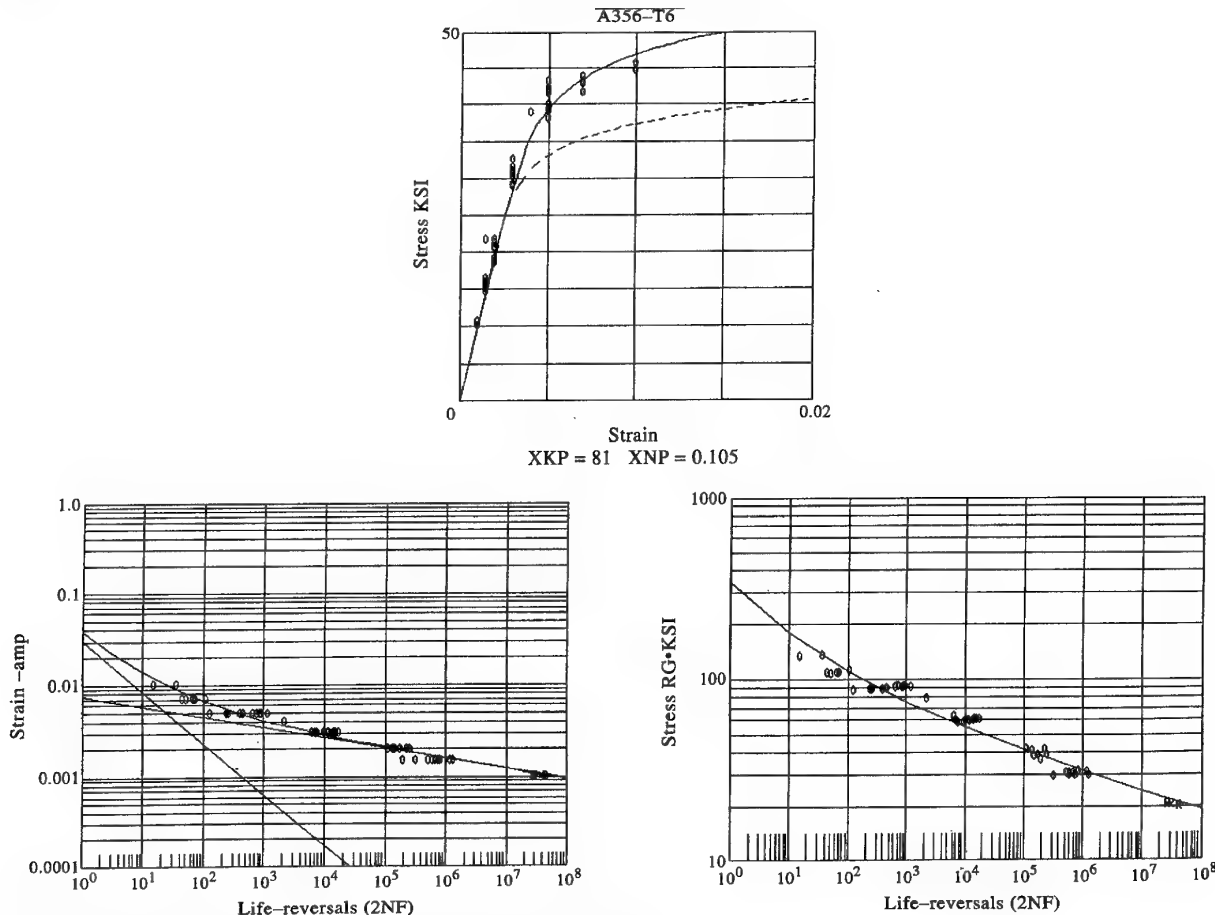


Figure 5 Material fatigue database data sheet for A356-T6 cast aluminum

large zones of elasticity. When one reaches general yielding of the components, the process breaks down.

At present it is still impractical to run large FEA models directly with plastic stress-strain material behavior. We must still use elastic analysis. Even in components or bodies that have a relatively small number of elements it is usually more useful to increase the element density in the high stress regions and use elastic analysis, rather than keep the same number of elements and use plastic analysis. If there were a way for fatigue analysts to perform a single plastic analysis of a load cycle and use the results for processing all the service loads, it would then be possible to utilize codes such as ABACUS™. Presently the superposition of stresses from different loads is not valid when the local strains are in the plastic region.

In Ref. 29 the Neuber plasticity correction method was extended to three dimensional stress-strain states. This technique is vital if one wishes to continue to use elastic FEA of large structures and account for any multiaxial local stress states.

LOADS

As FEA models grew in complexity in the late 1980s, it became more and more difficult for a car body or chassis component engineer to select a single critical load case. Figure 7 depicts a prototype component along with nine load vectors, each of whose time-load

histories was largely independent of any other. At the time of this fatigue analysis in 1989, the single 'hot element' approach was still common practice in the vehicular industry. It became apparent that in order to find the critical load case, a large number of different load cases had to be examined; so many that automation of the process was considered. This suggested that we could simply adopt the unit load-superposition approach used in civil engineering structural analysis, and subsequently run all the load cases for all the elements. At Ford this technique was translated into a program called FLAP³¹. The method is now used on most new car body structures. The number of load channels is usually 70 or more, with each channel's length greater than 1 million samples (from the test track history recording). The number of elements processed now routinely reaches 100 000; although simpler components models are much smaller (Figure 8).

Presently the best source of loads information still comes from FM tape recordings taken from prototype vehicles on the proving ground. Although this is reliable, it requires that a prototype vehicle be available. It would be highly desirable to be able to simulate the vehicle's progress over the proving grounds for calculation of the body or chassis component loads. Reference ³² partially solved this problem by using wheel-force recordings as input into a DADS vehicle dynamics simulation program. The weak links in the system are tire models and bushing models. As in

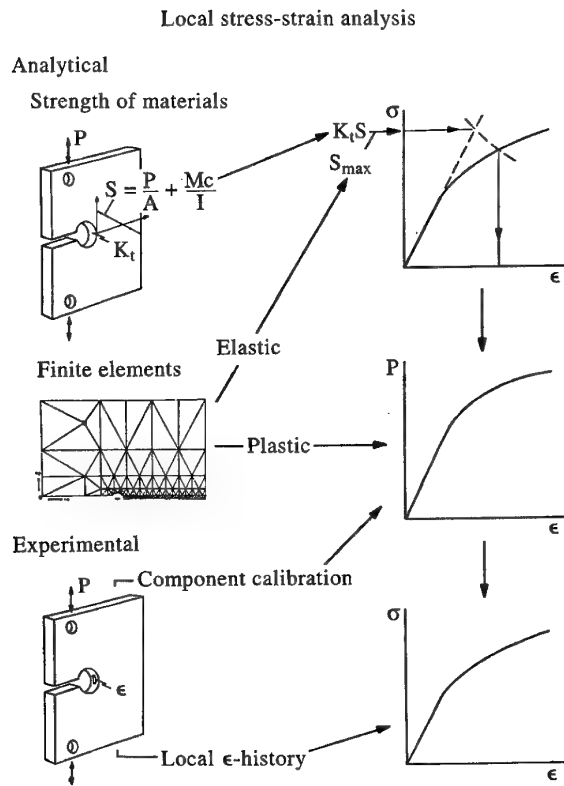


Figure 6 Approaches for performing the local stress-strain analysis of a notched member

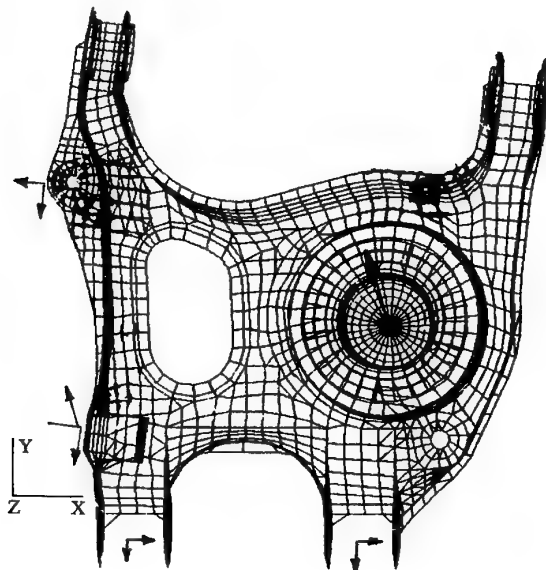


Figure 7 FEA geometry of a prototype suspension arm model with unit load vector locations

In the case of plasticity corrections, these areas contain components and materials that are highly non-linear. Substantial progress is being made in both areas, for example, Ref. 33, but at this time loads cannot be reliably derived from full vehicle computer simulations. There are certainly further difficulties to be overcome before this aspect of the fatigue analysis problem becomes routine (Figure 9).

SUMMARY

The present state of the art in ground vehicle durability analysis emphasizes the following features:

- Material properties derived from standard strain life test results.
- A three-dimensional stress-strain model, adapted from that of Mroz. The model must be able to simulate reversed multiaxial stress/strain paths.
- Damage assessment must be flexible enough to handle several multiaxial fatigue damage criteria. A critical plane search for the most damaging direction is necessary.
- A multiaxial Neuber type of plasticity correction method must be used to translate the elastic local stress estimates into approximations that are corrected for plastic stress-strain behavior.
- Large finite element models of vehicular components tend to have many load input points, and thus must utilize a elastic unit load analysis combined with a superposition procedure of each load points service history, to produce each element's stress history. It is critical that the time base of the loading events be preserved.

Present problem areas that require further research:

- The simulation of the non-linear stress-strain or load deflection behavior of elements such as tires and bushings.
- Accounting for 'small cycle' effects caused by periodic overload conditions in the loading.

Although the present software does not incorporate the latter two effects, the methods are already robust and accurate enough to make good estimates of component life. They are now used as standard tools in the fatigue design and analysis of automotive structures.

REFERENCES

- 1 Bauschinger, J., Ueber die Veraenderung der Elastizitaetsgrenze und der Festigkeit des Eisens und Stahls durch Strecken und Quetschen, durch Erwaemmen und Abkuhlen und durch oftmael wiederhol Beanspruchung. *Mitteilungen Mechanishes-technisches Laboratorium, Muenchen*, 1886, **13**(8), 1–115.
- 2 Jenkin, C. F., Fatigue in metals. *The Engineer*, 1922, **134**(3493), 612–614.
- 3 Masing, G., Eigenspannungen und Verfestigung beim Messing. In *Proceedings 2nd International Congress of Applied Mechanics*, Zurich, 1926.
- 4 Duwez, P., On the plasticity of crystals. *Physical Review*, 1935, **47**, 494–501.
- 5 Whiteman, I. R., A mathematical model depicting the stress-strain diagram and the hysteresis loop. *Journal of Applied Mechanics, ASME Transactions*, 1959, 95–100.
- 6 Martin, J. F., Topper, T. H. and Sinclair, G. M., Computer based simulation of cyclic stress-strain behavior. Report No. 326. Department of Theoretical and Applied Mechanics, University of Illinois, July 1969. Also published in *ASTM Materials Research and Standards*, 1971, **11** (2).
- 7 Wetzel, R. M., A method of fatigue damage analysis. Ph.D. Thesis, University of Waterloo, Canada, 1971.
- 8 Jhansale, H. R. and Topper, T. H., Cyclic deformation and fatigue behavior of axial and flexural members—a method of simulation and correlation. In *Proceedings 1st International Conference on Structure Mechanics in Reactor Technology*, Berlin, September 1972, Part L, pp. 433–455.
- 9 Conle, A. and Topper, T. H., Sensitivity of fatigue life predictions to approximations in the representation of metal cyclic deformation response in a computer-based fatigue analysis model. In *Proceedings 2nd International Conference on Structure Mechanics in Reactor Technology*, Berlin, September 1973.

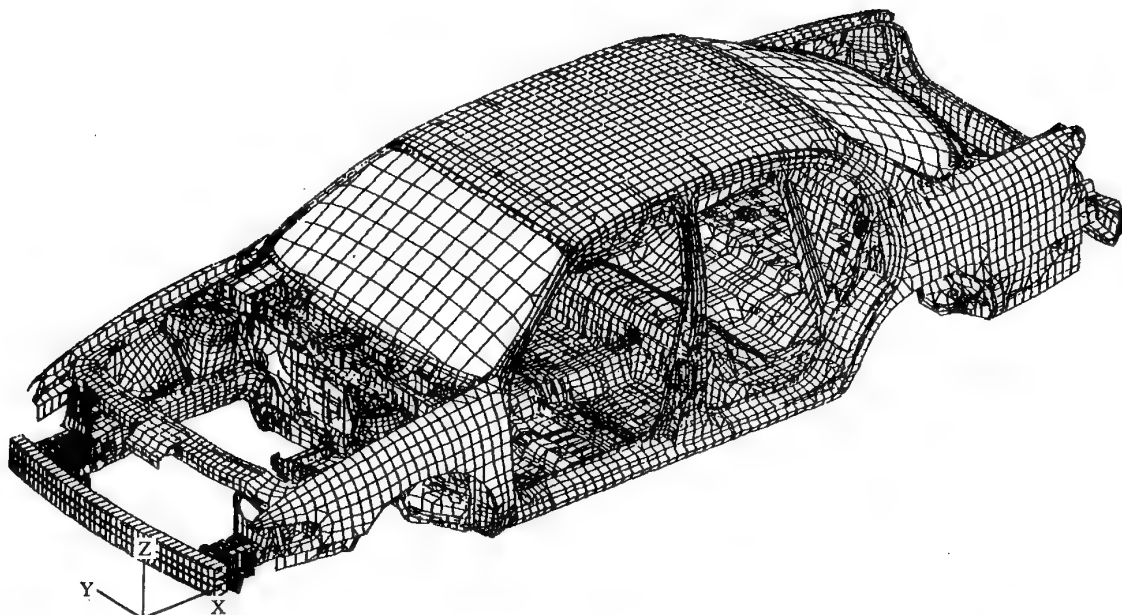


Figure 8 Large scale durability model used to analyze prototype car body fatigue life

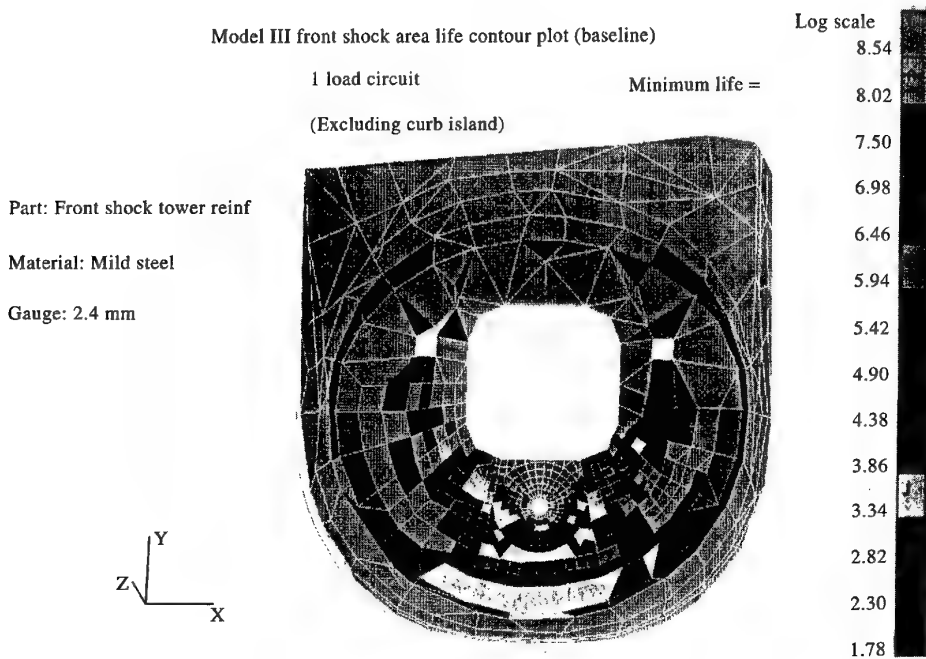


Figure 9 Prototype shock tower model section showing durability life prediction by shaded elements

- 10 Hanschmann, D., Ph.D. thesis. Technische Hochschule Aachen, Germany, 1981.
- 11 Conle, A. and Landgraf, R. W., A fatigue analysis program for ground vehicle components. *Proceedings International Conference on Digital Techniques in Fatigue*, Society of Environmental Engineers Conference at City University, 1983.
- 12 Conle, F. A., et al., *Tracking Time in Service Histories for Multiaxial Fatigue Problems*. ASTM STP-1006. American for Testing and Materials, Philadelphia, PA, 1989, pp. 198-210.
- 13 Fash, J. W., et al., Enhancing the design development cycle through computer integrated engineering for durability. SAE SP-730, Paper 871942. SAE, 1987.
- 14 Bonnen, J. J. F., et al., Biaxial torsion-bending fatigue of SAE axle shafts. SAE Paper No. 910164, SAE.
- 15 Fash, J. W. and Conle, F. A., Analysis of strain gage rosette data for fatigue life predictions. SAE Paper No. 92114. SAE, 1992.
- 16 Mroz, Z., On the description of anisotropic work-hardening. *Journal of the Mechanics and Physics of Solids*, 1967, **15**, 163-175.
- 17 Chu, C.-C., A three-dimensional model of anisotropic hardening in metals and its application to the analysis of sheet metal formability. *Journal of the Mechanics and Physics of Solids*, 1984, **32**, 197-212.
- 18 Krieg, R. D., A practical two surface plasticity theory. *Journal of Applied Mechanics*, 1975, **42**, 641-646.
- 19 McDowell, D. L., A two surface model for transient nonproportional cyclic plasticity. *Journal of Applied Mechanics*, 1985, **52**, 298-308.

- 20 Bannantine, J. A., A variable amplitude multiaxial fatigue life prediction method. Report No.151/UILU-ENG 89-3605. University of Illinois, October 1989.
- 21 Chu, C.-C., A constitutive model for cyclic creep/relaxation. *Proceedings of International Conference on Constant Laws for Engineering Materials*, ed. Fan Jinghong and Sumio Murakami, 11–13 August, P. R. China, 1989, Vol. II, pp. 709–713.
- 22 Chu, C.-C., et al., Multiaxial stress-strain modeling and fatigue life prediction of SAE axle shafts. *ASTM STP of Symposium on Multiaxial Fatigue*, San Diego, 1991, in press.
- 23 Chu, C.-C., Critical plane fatigue analysis of various constant amplitude tests for SAE1045 steel. SAE Paper No. 940246. SAE, 1994.
- 24 Nowack, H., Biharmonische Beanspruchungsablaufe zur Beurteilung der Schädigung unregelmässiger Beanspruchungen (Biharmonic load cases for determination of damage due to irregular loading). *VDI-Z Fortschritt Berichte*, 1969, 5(7).
- 25 Haibach, E., Modifizierte Lineare Schadensakkumulations Hypothese zur Berücksichtigung des Dauerfestigkeits-abfalls mit Fortschreitender Schädigung. LBF Report TM-50/70, Darmstadt, 1970.
- 26 Conle, A. and Topper, T. H., Overstrain effects during variable amplitude service history testing. *International Journal of Fatigue*, 1980, 130–136.
- 27 Yan, X., et al., A Property Fitting Approach for Improved Estimates of Small Cycle Fatigue Damage. SAE Report No. 920665. SAE, 1992.
- 28 DuQuesnay, D. L., Pompetzki, M. A. and Topper, T. H., Fatigue life prediction for variable amplitude strain histories. SAE Paper No. 930400. SAE, 1993.
- 29 Chu, C.-C. and Conle, F. A., Multiaxial Neuber-type of elastic to elastic-plastic stress-strain correction. *Proceedings of 4th International Conference on Biaxial Multiaxial Fatigue*, St. Germain en Laye, France, 31 May–4 June 1994, pp. 489–495.
- 30 Neuber, H., Theory of stress concentration for shear strained prismatical bodies with arbitrary non-linear stress-strain law. *Journal of Applied Mechanics*, 1961, **28**, 544–550.
- 31 Agrawal, H., et al., Up-front durability CAE analysis for automotive sheet metal structures. SAE Paper No. 961053. SAE, 1996.
- 32 Conle, F. A. and Mousseau, C. W., Using vehicle dynamics simulations and finite-element results to generate fatigue life contours for chassis components. *International Journal of Fatigue*, 1991, **13**, 195–205.
- 33 Mousseau, C. W., Hulbert, G. M. and Clark, S. K., On the modeling of tires for the prediction of automotive durability loads. *Vehicle System Dynamics*, 1996, **25**(Suppl.), 466–488.

PII: S0142-1123(97)00018-2

Multiaxial fatigue life prediction method in the ground vehicle industry

C.-C. Chu

MD 3182, SRL Ford Motor Company, Dearborn, MI 48121-2053, USA

The extensive progress which has been made in the multiaxial fatigue area over the past 5 to 10 years has allowed wider application of the multiaxial fatigue method in component durability design in the ground vehicle industry. The method adopts the long established local strain-life approach and includes several new features. (1) A three-dimensional cyclic stress-strain model, used to simulate the elastic-plastic material behavior under complicated loadings. (2) The critical plane approach, which requires the fatigue analysis to be performed on various potential failure planes before determining the lowest fatigue life. (3) A biaxial damage criterion, to better quantify fatigue damage under various loading conditions. (4) A multiaxial Neuber equivalencing technique, used to estimate, from the elastic finite element stress results, the multiaxial stress and strain history of plastically deformed notch areas. This paper examines the application of the above features to the fatigue analyses of three generic service/test histories: a constant amplitude (baseline) test history, a history directly recorded by strain gages mounted on the critical location of a structural component, and a loading history recorded in multichannels for a complex structure. © 1998. Published by Elsevier Science Ltd.

(Keywords: multiaxial fatigue; biaxial damage criterion; critical plane; parameter life curve; plasticity; notch; Neuber)

INTRODUCTION

It has been almost 20 years since the introduction of the local strain-life approach and almost 15 years since it became a widely accepted tool for predicting the fatigue life of structural components¹. The application of this technique however has been limited to uniaxially or proportionally loaded structures, a restriction that principally arose from the lack of reliable three-dimensional cyclic stress-strain models which could adequately simulate experimentally observed cyclic stress-strain behavior.

Several plasticity models have since been developed and, more importantly, implemented for cyclic stress analysis²⁻⁴. In the meantime, for the past 5 to 10 years much effort in the fatigue area has been focused on various multiaxial subjects such as biaxial damage parameters⁴⁻⁸, the critical plane approach⁹⁻¹², and multiaxial notch stress correction methods¹³⁻¹⁶. Although there has been no consensus yet as to which is the best approach among various stress-strain models, damage criteria, and notch stress correction methods, the need to use multiaxial fatigue methods for non-proportional loading conditions has been recognized by the significant improvement in fatigue life prediction accuracy these analyses yield over the traditional uniaxial method⁴.

In this paper, features of the multiaxial fatigue method are reviewed through application to the analysis

of three types of input history. (1) Load or strain controlled constant amplitude test results. For this simplest type of stress and strain history, it is shown that, instead of using the standard fatigue life prediction routines, data from all constant amplitude tests can be used to identify the proper damage criterion and thus the damage parameter versus fatigue life curve for the material. (2) A local strain history recorded by rosette strain gages installed at a critical location. A general three-dimensional cyclic stress-strain model is required to obtain the corresponding stress history before the fatigue analysis is performed. Such directly measured histories, with minimum error introduced by structural stress analysis, makes this type of history a good means to test the damage analysis part of the methodology. (3) An external load history of a real structural component. The local stress and strain history is first obtained by an elastic finite element analysis of the structure. At critical locations where the material elastic limit has been exceeded, a multiaxial stress correction method is currently used to estimate the elastic-plastic stress and strain histories. Although such correction methods have been widely used in uniaxial cases, and there are encouraging results comparing corrected and directly calculated multiaxial notch stresses, the general usage of multiaxial stress correction techniques is still a subject of research.

GENERAL DESCRIPTION OF THE METHOD

As shown by the flow chart in *Figure 1*, our multiaxial fatigue analysis program can be separated into two parts: the stress analysis part and the fatigue damage analysis part. The objective of the stress analysis is to obtain the complete 3D stress and strain history of a potential failure site. Depending on the complexity of the problem, this part of the analysis can vary from simple solutions attainable in closed form (such as the case for uniformly deformed fatigue samples) to complicated but direct multiaxial stress calculations made from recorded local strains using a three-dimensional cyclic plasticity model, and further to multiaxial elastic-plastic stress and strain estimation based on simpler elastic solutions from the finite element analysis of a complete structure. The examples reviewed in this paper are organized according to this gradation in difficulty.

The fatigue damage analysis involves rainflow counting of the fatigue events and the summing up of their damage. The method is similar to that used for uniaxial

problems, with the additional complexity of the biaxial damage criterion and the critical plane approach: using Brown and Miller's biaxial damage criterion as an example, for every potential failure plane, damage events are determined by rainflowing the shear strain component (γ). During each shear strain defined damage event, the variation of normal strain (ϵ) is also recorded. The damage caused by each event is then assessed by the biaxial damage parameter ($\gamma_a + K\epsilon_a$). The (shortest) fatigue life (on the most critical plane) can be determined only after the fatigue analysis is performed on each and every potential failure plane.

As input to the method, the description of the material fatigue properties requires a cyclic equivalent stress-equivalent strain relationship and a fatigue curve. As will be explained later, the fatigue curve, which traditionally has been the *S-N* curve or the strain-life curve for uniaxial or proportional problems, is here redefined as a damage parameter versus fatigue life curve. This parameter-life curve must be constructed for each multiaxial damage criterion.

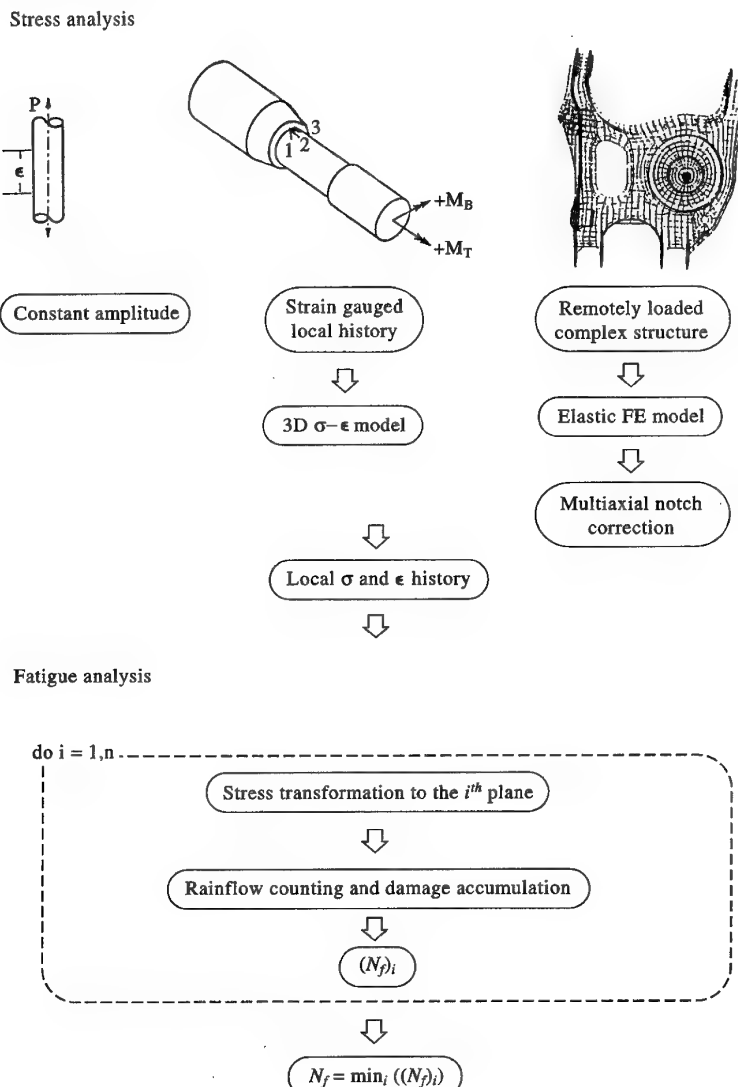


Figure 1 Flow chart of the multiaxial fatigue method

CONSTANT AMPLITUDE TEST DATA

In constant amplitude tests, the stress-strain hysteresis loop and its associated damage parameter remain constant throughout the stabilized portion of history. By assuming the Miner's linear damage accumulation rule, there should then exist a relationship between the measured (constant) damage parameter and the observed fatigue life. Both the traditional $S-N$ curve and the strain-life equation are examples of such a relationship. Therefore, instead of using the standard fatigue life prediction routines, it has been realized that the constant amplitude test data can be more directly analysed to help evaluate the appropriateness of a damage criterion than to test the fatigue analysis algorithms.

To analyse data from general multiaxial constant amplitude tests the critical plane approach has to be adopted. That is, by using coordinate transformation formulae for the stress and strain tensors, the damage parameter on individual material planes can be expressed, in terms of the measured stress and strain quantities, as a function of the plane orientation. The most critical plane can therefore be determined by maximizing the damage parameter with respect to the plane orientation. For example, the variation of the Brown and Miller damage criterion⁵ on different planes for a uniaxial tension-compression test and a pure shear test is shown in *Figure 2*. (A detailed formulation for the critical value of several damage

criteria for constant amplitude proportional loadings can be found in Ref. 12.)

By plotting the maximized (critical) damage parameter against the observed fatigue life, one can evaluate the adequacy of the parameter. If the data points are widely scattered, the parameter is inappropriate. If the data points lie in a tight band, the parameter is suitable to be used for fatigue life analysis.

A large collection of constant amplitude tests for normalized SAE1045 steels, compiled in Ref. 17, was analysed using the above-mentioned approach in Ref. 18. *Figure 3* reproduces the results from one uniaxial (γ_a) and one biaxial ($(\sigma_{max}\epsilon_a + |\tau|_{max}\gamma_a)$) damage criterion. It should be noted that these plots contain data from (1) baseline fatigue tests, i.e. uniaxial tension-compression and simple torsional tests; (2) proportional tests with various tension-torsion ratios; and (3) out-of-phase tests. It is believed that by including more types of test data in such plots, the damage parameter as well as the damage parameter versus fatigue life curve can be more accurately determined, and then successfully used for fatigue analysis of complicated structures, where many modes of loading occur in the same test.

RECORDED LOCAL STRAIN HISTORY

After the appropriate damage parameter-fatigue life curve has been determined for the material, the overall

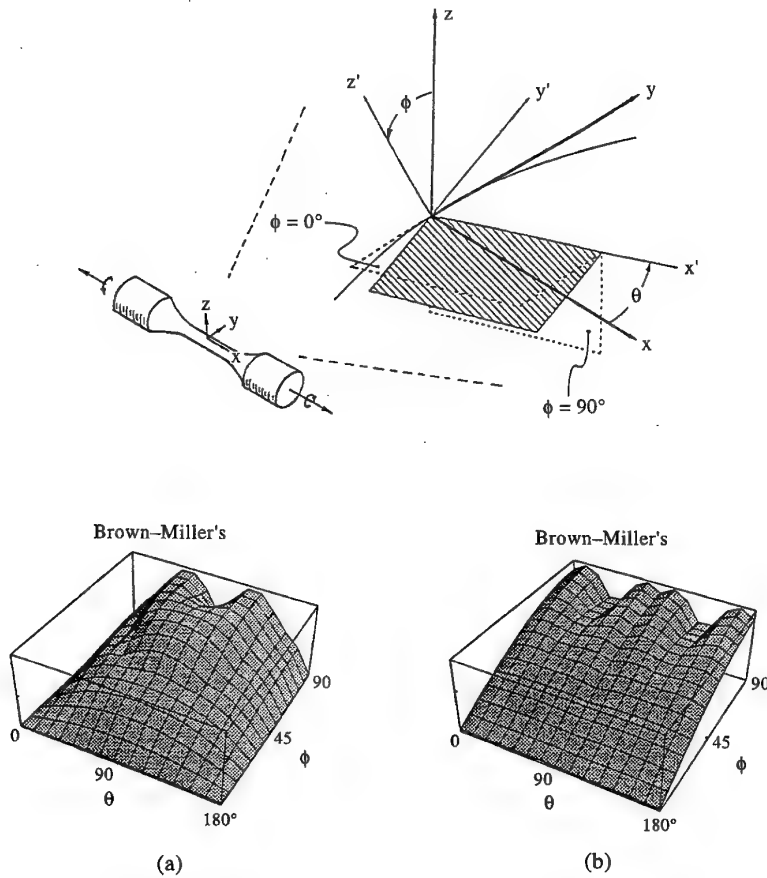


Figure 2 Variation of Brown and Miller's criterion for (a) uniaxial tension-compression test and (b) pure shear test

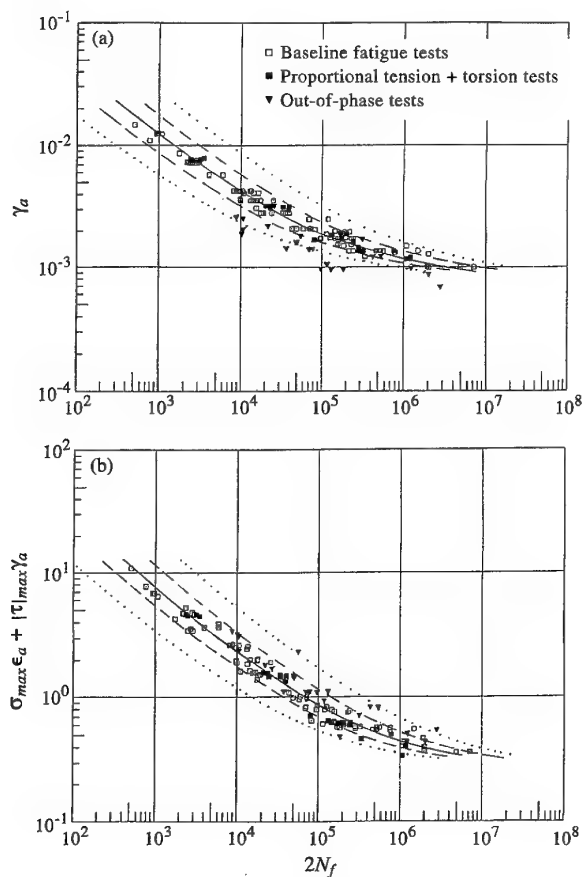


Figure 3 Fatigue curve for SAE1045 steels if (a) shear strain amplitude and (b) modified Smith-Watson-Topper is the damage criterion (figures 1 and 3 of Ref. 18)

multiaxial fatigue method can be tested by predicting fatigue life from strain histories recorded at a known failure site of a component test. Direct strain measurements avoid additional errors that may be introduced by the stress analysis due to geometric effects between the load measurement position and the failure location. Examples of such direct measurement tests using complicated bending and torsion log-skidder histories on the SAE axle shaft specimens can be found in Refs 17,19.

A general three-dimensional cyclic stress-strain model is needed to obtain the stress response to these recorded strain histories. As mentioned earlier, there have been several models proposed and implemented lately^{2,4}. All the models have been based on yield surface formulations, and were developed to meet the minimum requirements that they reproduce the two widely accepted material behavioral characteristics: (1) the classical flow theory for monotonic loadings, and (2) Masing's behavior for cyclic proportional loadings. The major difference among the models seems to lie in the evolution rules of the yield surfaces. While it is not difficult to see the difference in formulations, there is a lack of published work comparing quantitatively the model's ability to predict material behavior under complex loadings and hence its impact on multiaxial fatigue life assessment.

An example of results using a generalized Mróz model²⁰ to obtain the stress response to a recorded

local strain history is shown in *Figure 4*. The predicted life versus observed life comparison for several multiaxial tests, as reported in Ref. 3, is shown in *Figure 5*. Although many damage criteria were used in the study, only the Smith-Watson-Topper ($\sigma_{max}\epsilon_a$) and a modified biaxial version of it ($\sigma_{max}\epsilon_a + |\tau|_{max}\gamma_a$) are included here to emphasize the improvement in fatigue life prediction capability achieved by using the multiaxial approach.

HISTORY FROM ELASTIC FINITE ELEMENT ANALYSIS

Since a measured local strain history is generally not available, especially in the early design stages, the local history in most of our problems can only be obtained by using finite element analysis of the complete structure. Unfortunately, even with today's explosive improvements in computer speed, a full scale elastic-plastic FE analysis of a complex structure subjected to random multiaxial loading history is still too time consuming and costly.

As commonly practiced now for proportional loadings, we use the superimposed elastic finite element stress results as the input to the stress analysis part of the program. If the FE stress results exceed the elastic limit, then a Neuber type of stress correction method is adopted to estimate the real stress and strain states at the plastically deformed notch area. When loading is multiaxial and non-proportional, however, we must use an extension of this uniaxial Neuber stress correction method²¹⁻²³ to multiaxial cases. Since the correction method is largely an engineering approach with no rigorous support from the mechanics point of view, only extensive comparison with either experimental or numerical results can justify a particular scheme's applicability to different notches.

Most comparisons published so far, however, concentrated on monotonic biaxial proportional loadings. A few examples of the applications to complicated cyclic loadings can be found in Ref. 14 where comparisons were found between the corrected stresses and those obtained by elastic-plastic finite element analysis of a notched round bar. Both this and the ongoing comparisons between the corrected notch stresses, using the technique proposed in Ref. 16, with those calculated from strains recorded by gages at the notch root of an SAE axle shaft²⁴, show encouraging results, within 10% of the more directly simulated stress results.

Unfortunately, since our fatigue life prediction capability depends on the accuracy in both the stress analysis and the fatigue damage analysis, a say 10% error in stress, which by stress analysis standards seems acceptable, is likely to double the fatigue life prediction error mentioned in the previous section where direct measurement of local history is available.

CONCLUSION

This paper has reviewed the progress that has been made in the multiaxial fatigue analysis area in the ground vehicle industry: biaxial damage criteria have been developed; the critical plane approach has been adopted; and cyclic multiaxial stress-strain models are implemented. In consequence, fatigue life predictions

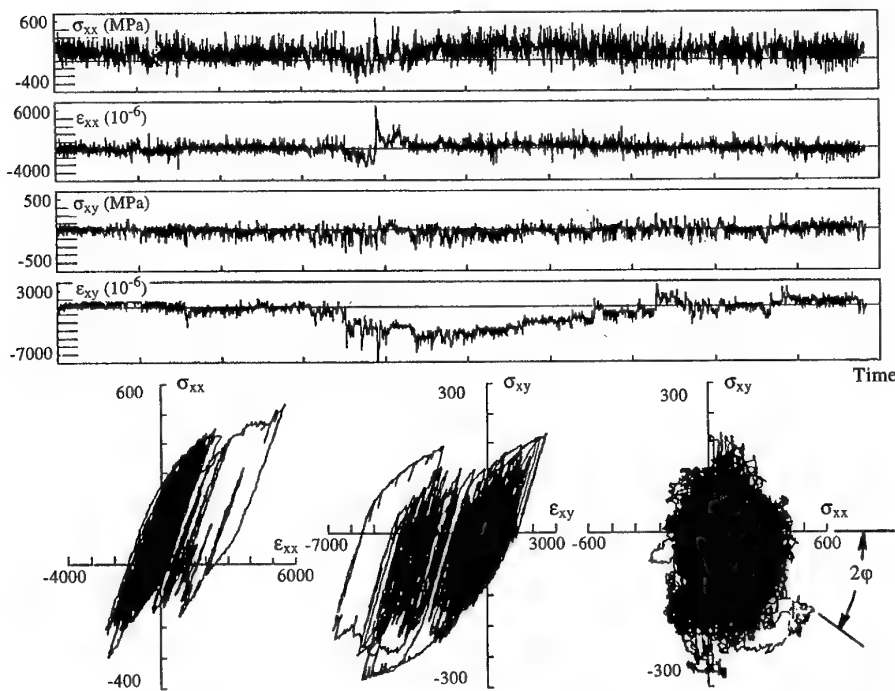


Figure 4 Stress and strain results calculated from measured rosette strains for biaxial tests on SAE axle shafts (figure 3 of Ref. 4)

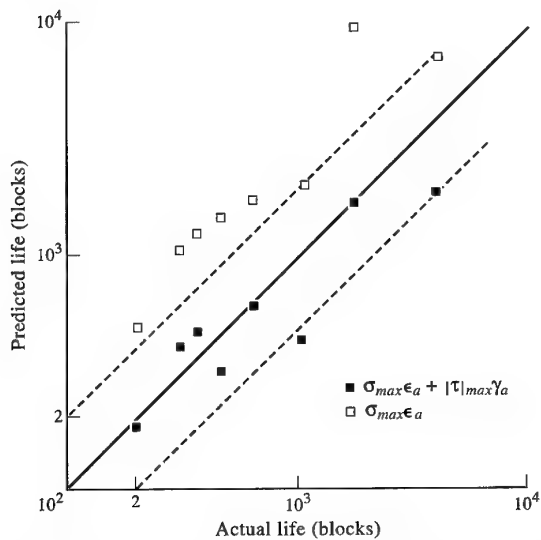


Figure 5 Comparison between predicted and observed fatigue lives for random amplitude combined bending and torsion tests on SAE axle shafts (figure 7 of Ref. 4)

for simple components subjected to complicated loading have seen at least a two- to three-fold improvement over the results of the traditional uniaxial approach. Since the success in our multiaxial fatigue life method also depends on the ability to obtain accurate local histories, the challenge we are facing immediately seems to have shifted from the fatigue analysis part to the stress analysis part of the method; that is, the development of an efficient and consistently accurate method to obtain the stress and strain histories at critical locations of complicated structures subjected to multiaxial loadings.

REFERENCES

- 1 Conle, A. and Landgraf, R., A fatigue analysis program for ground vehicle components. Proceedings of International Conference on Digital Techniques in Fatigue, London, 1983, pp. 1–28.
- 2 Kötgen, V. B., Anthes, R. J. and Seeger, T., Implementation des Werkstoffmodells von Mróz in das Finite Element Program ABAQUS. Report FF-7/1991, Fachgebiet Werkstoffmechanik Technische Hochschule Darmstadt, 1991.
- 3 Bannantine, J. A. and Socie, D. F., A multiaxial fatigue life estimation technique. In *Advances in Fatigue Lifetime Predictive Techniques*, eds M. R. Mitchell and R. W. Landgraf. ASTM STP 1122, ASTM, Philadelphia, 1992, pp. 249–275.
- 4 Chu, C. C., Conle, F. A. and Bonnen, J. J. F., Multiaxial stress-strain modeling and fatigue life prediction of SAE axle shafts. In *Advances in Multiaxial Fatigue*, eds D. L. McDowell and R. Ellis. ASTM STP 1191, ASTM, Philadelphia, 1993, pp. 37–54.
- 5 Brown, M. W. and Miller, K. J., A theory for fatigue failure under multiaxial stress-strain conditions. *Proceedings of Institute of Mechanical Engineers*, 1973, **187**, 745–755.
- 6 Garud, Y. S., A new approach to the evaluation of fatigue under multiaxial loadings. *Journal of Engineering Materials Technology, Transactions ASME*, 1981, **103**, 118–125.
- 7 Socie, D. F., Waill, L. A. and Dittmer, D. F., Biaxial fatigue of Inconel 718 including mean stress effects. In *Multiaxial Fatigue*, eds K. Miller and M. W. Brown. ASTM STP 853, ASTM, Philadelphia, 1985, pp. 463–481.
- 8 Fatemi, A. and Kurath, P., Multiaxial fatigue life predictions under the influence of mean stresses. *Journal of Engineering Materials Technology, Transactions ASME*, 1988, **110**, 380–388.
- 9 Findley, W. N., Coleman, J. J. and Handley, B. C., Theory for combined bending and torsion fatigue data for 4340 steel. Proceedings of International Conference on Fatigue of Metals. The Institute of Mechanical Engineers, 1956, pp. 150–157.
- 10 Lohr, R. D. and Ellison, E. G., A simple theory for low cycle multiaxial fatigue. *Fatigue and Fracture of Engineering Materials and Structures*, 1980, **3**, 1–17.
- 11 Socie, D. F., Multiaxial fatigue damage models. *Journal of Engineering Materials Technology, Transactions ASME*, 1987, **109**, 293–298.
- 12 Chu, C. C., Fatigue damage calculation using the critical plane approach. *Journal of Engineering Materials Technology, Transactions ASME*, 1995, **117**, 41–49.
- 13 Hoffman, M. and Seeger, T., Estimating multiaxial elastic-plastic notch stresses and strains in combined loading. In *Biaxial and*

- 14 *Multiaxial Fatigue*, eds M. W. Brown and K. J. Miller, EGF3, 1989, pp. 3–24.
- 15 Köttingen, V. B., Barkey, M. E. and Socie, D. F., Pseudo stress and pseudo strain based approaches to multiaxial notch analysis. *Fatigue and Fracture of Engineering Materials and Structures*, 1995, **18**(9), 981–1006.
- 16 Barkey, M. E., Socie, D. F. and Hsia, K. J., A yield surface approach to the estimation of notch strains for proportional and nonproportional cyclic loading. *Journal of Engineering Materials Technology, Transactions ASME*, 1994, **116**, 173–180.
- 17 Chu, C. C. and Conle, F. A., Multiaxial Neuber-type of elastic to elastic-plastic stress-strain correction. Proceedings of Fourth International Conference on Biaxial/Multiaxial Fatigue, St. Germain en Laye, France, 1994, pp. 489–495.
- 18 *Multiaxial Fatigue, Analysis and Experiments*, eds G. E. Leese and D. F. Socie. SAE AE-14, Warrendale, PA, 1989.
- 19 Chu, C. C., Critical plane fatigue analysis of various constant amplitude tests for SAE1045 steels. SAE Paper 940246, 1994.
- 20 Bonnen, J. J. F., Conle, F. A. and Chu, C. C., Biaxial torsion-bending fatigue of SAE axle shafts. SAE Paper 910164, 1991 (also SAE Transactions, 1993).
- 21 Chu, C. C., Programming of a multiaxial stress-strain model for fatigue analysis. SAE Paper 920662, 1992.
- 22 Neuber, H., Theory of stress concentration for shear strained prismatical bodies with arbitrary nonlinear stress-strain law. *Journal of Applied Mechanics*, 1961, **28**, 544–550.
- 23 Glinka, G., Energy density approach to calculation of inelastic strain-stress near notches and cracks. *Engineering Fracture Mechanics*, 1985, **22**(3), 485–508.
- 24 Topper, T. H., Wetzel, R. M. and Morrow, J., Neuber's rule applied to fatigue of notched specimens. *ASTM Journal of Materials*, 1969, **4**(1), 200–209.
- 25 Hartline, R., Minutes of SAE FD&E Committee Component Testing Division, Detroit, Michigan, 4–5 October 1994.

PII: S0142-1123(97)00046-7

Fatigue crack initiation and growth in riveted specimens: an optical and acoustic microscopic study

Z. M. Connor, W. Li, M. E. Fine and J. D. Achenbach*Northwestern University, Center for Quality Engineering and Failure Prevention,
Evanston, IL 60208, USA*

While optical microscopy on riveted specimens reveals only surface cracks, the acoustic C-scan images reveal subsurface and buried cracks emerging to the surface. This is of particular interest for fatigue cracks that initiate below the outer surface such as with chamfered riveted panels. Fatigue crack initiation and growth in riveted panels of Alclad 2024-T3 were characterized using optical microscopy and scanning acoustic microscopy to obtain C-scan images. The C-scan images were obtained using a focused transducer with a center frequency of *ca* 50 MHz, and the peak value of the back surface echo of the plate with countersunk rivet holes was recorded in the C-scan images. Data on the initiation and development of fatigue cracks at rivets in riveted Alclad 2024-T3 are given. © 1998 Elsevier Science Ltd.

(Keywords: fatigue cracks; rivets; nondestructive evaluation)

INTRODUCTION

Fatigue crack initiation and microcrack development at rivets in riveted panels is much more complex than at notches or holes. This subject is of particular interest in aircraft where the skin is riveted to the frame. In riveted aircraft skin panels, fatigue cracks generally initiate in the subsurface and then grow from individual rivets. Interaction of cracks at more than one rivet leads to multi-site damage. The process starts at individual rivets and that is the subject of this paper.

Since the cracks initiate in the subsurface, the initial stages cannot be studied by surface observation. Fortunately, a scanning acoustic microscope (SAM) was available for this research to study fatigue crack development in the subsurface. In riveted joints where there is no effective adhesive to help transfer the load, the load is completely transferred through the rivets. The transfer process and stress state in the panels around and near the rivet is very complex due to many factors. Schijve has published a review¹.

Load by-pass occurs. For this reason, the load on each rivet and the load transferred to and from the rivet to the surrounding plates are not equal for each rivet in a multiple riveted joint. The load transfer process itself is between tight fitting pins inserted in holes in panels. *Figure 1* depicts pin loaded holes and by-pass. Residual stresses result from the riveting process. Using X-ray diffraction, Fitzgerald and Cohen² measured the residual stresses at countersunk riveted joints of Alclad 2024-T3 aluminum alloy plates as a

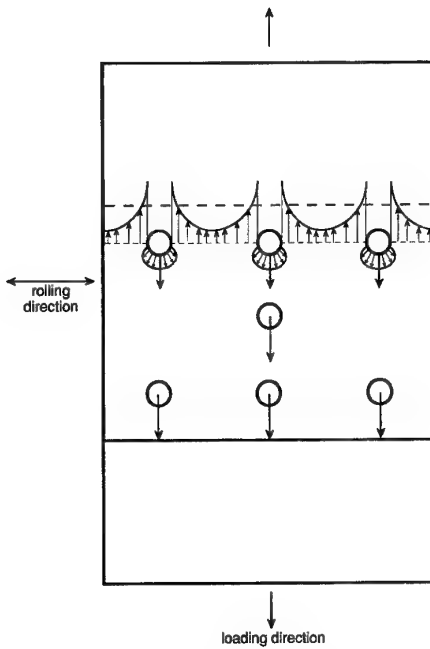


Figure 1 Drawing depicting pin loaded holes and by-pass load. Plastic deformation is observed in the region of the small arrows in the plates close to some of the rivets

function of riveting stress as indicated by the bucktail diameter. The stress on the rivet head was always compressive, but the residual stress in the sheet near the rivet for both cladding and alloy was tensile for



Figure 2 Sketch depicting bending of a lap joint when loaded in uniaxial tension due to load asymmetry

small diameter bucktails but changed to compressive as the riveting stress was increased.

With a lap joint or asymmetric butt joint, there is a bending moment when uniaxial tension is applied. This is schematically shown in *Figure 2* for a lap joint. Schijve¹ observed that the fatigue stress amplitude-cycles to failure curves for lap joints and asymmetric butt joints are nearly the same; however, symmetric butt joints where the bending moments are much less gave much better fatigue resistance. The present research is with lap joint specimens.

Plastic deformation in the plates occurs from the load transfer to and from the rivet and is easily noticeable if the load is sufficiently high to give failure in a few hundred thousand fatigue cycles. Such plastic deformation occurs at some of the rivets in an array in the regions of high compressive stress during the fatigue cycle. This is also indicated in *Figure 1* in the region of the small arrows beneath the top row of rivets. In flush head rivets, the holes in one plate are countersunk and the rivets are chamfered. This results in greater complexity of the stress pattern, the plastic deformation that occurs, and the microcrack generation processes. The microcrack development is further complicated by fretting that may occur between the rivet and the rivet hole and between the plates that are riveted together.

The current results of an experimental study of the factors determining microcrack development and the microcrack development processes themselves in flush-riveted aluminum alloy joints are presented. The development of the microcracks and how they formed major propagating cracks were followed using both optical and acoustic microscopes. While the optical microscope gives information about the specimen surface, the SAM gives an image through the thickness projected onto a plane. The hidden surface of the specimen is included in the projection. Thus cracks are revealed that are not on the outer surface of the flush head riveted panel. Since cracks initiate below the outer surface of the specimen, the SAM is essential to this investigation.

EXPERIMENTAL

Each lap joint specimen was assembled from two Alclad 2024-T3 aluminum alloy panels, 1.02 mm thick,

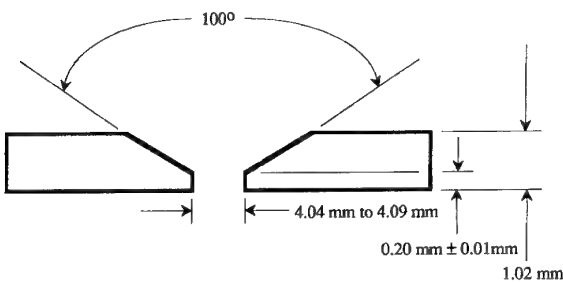


Figure 3 Side view of countersunk panel with a knife edge equal to 20% of the thickness of the panel

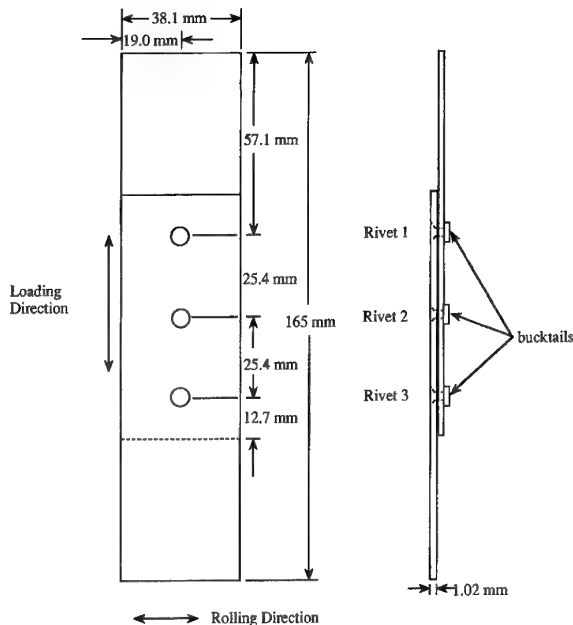


Figure 4 Drawing of three rivet specimen showing geometry and dimensions

using 2017-T4 aluminum alloy rivets. The chamfered rivets were 3.97 mm in diameter in the stem and 6.35 mm in length. The rivet head was *ca* 6 mm in diameter. The cladding on the 2024-T3 panels was 1050 aluminum alloy, 0.05 mm thick on each side. One piece of the sheet in each pair had countersunk rivet holes and one had straight holes. Two types of panels were prepared, one set with three holes and one set with nine holes. The three hole panels were 38 mm wide by 165 mm long, the nine hole panels were three times wider and 178 mm long. The holes and

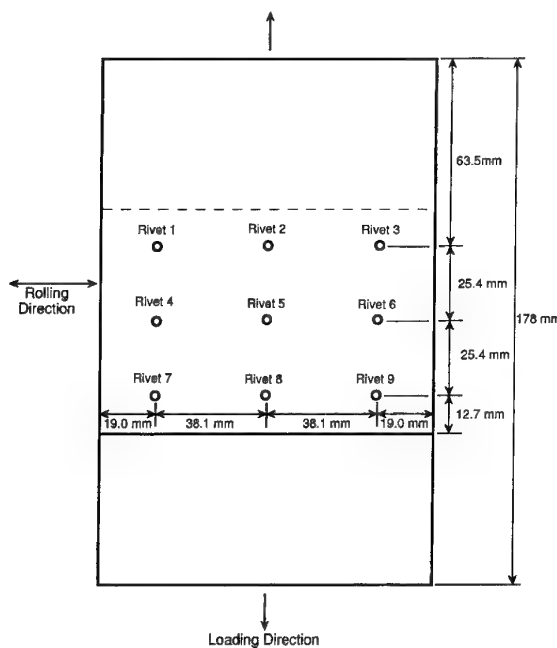


Figure 5 Drawing of nine hole specimen showing dimensions

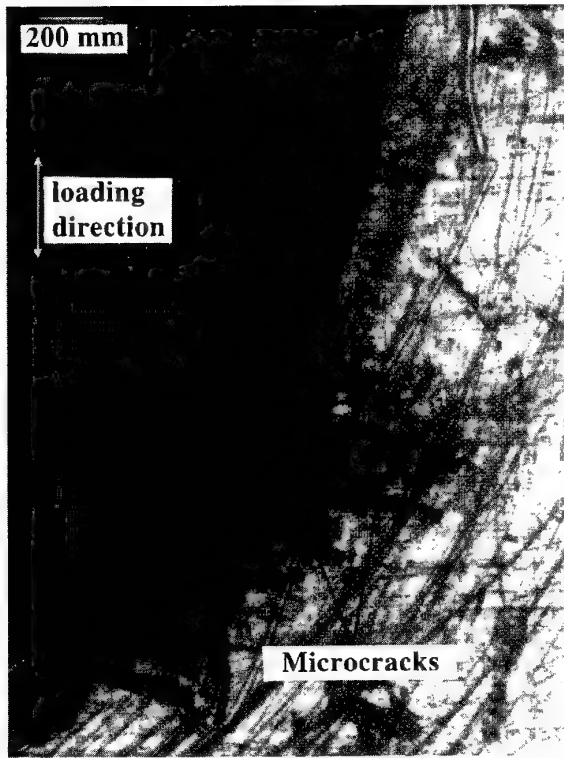


Figure 6 Optical photomicrograph showing the rumpled region after 215 000 cycles. Two microcracks are pointed out with arrows

countersinks were drilled with a computer controlled machining center. The hole diameters were between 4.04 and 4.09 mm. The limits for the hole diameter given in the Boeing specification are between 4.04 and 4.24 mm, with the smaller diameter being favored^{3,4}. The included angle of the countersink is 100°. The depth of the countersink was gradually increased until a knife edge of 0.20 ± 0.01 mm was obtained. This gives a knife edge of *ca* 20% of the thickness of the

material as given in *Figure 3*. Also, this meets typical flushness requirements for the rivet heads in aircraft panels, + 0.102 to - 0.000 mm³.

The panels were riveted together on a manually operated hydraulic press. The three rivet specimens were compressed between two flat plates at a constant load of 44.6 kN. This load was used to obtain a bucktail diameter of 6.12 ± 0.05 mm in accordance with Boeing Company 737 Structural Repair Standard (1970)⁴. The rivets were in line with the loading direction and were 25.4 mm apart in the loading direction. The nine hole pairs were riveted together with seven rivets, three rivets on top and bottom and one rivet in the center, using a load of 133.4 kN, which gave the desired bucktail diameter. The rivet specimen geometries and dimensions are given in *Figures 4 and 5*.

The three rivet specimens were loaded in uniaxial tension and tested in load control using an MTS Machine (comparable to an MTS 810 system) with a maximum load of 4.0 kN and an *R* ratio of 0.1. This load was selected on the basis of preliminary experiments to give failure in several hundred thousand cycles⁵. Only two of the seven rivet specimens have been tested to date. In the first experiment with the seven rivet specimens, the load was increased after a set amount of cycling until cracks were observed. A load of 12 kN was used in the other test.

The flush head riveted specimen surface was observed during the tests with an Olympus microscope (model 225143) at a magnification of $40 \times$. This microscope was mounted on the MTS machine so the observations of surface breaking microcracks and later propagating crack length could be measured without removing the sample from the MTS machine. Many tests were continued until failure. Some tests were stopped much earlier in the fatigue process and examined more carefully with other microscopes in a metallurgy laboratory. Crack growth measurements were obtained on five specimens. A few specimens were

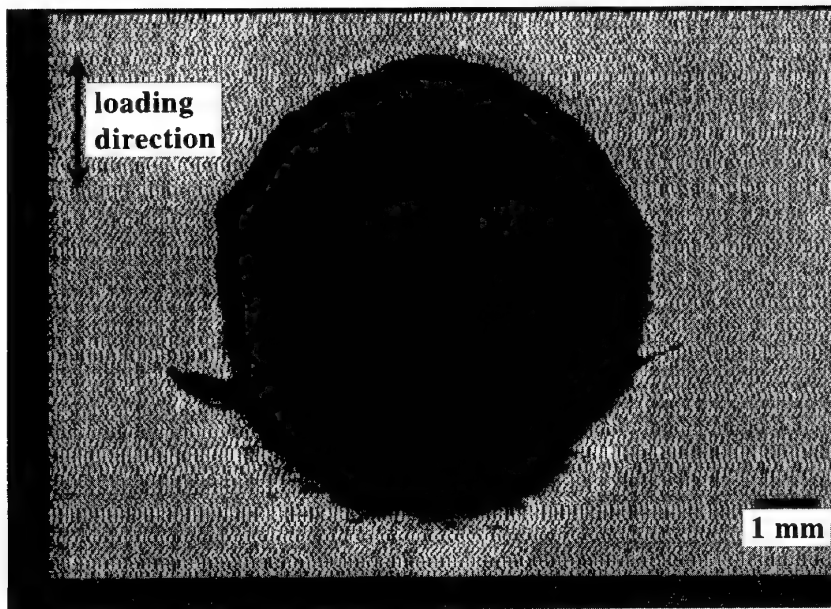


Figure 7 Scanning acoustic microscope C-scan image of the specimen shown in Figure 6

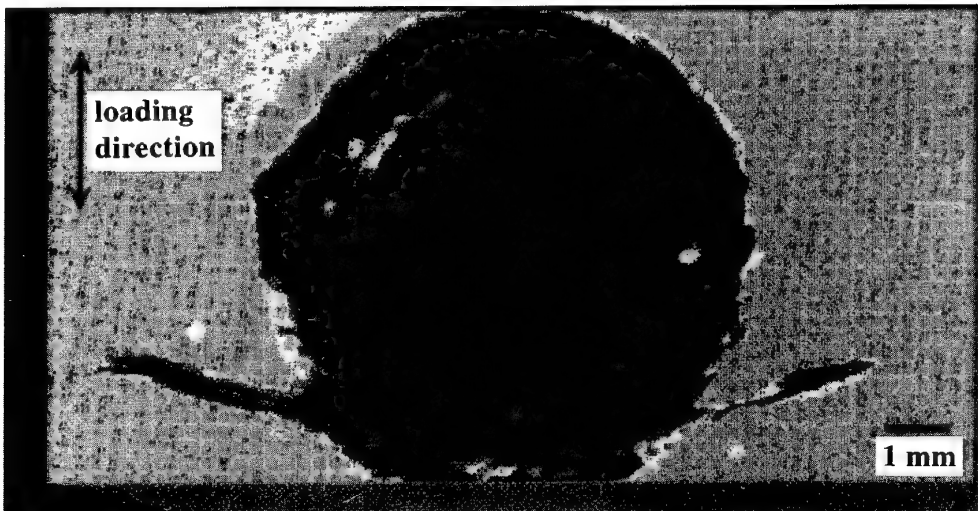


Figure 8 Scanning acoustic microscope C-scan image of a specimen showing a well developed eyebrow crack after 200 000 cycles

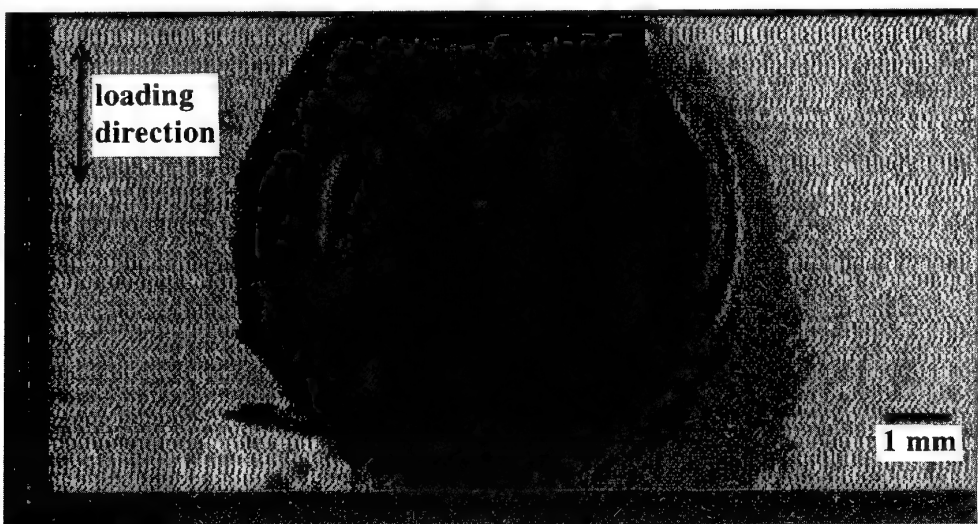


Figure 9 Scanning acoustic microscope C-scan image of a specimen showing a crack on only one side after 160 000 cycles

disassembled by grinding off the bucktail and carefully separating the plates. Then all surfaces were microscopically examined. A total of 25 specimens were tested.

Specimens at various stages in the fatigue process that had already been carefully examined with optical microscopes were investigated using a SAM to obtain C-scan images of the specimens[†]. A focused transducer with a center frequency of *ca* 50 MHz was used in conjunction with a Panametrics Hyscan system⁶. The specimens to be examined are submerged in a water tank. The focused transducer, attached to the *x*, *y*, *z* stages, is excited by a Panametrics Pulser-Receiver (model 5601A/ST) to generate ultrasonic waves. The focused beam is reflected by the specimen and returned to the transducer which now acts as a receiver. The transducer output signals, digitized by a Tektronix TDS-540 four channel digitizing oscilloscope and pro-

cessed by a Panametrics gated peak detector (model 5608), are finally acquired by a personal computer to produce a C-scan image.

The signal reflected from the back surface of the plate with countersunk rivet holes was gated and its peak value provided the data for the C-scan image of this plate. C-scan imaging reveals two dimensional projected images of cracks located throughout the specimen thickness.

RESULTS AND DISCUSSION

With the optical microscope, a surface rumpling consisting of plastic deformation markings and microcracks was the first feature observed by us in the three rivet specimens. This surface rumpling occurred adjacent to the rivet head of the outer rivet where the load was directly applied to the countersunk panel. These surface microcracks when first seen in this study were both circumferential and radial and were roughly 0.050–0.150 mm long when first observed. A typical example

[†]C-scan images were first obtained on specimens from this research by David Hsu at Iowa State University.

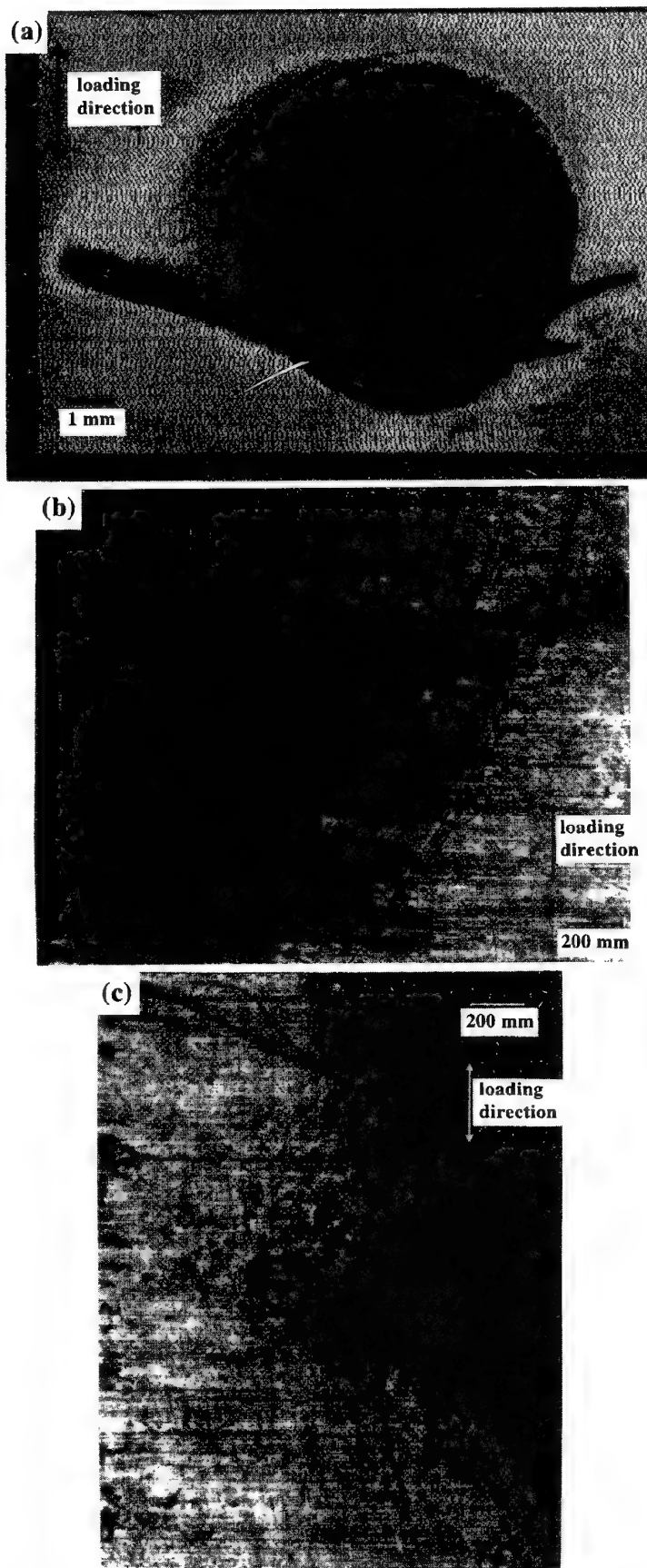


Figure 10 Specimen with eyebrow crack after 220 000 cycles. (a) C-scan image; (b) micrograph of left side in crack region; (c) micrograph of right side in crack region

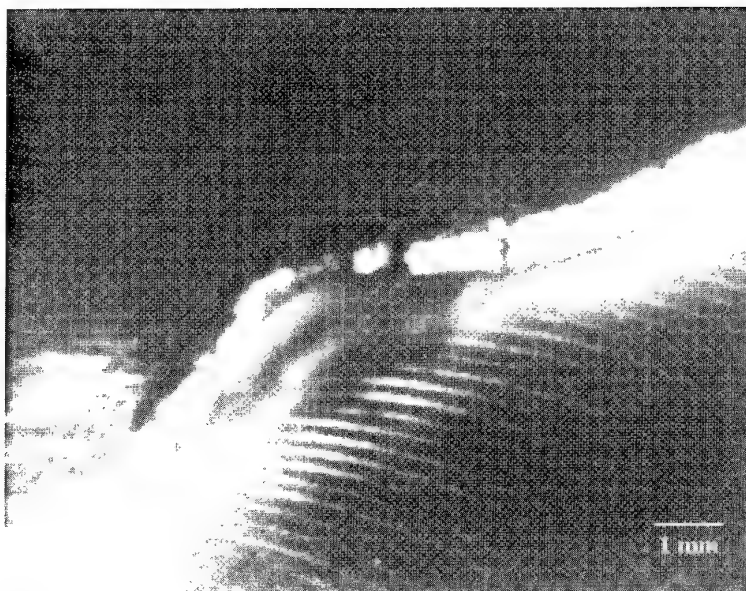


Figure 11 Micrograph of short crack in a specimen which was cycled to failure (293 000 cycles)

of the rumpled region is shown in the micrograph in *Figure 6* and a C-scan image of the same specimen is shown in *Figure 7*. The length of the rumpled region in the micrograph is *ca* 0.8 mm; whereas, the length of the radial crack in the C-scan image is *ca* 1.3 mm. The radial cracks initiate on the hidden surface of the countersunk panel and penetrate the rivet head surface later in their development. The surface microcracks do not appear to be directly responsible for the generation of the propagating cracks which initiate on a hidden surface. The rumpled regions and subsurface radial cracks are not located next to the center of the side of the rivet 90° to the loading direction, but rather closer to the top or bottom of the rivet forming an 'eyebrow' configuration. While the 'eyebrow' is seen optically only on the surface on one side of the rivet, the C-scan image of this specimen shows they occur on both sides of the rivet, but one side is more developed than the other and the other has not yet reached the surface. The shorter subsurface crack is *ca* 0.2 mm long. In this instance the subsurface radial crack was seen before any rumpling (shear bands and microcracks) was seen on the surface using an optical microscope. This is further evidence that the subsurface radial crack generation is not directly related to the surface rumpling even though the latter indicates fatigue damage, but the surface rumpling may result from the propagating crack.

Figure 8 is an example of a C-scan image of a specimen with a fully developed eyebrow crack on each side of the rivet. The cracks are *ca* 3.3 and 3.1 mm long. *Figure 9* is an example of a C-scan image of a specimen with the eyebrow crack detected only on one side. *Figure 10(a)* is another example of cracks on both sides of the rivet. This specimen was cycled for 220 000 times and the cracks are 4.8 and 1.5 mm long in the C-scan image. Optically measured, these cracks were 3.9 and 1.1 mm. *Figures 10(b)* and *(c)* are micrographs of the left and right side of the area of the specimen in which the cracks occur, respectively. *Figure 10(b)* clearly shows the long crack on the left

side of the rivet and a rumpled region on both sides of the crack near the rivet head. In *Figure 10(c)*, a short crack is seen which is not adjacent to the rivet head. The authors believe that this is due to the crack not having reached the surface in the region between the crack and the rivet head. Note that two cracks appear on the right side of this specimen in the C-scan image. This has been observed in other specimens. It is not known if this shorter crack has arrested or

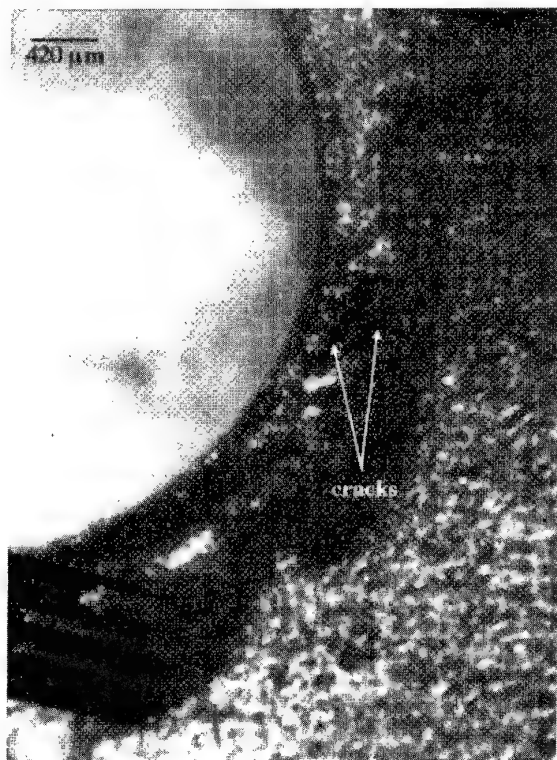


Figure 12 Micrograph showing cracks in the region where fretting occurs. Specimen was cycled 120 000 times and then disassembled

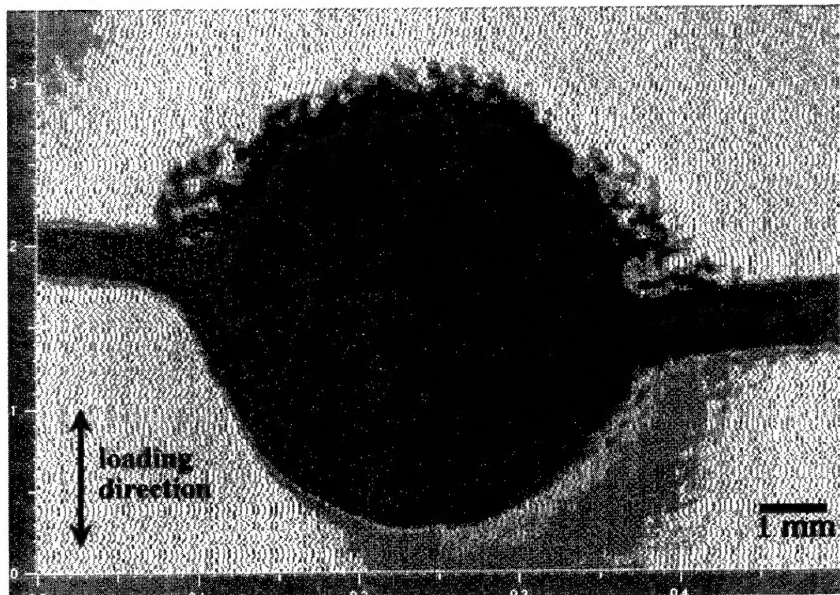


Figure 13 Scanning acoustic microscope C-scan image of the centrally located crack in a seven-rivet specimen run at a load of 12 kN for 30 000 cycles

whether it will grow with additional cycling until it meets the longer crack. Evidence of a shorter crack that has arrested is given in *Figure 11*, an optical micrograph showing a short crack in a specimen which was cycled to failure from another crack.

The C-scan images of a crack extending beneath the surface is not a line because the crack is not oriented normal to the surface. The rumpled regions were always seen on one side of the specimen before the other by *in situ* optical examination. Later a dominant radial crack emerged from these regions at an angle of *ca* 70° to the loading direction. It subsequently grows into a direction normal to the loading direction.

The approximate number of cycles until a propagating radial crack on the rivet head surface was seen to have emerged from beneath the rivet head in five three-rivet specimens on which crack growth measurements were taken was defined as N_i . The average N_i was found to be 286 000 cycles with an average deviation of 79 200 cycles. Observations were made every 10 000 cycles. The crack when first seen was already 0.5–1.7 mm long. The variation in initial crack size seen with the optical microscope on the flat surface of the panel arises in part because the initial cracks are sub-surface and take different paths to reach the surface. The average number of cycles to an 8 mm long crack was 375 000 cycles with an average deviation of 84 000. Thus *ca* 75% of the cycles to an 8 mm crack are spent generating a surface breaking radial crack.

After fatiguing and disassembling, the plate with the countersunk holes showed microcracks near the rivet hole on the hidden surface that contacts the other plate (*Figure 12*). This was observed in most of the disassembled specimens. The forementioned region is where fretting occurs in the plates. These microcracks had not penetrated to the outer plate surfaces.

Only two seven-rivet specimens have been studied to date. The first was run at 4.8 kN for 400 000 cycles and then the load was increased every 100 000 cycles. Cracks were optically observed on the specimen at

720 000 cycles, after a final load of 12.0 kN. Eyebrow cracks were observed in the countersunk panels adjacent to the three rivet heads which were closest to the load application, rivets 1, 2 and 3 in *Figure 5*. A second specimen was run at 12 kN and stopped at 30 000 cycles after a crack was observed in the countersunk panel adjacent to one of the rivet heads. This crack was oriented 90° to the load axis and centrally located with respect to the rivet (see *Figure 13* which shows the centrally located crack). While only two seven-rivet specimens have been examined, it is attractive to suggest that crack orientation is a function of applied load.

SUMMARY AND CONCLUSIONS

While the optical microscope reveals only surface cracks, the SAM in the C-scan mode images subsurface cracks projected onto a plane. Since microcracks initially form in the subsurface in riveted aluminum alloy panels and then grow to the surface, the SAM is useful to detect cracks before they can be seen by the optical microscope. These subsurface microcracks cannot be investigated by examination of the surface. Thus the acoustic microscope presents an opportunity for crack detection prior to their detection optically. With optical microscopy, surface rumpling consisting of microcracks and roughness is an early indication of fatigue cracking on the flush surface of lap joint panels riveted with flathead chamfered rivets. Defining N_i as the number of cycles to first optical microscopic observance of a propagating radial crack from the rivet, the average N_i has been found to be 286 000 cycles with an average deviation of 79 200 whereas the average number of cycles to the observance of an 8 mm crack was 375 000 cycles with an average deviation of 84 000.

ACKNOWLEDGEMENTS

This research was funded by the Federal Aviation Administration and the National Science Foundation by a fellowship to Z. M. Connor. We are grateful to Lynette Karabin from Alcoa for providing the material. We would like to thank David Hsu of Iowa State University for the initial C-scan images which he obtained on specimens from this research. We also wish to thank Richard Dojutrek from Northwestern University for machining the specimens.

REFERENCES

- 1 Schijve, J., Multi-site-damage fatigue of riveted joints. In *Durability of Metal Aircraft Structures, Proceedings of the International Workshop on Structural Integrity of Aging Airplanes*, ed. S. N. Atluri, C. E. Harris, A. Hoggard, N. Miller and S. G. Sampath, Atlanta Technology Publications, Georgia, 1992, pp. 2-27.
- 2 Fitzgerald, T. J. and Cohen, J. B., Residual stresses in and around rivets in clad aluminum alloy plates. *Materials Science and Engineering*, 1994, **A188**, 51-58.
- 3 Boeing Part Standard, BACR15CE RIVET, 100° Shear Head, 22 July. Boeing Co., 1987.
- 4 Boeing Company 737 Structural Repair Standard, Boeing Co., 1970.
- 5 Connor, Z. M., Fine, M. E. and Moran, B., A study of fatigue crack generation and growth in riveted Alclad 2024T3 specimens. *FAA-NASA Symposium on Continued Airworthiness of Aircraft Structures*, Atlanta, GA, 28-30 August 1996, in press.
- 6 Li, W., Achenbach, J. D. and Cheng, A., A time-resolved line-focus acoustic microscopy technique for surface-breaking crack depth determination. In *Review of Progress in Quantitative Non-destructive Evaluation*, Vol. 16, ed. D. O. Thompson and D. E. Chimenti. Plenum, New York, in press.

Epilogue

This conference was held to enhance the capability to predict and analyze fatigue damage of critical components under service environments. Hence, the application of fatigue research methodology to solve practical fatigue problems is clearly the primary target. In fact, we should not forget that the reason why fatigue is such a popular research subject (both in applied and basic research) is due to its enormous importance in engineering design, and reliability and performance of every engineering component. The conference consisted of forty-eight presentations, including five overview talks, six on fatigue crack initiation, six on short cracks, and thirteen on long cracks. Other talks were two on microscopy, seven on modeling, four on probability and statistics, and five on applications.

The interest of the attendees and the contents of the reports presented in the conference can be conveniently divided into three groups (as shown in *Figure 1*). The group on the top of the figure are fatigue practitioners, the front line fighters in the battle against fatigue. In the early days of the battle, they had to fight tooth and nail, as not many weapons were available to them. Consequently, the second group was called upon to provide essential weapons, i.e., laboratory fatigue data. The second group has provided some essential data, although the first group certainly need much more than what are currently available. The second group is like the logistics team behind the front line, working on a supply mission. The information that the second group produces is usually macroscopic in nature. It provides the first layer of understanding of the fatigue process under examination. However, it is often necessary to carry out further investigation to understand the process more deeply and thoroughly. This often requires micro-

scopic information in conjunction with macroscopic data. The design of such an investigation must be unique and original. The third group carries out this type of research and influences the quality of fatigue engineering and research on a long term basis. Casual observers may not see its value at all, as their progress does not reflect immediately on day-to-day fatigue engineering, or even on the activities of the second group; however, the ultimate success of the first and second groups is limited by the extent of success in understanding and characterizing the fundamental nature of fatigue by the third group.

There was a period that the research activities of this group was overvalued. There should be a good balance in promoting the activities of each group, and good communication among them is essential. In this conference, we witnessed significant successes in characterizing fatigue processes especially in crack growth analysis. There is still considerable disagreement in the interpretation of findings. It is the time to push the fundamental understanding of the parameters involved in growth analysis, down to the atomic dimension. A similar need certainly exists in the area of crack initiation, and the role of environment.

The increasing emphasis in reliability engineering and safe operation of aging military fleets point to increased employment of NDE techniques. It is highly desirable that the fatigue researchers work closely together with the NDE community to identify inspection requirements based on serious fatigue analysis and define the need of improving instrumentation to detect the critical states of fatigue. At the same time, the third group underutilizes NDE techniques in their investigation. New techniques and critical NDE criteria will be developed out of such collaboration. Examples of some such new techniques were reported in the conference.

The size of the conference was conducive to carrying out post-presentation dialogues among the three groups and the mix of these groups was just right. Those in Group Three benefited greatly in learning from Group One. The total moon eclipse, which occurred soon after the conclusion of the conference banquet, made the conference even more memorable.

Professor M. Meshii

*Department of Materials Science and Engineering,
 Northwestern University,
 Evanston, IL 60208, USA*

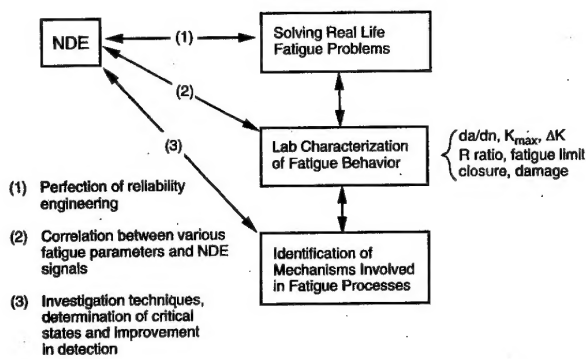


Figure 1

Instructions to Authors

Please follow these instructions carefully to ensure that the review and publication of your paper is as swift and efficient as possible. These notes may be copied freely.

Aims and scope

International Journal of Fatigue publishes papers dealing with the fundamental aspects of the fatigue of materials and, more importantly, with the relevance of fatigue to engineering and design.

Submissions

Contributions falling into the following categories will be considered for publication:

- ◆ Original high-quality research papers (preferably no more than 20 double line spaced manuscript pages, including tables and illustrations)
- ◆ Short communications, for rapid publication (no more than 10 double line spaced manuscript pages including tables and figures).
- ◆ Short contributions of up to 1200 words plus key illustrations for inclusion in 'Designer's Corner', covering topical issues associated with design against fatigue failure.

International Journal of Fatigue also publishes book reviews, conference reports and a calendar of forthcoming events. Contributions of this type should be sent to the Group Editor.

Contributions are normally received with the understanding that they comprise original, unpublished material and are not being submitted for publication elsewhere. Translated material, which has not been published in English, will also be considered. However, such material should be accompanied by a cover letter referring to the original article translated and declaring that permission of the original publisher has been obtained. All submissions should be accompanied by a written declaration, signed by all authors, that the paper has not been submitted for consideration elsewhere. Authors are solely responsible for the factual accuracy of their papers. The receipt of manuscripts will be acknowledged.

All authors must sign the 'Transfer of Copyright' agreement before the article can be published. This transfer agreement enables Elsevier Science Ltd to protect the copyrighted material for the authors, but does not relinquish the author's proprietary rights. The copyright transfer covers the exclusive rights to reproduce and distribute the article, including reprints, photographic reproductions, microform or any other reproductions of similar nature and translations, and includes the right to adapt the article for use in conjunction with computer systems and programs, including reproduction or publication in machine-readable form and incorporation in retrieval systems. Authors are responsible for obtaining from the copyright holder permission to reproduce any figures for which copyright exists.

Address for submissions

Editor: Les P. Pook, Department of Mechanical Engineering, University College London, Torrington Place, London WC1E 7JE. Facsimile +44 (0)171 383 0831.

North American Editor: Ken L. Reifsneider, Department of Engineering Science and Mechanics, Virginia Polytechnic Institute and State University, Blacksburg, Virginia 24061-0219, USA. Facsimile +1 703 231 4574.

Japanese Editor: Yukitaka Murakami, Department of Mechanical Science and Engineering, Kyushu University, 6-10-1 Hakozaki, Higashi-Ku, Fukuoka, 812 Japan. Fax: 092 641 9744.

Any queries regarding accepted papers, proofs or offprints should be addressed to the Editorial Office, *Fatigue*, Elsevier Science Ltd, The Boulevard, Langford Lane, Kidlington, Oxford OX5 1GB, U.K. Tel: (+1865) 843000; Fax: (+1865) 843010.

Review process

All contributions are read by two or more referees to ensure both accuracy and relevance, and revisions to the script may thus be required. On acceptance, contributions are subject to editorial amendment to suit house style. When a manuscript is returned for revision prior to final acceptance, the revised version must be submitted as soon as possible after the author's receipt of the referees' reports. Revised manuscripts returned after four months will be considered as new submissions subject for full re-review.

Copyright

The submission of a paper will imply that, if accepted for publication, it will not be published elsewhere in the same form, in any language, without the consent of the Publisher. Before publication, authors are requested to assign Copyright to Elsevier Science Ltd to sanction reprints and photocopies, and to authorize the reprinting of complete issues or volumes according to demand. It is the author's responsibility to obtain written permission to quote material that has appeared in another publication.

Disk submission

International Journal of Fatigue welcomes contributions prepared on disk. Disks should be sent with the final revised manuscript, and not the original submission. Please contact the editorial office for full instructions or refer to back issues of the journal for notes on disk preparation.

Preparation of scripts

You should write in clear and concise English. Spelling should follow the Oxford English Dictionary. Authors whose native tongue is not English are assured that in-house editorial attention to their contributions will improve clarity and acceptability to readers. Three copies of each article are required, typed on one side of A4 only, in double spacing (including abstract and references) and with wide margins. Please number every sheet of paper. Authors are responsible for ensuring that all manuscripts (whether original or revised) are accurately typed before final submission. Manuscripts will be returned to the authors with a set of instructions if they are not presented according to these Notes for Authors.

Arrangement of papers

You should arrange your contribution in the following order:

- 1 Paper title, author's name, affiliation, full postal address and telephone and fax numbers. Affiliations and addresses of co-authors should be clearly indicated. The title should be short, specific and informative.
- 2 Self-contained abstract of approximately 100 words, outlining in a single paragraph the aims, scope and conclusions of the paper; between one and five keywords, for indexing purposes, taken from the list appearing at the back of each issue or which can be accessed from the journal homepage; abbreviated article title, for use as a running headline.
- 3 The text, suitably divided under headings.
- 4 Acknowledgements (if any).

5 References (double spaced, and following the journal style).

6 Appendix (if any).

7 Tables (each on a separate sheet).

8 Captions to illustrations (grouped on a separate sheet or sheets).

9 Illustrations, each on a separate sheet containing no text, and clearly labelled with the journal title, author's name and illustration number.

Style of text

Subdivide your paper in the simplest way possible, consistent with clarity. The text should usually follow the standard sequence of introduction, method, results and discussion. Headings and subheadings for different sections of the paper should be clearly indicated. Do not number the sections. Ensure that all figures and tables are mentioned in the text, and that all references are cited in number order. Note that trade names should have an initial capital letter.

Units and abbreviations

All measurements and data should be given in SI units, or if SI units do not exist, in an internationally accepted unit. If you use any symbol or unit that may not be generally recognized, please include an explanatory footnote the first time it is used, to help the referees, editors and readers. It is also helpful to identify Greek symbols by name in the margin the first time they appear. Abbreviations and acronyms should only be used for unwieldy terms and names which occur frequently in the manuscript. Abbreviations should be used consistently throughout the text, and must be clearly defined in full on first use.

Mathematical and technical setting

Detailed mathematical discussion should be placed in an appendix. Equations and formulae should be typewritten wherever possible. Equations should be numbered consecutively with Arabic numerals in parentheses on the right hand side of the page. Special symbols should be identified in the margin, and the meaning of all symbols should be explained in the text where they first occur. If you use several symbols, a list of definitions (not necessarily for publication) should be submitted with the manuscript. Type or mark mathematical equations exactly as they should appear in print. Journal style for letter symbols is as follows: variables, *italic type* (indicated by underlining); constants, *roman type*; matrices and vectors, **bold type** (indicated by wavy underlining).

Tables

Tables should be numbered consecutively in Arabic numerals, and given a suitable caption. All table columns should have an explanatory heading, and, where appropriate, units of measurement. Footnotes to tables should be typed below the table, and should be referred to by superscript letters. Avoid the use of vertical rules. Tables should not duplicate results presented elsewhere in the manuscript, e.g. in graphs.

Illustrations

All graphs, photographs, diagrams and other drawings (including chemical structures) should be referred to as Figures, and numbered consecutively in Arabic numerals. All illustrations must be clearly labelled with the journal title, author's name and figure number.

Illustrations should be provided in camera ready form, suitable for reproduction without retouching. They will be photographically reduced in size, typically to fit one or two columns of the journal (approximately 85 or 175 mm), and this should be borne in mind to ensure that lines and lettering remain clear and do not break up on reduction. After reduction, lettering should be approximately the same size as the type used for the text in the journal.

Please ensure that all illustrations within a paper are consistent in style and quality. A table is usually more effective than a graph or a paragraph of text for recording data.

Graphs and line drawings

The minimum amount of descriptive text should be used on graphs and drawings; label curves, etc. with single-letter symbols (i.e. a, b, c, etc.) and place descriptive matter in the figure caption. Scale grids should not be used in graphs unless required for actual measurements. Please use a selection of the following symbols on graphs: +, ∂ , \square , \circ , \blacksquare , \bullet , \blacktriangle , ∇ . Graph axes should be labelled with the variable written out in full, along the length of the axis, with the unit in parentheses (for example, Length of sample (mm)). Lower case letters should be used throughout, with an initial capital letter for the first word only.

If your illustrations are computer generated, please supply the blackest possible laser output.

Photographs

Supply four sets of black and white prints. If necessary, a scale should be marked on the photograph. Please note that photocopies of photographs are not acceptable. Colour reproduction is available if the author is willing to bear the additional incremental reproduction and printing costs. Please contact the editorial office for details. A letter confirming the author's willingness to accept these costs should be sent with the revised manuscript.

Authors should note that illustrations will not be returned unless specifically requested.

References

In the text, indicate references to the literature by superior Arabic numerals which run consecutively through the paper. If you cite a reference more than once in the text, use the same number each time. References should follow the style in the journal. Please ensure that references are complete, i.e. that they include, where relevant, author's name, journal or book title, year of publication, volume number, page number, editors, publishers and place of publication. If in doubt, please include all available information. Take care that references are mentioned in the text in the correct number order.

Proofs

Correspondence and proofs for correction will be sent to the first named author unless otherwise indicated.

Proofs should be checked carefully for typesetting errors, and any queries should be answered in full. It is important that proofs are returned within the time stated or publication will be delayed/errors may not be corrected. Authors may be charged for any alterations other than typesetters errors.

Offprints and reprints

The corresponding author will receive 25 offprints of the paper and one copy of the journal free of charge. Extra copies of offprints, minimum 50, can be ordered when proofs are returned. Reprints, minimum 100 copies, can be ordered at any time from the Reprints Department, Elsevier Science Ltd, The Boulevard, Langford Lane, Kidlington, Oxford OX5 1GB.